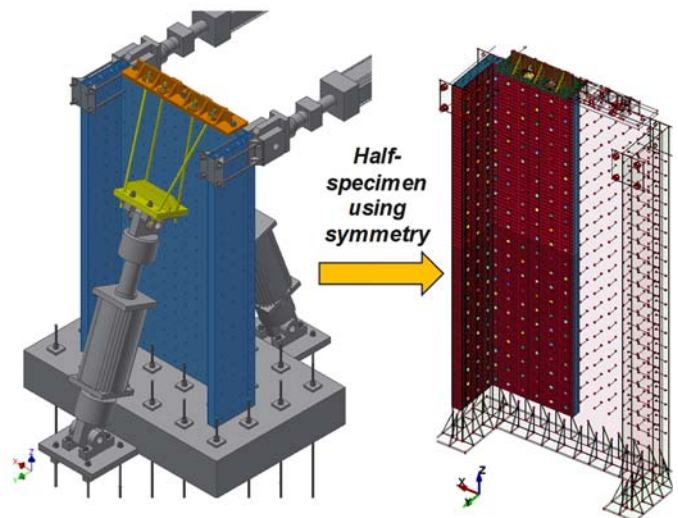
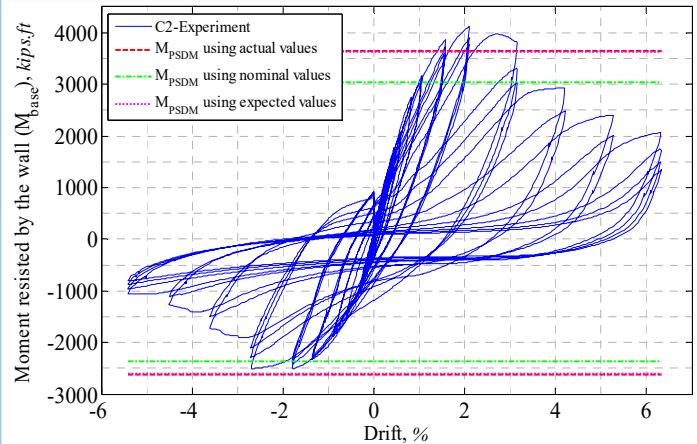


Cyclic Inelastic Behavior of C-Shaped Composite Plate Shear Walls/Concrete Filled (C-PSW/CF)

(CPF Research Grant # 06-16)



Hadi Kenarangi
Emre Kizilarslan
Erkan Polat
Michel Bruneau



University at Buffalo
Department of Civil, Structural and Environmental Engineering

Project: CPF#06-16

**Cyclic Inelastic Behavior of C-Shaped Composite Plate Shear
Walls/Concrete Filled (C-PSW/CF)**

Final Report

Prepared for

Charles Pankow Foundation & American Institute of Steel Construction

by

Hadi Kenarangi

Structural Engineer, Modjeski and Masters, Inc.

Emre Kizilarslan

Graduate Research Assistant

Erkan Polat

Assistant Professor at Munzur University

Michel Bruneau

SUNY Distinguished Professor

University at Buffalo

Department of Civil, Structural and Environmental Engineering
Buffalo, NY



University at Buffalo

The State University of New York

September, 2020

ACKNOWLEDGMENTS

This research was conducted with support from the Charles Pankow Foundation (CPF) and the American Institute of Steel Construction (AISC), through CPF research grant #06-16 “Seismic and Wind Behavior and Design of Coupled C-PSW/CF Core Walls for Steel Buildings” awarded to co-PIs Michel Bruneau, from the University at Buffalo, and Amit Varma, from Purdue University.

The researchers are also grateful to members of Project Advisory Team:

- Ron Klemencic, *Chairman & CEO*, Magnusson Klemencic Associates (MKA);
- Jim Malley, *Senior Principal*, Degenkolb Engineers;
- Ron Hamburger, *Senior Principal*, Simpson Gumpertz & Hager;
- Larry Kruth, *Vice President*, American Institute of Steel Construction (AISC);
- Devin Huber, *Director of Research*, AISC, and;
- Peter Timler, *President*, West-Cascadia Consultants;

for their technical guidance.

The researchers also thank all at Magnusson Klemencic Associates (MKA), Cives Steel Co., Supreme Group, J.F.Stearns Co., and Turner Construction, for their outstanding support, donation of steel, and fabrication of specimens in the experimental part of this study, as well as Anne Ellis *Executive Director of* the Charles Pankow Foundation, Thomas J. Schlafly, *Chief of Engineering Staff*, AISC, Devin Huber, *Director of Research*, AISC, and Mike Gannon, *Senior Engineer*, AISC, for their valuable support.

Finally, although this report focuses solely on the work conducted at the University at Buffalo, the authors are appreciative of the valuable technical exchanges with Amit Varma throughout this collaborative project, and as part of another related project from the same sponsors.

TABLE OF CONTENTS

SECTION 1 INTRODUCTION.....	3
1.1 Objective and Scope of Work.....	3
SECTION 2 DESIGN OF SPECIMENS	6
2.1 General.....	6
2.2 Preliminary Specimen Design.....	6
2.2.1 Initial Design Assumptions and Constraints.....	6
2.2.2 Plastic Moment Capacity	8
2.2.2.1 Compression Depths and M_p for Case (a).....	11
2.2.2.2 Compression Depths and M_p for Case (b).....	13
2.2.2.3 Compression Depths and M_p for Case (c).....	15
2.2.3 Details of Preliminary Specimen	17
2.2.4 Preliminary analysis.....	22
2.2.4.1 Moment-Curvature and Moment-Axial Load Diagrams)	22
2.2.4.2 Elastic Buckling of Skin Plate	26
2.2.5 Test Set-up Design.....	27
2.2.5.1 General.....	27
2.2.5.2 Lateral loading system set-up	31
2.2.5.3 Axial loading system set-up.....	32
2.2.6 Finite element analysis and Pushover Analysis of C100x30x5 using LS-Dyna.....	39
2.3 Final Design.....	50
2.3.1 Updated Initial Design	50
2.3.2 Note on Relationship of T-Shape C-PSW/CF Specimens	58

2.3.3	Preliminary finite element analyses and results of C-shaped specimens	61
-------	---	----

SECTION 3 TESTING OF C-SHAPED COMPOSITE PLATE SHEAR WALLS-CONCRETE

FILLED (C-PSW/CF)..... 64

3.1	General.....	64
3.2	Properties of Tested Specimens	64
3.3	Preparation of Specimens	66
3.4	Material Properties of Specimens	68
3.5	Loading Protocol of C-Shape Specimens	70
3.6	Application of Axial Loading on the C-Shape Specimens	71
3.7	Test Observations and Results	74
3.7.1	Specimen C1	75
3.7.2	Specimen C2.....	89
3.7.3	Test Data Analysis	103

SECTION 4 TESTING OF REPAIRED C-SHAPED COMPOSITE PLATE SHEAR WALLS-

CONCRETE FILLED (C-PSW/CF)..... 131

4.1	General.....	131
4.2	Repair Concept	131
4.3	Implementation of Repair Concept.....	136
4.4	Material Properties of Specimens	141
4.5	Loading Protocol of Repaired C-Shape Specimen	143
4.6	Application of Axial Loading on the C-Shape Specimens	145
4.7	Test Observations and Results	149
4.8	Test Data Analysis	167

SECTION 5 SUMMARY AND CONCLUSIONS	185
SECTION 6 REFERENCES.....	189
APPENDIX A Design details of Initial Specimen (Mathcad sheets)	194
APPENDIX B Initial Specimen and Initial Test Set-up Details: CAD Drawings	211
APPENDIX C Final Specimen Design Detail and Drawings.....	222
C.1 Tie Bar Design.....	222
C.2 Foundation reinforcing cage details.....	227
C.3 Test setup and specimens' drawings submitted to fabricator	236
C.4 Drawings received from fabricator	260
APPENDIX D Instrumentation of C-Shaped Walls	269
APPENDIX E Drawings of Repaired C-Shaped Wall.....	277
E.1 Repaired C-Shaped Specimen: Instrumentation Plan	283

“This Page Intentionally Left Blank”

LIST OF FIGURES

Figure 1-1. The main components of C-shaped Concrete Filled Composite Plate Shear Walls (C-PSW/CF)	3
Figure 2-1. The cross-section of a prototype wall.....	8
Figure 2-2. The axial stress blocks of a general cross section of a C-shaped C-PSW/CF under positive and negative drift.....	9
Figure 2-3. Cross-section of the C-shaped C-PSW/CF and its plastic stress distribution under positive (left) and negative wall drift.....	19
Figure 2-4. Percentage of axial load achieved for C100x30 C-PSW/CF based on t_c and f'_c	21
Figure 2-5. Percentage of axial load achieved for C60x20 C-PSW/CF based on t_c and f'_c	21
Figure 2-6. Moment-curvature relationship of the C100x30x5.375 C-PSW/CF model ($f'_c=4\text{ksi}$).....	23
Figure 2-7. Moment-curvature relationship of the C100x30x5.375 C-PSW/CF model ($f'_c=8\text{ksi}$).....	24
Figure 2-8. P-M interaction diagram for the C100x30x5.375 C-PSW/CF model.....	24
Figure 2-9. Neutral axis-curvature relation of the C100x30x5.375 wall model with: (a) $f'_c=4\text{ksi}$,.....	25
Figure 2-10. Perspective view of the test setup.....	28
Figure 2-11. Elevation and top views of the test setup.....	29
Figure 2-12. Perspective view of the test setup.....	29
Figure 2-13. Alternative designed (but not retained) vertical loading systems using: (a) W-shaped beam, (b) 3D steel truss.....	30
Figure 2-14. Details of the lateral loading system.....	31
Figure 2-15. Effective stress field in the lateral loading system under maximum negative loading.	32
Figure 2-16. Schematic view of the vertical loading system.....	34
Figure 2-17. Elevation view of the vertical loading system (South elevation).....	35
Figure 2-18. Threaded bars connection details in the vertical loading system.....	36
Figure 2-19. Vertical load spreading fixture of the vertical loading system.....	36

Figure 2-20. Vertical actuators top attachment fixture of the vertical loading system	37
Figure 2-21. Threaded bars connection details in the vertical loading system	38
Figure 2-22. Effective stress field in the vertical loading system under maximum vertical and lateral loading	39
Figure 2-23. Schematic of the developed finite element model of the test set-up in LS-Dyna	43
Figure 2-24. Base Shear vs. Drift Ratio of the FE Model of the C-Shaped C-PSW/CF under: a) Negative Drift, b) Positive Drift.....	43
Figure 2-25. P-M interaction curve comparisons between LS-Dyna model and material-based fiber-section analysis.....	44
Figure 2-26. Base-moment of the composite wall, concrete core, and steel plate under positive drifts	44
Figure 2-27. 3D view of the progression of local buckling and plastic regions at the bottom of the flange under positive drifts (West elevation).....	45
Figure 2-28. Base-moment of the composite wall, concrete core, and steel plate under negative drifts	45
Figure 2-29. 3D view of progression of local buckling and plastic regions at the bottom of the flange under negative drifts (East elevation).	46
Figure 2-30. Vertical (Z direction) stress field on the concrete core under axial loading (normalized by f'_c).	47
Figure 2-31. Vertical stress distribution on the flange solid elements along the concrete core (normalized by f'_c).....	48
Figure 2-32. Vertical stress distribution on the web solid elements along the concrete core (normalized by f'_c).....	49
Figure 2-33. (a) P-M interaction curve for prototype model; (b) P-PNA curve for prototype model	51
Figure 2-34. Change in the steel plate strain in half of a cycle for prototype model	52
Figure 2-35. Definitions of maximum and minimum strains on the web and flanges at a certain positive or negative curvature.....	52

Figure 2-36. (a) P-M interaction curve for prototype model; (b) P-PNA curve for geometrically scaled model	53
Figure 2-37. Change in strain in half of a cycle for geometrically scaled model	53
Figure 2-38. Cross-sectional aspect ratios	55
Figure 2-39. Possible designs within the existing objective constraints	55
Figure 2-40. Position of the wall on the foundation plan.....	55
Figure 2-41. (a) P-M interaction curve for the updated specimen; (b) Normalized P-M curve for the updated specimen	57
Figure 2-42. P-PNA curve for the updated specimen	57
Figure 2-43. Change in the steel plate strain in half of a cycle for the updated specimen.....	57
Figure 2-44. P-M interaction curve comparison for variations of material properties.....	58
Figure 2-45. C-PSW/CF Specimens testing program	58
Figure 2-46. T-shape specimen cross-section dimensions.....	59
Figure 2-47. (a) P-M interaction curve for the T-shape specimen; (b) Normalized P-M curve for the T-shape specimen	60
Figure 2-48. P-PNA curve for the T-shape specimen	60
Figure 2-49. Change in the steel plate strain in half of a cycle for the T-shape specimen.....	61
Figure 2-50. Details of the finite element model of C-shape specimen.....	61
Figure 2-51. Details of the finite element model of the C-shape specimen's Axial Loading Setup (ALS) and Lateral Loading Setup (LLS)	62
Figure 2-52. Preliminary monotonic and cyclic analyses of C-shape specimen.....	62
Figure 3-1. Construction sequence of specimens.....	68
Figure 3-2. Coupon tests of steel plates at web (p261) and flange (p307) for Specimen C1.....	69
Figure 3-3. Coupon tests of steel plates at web (p261) and flange (p307) for Specimen C2.....	69

Figure 3-4. Pushover results of the FEA model of C1 specimen and bi-linear approximation of the curves in positive and negative directions.....	71
Figure 3-5. Loading protocol for C-Shaped specimens.	71
Figure 3-6. Location of centroid and center line of axial load for C-Shaped wall specimens.....	72
Figure 3-7. Two options for the testing scheme of C-Shaped walls.	73
Figure 3-8. The axial force applied to C1 specimen during test	74
Figure 3-9. Normalized axial strains of the strain gauges at 17.4 in from the top of footing on Specimen C1	74
Figure 3-10. South-West views of the North Web of Specimen C1 at positive peaks	81
Figure 3-11. South-West views of the North Web of Specimen C1 at negative peaks	82
Figure 3-12. North-West views of the South Web of Specimen C1 at positive peaks	83
Figure 3-13. North-West views of the South Web of Specimen C1 at negative peaks.....	84
Figure 3-14. East view of the flange and South-East view of the South web of Specimen C1 at positive peaks	85
Figure 3-15. East view of the flange and South-East view of the South web of Specimen C1 at negative peaks	86
Figure 3-16. North-West views of the North Web of Specimen C1 at positive peaks	87
Figure 3-17. North-West views of the North Web of Specimen C1 at negative peaks	88
Figure 3-18. South-West views of the North Web of Specimen C2 at positive peaks	95
Figure 3-19. South-West views of the North Web of Specimen C2 at negative peaks	96
Figure 3-20. North-West views of the South Web of Specimen C2 at positive peaks	97
Figure 3-21. North-West views of the South Web of Specimen C2 at negative peaks.....	98
Figure 3-22. East view of the flange and North-East view of the North web of Specimen C2 at positive peaks	99

Figure 3-23. East view of the flange and North-East view of the North web of Specimen C2 at negative peaks	100
Figure 3-24. North-West views of the North Web of Specimen C2 at positive peaks	101
Figure 3-25. North-West views of the North Web of Specimen C2 at negative peaks	102
Figure 3-26. Applied lateral force vs. top drift relationship for a) Specimen C1 and b) Specimen C2....	105
Figure 3-27. Marked Cycle 18 in the applied lateral force vs. top drift relationship for Specimen C1....	106
Figure 3-28. (a) Inclination angle of vertical actuators at zero displacement; (b) Free body diagram of the specimen wall at zero displacement.....	106
Figure 3-29. Calculated experimental base moment vs. top drift relationship for a) Specimen C1 and b) Specimen C2.....	107
Figure 3-30. Strain profiles at first yield on: (a) positive displacement; (b) negative displacement for Specimen C1	114
Figure 3-31. Strain profiles at first yield on: (a) positive displacement; (b) negative displacement for Specimen C2	115
Figure 3-32. Strain profiles at the positive peak of Cycle 15 where the local buckling was visually observed on the web for Specimen C1	116
Figure 3-33. Strain profiles at the positive peak of Cycle 15 where the local buckling was visually observed on the web for Specimen C2.....	117
Figure 3-34. Strain profiles at the negative peak of Cycle 18 where the local buckling was visually observed on the flange for Specimen C1.....	118
Figure 3-35. Strain profiles at the negative peak of Cycle 17 where the local buckling was visually observed on the flange for Specimen C2.....	119
Figure 3-36. Strain profiles at: (a) the positive maximum strength point (Cycle 19); (b) the negative maximum strength point (Cycle 19) for Specimen C1	120

Figure 3-37. Strain profiles at: (a) the positive maximum strength point (Cycle 17); (b) the negative maximum strength point (Cycle 17) for Specimen C2	121
Figure 3-38. Comparison of Specimen C1 flexural resistances with P-M interaction curve.....	122
Figure 3-39. Comparison of Specimen C2 flexural resistances with P-M interaction curve.....	122
Figure 3-40. Comparison of calculated theoretical resistance moments and the experimental base moment for Specimen C1	123
Figure 3-41. Comparison of calculated theoretical resistance moments and the experimental base moment for Specimen C2	123
Figure 3-42. location of Krypton LEDs placed on the web of Specimen C1 at the north elevation.....	124
Figure 3-43. Out-of-plane movement of LEDs 14, 11, 08, and 02 located on the web of Specimen C1 .	124
Figure 3-44. Post-test damage inspection of the wall steel plates for Specimen C1.....	125
Figure 3-45. Out-of-plane movement of LEDs 14, 11, 08, and 02 located on the web of Specimen C2 .	125
Figure 3-46. Post-test damage inspection of the wall steel plates for Specimen C2.....	126
Figure 3-47. Tie bar fracture during testing of Specimen C2	126
Figure 3-48. Composition of wall rotations at the base of the wall	127
Figure 3-49. Calculated experimental base moment vs. wall base rotation relationship for Specimen C1	127
Figure 3-50. Comparison of calculated experimental base moment vs. wall base rotation and vs. total base rotation for Specimen C1	128
Figure 3-51. Calculated experimental base moment vs. wall base rotation relationship for Specimen C2	128
Figure 3-52. Comparison of calculated experimental base moment vs. wall base rotation and vs. total base rotation for Specimen C2	129
Figure 4-1. Repair concept for the C2 Specimen.....	133
Figure 4-2. Free body diagram of existing and splice plates load transfer	135

Figure 4-3. Scupper attachment and direction of concrete flow.	136
Figure 4-4. Fillet welding detail at the footing.	139
Figure 4-5. Repair sequence of flanges.....	140
Figure 4-6. Repair sequence of webs.....	140
Figure 4-7. Coupon tests of steel plates at flange (p307) and web (p261) for C2	142
Figure 4-8. Coupon tests of repairing steel plates.....	142
Figure 4-9. Pushover result of the FEA model of Repaired Specimen C2 and bi-linear approximation of the curves in positive and negative directions	144
Figure 4-10. Loading protocol for C-Shaped specimens	144
Figure 4-11. Location of centroid and centerline of axial load for C-Shaped wall specimens.....	145
Figure 4-12. Testing scheme of repaired C-Shaped wall.....	146
Figure 4-13. Sum of axial forces in the vertical actuators during test of Repaired Specimen C2	147
Figure 4-14. Normalized axial strains a) 2D and b) 3D of the strain gauges at 29-7/16 in. from the top of footing on Repaired Specimen C2	148
Figure 4-15. North-West views of the North Web of Repaired Specimen C2 at positive peaks	156
Figure 4-16. North-West views of the North Web of Repaired Specimen C2 at negative peaks	158
Figure 4-17. East view of the flange and North-East view of the North web of Repaired Specimen C2 at positive peaks.....	160
Figure 4-18. East view of the flange and North-East view of the North web of Repaired Specimen C2 at negative peaks.....	161
Figure 4-19. South-West views of the South Web of Repaired Specimen C2 at positive peaks	162
Figure 4-20. South-West views of the South Web of Repaired Specimen C2 at negative peaks.....	164
Figure 4-21. Vertical weld fracture at the corner of the NWS and NWW surfaces.....	166
Figure 4-22. Weld fractures at: a) NWS, b) NWN, c) SWN and d) SWS	166

Figure 4-23. Close-up pictures of the fracture propagation at SWS from: a) front view and b) side view	167
Figure 4-24. Applied lateral force vs. top drift relationship for Repaired Specimen C2	169
Figure 4-25. Some important points marked in the applied lateral force vs. top drift relationship for Repaired Specimen C2	169
Figure 4-26. (a) Inclination angle of vertical actuators at zero displacement; (b) Free body diagram of the specimen wall at zero displacement.....	170
Figure 4-27. Calculated experimental base moment vs. top drift relationship for Repaired Specimen C2	170
Figure 4-28. Strain profiles at first yield on: (a) positive displacement; (b) negative displacement	175
Figure 4-29. Strain profiles at the positive peak of Cycle 14 where the local buckling was visually observed on the web.....	176
Figure 4-30. Strain profiles at the negative peak of Cycle 19 where the local buckling was visually observed on the flange.....	177
Figure 4-31. Strain profiles at: (a) the positive maximum strength point (Cycle 17); (b) the negative maximum strength point (Cycle 17)	178
Figure 4-32. Comparison of Repaired Specimen C2 flexural resistances with P-M interaction curve	179
Figure 4-33. Comparison of calculated theoretical resistance moments and the experimental moment at cross-section above repair for Repaired Specimen C2	179
Figure 4-34. Sketch of post-test damage inspection of the wall steel plates for Repaired Specimen C2 .	180
Figure 4-35. Post-test damage inspection of the wall steel plates for Repaired Specimen C2	181
Figure 4-36. Weld fracture of tie bar at 3 rd row and 1 st column from West side of North Web.	181
Figure 4-37. Composition of wall rotations above repaired part of the wall	182
Figure 4-38. Calculated experimental base moment vs. wall rotation above repaired part for Repaired Specimen C2	182

Figure 4-39. Comparison of calculated experimental base moment vs. wall base rotation and vs. total base rotation for Repaired Specimen C2..... 183

“This Page Intentionally Left Blank”

LIST OF TABLES

Table 2-1. Closed form equations for C , and M_p under positive and negative drift.....	10
Table 2-2. Properties of the Initial Specimen.....	20
Table 2-3. Available friction forces at the interface of the top fixture and top of the wall.....	39
Table 2-4. Properties of the C-shape Specimen.....	56
Table 3-1. Properties of the C-shape Specimens	65
Table 3-2. Experiment log of Specimen C1.....	80
Table 3-3. Experiment log of Specimen C2.....	94
Table 3-4. Peak displacements and corresponding base moments for each cycle of Specimen C1 test...	108
Table 3-5. Peak displacements and corresponding base moments for each cycle of Specimen C2 test...	109
Table 3-6. Actual, nominal, and expected material properties and Calculated flexural resistances for Specimen C1	111
Table 4-1. Experiment log of Repaired Specimen C2	155
Table 4-2. Peak displacements and corresponding base moments for each cycle of Repaired Specimen C2 test.....	171
Table 4-3. Actual, nominal, and expected material properties and Calculated flexural resistances for Repaired Specimen C2.....	173

“This Page Intentionally Left Blank”

Abstract

A Composite Plate Shear Wall/Concrete Filled (C-PSW/CF) is a special lateral-force resisting system consisting a sandwiched panel of two steel plates with concrete infill in between them, ideally suited for core-wall structures in high-rise construction. The steel plates are connected to each other using tie bars that are embedded in the concrete infill and, in some instances, steel-headed stud anchors. This research project was conducted to investigate the cyclic lateral load behavior of these walls, in terms of strength, and drift capacity. Findings from this project are provided in a series of report. The current report presents findings from the testing of two large-scale C-shaped concrete filled composite plate shear core walls subjected to flexure and axial loads together. Their dimensions were the same, but different axial loads were applied, up to 19% of axial loading capacity. Moreover, one of the walls was repaired and retested. The composite behavior and the plastic hinge development were investigated and compared to results from plastic moment calculations. This provides valuable results on the expected behavior of one composite cross-section that is frequently used in full core wall. This is done to support the development of design guidelines for high-rise core-wall steel buildings having C-PSW/CF as the primary lateral force resisting system.

SECTION 1

INTRODUCTION

1.1 Objective and Scope of Work

This document presents findings from experiments conducted on C-shaped Concrete Filled Composite Plate Shear Walls (C-PSW/CF) specimens subjected to axial force and flexure, together with information on design of the corresponding test set-up. A Composite Plate Shear Wall/Concrete Filled (C-PSW/CF) is a special lateral-force resisting system consisting of a sandwiched panel of two steel plates with concrete infill in between them. The steel plates are connected to each other using tie bars that are embedded in the concrete infill, as shown in Figure 1-1. In some instances, steel-headed stud anchors are used together with the tie bars. C-PSW/CF is a lateral load resisting system ideally suited for core-wall structures in high-rise construction (as well as for other shear wall applications).

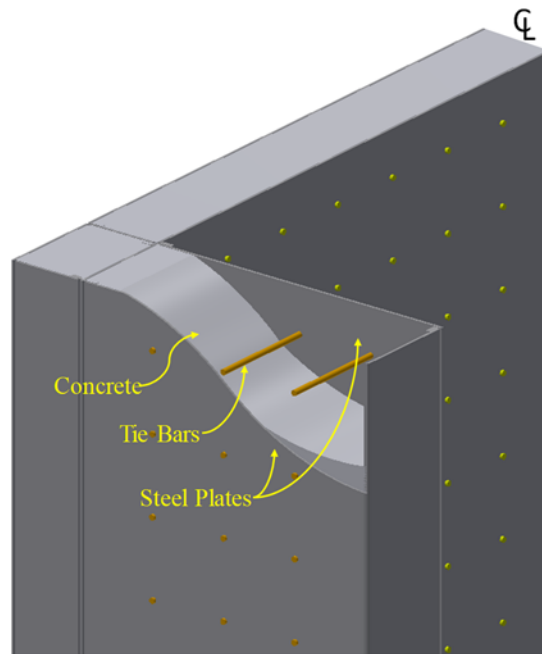


Figure 1-1. The main components of C-shaped Concrete Filled Composite Plate Shear Walls (C-PSW/CF)

In tall building construction, reinforced concrete shear walls with coupling beams are commonly used. C-PSW/CF can similarly be used with composite coupling beams. Their appeal lies in the fact that the steel panels of C-PSW/CF can be fabricated off-site, shipped and erected on-site, and serve as formwork for the concrete. Most importantly, this can significantly accelerate construction time (MSC 2019). While this structural system has been used in mid-rise construction in non-seismic regions (Bowerman and Chapman 2002), as well as in nuclear structures to provide (among many load cases considered) missile and aircraft impact resistance in addition to elastic resistance to seismic and wind lateral loads (Bhardwaj and Varma 2017; Varma et al. 2011; Varma et al. 2014), knowledge on its cyclic inelastic non-linear behavior is needed for application in regions where severe earthquakes are expected. In a somewhat related topic, past research that has shown that concrete-filled steel tubes can have a ductile cyclic inelastic behavior (Brown et al. 2015; Denavit et al. 2016; Hajjar 2000; Kenarangi and Bruneau 2019; Leon et al. 2007; Stephens et al. 2018; Tsai 1992; Usami and Ge 1994; Varma et al. 2002; Varma et al. 2004) is instructive and suggests that similar performance is possible for C-PSW/CF, although this cannot be inferred directly from those past tests.

Some research has investigated the in-plane cyclic inelastic behavior of these walls. Alzeni and Bruneau (2014) tested four concrete-filled sandwich steel panel (CFSSP) walls with and without circular boundary elements. The specimens showed stable ductility up to 3% drift. A few wall specimens having square ends rather than circular ones have also been tested (Bruneau and Kizilarslan 2019; Cho et al. 2015; Eom et al. 2009; Yu et al. 2019). However, no research has been conducted on C-Shaped walls, especially when subjected to simultaneously axial and lateral loadings. Given that C-shaped walls can be parts of the lateral-load resisting core of building (around elevator shafts), investigating the behavior of such walls is important. Note that in these walls, the plastic neutral axis can move quite significantly in alternating directions of loading. Knowledge on the cyclic inelastic behavior of C-shaped walls is necessary for the development of design guidelines when high-rise core-wall steel buildings having C-PSW/CF are used as the primary lateral force resisting system.

With the above in mind, two C-PSW/CFs were tested at the Structural Engineering and Earthquake Simulation Laboratory (SEESL) at State University of New York (SUNY) at Buffalo. The dimensions of the walls were the same, but slightly different axial load ratios were applied, namely corresponding to 19% and 15% of the crushing load of the infill concrete ($A_c f'_c$). Testing two specimens was helpful to establish replicability of the test results. Moreover, for one of the walls, a repair strategy that was deemed practical and applicable for post-earthquake repairs (irrespective of the severity of wall damage) was developed and verified experimentally, subjected to the same testing protocol. This repair strategy involved replacement of the buckled plates and, if necessary, partial or complete replacement of the concrete located between the removed plates, with re-use or replacement of existing tie bars as appropriate.

Section 2 provides the steps of the design process for the specimens tested. The initial design is presented in Section 2.2 and the final dimensions of the specimens and test setup are in Section 2.3. Section 3 provides results and observations from the experiments. This includes information on preparation of the specimens (Section 3.3), the protocols for cyclic loading and axial loading application (Sections 3.5 and 3.6), and step-by-step descriptions of the specimens' cyclic response and progressive failure modes throughout the tests (Section 3.7). Section 4 presents a repair concept for C-PSW/CFs and experimental validation of the concept. The details of the repair concept and its implementation are presented in Sections 4.2 and 4.3. Loading protocol and procedure for application of axial loading are outlined in Sections 4.5 and 4.6. Step-by-step description of the tests, behaviors observed, and analysis of results are in Sections 4.7 and 4.8. Finally, summary and conclusions are provided in Section 5.

SECTION 2

DESIGN OF SPECIMENS

2.1 General

This section provides information on preliminary and final design of C-Shaped Composite Plate Shear Walls/Concrete Filled (C-PSW/CF). Section 2.2 outlines the initial design assumptions related to prototype model chosen and the various constraints that drove the specimens' design. As such, it documents some of the iterations that took place in the process, to converge on the final characteristics of the specimens, test set-up, and testing program described in Section 2.3. The reader solely interested in the final specimen characteristics and details of the test set-up can skip to Sections 2.3 and 2.2.5, respectively.

2.2 Preliminary Specimen Design

2.2.1 Initial Design Assumptions and Constraints

The specimens considered here are Composite Plate Shear Walls/Concrete Filled (C-PSW/CF) having a C-shaped cross section subjected to weak axis flexure and axial loads. Given that C-shaped walls can be parts of the lateral-load resisting core of building (around elevator shafts), investigating the behavior of such walls is important.

The specimens were designed based on the assumption that the walls would attain their plastic moment capacity at their base. The plastic moment capacity of each wall is based on the assumption of a uniform yield stress distribution of steel, F_y , and uniform compressive stress distribution of concrete, f_c , (Alzeni and Bruneau 2014). The required lateral force (actuator force to be developed during testing) was taken equal to the wall's plastic moment divided by its height from the point of maximum moment to the applied force level.

The initial specimen design constraints were mainly:

- The desired wall cross-section;

- Reinforcement ratio (limited to less than 10%);
- Laboratory constraints for test set-up;
- Disposal costs of the specimens.

The cross-section geometry was also driven by the desire to test vertical walls cantilevering from their base and simultaneously subjected to lateral forces applied at their top and axial forces. The geometry of that test set-up configuration is presented in more details in Section 2.2.5. As described in that section, the MTS servo-controlled hydraulic actuators available for this purpose at the University at Buffalo's (UB) Structural Engineering and Earthquake Simulation Laboratory (SEESL) included two 220kips actuators, for a total possible horizontally applied force of 440kips, and two 430kips actuators, for a potential total vertical loading of 860kips. For design purposes, to design the test set-up, the assumed upper limit for the lateral force was taken as 220kips. This provided a “margin” of two for the initial design to account for strengths greater than the theoretical plastic moment value due to strain hardening of steel, confinement of concrete, and expected strengths of the material exceeding the specified values.

On the basis of input from the Project Advisory Team, a prototype wall cross-section (Figure 2-1) was assumed to have a flange width, h , of 30ft., a web depth, b , of 10ft., and a minimum wall thickness, c , of 24 in. Based on the design assumptions and constraints mentioned above, a specimen was designed at 1/4th scale of the cross-section of the prototype wall model. Once specimen cross-section was defined for the specimen at this 1/4th scale, height of the specimen was defined such as to develop the plastic moment calculated from specified material properties on the basis of the above constraints on hydraulic actuators and the assumed margin of 2 for the lateral load needed to fail the specimen. There also was a desire to subject the specimens to axial loads of a magnitude equal to, if possible, up to 30% of the squash load of the infill concrete ($A_c f'_c$). A large number of preliminary analyses were conducted to determine the appropriate size and dimensions of the specimen to be tested; some of these are reported below.

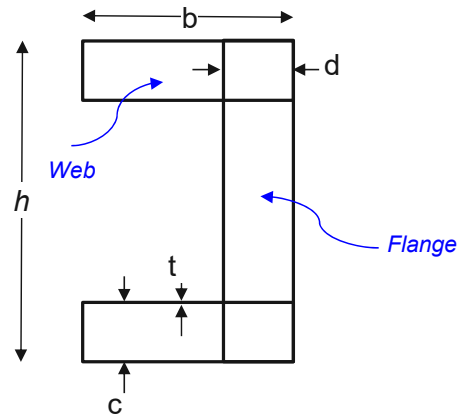


Figure 2-1. The cross-section of a prototype wall

2.2.2 Plastic Moment Capacity

Flexural capacity of this wall was first estimated by using simple plastic theory based on the assumption of uniform plastic stress distribution on steel and concrete sections used by Alzeni and Bruneau (2014). Figure 2-2 illustrates the axial stress blocks of a general cross section of a C-shaped C-PSW/CF with the variables used to develop closed form equations to calculate plastic moment capacity of C-Shaped C-PSW/CF with any geometric properties, under positive and negative drift. Table 2-1 presents the resulting closed form equations for C , and M_p for the possible location of plastic neutral axis illustrated in Figure 2-2. Derivation of the terms used in these equations is provided in more details in Section 2.2.2.1 to 2.2.2.3.

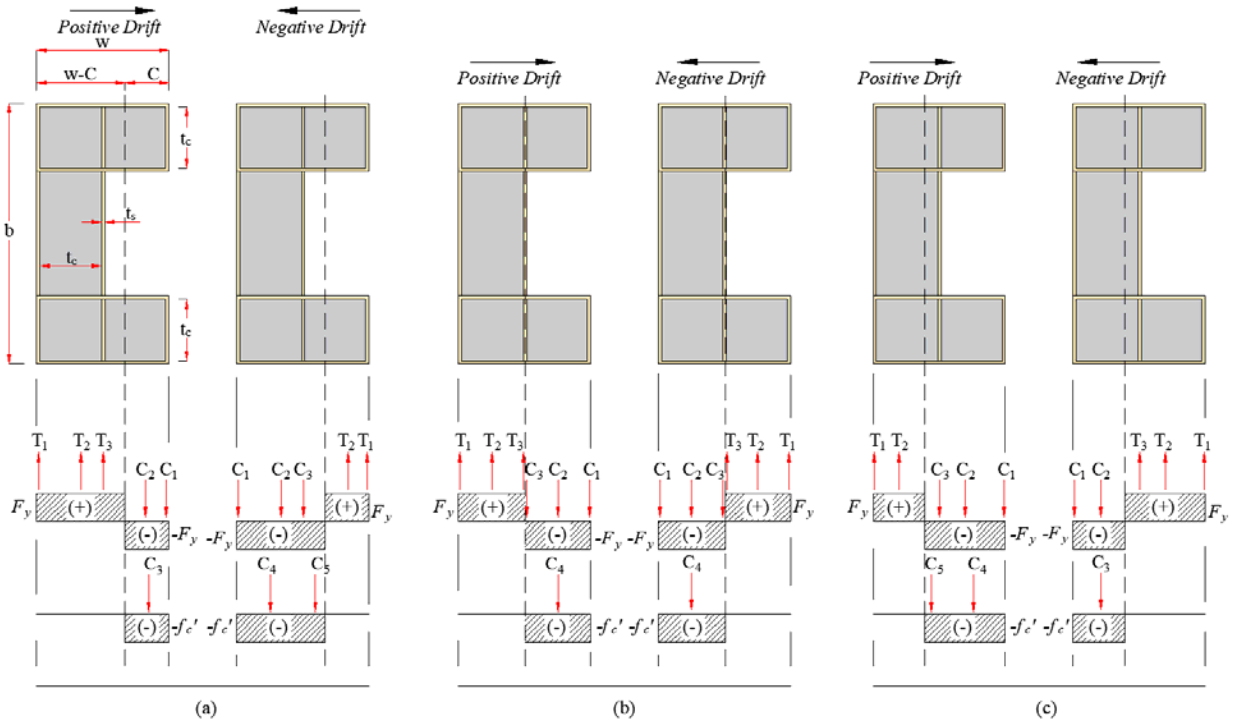


Figure 2-2. The axial stress blocks of a general cross section of a C-shaped C-PSW/CF under positive and negative drift

Table 2-1. Closed form equations for C, and Mp under positive and negative drift

CASE A – NEGATIVE DRIFT
$C = \frac{8 * Fy * ts^2 + ((-2 * b + 4 * w + 2 * tc) * Fy + 6 * fc * tc) * ts - b * fc * tc}{2 * (4 * Fy * ts + fc * tc)}$
$M_p = (6.0 * tc * ts^2 + (3.0 * tc^2 + (-1 * b - 7.0 * C) * tc) * ts + (-0.5 * b - 1 * C) * tc^2 + C * (C + b) * tc) * fc$ $+ (8.0 * ts^3 + (3.0 * tc - 2.0 * b - 8.0 * C) * ts^2 + ((2 * w - 1 * b - 2 * C) * tc + 4.0 * C^2 + (-4.0 * w + 2 * b) * C + 2.0 * w^2) * ts) * Fy$
CASE A – POSITIVE DRIFT
$C = \frac{ts * (b + 2 * w - tc - 4 * ts) * Fy + fc * tc}{4 * Fy * ts + fc * tc}$
$M_p = (tc * ts^2 - 2.0 * tc * C * ts + tc * C^2) * fc$ $+ (8.0 * ts^3 + (-8.0 * w + 3.0 * tc - 2.0 * b + 8.0 * C) * ts^2$ $+ (4.0 * C^2 + (-4.0 * w - 2 * b + 2 * tc) * C + 2.0 * w^2 - 1 * tc * b + 2 * b * w) * ts) * Fy$
CASE B – NEGATIVE DRIFT
$C = \frac{(-8 * ts^2 + (2 * b + 4 * w - 6 * tc) * ts + 2 * tc * b) * Fy - tc * (b - 4 * ts) * fc}{2 * b * Fy}$
$M_p = (4 * ts^2 * tc + (2.0 * tc^2 + (-4 * C - 1 * b) * tc) * ts - 0.5 * b * tc^2 + tc * C * b) * fc$ $+ (-8.0 * ts^3 + (8.0 * C + 2.0 * b - 13.0 * tc) * ts^2$ $+ (-4.0 * tc^2 + (2 * w + 6.0 * C + 3.0 * b) * tc - 4.0 * w * C - 2.0 * C * b + 2.0 * w^2) * ts + b * tc^2 - 2.0 * tc * C * b + C^2 * b) * Fy$
CASE B – POSITIVE DRIFT
$C = \frac{(4 * ts^2 + (-b - 2 * w + 3 * tc) * ts + b * (w - tc)) * Fy + tc * fc * ts}{Fy * b + fc * tc}$
$M_p = (tc * C^2 + ts^2 * tc - 2.0 * ts * tc * C) * fc$ $+ (-8.0 * ts^3 + (2.0 * b + 8.0 * w - 8.0 * C - 13.0 * tc) * ts^2$ $+ (-4.0 * tc^2 + (8.0 * w - 6.0 * C + 3.0 * b) * tc + (-2.0 * w + 2.0 * C) * b + 4.0 * w * C - 2.0 * w^2) * ts + tc^2 * b$ $+ (-2.0 * w + 2.0 * C) * b * tc + (-2.0 * w * C + C^2 + w^2) * b) * Fy$
CASE C – NEGATIVE DRIFT
$C = \frac{(b - 4 * ts) * fc + 4 * Fy * w * ts}{(b - 4 * ts) * fc + 8 * ts * Fy}$
$M_p = (-2.0 * ts^3 + (4.0 * C + 0.5 * b) * ts^2 + (-2.0 * C^2 - b * C) * ts + 0.5 * b * C^2) * fc$ $+ (-4.0 * ts^3 + (-5.0 * tc + b) * ts^2 + (4.0 * C^2 + (-2 * tc - 4.0 * w) * C + 2.0 * w^2 + 2 * tc * w + b * tc) * ts) * Fy$
CASE C – POSITIVE DRIFT
$C = \frac{(4 * ts^2 + (-b - 4 * w + 8 * tc) * ts + (w - tc) * (b - 2 * tc)) * fc + 4 * (w - \frac{tc}{2}) * Fy * ts}{(b - 4 * ts) * fc + 8 * ts * Fy}$
$M_p = (-4.0 * ts^3 + (b - 5.0 * tc) * ts^2 + ((2 * C + b) * tc + 2.0 * w^2 + 4.0 * C^2 - 4.0 * C * w) * ts) * fc$ $+ (-2.0 * ts^3 + (0.5 * b + 4.0 * w - 4.0 * C - 2.0 * tc) * ts^2$ $+ (tc^2 + (b + 5.0 * w - 8.0 * C) * tc - 2.0 * C^2 + (b + 4.0 * w) * C - 2.0 * w^2 - 1 * b * w) * ts + tc^3 + (0.5 * b - 2 * C) * tc^2$ $+ ((b + 2 * w) * C - 1 * w^2 - 1 * b * w) * tc + 0.5 * b * w^2 + 0.5 * C^2 * b - 1 * C * b * w) * fc$

2.2.2.1 Compression Depths and Mp for Case (a)

Negative drift case:

Forces:

$$T1 = 2 * ts * (2 * ts + tc) * Fy$$

$$T2 = 4 * ts * (w - C - ts) * Fy$$

$$C1 = Fy * b * ts$$

$$C2 = 4 * ts * (C - ts) * Fy$$

$$C3 = ts * (b - 4 * ts) * Fy$$

$$C4 = tc * (b - 4 * ts) * fc$$

$$C5 = 2 * tc * (C - ts) * fc$$

$$T1 + T2 = C1 + C2 + C3 + C4 + C5$$

$$C = \frac{8 * Fy * ts^2 + ((-2 * b + 4 * w + 2 * tc) * Fy + 6 * fc * tc) * ts - b * fc * tc}{2 * (4 * Fy * ts + fc * tc)}$$

Lever arms of forces about the centroid:

$$LT1 = w - C - 0.5 * ts$$

$$LT2 = 0.5 * w - 0.5 * C - 0.5 * ts$$

$$LC1 = C - 0.5 * ts$$

$$LC2 = 0.5 * C - 0.5 * ts$$

$$LC3 = C - 1.5 * ts - tc$$

$$LC4 = C - ts - 0.5 * tc$$

$$LC5 = 0.5 * C - 1.0 * ts - 0.5 * tc$$

Plastic moment:

$$Mp = T1 * LT1 + T2 * LT2 + C1 * LC1 + C2 * LC2 + C3 * LC3 + C4 * LC4 + C5 * LC5$$

$$\begin{aligned}
M_p = & (6.0 * tc * ts^2 + (3.0 * tc^2 + (-1.* b - 7.0 * C) * tc) * ts + (-0.5 * b - 1.* C) * tc^2 + C * (C + b) \\
& * tc) * fc \\
& + (8.0 * ts^3 + (3.0 * tc - 2.0 * b - 8.0 * C) * ts^2 \\
& + ((2.* w - 1.* b - 2.* C) * tc + 4.0 * C^2 + (-4.0 * w + 2.* b) * C + 2.0 * w^2) * ts) \\
& * Fy
\end{aligned}$$

Positive drift case:

Forces:

$$T1 = ts * b * Fy$$

$$T2 = 4 * ts * (w - C - ts) * Fy$$

$$T3 = ts * (b - 4 * ts) * Fy$$

$$C1 = 2 * ts * (2 * ts + tc) * Fy$$

$$C2 = 4 * ts * (C - ts) * Fy$$

$$C3 = 2 * tc * (C - ts) * fc$$

$$T1 + T2 + T3 = C1 + C2 + C3$$

$$C = \frac{ts * (b + 2 * w - tc - 4 * ts) * Fy + fc * tc}{4 * Fy * ts + fc * tc}$$

Lever arms of forces about the centroid:

$$LT1 = w - C - 0.5 * ts$$

$$LT2 = 0.5 * w - 0.5 * C - 0.5 * ts$$

$$LT3 = w - C - tc - 1.5 * ts$$

$$LC1 = C - 0.5 * ts$$

$$LC2 = 0.5 * C - 0.5 * ts$$

$$LC3 = 0.5 * C - 0.5 * ts$$

Plastic moment:

$$Mp = T1 * LT1 + T2 * LT2 + T3 * LT3 + C1 * LC1 + C2 * LC2 + C3 * LC3$$

$$\begin{aligned}
M_p &= (tc * ts^2 - 2.0 * tc * C * ts + tc * C^2) * fc \\
&\quad + (8.0 * ts^3 + (-8.0 * w + 3.0 * tc - 2.0 * b + 8.0 * C) * ts^2 \\
&\quad + (4.0 * C^2 + (-4.0 * w - 2. * b + 2. * tc) * C + 2.0 * w^2 - 1. * tc * b + 2. * b * w) * ts) \\
&\quad * Fy
\end{aligned}$$

2.2.2.2 Compression Depths and Mp for Case (b)

Negative drift case:

Forces:

$$T1 = 2 * ts * (2 * ts + tc) * Fy$$

$$T2 = 4 * ts * (w - C - ts) * Fy$$

$$T3 = (2 * ts + tc - C) * (b - 4 * ts) * Fy$$

$$C1 = ts * b * Fy$$

$$C2 = 4 * ts * (C - ts) * Fy$$

$$C3 = (C - ts - tc) * (b - 4 * ts) * Fy$$

$$C4 = tc * (b - 4 * ts) * fc$$

$$T1 + T2 + T3 = C1 + C2 + C3 + C4$$

$$C = \frac{(-8 * ts^2 + (2 * b + 4 * w - 6 * tc) * ts + 2 * tc * b) * Fy - tc * (b - 4 * ts) * fc}{2 * b * Fy}$$

Lever arms of forces about the centroid:

$$LT1 = w - C - 0.5 * ts$$

$$LT2 = 0.5 * w - 0.5 * C - 0.5 * ts$$

$$LT3 = 1.0 * ts + 0.5 * tc - 0.5 * C$$

$$LC1 = C - 0.5 * ts$$

$$LC2 = 0.5 * C - 0.5 * ts$$

$$LC3 = 0.5 * C - 0.5 * ts - 0.5 * tc$$

$$LC4 = C - ts - 0.5 * tc$$

Plastic moment:

$$Mp = T1 * LT1 + T2 * LT2 + T3 * LT3 + C1 * LC1 + C2 * LC2 + C3 * LC3 + C4 * LC4$$

$$\begin{aligned} Mp = & (4 * ts^2 * tc + (2.0 * tc^2 + (-4 * C - 1 * b) * tc) * ts - 0.5 * b * tc^2 + tc * C * b) * fc \\ & + (-8.0 * ts^3 + (8.0 * C + 2.0 * b - 13.0 * tc) * ts^2 \\ & + (-4.0 * tc^2 + (2 * w + 6.0 * C + 3.0 * b) * tc - 4.0 * w * C - 2.0 * C * b + 2.0 * w^2) \\ & * ts + b * tc^2 - 2.0 * tc * C * b + C^2 * b) * Fy \end{aligned}$$

Positive drift case:

Forces:

$$T1 = ts * b * Fy$$

$$T2 = 4 * ts * (w - C - ts) * Fy$$

$$T3 = (w - C - ts - tc) * (b - 4 * ts) * Fy$$

$$C1 = 2 * ts * (2 * ts + tc) * Fy$$

$$C2 = 4 * ts * (C - ts) * Fy$$

$$C3 = (b - 4 * ts) * (2 * ts + tc - w + C) * Fy$$

$$C4 = 2 * tc * (C - ts) * fc$$

$$T1 + T2 + T3 = C1 + C2 + C3 + C4$$

$$C = \frac{(4 * ts^2 + (-b - 2 * w + 3 * tc) * ts + b * (w - tc)) * Fy + tc * fc * ts}{Fy * b + fc * tc}$$

Lever arms of forces about the centroid:

$$LT1 = w - C - 0.5 * ts$$

$$LT2 = 0.5 * w - 0.5 * C - 0.5 * ts$$

$$LT3 = 0.5 * w - 0.5 * C - 0.5 * ts - 0.5 * tc$$

$$LC1 = C - 0.5 * ts$$

$$LC2 = 0.5 * C - 0.5 * ts$$

$$LC3 = 1.0 * ts + 0.5 * tc - 0.5 * w + 0.5 * C$$

$$LC4 = 0.5 * C - 0.5 * ts$$

Plastic moment:

$$Mp = T1 * LT1 + T2 * LT2 + T3 * LT3 + C1 * LC1 + C2 * LC2 + C3 * LC3 + C4 * LC4$$

$$\begin{aligned} Mp = & (tc * C^2 + ts^2 * tc - 2.0 * ts * tc * C) * fc \\ & + (-8.0 * ts^3 + (2.0 * b + 8.0 * w - 8.0 * C - 13.0 * tc) * ts^2 \\ & + (-4.0 * tc^2 + (8.0 * w - 6.0 * C + 3.0 * b) * tc + (-2.0 * w + 2.0 * C) * b + 4.0 * w \\ & * C - 2.0 * w^2) * ts + tc^2 * b + (-2.0 * w + 2.0 * C) * b * tc \\ & + (-2.0 * w * C + C^2 + w^2) * b) * Fy \end{aligned}$$

2.2.2.3 Compression Depths and Mp for Case (c)

Negative drift case:

Forces:

$$T1 = 2 * ts * (2 * ts + tc) * Fy$$

$$T2 = 4 * ts * (w - C - ts) * Fy$$

$$T3 = ts * (b - 4 * ts) * Fy$$

$$C1 = ts * b * Fy$$

$$C2 = 4 * ts * (C - ts) * Fy$$

$$C3 = (C - ts) * (b - 4 * ts) * fc$$

$$T1 + T2 + T3 = C1 + C2 + C3$$

$$C = \frac{((b - 4 * ts) * fc + 4 * Fy * w) * ts}{(b - 4 * ts) * fc + 8 * ts * Fy}$$

Lever arms of forces about the centroid:

$$LT1 = w - C - 0.5 * ts$$

$$LT2 = 0.5 * w - 0.5 * C - 0.5 * ts$$

$$LT3 = 1.5 * ts + tc - C$$

$$LC1 = C - 0.5 * ts$$

$$LC2 = 0.5 * C - 0.5 * ts$$

$$LC3 = 0.5 * C - 0.5 * ts$$

Plastic moment:

$$Mp = T1 * LT1 + T2 * LT2 + T3 * LT3 + C1 * LC1 + C2 * LC2 + C3 * LC3$$

$$Mp = (-2.0 * ts^3 + (4.0 * C + 0.5 * b) * ts^2 + (-2.0 * C^2 - b * C) * ts + 0.5 * b * C^2) * fc$$

$$+ (-4.0 * ts^3 + (-5.0 * tc + b) * ts^2$$

$$+ (4.0 * C^2 + (-2. * tc - 4.0 * w) * C + 2.0 * w^2 + 2. * tc * w + b * tc) * ts) * Fy$$

Positive drift case:

Forces:

$$T1 = ts * b * Fy$$

$$T2 = 4 * ts * (w - C - ts) * Fy$$

$$C1 = 2 * ts * (2 * ts + tc) * Fy$$

$$C2 = 4 * ts * (C - ts) * Fy$$

$$C3 = ts * (b - 4 * ts) * Fy$$

$$C4 = 2 * tc * (w - 2 * ts - tc) * fc$$

$$C5 = (b - 4 * ts) * (ts + tc - w + C) * fc$$

$$T1 + T2 + T3 = C1 + C2 + C3$$

$$C = \frac{(4 * ts^2 + (-b - 4 * w + 8 * tc) * ts + (w - tc) * (b - 2 * tc)) * fc + 4 * \left(w - \frac{tc}{2}\right) * Fy * ts}{(b - 4 * ts) * fc + 8 * ts * Fy}$$

Lever arms of forces about the centroid:

$$LT1 = w - C - 0.5 * ts$$

$$LT2 = 0.5 * w - 0.5 * C - 0.5 * ts$$

$$LC1 = C - 0.5 * ts$$

$$LC2 = 0.5 * C - 0.5 * ts$$

$$LC3 = 1.5 * ts + tc - w + C$$

$$LC4 = C - 0.5 * w - 0.5 * ts - 0.5 * tc$$

$$LC5 = 0.5 * ts + 0.5 * tc - 0.5 * w + 0.5 * C$$

Plastic moment:

$$Mp = T1 * LT1 + T2 * LT2 + C1 * LC1 + C2 * LC2 + C3 * LC3 + C4 * LC4 + C5 * LC5$$

$$Mp = (-4.0 * ts^3 + (b - 5.0 * tc) * ts^2 + ((2.* C + b) * tc + 2.0 * w^2 + 4.0 * C^2 - 4.0 * C * w) * ts)$$

* F_y

$$+ (-2.0 * ts^3 + (0.5 * b + 4.0 * w - 4.0 * C - 2.0 * tc) * ts^2$$

$$+ (tc^2 + (b + 5.0 * w - 8.0 * C) * tc - 2.0 * C^2 + (b + 4.0 * w) * C - 2.0 * w^2 - 1.* b$$

$$* w) * ts + tc^3 + (0.5 * b - 2.* C) * tc^2 + ((b + 2.* w) * C - 1.* w^2 - 1.* b * w) * tc$$

$$+ 0.5 * b * w^2 + 0.5 * C^2 * b - 1.* C * b * w) * fc$$

2.2.3 Details of Preliminary Specimen

The selected 1/4th scale cross-section of the wall specimen is shown in Figure 2-3, together with the assumed plastic stress distribution. It is referred to as C100x30x5.375 because it has a full flange width, b , of 100 *in.*, a web depth, w , of 30 *in.*, and a cross-section (web and flange) total thickness of 5.375 *in.* It also has a concrete thickness of, t_c , 5 *in.* and steel plate thickness, t_s of 3/16 *in.* Table 2-2 provides the other properties of the cross-section as well as the material properties of the steel and the concrete material assumed in calculating nominal strength. Provided in the table is also the plastic moment capacity and the percentage of the axial squash load that could theoretically be applied to the wall section by the vertical actuators at full capacity (i.e., ratio of available axial load to axial load capacity of the infill concrete ($A_c f'_c$)). This indicates that, at the capacity of the vertical actuators, the C100x30x5.375 wall model would be subjected to a maximum axial loading that corresponds to 27% of the squash load (based on concrete axial strength) if the concrete strength is 4ksi, where the squash load is defined as crushing load of the infill concrete. Smaller specimens would have been required to achieve axial stresses equal to higher percentages of the squash load. For example, Figure 2-4 shows the percentage of the maximum achievable squash load as a function of concrete thickness (t_c) and concrete compressive strength (f'_c). For example, to illustrate how various parameters would impact this percentage (Figure 2-5), with the current wall geometry ($t_c = 5in$) and with an expected concrete compressive strength (e.g., $f'_c = 6ksi$), the maximum load applied

corresponds to 18% of the axial capacity of the infill concrete. Alternatively, if reducing the thickness of concrete to 4 in. while keeping the other parameters of the wall section the same ($F_y = 50ksi$, $f'_c = 6ksi$), 23% of the axial strength would be achieved.

An alternative to the C100x30x5.375 wall model that was considered is a C60x20x5.375 wall (which would be closer to a 1/6th scale model), which has less concrete area and therefore allows for more variability in f'_c as far as reaching large percentages of the squash load. The 1/6th scale model has a full flange width, b , of 60 in., web depth, w , of 20 in., steel plate thickness, t_s , of 3/16 in. The wall cross-section width-to-depth aspect ratio of this section is 3, whereas it is 3.33 for the 1/4th scale model (C100x30x5.375). Theoretically, 30% axial load can be achieved for the 1/6th scale model with $t_c = 5in$, if the expected strength of the concrete is $f'_c = 6ksi$. This would also be the case with a concrete thickness, t_c , of 8in. if $f'_c=4ksi$. Figure 2-5 shows the percentage of the maximum achievable axial force (as a function of t_c and f'_c) for the 1/6th scale wall model. However, the larger scale C100x30x5.375 was preferred and was selected as the recommended preliminary specimen to be considered for the subsequent analyses thereafter.

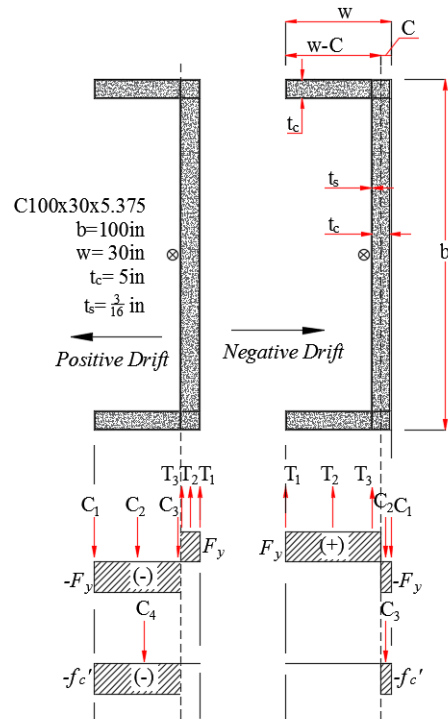


Figure 2-3. Cross-section of the C-shaped C-PSW/CF and its plastic stress distribution under positive (left) and negative wall drift.

Table 2-2. Properties of the Initial Specimen.

Wall Parameters	Units	C100X30X5.375
Wall Height, H	<i>in</i>	166
Flange length, b	<i>in</i>	100
Web length, w	<i>in</i>	30
Steel thickness, t_s	<i>in</i>	0.1875
Concrete thickness, t_c	<i>in</i>	5.0
Total thickness, t	<i>in</i>	5.375
Wall aspect ratio, H/w	-	5.80
Cross-section aspect ratio, b/w	-	3.33
Steel area, A_s	<i>in</i> ²	62.0
Concrete area, A_c	<i>in</i> ²	741.0
Gross area, A_g	<i>in</i> ²	802.0
Reinforcement ratio, ρ_s	%	8.0
Yield strength, F_y	<i>ksi</i>	50.0
Concrete strength, f'_c	<i>ksi</i>	4.0
Max moment (+ Drift), M_p	<i>kip-in</i>	31508
Max. base shear, V_{max}	<i>kip</i>	176.0
Safety factor, SF	-	2.51
30% axial capacity of concrete, $0.3A_c f'_c$	<i>kip</i>	963.0
Max. achievable axial load,	%	27.0

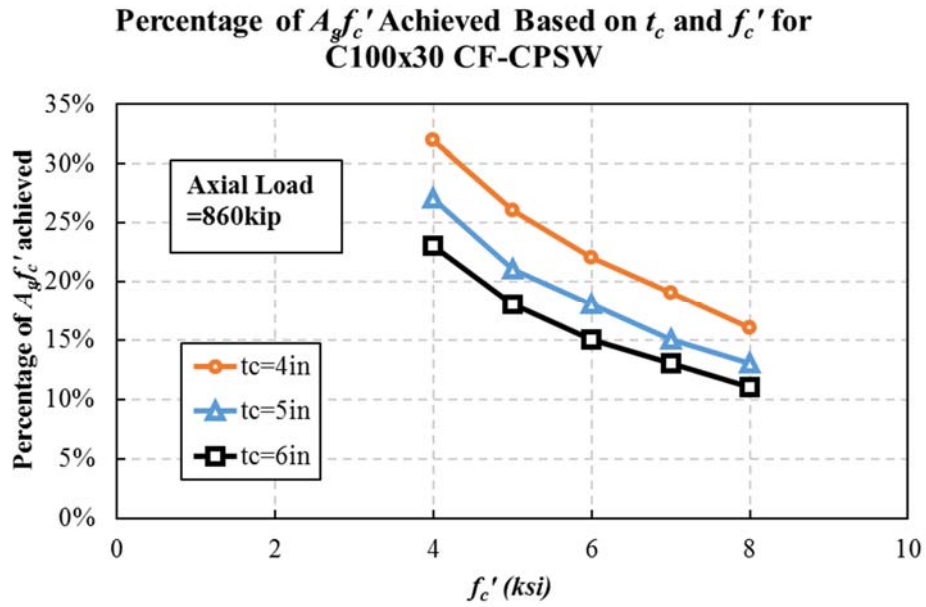


Figure 2-4. Percentage of axial load achieved for C100x30 C-PSW/CF based on t_c and f_c'

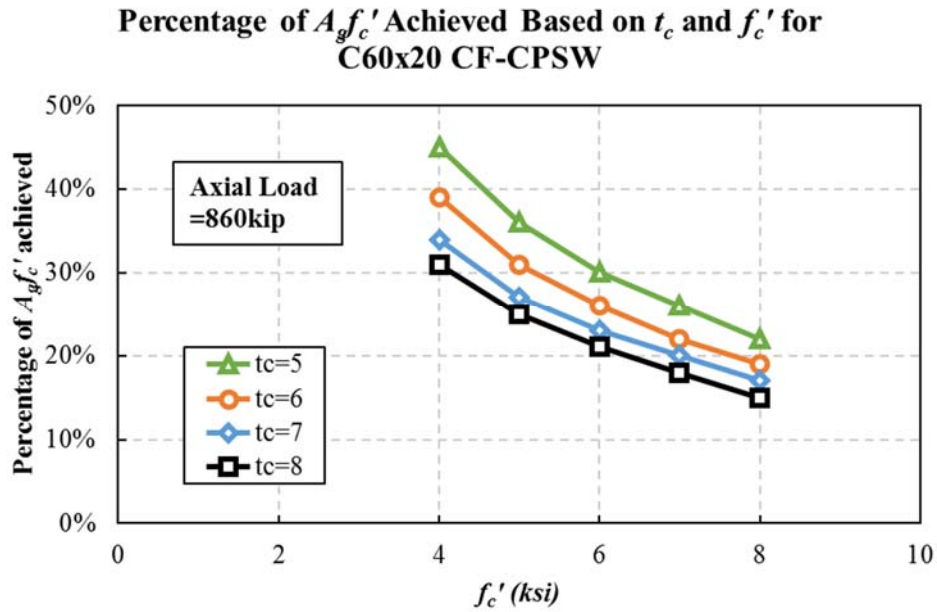


Figure 2-5. Percentage of axial load achieved for C60x20 C-PSW/CF based on t_c and f_c'

Note that assuming a C100x30x5.375 wall, a wall height of approximately 14ft above the concrete foundation was chosen to be able develop the plastic moment at the base of the wall with the specified actuator and contingencies. Maximum wall strength and drifts, as well as other practical consideration, supported this decision at that time.

To conservatively determine the needed lateral force to test the chosen specimen, considering a yield strength of steel, $F_y = 50ksi$ and uniaxial compressive strength of concrete, $f'_c = 8ksi$, the plastic moment of the cross-section is 39,962 kip-in (under positive wall drift) and the lateral force required at the wall top to achieve this moment is 186 kips. Using an expected yield strength of 60ksi would increase this value by approximately 20%. The lateral force applied using two 220kips actuators that provide a total force of 440kips was deemed an adequate lateral load capacity to test the specimens while also countering the horizontal component of the vertical actuators at large drifts.

2.2.4 Preliminary analysis

2.2.4.1 Moment-Curvature and Moment-Axial Load Diagrams)

The moment-curvature diagram of the C100x30x5.375 wall model having concrete strength, $f'_c = 4ksi$, and $f'_c = 8ksi$, under negative and positive wall drift is shown in Figures 2-6 and 2-7, respectively. The section moment obtained from the fiber analysis gradually converges to the plastic moment with increasing wall curvature. The section attains its plastic moment with less curvature under positive drift than under negative drift. This figure also indicates the increase in flexural strength of the section under negative drift, and the decrease under positive drift, with increasing axial load (e.g., $P=0.0$, $P = 0.15P_{oc}$, and $P = 0.3P_{oc}$, where P_{oc} is the axial strength of the concrete).

Figure 2-8 shows the P-M interaction diagram of the C100x30x5.375 specimen under positive and negative wall drift, for C-PSW/CFs having concrete strength of $f'_c = 4ksi$, and $f'_c = 8ksi$. The P-M interaction diagram indicates that the moment capacity of the section is reduced under increasing axial load under positive drift. On the other hand, it is gradually increased when subjected to higher axial loads under

negative drift. The observed moment capacity increase of the section is best understood by observing the history of the neutral axis location of the section that is illustrated graphically in Figure 2-9. The main observations from Figure 2-9 are as follows:

- Compression depth increases with greater axial load;
- In a given direction of bending, the increase in moment capacity (when axial load is zero) is inversely proportional to the distance between the plastic neutral axis and the section centroid axis;
- The section attains its largest strength when the plastic neutral axis is at the center of gravity (or centroid axis), which is true for any section (but for the C-shape, it will not be the same value for negative and positive bending);
- Under negative drift, the plastic neutral axis is always located within the wall flange, and;
- Under positive drift, the compression depth, under zero axial load, almost matches with the centroid of the section (i.e., corresponds to peak moment capacity of the section).

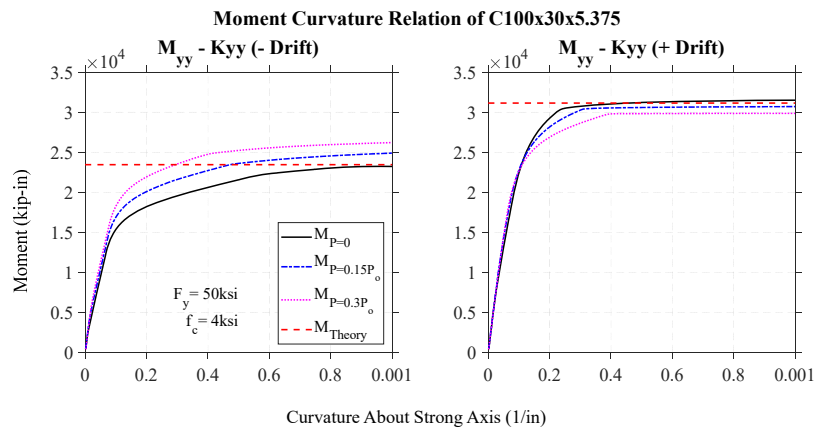


Figure 2-6. Moment-curvature relationship of the C100x30x5.375 C-PSW/CF model ($f_c=4\text{ksi}$)

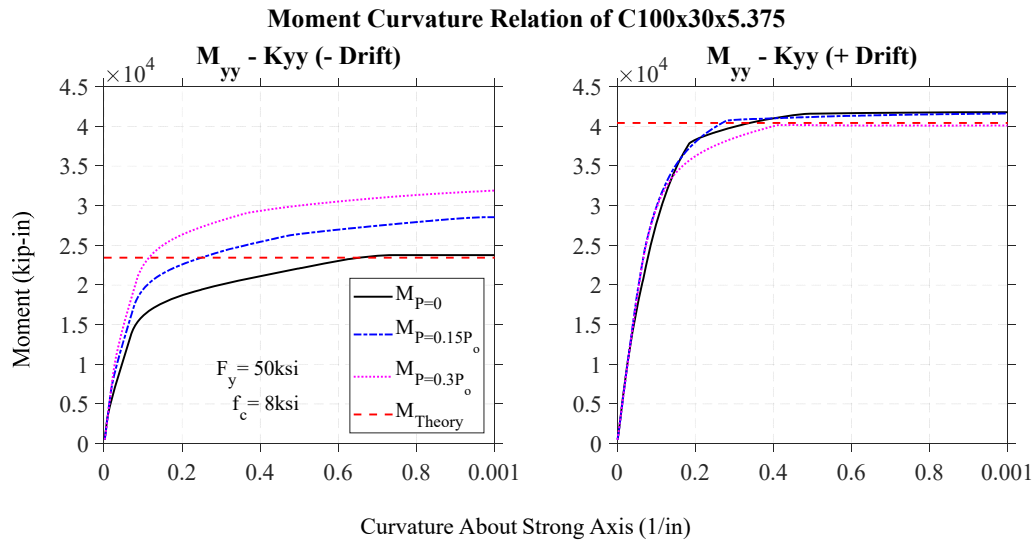


Figure 2-7. Moment-curvature relationship of the C100x30x5.375 C-PSW/CF model ($f_c=8\text{ksi}$)

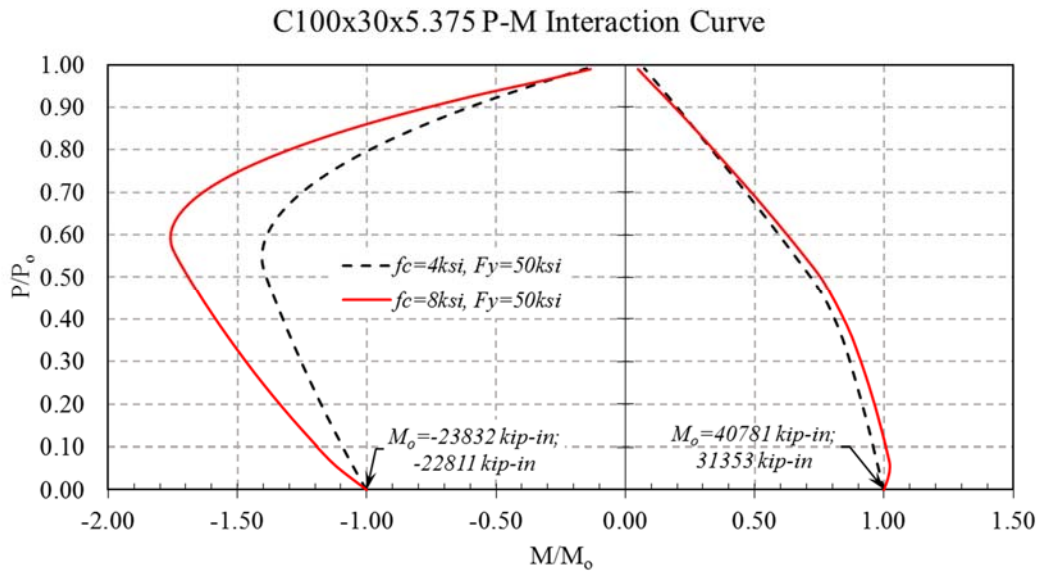
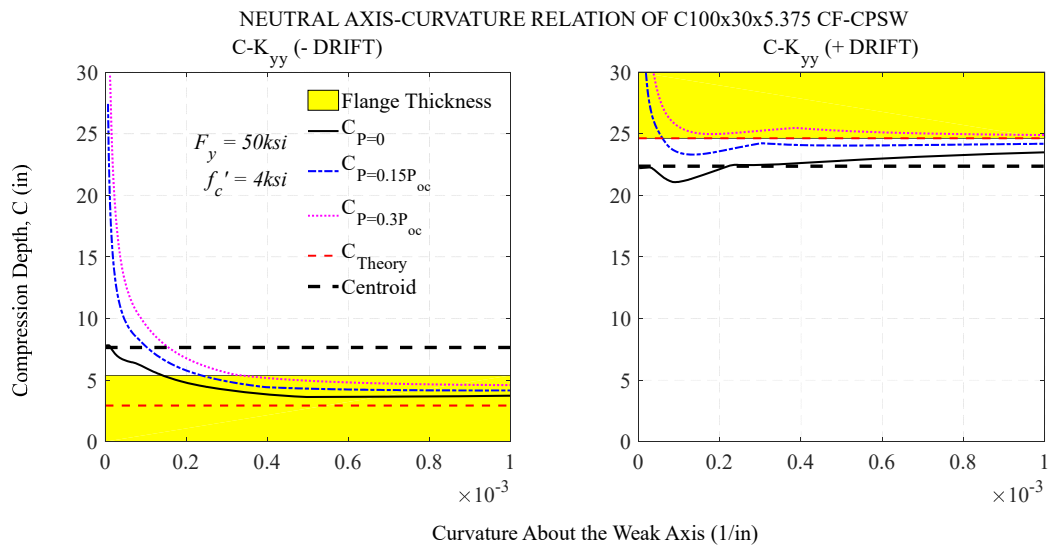
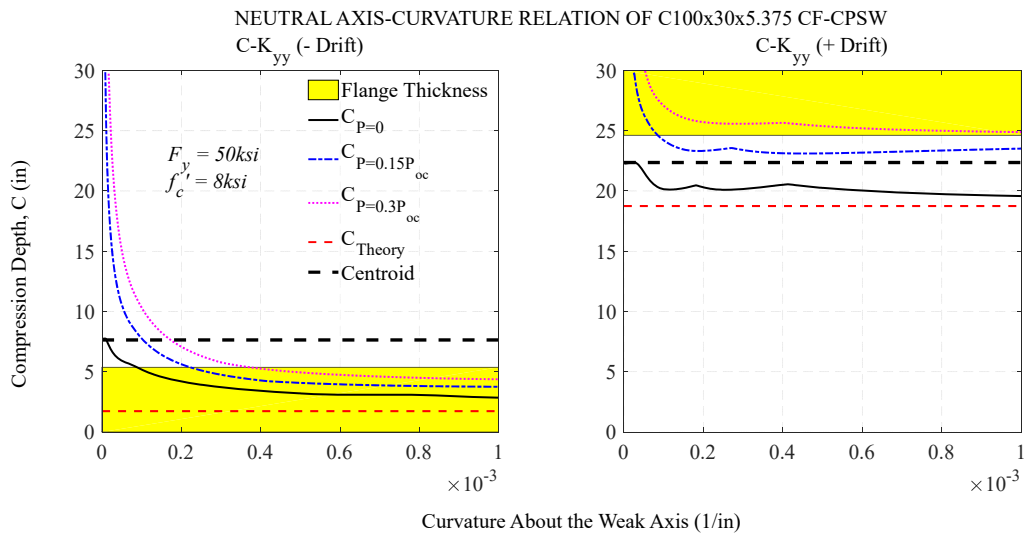


Figure 2-8. P-M interaction diagram for the C100x30x5.375 C-PSW/CF model



(a) $f'_c=4ksi$



(b) $f'_c=8ksi$

Figure 2-9. Neutral axis-curvature relation of the C100x30x5.375 wall model with: (a) $f'_c=4ksi$,

and; (b) $f'_c=8ksi$

2.2.4.2 Elastic Buckling of Skin Plate

Once satisfactory wall dimensions have been selected and satisfactory flexural strength is provided, the ability of a walls to develop this plastic moment requires that premature local buckling of the steel plate be prevented. To ensure yielding of the web plate prior to its local buckling, Alzeni and Bruneau (2014) proposed the following equation:

$$\frac{s}{t_p} = 1.8 \sqrt{\frac{E}{F_y}} \quad (2.1)$$

where s is vertical spacing of the tie bars, and t_p is thickness of the plate.

This equation is identical to Equation (H7-1) given in Article H7.4a of AISC341-16 (2016) for the maximum allowable spacing of tie bars in both the vertical and horizontal directions for the steel plate of C-PSW/CF with boundary elements. Based on this equation, for a steel plate thickness, t_p , of $\frac{3}{16}in.$, and properties of $E = 29000ksi$ and $F_y = 50ksi$, the maximum allowable spacing, s , of tie bars in both the vertical and horizontal directions is equal to $8.13in.$ The spacing of tie bars in vertical and horizontal directions for the specimen was therefore taken as $8in.$

Tie bars diameter was selected per Article H7.4e of AISC341-16 (2016) by adding the tension force that develop due to locally buckled steel face plates (Equation (H7-5) of AISC341-16), and the required tension force that develops along the tie bar to prevent splitting of the concrete core between the steel plates (Equation (H7-6) of AISC341-16 (2016)). The corresponding required tensile strength for each tie bar was calculated equal to $11.8kips$. At this stage, a Grade 50 tie bar with $0.625in.$ diameter was chosen based on the required tensile strength. The connection of tie bars to the steel plates was designed to develop the tensile strength of the tie bars using fillet welds. Details of the design procedure are presented in Appendix A.

2.2.5 Test Set-up Design

2.2.5.1 General

Each wall specimen to be tested is a cantilever embedded at its base into a reinforced concrete footing needed to transfer the base moment into the laboratory strong floor. Therefore, the entire test set-up consists of four main components, namely: (1) the wall reinforced concrete footing; (2) the C-shaped C-PSW/CF specimen; (3) the Lateral Loading System (LLS), and; (4) the Axial Loading System (ALS). The corresponding test set-up is illustrated in Figures 2-10 and 2-11. The CAD drawings of the test setup are presented in Appendix B.

The height of the wall, from top of the footing to the centerline of the actuator plates is about 14 *ft.* The total height of the test set-up from the strong floor is 16.5 *ft.* Figure 2-10 shows a schematic view of the C-shaped C-PSW/CF wall.

The dimensions of the footing and post-tension forces of the DYWIDAGs used to tie it to the strong floor of the structural laboratory were chosen to prevent any uplift due to wall over-turning moment under development of its plastic moment capacity calculated with expected material properties and multiplied by a safety factor of 1.5 to account for possible strain hardening. The design dimensions of the footing are 8 *ft.* × 12 *ft.* in plan, and 2 *ft.* in thickness. The number of DYWIDAGs used for this footing is 24, each pre-tensioned 130 *kips* (per DYWIDAG bar) to prevent uplift on the tension side of the footing.

At the top of the wall, horizontal loading is applied to the specimen's two wall webs, and vertical force is applied to the wall flange, as illustrated in Figures 2-10 and 2-11. In this approach, the horizontal loading system consists of two MTS Model 244.51S (220 *kips*) actuators with its connecting hardware (namely head washer plates, post-tension bars, and stiffeners).

The axial loading system consists of two MTS Model 243.90T (440 *kips*) actuators attached between the top of the wall and the strong floor. The setup for attachment of these actuators to the wall needed to be able to transfer and keep constant the vertical axial load at the top of the wall throughout the

cyclic test and when the wall is laterally deformed. For this purpose, an iterative design and analysis process was conducted by which different test set-ups were designed. Feasibility, constructability, and reliability of each set-ups was considered in order to find the best possible configuration. Hence, in addition to the vertical loading system shown in Figure 2-10, two alternative systems were fully designed and investigated in details; they consisted of: (i) a W40x211 beam having large stiffeners, spreader plates, tension bars, and angles; (ii) a 3D truss system spanning over the full length of the wall. These alternatives are also shown in Figure 2-13, but were found to be heavier, more problematic to erect in the laboratory, and less stable. Details on these other fully developed alternatives are not presented here. Details of the preferred vertical loading system that has been retained here are presented in Section 2.2.5.3.

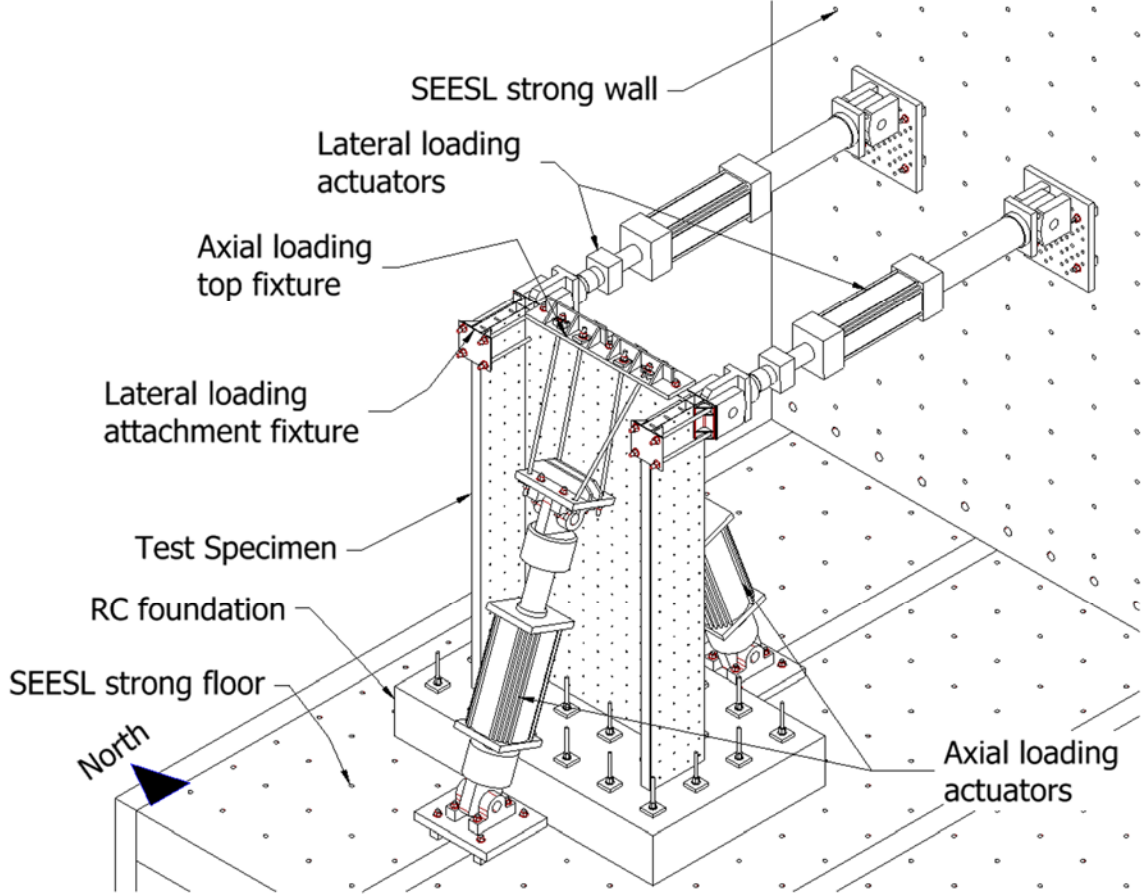


Figure 2-10. Perspective view of the test setup

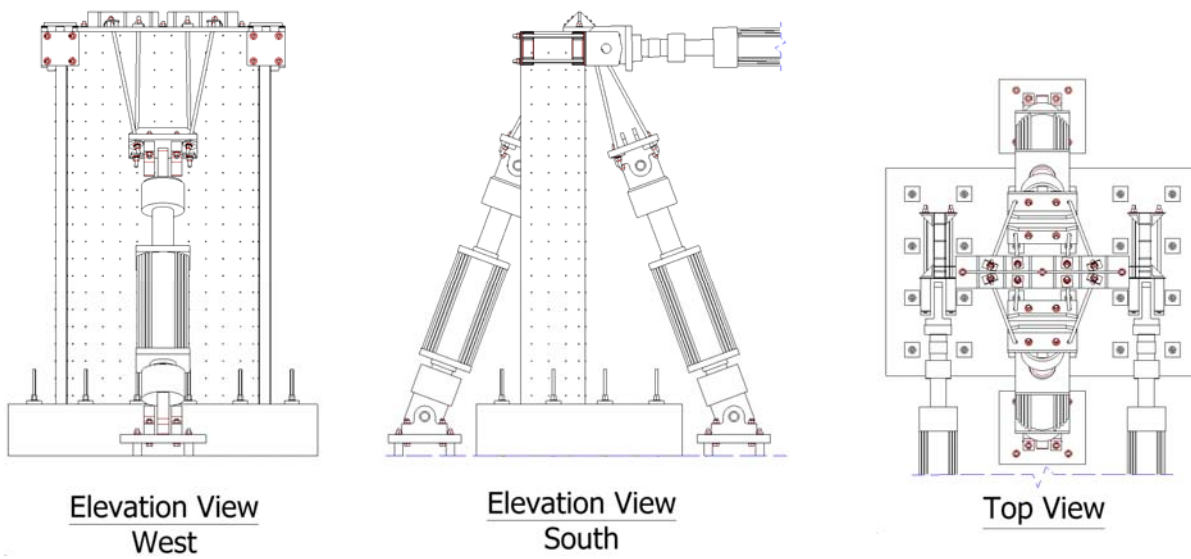


Figure 2-11. Elevation and top views of the test setup

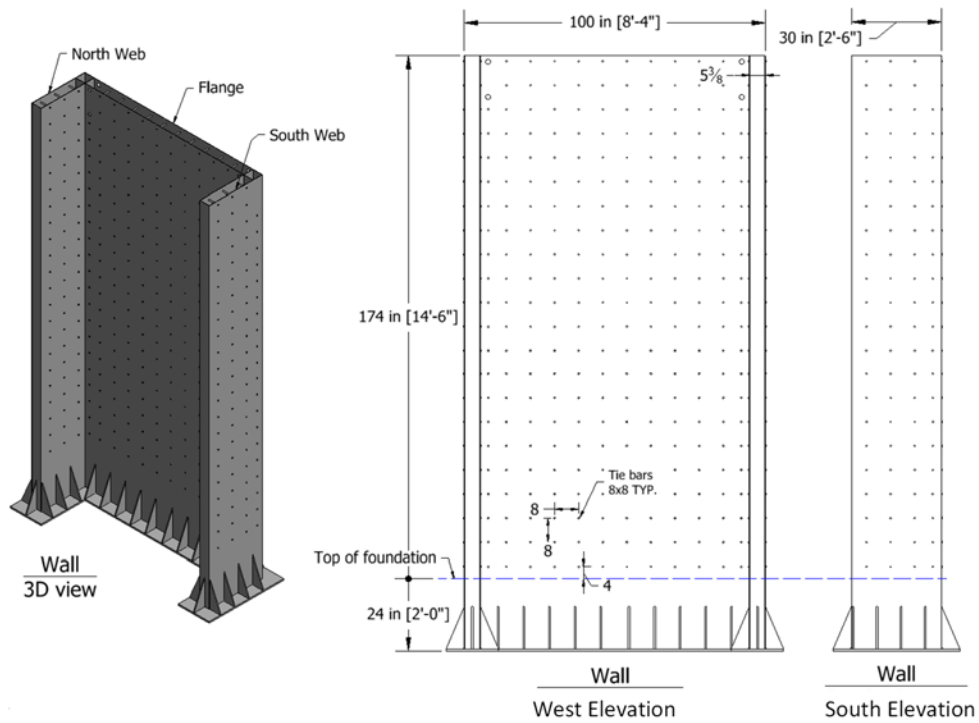
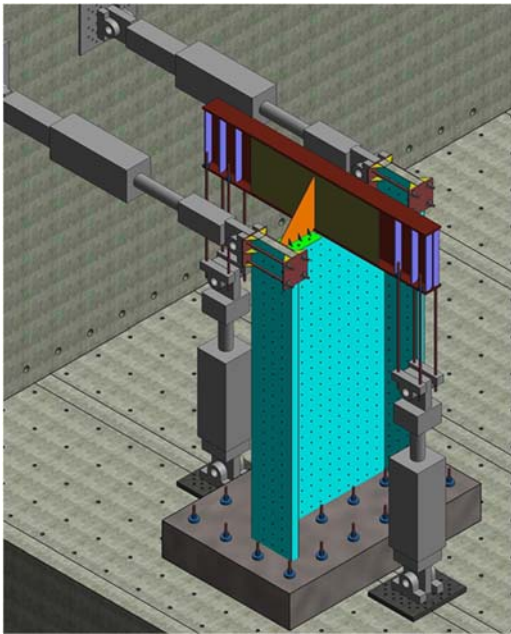
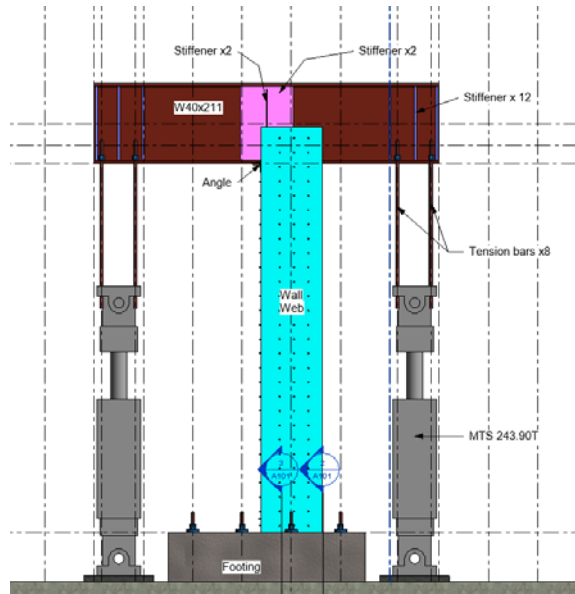


Figure 2-12. Perspective view of the test setup

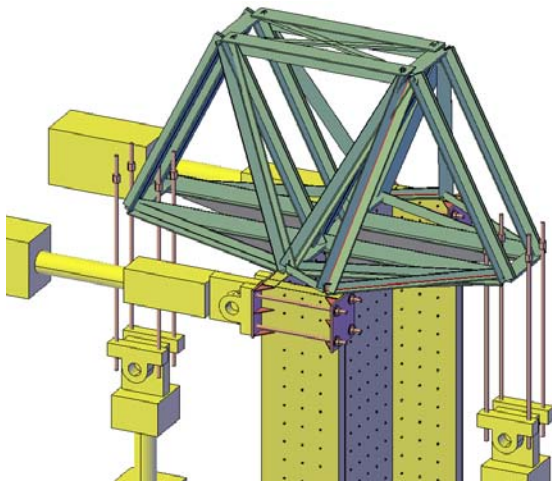


3D view

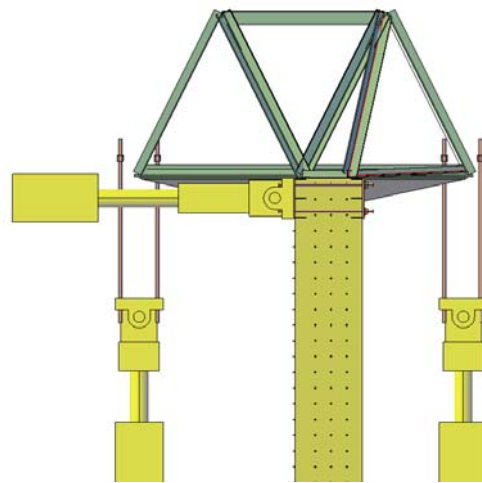


North elevation

(a) Vertical loading system using W shape beam on top of the wall



3D view



South elevation

(b) Vertical loading system using a 3D truss on top of the wall

Figure 2-13. Alternative designed (but not retained) vertical loading systems using: (a) W-shaped beam, (b) 3D steel truss

2.2.5.2 Lateral loading system set-up

As mentioned above, the lateral loading system consists of the two MTS Model 244.51S (220kips) actuators and their connection elements, namely head washer plates, post-tension actuator rods, and stiffeners. Figure 2-14 shows a schematic view of the lateral loading system. The lateral loading system was designed such that the capacity of these two horizontal actuators would be sufficient to develop up to 1.5 times the plastic moment of the specimens. Detailed design of the stiffeners and joint welds are presented in Appendix A. Due to complexity of the wall geometry and to prevent any unwanted eccentric loadings, the stiffeners were designed to be welded to each test specimen. Detailed finite element analyses of the lateral loading system were carried out using LS-Dyna to ensure proper and stable behavior of the system under positive and negative loadings. Figure 2-15 representatively shows the effective stress field in the system under maximum negative strength.

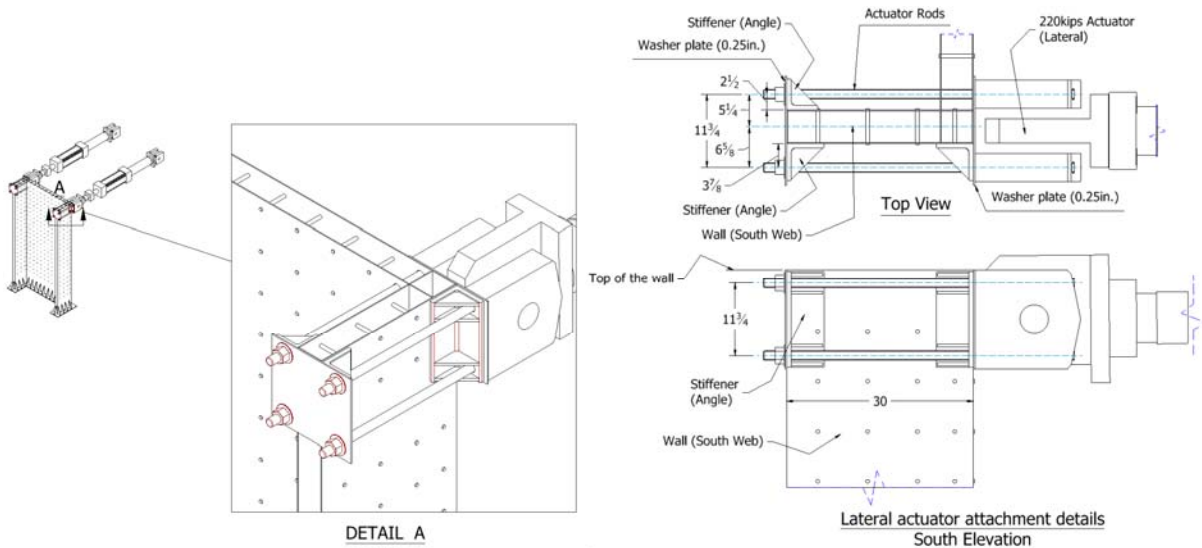


Figure 2-14. Details of the lateral loading system

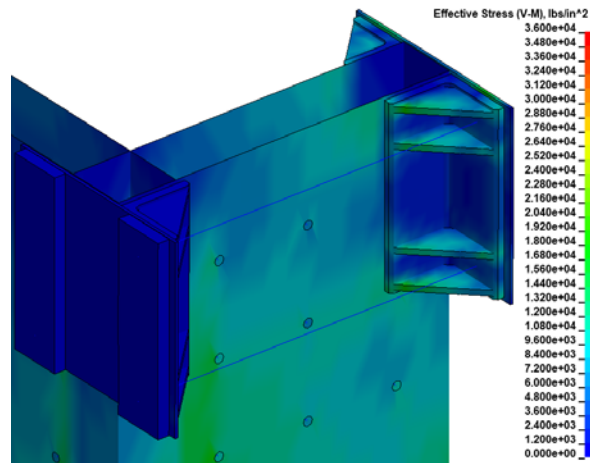


Figure 2-15. Effective stress field in the lateral loading system under maximum negative loading.

2.2.5.3 Axial loading system set-up

The designed set-up to apply vertical loading to the specimen consists of a top attachment fixture that is a stiffened inverted T-shape built-up beam sitting on top of the wall's flange. The top fixture spreads the downward load of the actuators on top of the wall. Two inclined vertical actuators are post-tensioned to the strong floor and located symmetrically on the east and west sides of the wall. The load of each actuator is transferred to the top attachment fixture by means of four high impact threaded bars. Figure 2-16 shows a schematic view of this system. The axial load in both of the vertical actuators was servo-controlled to remain equal to each other throughout the test.

Figure 2-17 shows an elevation view of the vertical loading system. As shown in this figure, the angle between the inclined actuators and the strong floor is 70° . This angle changes about $\pm 5^\circ$ during the test as the top of the wall drifts back and forth (considering the maximum displacements that can be applied by the actuators). The running threaded bars between the actuator plates and the top fixture were arranged in such a way that the central axes of both actuators coincide with the center plane of the wall flange in order to balance the tensile load among the threaded bars. Double spherical washers were used at the threaded bar joints in order to avoid moment concentrations due to accidental eccentricities. Figure 2-18

shows the details of the threaded bar end joints. Details of the top fixture and the actuator attachment plates are shown in Figures 2-19 and 2-20. Details of the design procedure for the top fixture and the actuator attachment plates are presented in Appendix A. Finite element analyses were carried out to control the stability of the vertical loading system. Figure 2-21 shows the developed finite element model of the vertical loading system and its deformed state. Figure 2-22 representatively shows the effective stress field in the top attachment fixture and the actuator attachment plate under maximum vertical loading.

The top fixture was anchored to the top of the wall at three locations by means of threaded bars embedded in the flange of the wall. The shear load demand on these embedded bars were calculated by considering worst case of the following scenarios:

- Unbalanced load from hanging only one vertical actuator on one side of the wall during set-up assembly process.
- Unbalanced actuator loads due to control errors during the test.
- The maximum horizontal resultant load produced by the vertical actuators having equal axial loads at maximum drift of the specimen, calculated to be 80kips when at maximum capacity of both vertical actuators (i.e., 440kips axial load per actuator).
- The resulting unbalanced lateral load due to unexpected accidental rupture of one of the 8 threaded bars running between the actuator and top fixture during the test, calculated as 165kips .

Analyses showed that the latter case is the most critical case producing a shear demand of 165kips on the vertical anchors. Note that in calculating the provided strength to resist this load, the friction at the interface between the top fixture and the concrete at the top of the wall was neglected. With respect to the other scenarios, the interface friction alone is sufficient to prevent lateral slippage at the interface between the top fixture and the top of wall flange during the test, which is desirable because slippage at the interface during the test would introduce some errors in the test data. In other words, the friction force was designed to transfer the maximum resultant horizontal component of the load produced by the vertical actuators at

maximum drift of the specimen (i.e., the 80kips mentioned in the third bullet above). Considering a conservative value of friction coefficient equal to 0.3 between the concrete and steel plate, the available interface force is shown in Table 2-3 for two cases of 15% and 30% axial loads. Nonetheless, the vertical anchors were also designed be able to resist alone the same forces, for conservatism and practical considerations.

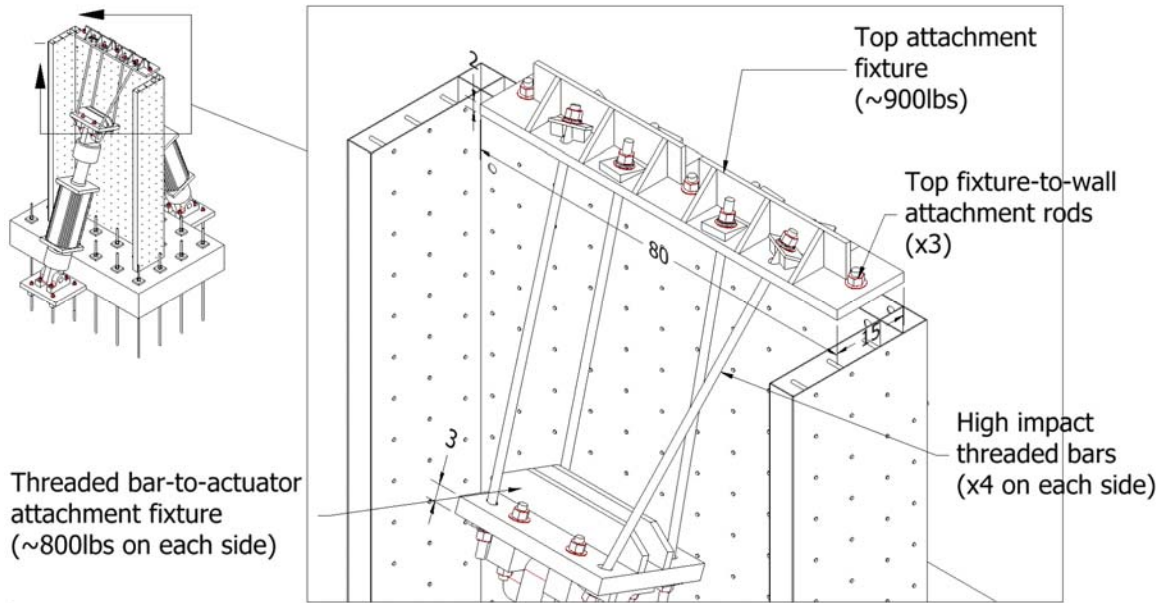


Figure 2-16. Schematic view of the vertical loading system

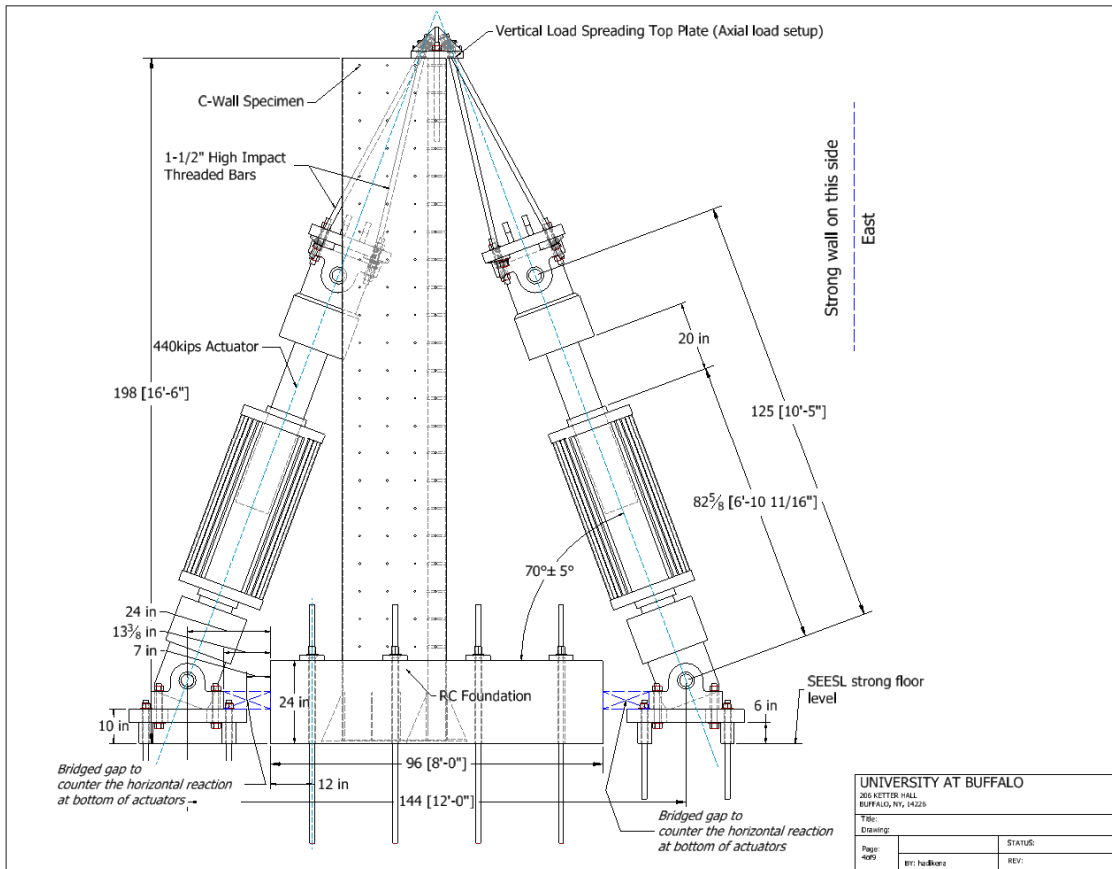


Figure 2-17. Elevation view of the vertical loading system (South elevation)

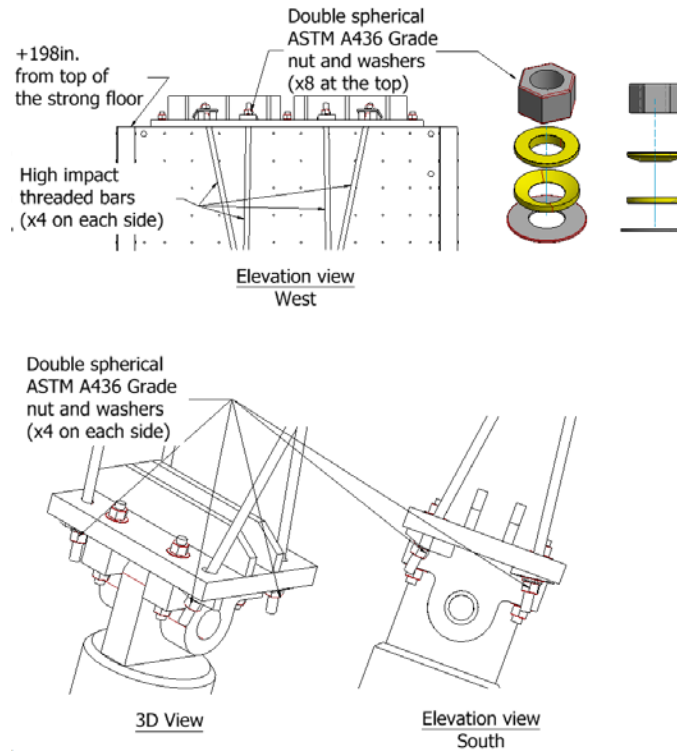


Figure 2-18. Threaded bars connection details in the vertical loading system

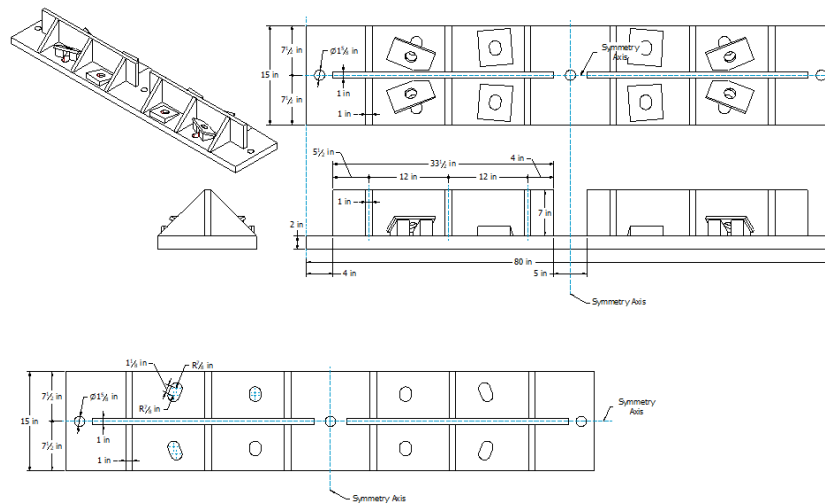


Figure 2-19. Vertical load spreading fixture of the vertical loading system

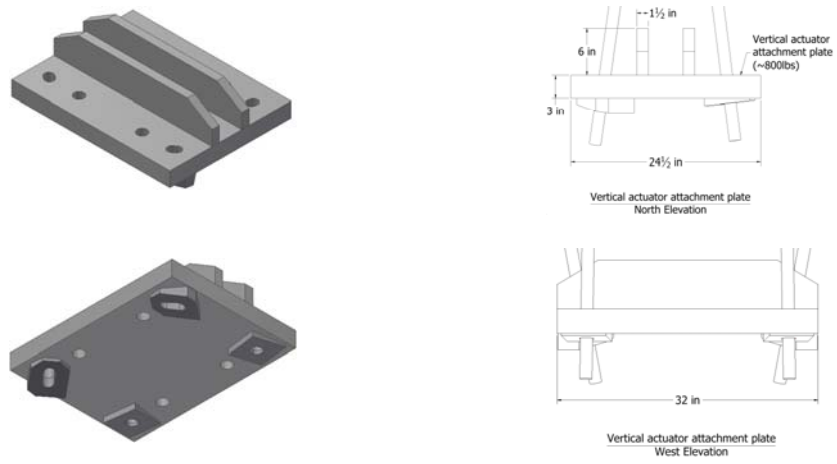


Figure 2-20. Vertical actuators top attachment fixture of the vertical loading system

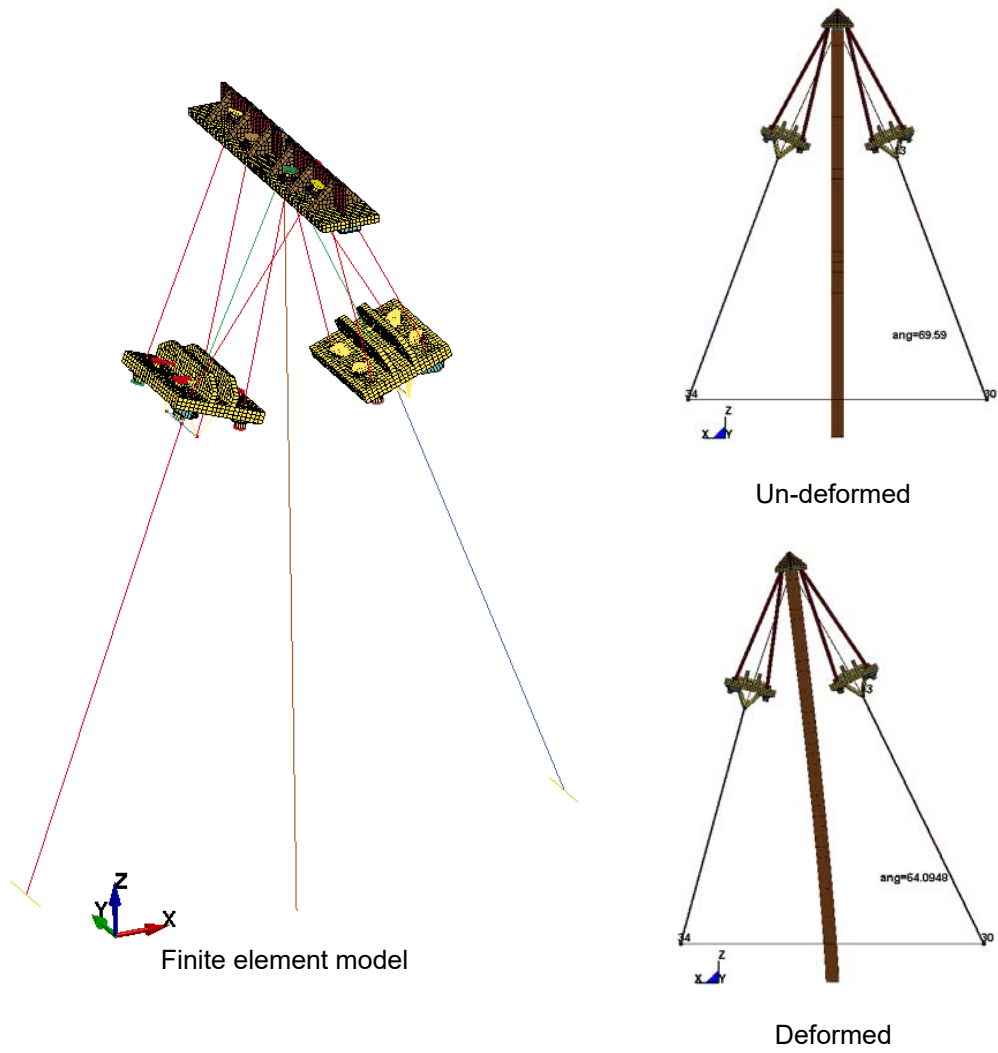


Figure 2-21. Threaded bars connection details in the vertical loading system

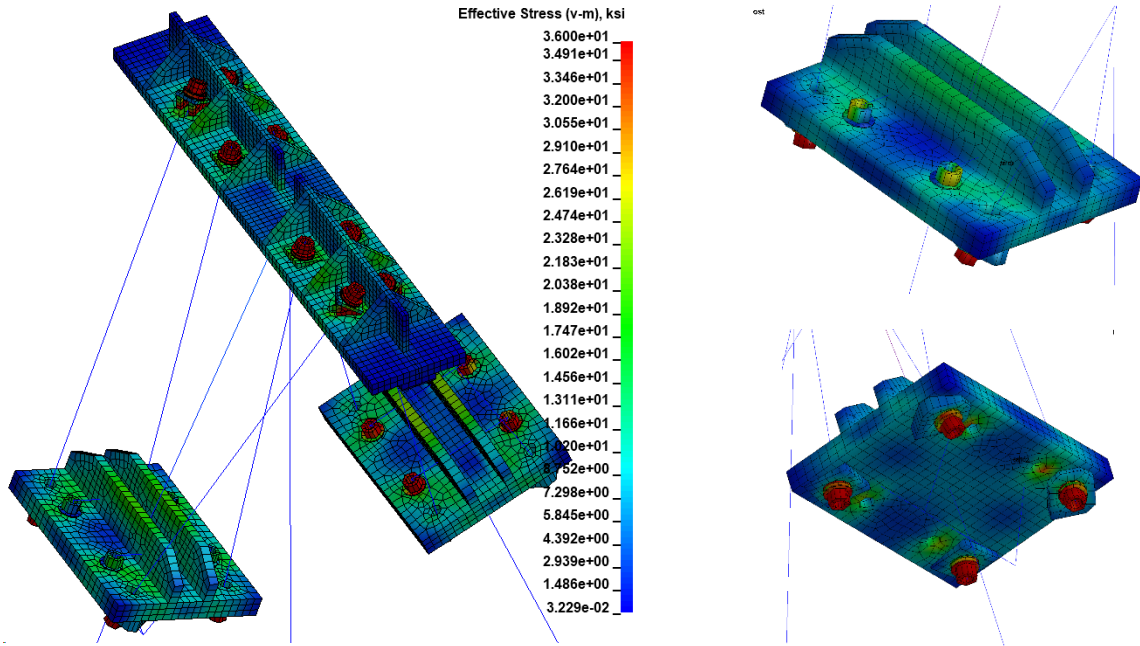


Figure 2-22. Effective stress field in the vertical loading system under maximum vertical and lateral loading

Table 2-3. Available friction forces at the interface of the top fixture and top of the wall

Axial load percentage	Available friction force from vertical actuators	Available friction force from anchorage bars	Ratio of available friction force to the required transferring force
30%	$2 \times 440 \times \sin(70^\circ) \times 0.3 = 248 \text{ kips}$	0 (No pre-tension)	3.1
15%	$2 \times 220 \times \sin(70^\circ) \times 0.3 = 124 \text{ kips}$	0 (No pre-tension)	1.6

2.2.6 Finite element analysis and Pushover Analysis of C100x30x5 using LS-Dyna

Preliminary analyses of the behavior of the specimens were conducted to establish expected experimental behavior and verify adequacy of the test set-up load transfer mechanism. The finite element study of the

wall, with fixed-base boundary condition, was performed using LS-Dyna. Plastic kinematic material model, with properties, $F_y = 50ksi$, $E = 29000ksi$ and $E_T = 100ksi$ were used for the steel, and Winfrith concrete model with $f'_c = 4ksi$ was used for the concrete. Analysis included pushover of the wall in the negative and positive directions, with and without axial load. Lateral and axial loads were applied to the finite element model following the same approach proposed for testing (i.e., axial load applied to the wall flange top only) by combining the models developed for the lateral and axial load fixtures (presented in Sections 2.2.5.2 and 2.2.5.3, respectively) with the model of the specimen. Figure 2-23 shows a schematic view of the resulting finite element model. Only half of the test specimen and set-up was modeled using symmetry principles to reduce the computational costs.

Figure 2-24 shows the pushover curves obtained from the finite element analyses of the C-shaped C-PSW/CF model under positive and negative wall drifts. The maximum base shear force obtained under positive and negative drift exceed the theoretical M_p values, reaching 186kips and 148kips, respectively. Web plate buckling was observed to start developing at about +1% positive drift ratio, and buckling of the steel plate on the east side of the flange (East is defined with respect to the North sign shown in Figure 2-10) was observed at about -3% drift ratio. Figure 2-25 shows a comparison of the results obtained with LS-Dyna and those obtained using fiber-section analysis in OpenSees (2006). Note that in the OpenSees analyses a material-based P-M interaction curve was used and no strain hardening was assumed for the steel; for comparison, a similar material model was used for the LS-Dyna analyses in Figures 1-24 and 1-26.

Figures 2-26 and 2-28 show the base-moment of the composite wall as well as the contributions of the concrete core and the steel plates to the total composite base-moment under positive and negative drifts, respectively. Figures 2-27 and 2-29 show the development of local buckling and of the plastic regions at the bottom of the steel plate for positive and negative drifts, respectively, at a six different points along the push-over curves for positive and negative drifts shown in Figures 2-26 and 2-28.

Finite element analysis was also performed to verify that a uniform axial stress distribution over the lower half of the wall is achieved even though only the flange is axially loaded at the top of the wall. The axial stress distribution from these models were compared against the actual stress distribution expected under uniform axial loading on each component of the wall (i.e., the concrete core and the steel plate). Note that for a fully composite wall, the applied axial load is expected to distribute between the steel plate and the concrete core proportionally to each part's axial stiffness. In other words, the axial load on each component is proportional to the product of the modulus of elasticity and cross-section area of that component. The expected axial load distribution on each component was calculated as follows (from a Mathcad sheet):

Axial strength:

$$f_c := 4 \text{ksi} \quad F_y := 50 \text{ksi}$$

$$P_c := f_c \cdot A_c = 2.985 \times 10^3 \text{-kip} \quad \text{Axial strength of the cross-section (Concrete core)}$$

$$P_o := f_c \cdot A_c + F_y \cdot A_s = 6.086 \times 10^3 \text{-kip} \quad \text{Axial strength of full composite cross-section}$$

$$P_{\text{axial}} := 840 \text{kip} \quad \text{Applied axial load on the wall (vertical components of actuators)}$$

$$\frac{P_{\text{axial}}}{P_c} = 28.141\% \quad \frac{P_{\text{axial}}}{P_o} = 13.803\%$$

Expected distribution of the axial load on the concrete core and steel plates:

$$E_c := 3240 \text{ksi} \quad \text{Concrete elasticity modulus}$$

$$E_s := 29000 \text{ksi} \quad \text{Steel elasticity modulus}$$

$$\sigma_c := \frac{E_c}{E_c \cdot A_c + E_s \cdot A_s} \cdot P_{\text{axial}} = 0.645 \text{-ksi} \quad \text{Axial stress on the concrete core}$$

$$\sigma_{\text{c_ratio}} := \frac{\sigma_c}{f_c} = 16.137\% \quad \text{Axial stress ratio on the concrete core}$$

$$F_c := \sigma_c \cdot A_c = 481.7 \text{-kip} \quad \text{Axial load on the concrete core}$$

$$\sigma_s := \frac{E_s}{E_c \cdot A_c + E_s \cdot A_s} \cdot P_{\text{axial}} = 5.778 \cdot \text{ksi} \quad \text{Axial stress on the steel plate}$$

$$\sigma_{s_ratio} := \frac{\sigma_s}{F_y} = 11.555\% \quad \text{Axial stress ratio on the steel plate}$$

$$F_s := \sigma_s \cdot A_s = 358.3 \cdot \text{kip} \quad \text{Axial load on the steel plate}$$

Per the above calculations, the expected uniform stress acting on the concrete core cross-section should be equal to approximately 16% of f'_c . Verifying this with the finite element analyses, Figure 2-30 shows the vertical (Z direction) stress field in terms of f'_c on the concrete core. The distribution of the vertical stresses on the flange and web's concrete core cross-section solid elements at different levels along the wall are shown in Figures 2-31 and 2-32, respectively. As shown in Figure 2-31, at the top of the wall and immediately under the top axial load fixture, large axial stresses on the cross-section are concentrated near the top fixture. However, the vertical stress distribution becomes more uniform with increased distance from the top fixture and it becomes effectively uniform over the lower 2/3 of the wall. The average vertical stress in the concrete at 110in, 80in, 15in, and 5in elevations are 17.8%, 16.3%, 14.2%, and 14.0% respectively, which is acceptably close to the expected distribution stress. As shown in Figure 2-32 at top of the wall there is no axial stress on the web's cross-section. The axial stresses on the web's cross-section increase to an average stress of 8.6% at Z=110in and increases to average stress of 13.9% at Z=5in. As shown in this figure, the axial stress within the web's cross-section is less uniform comparing to the flange. This is partly because of the existing eccentricity between the point of the applied axial load and the center of gravity of the C-shaped wall's cross-section, which results in a moment, and the development of a diagonal compression strut in the web near the base of the wall.

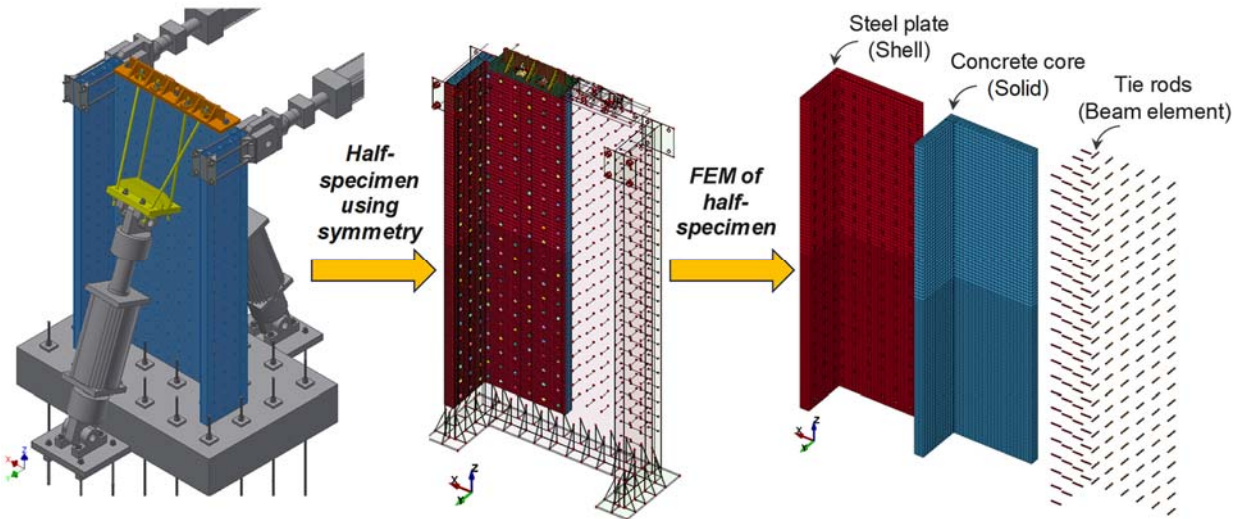


Figure 2-23. Schematic of the developed finite element model of the test set-up in LS-Dyna

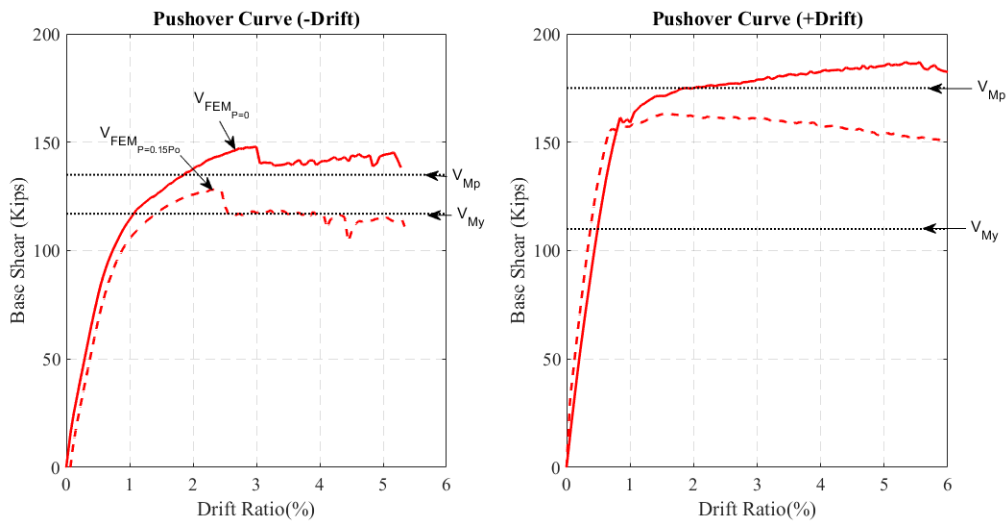


Figure 2-24. Base Shear vs. Drift Ratio of the FE Model of the C-Shaped C-PSW/CF under: a) Negative Drift, b) Positive Drift

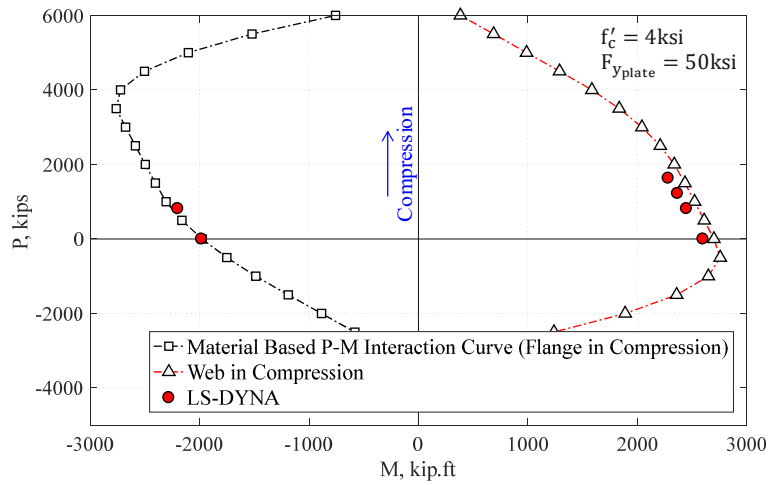


Figure 2-25. P-M interaction curve comparisons between LS-Dyna model and material-based fiber-section analysis

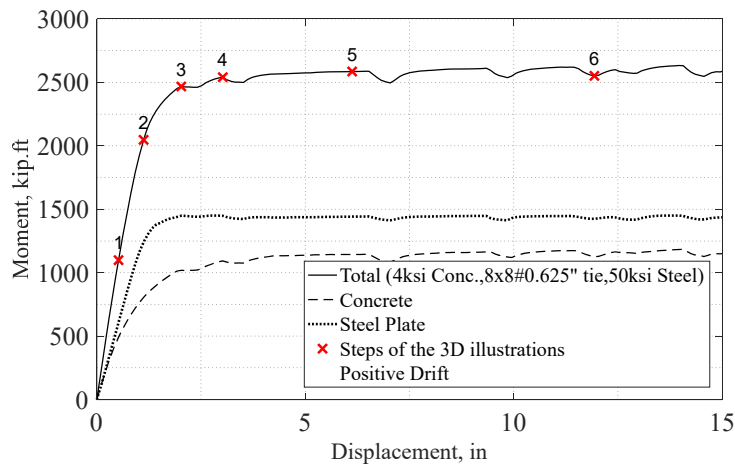


Figure 2-26. Base-moment of the composite wall, concrete core, and steel plate under positive drifts

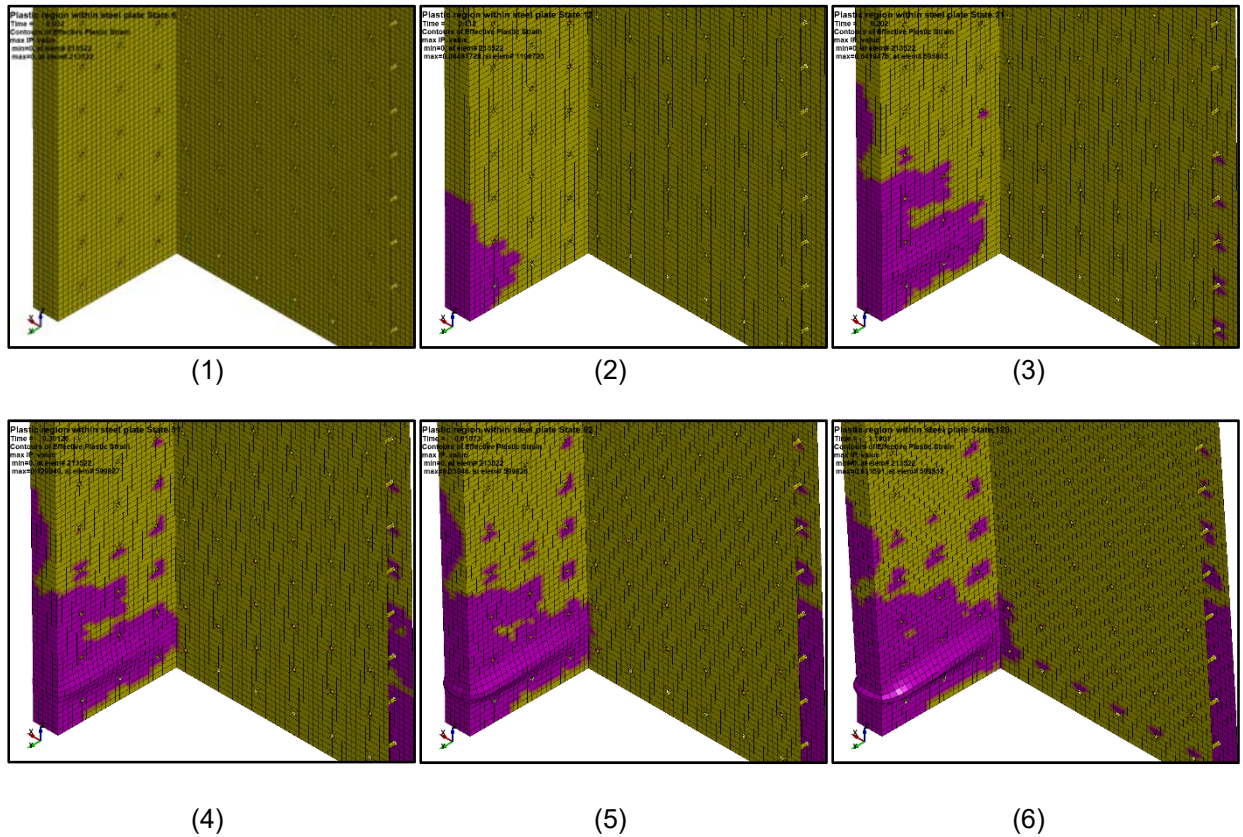


Figure 2-27. 3D view of the progression of local buckling and plastic regions at the bottom of the flange under positive drifts (West elevation).

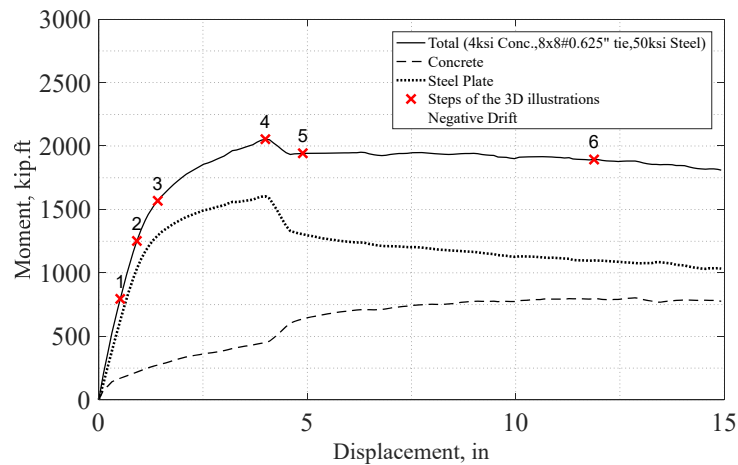


Figure 2-28. Base-moment of the composite wall, concrete core, and steel plate under negative drifts

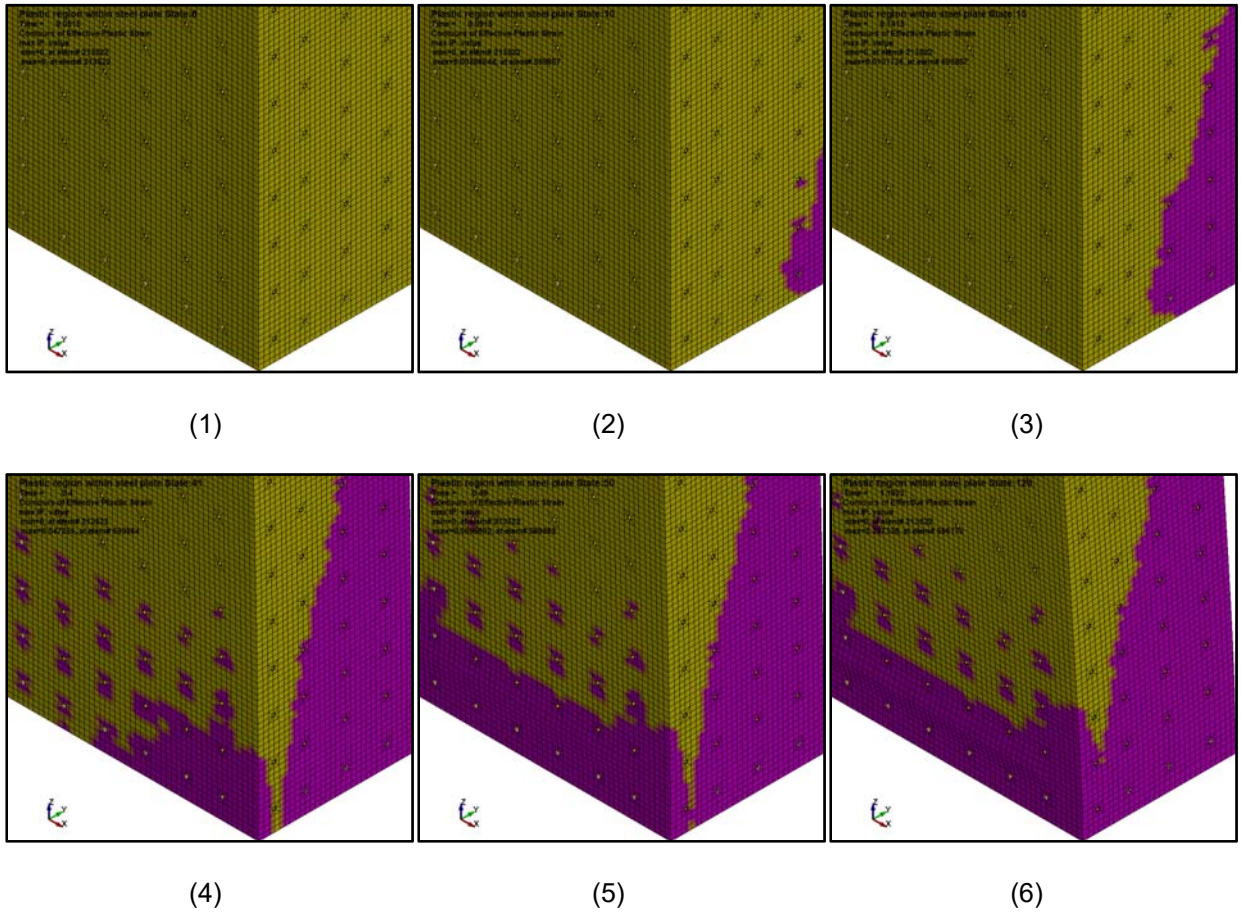


Figure 2-29. 3D view of progression of local buckling and plastic regions at the bottom of the flange under negative drifts (East elevation).

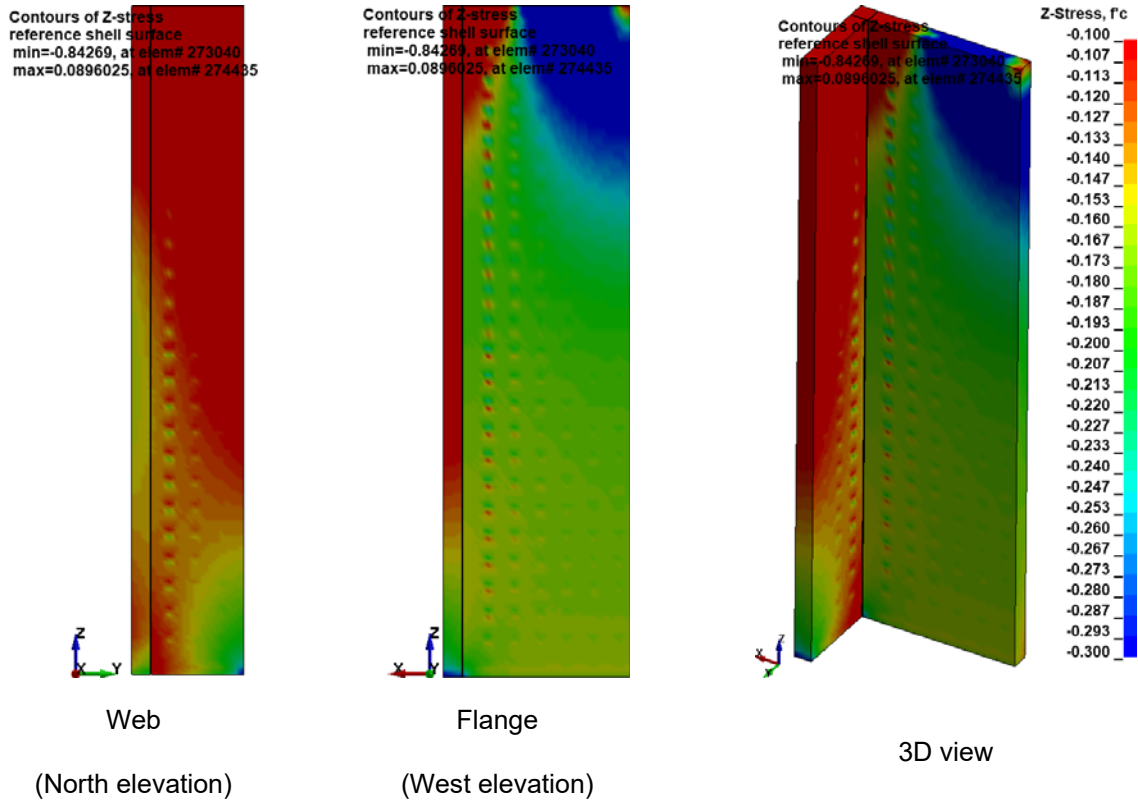


Figure 2-30. Vertical (Z direction) stress field on the concrete core under axial loading (normalized by f'_c).

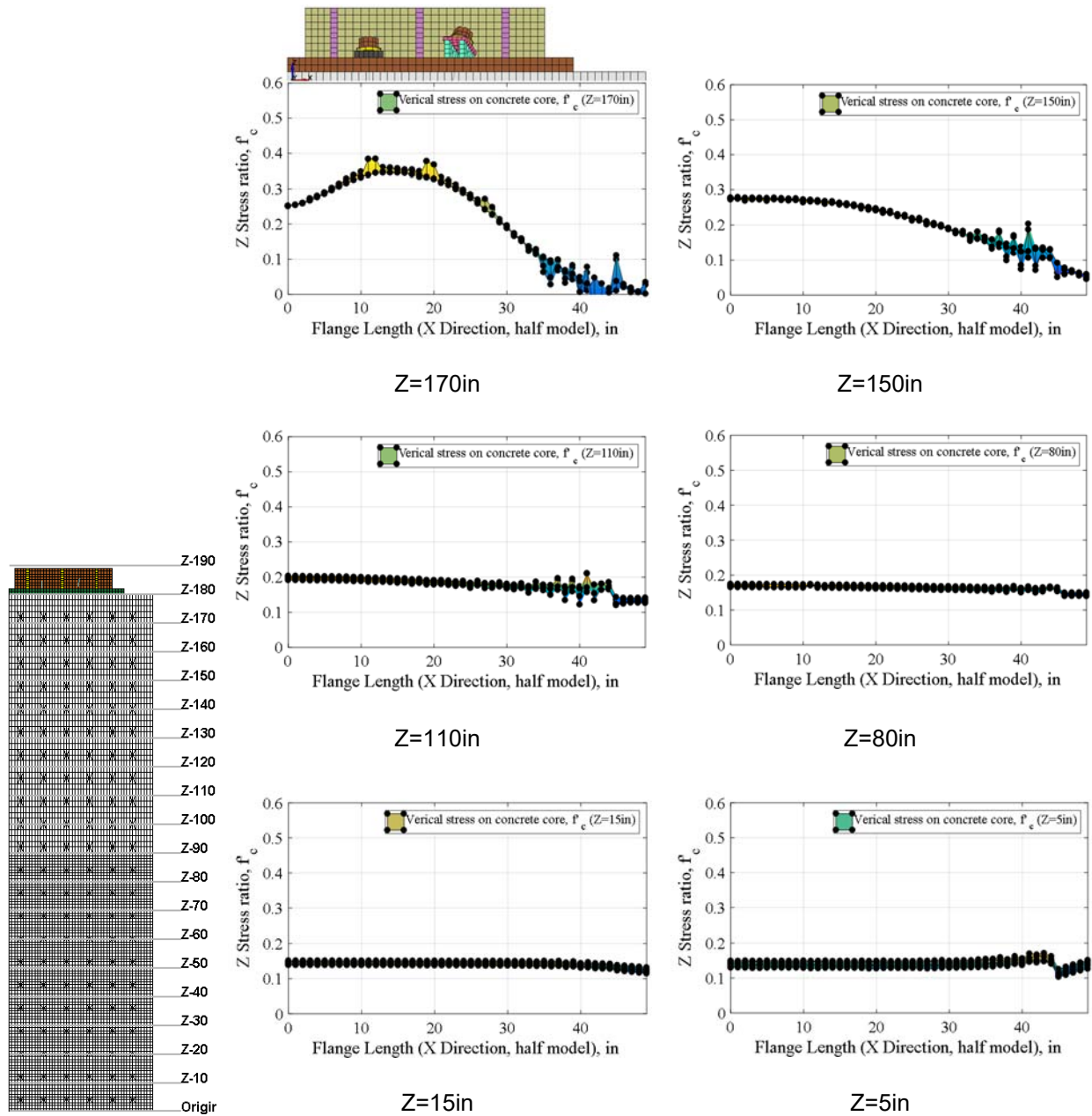


Figure 2-31. Vertical stress distribution on the flange solid elements along the concrete core (normalized by f'_c)

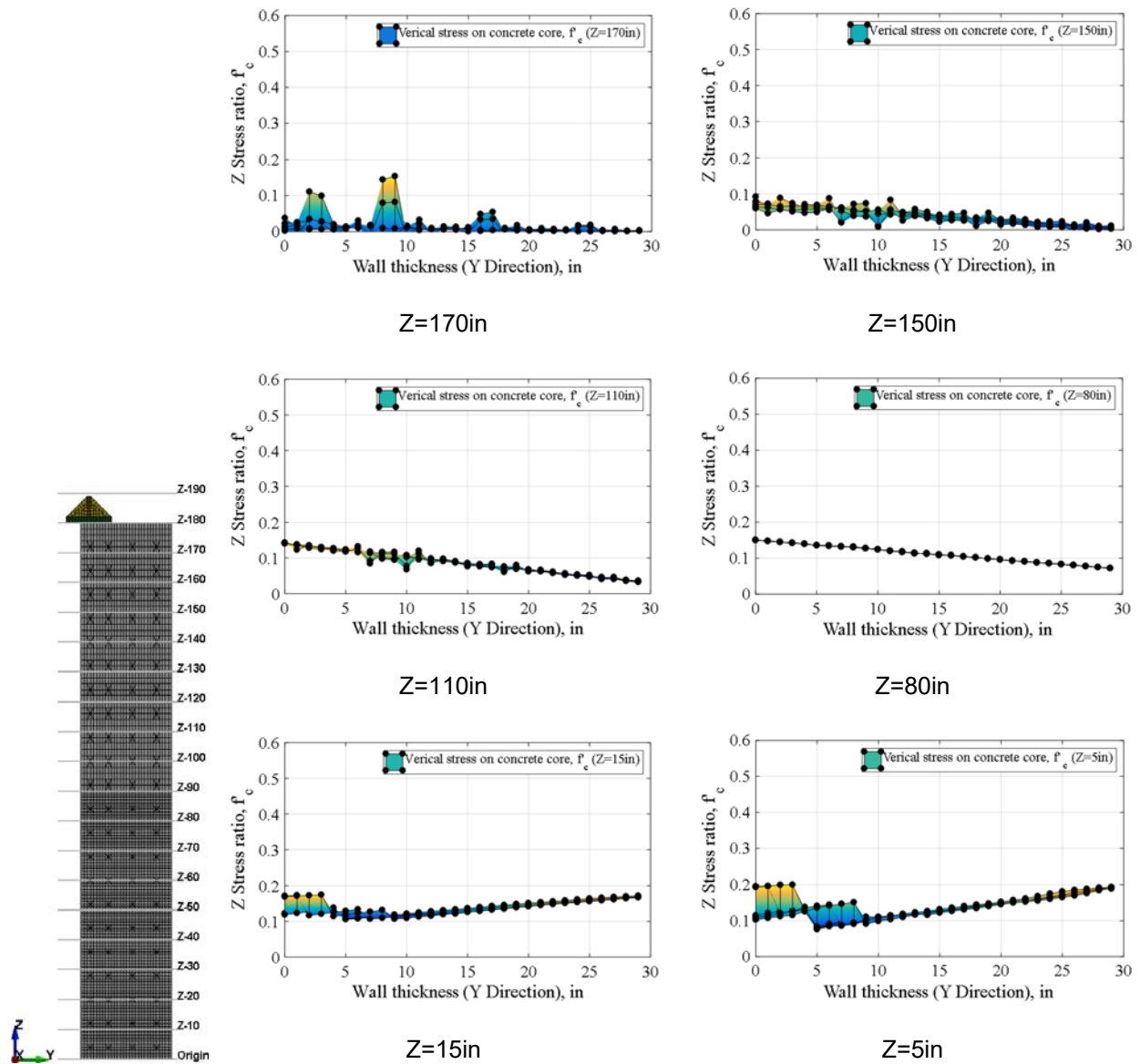


Figure 2-32. Vertical stress distribution on the web solid elements along the concrete core (normalized by f'_c)

2.3 Final Design

2.3.1 Updated Initial Design

The above designed C-shape C-PSW/CF testing program and test specimens were submitted to the Project Review Panel (PRP) for its review and comments. For convenience, the properties of the initially designed base C-shape specimen are repeated in Table 2-4. Based on the discussion between the research team and the PRP at that time, it was decided to modify the C-shape C-PSW/CF testing program and test specimens based on the following modified objectives:

- The steel-to-concrete ratio of the cross-section had to less than 4.5%.
- The applied axial load ratio (i.e., the ratio of applied axial load to the crushing load of the concrete core) could be reduced to approximately 25% (even though a value of 30% was more desirable). This made it possible to select larger dimensions for the web and flange thickness in order to reduce the steel ratio in these parts. (Note: To allow investigating the effect of larger axial stresses on behavior, it was decided that specimens having T-shape cross-sections corresponding to half of the C-shape specimen would be tested subsequently – results from these tests will be provided in a separate report).
- Dimensions of the specimen should be proportional to those of the representative prototype cross-section provided by the PRP. Dimensions of the prototype are provided in Table 2-4.

The material-based $P - M_p$ interaction curve for prototype cross-section (also referred to as the prototype model) is shown in Figure 2-33a. The corresponding Plastic Neutral Axis (PNA) locations are also shown in Figure 2-33b for various levels of compressive axial load on the cross-section. Also, the change in the steel face plate's maximum strain during a half cycle between maximum and minimum curvatures of 4 and 8 times the curvature corresponding to initial yield under positive moment are shown in Figure 2-34. These values were calculated using Equations (2.2) and (2.3) and Figure 2-35.

$$\Delta\epsilon_{(at\ web\ side)} = |\epsilon_{wc}| + |\epsilon_{wt}| \quad (2.2)$$

$$\Delta\epsilon_{(at\ flange\ side)} = |\epsilon_{fc}| + |\epsilon_{ft}| \quad (2.3)$$

To test C-shape walls in the laboratory, the dimensions of the prototype model needed to be scaled down. The thickness of the steel plates dictated the geometric scale factor of the specimens, considering that the structural steel plate thickness to use should not be less than $3/16in$. Using this plate thickness, the scale factor is equal to $3/8$. The dimensions and properties of the geometrically scaled specimen are shown in Table 2-4. Figures 2-36 and 2-37 show the $P-M_P$ interaction curve, location of PNA, and strain changes in the steel face plate under various axial load ratio for the scaled cross-section, respectively.

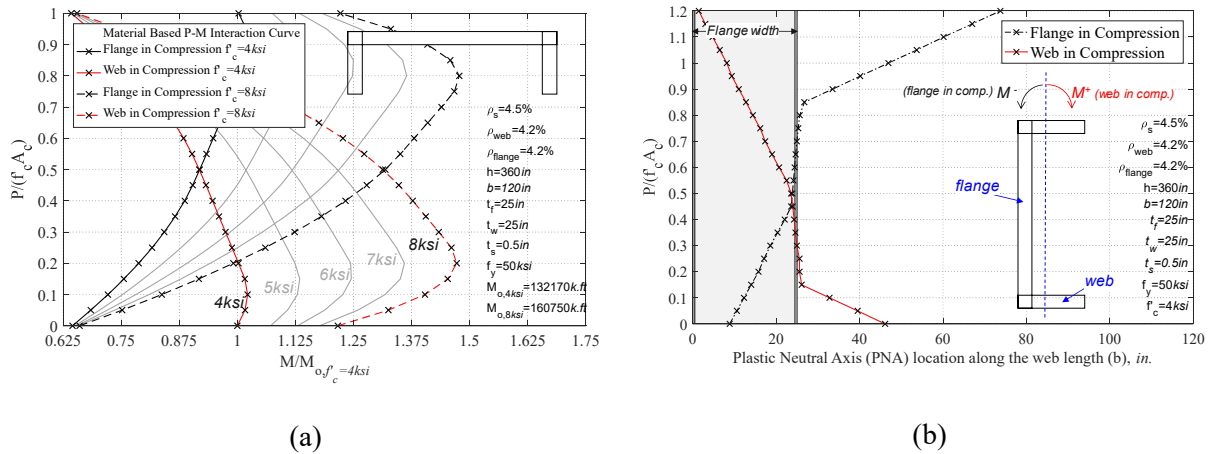


Figure 2-33. (a) P-M interaction curve for prototype model; (b) P-PNA curve for prototype model

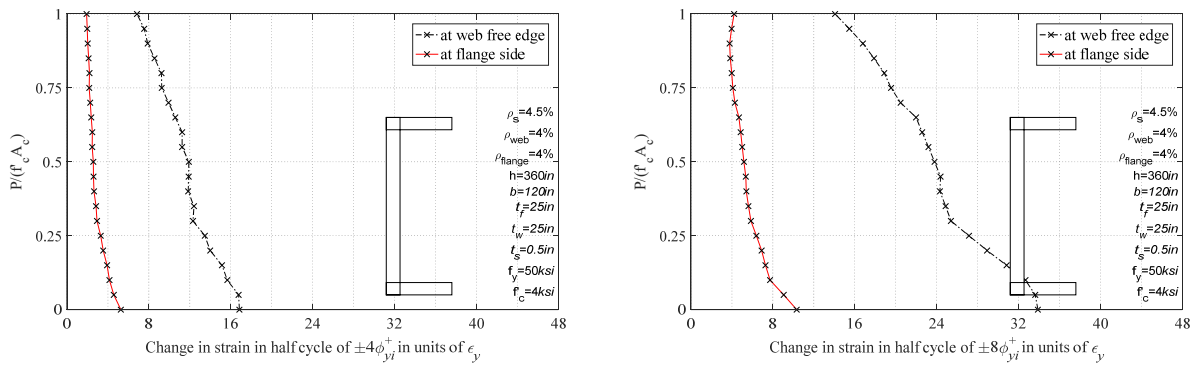


Figure 2-34. Change in the steel plate strain in half of a cycle for prototype model

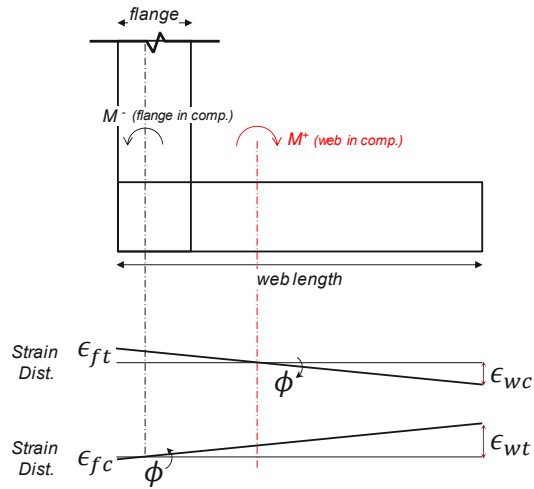


Figure 2-35. Definitions of maximum and minimum strains on the web and flanges at a certain positive or negative curvature

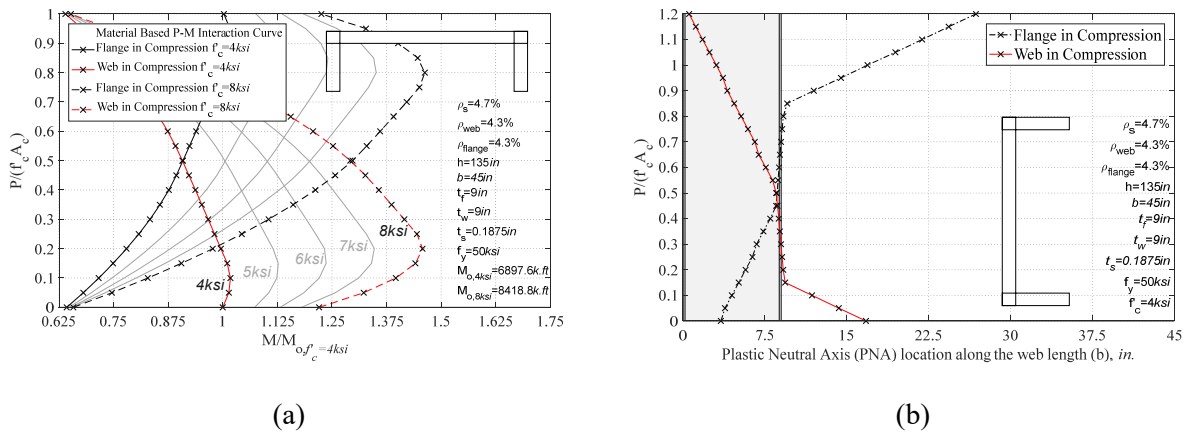


Figure 2-36. (a) P-M interaction curve for prototype model; (b) P-PNA curve for geometrically scaled model

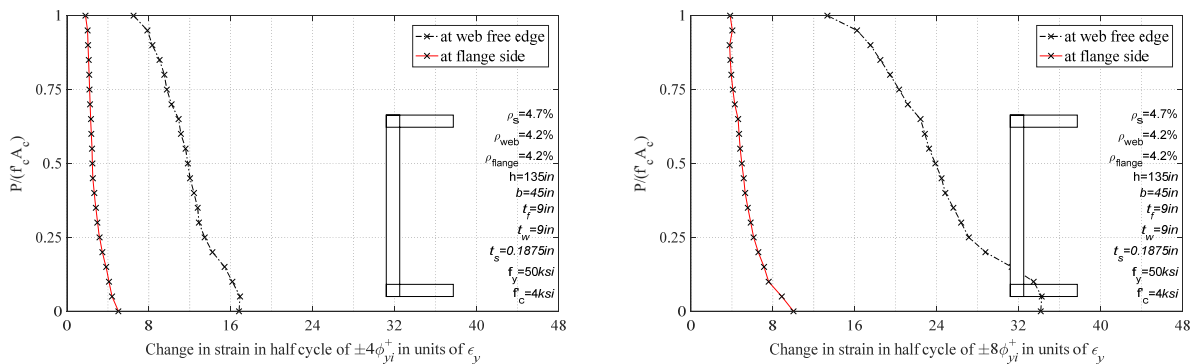


Figure 2-37. Change in strain in half of a cycle for geometrically scaled model

Comparing these figures with the ones corresponding to the prototype model shows that the scaled specimen and prototype models have similar behaviors. However, as presented in Table 2-4, the maximum axial load ratio that can be applied using the vertical actuators in the SEESL on this cross-section is 12%, which was less than the desirable axial load ratio for the testing program. Also, the foundation size that would have been required for the testing of such specimen would have been very large and the construction and recycling costs excessive. Therefore, the option of testing a geometrically scaled specimen couldn't be

considered in the testing program. Instead, the specimens were designed with cross-section ($\gamma=b/h$), web ($\beta=t_w/b$), and flange ($\alpha=t_f/h$) aspect ratios within $\pm 35\%$ of those from the prototype model (i.e., $\gamma_p=0.31$, $\beta_p=0.28$, and $\alpha_p=0.06$). Figure 2-38 shows the definition of these cross-sectional aspect ratios. Also, the updated specimens were designed to have flexural strength approximately equal to the initially designed specimens in order to keep the dimensions of the foundation un-changed.

Figure 2-39 shows about 15000 possible cross-sections that fall within the mentioned constraints. The rectangular box shown in this figure, indicates the boundaries of the imposed cross-sectional constraints. Figure 2-40 shows the cross-section of the selected final design and its position on the foundation. The final design was chosen from the points that are located inside the box shown in Figure 2-39. Note that the final dimensions were chosen considering that none of the DYWIDAG bar locations shown in Figure 2-40 were blocked by the cross-section of the specimen, which further limited the possible choice of specimens down to only a few nearly similar options. The dimensions and properties of the resulting updated specimen are shown in Table 2-4.

Figures 2-41 to 2-43 show the $P-M_p$ interaction curve, location of PNA, and strain changes in the steel face plate under various axial load ratio for the scaled cross-section, respectively. Figure 2-44 shows the $P-M_p$ interaction curve for variations of concrete uniaxial compressive strength between 4 and 6ksi and steel face plate yield strength between 50 and 60ksi. The values of concrete strength and steel yield for test specimen and the day of test were expected to be within these considered ranges.

The test setup including the axial loading system and lateral loading system for the C-shape specimens remained similar to what was presented above. Upon submission of the detailed drawings by the research team, the steel fabricator who detailed and erected the steel for the specimens develop a revised set of drawings identical except for one change in the wall-to-foundation connection detail where the doubler plate in the part of the wall embedded into the footing was replaced by a thicker plate instead. The updated details and drawings of the C-shape specimen are presented in Appendix C of this report.

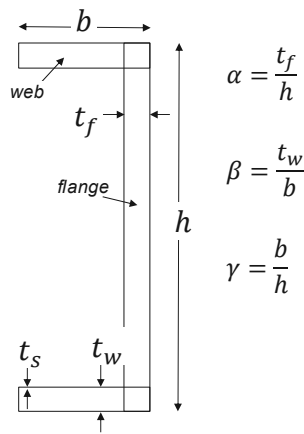


Figure 2-38. Cross-sectional aspect ratios

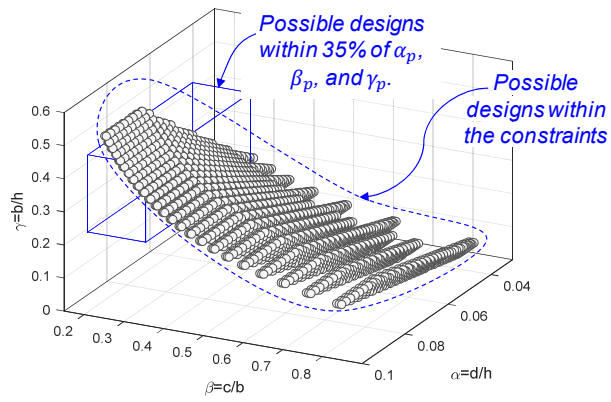


Figure 2-39. Possible designs within the existing objective constraints

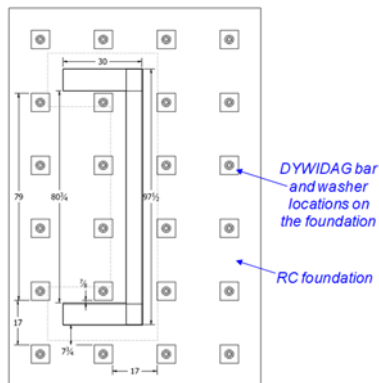


Figure 2-40. Position of the wall on the foundation plan

Table 2-4. Properties of the C-shape Specimen

Wall Parameters	Units	Prototype	Initial Specimen	Updated Specimen
Wall Height, H	<i>in.</i>	-	166	166
Flange length, h	<i>in.</i>	360.0	100	97.5
Web length, b	<i>in.</i>	120.0	30.0	30.0
Steel plate thickness, t_s	<i>in.</i>	1/2	3/16	3/16
Flange thickness, t_f	<i>in.</i>	25.0	5.375	6.0
Web thickness, t_w	<i>in.</i>	25.0	5.375	8.375
Tie bar spacing (vertical and horizontal)	<i>in.</i>	12	8	6
Tie bar diameter	<i>in.</i>	1	5/8	7/16
Wall aspect ratio (height to web), H/b	-	-	5.53	5.53
Cross-section aspect ratio, $\gamma=b/h$	-	0.33	0.30	0.31 ($=\gamma_p$)
Flange aspect ratio, $\alpha=t_f/h$	-	0.07	0.054	0.06 ($=\alpha_p$)
Web aspect ratio, $\beta=t_w/b$	-	0.21	0.18	0.28 ($=\beta_p$)
Steel area, A_s	<i>in.</i> ²	622	62.0	61.8
Concrete area, A_c	<i>in.</i> ²	13128	741.0	925.2
Gross area, A_g	<i>in.</i> ²	13750	802.0	987
Reinforcement ratio of web, ρ_{web}	%	4.2	8.0	4.5
Reinforcement ratio of flange, ρ_{flange}	%	4.2	6.9	6.3
Reinforcement ratio, ρ_s	%	4.5	6.9	6.3
Yield strength, F_y	<i>ksi</i>	50	50.0	50
Concrete strength, f'_c	<i>ksi</i>	6	4	4-6
Crushing load of concrete, $A_c f'_c$	<i>kips</i>	78770	2964	3700-5550
Max. achievable axial load, $P/A_c f'_c$	%	-	27	15-22

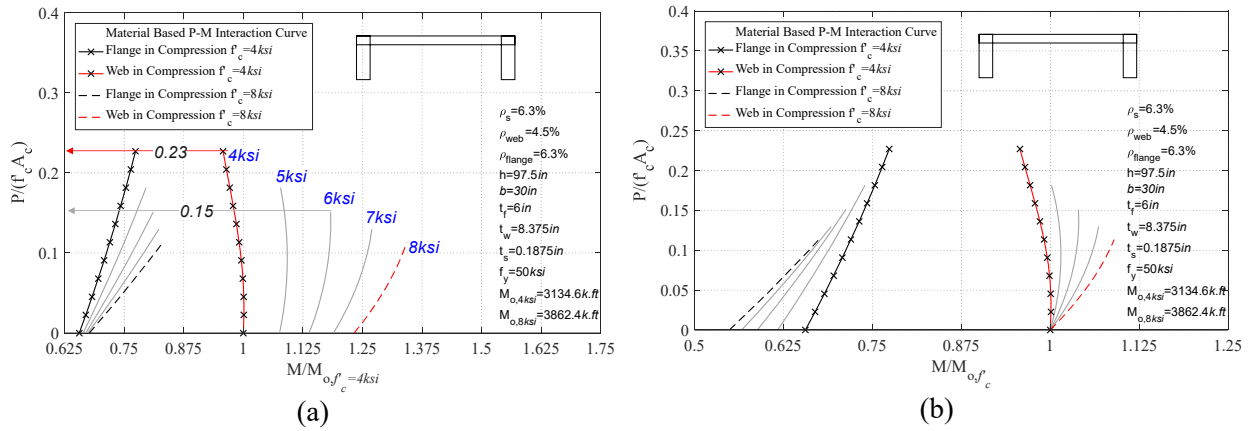


Figure 2-41. (a) P-M interaction curve for the updated specimen; (b) Normalized P-M curve for the updated specimen

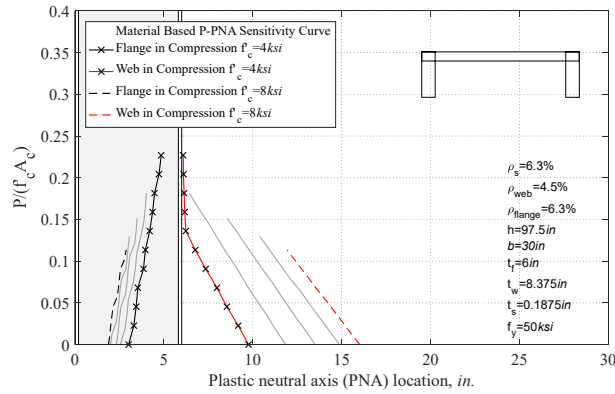


Figure 2-42. P-PNA curve for the updated specimen

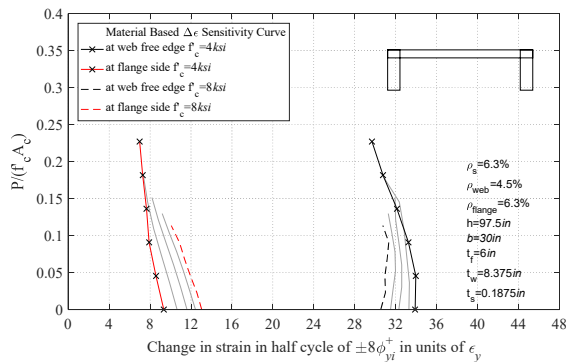


Figure 2-43. Change in the steel plate strain in half of a cycle for the updated specimen

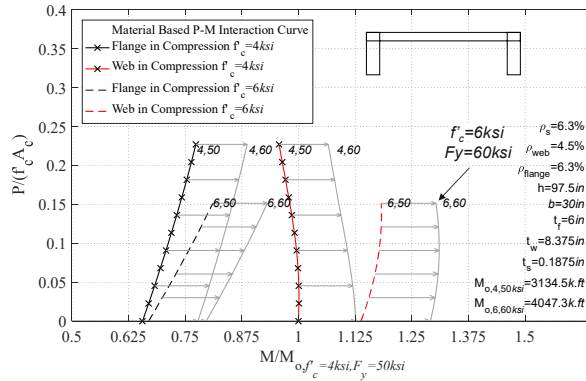


Figure 2-44. P-M interaction curve comparison for variations of material properties

2.3.2 Note on Relationship of T-Shape C-PSW/CF Specimens

Although testing of T-shaped C-PSW/CF is the subject of a separate report, some aspects of the intended T-shape wall tests are worth mentioning here. First, the intent of those separate tests is to subject the walls to higher axial load ratio of up to 30% and give valuable experimental data on the behavior of these walls under these conditions. For comparison, the maximum axial load ratio that was possible to apply on the C-shape specimen was 15% and 22% of $A_c f'_c$, for f'_c of 6 and 4ksi, respectively (which is still significant). As a result, it was foreseen when the final C-shaped walls were designed and ready to be tested, that the combined testing of T-shaped and C-shaped would allow to explore cyclic inelastic behavior for a range for different values of axial load ratio, following the testing matrix shown in Figure 2-45.

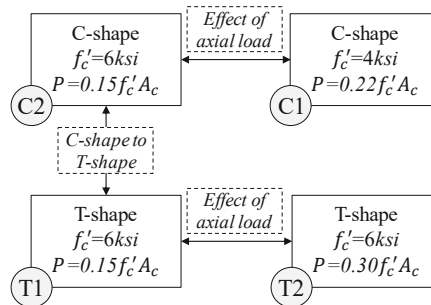


Figure 2-45. C-PSW/CF Specimens testing program

The intent was to design and test T-shape walls having a flange of half of the length of the C-shape wall and similar web dimensions. Figure 2-46 shows the dimensions of the resulting T-shape specimen cross-section. Using a similar test set-up to the one shown above, an axial load ratio of 30% can be applied on such a T-shape specimen with concrete infill f'_c of $6ksi$. The T-shape specimen was expected to have similar resisting characteristics as the C-shape specimen under positive and negative moments. However, note that local buckling of the steel plates along the flange at the bottom of the wall would have different shape compared to C-shape specimen. This is because of the shorter available free cross length between the steel plates of the web that are welded to the interior face of the flange plates and both ends of the flange, as shown on Figure 2-46.

Figures 2-47 to 2-49 show the $P-M_p$ interaction curve, location of PNA, and strain changes in the steel face plate under various axial load ratio for the scaled cross-section, respectively, which compares well with the above results.

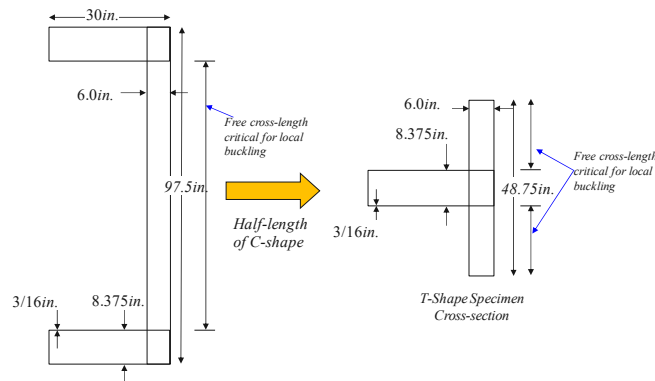
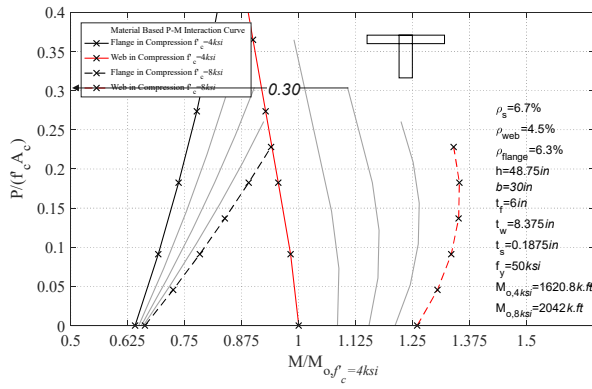
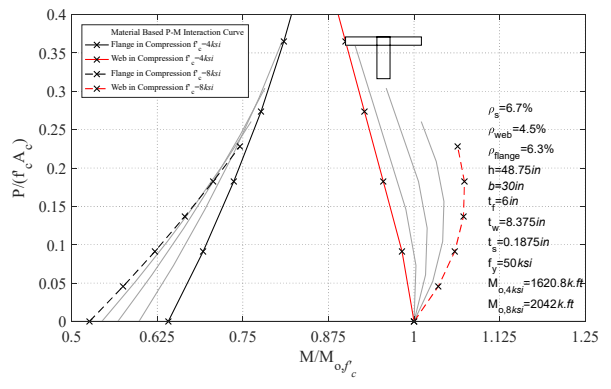


Figure 2-46. T-shape specimen cross-section dimensions



(a)



(b)

Figure 2-47. (a) P-M interaction curve for the T-shape specimen; (b) Normalized P-M curve for the T-shape specimen

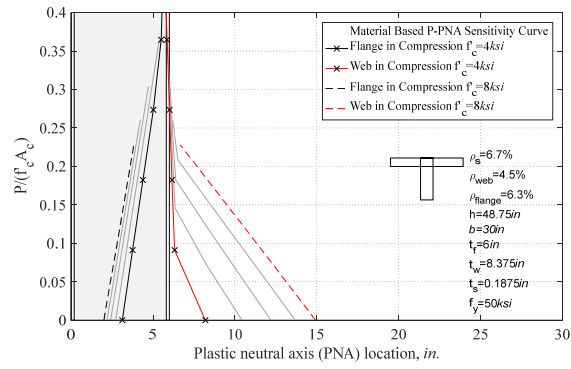


Figure 2-48. P-PNA curve for the T-shape specimen

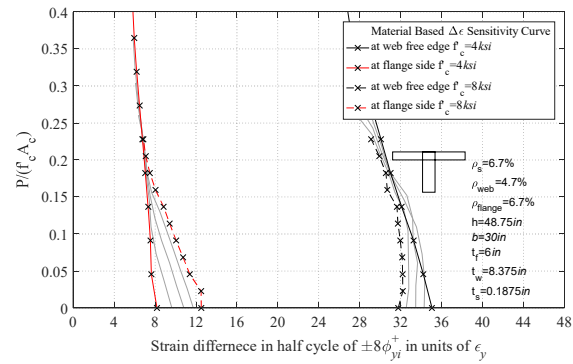


Figure 2-49. Change in the steel plate strain in half of a cycle for the T-shape specimen

2.3.3 Preliminary finite element analyses and results of C-shaped specimens

The details of the developed finite element model for the C-shape specimen are shown in Figures 2-20 and 2-51. Figure 2-52 shows preliminary monotonic and cyclic analyses of the C-shape specimen (under no axial load). These results were used to develop the testing protocol described in the subsequent sections.

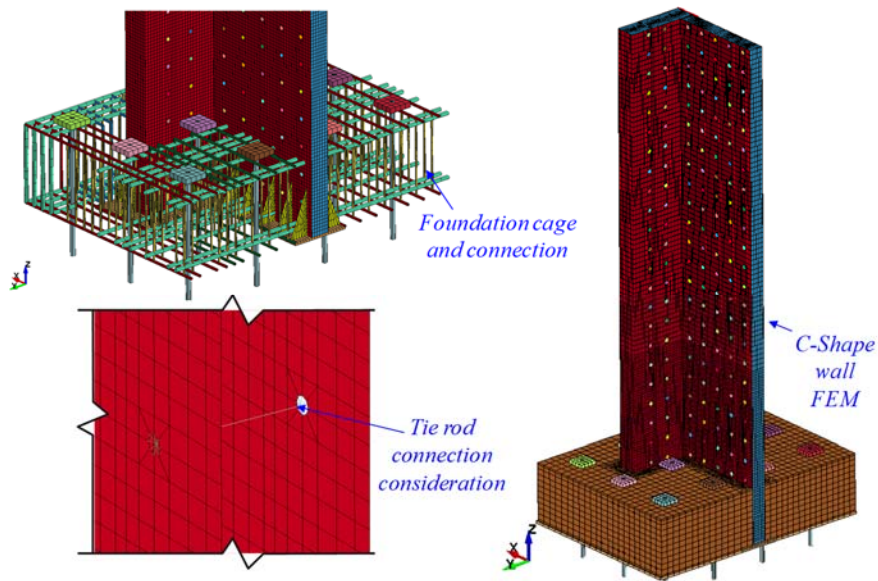


Figure 2-50. Details of the finite element model of C-shape specimen

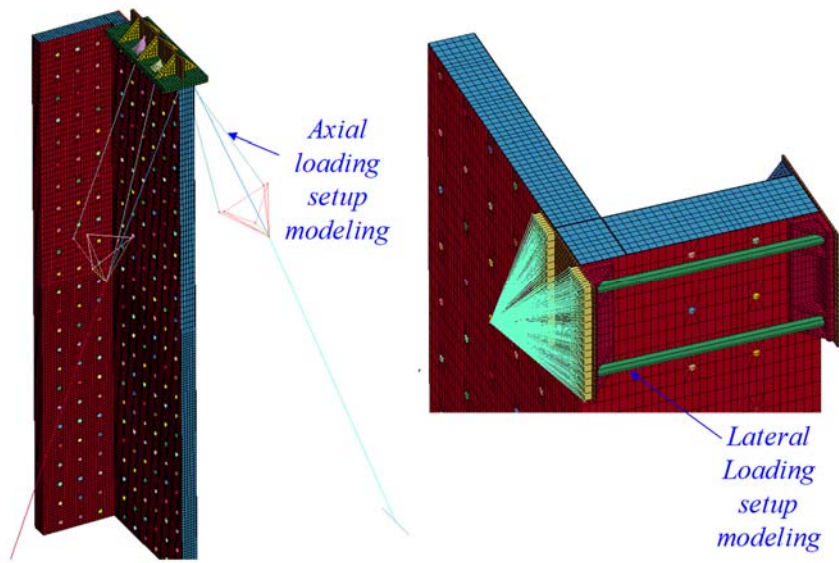


Figure 2-51. Details of the finite element model of the C-shape specimen's Axial Loading Setup (ALS) and Lateral Loading Setup (LLS)

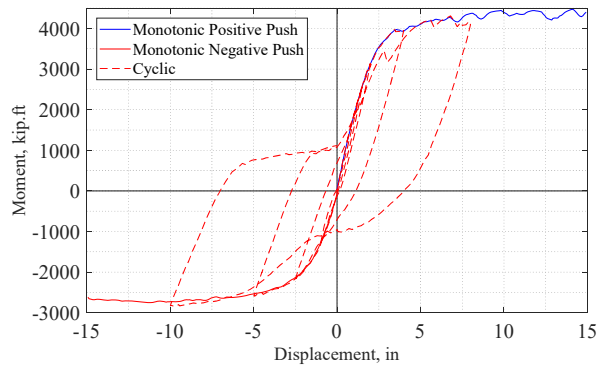


Figure 2-52. Preliminary monotonic and cyclic analyses of C-shape specimen

“This Page Intentionally Left Blank”

SECTION 3

TESTING OF C-SHAPED COMPOSITE PLATE SHEAR WALLS- CONCRETE FILLED (C-PSW/CF)

3.1 General

This section presents the results for the two C-Shape Concrete Filled-Composite Plate Shear Walls (C-PSW/CFs) tested. The properties of tested specimens are presented in Section 3.2. Details of their fabrication are provided in Section 3.3, with material properties of concrete and steel for both specimens presented in Section 3.4. Loading protocol and application of axial loading is discussed in Sections 3.5 and 3.6. Finally, step-by-step description of the tests, behaviors observed, and analysis of results are in Section 3.7.

3.2 Properties of Tested Specimens

Table 3-1 summarizes many relevant dimensions and properties for the two C-shapes specimens, namely: overall dimensions; tie bar spacing and diameter; wall aspect ratios; steel, concrete and gross areas; reinforcement ratios; yield strength and concrete compressive strength, and target axial loads.

Table 3-1. Properties of the C-shape Specimens

Wall Parameters	Units	Prototype	C1	C2
Wall Height, H	<i>in.</i>	N/A	166	166
Flange length, h	<i>in.</i>	360.0	97.5	97.5
Web length, b	<i>in.</i>	120.0	30.0	30.0
Steel plate thickness, t_s	<i>in.</i>	1/2	3/16	3/16
Flange thickness, d	<i>in.</i>	25.0	6.0	6.0
Web thickness, c	<i>in.</i>	25.0	8.375	8.375
Tie bar spacing (vertical and horizontal)	<i>in.</i>	12	6	6
Tie bar diameter	<i>in.</i>	1	1/2	1/2
Wall aspect ratio (height to web), H/b	N/A	N/A	5.53	5.53
Cross-section aspect ratio, $\gamma=b/h$	N/A	0.33	0.31 ($=\gamma_p$)	0.31 ($=\gamma_p$)
Flange aspect ratio, $\alpha=d/h$	N/A	0.07	0.06 ($=\alpha_p$)	0.06 ($=\alpha_p$)
Web aspect ratio, $\beta=c/b$	N/A	0.21	0.28 ($=t_w$)	0.28 ($=t_w$)
Steel area, A_s	<i>in.</i> ²	622	61.8	61.8
Concrete area, A_c	<i>in.</i> ²	13128	925.2	925.2
Gross area, A_g	<i>in.</i> ²	13750	987	987
Reinforcement ratio of web, ρ_{web}	%	4.2	4.5	4.5
Reinforcement ratio of flange, ρ_{flange}	%	4.2	6.3	6.3
Reinforcement ratio, ρ_s	%	4.5	6.3	6.3
Yield strength, F_y	<i>ksi</i>	50	55.4	55.4
Concrete strength, f'_c	<i>ksi</i>	6	4.5	5.1
Crushing load of concrete, $A_c f'_c$	<i>kips</i>	78770	4163	4719
Target axial load ratio	%	N/A	22	15

3.3 Preparation of Specimens

According to the constraints imposed by the SEESL lab equipment and PRP that were described in Section 2.3, in order to reach the target axial load ratio of $0.22 A_c f'_c$ using the capacity of the available actuators in the SEESL lab, the first C-shape specimen (i.e., Specimen C1) had to be tested with a concrete strength equal to $4ksi$ in its core. In this regard, at regular interval in the days following pouring of the concrete in the first wall specimen (i.e., Specimen C1), concrete cylinders were tested and the resulting concrete strength of Specimen C1 was tracked until it reached $4ksi$; testing started the day after this strength was reached. On the other hand, the concrete was allowed to cure for more than 28 days in order to reach its expected strength of $6ksi$ for the second specimen (i.e., Specimen C2); although it was the intent to reach a strength of $6ksi$ to apply 15% of concrete force as an axial load, the maximum concrete strength reached $5.1ksi$ after 30 days, with no significant strength gains after a period of 21 days, and it was decided to proceed with testing (adjusting the axial load to retain the $0.15 A_c f'_c$ axial load target).

For each one of the specimens, the formwork for the concrete footing was first constructed. PVC pipes were placed inside the footing on a $2ft.$ center-to-center grid at the locations where DYWIDAG bars were to be later used to connect the specimens to the SEESL strong floor. The reinforcing cage of the foundation was tied outside the formwork and then placed in the formwork. Then the empty module of the wall was positioned into the formwork, clearing the reinforcing bar cages. Additional #10 bars were then ran through the wall's flange (in pre-drilled holes) to achieve continuity of the horizontal reinforcement in the cage in the East-West direction. The pre-drilled holes on the flange through which the #10 bars passed were sealed to prevent the flow of wet concrete between the wall and the foundation.

For Specimen C1, the concrete of the foundation and wall was poured separately and on different days. As it was mentioned before, the strength of the concrete poured in the wall had to be monitored closely in order to not exceed the target strength of $4ksi$, but a stronger concrete for the foundation was acceptable.

Note that many of the tasks required to complete the test setup and instrumentation could only be done after pouring the foundation concrete. Therefore, the test setup preparation for Specimen C1 was scheduled such as to have a maximum 5-day window between the wall concrete pouring and the test day.

After one week from the foundation concrete pour, the foundation formwork was removed and the specimen was positioned (using the over-head crane) at its testing location in front of the SEESL strong wall. Finite element analysis was performed with the available concrete strength of the foundation to make sure that the foundation could resist the total specimen weight held from the lifting hooks placed near its mid-length (see Figure 1-2). Note that, a few minor surface cracks at the top surface of the concrete foundation were observed during the curing of the foundation. These cracks were considered to be insignificant and had no structural effect on the behavior of the specimen. The specimen was then post-tensioned to the strong floor using 24 DYWIDAG bars with $1\frac{3}{8}$ in. nominal diameter. The DYWIDAGs were post-tension with 130kips force, which was equal to 70% of their nominal yield load. Next, the strain gauges, displacement transducers, and other instrumentation were installed. The instrumentation plan for the C-shape specimens is presented in Appendix D. The wall concrete was poured after installation of the strain gages. The vertical test setup was assembled and attached afterwards. The lateral actuators were attached as a final step before testing the specimen.

By contrast, in preparation of Specimen C2, the concrete of the foundation and wall parts were poured within only a few days of each other; all remaining aspect of test set-up and instrumentation assembly for the test setup preparation were completed following the above sequence.

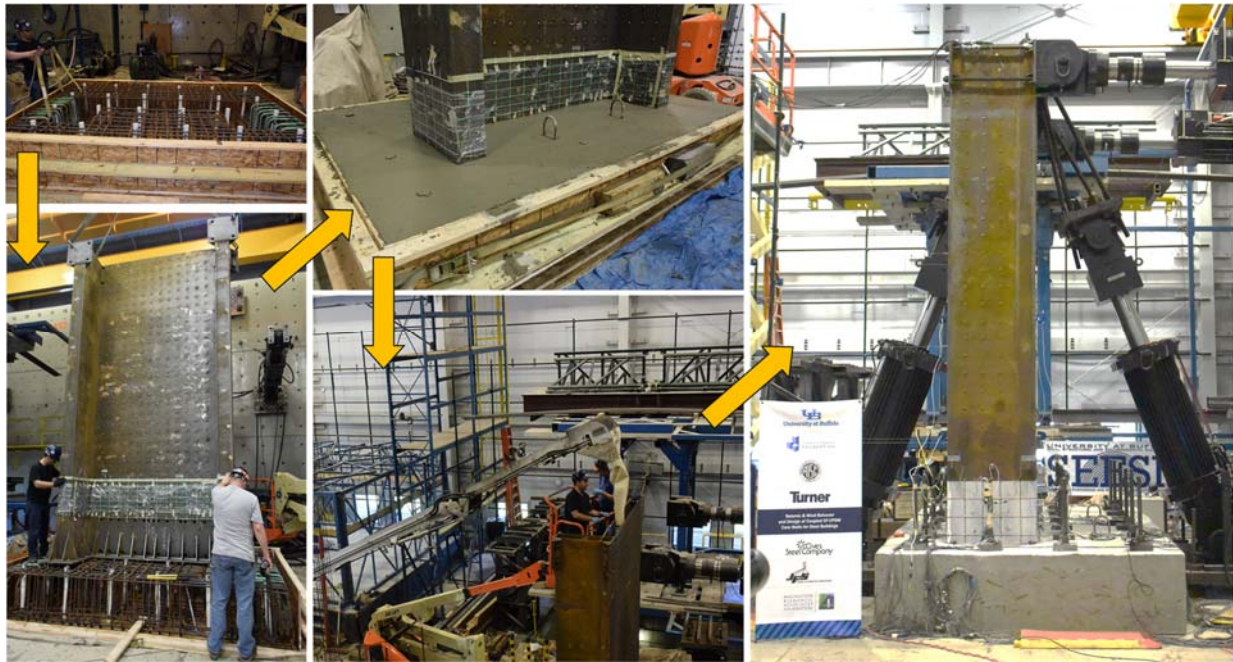


Figure 3-1. Construction sequence of specimens

3.4 Material Properties of Specimens

Three coupons for the steel used in the web and flange of the specimen (identified as p261 and p307, respectively in the shop drawings of the specimens presented in Appendix C5) were tested under uniaxial tension, for six coupon tests for each wall specimen. Results are presented in Figures 3-2 and 3-3. A572Gr50 steel was used in construction of the flange and web plates. However, no “yield plateau” was observed in the stress-strain behavior of the tested coupons. Using the 0.2% offset method, the yield strengths of the plates were determined to be 54.6 *ksi* and 56.2 *ksi* for web and flange plates of Specimen C1, and 52.65*ksi* and 57.79*ksi* for web and flange plates of Specimen C2, respectively. The average yield strengths of the plates are 55.4*ksi* for Specimen C1 and 55.2*ksi* for Specimen C2.

For concrete, fifteen 3in.×6in. and six 6in.×12in. cylinders were taken for each specimen on the day of concrete pouring from the concrete batches used for the foundation and the infill of the wall. This unusually large number of cylinders was taken to allow to keep track of concrete strength over time, to ensure that the concrete strength in the first C-Shape Wall would not significantly exceed 4 *ksi* on the day

of testing, to allow applying close to the target value of $0.22A_c f'_c$ as an axial load when using the vertical actuators at full capacity. The concrete strength obtained for Specimens C1 and C2 are $4.5ksi$ and $5.1ksi$, respectively.

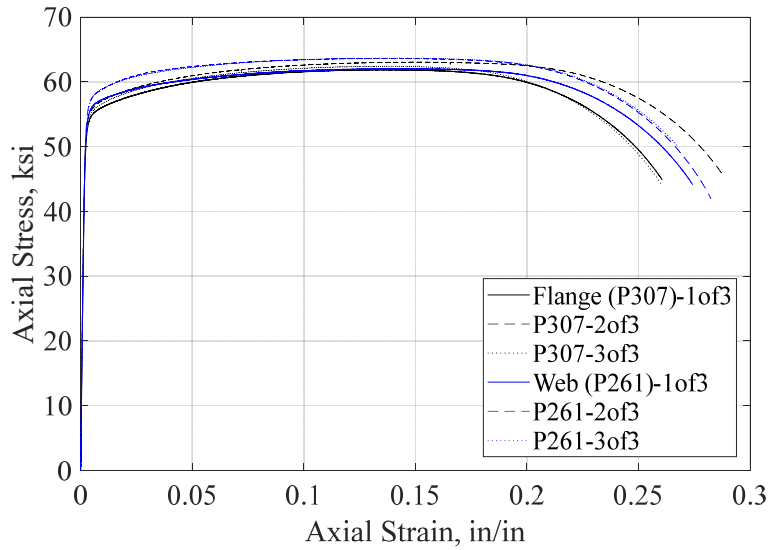


Figure 3-2. Coupon tests of steel plates at web (p261) and flange (p307) for Specimen C1.

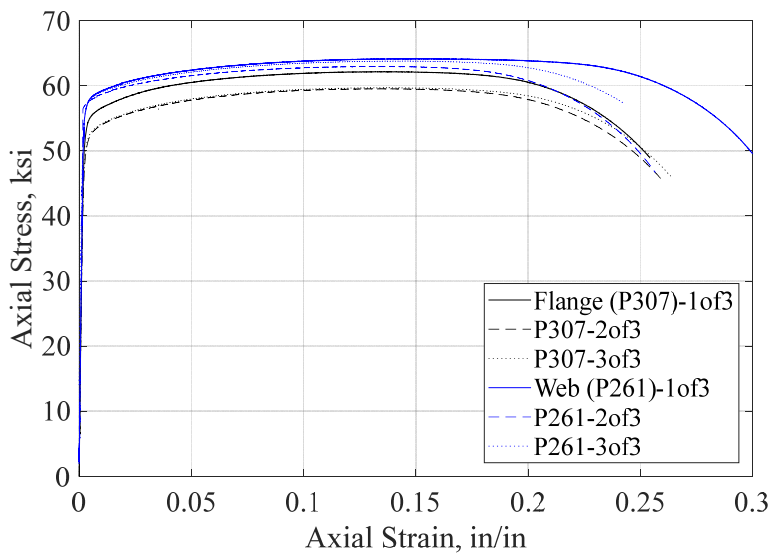


Figure 3-3. Coupon tests of steel plates at web (p261) and flange (p307) for Specimen C2.

3.5 Loading Protocol of C-Shape Specimens

The cyclic testing protocol was designed based on the yield displacements obtained from the Finite Element Analysis (FEA) of Specimen C1. The model was run based on the expected material behavior of the steel and concrete. The result of the average of steel coupon tests ($F_y = 55.4 \text{ ksi}$) was directly input into the model and the concrete strength was assumed to be 4 ksi . Figure 3-4 shows the result of pushover curves both in positive and negative direction and the bi-linear curve estimation for the pushover curves. The yield displacements (Δ_y) in positive and negative directions are 1 in. and 0.5 in. , respectively. However, the loading protocol was created based on yield displacements obtained from the estimated bi-linear curve estimation for both directions (Δ_y'), which are 1.75 in. in the positive direction and 1.5 in. in the negative direction as in Figure 3-4. To facilitate the comparison, both C-Shaped specimens were subjected to the same cyclic displacement loading protocol that was created for Specimen C1.

Up to the equivalent yield displacements ($+1.75 \text{ in.}/-1.5 \text{ in.}$) obtained from bi-linear estimation of pushover curves, specimens are cycled in force-controlled mode for the first 10 cycles. Beyond that, specimen is tested in displacement-controlled mode. The resulting loading protocol is shown in Figure 3-5. There are only two cycles per drift amplitude in force-controlled cycles. However, the number of cycles per drift amplitude in the displacement-controlled cycles is increased to three up to maximum capacity of specimens ($+5.25 \text{ in.}/-4.50 \text{ in.}$), and then the number of cycles is decreased to two for the subsequent cycles. Note that the original protocol contains only two cycles at 6% drift, but, as will be shown later, specimens were cycled repeatedly beyond that, as needed to observe the further progression of fracture. Drifts were limited to 6% for safety reasons, to keep the specimen stable upon substantial strength degradation.

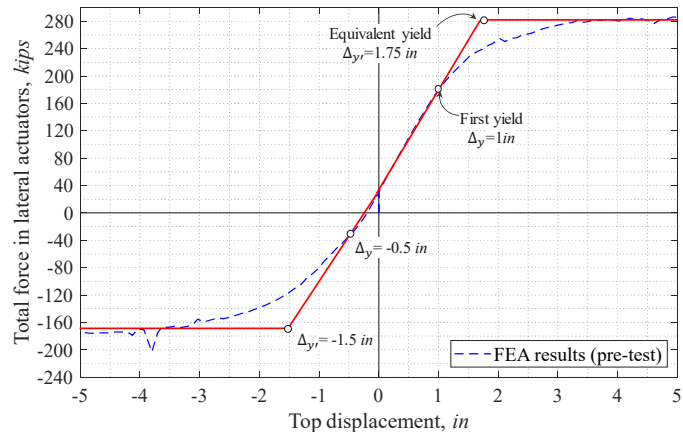


Figure 3-4. Pushover results of the FEA model of C1 specimen and bi-linear approximation of the curves in positive and negative directions.

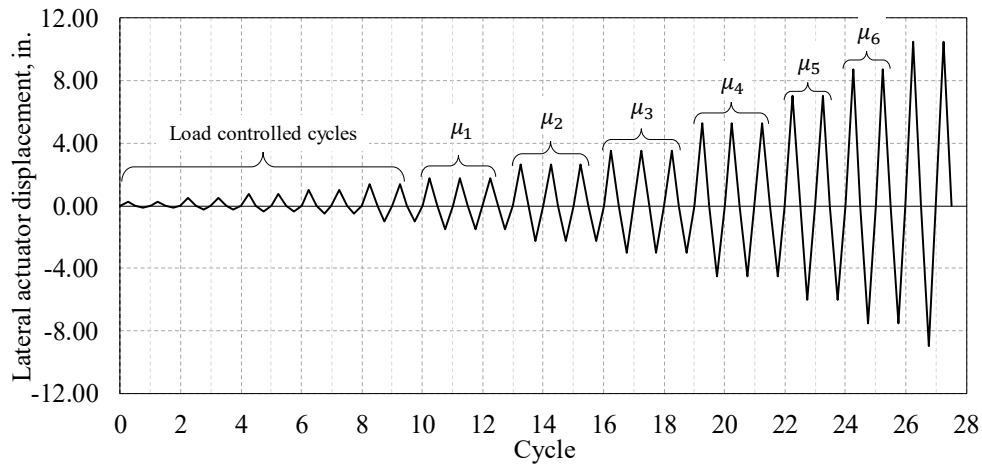


Figure 3-5. Loading protocol for C-Shaped specimens.

3.6 Application of Axial Loading on the C-Shape Specimens

The centroid of C-Shaped specimens is located at 9.11 in. from the flange. However, for practical reasons, the axial loading was applied centered on the top of flange rather than at the centroid. This resulted in a moment due to the eccentricity of the axial load, as shown in Figure 3-6, which was taken into account when post-processing the experimental results.

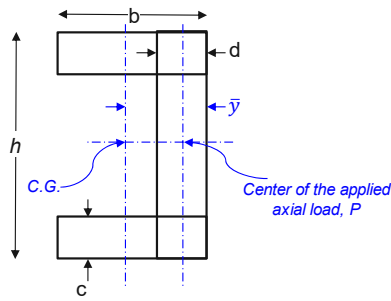


Figure 3-6. Location of centroid and center line of axial load for C-Shaped wall specimens.

Two options for applying the axial load, as part of the test protocol, were considered. In Option 1, before applying the axial loading, the horizontal actuators are locked at the initial point of zero horizontal displacement. By contrast, in Option 2, the lateral actuators are not locked. Option 1 was deemed preferable and chosen for this experimental program because, without locking the lateral actuator, the specimens could have moved laterally upon application of the axial load due to the moment created by the eccentricity of the axial load.

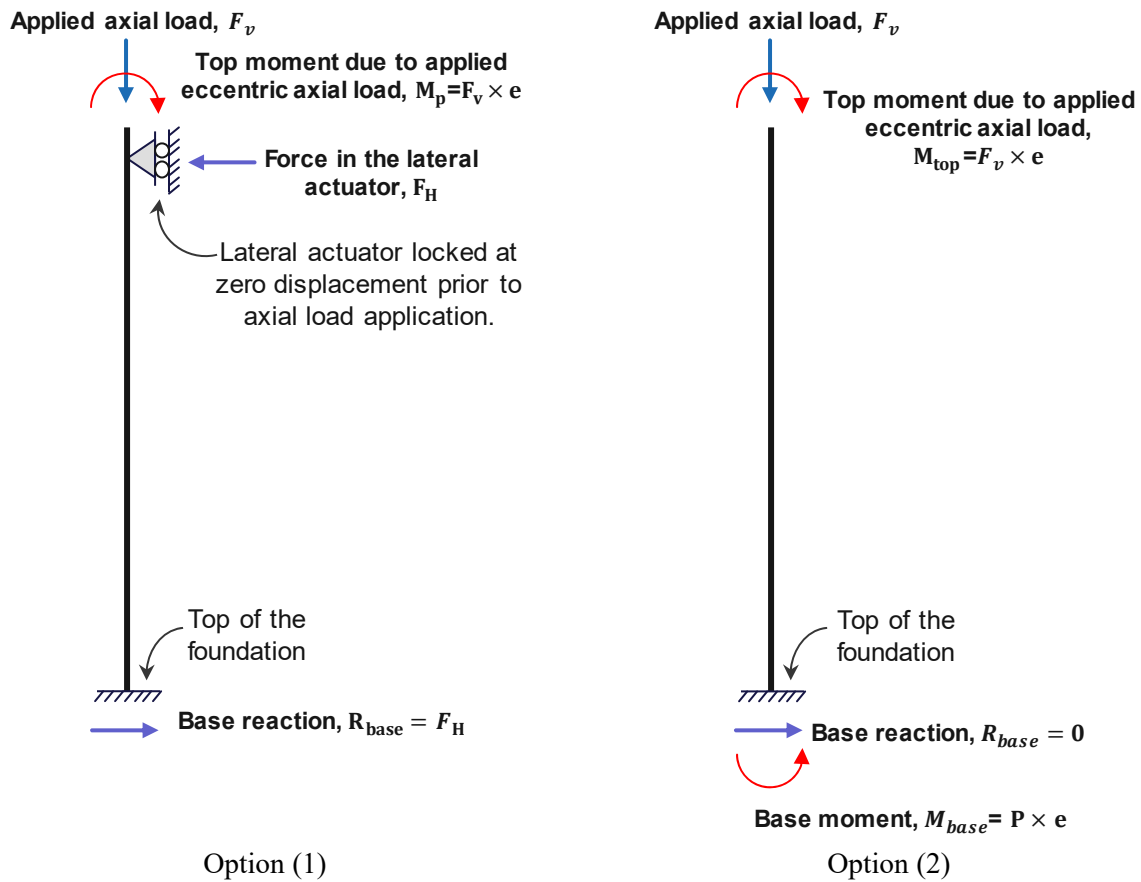


Figure 3-7. Two options for the testing scheme of C-Shape walls.

The vertical actuators were driven in a force-controlled mode such as to apply constant axial force to the specimen cross-section. The summation of the axial force in the vertical actuators was tracked during testing to verify that it remained constant throughout the tests, as shown in Figure 3-8. The distribution of axial strains across the cross-section were also tracked after engaging the vertical actuators, to verify that the cross-section was subjected to uniform stresses under the applied axial loading, even though loading was only applied to the flange. Results obtained from the strain gauges located in the plastic hinge region of the specimen confirmed that this was the case, as shown in Figure 3-9 for normalized axial strains across a cross-section at 17.4in. from the top of footing on Specimen C1.

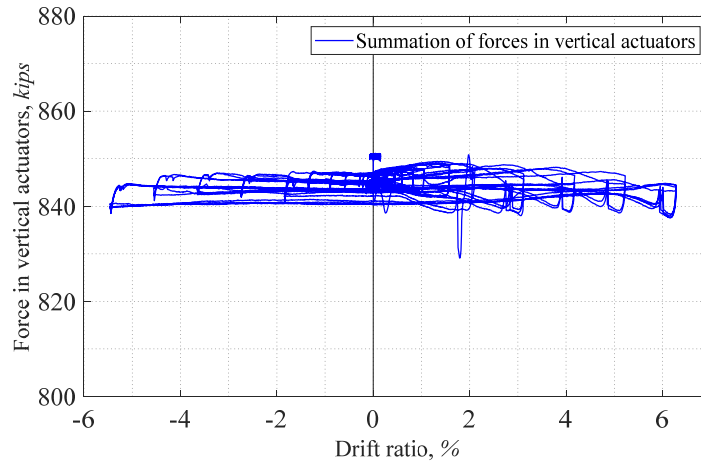


Figure 3-8. The axial force applied to C1 specimen during test

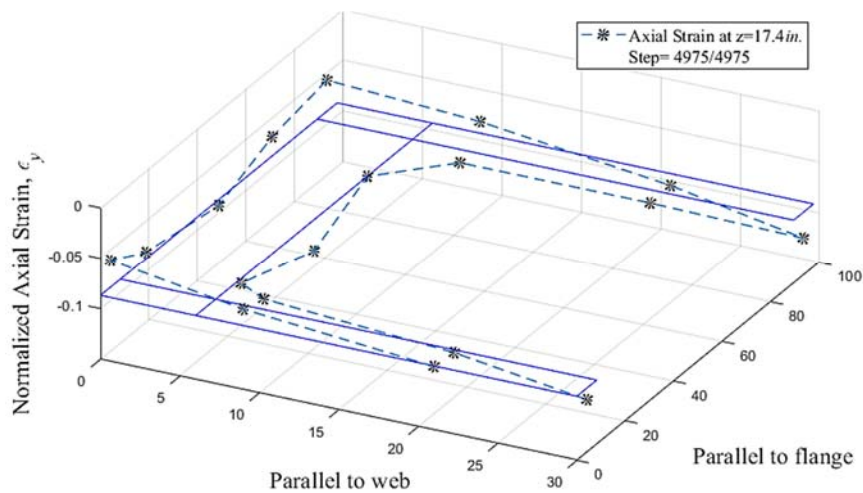


Figure 3-9. Normalized axial strains of the strain gauges at 17.4 in from the top of footing on Specimen C1

3.7 Test Observations and Results

Specimens C1 and C2 were tested under the axial and cyclic loading protocols discussed in Section 3.5. As discussed before, the cyclic lateral displacement testing protocol was designed based on a computation of the yield points (for both positive and negative bending) obtained from finite element analysis of Specimen

C1. To facilitate comparison of results, Specimen C2 was also subjected to the same cyclic lateral displacement history as Specimen C1.

3.7.1 Specimen C1

Testing started by loading the vertical actuators while the horizontal actuators were held at zero displacement. The forces in the vertical actuators were increased up to their full capacity. The vertical actuators that were used for applying the axial load on the specimen were two MTS ASSY-243.90T actuators with a nominal capacity of 450*kips* in tension. However, it turned-out that the controller device at SEESL lab only allowed the actuators to be loaded up to 425*kips*, which resulted in application of 19% of $A_c f'_c$ on the cross-section of the C-shape wall (note that the actuators are regularly calibrated, so the inability to apply the full 450 *kips* could not be resolved). Then, the lateral actuators were loaded to apply the lateral cyclic displacements at the top of the specimen according to the pre-determined cyclic protocol. The first cycle of the loading protocol, at the displacement of $\Delta_y/4$, enabled to verify if all the attached data recording instruments were working properly and that no un-foreseen deficiencies existed in the specimen and the test setup. None of the components of steel plates of the specimen experienced any buckling or yielding and the same behavior was observed in all of excursions cycles at amplitudes of $\Delta_y/2$, and $3\Delta_y/4$.

At the positive peak of the estimated displacement of Δ_y , the strain recorded at the farthest end of the web was -1940.6 $\mu strain$, which is 101.6 % of the average measured yield strain (i.e., 1910 $\mu strain$) of the steel plate based on the coupon tests. The strain recorded at the negative peak of the estimated displacement of Δ_y at the flange was -584.8 $\mu strain$ (30.6 % of the average measured yield strain). In the second excursion at the same drift, the strain values did not change much (103.7% in the web and 30.98% in the flange). In addition, no local buckling was observed at this cycle amplitude.

The specimen was cycled with an additional displacement amplitude of $1.375\Delta_y$. In the first excursion of the cycle, the strains in the web at the peak positive drift and in the flange at the peak negative drift were -2897 $\mu strain$ and -887.2 $\mu strain$ (151.7% and 46.5% of the estimated yield strain, ϵ_y) and the

strains did not change much during the following excursion at the same drift (161% and 46.8% of the estimated yield strain, ε_y in the web and flange, respectively).

Note that from that point onward, the specimen was cycled following a protocol defined by yield displacements obtained from the estimated bi-linear curve for both directions (Δ_y'), which are 1.75in. in the positive direction and 1.5in. in the negative direction, as shown in Figure 3-4. This equivalent bi-linear yield defined the size of displacement increments (such as 1.5 Δ_y' , 2.0 Δ_y' , 3.0 Δ_y' , 4.0 Δ_y' , 5.0 Δ_y' , and 6.0 Δ_y') instead of first yield displacement (Δ_y) corresponding to when the outermost cross-section fiber has yielded. At a lateral displacement equal to 1 Δ_y' (i.e., Cycle 11), strain gauges showed that approximately 26.7% of the entire cross-section (30in.) between the first and second tie bar rows and 13% between the second and third tie bar rows above the top of foundation had yielded with no visual observation of local buckling. During the second excursion at the same drift (i.e., Cycle 12), yield percentage of the cross section between the first and second tie bar rows and between the second and third tie bar rows remained the same as in the previous cycle. Note that during the test, the third excursion at this amplitude was skipped (i.e., Cycle 13). In an attempt to capture the drift at which the plastic moment capacity was reached at the cross-section, the specimen was cycled with an additional displacement amplitude of 1.5 Δ_y' (i.e., Cycle 14) even though this cycle amplitude was not defined in the original loading protocol. In the first excursion of the cycle, strain gauges showed that approximately 30% of the entire cross-section had yielded with no visual observation of local buckling. Some minor cracks at the surface of the concrete foundation were observed locally near the wall's web and flange corners. The white wash paint on the interface of foundation and steel plate also flaked off a bit.

During the second excursion at the same drift (i.e., Cycle 15), when the strain gauge recorded 3672 $\mu strain$, local buckling was observed on the web at approximately 3in. from the top of the foundation at the end of the North Web (NW) and between the 1st and 2nd tie bar rows on the South face of the North Web (referred to labeled as NWS afterwards) (C15P in Figure 3-10). At peak displacement during the third excursion (i.e., Cycle 16), the steel plate between the 1st and 2nd tie bar rows started to buckle at the North

face of the South Web (referred to as SWN afterwards) and at the North face of North Web (referred to as NWN afterwards), and at the South face of the South Web (referred to as SWS afterwards). Also, another occurrence of local buckling was observed between the foundation level and the 1st tie bar row at NWS and SWN (refer to C16P in Figures 3-10, 3-12, 3-14, and 3-16).

At the lateral displacement equal to $2\Delta_y$ ' (i.e., Cycle 17), the lateral load capacity reached the maximum values of $280kip / -158kip$ in the positive and in the negative drift directions, respectively. After first cycle at the same drift (i.e., Cycle 17 with amplitude of $3.5in.$ and $-3in.$), the test was stopped to be continued next day. In order to return the specimen to an unloaded condition first, the horizontal actuators were held at zero displacement, then the vertical actuators were unloaded, and eventually the displacement control of the horizontal actuators was released and the actuator hydraulic pumps were shot off. Testing on the second day started by loading the actuators using the same sequence that was followed on the previous day at the beginning of the test. Testing resumed with execution of Cycle 18. It should be noted that the maximum force of $328.9kips$ was reached in the positive direction of Cycle 18 ($+3.5 in.$), on the second day of the test during the second displacement excursion after axial load reloading. In addition to the previously observed buckled locations, a slight buckling was observed to develop in the steel plate between the 3rd and 4th tie bar rows at SWN, NWS, SWS, and NWS. Moreover, local buckling initiated at the East elevation of the Flange (referred to as FE afterwards) between the 1st and 2nd tie bar rows (refer to C18N cycle in Figure 3-15). A small fracture initiation was detected in the steel plate at SW with no drop in the strength in the last excursion (i.e., Cycle 19).

In the first cycle of $3\Delta_y$ ' displacement (i.e., Cycle 20), the lateral horizontal force dropped by about 15% in the positive displacement direction. In the negative drift, a maximum force of $160.5kips$ was reached when the specimen was displaced by $-4.5 in.$ An additional local buckling was observed to initiate between the 2nd and 3rd tie bar rows at SWS and NWN. Also, fracture started to occur at the corners of NWS and NW at the foundation level and propagated towards the buckled locations on each side, following an inclined path. The fractures were approximately $4in.$ long at NWS; and $1.5in.$ at NW. The East face of

North Web (referred to as NWE this point forward) buckled between the 1st and 2nd tie bar rows. Moreover, an additional buckling wave was observed to develop at NW and SW at approximately 11 *in.* from the top of the foundation. In the second excursion (i.e., Cycle 21), the cracks on the steel plate grew to 5 *in.* and 4 *in.* at NWS and NW, respectively. Also, another fracture was observed to initiate at the corner of SW and SWN at 1 *in.* above the top of the foundation, being approximately 1 *in.* in length on both sides. In the last cycle of the displacement amplitude of $3\Delta_y$ ' (i.e., Cycle 22), the fractures reached lengths of 6 *in.* at NWS; 6 *in.* at NW; 2.5 *in.* at SW, and 3 *in.* at SWN.

In the displacement that was equal to $4\Delta_y$ ' (i.e., positive peak of Cycle 23), the drop in lateral horizontal force in the positive direction was 34.7 %, but 23.7 % in the negative direction. Another buckling wave was observed to develop at the SW at 17 *in.* from the top of the foundation. Cracks grew to 4.5 *in.* at SW; 6.125 *in.* at NW; 8 *in.* at NWS; and 5 *in.* at SWN. Additional cracks occurred at this drift, namely: a 2 *in.* crack at SW at 5 *in.* from the foundation; a 2 *in.* crack at NW at 4 *in.* from top of the foundation; a 6 *in.* crack at NWN, and; a 2 *in.* crack at SWS. Also, the East face of South Web (referred to as SWE after this point) buckled between the 1st and 2nd tie bar rows. Two tie bars at the 1st row at SWS failed. The failure consisted of a fracture at the tie bar weld to the steel plate. In the second excursion (i.e., Cycle 24), weld where the thicker wall plate (inside the foundation) was welded to the wall plate was observed to be fractured for about 0.75 *in.* at the corner of the wall at the South-East corner. At this stage, 34 % of the web length (8.25 *in.* out of 24 *in.*) at NW and 28% of web length (6.75 *in.* out of 24 *in.*) at SW was fractured.

The lateral horizontal force dropped by 43.4 % in the positive and 55 % in the negative directions when the specimen was displaced by $5\Delta_y$ ' (i.e., Cycle 25). The cross-section fractured by 58% at SW and 42% at NW in this cycle. Also, two tie bars at NWS in the first tie bar rows was observed to be fractured. In the second cycle (i.e., Cycle 26), the fracture in SWE grew to 1.5 *in.*, and 64% at SW and 60% at NW.

At the $6\Delta_y$ ' displacement amplitude (i.e., Cycle 27), peak lateral horizontal force had dropped by 53.3 % in the positive and 71.4 % in the negative directions. The web steel was fractured over 75% of its original area at SW and 73 % at NW. Also, a 1 *in.* fracture along flange was detected at NWE. In the next

excursion (i.e., Cycle 28), the cracks at SWE and NWE grew to 8in. and 2.5in. along the flange, respectively. During the third excursion at that displacement amplitude (i.e., Cycle 29), 77 % of the SW web steel and 81 % of the NW one was fractured. The cracks at SWE extended to 36.75in. along the flange and 3.5in. toward the web, but the length of fracture at NWE stayed at 4 in along the flange and 3.5in. towards the web. In the last cycle (i.e., Cycle 30), onset of cracking in the steel plate around some of the tie bars was observed in some locations along the first and second tie bar rows in the FE, where the largest crack width observed was ¼” but less in most cases (it could not be ascertained if the crack was across the full thickness of the plate or just a surface crack). The test was stopped at this point due to safety concerns.

The details on the progression of buckling and fracture is tabulated in Table 3-2. Also, Figures 3-10 to 3-17 show the progressive development of the phenomena described above at locations NW and NWS; SW and SWN; SWS and FE; and NWN of Specimen C1. Labels C_nP and C_nN in these figures respectively refer to peak positive and negative displacements during Cycle n. For example, $C_{15}P$ means the maximum positive displacement attained during the fifteenth cycle during the test.

Table 3-2. Experiment log of Specimen C1

(Note: 1 in. = 25.4 mm; 1ft=0.3048 m; 1sq in.=645.2 mm²; 1 in⁴=416231 mm⁴; 1 psi=0.0069 MPa; 1 ksi=6.9 MPa)

Cycle No	Cycle Drift, in	Laterally Applied Force, V, kips	FE	NWW	NWN	NWS	SWW	SWN	SWS	NWE	SWE
15	2.63/-2.25	254.4 /-140		B @ 3in FF		B @ 1st-2nd TR	B @3in FF				
16	2.63/-2.25	249.6/-138.4			B @1st-2nd TR			B @1st-2nd TR	B @1st-2nd TR		
17	3.5/-3	280.3/-157.6			B @3rd-4th TR	B @FF-1st TR		B @FF-1st TR	B @FF-1st TR		
18	3.5	328.9	B @1st-2nd TR			B @3rd-4th TR		B @3rd-4th TR	B @3rd-4th TR		
	-3	-154.4									
19	3.5	260									
	-3	-148.8									
20	5.25	282.2			B @2nd-3rd TR				B @2nd-3rd TR		
	-4.5	-160.8		1.5in. FR		4in. FR					B @1st-2nd TR
21	5.25	234		B @ 11in FF			B @11in FF				
	-4.5	-146.3		4in. FR		5in. FR	1in. FR	1in. FR			
22	5.25	216									
	-4.5	-132.1		6in. FR		6in. FR	2.5in. FR	3in. FR			
	7	214.9					B @17in FF				
23	-6	-122.8		6.125in. FR	6in. FR	8in. FR	4.5in. FR	5in. FR	2in. FR WFR @1r1c & 1r2c		B @1st-2nd TR
24	7	187.4									0.75in. FR
	-6	-88.71			34% FR	34% FR		28% FR	28% FR		
	8.75	185.8									
25	-7.5	-73.27			42% FR	42% FR, WFR @1r1c, @1r2c		58% FR	58% FR		
26	8.75	156.7									1.5in. FR
	-7.5	-52.5			60% FR	60% FR		64% FR	64% FR		
27	10.5	153.6								1in. FR	
	-9	-47.48			73% FR	73% FR		75% FR	75% FR		
28	10.5	125.6								2.5in. FR	8in. FR
	-9	-37.12									
29	10.5	108.8	36.75in. FR							4in. FR	
	-9	-31.97			81% FR	81% FR		77% FR	77% FR		
30	10.5	98.35									
	-9	-28.22			81% FR	81% FR		77% FR	77% FR		

Note: The steel plate faces are abbreviated as follows: FE = the East Flange, NWW = West of North Web, NWN = North of North Web, NWS = South of North Web, SWW = West of South Web, SWN = North of South Web, SWS = South of South Web, NWE = East of North Web, and SWE = East of South Web. Also, FF means "from footing", FR is fracture, B is buckling, TR is tie bar row, WFR is tie bar weld fracture, r is tie bar row, and c is tie bar column

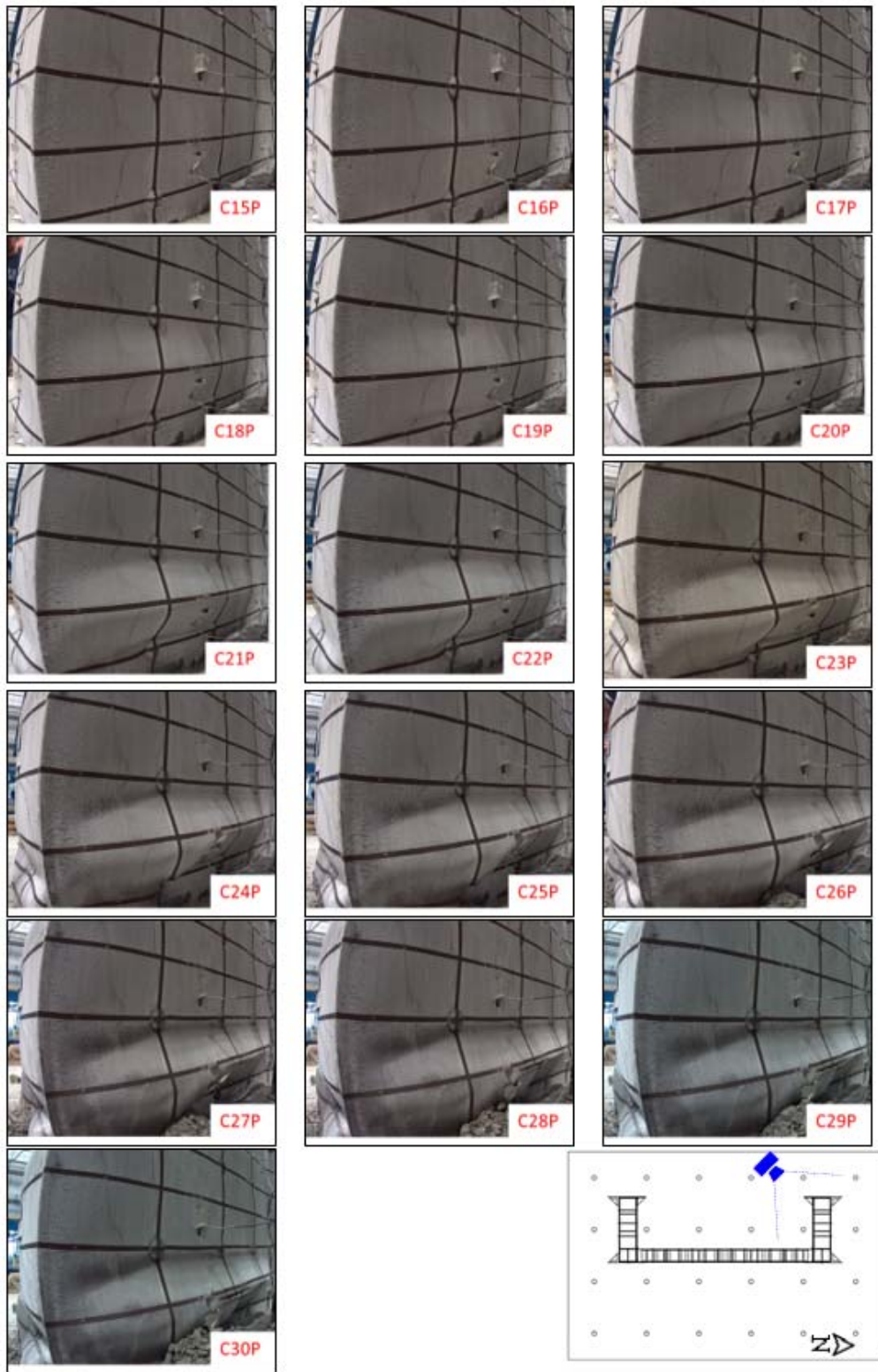


Figure 3-10. South-West views of the North Web of Specimen C1 at positive peaks

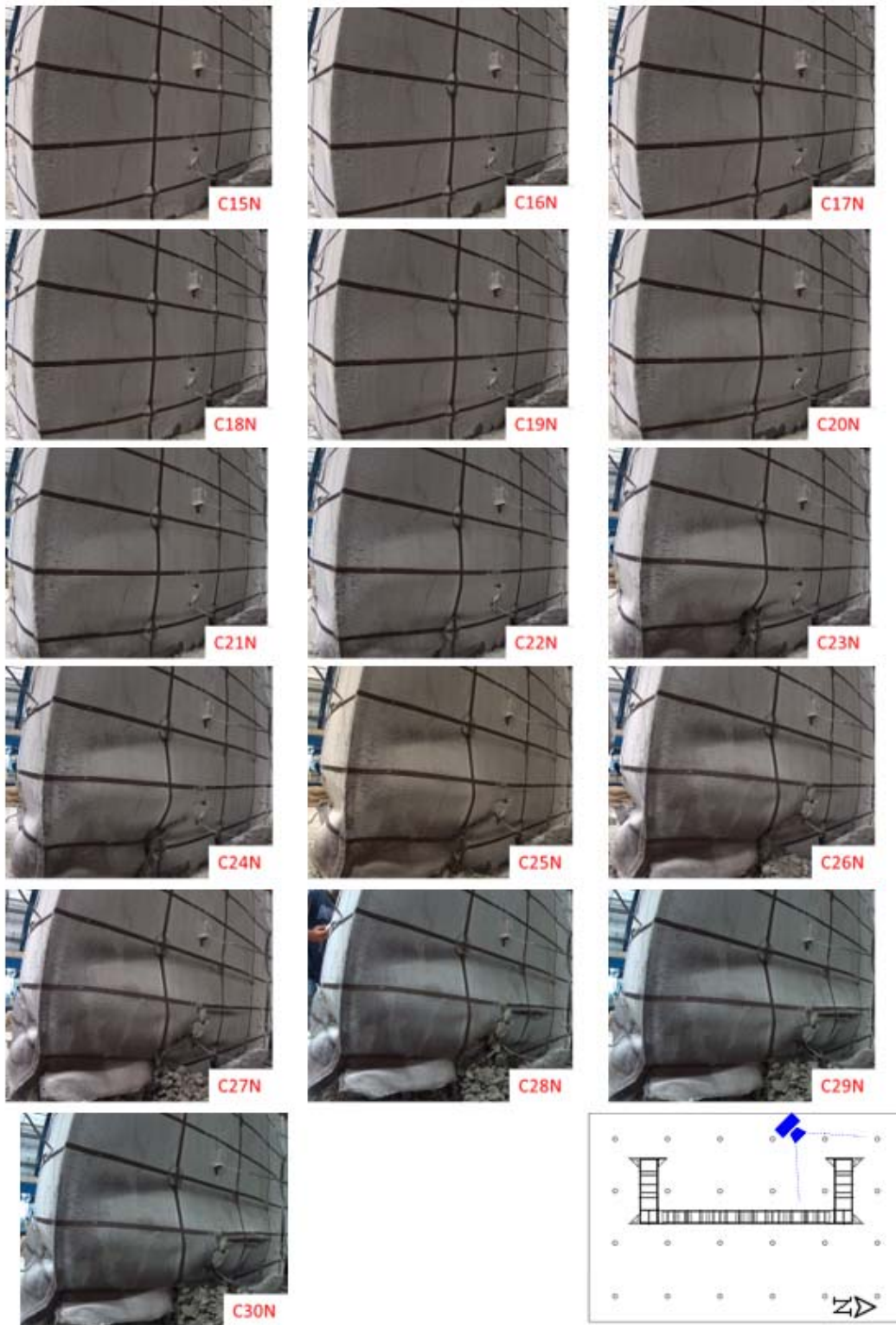


Figure 3-11. South-West views of the North Web of Specimen C1 at negative peaks

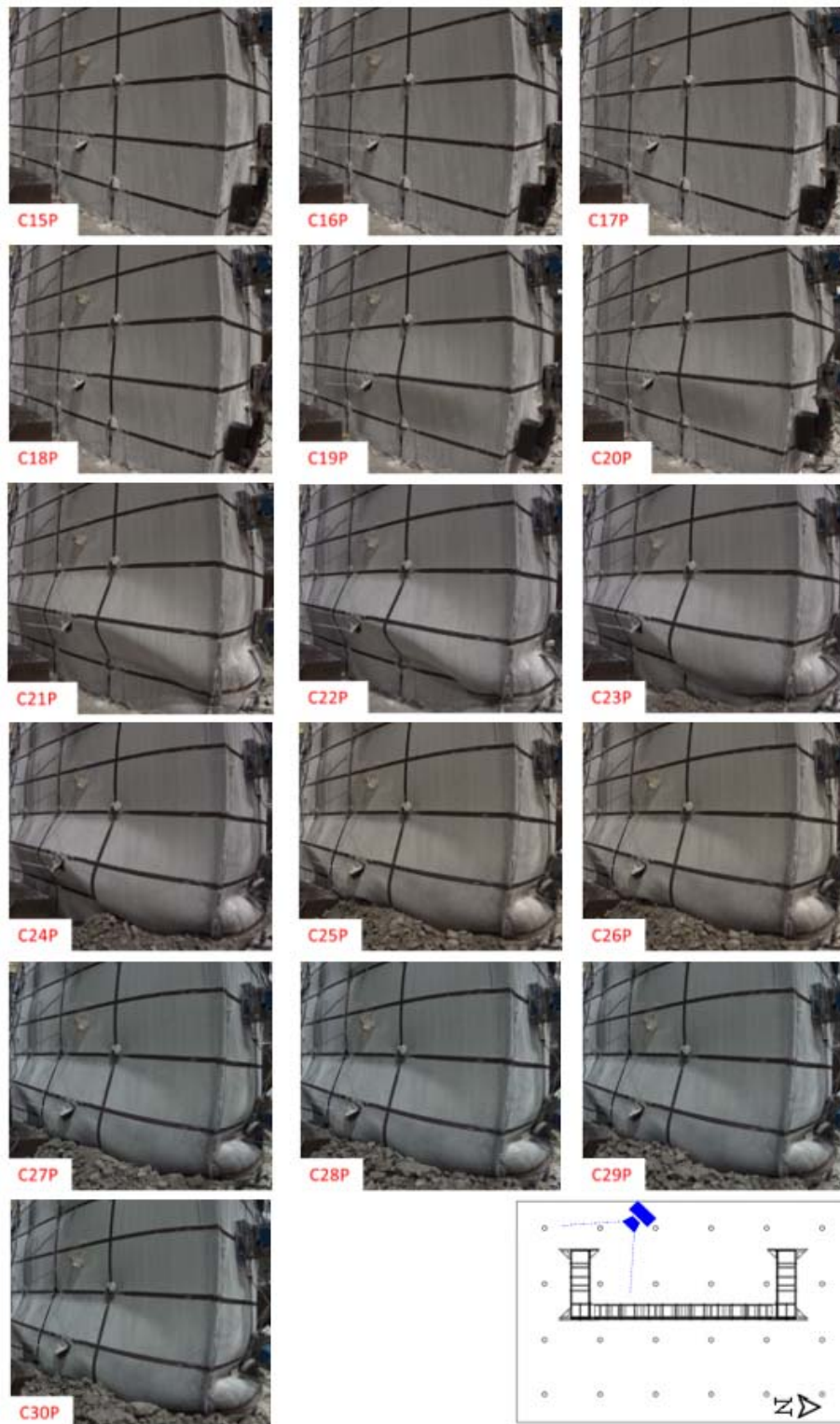


Figure 3-12. North-West views of the South Web of Specimen C1 at positive peaks

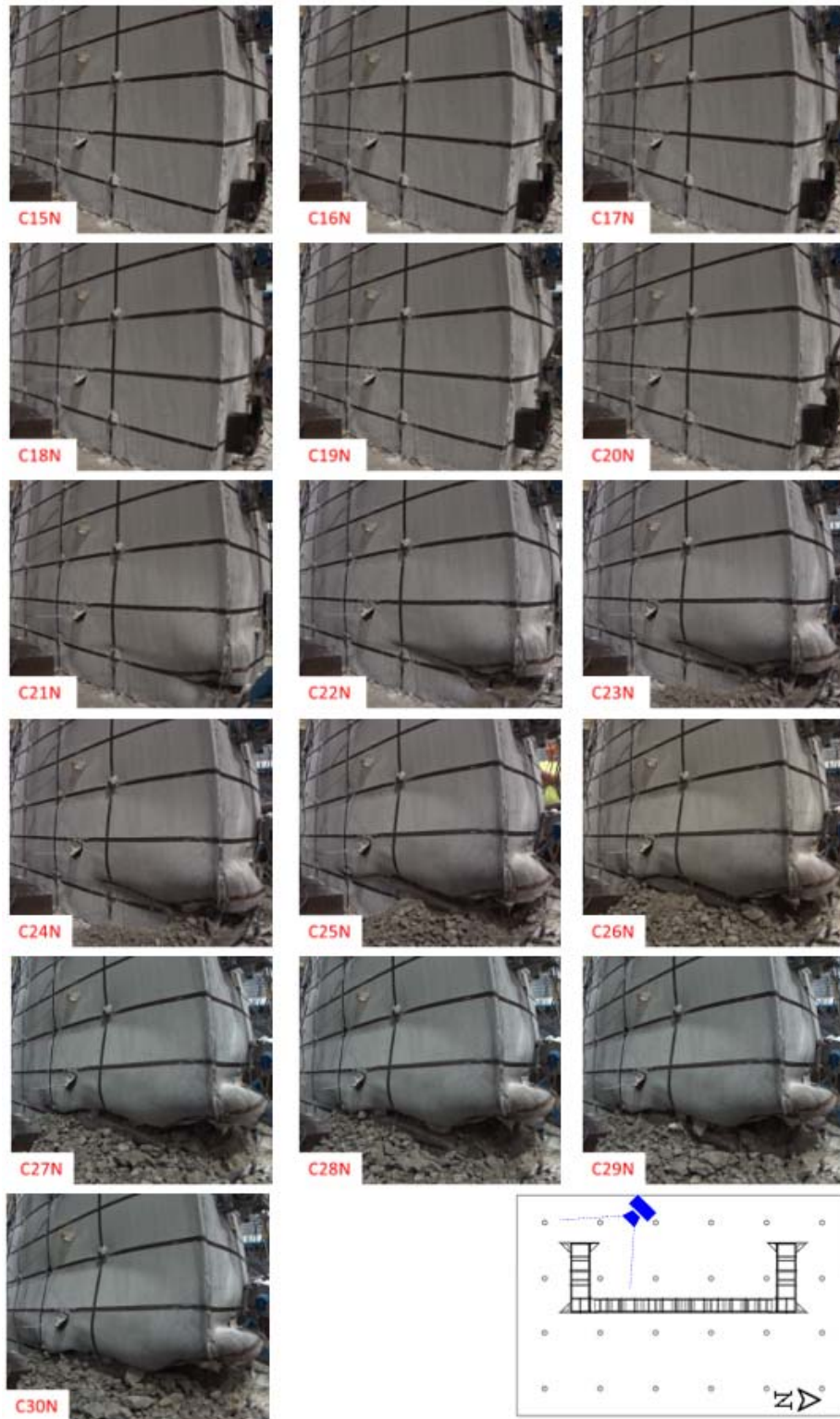


Figure 3-13. North-West views of the South Web of Specimen C1 at negative peaks

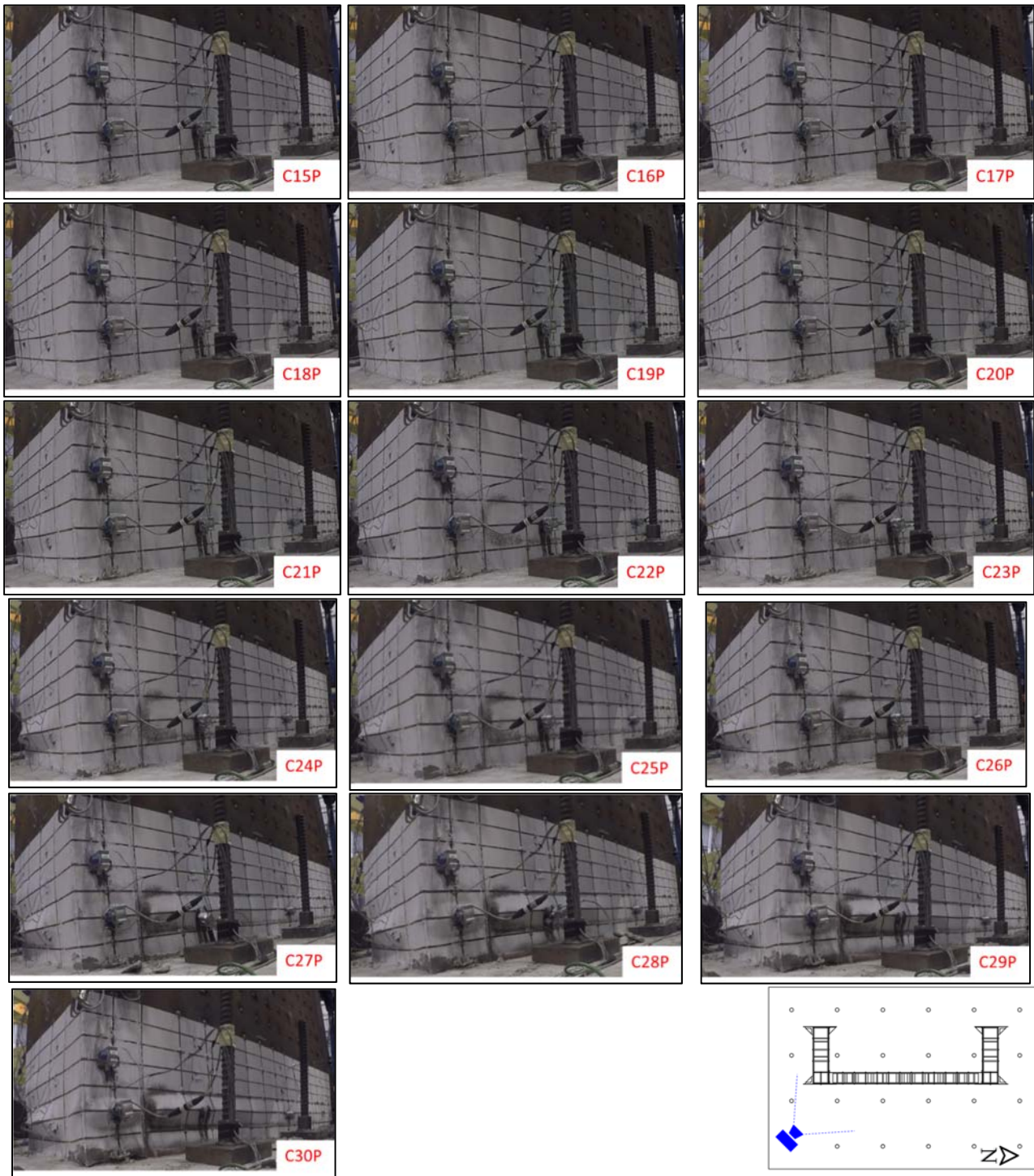


Figure 3-14. East view of the flange and South-East view of the South web of Specimen C1 at positive peaks

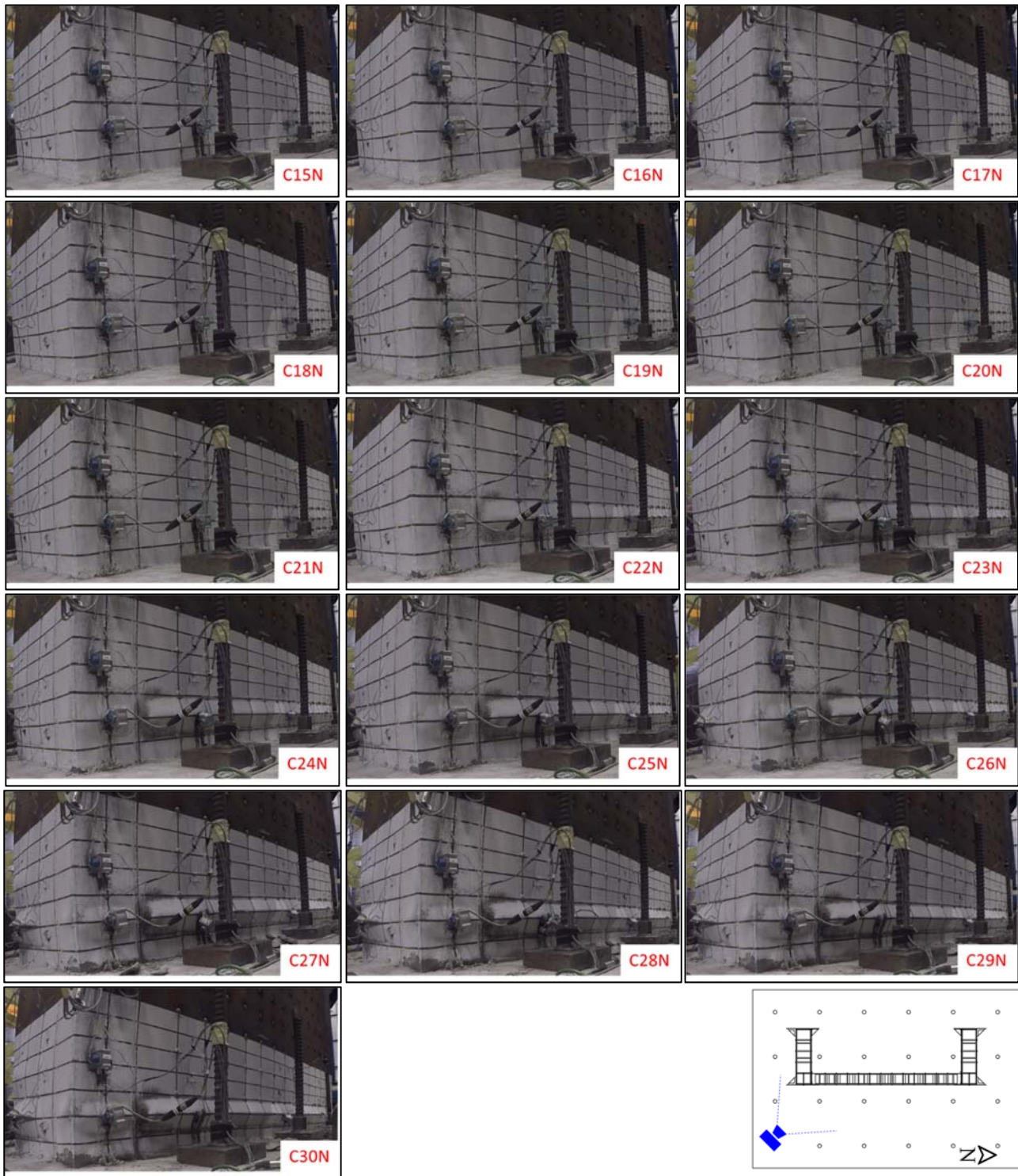


Figure 3-15. East view of the flange and South-East view of the South web of Specimen C1 at negative peaks

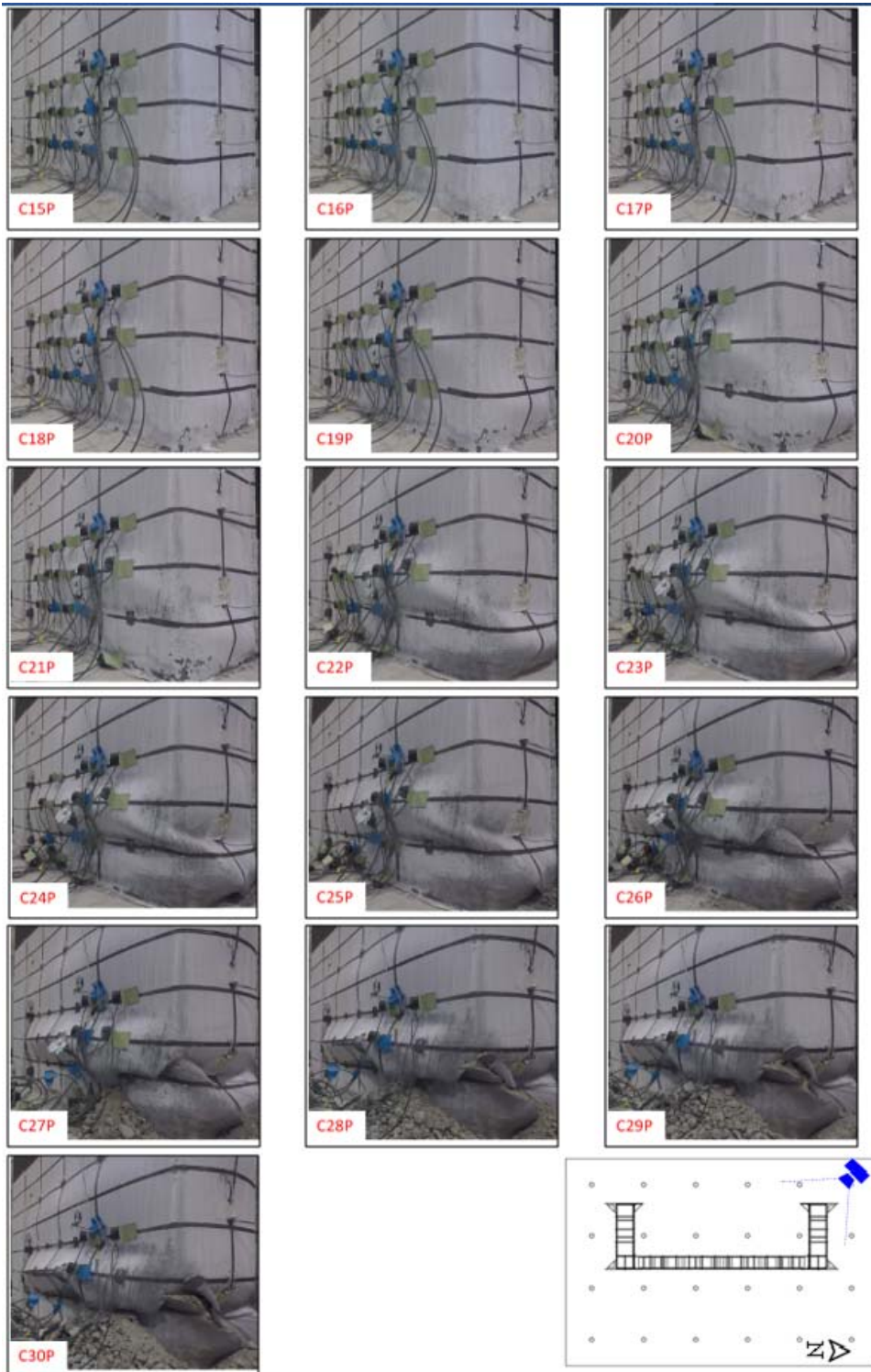


Figure 3-16. North-West views of the North Web of Specimen C1 at positive peaks

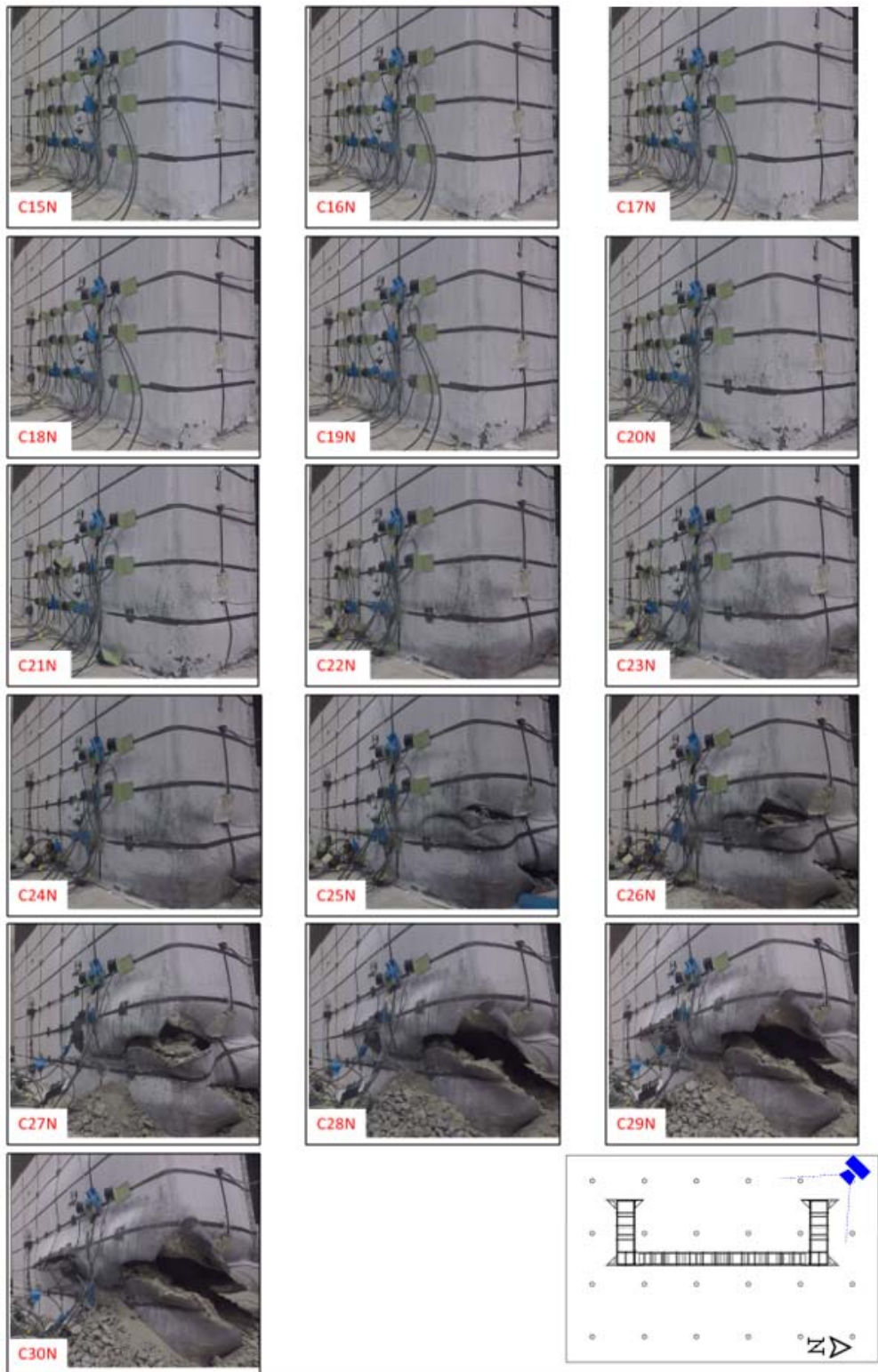


Figure 3-17. North-West views of the North Web of Specimen C1 at negative peaks

3.7.2 Specimen C2

As was done for Specimen C1, testing started by loading the vertical actuators while the horizontal actuators were held at zero displacement. The forces in the vertical actuators were increased up to 400kips to apply 15% of $A_c f'_c$ on the cross-section of the C-shape wall. Then, the lateral actuators were loaded to apply the lateral cyclic displacements at the top of the specimen according to the pre-determined cyclic protocol.

The first cycle of the loading protocol, at the displacement of $\Delta_y/4$, enabled to verify if all the attached data recording instruments were working properly and that no unforeseen deficiencies existed in the specimen and the test setup. The second cycle of the same displacement ($\Delta_y/4$) was skipped. None of the components of steel plates of the specimen experienced any buckling or yielding through all of the excursion cycles at amplitudes of $\Delta_y/2$, and $3\Delta_y/4$.

At the positive peak of the estimated displacement of Δ_y , the strain recorded at the farthest end of the web was $-2041 \mu\text{strain}$, which is 105 % of the average measured yield strain (i.e., $1944 \mu\text{strain}$) of the steel plate based on the coupon tests. The strain recorded at the negative peak of the estimated displacement of Δ_y in the flange was $-534.6 \mu\text{strain}$ (27.5 % of the average measured yield strain). In the second excursion at the same drift, the strain values did not change much (107% in the web and 27.8% in the flange). In addition, no local buckling was observed at this cycle amplitude.

The specimen was cycled with an additional displacement amplitude of $1.375\Delta_y$. In the first excursion of the cycle, the strains in the web at the peak positive drift and in the flange at the peak negative drift were $-3360 \mu\text{strain}$ and $-837.8 \mu\text{strain}$ (173% and 43.1% of the estimated yield strain of ϵ_y) and during the following excursion at the same drift (i.e., Cycle 10), strain gauges showed similar results (175% and 45% of ϵ_y in the webs and in the flange) showed 250% with no visual buckling.

After Cycle 10 (i.e., amplitude of $1.375in.$ and $-1in.$), the test was paused to continue the next day. First, the horizontal actuators were held at zero displacement, then the vertical actuators were unloaded, and finally the displacement control of the horizontal actuators was released. Testing on the second day started by loading the actuators using the same sequence that was followed on the previous day at the

beginning of the test. However, after getting the true strength of concrete from unconfined cylinders tested overnight, the forces in the vertical actuators were changed from 400kips to 360kips to apply an axial force closer to the target of 15% of $A_c f'_c$ on the cross-section of the C-shape wall. This is because, in the early part of the test, the concrete strength was assumed to be 6ksi but it was found out to be only 5.1ksi from the cylinder tests. Then, testing resumed with execution of Cycle 11.

As done for Specimen C1, from this point onward, the specimen was cycled with yield displacements obtained from the estimated bi-linear curve for both directions (Δ_y '), and target amplitudes calculated as $1.5\Delta_y$ ', $2.0\Delta_y$ ', $3.0\Delta_y$ ', $4.0\Delta_y$ ', $5.0\Delta_y$ ', and $6.0\Delta_y$ ' (instead of values calculated as a function of first yield displacement, Δ_y). At a lateral displacement equal to $1.0\Delta_y$ ' (i.e., Cycle 11), strain gauges showed that approximately 26.7% of the entire cross-section (30in.) between the first and second tie bar rows and 17% between the second and third tie bar rows above the top of foundation had yielded with no visual observation of local buckling. During the second excursion at the same drift (i.e., Cycle 12), yield percentage of the cross section between the first and second tie bar rows and between the second and third tie bar rows increased a bit (up to the values of 27% and 17.3%, respectively). Note that during the test, the third excursion at this amplitude was skipped (i.e., Cycle 13).

At the displacement amplitude of $1.5\Delta_y$ ' (i.e., Cycle 14), local buckling initiation was observed from 2in. above the top of foundation on the West face of the North Web (NWW) and the West face of the South Web (SWW). During the second excursion at the same drift (i.e., Cycle 15), local buckling was observed in the steel plate between the 1st and 2nd tie bar rows on the South face of the South Web (SWS), 3rd and 4th tie bar rows on the North face and South face of North Web (NWN and NWS), and 3rd and 4th tie bar rows on the North face of the South Web (C15P in Figure 3-18). At peak displacement during the third excursion (i.e., Cycle 16), the steel plate between the 1st and 2nd tie bar rows started to buckle at NWS. Also, another occurrence of local buckling was observed between the 2nd and 3rd tie bar rows on the North face of the South Web (SWN) (refer to C16P in Figures 3-18 and 3-20).

At the lateral displacement equal to $2\Delta_y$ ' (i.e., Cycle 17), a maximum lateral force of 319.8kips/-156.6kips was reached both in the positive and negative drift directions, respectively. In addition to the previously observed buckled locations, buckling was observed to develop in the steel plate between the top of the foundation and the 1st tie bar row and between the 1st and 2nd tie bar rows at NWN (C17P in Figure 3-24) and a slight buckling was detected between the 5th and 6th tie bar rows at NWS. In the negative drift direction, buckling started to initiate in the East face of Flange (FE) between the 1st and 2nd tie bar rows (C17N in Figure 3-23). Also, over a depth of 1in., concrete in the foundation at the corners of NWW and NWS; and SWW and SWN detached and lifted a bit. In the second excursion of the same drift (i.e., Cycle 18), additional buckling was observed between the 3rd and 4th tie bar rows and between the top of foundation and the 1st tie bar row at SWN. No significant change was observed during the last excursion at the same drift (i.e., Cycle 19).

In the first cycle of $3\Delta_y$ ' displacement (i.e., Cycle 20), the lateral horizontal force dropped by about 4% in the positive displacement direction and by 10% in the negative drift. No change was observed in the positive direction, but in the negative direction, the steel fractured at the corners of NWS and NWW; and SWN and SWW at the foundation level. The fracture at NWW was 0.5in. along the plate and the fracture at South Web (SW) was 3.5in. along SWW and 4.5in. along SWN. During the positive drift of the second excursion (i.e., Cycle 21), buckling started at 13in. from the top of the foundation at NWW. During the negative drift of the cycle, the steel plate on the East face of the South Web (SWE) in the box section in the corner of FE and SWS started to buckle. The fractures grew to 5-1/8in. at NWW and 4in. at NWS starting from the foundation level and propagating towards the buckled location, following an inclined path. Also, the growth in fractures were 4-3/4in. at SWW and 5-1/4in. at SWN at foundation level. In the last cycle at the displacement amplitude of $3\Delta_y$ ' (i.e., Cycle 22), the fractures reached lengths of 5in. (inclined) at NWS; 6in. at NWW; 5.25in. at SWW, and 6.5in. (horizontal) at SWN. Moreover, the steel plate at the East face of the North Web (NWE) in the box section in the corner of FE and NWN buckled.

At the peak of the displacement at a drift equal to $4\Delta_y'$ (i.e., positive peak of Cycle 23), the drop in lateral horizontal force in the positive direction was 27.9%, and 28.8% in the negative direction. Another buckling wave was observed at the SWW at 13in. from the top of the foundation. During the negative drift, additional cracks developed at 4.5in. from the top of foundation; 2.5in. long at NWN and 1.5in. long at NWW. The existing cracks from previous cycles grew to 7.25in. at NWW at the foundation level; 8in. (inclined) at NWS; reached complete fracture (inclined) at SWW; and 10.5in. at SWN. Additional cracks occurred 4in. from the top of foundation and 7.25in. long at SWS. Note that the crack at NWS passed through tie bar at the 1st row and 1st column of tie bars (recall that vertical lines of ties, called “columns” here, are numbered starting from the tip of the web, i.e. farthest point from the flange) and the crack at SWN passed through tie bar at 1st row and 2nd column of tie bars and at the peak of negative drift of the second excursion (i.e., Cycle 24), 42% of the web length (10in. out of 24in.) at North Web (NW) and 46.4% of web length (11-1/8in. out of 24in.) at South Web (SW) were fractured).

The lateral horizontal force dropped by 40% in the positive and 52.2% in the negative directions when the specimen was displaced by $5\Delta_y'$ (i.e., Cycle 25). In the positive direction, the steel plates between the 2nd and 3rd tie bar rows at NWS, NWN, and SWS buckled. The cross-section fractured by 57.3% at SW and 46% at NW during the negative drift of the cycle. Also, the weld of tie bar at SWS in the first tie bar rows and second tie bar column on the web face plate was observed to be fractured. In the second cycle (i.e., Cycle 26), the fractures grew to 64% at SW and 62.5% at NW. Also, the welds of the tie bars in the first row at NWN fractured.

At the $6\Delta_y'$ displacement amplitude (i.e., Cycle 27), peak lateral horizontal force had dropped by 48% in the positive and 69.3% in the negative directions. The web steel was fractured over 60.4% of its original area at SW and 68.8% at NW. The following tie bar welds were fractured: the weld around all tie bars in the 1st row at SWS and 1st row and 3rd column from end web plate at SWN. After this cycle, the test was paused to continue the next day. The same procedure explained before was accomplished to unload the specimen and reload it the next day. The test continued with cycle 28. In the next excursion (i.e., Cycle 28),

a crack developed in the foundation level at the corner of SWE and SWS; 1.5in. at SWS and 2.5in. along the flange, respectively. The fracture grew to 64.6% at SW and 70.8% at NW. Two tie bars on the 2nd row, at the 1st and 2nd column from web plate, fractured. Also, a vertical crack developed (2in. long) at the corner weld of NWW and NWN. During the third excursion at that displacement amplitude (i.e., Cycle 29), the cracks at SWE corner extended to 3in. along the flange and 2.75in. toward the web in the positive drift of the cycle. In the negative drift, 66.7% of the SW web steel and 71% of the NW one were fractured. Also, another weld of a tie bar on the 2nd row at the 3rd column from web plate was fractured. In the last cycle (i.e., Cycle 30), the cracks grew to 3-1/8in. along the flange and 3in. toward the web. In the negative excursion, the fracture at SW grew to 68.75% of the web length and the fracture at NW became 73%.

The details on the progression of buckling and fracture is tabulated in Table 3-3. Also, Figures 3-18 to 3-25 show the progressive development of the phenomena described above at locations NWW and NWS; SWW and SWN; NWN and FE; and NWN of Specimen C2. Labels CnP and CnN in these figures refer to peak positive and negative displacements during Cycle n. For example, C16P means the maximum positive displacement attained during the sixteenth cycle during the test.

Table 3-3. Experiment log of Specimen C2

(Note: 1 in. = 25.4 mm; 1ft=0.3048 m; 1sq in.=645.2 mm²; 1 in⁴=416231 mm⁴; 1 psi=0.0069 MPa; 1 ksi=6.9 MPa)

Cycle No	Cycle Drift, in	Laterally Applied Force, V, kips	FE	NWW	NWN	NWS	SWW	SWN	SWS	NWE	SWE
14	2.63/-2.25	301.3/-143.3		B @2in FF			B @2in FF				
15	2.63/-2.25	292.1/-141.7			B @3rd-4th TR	B @3rd-4th TR		B @3rd-4th TR	B @1st-2nd TR		
16	2.63/-2.25	285.4/-139.5				B @1st-2nd TR		B @2nd-3rd TR			
17	3.5/-3	319.8/-156.6	B @1st-2nd TR		B @1st-2nd TR	B @5th-6th TR					
18	3.5	303						B @3rd-4th TR			
	-3	-149.8									
19	3.5	294.1									
	-3	-143.9									
20	5.25	308.1									
	-4.5	-154.9		0.5in. FR			3.5in. FR	4.5in. FR			
21	5.25	259.9		B @13in FF							
	-4.5	-138.6		5.125in. FR		4in. FR	4.75in. FR	5.25in. FR			B @1st-2nd TR
22	5.25	240.4									
	-4.5	-125.3		6in. FR		5in. FR	5.25in. FR	6.5in. FR		B @1st-2nd TR	
	7	230.9					B @13in FF				
23	-6	-111.7		7.25in. FR	2.5in. FR	8in. FR	8.375in. FR	10.5in. FR	7.25in. FR		
	7	198.7				WFR @1r1c		WFR @1r2c			
24	-6	-80.98									
	8.75	192.3			B @2nd-3rd TR	B @2nd-3rd TR		46.4% FR	46.4% FR		
25	-7.5	-74.78			46% FR	46% FR		57.3% FR	57.3% FR, WFR @1r2c		
	8.75	162.9									
26	-7.5	-51.96			62.5% FR, WFR @1r1c, 1r2c, 1r3c	62.5% FR		54% FR	54% FR		
	10.5	167									
27	-9	-48.12			68.8% FR	68.8% FR		60.4% FR, WFR @1r3c	60.4% FR WFR @1r1c, 1r3c		
	10.5	144.7							1.5in. FR		2.5in. FR
28	-9	-39.41			70.8% FR, Tie F @2r2c	70.8% FR, WFR @2r1c, Tie F @2r2c		64.6% FR	64.6% FR		
	10.5	126.6							2.75in. FR		3in. FR
29	-9	-32.97			71% FR, WFR @2r3c	71% FR		66.7% FR	66.7% FR		
	10.5	115.7							3in. FR		3.125in. FR
30	-9	-28.53			73% FR	73% FR		68.75% FR	68.75% FR		

Note: The steel plate faces are abbreviated as follows: FE = the East Flange, NWW = West of North Web, NWN = North of North Web, NWS = South of North Web, SWW = West of South Web, SWN = North of South Web, SWS = South of South Web, NWE = East of North Web, and SWE = East of South Web. Also, FF means "from footing", FR is fracture, B is buckling, TR is tie bar row, WFR is tie bar weld fracture, r is tie bar row, and c is tie bar column

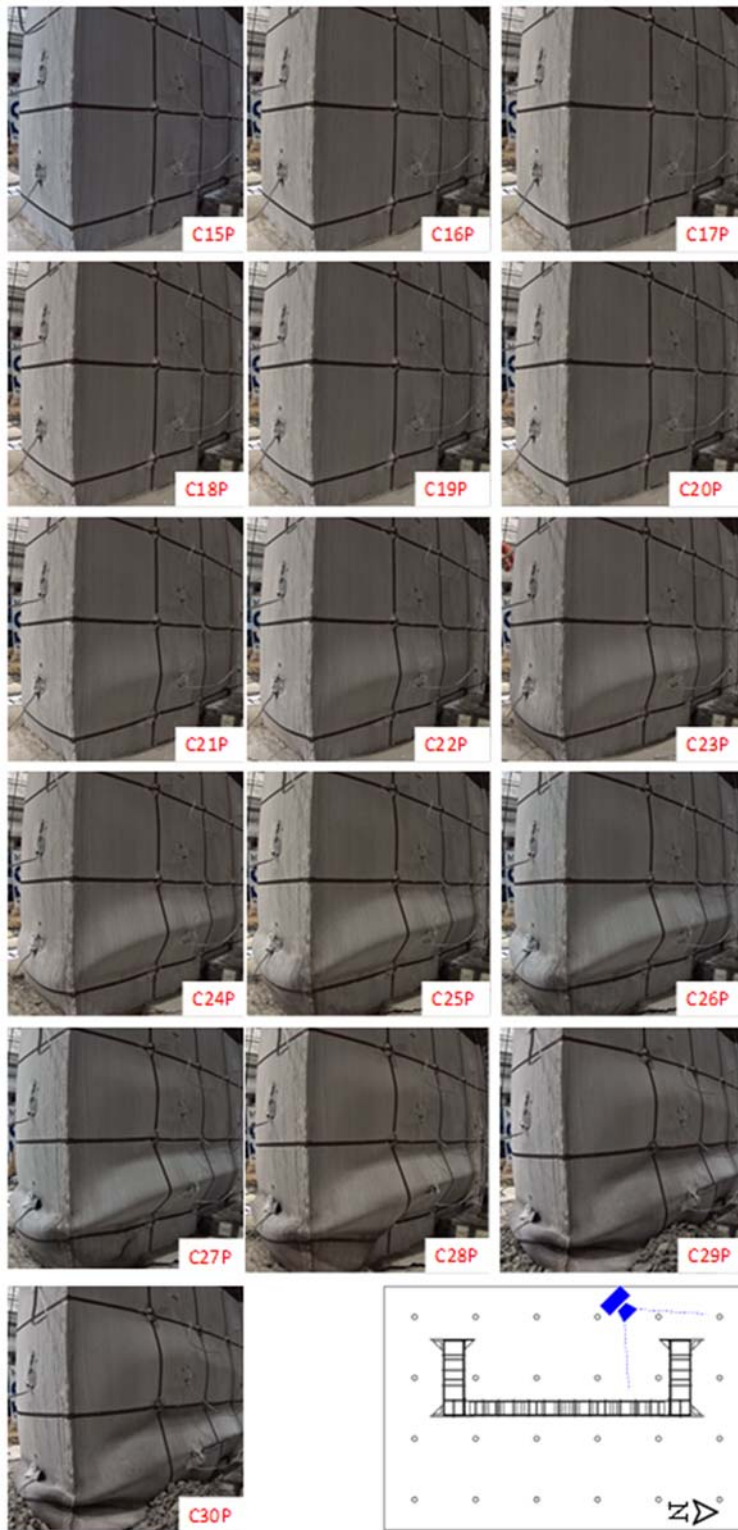


Figure 3-18. South-West views of the North Web of Specimen C2 at positive peaks

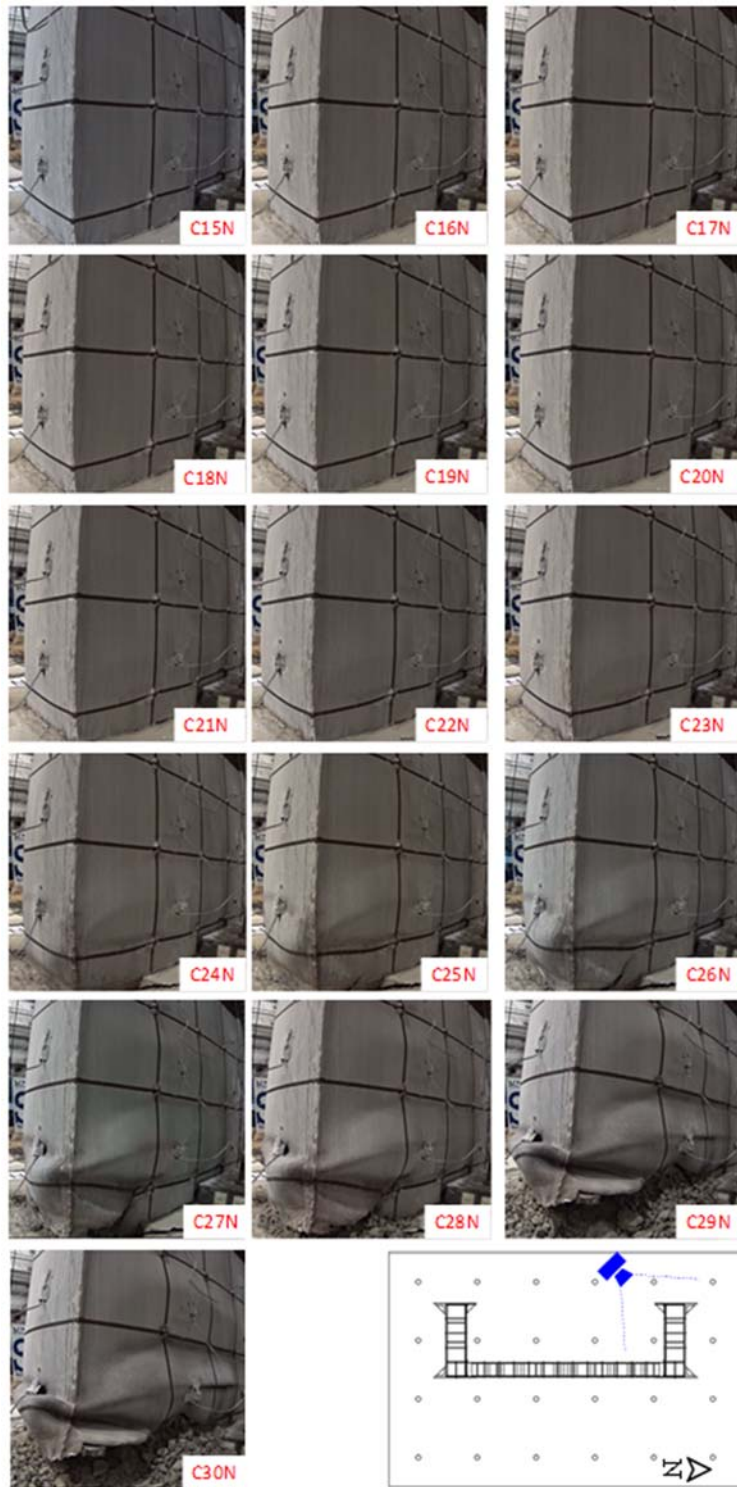


Figure 3-19. South-West views of the North Web of Specimen C2 at negative peaks

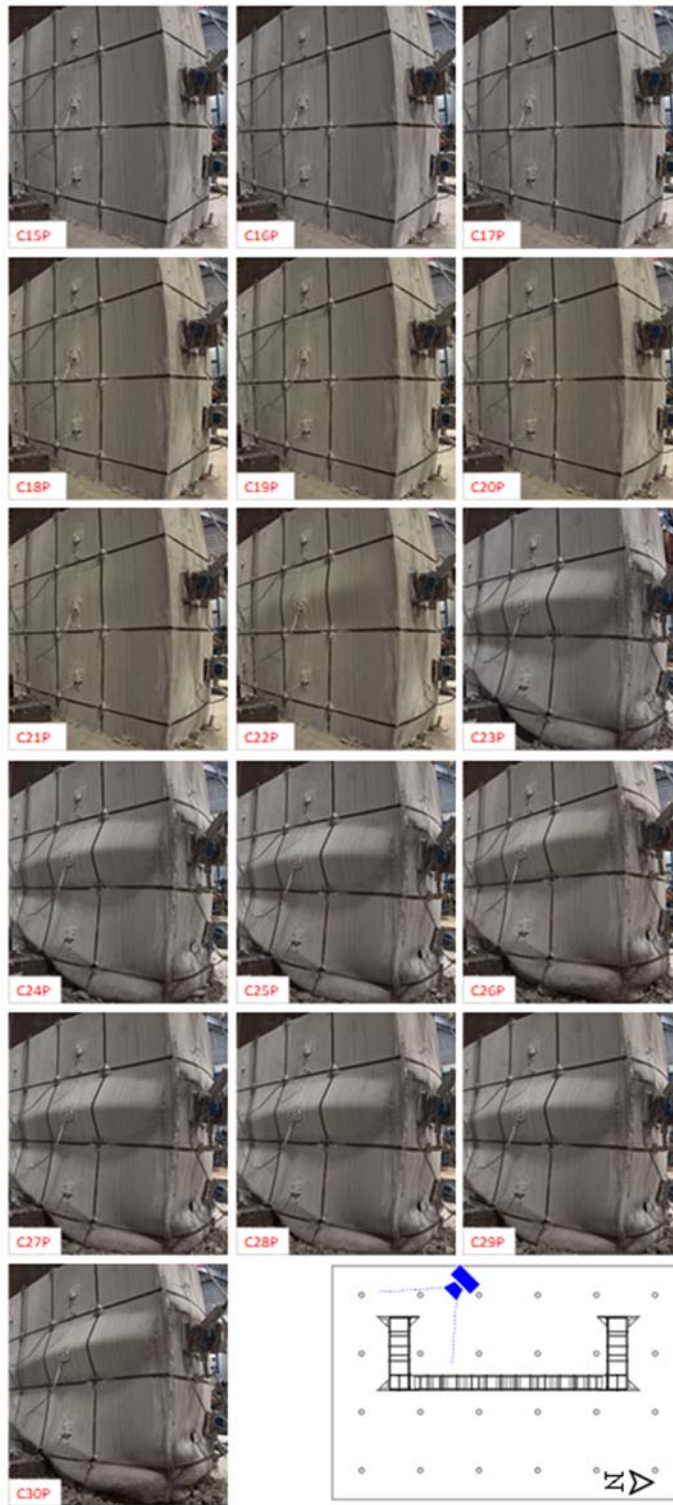


Figure 3-20. North-West views of the South Web of Specimen C2 at positive peaks

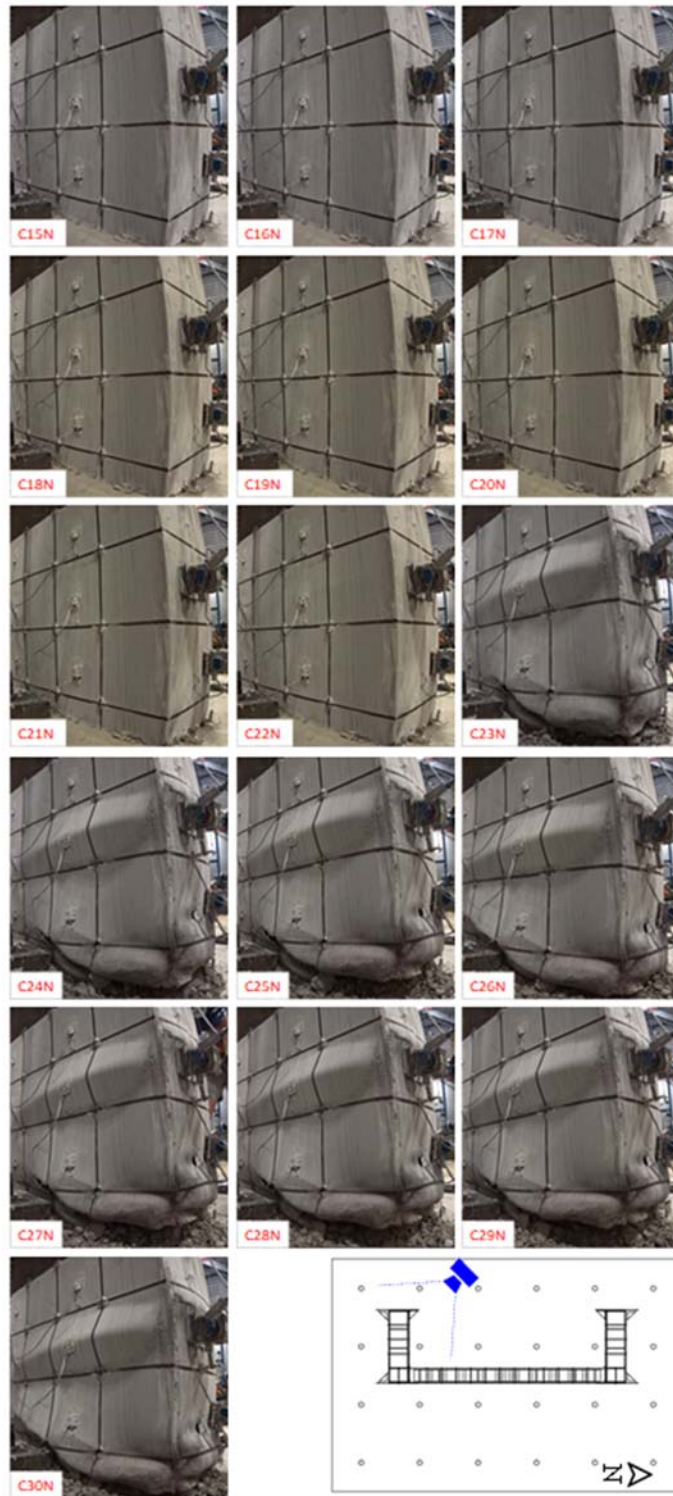


Figure 3-21. North-West views of the South Web of Specimen C2 at negative peaks

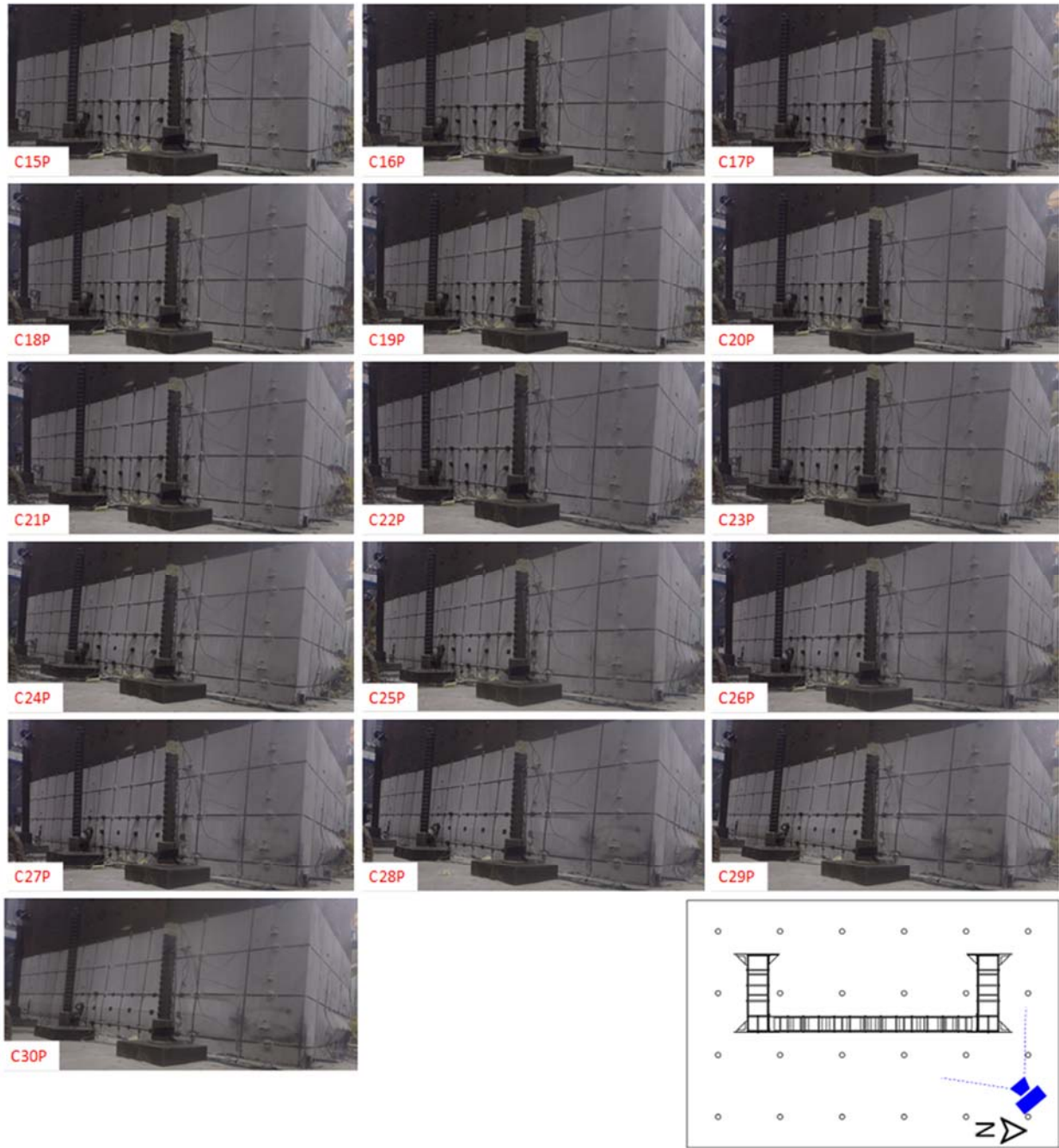


Figure 3-22. East view of the flange and North-East view of the North web of Specimen C2 at positive peaks

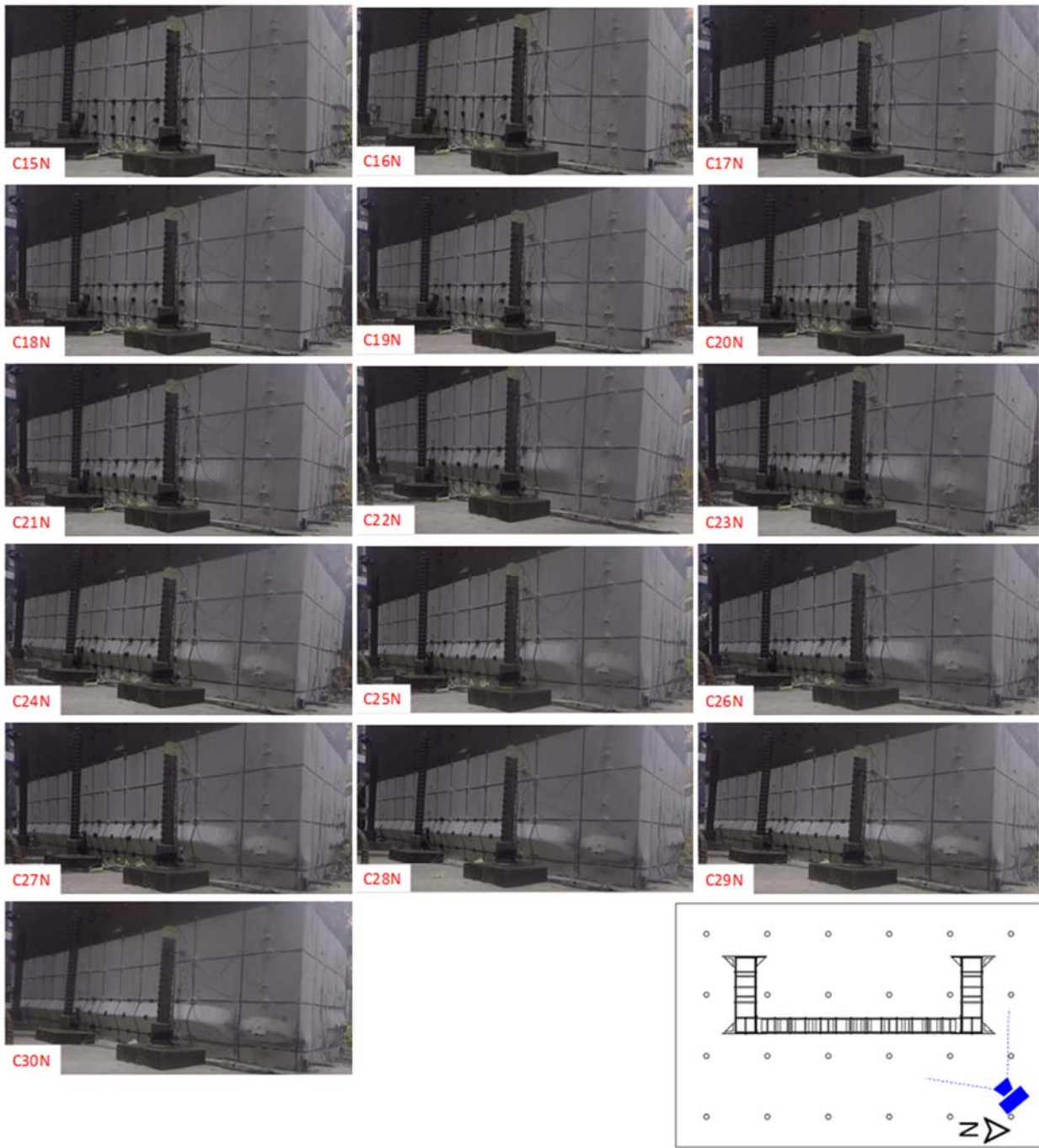


Figure 3-23. East view of the flange and North-East view of the North web of Specimen C2 at negative peaks

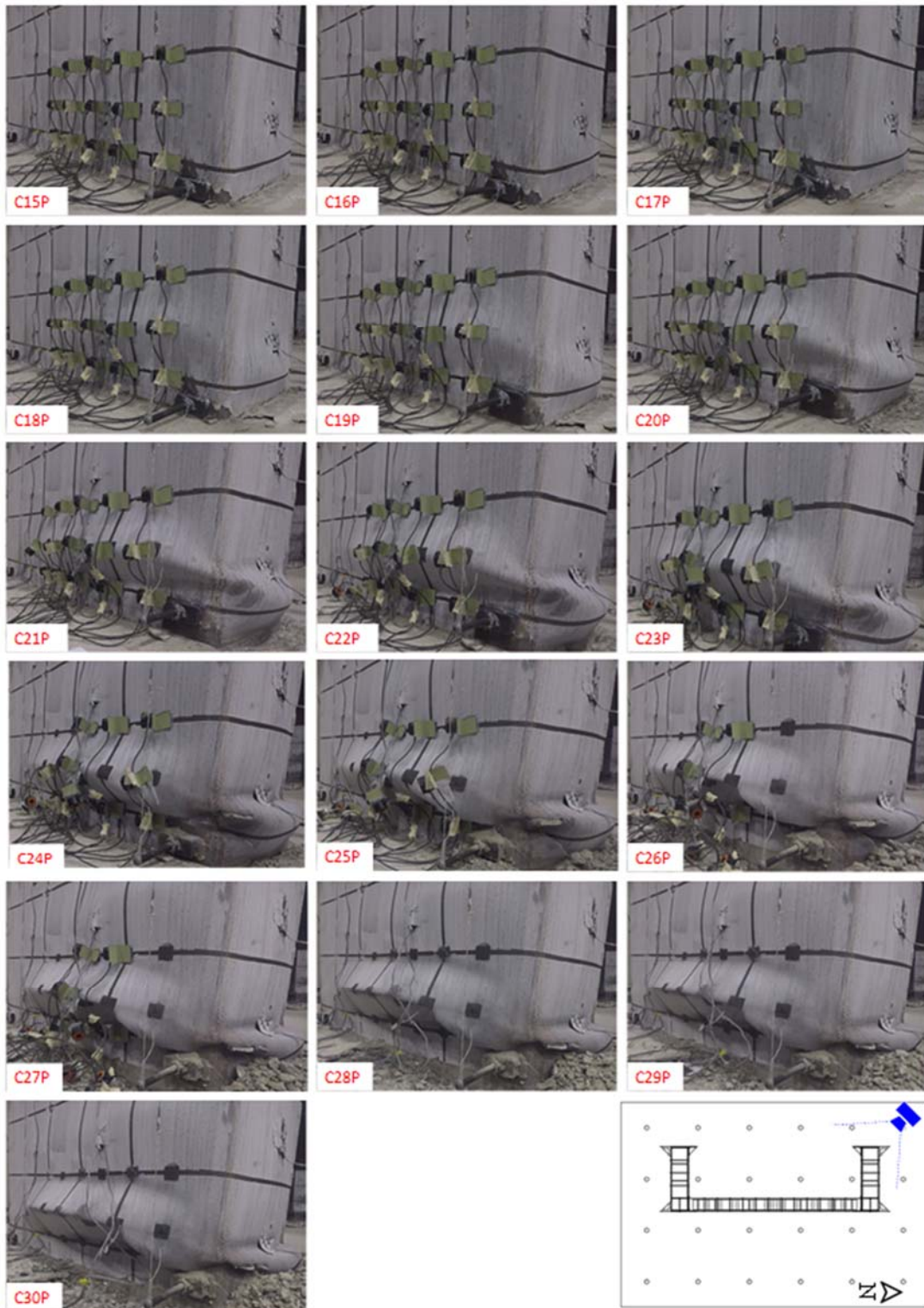


Figure 3-24. North-West views of the North Web of Specimen C2 at positive peaks

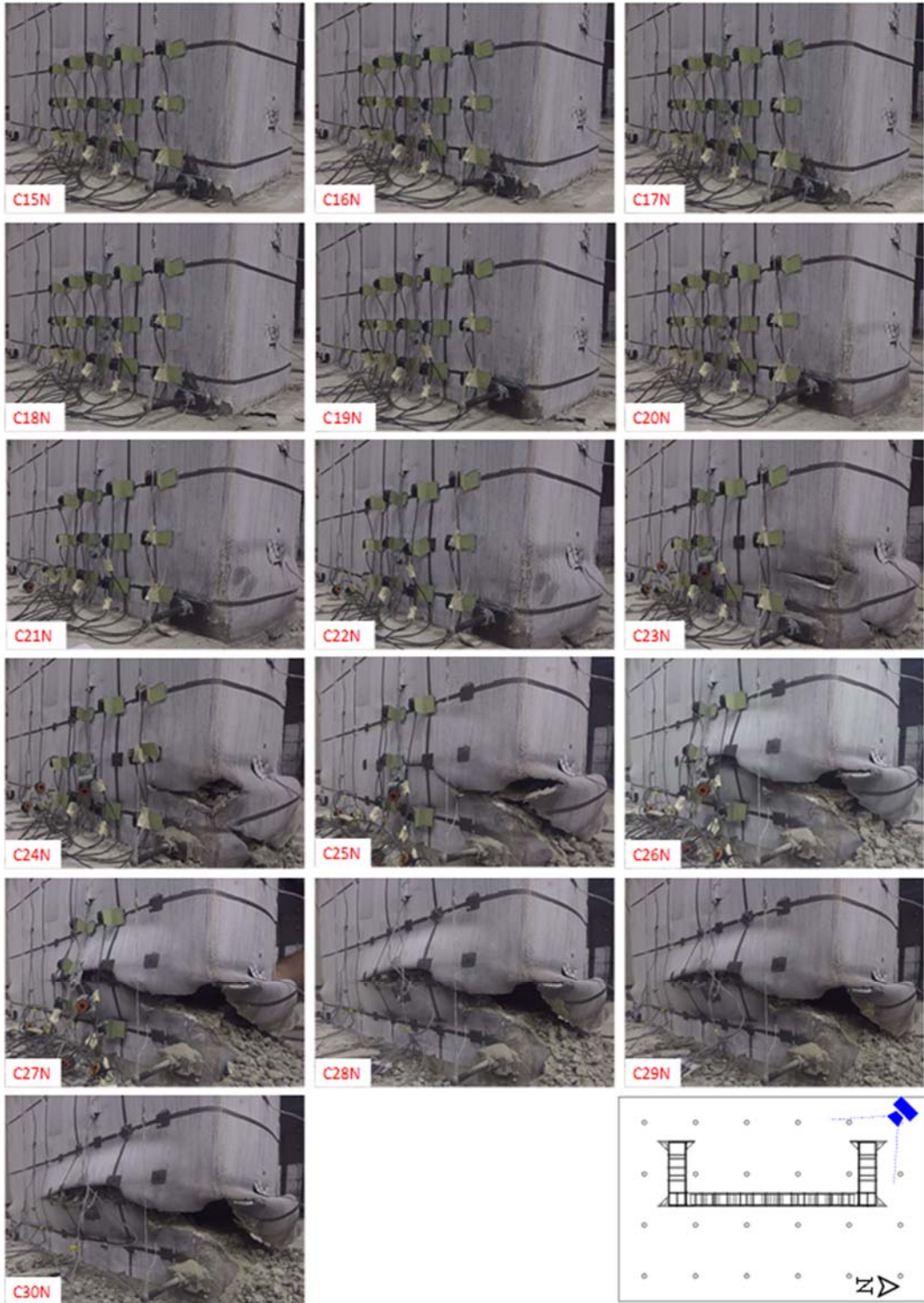


Figure 3-25. North-West views of the North Web of Specimen C2 at negative peaks

3.7.3 Test Data Analysis

The experimentally-obtained applied lateral force versus top lateral drifts for Specimen C1 and Specimen C2 are shown in Figure 3-26a and Figure 3-26b, respectively. The vertical axis shows the horizontal force applied to the specimen, which is equal to the value recorded by the lateral actuators (not equal to the shear force applied to the specimen, because the force shown in this figure is not yet corrected to subtract the horizontal components of the vertical actuator forces, which only cancel each other when the drift is equal to zero). The lateral drift was calculated by dividing the top of the wall's lateral displacement by the distance from top of the foundation to the centerline of the lateral actuator's attachment head. The points when some of the key observations were made during the test (corresponding to the onset of visible local buckling on the web and flange and maximum strengths at negative and positive displacements) are marked on these curves.

As it was mentioned before, the testing of each specimen was performed during several days. For Specimen C1, the loading protocol was executed until the end of Cycle 17, which was the first cycle with an amplitude of $+3.5in.$ and $-3.0in.$ in positive and negative directions, respectively. Then the vertical actuators were unloaded and the testing was continued and finished on the next day. It should be noted that during the first half-cycle of the second test day (i.e., Cycle 18), the force readings in the horizontal actuators went abnormally high when compared to prior and following cycles. The recorded peak value at this positive half-cycle was $328.9kips$. The difference of force between the positive peak at Cycle 18 and the corresponding peak at the following cycle, which had the same amplitude was $49.4kips$. This cycle is highlighted in Figure 3-27, which shows the same force-displacement relationship as in Figure 3-26a. This recorded peak value seems to be an outlier and is believed to be possibly due to a recording error in the lateral actuator controllers or the data acquisition system given that it only appeared during the first half-cycle of horizontal loading at the beginning of the test on the second day, even though such an error was not logged during the test. There are no reasons to believe that the specimen could have benefited from such an increase in material strength overnight. Therefore, the force values of the first half of Cycle 18 was

not taken into account in the subsequent calculations related to wall strength. However, this was not observed in the test result of Specimen C2.

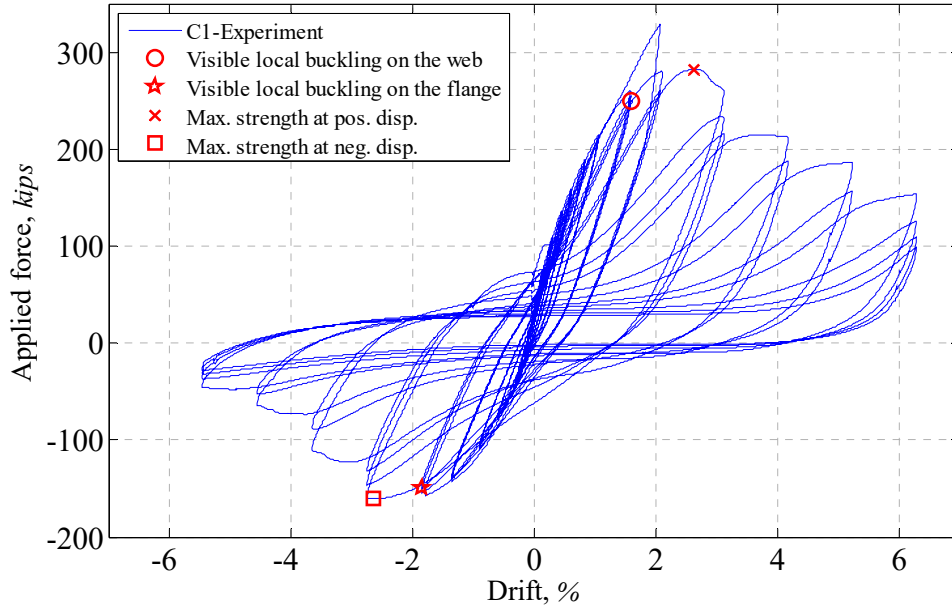
The moment resisted by the wall at its base was calculated by separating the horizontal components of the force of the two vertical actuators that applied axial load on the wall. As it was discussed before, the actuators used for the axial load application were placed with an inclination angle of 70 degrees from the strong floor and toward the wall (see Figure 3-28a). The trajectories of the axes of these actuators intersect above the centerline of the flange of the wall. At the point of zero horizontal displacement at the top of the wall, the horizontal components of the forces in the two vertical actuators are equal and in opposite directions. At non-zero displacements of the top of the wall, as the inclination angles of the vertical actuators change, the summation of the horizontal components of the forces in these actuators develops an extra force that has to be carried by the horizontal actuators. The free-body diagram of the forces (at zero displacement) is shown in Figure 3-28b. The moment resisted by the wall at its base was calculated according to the free-body diagram shown in Figure 3-28b by Equation (3.1):

$$\overrightarrow{M}_{base} = \overrightarrow{r}_{act} \times \overrightarrow{F}_H + \overrightarrow{r}_{top} \times (\overrightarrow{F}_{v1} + \overrightarrow{F}_{v2}) \quad (3.1)$$

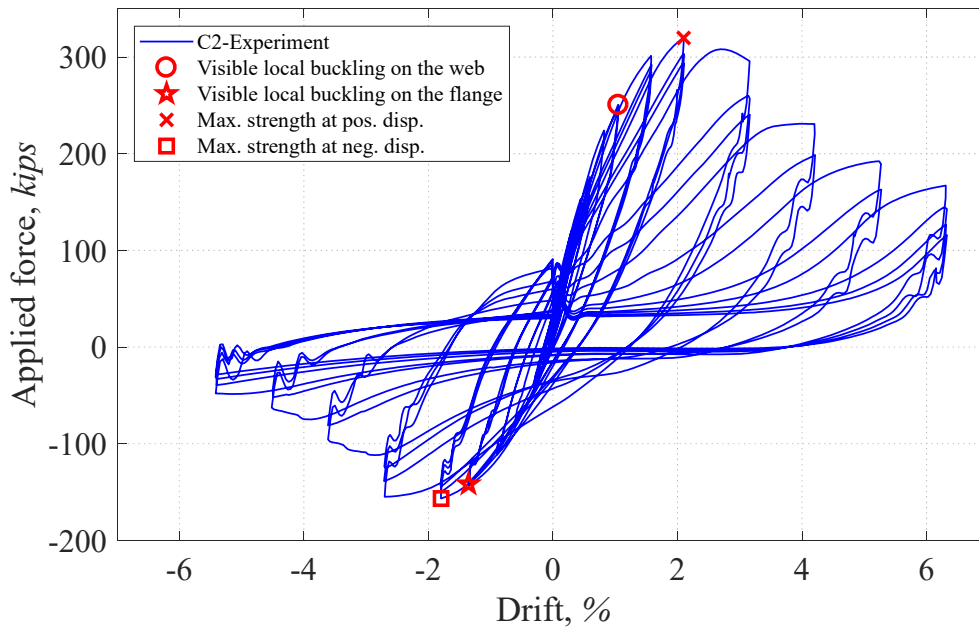
Figure 3-29a and Figure 3-29b show the calculated base moment resisted by the wall versus the top of the wall's drift for Specimen C1 and Specimen C2. The peak displacements and corresponding base moments for each cycle of the Specimen C1 and C2 test are presented in the Tables 3-4 and 3-5.

To determine the ductility reached (μ), an effective yield displacement ($\delta_{y,eff}$) was taken as the displacement corresponding to the intersection of a line tangent to the initial slope of the resulting pushover curve and a horizontal line set at the level of the maximum base moment obtained from test, $M_{base,max}$. The displacement obtained at $0.8M_{base,max}$ after post-peak of the backbone curve of the test setup was taken for the ultimate displacement (δ_u). Then, using Equation 3.2, ductility was calculated and was found to exceed 4 (i.e., 4.02/-4.3 in the positive and negative directions for both specimens).

$$\mu = \frac{\delta_u}{\delta_{y,eff}} \quad (3.2)$$



a)



b)

Figure 3-26. Applied lateral force vs. top drift relationship for a) Specimen C1 and b) Specimen C2

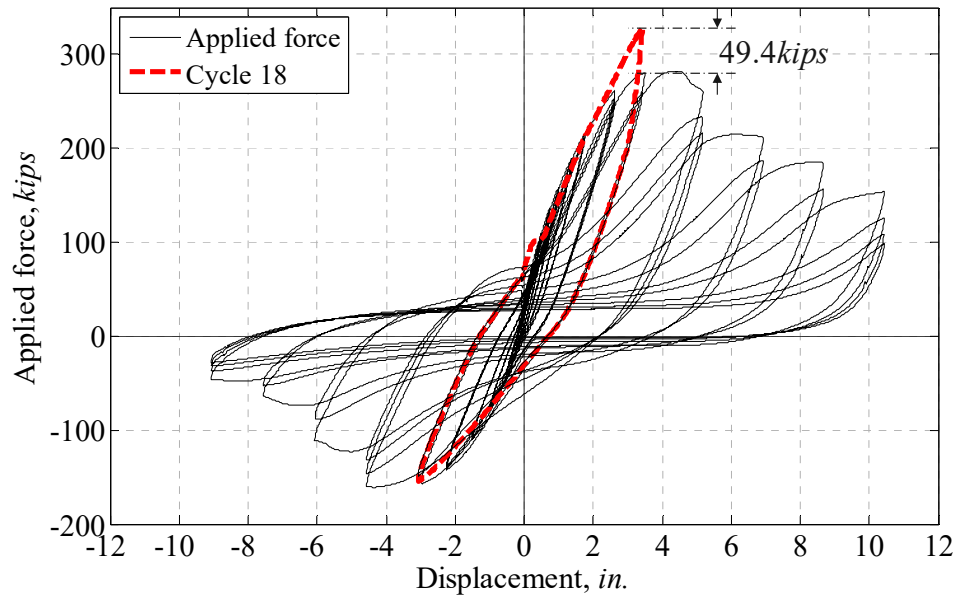


Figure 3-27. Marked Cycle 18 in the applied lateral force vs. top drift relationship for Specimen C1

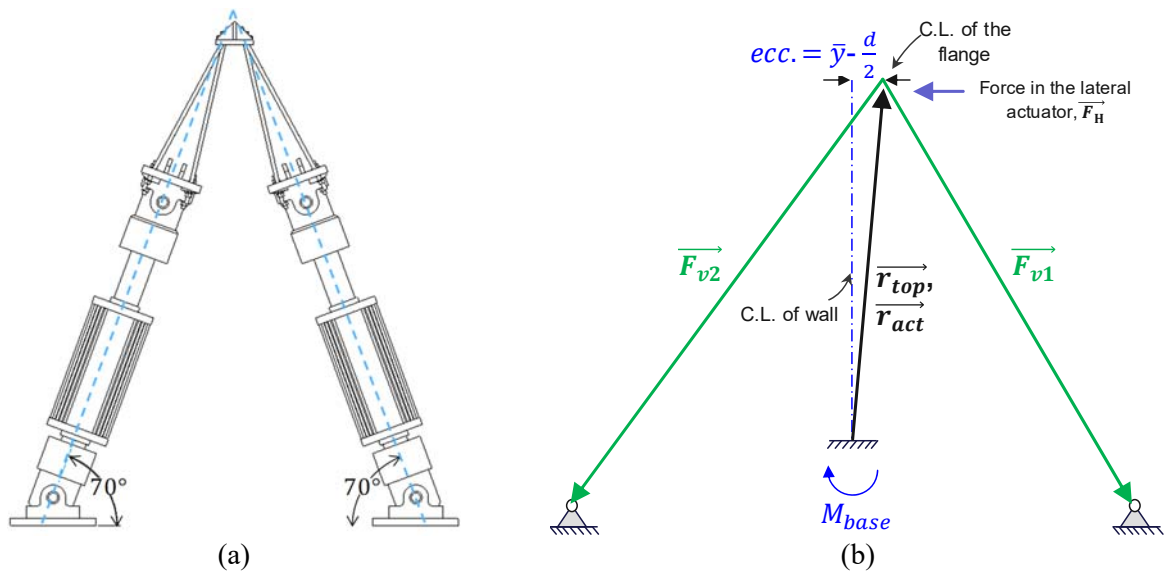
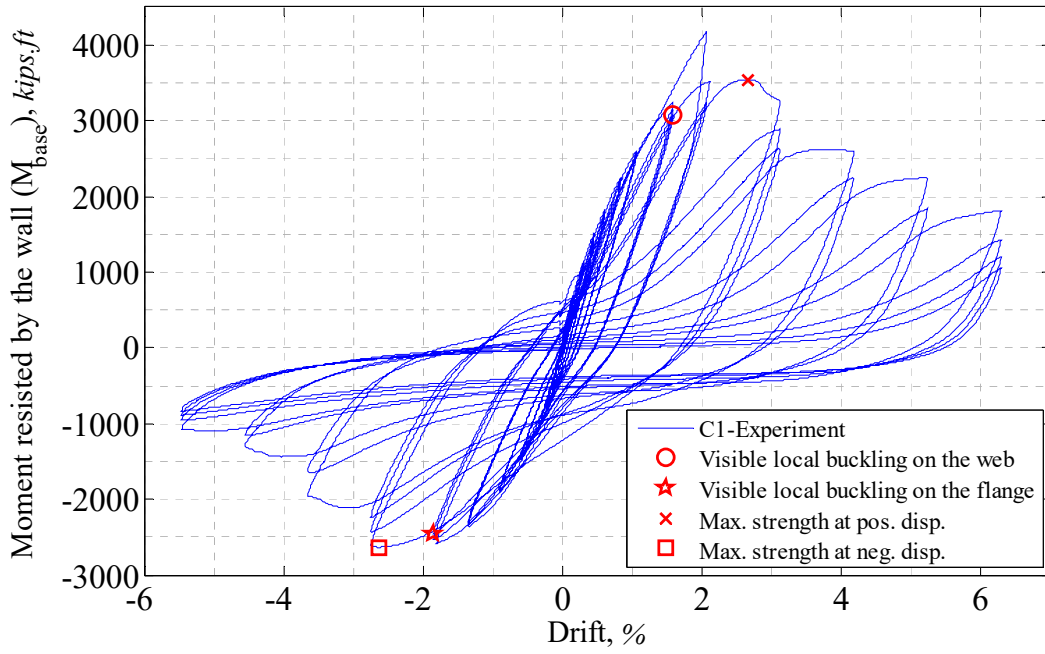
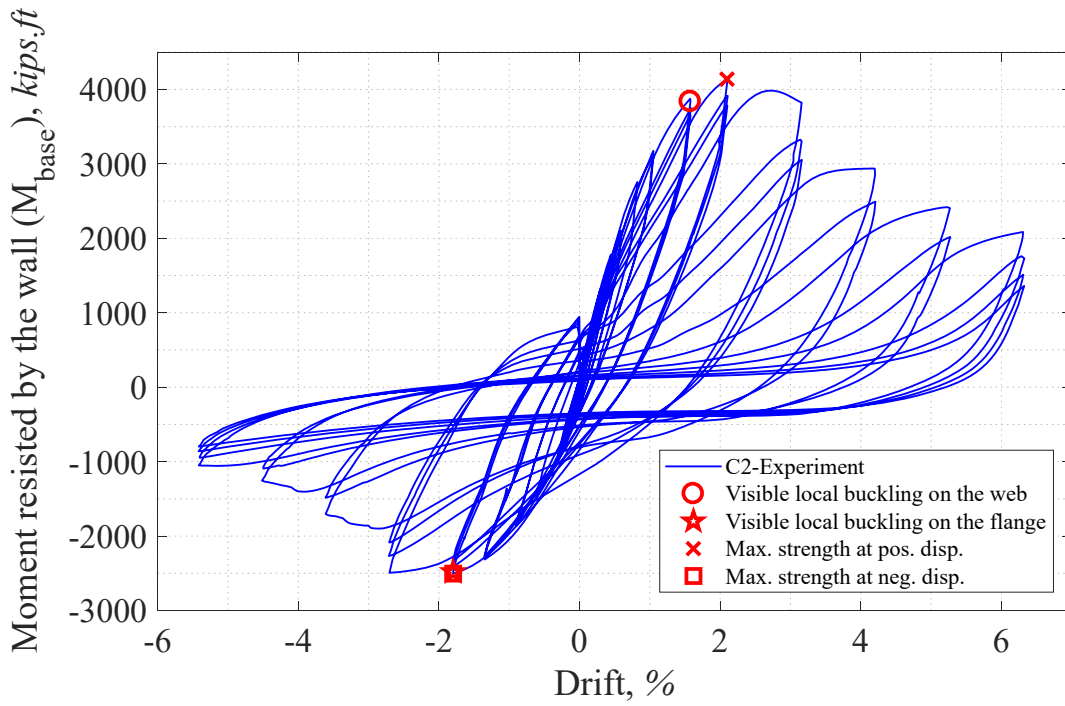


Figure 3-28. (a) Inclination angle of vertical actuators at zero displacement; (b) Free body diagram of the specimen wall at zero displacement



a)



b)

Figure 3-29. Calculated experimental base moment vs. top drift relationship for a) Specimen C1 and b) Specimen C2

Table 3-4. Peak displacements and corresponding base moments for each cycle of Specimen C1 test

Cycle	Label	Displacement, <i>in.</i>	Base Moment, <i>kip.ft</i>	Cycle	Label	Displacement, <i>in.</i>	Base Moment, <i>kip.ft</i>
1	C1P	0.25	679	16	C16P	2.63	3082
	C1N	-0.13	-286		C16N	-2.25	-2307
2	C2P	0.25	681	17	C17P	3.50	3511
	C2N	-0.13	-289		C17N	-3.00	-2584
3	C3P	0.50	1140	18	C18P	3.43	4178
	C3N	-0.25	-593		C18N	-3.07	-2538
4	C4P	0.50	1121	19	C19P	3.43	3235
	C4N	-0.25	-597		C19N	-3.07	-2461
5	C5P	0.75	1510	20	C20P	5.18	3254
	C5N	-0.38	-808		C20N	-4.57	-2631
6	C6P	0.75	1481	21	C21P	5.18	2875
	C6N	-0.38	-798		C21N	-4.57	-2435
7	C7P	1.00	1819	22	C22P	5.18	2633
	C7N	-0.50	-957		C22N	-4.57	-2240
8	C8P	1.00	1784	23	C23P	6.93	2593
	C8N	-0.50	-953		C23N	-6.07	-1956
9	C9P	1.38	2244	24	C24P	6.93	2252
	C9N	-1.00	-1484		C24N	-6.06	-1630
10	C10P	1.38	2222	25	C25P	8.68	2232
	C10N	-1.00	-1473		C25N	-7.56	-1318
11	C11P	1.75	2598	26	C26P	8.67	1840
	C11N	-1.50	-1907		C26N	-7.56	-1157
12	C12P	1.75	2556	27	C27P	10.42	1816
	C12N	-1.50	-1892		C27N	-9.06	-1079
13	C13P	Skipped	N/A	28	C28P	10.43	1429
	C13N	Skipped	N/A		C28N	-9.07	-958
14	C14P	2.63	3240	29	C29P	10.43	1197
	C14N	-2.25	-2363		C29N	-9.06	-887
15	C15P	2.63	3149	30	C30P	10.43	1053
	C15N	-2.25	-2329		C30N	-9.07	-836

Table 3-5. Peak displacements and corresponding base moments for each cycle of Specimen C2 test

Cycle	Label	Displacement, <i>in.</i>	Base Moment, <i>kip.ft</i>	Cycle	Label	Displacement, <i>in.</i>	Base Moment, <i>kip.ft</i>
1	C1P	0.25	703	16	C16P	2.63	3656
	C1N	-0.13	-302		C16N	-2.25	-2261
2	C2P	Skipped	N/A	17	C17P	3.50	4138
	C2N	Skipped	N/A		C17N	-3.00	-2503
3	C3P	0.50	1315	18	C18P	3.43	3915
	C3N	-0.25	-612		C18N	-3.07	-2410
4	C4P	0.50	1316	19	C19P	3.43	3783
	C4N	-0.25	-610		C19N	-3.07	-2332
5	C5P	0.75	1779	20	C20P	5.18	3984
	C5N	-0.38	-794		C20N	-4.57	-2493
6	C6P	0.75	1731	21	C21P	5.18	3325
	C6N	-0.38	-787		C21N	-4.57	-2268
7	C7P	1.00	2103	22	C22P	5.18	3054
	C7N	-0.50	-943		C22N	-4.57	-2085
8	C8P	1.00	2072	23	C23P	6.93	2937
	C8N	-0.50	-940		C23N	-6.07	-1897
9	C9P	1.38	2755	24	C24P	6.93	2494
	C9N	-1.00	-1479		C24N	-6.06	-1485
10	C10P	1.38	2754	25	C25P	8.68	2419
	C10N	-1.00	-1477		C25N	-7.56	-1403
11	C11P	1.75	3118	26	C26P	8.67	2019
	C11N	-1.50	-1864		C26N	-7.56	-1093
12	C12P	1.75	3174	27	C27P	10.42	2085
	C12N	-1.50	-1854		C27N	-9.06	-1055
13	C13P	Skipped	N/A	28	C28P	10.43	1761
	C13N	Skipped	N/A		C28N	-9.07	-948
14	C14P	2.63	3876	29	C29P	10.43	1511
	C14N	-2.25	-2314		C29N	-9.06	-860
15	C15P	2.63	3748	30	C30P	10.43	1360
	C15N	-2.25	-2291		C30N	-9.07	-797

The strains on the steel plates were recorded by strain gages placed at 5.4, 11.4, and 17.4*in.* from the top of the foundation on the webs and flange of the wall. The strain profiles at these three heights are shown in Figures 3-30 and 3-31 at the peak displacements of the cycle corresponding to the theoretical first yield points in the positive and negative direction for Specimen C1 and C2, respectively. The vertical axis

shows the recorded strain normalized to the yield strain of the steel plate, which was obtained as 0.0019 from the steel coupon tests. At this stage, the strain profiles across the wall cross-section are almost linear. Figures 3-32 and 3-35 respectively show the recorded strains at the points where the local buckling was observed, on the web for positive wall displacements, and on the flange for negative displacements for both Specimen C1 and C2. The strain profiles at the points where maximum resistance was reached are shown in Figures 3-36 and 3-37.

The points of maximum flexural strength experimentally obtained from Specimens C1 and C2 were compared to their corresponding values predicted by theoretical P-M interaction curves. These plots are shown in Figures 3-38 and 3-39 for Specimens C1 and C2, respectively. In calculation of the P-M interaction curves, the actual material properties of the steel plates and concrete infill measured from the tensile coupon and compression cylinder tests were used.

The experimentally obtained moment developing at the base of the walls were also compared to their theoretical plastic moment calculated using the Plastic Stress Distribution Method (PSDM), M_{PSDM} , and to the yield moment, M_y . Note that values of the yield moment and corresponding neutral axis location were calculated for strain diagrams obtained assuming an E_c value obtained using ACI equation (ACI 2019) (lower M_y values would have been obtained using lower values of E_c).

The theoretical values were calculated three different way, namely using the actual, nominal, and expected material properties. These comparisons are shown in Figures 3-40 and 3-41 for Specimens C1 and C2, respectively. The actual values are those obtained from the testing of steel coupons of samples from the wall's web and flanges, and of concrete cylinder cast during construction of the walls and tested on the corresponding specimen test day. The nominal yield value used for the steel plates was equal to 50ksi for the A572Gr50 steel used in the wall's construction. The nominal value for concrete was taken equal to 4ksi for both specimens. The expected values for the steel yield and concrete compressive strengths were calculated by multiplying those values by $R_y=1.1$ and $R_c=1.5 \times 0.85$, respectively. The material property values as well as the calculated theoretical resistances are shown in Table 3-6.

In Table 3-6, the ratio of Plastic Moment to First Yield Moment also provides information on the portion of the wall along its height over which yielding occurred in at least some part of the cross-section. Results indicated that over roughly 40% of the height of the wall experienced such yielding, given that this ratio was in the range of 1.45 to 1.66 (depending on direction of loading) for the measured material strengths.

Table 3-6. Actual, nominal, and expected material properties and Calculated flexural resistances for Specimen C1

(Note: 1 in. = 25.4 mm; 1ft=0.3048 m; 1sq in.=645.2 mm²; 1 in⁴=416231 mm⁴; 1 psi=0.0069 MPa; 1 ksi=6.9 MPa)

Specimen	Material property	Concrete f'_c , ksi	Steel plates F_y , ksi	M_y , kip.ft			M_{PSDM} , kip.ft			$\frac{M_{PSDM}}{M_y}$		$\frac{M_{exp}}{M_{PSDM}}$			
				Pos.	y_{NA} , in	Neg.	y_{NA} , in	Pos.	y_{NA} , in	Neg.	y_{NA} , in	Pos.	Neg.		
C1	Nominal	4.0	50.0	2079	7.52	-1507	9.52	3010	6.19	-2406	4.86	1.45	1.6	1.18	1.10
	Actual	4.5	55.4	2356	8.35	-1634	8.92	3387	6.27	-2640	4.64	1.44	1.62	1.04	1.00
	Expected	5.1	55.0	2486	8.78	-1632	8.60	3596	6.40	-2662	4.19	1.45	1.63	0.98	1.0
C2	Nominal	4.0	50.0	2100	8.15	-1449	9.05	3044	6.25	-2359	4.60	1.45	1.63	1.35	1.06
	Actual	5.1	55.4	2516	9.52	-1581	8.53	3639	6.92	-2623	4.00	1.45	1.66	1.13	0.96
	Expected	5.1	55.0	2506	9.51	-1573	8.53	3624	6.96	-2608	3.99	1.45	1.66	1.14	0.97

Note: y_{NA} is the location of the neutral axis from the face of flange.

Note that as described in Section 3.3, due to the testing program requirements, the strength of the steel plate and concrete materials had to be controlled. In order to control the maximum strength of the test walls, the steel plates of all the specimens were ordered to have yield strengths *less than 58ksi*. Also, to achieve the target level of the applied axial load for Specimen C1 using the full capacity of the SEESL lab actuators, the specimen's concrete strength was required to be *4ksi* at the day of the test. Therefore, as a result of these unusual controls, the actual and expected material properties were not close for Specimen C1.

A grid of Krypton LEDs were placed on the north elevation of the north web of the wall and east elevation of the flange. Figure 3-42 shows the location of these LEDs on the web for both specimens. The LEDs were placed at the bottom of the wall close to the foundation surface and between the first and second rows of the tie bars where severe local buckling developed during the test. The amplitude of the local buckling in this region was measured using the out-of-plane movement of the LEDs during the test. Figures 3-43 and 3-45 show the out-of-plane movement of the LEDs located between the tie bars shown in Figure 3-42 for Specimen C1 and C2, respectively, as an example. As shown in the figure, the buckling on the steel plate of the web was initiated during Cycle 6. The amplitude of the local buckling was dramatically increased after the 12th cycle in Specimen C1 and after 11th cycle in Specimen C2.

The specimens were inspected after their failure. Figures 3-44 and 3-46 show a schematic of the damage on the steel plates for Specimen C1 and C2, respectively. In this figure, the locally buckled areas are marked with green dashed line, the fracture lines are shown with solid blue line, the failed tie bar welds are shown with solid red lines and failed tie bar in Specimen C2 are shown by red crosses. Note that failures at tie bar locations, in all observed cases, were due to weld failure at their connection (typically at only one end of the tie bar) except for one tie bar in Specimen C2 (identified by the red cross in Figure 3-46 where the tie bar itself is known to have fractured as in Figure 3-47). The failed end of the tie bar is marked in the figure.

The rotations of the wall at the base where the plastic hinge was developed was also calculated. This was done using the recorded horizontal movements of the wall for the string pot attached to the wall closest to the foundation, and then dividing its readings by its distance to the top of the foundation (33in.), which resulted in total rotations at the wall base (i.e., θ_{wt}). Recognizing that this calculated rotation also included the rotations of the wall-foundation connection (i.e., θ_{wf}), these rotations at the wall-foundation connection (θ_{wf}) were subtracted from the total rotations (θ_{wt}) to obtain the wall rotations at the base (i.e., θ_{wb}). Figure 3-48 shows the composition of the rotations at the base of the wall. Note that there was no

slippage between the footing and the strong floor during the test and therefore the lateral displacements of the footing were considered zero in calculation of the rotation.

Note that the rotation at the wall-foundation connection (θ_{wf}) could have been calculated at each step of the test using the differences in the recorded displacements from the vertical string pots (i.e., along the axial axis of the wall) that were connected from the wall surface to the foundation's top surface at east and west elevations of the wall, divided by their distance from each other, but this would have not included rotations introduced locally near the base of the wall due to the flexibility/deformations of the foundation itself. Instead, the wall-foundation connection rotation was taken into account by substituting the foundation and wall-to-foundation connection with a linear rotational spring at the base of the wall. The rotational stiffness of this spring was calculated by finding the slope of a line that was fitted to the $M_{base}-\theta_{wf}$ relationship curve at the linear cycles (i.e., from the beginning of the test until end of Cycle 7) and then multiplying the rotational stiffness by the base moment (M_{base}) at each corresponding step of the test. The rotational spring stiffness was calculated as $1.13 \times 10^6 \text{ kip.ft/rad}$ for Specimen C1 and $1.26 \times 10^6 \text{ kip.ft/rad}$ for Specimen C2. Figures 3-49 and 3-51 show the calculated base moment versus the wall rotations ($M_{base}-\theta_{wb}$) relationship curve for Specimen C1 and C2, respectively. This curve was compared to the one with total rotations at the wall base ($M_{base}-\theta_{wt}$) in Figures 3-50 and 3-52.

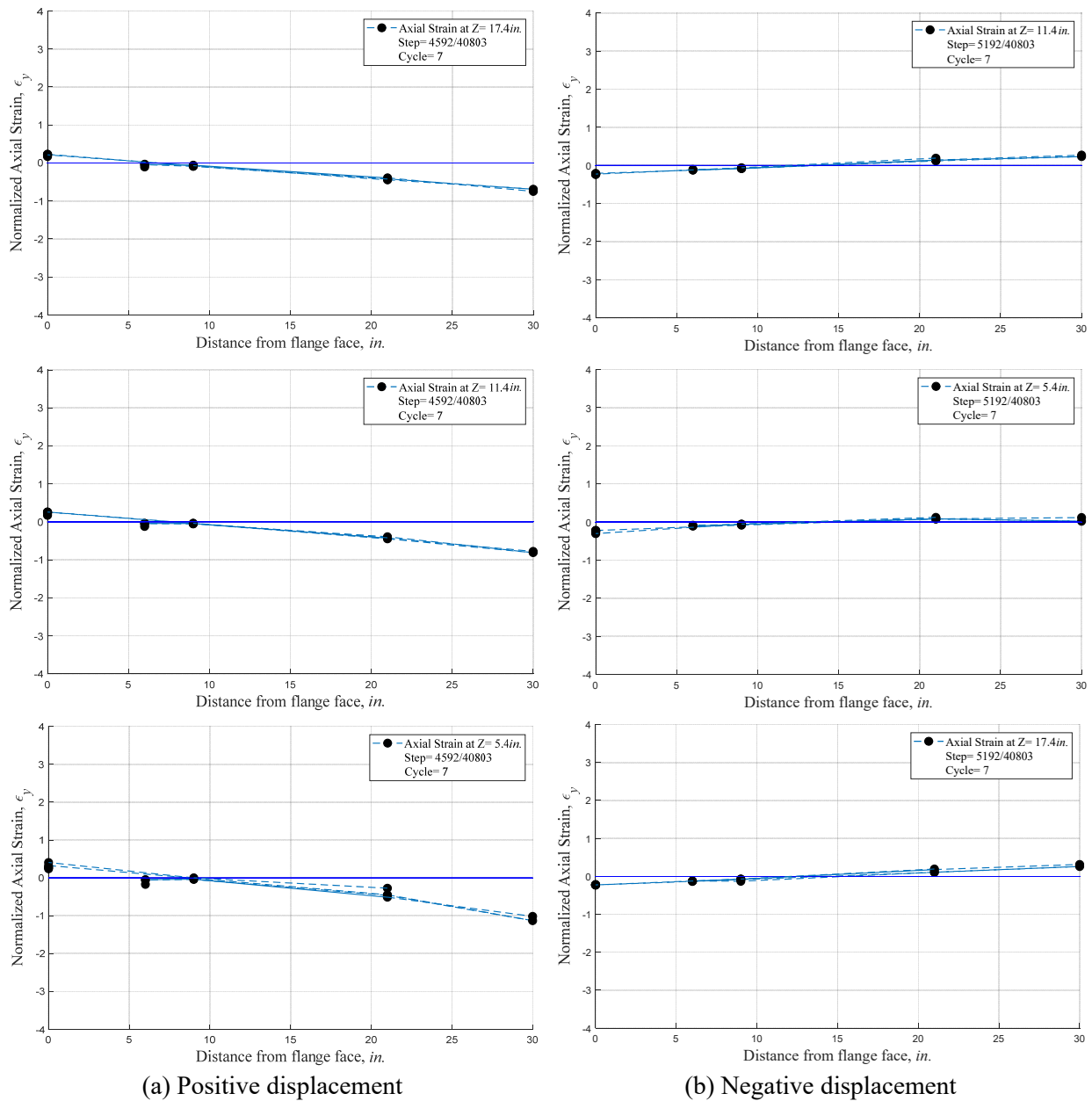
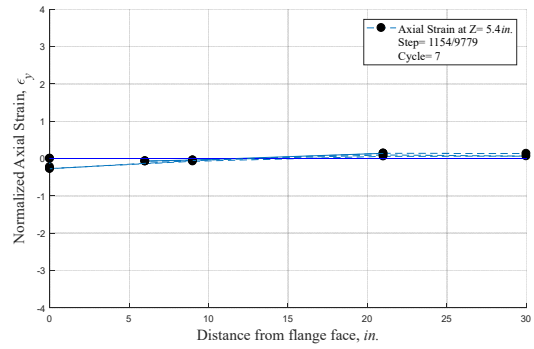
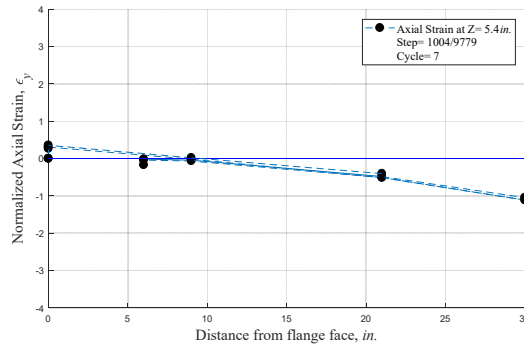
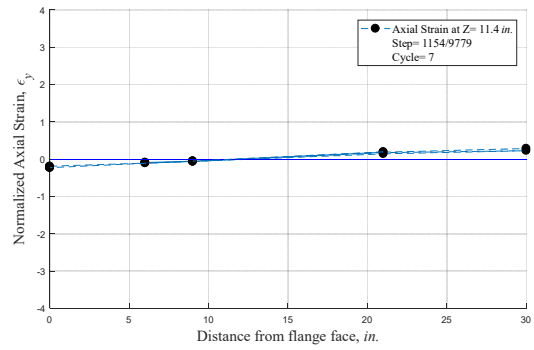
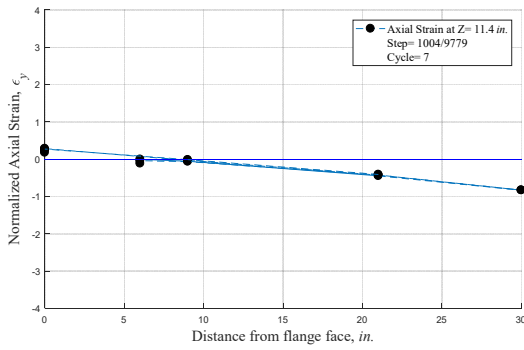
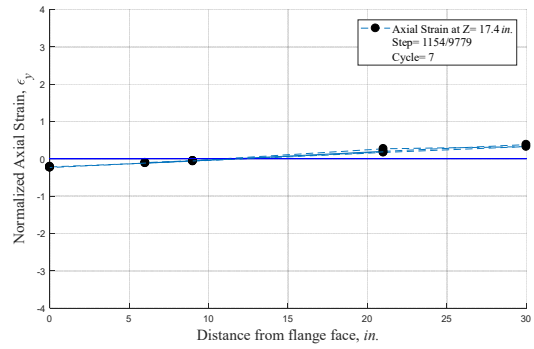
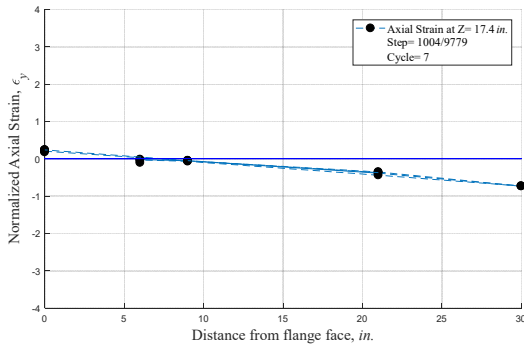


Figure 3-30. Strain profiles at first yield on: (a) positive displacement; (b) negative displacement for Specimen C1



(a) Positive displacement

(b) Negative displacement

Figure 3-31. Strain profiles at first yield on: (a) positive displacement; (b) negative displacement for Specimen C2

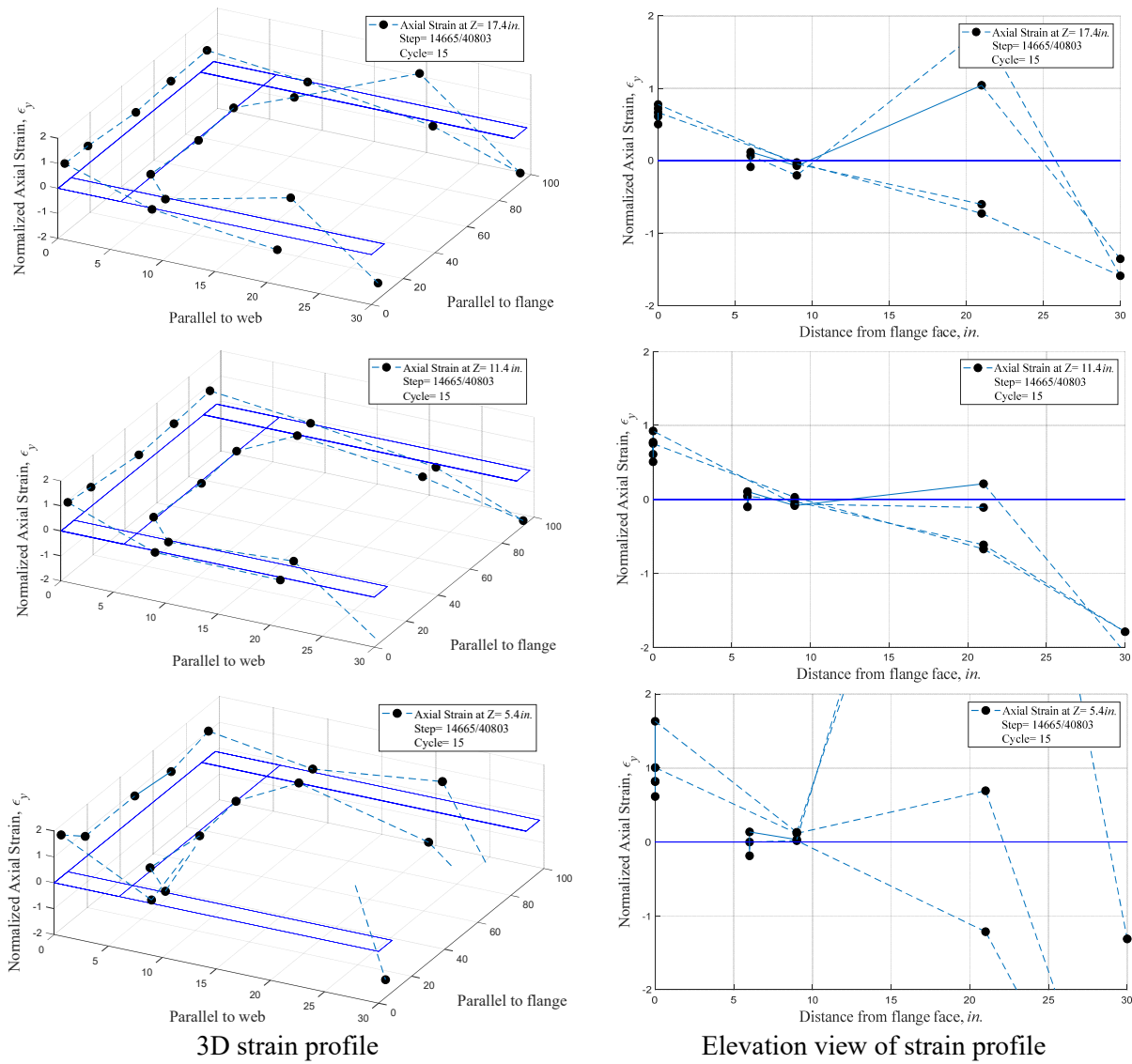
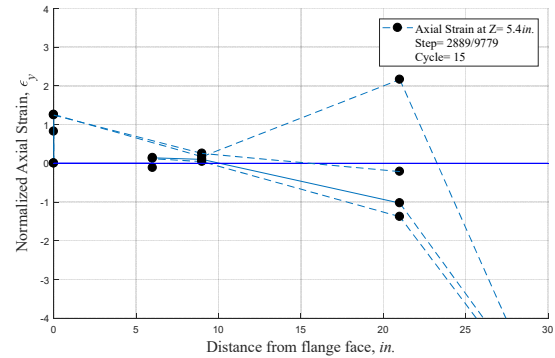
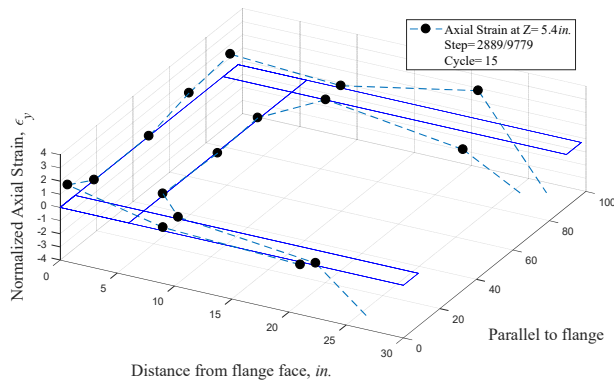
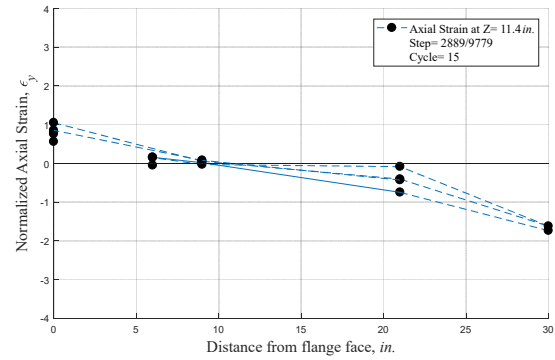
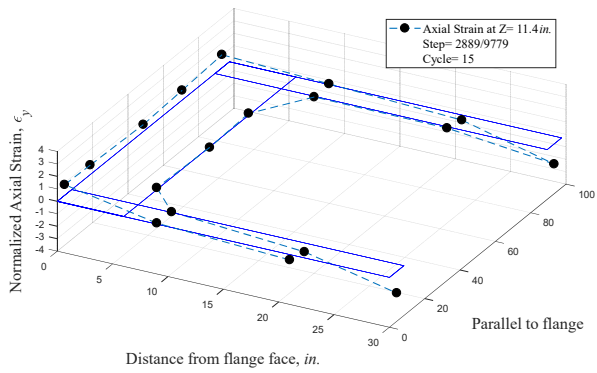
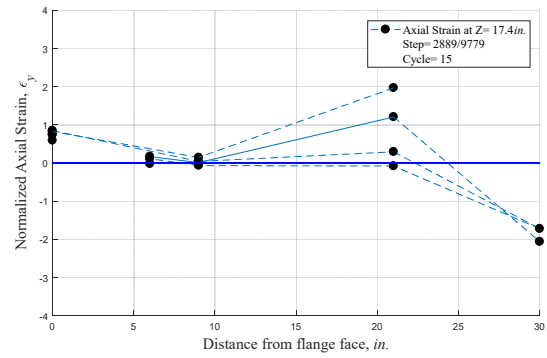
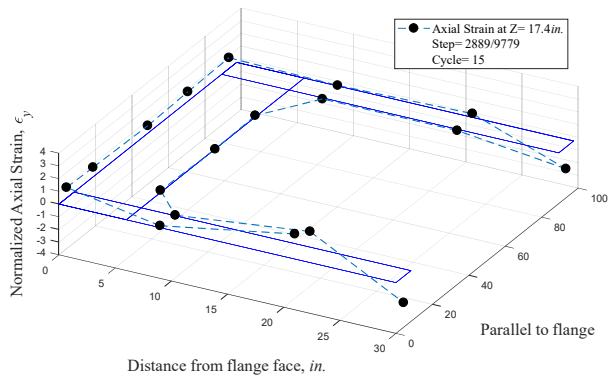


Figure 3-32. Strain profiles at the positive peak of Cycle 15 where the local buckling was visually observed on the web for Specimen C1



3D strain profile

Elevation view of strain profile

Figure 3-33. Strain profiles at the positive peak of Cycle 15 where the local buckling was visually observed on the web for Specimen C2

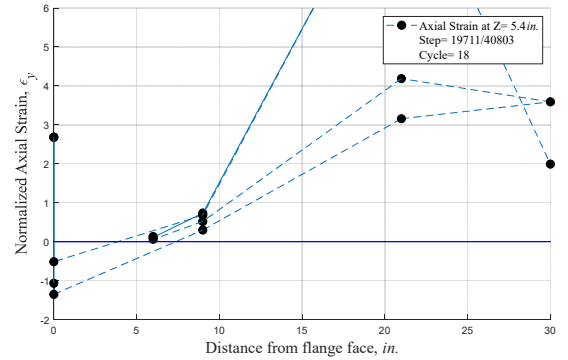
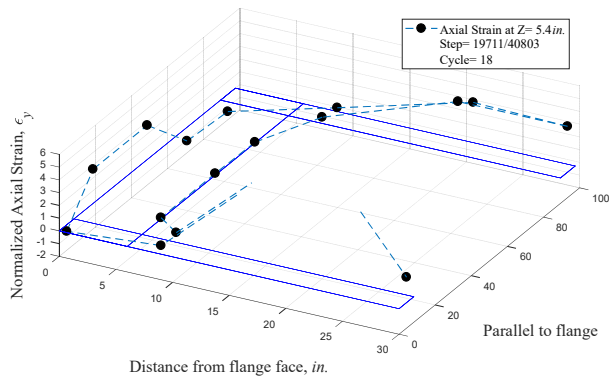
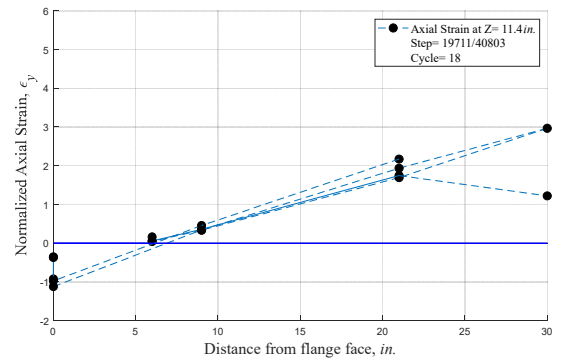
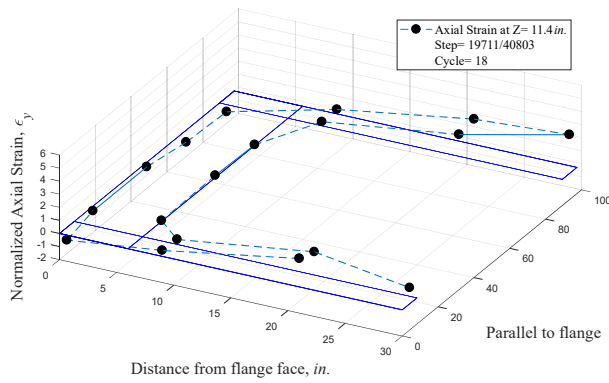
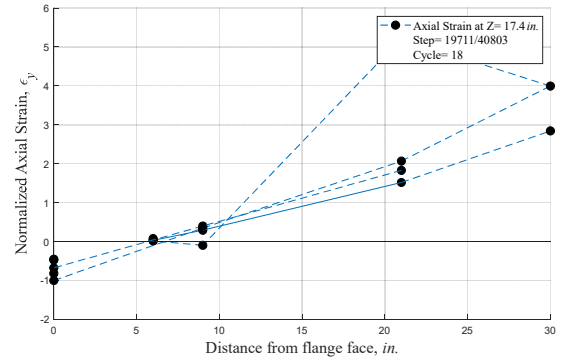
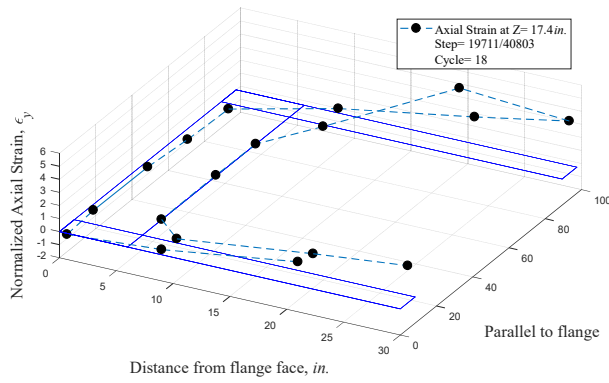


Figure 3-34. Strain profiles at the negative peak of Cycle 18 where the local buckling was visually observed on the flange for Specimen C1

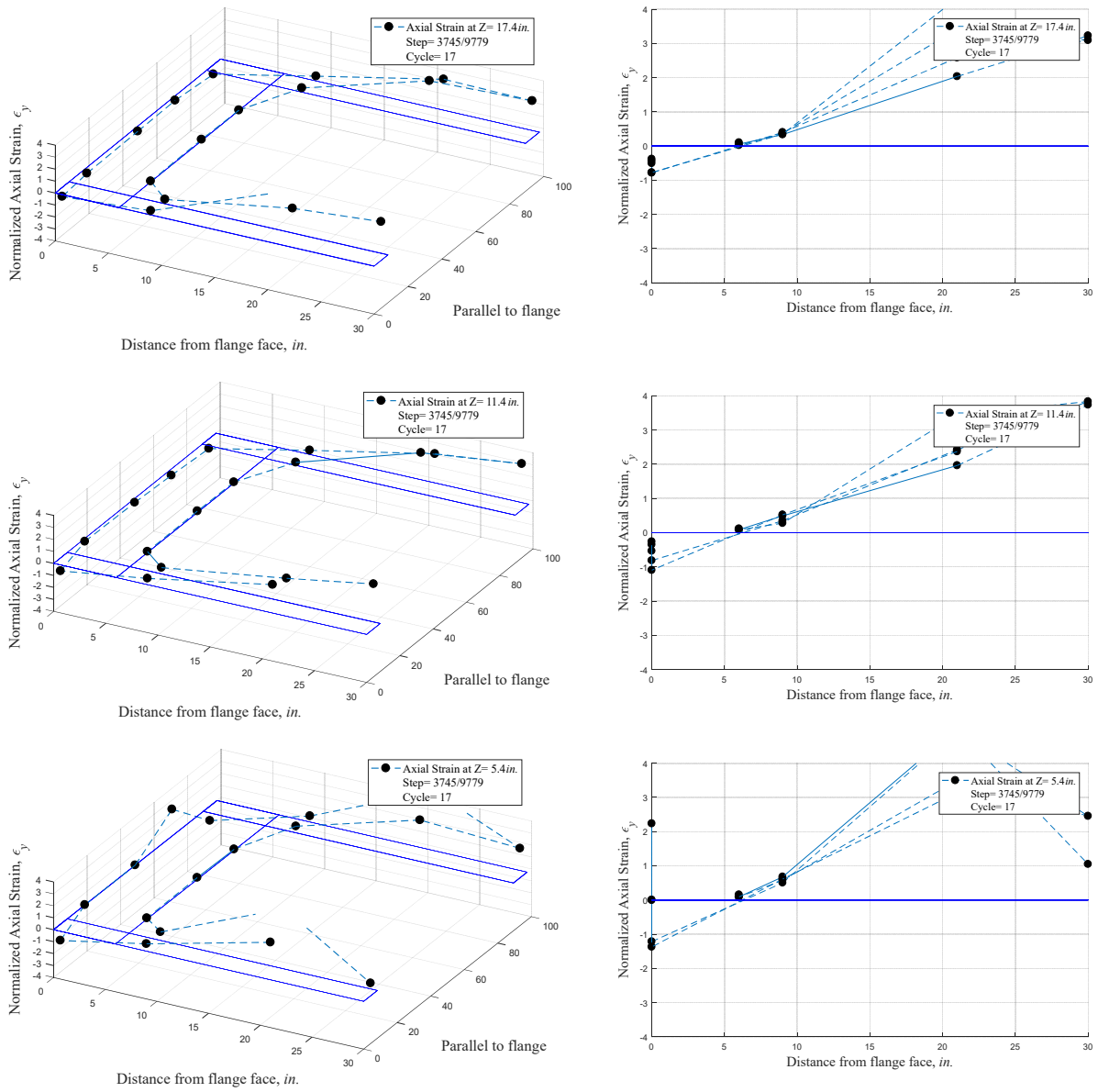
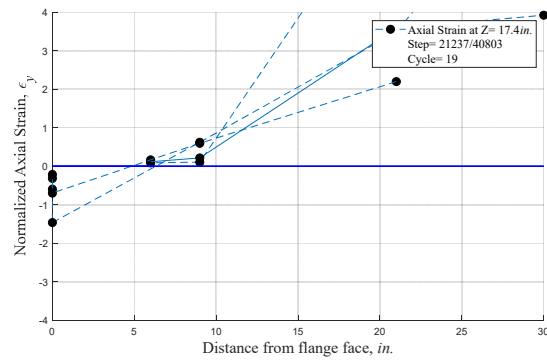
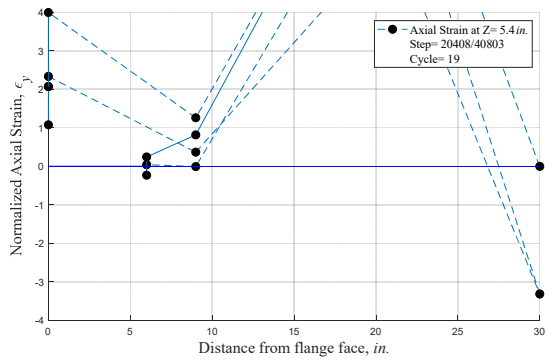
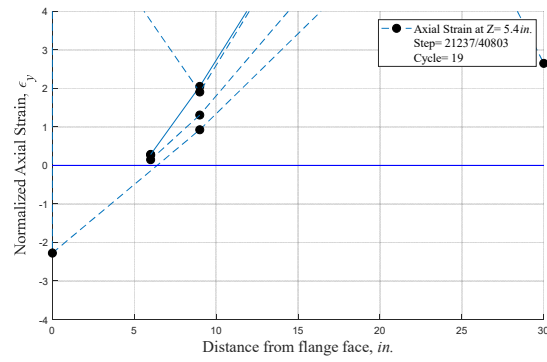
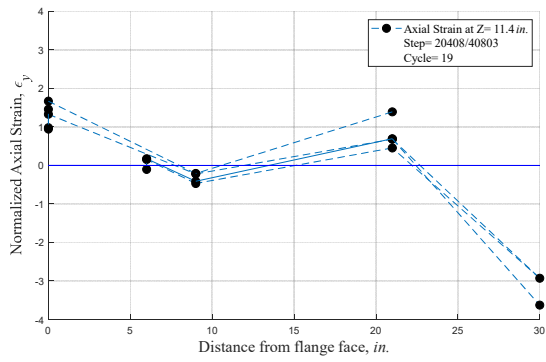
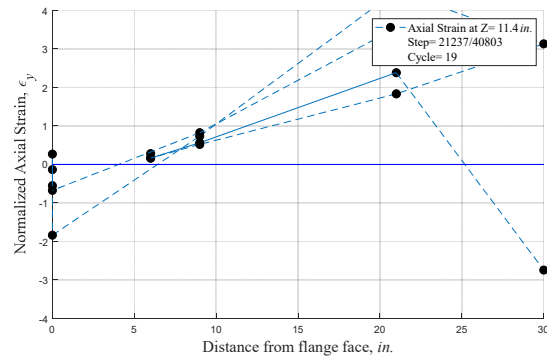
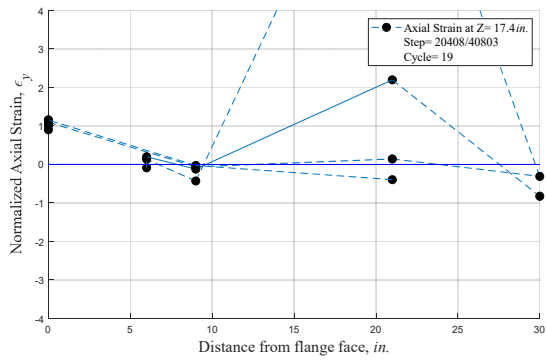


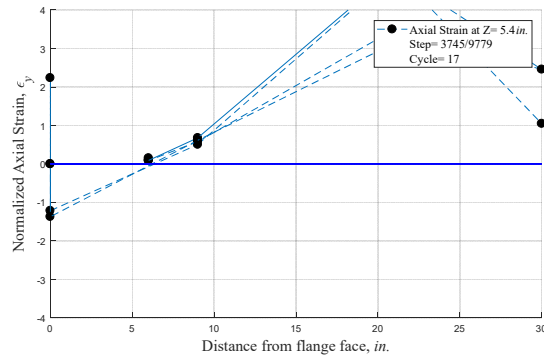
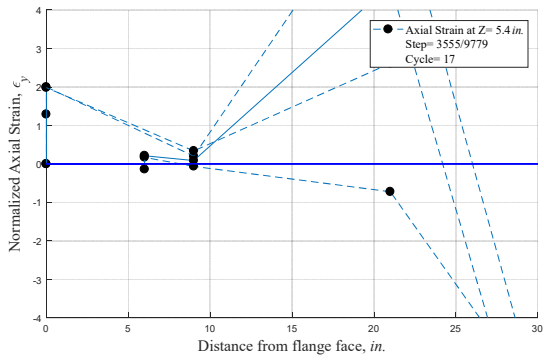
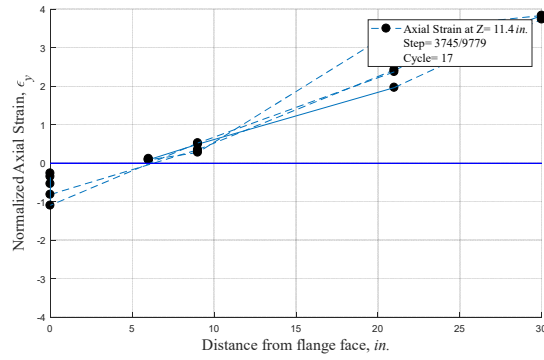
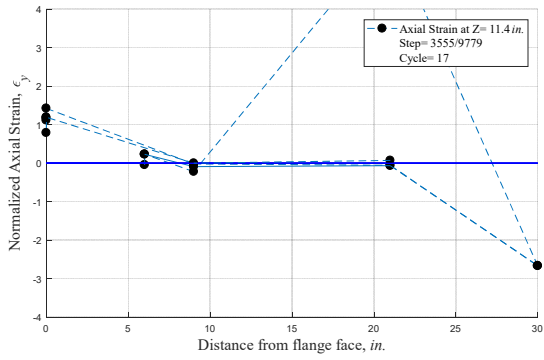
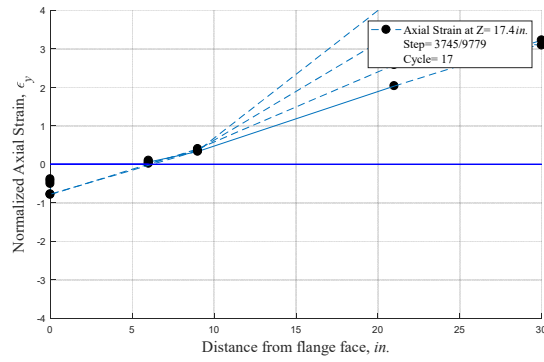
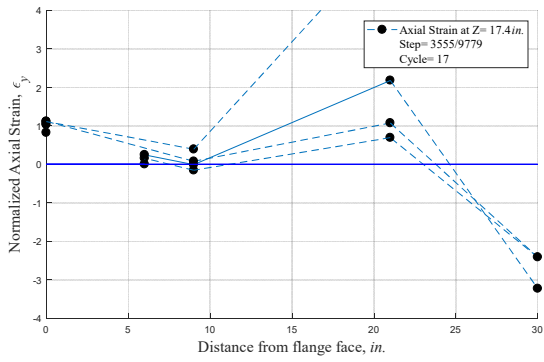
Figure 3-35. Strain profiles at the negative peak of Cycle 17 where the local buckling was visually observed on the flange for Specimen C2



(a) Positive maximum strength

(b) Negative maximum strength

Figure 3-36. Strain profiles at: (a) the positive maximum strength point (Cycle 19); (b) the negative maximum strength point (Cycle 19) for Specimen C1



(a) Positive maximum strength

(b) Negative maximum strength

Figure 3-37. Strain profiles at: (a) the positive maximum strength point (Cycle 17); (b) the negative maximum strength point (Cycle 17) for Specimen C2

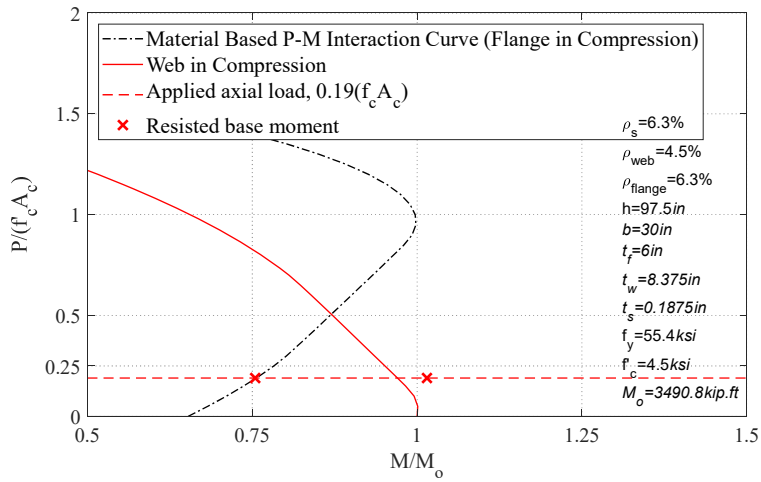


Figure 3-38. Comparison of Specimen C1 flexural resistances with P-M interaction curve

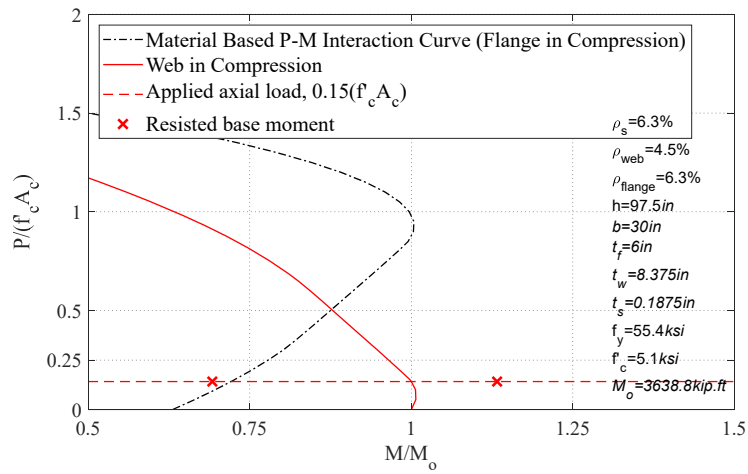


Figure 3-39. Comparison of Specimen C2 flexural resistances with P-M interaction curve

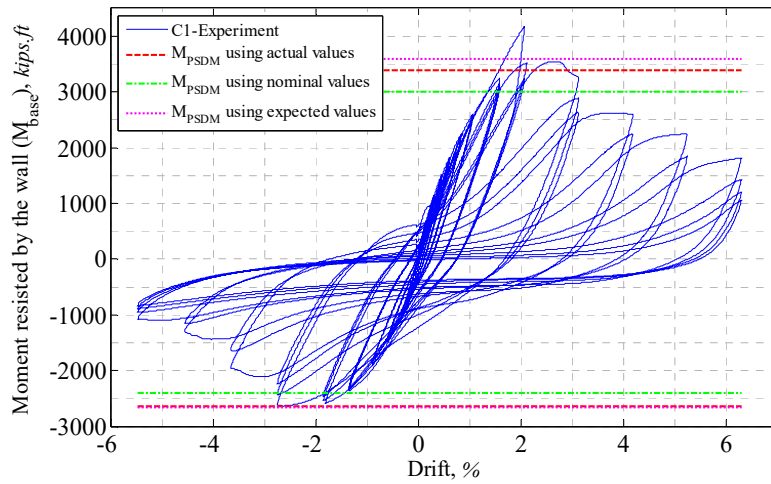


Figure 3-40. Comparison of calculated theoretical resistance moments and the experimental base moment for Specimen C1

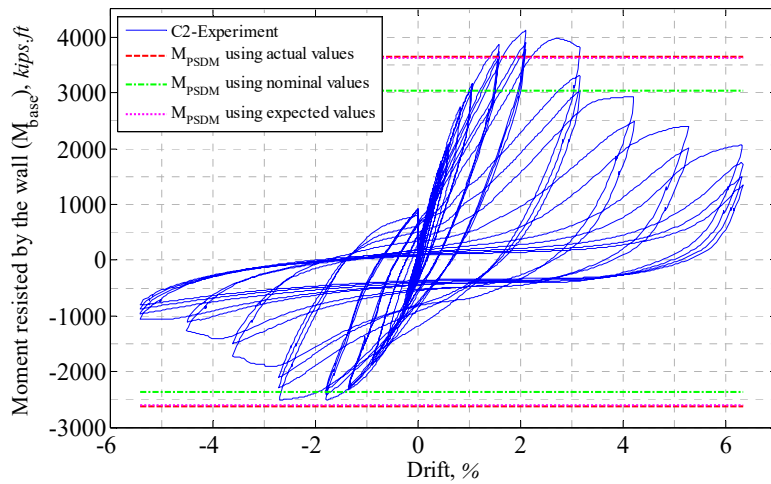


Figure 3-41. Comparison of calculated theoretical resistance moments and the experimental base moment for Specimen C2

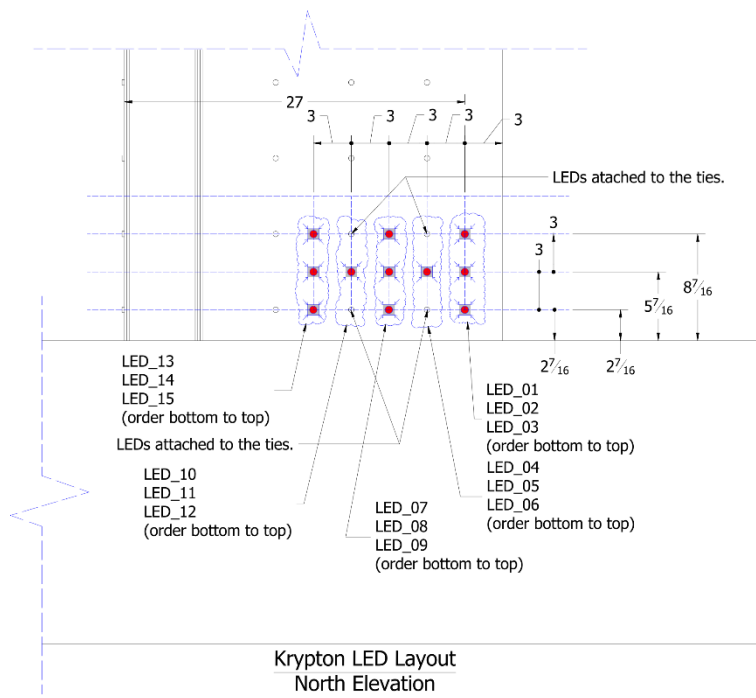


Figure 3-42. location of Krypton LEDs placed on the web of Specimen C1 at the north elevation

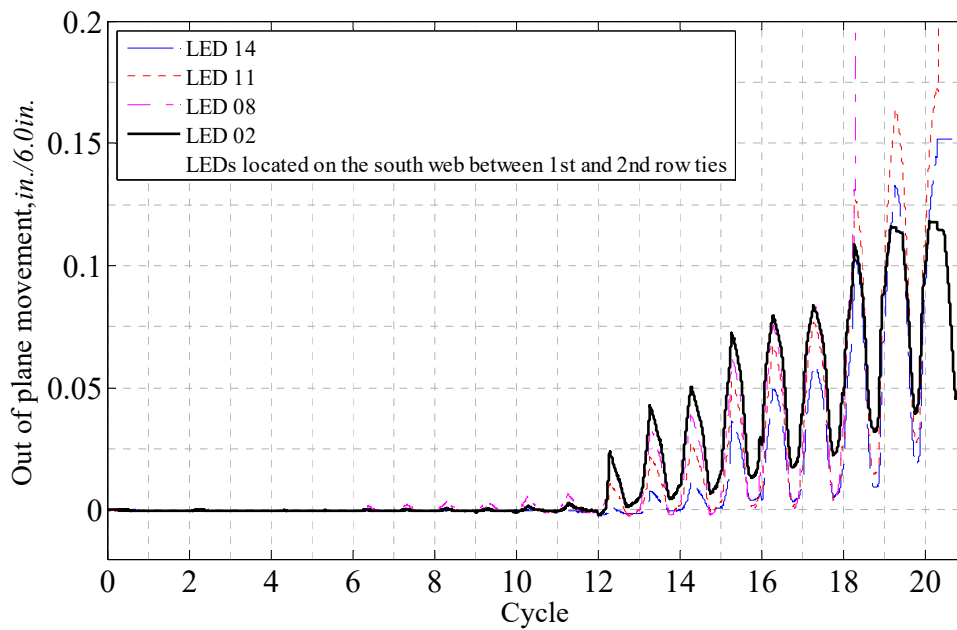


Figure 3-43. Out-of-plane movement of LEDs 14, 11, 08, and 02 located on the web of Specimen C1

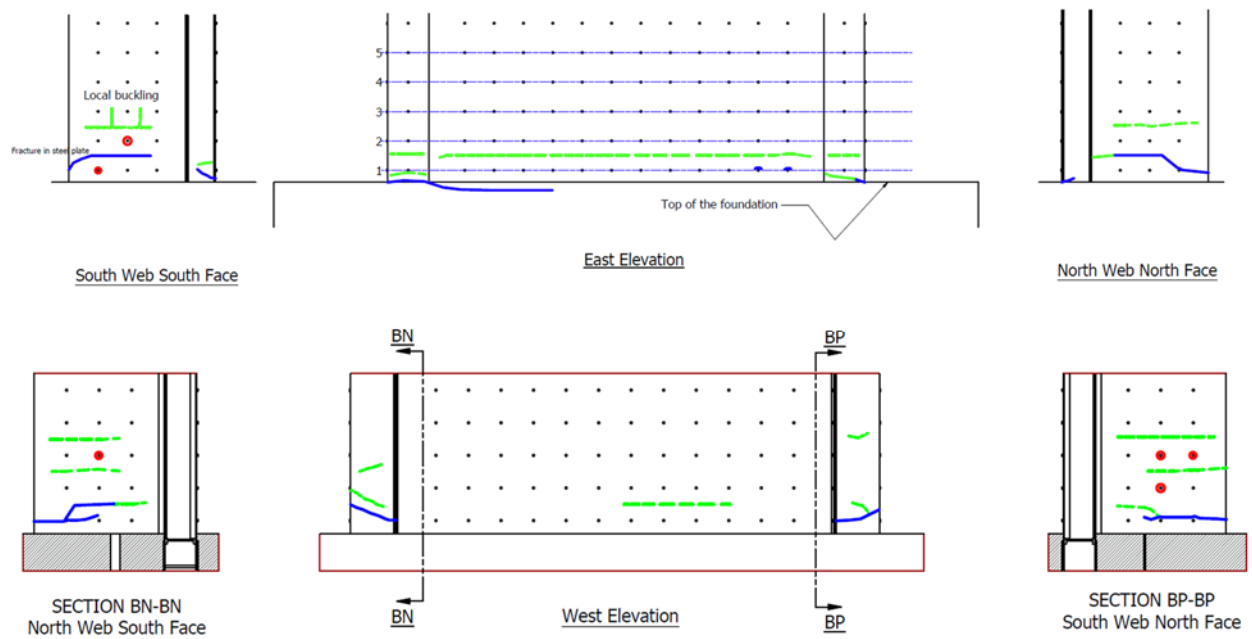


Figure 3-44. Post-test damage inspection of the wall steel plates for Specimen C1

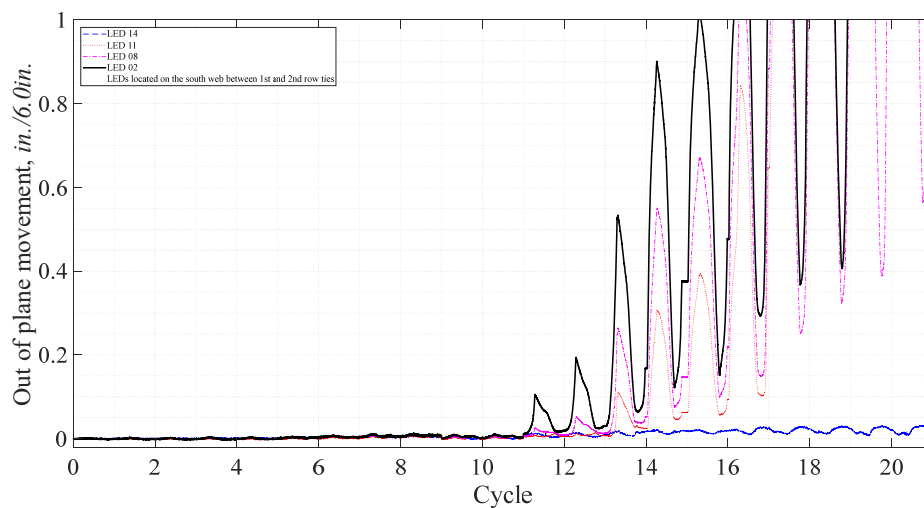


Figure 3-45. Out-of-plane movement of LEDs 14, 11, 08, and 02 located on the web of Specimen C2

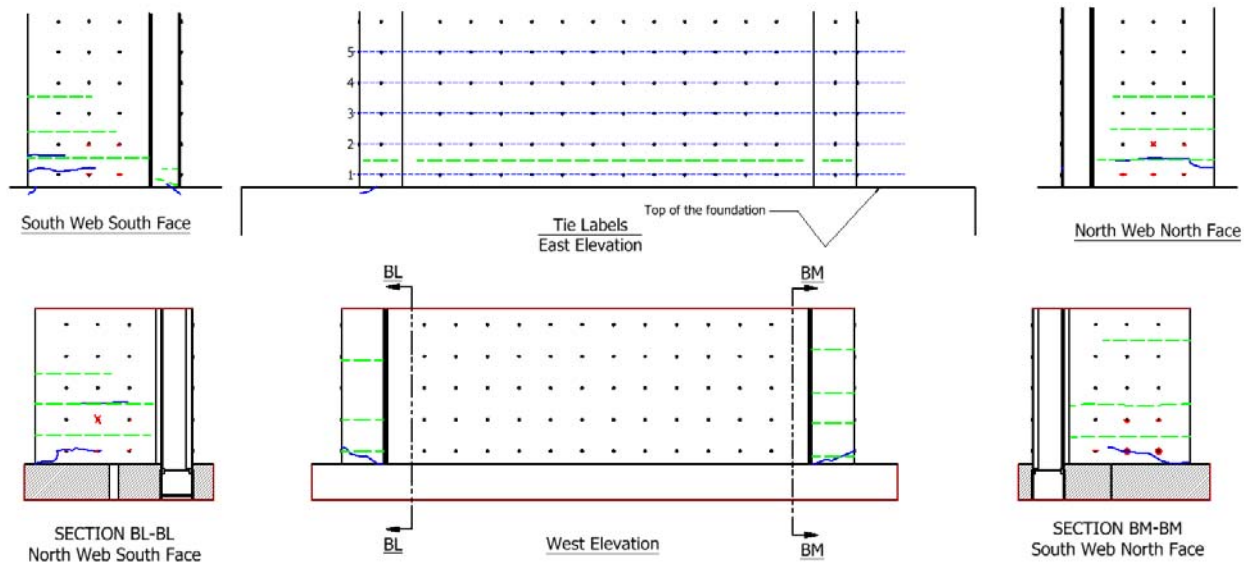


Figure 3-46. Post-test damage inspection of the wall steel plates for Specimen C2



Figure 3-47. Tie bar fracture during testing of Specimen C2

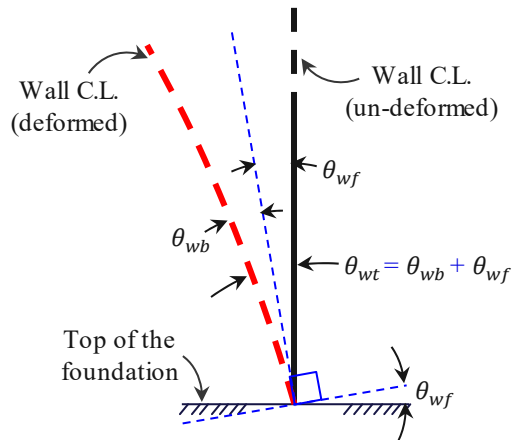


Figure 3-48. Composition of wall rotations at the base of the wall

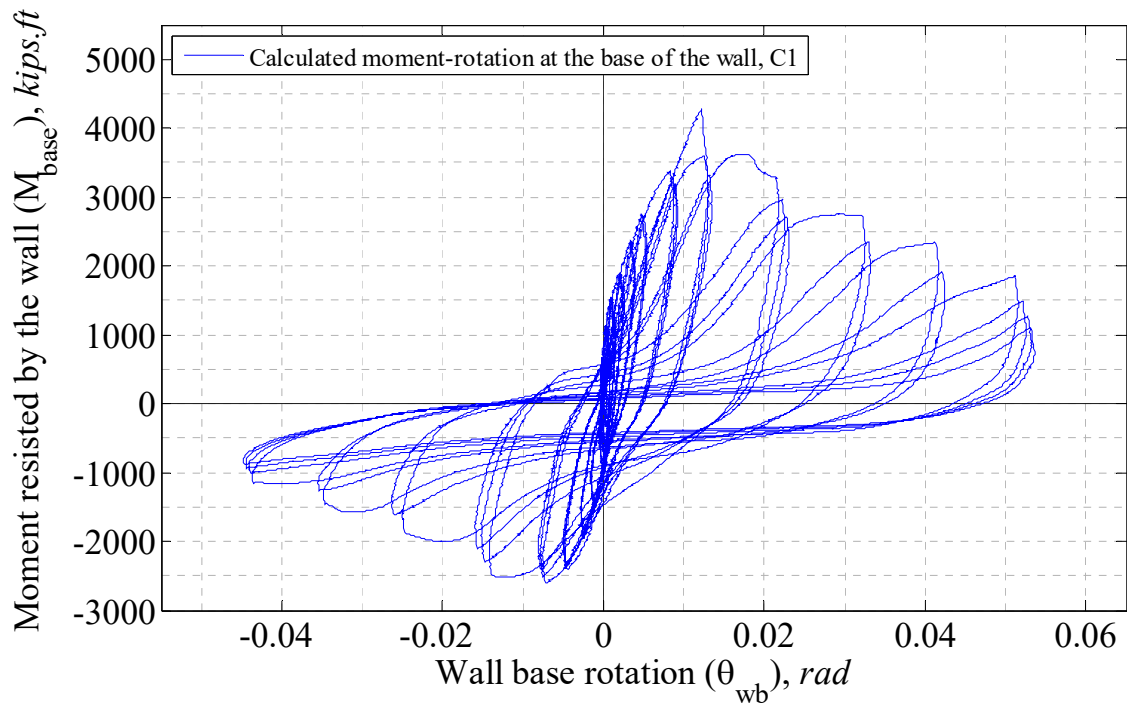


Figure 3-49. Calculated experimental base moment vs. wall base rotation relationship for Specimen C1

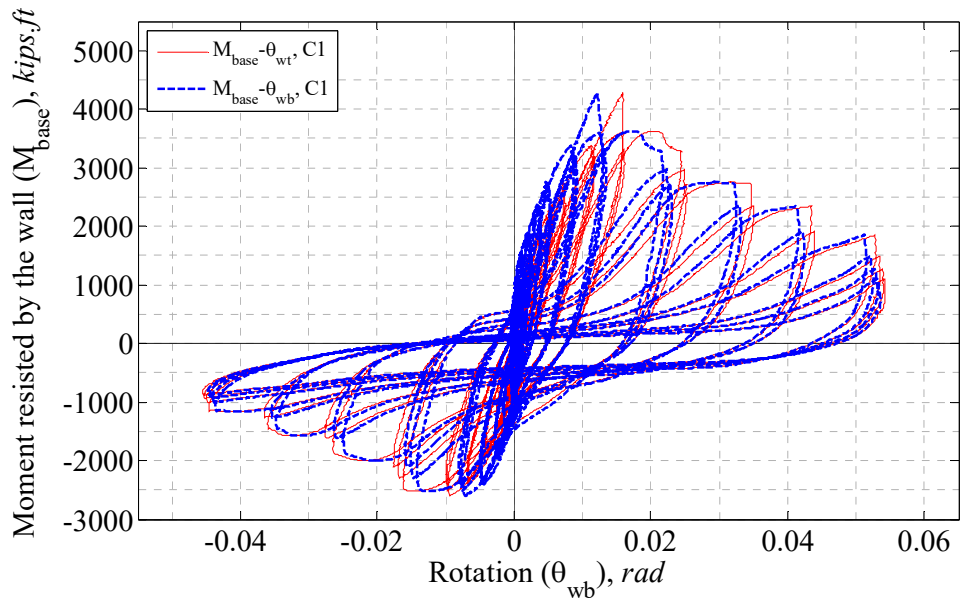


Figure 3-50. Comparison of calculated experimental base moment vs. wall base rotation and vs. total base rotation for Specimen C1

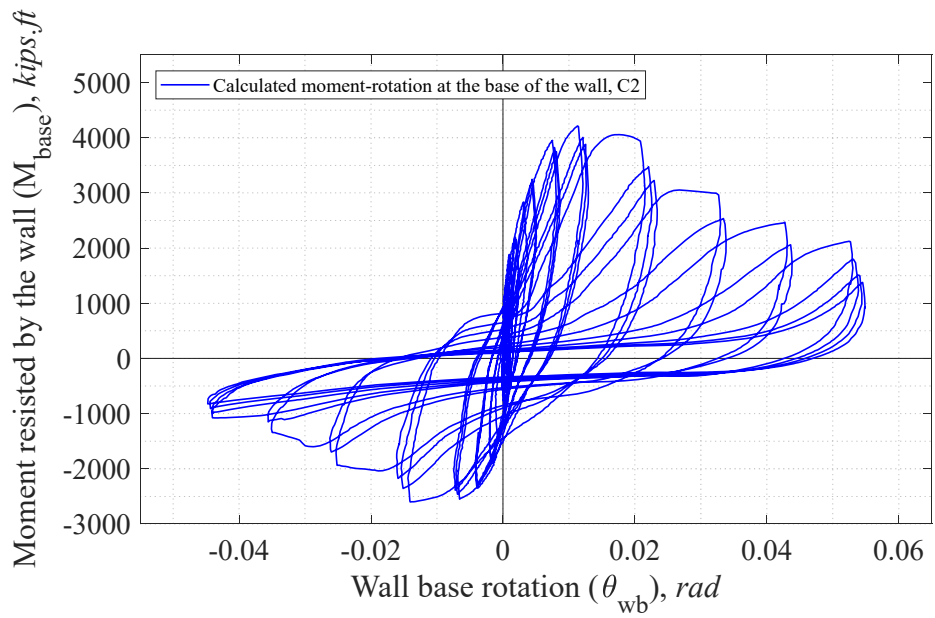


Figure 3-51. Calculated experimental base moment vs. wall base rotation relationship for Specimen C2

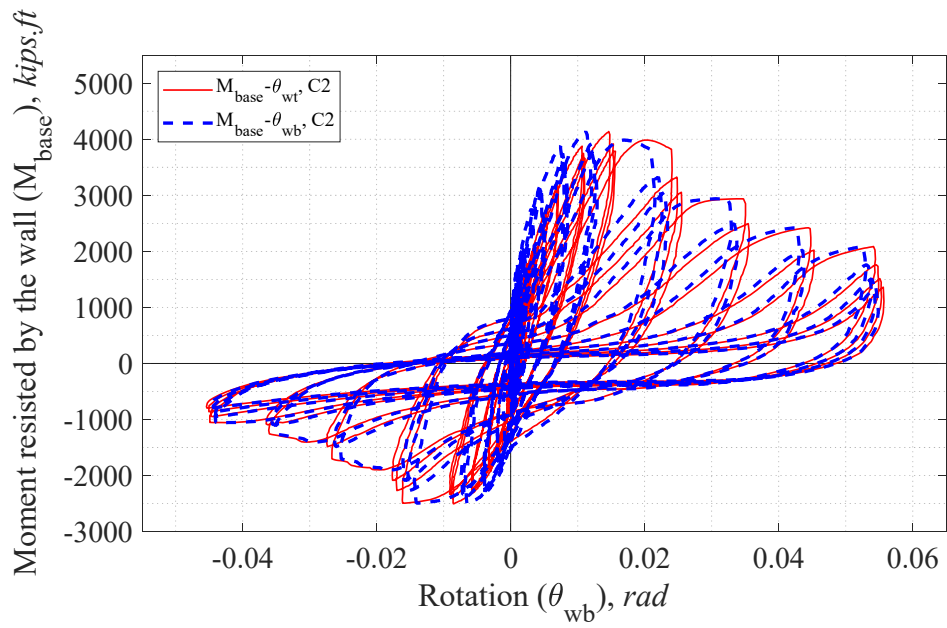


Figure 3-52. Comparison of calculated experimental base moment vs. wall base rotation and vs. total base rotation for Specimen C2

“This Page Intentionally Left Blank”

SECTION 4

TESTING OF REPAIRED C-SHAPED COMPOSITE PLATE SHEAR WALLS-CONCRETE FILLED (C-PSW/CF)

4.1 General

Information on the construction of the C1 and C2 wall specimens was described in details Section 3. In this section, the process of repairing and retesting Specimen C2 wall is described. The details of the repair concept and its implementation are presented in Sections 4.2 and 4.3. The properties of steel and concrete are provided in Section 4.4. Loading protocol and procedure for application of axial loading are outlined in Sections 4.5 and 4.6. Finally, step-by-step description of the tests, behaviors observed, and analysis of results are in Sections 4.7 and 4.8.

4.2 Repair Concept

Discussions took place between the research team and Brian Morgen from MKA who is the lead engineer involved in the design of the composite walls for the Rainier Square Project in Seattle, to assess various post-earthquake repair strategies for C-PSW/CF, and identify what seemed to be the most practical option. It was determined that composite walls would likely be repaired in segments, and that the repair would involve replacement of the buckled plate and, if necessary, partial or complete replacement of the concrete located between the removed plates. In the case of complete concrete replacement, new tie bars would be used, whereas existing tie bars would be re-used in the case of partial concrete replacement. Initial repair details were developed by the research team, and discussions were then held with the contractors (Turner Construction Company) and steel erector (James F Stearns Co Inc.) partnering on this project to establish a workable construction process and details needed to achieve the repair objectives.

Note that the repair scheme was to be implemented on Specimen C2 that had been tested, on purpose, to extreme inelastic deformations to investigate the rate of strength degradation at progressively

larger drifts; by all means, significantly lesser damage would be expected following actual earthquakes. After the test of Specimen C2, webs of the wall were buckled up to the 4th tie bar row and extensively fractured between 1st and 2nd tie bar rows. The flange steel plate on wall's East side had buckled between the 1st and 2nd tie bar rows but there was no buckling/fracture in the flange on its West side.

The repair strategy retained to address such extensive damage conceptually consisted of the following steps:

- Chipping away a part of the concrete footing at the face of the wall, removing enough concrete to expose the weld of the wall plate the thicker wall plate inside of footing.
- Cutting and removing the buckled and fractured steel and removing the loose concrete exposed by removal of the steel plates. This was expected to involve some chipping of the exposed concrete all around the wall, and removal of concrete through the entire thickness of the wall in some locations (such as in most of the webs).
- Adding steel plates along the entire perimeter of wall at its base where buckled/fractured plates were removed. These new steel plates, effectively acting as splice plates, were to be fillet-welded at their top and bottom ends. At the bottom end, this would be to the existing thicker plate located inside the wall's footing, and at the top end to the existing non-damaged steel plate. Note that, at the bottom, the splice plate was fillet-welded to the thicker wall plate to "by-pass" the thinner plate at the wall base, in order to achieve load transfer and ensure no yielding of the thinner plate there. The new splice would be made of plates of identical dimensions "wrapping" all around the wall, as shown in Figure 4-1.
- Filling the empty space between the splice plates with self-consolidating concrete that could easily flow through voids without the need for vibrations.

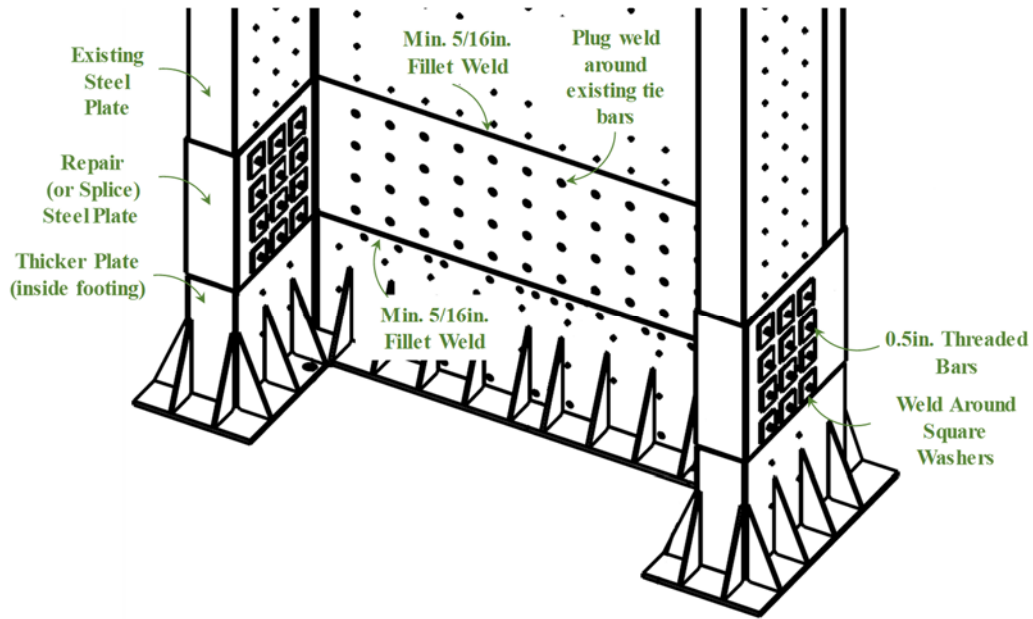


Figure 4-1. Repair concept for the C2 Specimen

The thickness of the repair steel plate (splice plate) was chosen based on a number of considerations, including finite element analysis done in LS-DYNA and required fillet weld size as described below. Note that the main objective was to make the repaired section stronger, such as to develop plastic hinging above the repaired part, therefore keeping the splice plates elastic.

First, the thickness of the fillet weld to the splice plate was calculated such as to be able to transfer a force equal to yielding of the steel plate in the above plastic hinge region. Considering a $0.707 \cdot w$ throat for the fillet welds, where w is the size of the weld, the required fillet weld size was required to be at least $5/16in.$, plus a $1/16in.$ clear distance from the plate edge, to resist the yield force from existing steel plate. Therefore, the required thickness of the splice plate was $3/8in.$, i.e., the twice in size of the existing plate. Note that in an initial approach, the size of the plate was checked for its adequacy to resist the combination of compressive yield force from the plate above the splice, and the moment created by the eccentricity of that force from the middle of existing plate to the middle of the splice plate. However, under such an assumption, to keep the splice plate elastic would have required it to be $1in.$ thick, which quickly appeared

to be excessive. More appropriately, the splice plate thickness was selected considering the free-body diagram shown in Figure 4-2, where the moment due to eccentricity of the force is resisted by the couple developed by the concrete force resulting from stresses developing behind the plates and the force the at tie bars. Note that finite element analysis also indicated that the tie bar also resisted a moment equal to 9.5% of the plastic moment of the tie bar, which is negligible. Also, note that the contribution of friction forces was neglected in this free-body-diagram, as it is not significant. Analysis using LS-DYNA confirmed that the 3/8in. splice plate provided was adequate.

Finally, as part of the repair concept, to achieve the goal of developing the wall's flexural plastic hinge above the repair zone, it was more logical to provide a repaired zone of constant height all around the wall. The height of the repair plate was chosen based on the webs, which were damaged up to the 4th tie bar row. Even though the steel in flanges was not damage beyond the 2nd tie bar row, the intent was to use a splice plate of same height to provide continuity between the webs and flange and facilitate formation of a plastic hinge at the same height all around the wall. Hence, the total splice plate height was chosen to be 25in. (extending 24.5in. above the top of footing and 0.5in. into the footing where it was connected to the thicker wall plate). Moreover, to bridge over locations of the flange where the steel plates and tie bars would not be removed, the splice plates were provided with a grid of pre-cut 1-3/4in. in diameter holes located to match the exiting tie bar spacing (6in. c/c in both the horizontal and vertical directions (refer to Appendix E)).

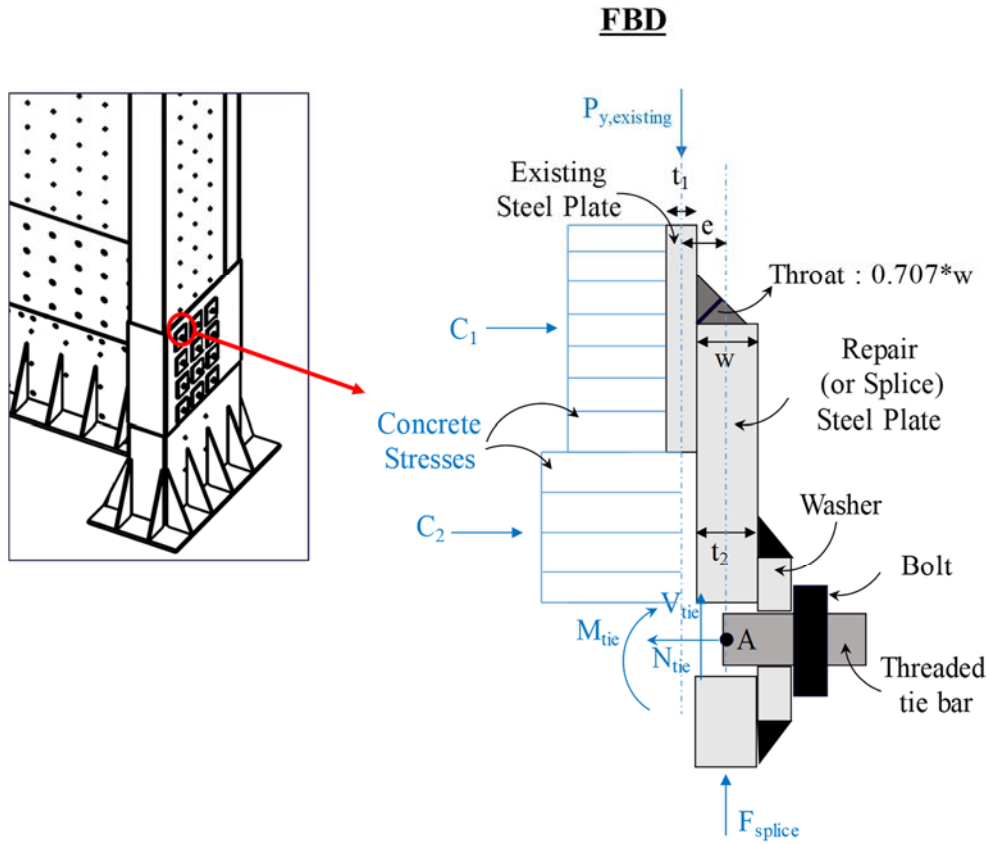


Figure 4-2. Free body diagram of existing and splice plates load transfer

The concrete used to fill the void between the new splice plates, to recreate a composite wall, was poured from $3in.x3in.$ holes that were cut at the top end of where the concrete was chipped and removed during the repair. For fluidity of the concrete, a MasterEmaco S-440CI self-consolidating repair mortar with $3/8in.$ aggregates and integral corrosion inhibitor was used. In order to help the concrete fill all the gaps, the splice plates were tapped with a hammer to provide some external vibration as it was poured from the holes. Also, “scuppers” were used to pour the concrete; they consisted of wood boxes with an opening at their bottom attached to the surface of the wall where the $3in.x3in.$ holes were located, as shown in Figure 4-3. Filling the scupper to the top pushed the concrete further to the other end due to pressure and up to the top level of the chipped concrete. Concrete leakage from small holes of $1/8in.$ diameter that were drilled at

the top level of the chipped concrete on the far ends of the splice plates was used as indicated that the concrete filled the void up to the top (to complement, this was also checked by passing fingers through the scupper holes as far as could reach).

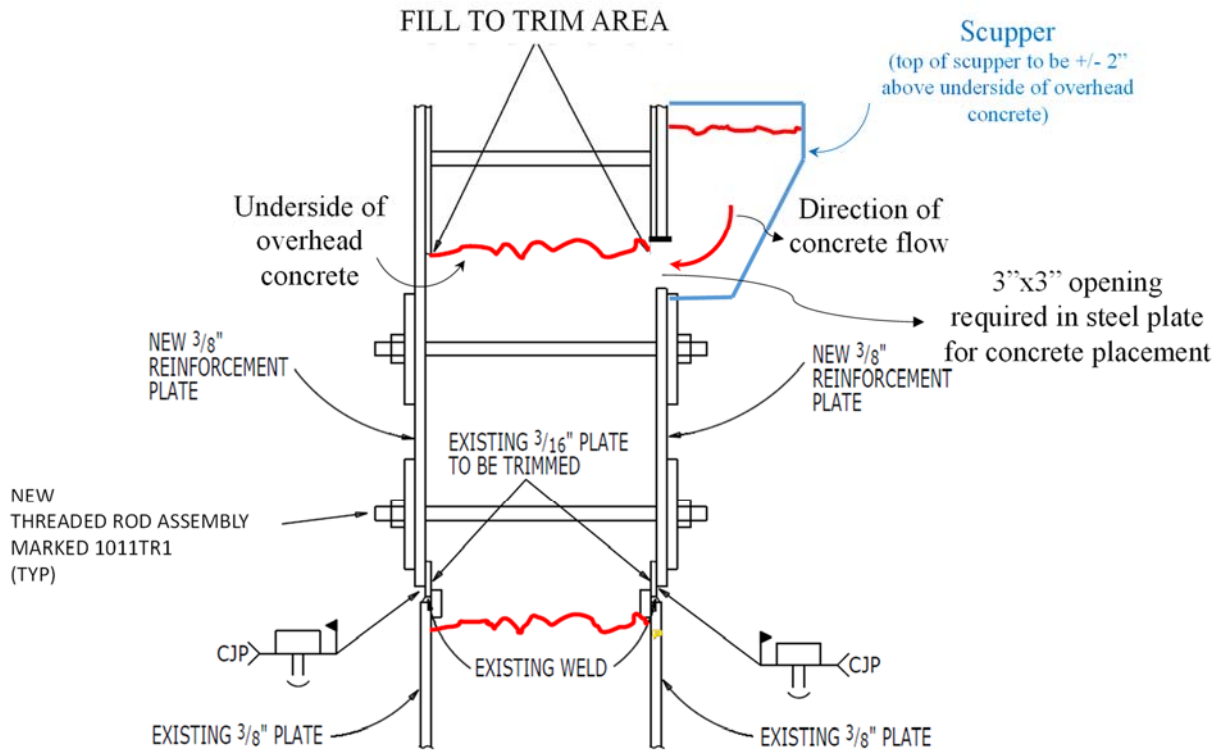


Figure 4-3. Scupper attachment and direction of concrete flow.

4.3 Implementation of Repair Concept

Implementation of the repair strategy started with chipping away the concrete in the footing at the face of the wall, removing the concrete up to a depth of approximately 0.75 in. over a width of 5 in. all around the wall specimen. This was done to make it possible for the welder to fillet-weld the splice plate to the thicker wall plate inside the footing in order to achieve load transfer and ensure no yielding of the thinner plate at the wall base. Then, two different methodologies were adopted for repairing the flanges and webs.

There was no damage in the west flange. Therefore, the ends of tie bars were smoothed and a 3/8 in. repair plate, with holes on a layout at the same spacing as the existing tie bars, was placed on top of the 3/16 in. existing steel plate. The top and bottom of the repair plate were fillet-welded with AWS E71T-1M-H8 UltraCore 71A85 flux-cored gas-shielded (FCAW-G) wires (which has minimum 20 Joules (ft*lbF) Charpy V-notch at 0 °F) to the existing plate and the tie bars were plug-welded to the repair plate around the holes. However, on the east flange, the steel between the 1st and 2nd tie bar rows had locally buckled during the test. Therefore, the buckled steel was cut out but some of steel around the tie bars was left for plug welding. Then, the damaged concrete behind the buckled steel was removed (approximately 3 in. in depth). The repair plate was placed on top of the existing steel plate and its top and bottom parts were filled welded to the existing steel plate. Note that in order to facilitate welding the splice plate to the thicker plate inside the footing, the bottom of the splice plates was beveled as shown in Figure 4-4. Also, existing tie bars were plug-welded to the repair plate around the holes. After that, three 3 in. x 3 in. holes were cut at mid-distance of the 1st and 2nd tie bar rows, 3 ft. apart from each other. Scuppers (Figure 3-1) were attached to the surface of the plate with screws. Then, self-consolidating concrete with small aggregates and high workability was poured through the scuppers and the plate was tapped with hammers to vibrate the concrete and help fill all voids. Also, small holes of 1/8 in. diameter were drilled at the top level of chipped concrete on the splice plates at half-distance between scuppers in order to see if the concrete flowed over the width of removed concrete. Then, the lids of the scuppers were slid to close the hole. The next day, the scuppers were removed and the surface was cleaned. Finally, the opened spots were capped by welding around slightly bigger plates.

The local buckling on both the north and south webs extended up over four rows of tie bars (Figure 4-6). Therefore, the same repairing strategy as described above was applied to both webs, which consisted of removing the steel plates and damaged concrete, placing new steel plates, filling with concrete, and adding new tie bars where needed. The existing steel plate were flame-cut to be removed. Then, the concrete and tie bars were removed with a drilling machine; in this case, concrete was removed over the entire

thickness of the wall. The repair plates were placed and fillet welded at their top and bottom. Then, 0.5 in. diameter threaded rods were placed through pre-cut holes in the repair plate and washers were put on each side of the webs and tightened with bolts. In order to prevent concrete leakage, the washers were welded around to the plate. Then, a scupper was mounted to a pre-cut hole (3 in. x 3 in.) on each repair plate. The concrete was poured through the scuppers and the plates were tapped with a hammer to produce vibrations to help even distribution and concrete flow between the plates. This was also checked by concrete leakage through small holes located at various places at the top height of the chipped concrete. Then, each scuppers' hole was closed by lowering a lid. The next day, the scuppers were removed, the surface was smoothed, and slightly bigger plate was welded all around to cap the opening.

After that, the concrete strength was monitored by periodically testing concrete cylinders until the strength reached ensured that moment capacity of the repaired cross-section was greater than the one of the existing cross-section above the repaired part. Meanwhile, all remaining aspect of test set-up and instrumentation were completed.

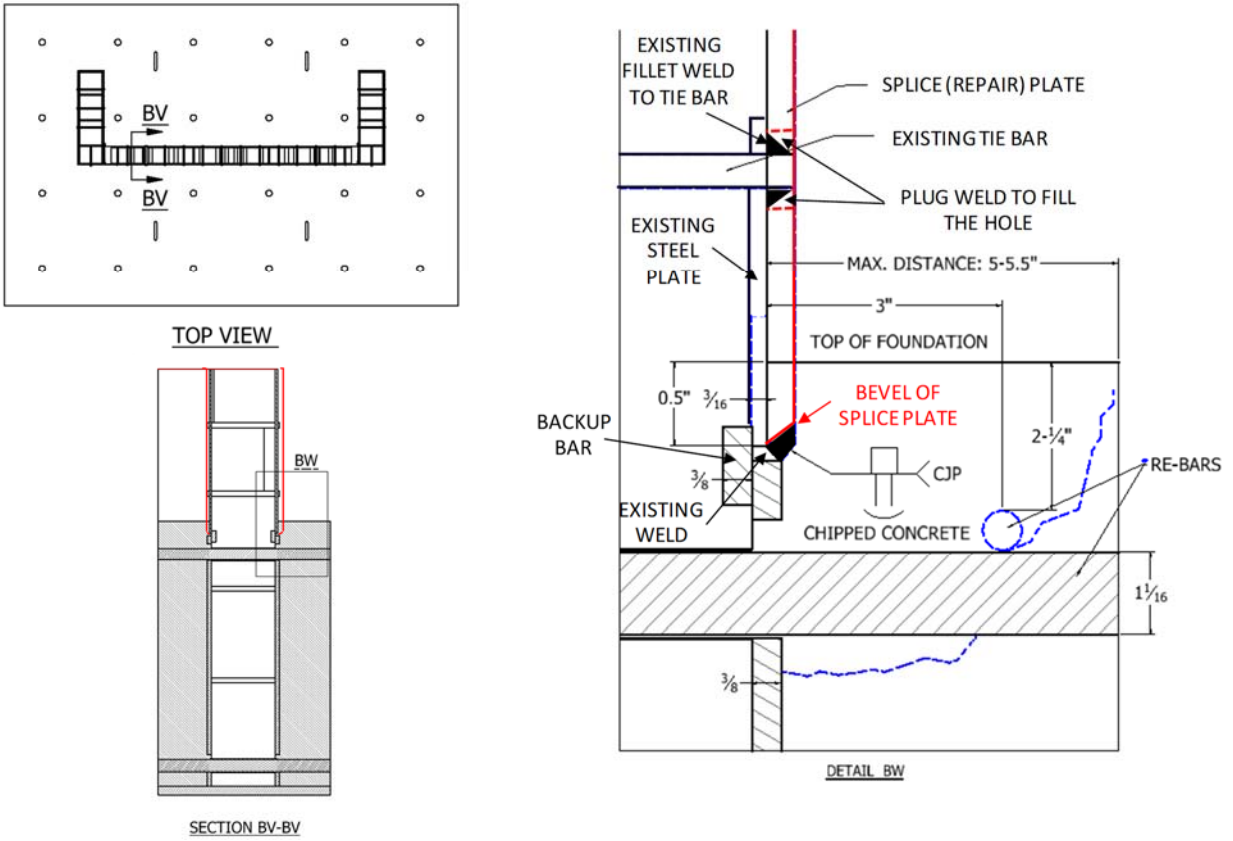


Figure 4-4. Fillet welding detail at the footing.

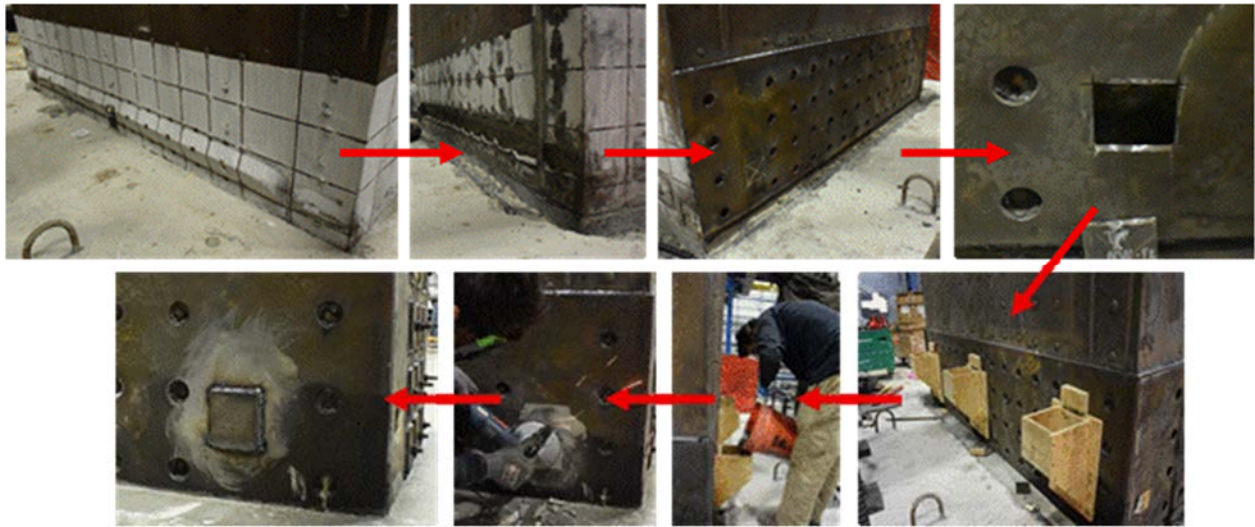


Figure 4-5. Repair sequence of flanges



Figure 4-6. Repair sequence of webs

4.4 Material Properties of Specimens

Three coupons for the steel used in the webs and flange of the C2 specimen (identified as p261 and p307, respectively in the shop drawings of the specimens presented in Appendix C5), and three coupons for the repair plates were tested under uniaxial tension. Results are presented in Figures 3-3 and 4-8. As mentioned before (Section 3.4), the average yield strength of the A572Gr50 steel used in construction of the flange and web plates of Specimen C2 was 55.2ksi (based on the 0.2% offset method, as no “yield plateau” was observed in the stress-strain behavior of the tested coupons). Figure 4-8 shows the results of the coupon tests for the repair steel plates. The 3/8in. thickness of these plates was too large for the MTS uniaxial tension/compression machine inside the SEESL Laboratory at State University of New York (SUNY) at Buffalo. Therefore, the thickness of the plates was machined down to half the original thickness. Unfortunately, during the test, two of the coupons broke outside of their gauge length, which is reflected by the discontinued elongation results in Figure 4-8. However, the average of the yield strength obtained for these three coupons, measured as 53.14ksi., was sufficient to ensure that the repair plates had adequate strength to prevent yielding in the splice itself.

To establish the strength of the concrete used for the repairs, 3in.×6in. and 6in.×12in. cylinders were taken from the concrete used to fill the space between the steel splice plates on the day of concrete pouring. The average compressive strength was measured to be 6.4ksi from the unconfined compression test. Moreover, the strength of the existing concrete inside of the C2 specimen was determined using three extra 6in.×12in. cylinders that had been cast the same day as the C2 wall; test of these cylinders indicated that the strength of concrete has not increased since the day C2 was tested, as the average strength obtained was still 5.1ksi.

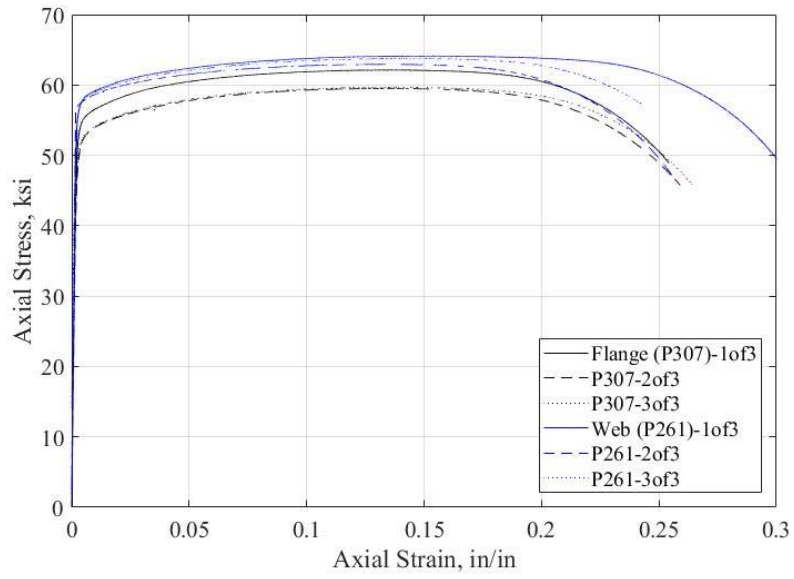


Figure 4-7. Coupon tests of steel plates at flange (p307) and web (p261) for C2

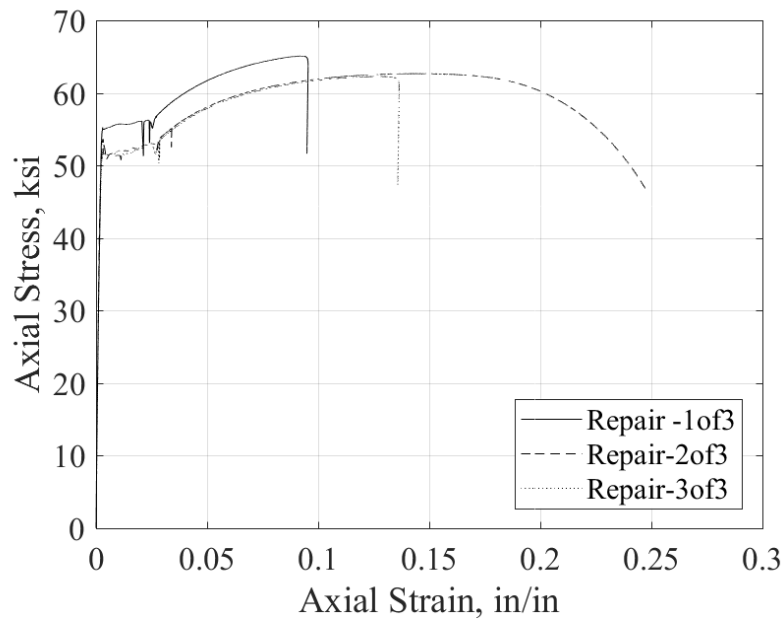


Figure 4-8. Coupon tests of repairing steel plates

4.5 Loading Protocol of Repaired C-Shape Specimen

The cyclic testing protocol was designed based on the yield displacements obtained from the Finite Element Analysis (FEA) of the Repaired Specimen C2. The model was run based on true material properties of existing steel plate and concrete, and the expected material behavior of the repair steel plate. The average strength of steel from the coupon tests for the existing steel plate (F_y is 55.2 *ksi*) was directly input into the model and the same steel properties were used for the repair steel plate as the average strength from coupons was not available at the time of the analyses.

There were a few cylinders left from the time Specimen C2 was cast; these were to be used to determine the compressive strength of the concrete on the test day of the repaired specimen. In the meantime, for the analyses conducted to determine the loading protocol, the concrete strength was presumed to be 5.6 *ksi* by extrapolating the slope obtained from the concrete strengths measured at 22 days and on the test day of Specimen C2, to the day of testing for the Repaired Specimen C2.

Figure 3-4 shows the result of the pushover curves obtained from the finite element model, both in the positive and negative directions, and a corresponding bi-linear curve estimation for the pushover curves. The yield displacements (Δ_y) as defined by any point reaching the yield strain on the cross-section, in the positive and negative directions, are 1 *in.* and 0.5 *in.*, respectively. However, the loading protocol was created based on yield displacements obtained from the estimated bi-linear curve for both directions (Δ_y'), which are 2 *in.* in the positive direction and 1.5 *in.* in the negative direction, as shown in Figure 3-4.

Up to the equivalent yield displacements (+2.0 *in.* / -1.5 *in.*) obtained from the bi-linear curves, the specimen was cycled in force-controlled mode for the first 10 cycles. Beyond that, the specimen was tested in displacement-controlled mode. The resulting loading protocol is shown in Figure 3-5. There are only two cycles per drift amplitude in the force-controlled cycles. However, the number of cycles per drift amplitude in the displacement-controlled cycles increased to three cycles, up to until the maximum capacity

of the specimen is reached (+6 in./-4.50 in.), and then the number of cycles is decreased to two for the subsequent cycles.

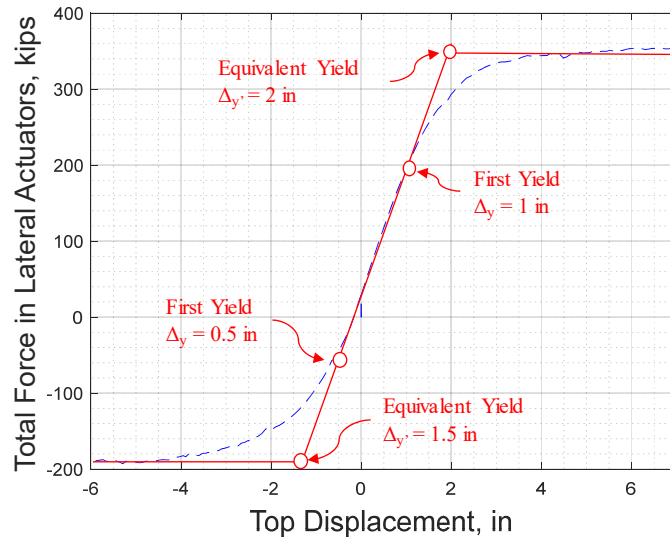


Figure 4-9. Pushover result of the FEA model of Repaired Specimen C2 and bi-linear approximation of the curves in positive and negative directions

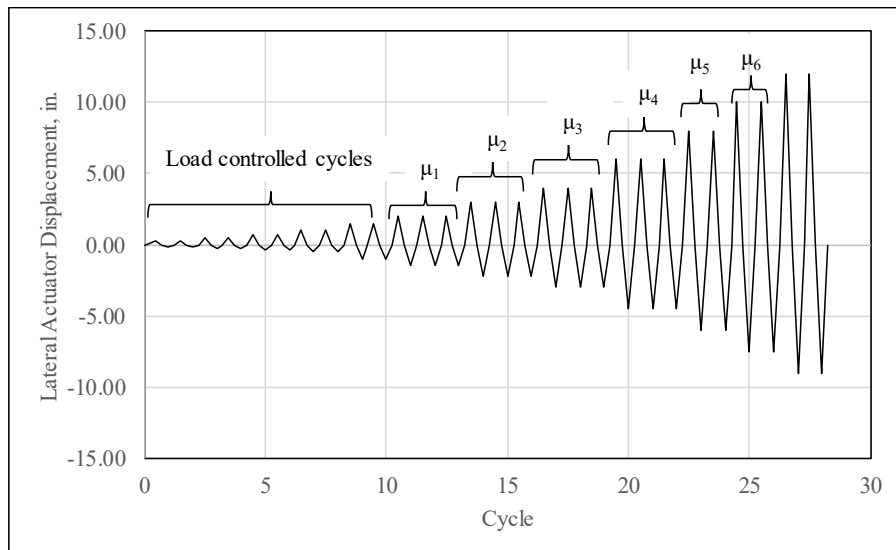


Figure 4-10. Loading protocol for C-Shaped specimens

4.6 Application of Axial Loading on the C-Shape Specimens

As described and done previously for Specimens C1 and C2, the axial loading was applied centered on the top of flange rather than at the centroid, which resulted in a moment due to the eccentricity of the axial load, as shown in Figure 3-6, which was taken into account when post-processing the experimental results.

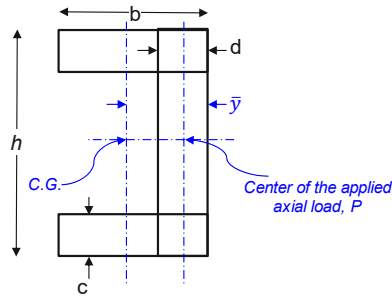


Figure 4-11. Location of centroid and centerline of axial load for C-Shaped wall specimens

To compare the results with the C2 specimen, the same testing scheme was applied to the repaired wall. Before applying the axial loading, the horizontal actuators were locked at the initial point of zero horizontal displacement because, without locking, the specimens could have moved laterally upon application of the axial load due to the moment created by the eccentricity of the axial load (Figure 4-12).

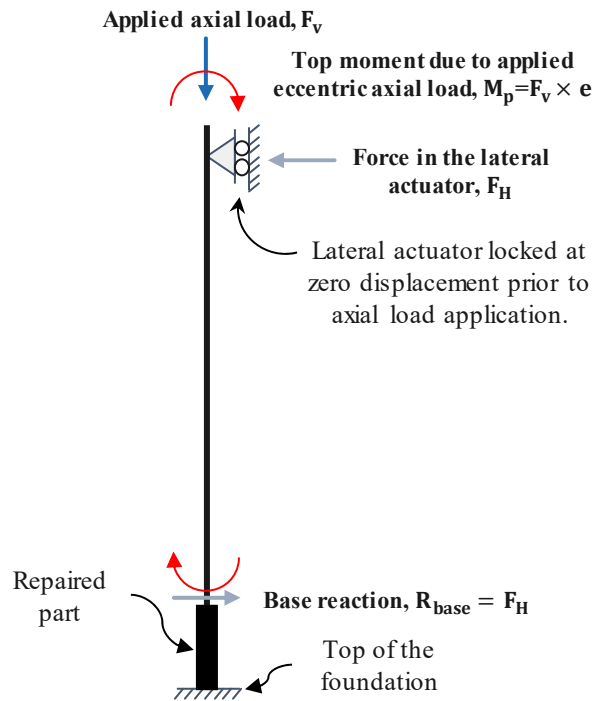


Figure 4-12. Testing scheme of repaired C-Shaped wall

The vertical actuators were driven in a force-controlled mode such as to apply constant axial force to the specimen cross-section. The summation of the axial force in the vertical actuators was tracked during the test to verify that it remained constant throughout testing, as shown in Figure 3-8. The distribution of axial strains across the cross-section were also tracked after engaging the vertical actuators, to verify that the cross-section was subjected to uniform stresses under the applied axial loading, even though loading was only applied to the flange. Results obtained from the strain gauges located in the plastic hinge region of the specimen confirmed that this was the case, as shown in Figure 3-9 for normalized axial strains across a cross-section at 29-7/16 in. from the top of footing on Repaired Specimen C2.

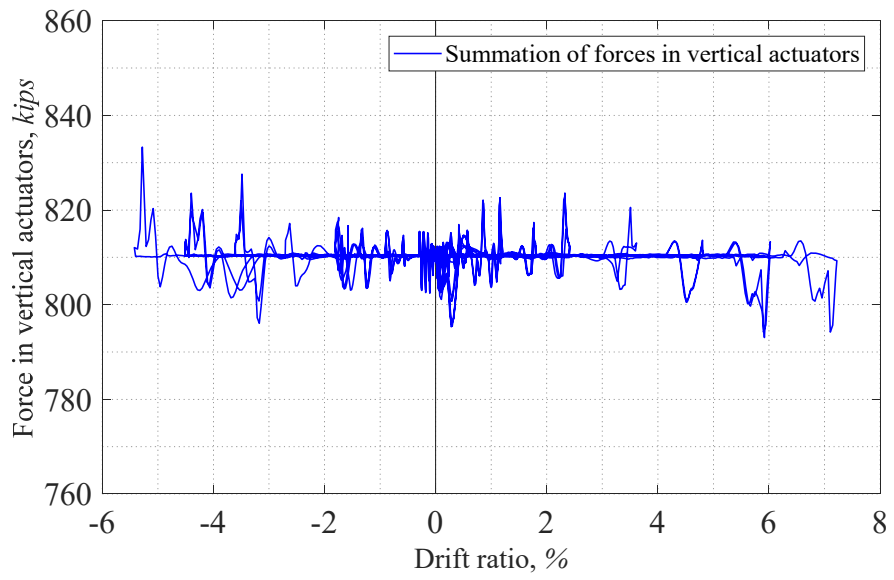
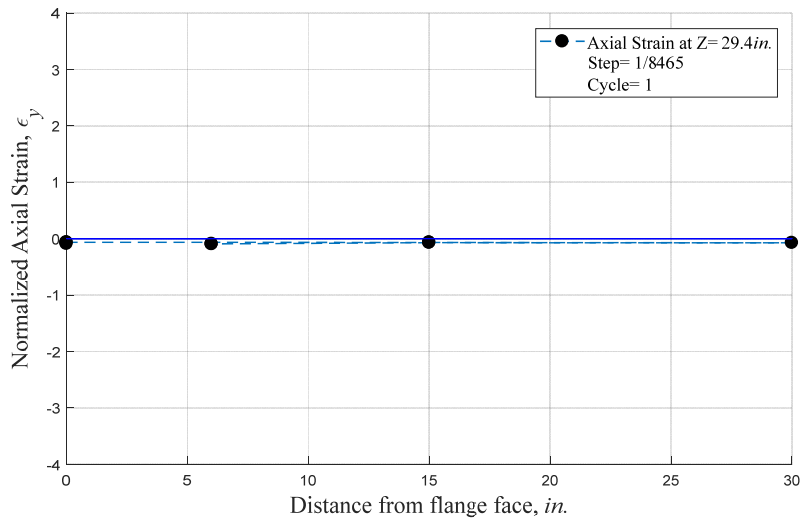
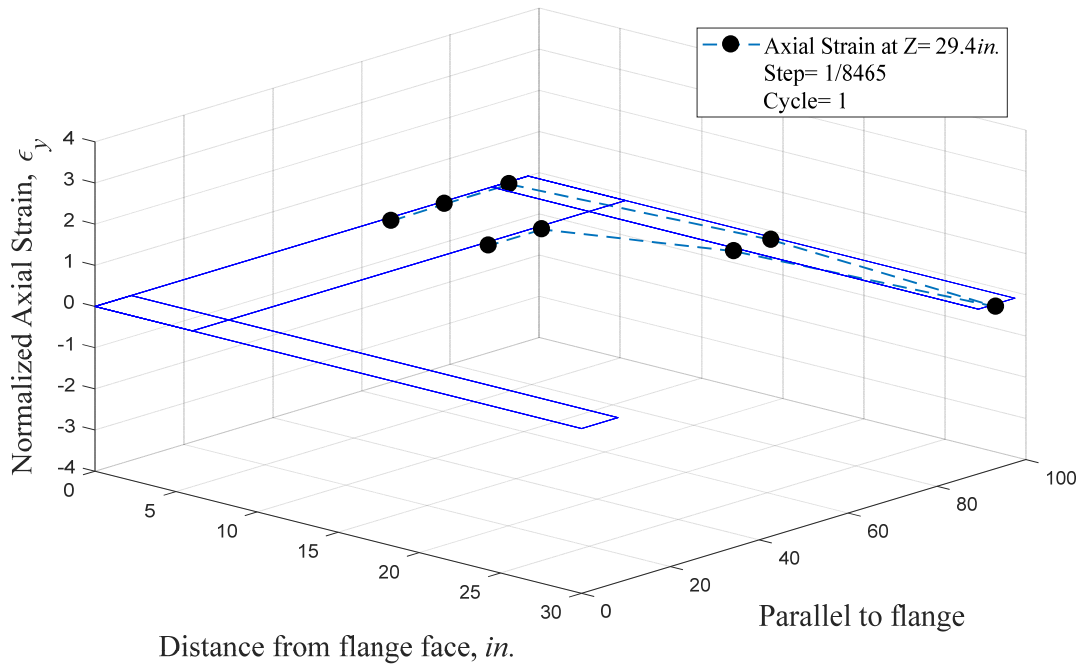


Figure 4-13. Sum of axial forces in the vertical actuators during test of Repaired Specimen C2



a)



b)

Figure 4-14. Normalized axial strains a) 2D and b) 3D of the strain gauges at 29-7/16 *in.* from the top of footing on Repaired Specimen C2

4.7 Test Observations and Results

Repaired Specimen C2 was tested under the axial and cyclic loading protocols discussed in Section 3.5. As discussed before, the cyclic lateral displacement testing protocol was designed based on a computation of the yield points (for both positive and negative bending) obtained from finite element analysis of the repaired wall.

Testing started by loading the vertical actuators while the horizontal actuators were held at zero displacement. The forces in the vertical actuators were increased up 400*kips*, which resulted in application of 15% of $A_c f'_c$ on the cross-section of the C-shape wall. Then, the lateral actuators were loaded to apply the lateral cyclic displacements at the top of the specimen according to the pre-determined cyclic protocol. The first cycle of the loading protocol, at the displacement of $\Delta_y/4$, enabled to verify if all the attached data recording instruments were working properly and to point out all existing deficiencies in the specimen or the test setup. None of the components of steel plates of the specimen experienced any buckling or yielding and the same behavior was observed in all of excursions cycles at amplitudes of $\Delta_y/2$, and $3\Delta_y/4$.

At the positive peak of the estimated displacement of Δ_y , the strain recorded in the farthest end of the web was -1305.8 $\mu strain$, which is 66.93 % of the average yield strain (i.e., 1951 $\mu strain$) of the steel plate based on the coupon tests. The strain recorded in the negative peak of the estimated displacement of Δ_y was -424.5 $\mu strain$ (21.76 % of the average measured yield strain). In the second excursion at the same drift, the strain values did not change much (66.47% in the web and 21.98% in the flange). In addition, no local buckling was observed at this cycle amplitude.

In an attempt to capture the drift at which first yielding was reached at the cross-section, the specimen was cycled with an additional displacement amplitude of $1.5\Delta_y$. In the first excursion of the cycle, the strains in the web and flange were -1898 $\mu strain$ and -727 $\mu strain$ (97.27% and 37.27% of the estimated displacement of Δ_y) and the strains did not change much in the following excursion at the same drift (96.67% and 37.61% of Δ_y in the web and flange, respectively).

Note that from that point onward, the specimen was cycled following a protocol defined by yield displacements obtained from the estimated bi-linear curve for both directions (Δ_y'), which are 2in. in the positive direction and 1.5in. in the negative direction, as shown in Figure 3-4. This equivalent bi-linear yield defined the size of displacement increments (such as $1.5\Delta_y'$, $2.0\Delta_y'$, $3.0\Delta_y'$, $4.0\Delta_y'$, $5.0\Delta_y'$, and $6.0\Delta_y'$) instead of first yield displacement (Δ_y') corresponding to when the outermost cross-section fiber has yielded. At a lateral displacement equal to $1\Delta_y'$, strain gauges showed that approximately 20% of the entire cross-section (30in.) between the first and second tie bar rows above the repaired part and 16.7% between the second and third tie bar rows above the repaired part had yielded with no visual observation of local buckling. During the second excursion at the same drift, 26.7% of the cross section between first and second tie bar rows had yielded but yield percentage of the cross-section remained the same as in the previous cycle (20% and 16.7% of cross-section between 1st and 2nd and 2nd and 3rd rows, respectively had yielded). In the third excursion, the yield percentage of the cross-section did not change.

At the lateral displacement equal to $1.5\Delta_y'$ (i.e., Cycle 14), when the strain gauge recorded $4985\mu strain$, local buckling was observed on the web between the 1st and 2nd tie bar rows on the South face of the North Web (labeled NWS afterwards) and North face of South Web (referred to as SWN afterwards). In the following excursion (i.e., Cycle 15), 53.3% and 66.7% of the cross-section between the 1st and 2nd tie bar rows and the cross-section between 2nd and 3rd tie bar rows, respectively yielded. In addition, buckling was observed in the steel plates between the 2nd and 3rd tie bar rows on the South face of South Web as in C15P in Figure 4-19 (referred to as SWS afterwards); note that prior to start of the Repaired Specimen C2 test, it was observed that a hollow sound could be heard when tapping on the plate at that location, which confirmed that a slight bulge existed there due to detachment of the steel plate from the face of concrete, as a consequence of the previous testing of C2 Specimen. Therefore, during testing of Repaired Specimen C2, that cross-section buckled first. The same sound was observed for the steel plate between the 1st and 2nd tie bar rows above the repaired part on the South face of North web (NWS). Moreover, steel at 4in. from the top of the repair plate also started to buckle on the West surface of North

web (NWW) as in C15P in Figure 4-15. During the last excursion at the same cycle amplitude (i.e., Cycle 16), in addition to all previously buckled plate locations, the steel plate between the 1st and 2nd tie bar rows also started to buckle at the North face of the North Web (referred to as NWN afterwards) and steel located at 4.5in. and 11in. from the top of the repaired part on the West surface of South web (SWW) also started to buckle (C16P in Figure 4-19).

At the lateral displacement equal to $2\Delta_y$ ' (i.e., Cycle 17 with amplitude of 4in. and -3in.) the lateral load capacity reached to maximum value 427kip /-197kip in the positive and in the negative drift directions. In the positive drift, the steel plate between the 1st and 2nd tie bar rows at SWS started to buckle (C17P in Figure 4-19). However, in the negative drift part of this cycle, at 0.5in. drift, a relative upward movement of the wall relative to the top its footing was observed at the South web (called "uplift" hereafter). Also, there was a sudden drop in the applied horizontal load, which was suspected to be due to a weld fracture at the connection between the repair plate and the existing thicker plate embedded inside the footing but this could not be confirmed without chipping the concrete in the footing. In the second excursion at the same cyclic amplitude (i.e., Cycle 18), the steel plate between the 2nd and 3rd rows buckled on the East flange (labeled FE afterwards) for about 27in. from the North side of the wall in the negative direction, as in C18N in Figure 3-15. Also, the wall uplift at the South web was observed to increase. At that time, a small part of the footing was chipped off, which allowed to visually confirm that the weld connecting the repair plate to the thicker plate had fractured. During last excursion at the negative drift (i.e., Cycle 19), local buckling initiated on the steel plate between the 1st and 2nd tie bar rows on FE (C19N in Figure 3-15), except for the place on FE that had buckled between the 2nd and 3rd tie bar rows in the previous cycle (refer to C20N in Figure 3-15). After this cycle, the test was stopped, to be continued on the next day. In order to return the specimen to an unloaded condition first, the horizontal actuators were held at zero displacement, then the vertical actuators were unloaded, and eventually the displacement control of the horizontal actuators was released and the actuator hydraulic pumps were turned off.

Testing on the second day started by loading the actuators using the same sequence that was followed on the previous day at the beginning of the test. Testing resumed with execution of Cycle 20 (displacement of $3\Delta_y$ with amplitude of $6in.$ and $-4.50in.$). In addition to the previously observed buckled locations, a slight buckling was observed to develop in the steel plate between the 3rd and 4th tie bar rows at SWN, and in the steel plate between the 2nd and 3rd tie bar rows at NWS. In the negative drift, local buckling was observed in the steel plate between the 2nd and 3rd tie bar rows on the east side of the North web (NWE), as in C20N in Figure 3-15. Also, the fracture at the footing on the South web increased to $11in.$ into the web. Moreover, a slight uplift of the wall at the top of footing was also observed at the North web but the exact amount of presumed fracture could not be determined at the time as no such fracture was visible. Note that during the test, the second and third excursions planned to be executed at this amplitude were skipped (i.e., Cycle 21 and 22). This was done based on the assumption that since the base of the wall was most possibly fractured; it would have not been possible to “unbuckle” the plate on the east side of the South web with the same cyclic amplitude. However, by pushing the specimen further to a larger displacement, this would allow the specimen to buckle further and presumably help identify if failure would happen at larger displacements and see strength degradation at the same time.

In the displacement cycle of amplitude equal to $4\Delta_y$ (i.e., positive peak of Cycle 23 with amplitude of $8in.$ and $-6in.$), the drop in lateral horizontal force in the positive direction was 28.87%, but only 15.4% in the negative direction. Another buckling wave was observed to develop in the steel plate between the 1st and 2nd tie bar rows at the NWE. In addition, the weld inside the footing was fractured up to the flange. Fracture started to occur at the corners of NWS and NW at the buckled location ($4.5in.$ from the top of the repair plate). The fractures were approximately $0.5in.$ long at NWS; and $1in.$ at NW. After the cycle was complete, there was a $3in.$ vertical fracture in the corner of NWS and NW (Figure 4-21), which is a condition that has been previously encountered in rectangular end plates of composite sections (e.g., see other examples in El-Bahey and Bruneau (2011), Fujimoto et al. (1988), Iwata et al. (2000), and Saeki et al. (1995)). In the negative drift of the next excursion (i.e., Cycle 24), the welds of six tie bars fractured, namely

at: 1st row 2nd column (from West) at NWS; 1st row 1st column; 1st row 2nd column; 2nd row 2nd column; 3rd row 1st column; and 3rd row 2nd column at NWN. In addition, the corner of NW and NWN fractured for about 1.5in.

The lateral horizontal force dropped by 20.8% in the positive and 21.06% in the negative directions when the specimen was displaced by $5\Delta_y$ (i.e., Cycle 25). The cross-section fractured by 38% of the web length (9.125 in. out of 24 in.) at NW in this cycle. Also, one additional tie bar weld (2nd row 1st column from West) at NWN was observed to be fractured. In the second cycle (i.e., Cycle 26), the fracture in the North web grew to 12.5in. (52.08%). Also, a 2.5in. vertical crack was observed in the corner of SW and SWN around where it buckled (4in. from the top of repair plate).

At the $6\Delta_y$ displacement amplitude (i.e., Cycle 27), peak lateral horizontal force had dropped by 5.34% in the positive and 18.66% in the negative directions. The web steel was fractured over 68.75% of its original area at NW. Also, a new local buckling was observed in the corner of NWN and NEW. Since the drop in strength in successive cycles at drift was not much, and for safety reasons as drifts were already large in this cycle, the test was stopped at this point.

The details on the progression of buckling and fracture is tabulated in Table 4-1. Also, Figures 3-12 to 3-17 show the progressive development of the phenomena described above at locations NW and NWN; NWN and FE; and SW and SWS of Repaired Specimen C2.

When the test was over, the concrete all around the webs and at the corners of the flanges in the footing was chipped off to reveal how much the fracture propagated in both webs of the wall. Figure 4-22 shows the fractures of welds connecting the repair plate to the thicker plate inside of the foundation at NWS, NWN, SWN and SWS, respectively. The weld in the south web fractured almost all of the web's cross section, up to the flange (24.5in. at SWS and 24in. at SWN). However, the weld fractures at NWN and at NWS were shorter, at 20.5in. and 9.25in, respectively. The initial fractures at SWS and SWN were attributed to the fact that, around the webs, the bottom end of the repair plate did not perfectly reach the location of the existing weld that connected the wall steel plate to the thicker plate in the footing. This

made it difficult to weld the splice plate to the thicker plate in the footing, as originally intended as part of the repair scheme. Therefore, in order to transfer loads to the thicker plate inside the footing, five passes of fillet weld were done at that bottom location, trying to span the distance. However, in some places at the bottom end of the web, not enough weld material was added, and the splice plate ended-up being connected to the thinner part of the wall above the footing plate. As a result, a fracture initiated in the existing weld on the South Web. Furthermore, observation of the fracture surface after completion of the test showed that the fracture of the new weld at that location revealed lack of fusion with the beveled splice plate, as shown in Figure 4-23. This fracture propagated more through the web during the negative drift of the Cycle 23, and did not change in the following cycles. The same phenomenon happened for the fracture at NWN, but the fracture at NWS was through the thicker plate in the footing. Note that in the laboratory setting, due to the presence of the footing, the weld connecting the splice plate to the thicker plate was difficult to accomplish, as it was hard for the welders to see the bottom of the splice plate, even though it was beveled.

Table 4-1. Experiment log of Repaired Specimen C2

(Note: 1 in. = 25.4 mm; 1ft=0.3048 m; 1sq in.=645.2 mm²; 1 in⁴=416231 mm⁴; 1 psi=0.0069 MPa; 1 ksi=6.9 MPa)

Cycle No	Cycle Drift, in	Laterally Applied Force, V, kips	FE	NWW	NWN	NWS	SWW	SWN	SWS	NWE	SWE
14	3.0/-2.25	388/-173				B @1st-2nd TR		B @1st-2nd TR			
15	3.0/-2.25	381.5/-171.8		B @4in FRP	B @1st-2nd TR B @3rd-4th TR				B @2nd-3rd TR		
16	3.0/-2.25	371.6/-169.2					B @4.5in FRP B @11in FRP FR at footing				
17	4.0/-3	427/-197							B @1st-2nd TR		
18	4.0	413.6	B @2nd-3rd TR								
	-3	-186.1									
19	4.0	397.1	B @1st-2nd TR								
	-3	-182.6									
20	6.0	398.7				B @2nd-3rd TR		B @3rd-4th TR			
	-4.5	-196.2		Slight uplift at footing (slight FR)				11in. FR at Footing		B @2nd-3rd TR	
21	6.0	n/a									
	-4.5	n/a									
22	6.0	n/a									
	-4.5	n/a									
	8	283.8									
23	-6	-165.8		1in. FR @4.5in FRP		0.5in. FR @4.5in FR		Full Web FR at Footing		B @1st-2nd TR	
	8	230.6									
24	-6	-146.1			1.5in. FR WFR @1r1c; @1r2c; @2r2c; @3r1c; @3r2c;	WFR @1r2c					
25	10.0	224.5									
	-7.5	-131.5		38% FR; WFR @2r1c on NWN							
26	10.0	193.3									
	-7.5	-111.5		52% FR							
27	12.0	212.5									
	-9	-105		68.75% FR							
28	12.0	n/a									
	-9	n/a									skipped

Note: The steel plate faces are abbreviated as follows: FE = the East Flange, NWW = West of North Web, NWN = North of North Web, NWS = South of North Web, SWW = West of South Web, SWN = North of South Web, SWS = South of South Web, NWE = East of North Web, and SWE = East of South Web. Also, FF means "from footing", FRP means "from repair", FR is fracture, B is buckling, TR is tie bar row, WFR is tie weld fracture, r is tie bar row, and c is tie column. n/a means not applicable.

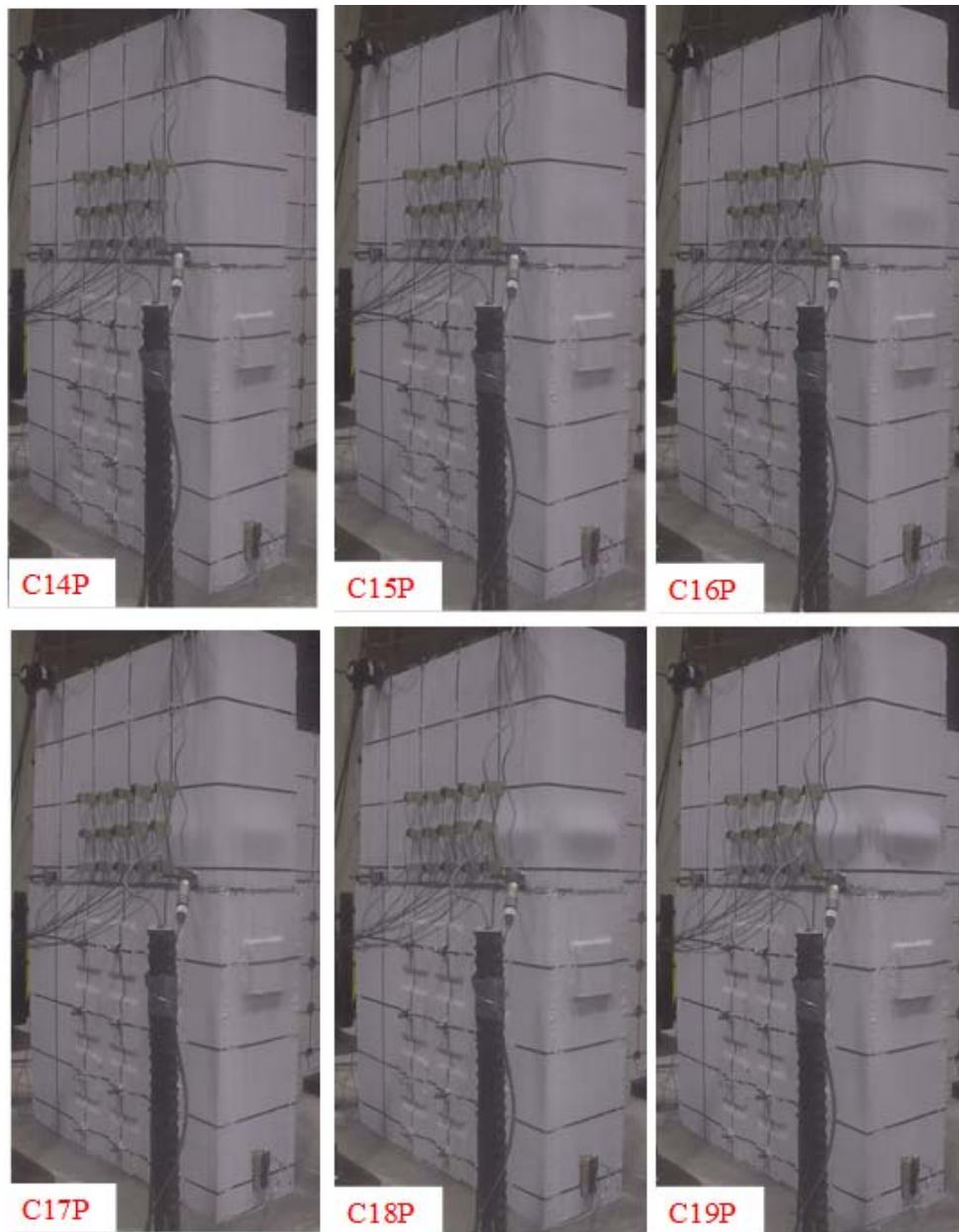


Figure 4-15. North-West views of the North Web of Repaired Specimen C2 at positive peaks

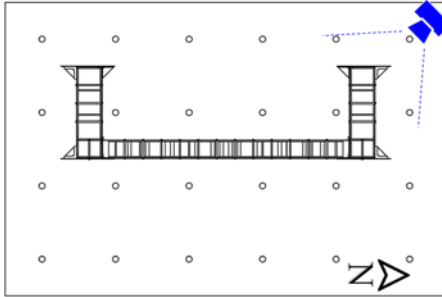


Figure 4-15. (Continued)

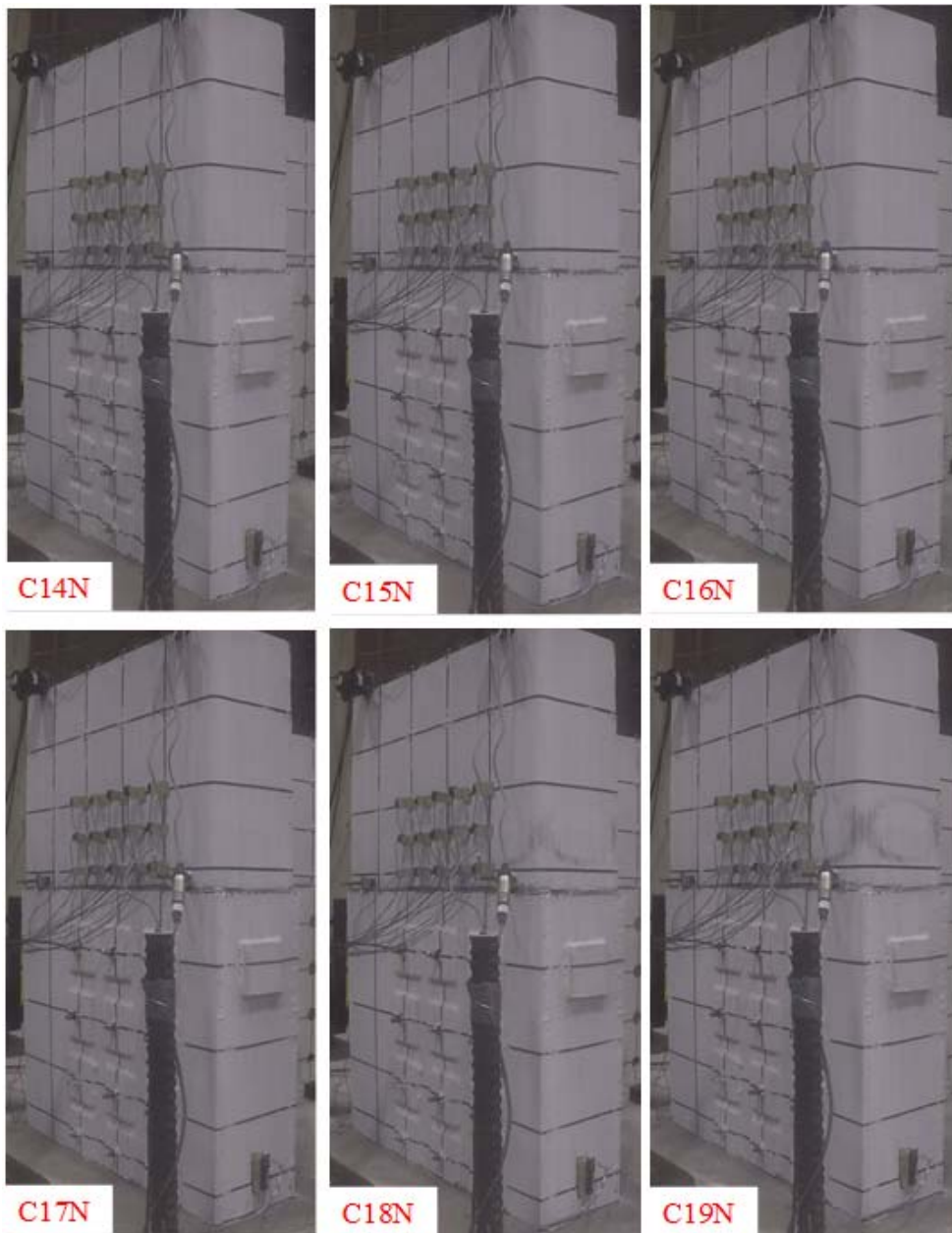


Figure 4-16. North-West views of the North Web of Repaired Specimen C2 at negative peaks

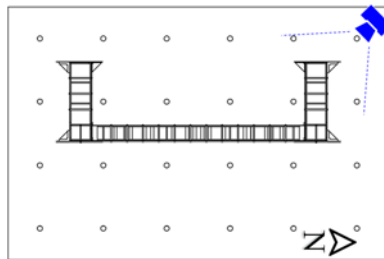
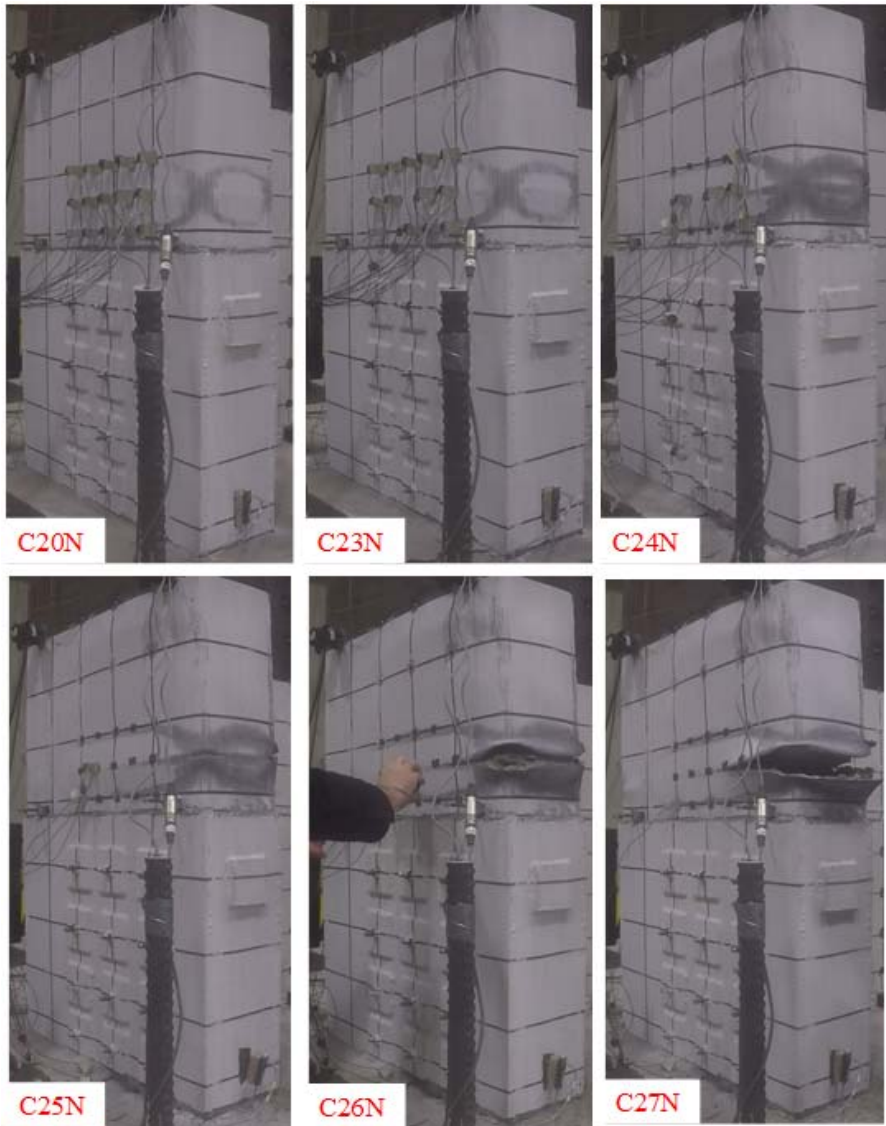


Figure 4-16. (Continued)

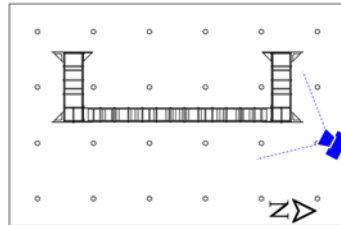
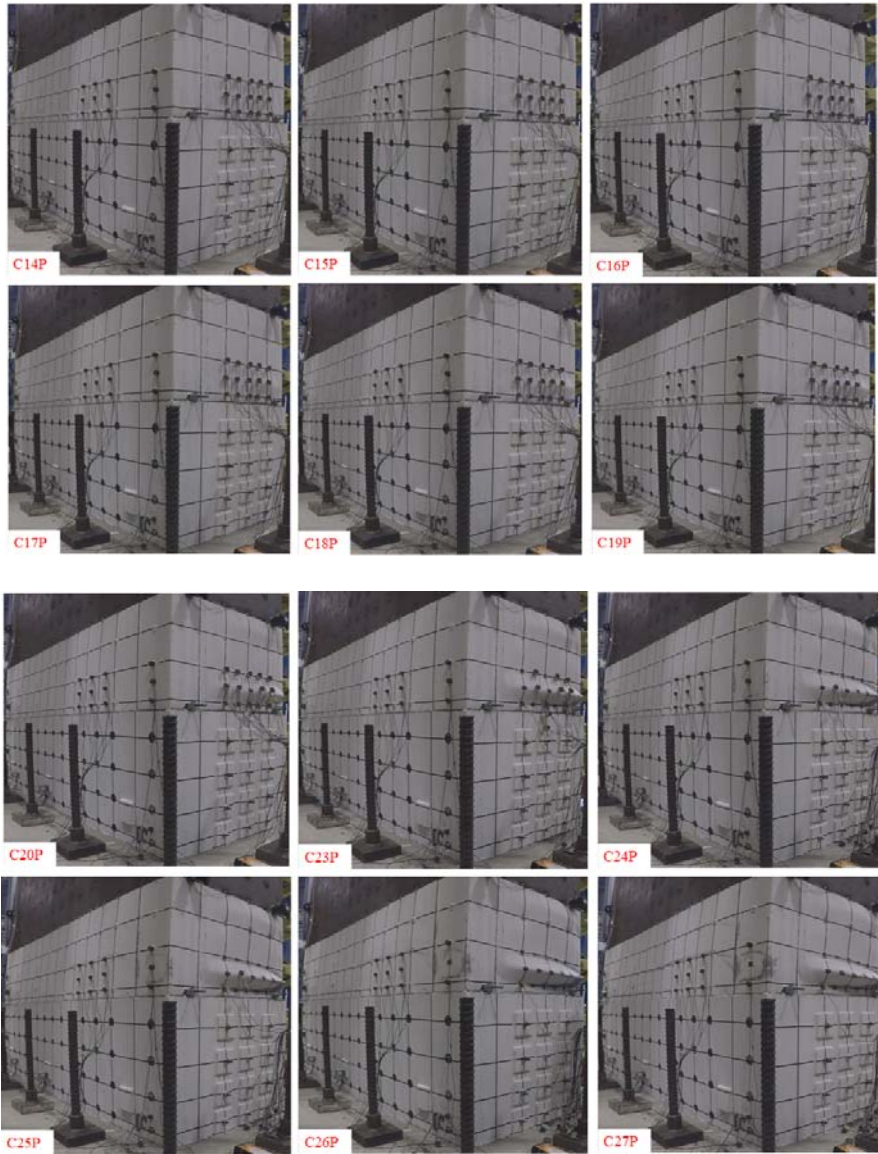


Figure 4-17. East view of the flange and North-East view of the North web of Repaired Specimen C2 at positive peaks

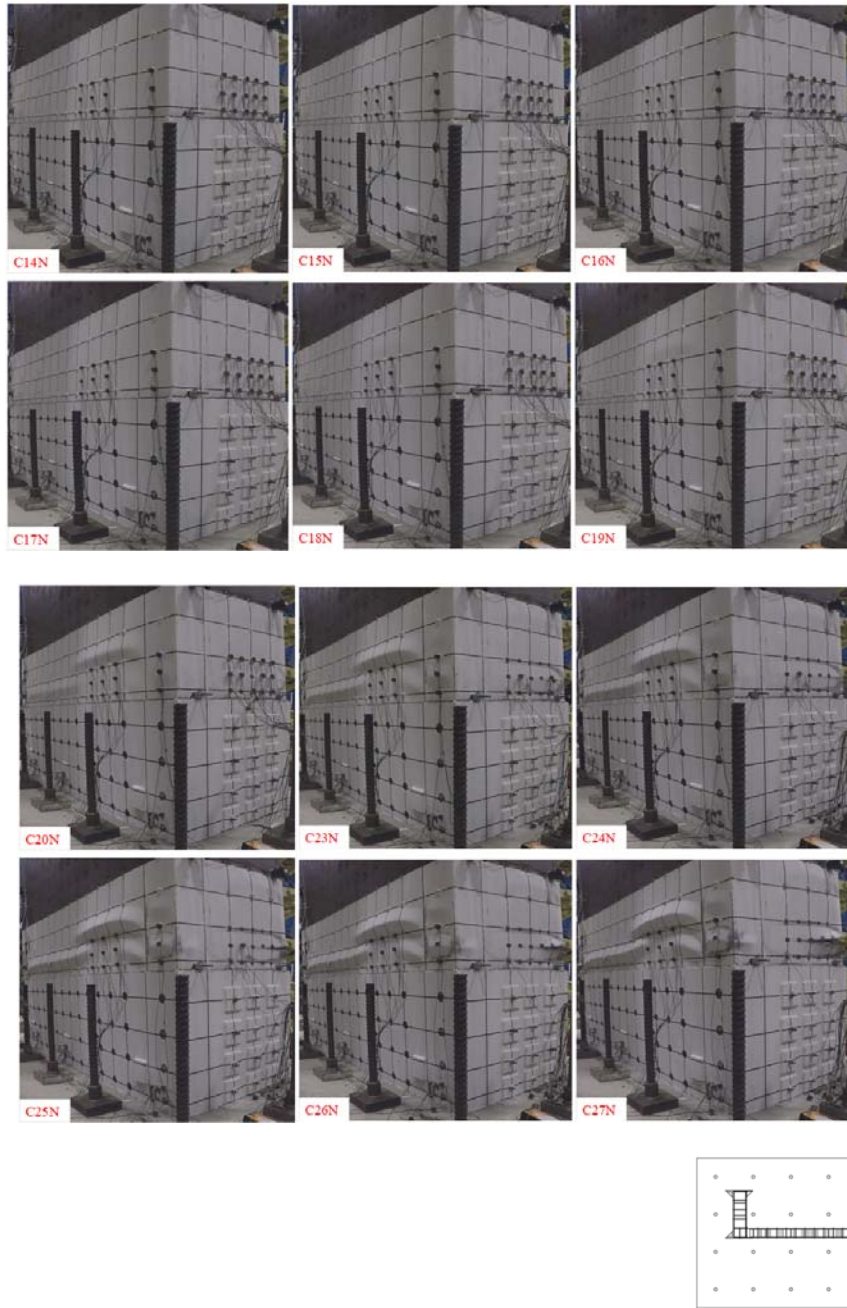


Figure 4-18. East view of the flange and North-East view of the North web of Repaired Specimen C2 at negative peaks



Figure 4-19. South-West views of the South Web of Repaired Specimen C2 at positive peaks

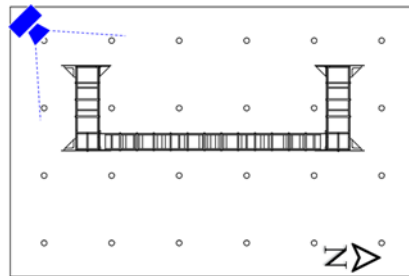


Figure 4-19. (Continued)

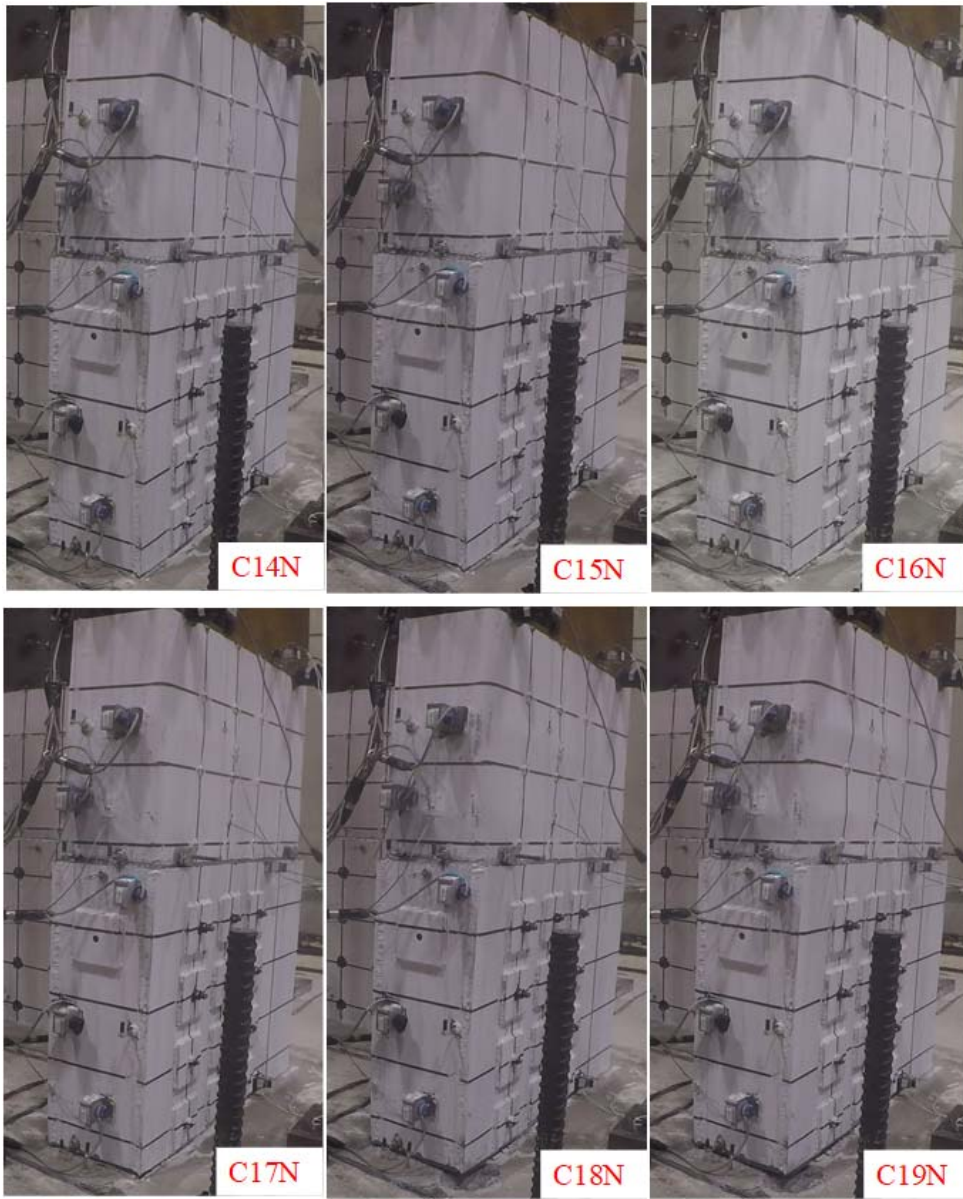


Figure 4-20. South-West views of the South Web of Repaired Specimen C2 at negative peaks

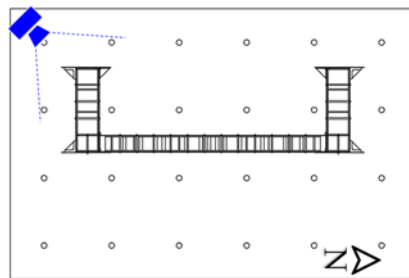
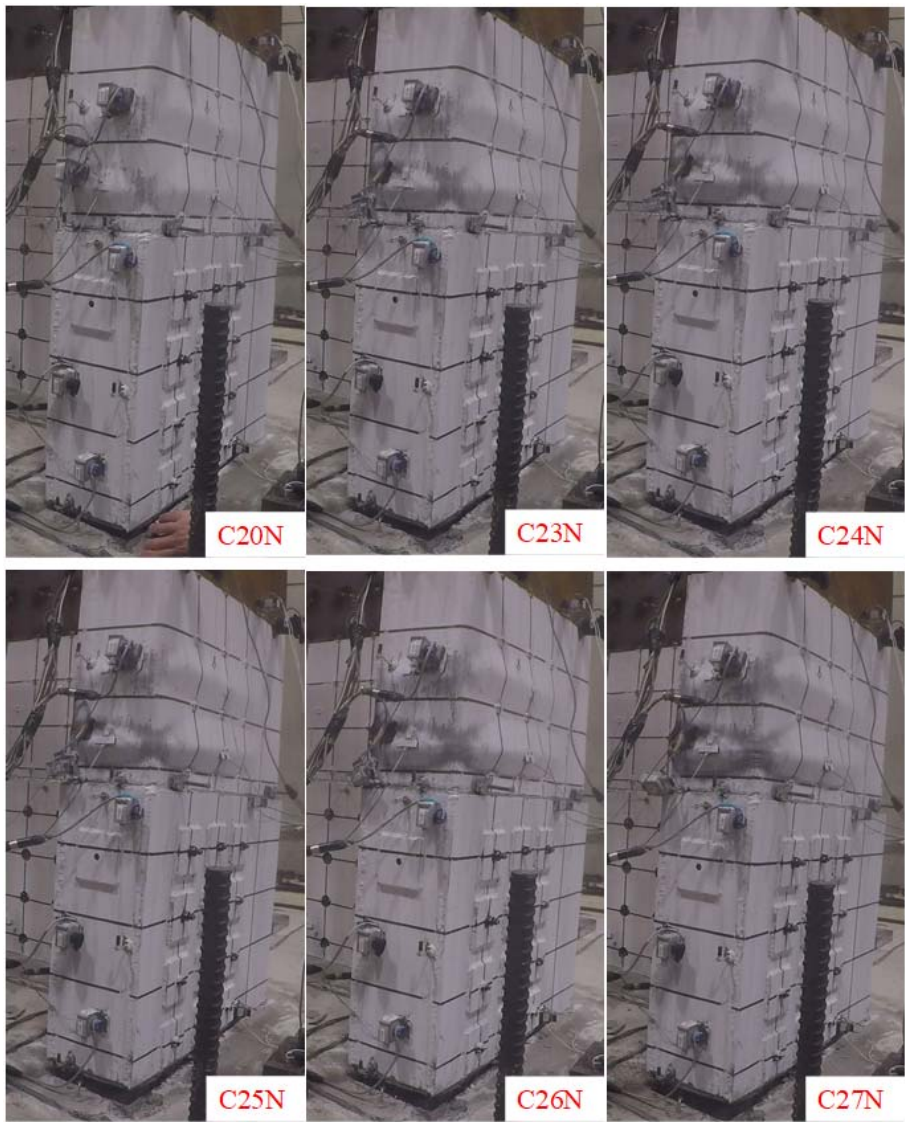


Figure 4-20. (Continued)



Figure 4-21. Vertical weld fracture at the corner of the NWS and NWW surfaces



a)



b)



c)



d)

Figure 4-22. Weld fractures at: a) NWS, b) NWN, c) SWN and d) SWS



Figure 4-23. Close-up pictures of the fracture propagation at SWS from: a) front view and b) side view

4.8 Test Data Analysis

The experimentally obtained applied lateral force versus top lateral drifts for Repaired Specimen C2 is shown in Figure 3-26. The vertical axis shows the horizontal force applied to the specimen, which is equal to the value recorded by the lateral actuators (not equal to the shear force applied to the specimen, because the force shown in this figure is not yet corrected to subtract the horizontal components of the vertical actuator forces, which only cancel each other when the drift is equal to zero). The lateral drift was calculated by dividing the top of the wall's lateral displacement by the distance from the top of the repaired part to the centerline of the lateral actuator's attachment head. As mentioned before, the weld inside the footing in the South web fractured. Therefore, the lateral load capacity of the wall in the negative drift direction was anticipated to be more than what was obtained experimentally, which is the summation of the two recorded horizontal actuator forces. Hence, in Figure 3-26, the applied horizontal force is also compared with twice of the horizontal force from the North actuator ($2 \times \text{North}$), as the weld inside the footing of the North web fractured at a relatively later stage. Given that the applied horizontal forces from both method are almost the same for the positive drifts, this confirmed that it can be assumed that the capacity of the wall in the

negative direction would have been close to the value obtained as “*twice of the horizontal force from the North actuator (2xNorth)*” if early fracture had not happened at the base of the South web, and this was used as a “proxy” here for the capacity of the wall in the negative direction.

Building from the results in Figure 3-26, Figure 3-27 shows the points when some of the key observations were made during the test. In particular, these points correspond to the onset of visible local buckling on the web and flange and maximum strengths at negative and positive displacements.

The moment resisted by the wall above the repair was calculated by separating the horizontal components of the force of the two vertical actuators that applied an axial load to the wall. As discussed before, the actuators used for the axial load application were placed at an inclination angle of 70 degrees from the strong floor, leaning toward the wall (see Figure 3-28a). The trajectories of the axes of these actuators intersect above the centerline of the flange of the wall. At the point of zero horizontal displacement at the top of the wall, the horizontal components of the forces in the two vertical actuators are equal and in opposite directions. At non-zero displacements of the top of the wall, as the inclination angles of the vertical actuators change, as a result, the summation of the horizontal components of the forces in these actuators develops an extra force that has to be carried by the horizontal actuators. The free-body diagram of the forces (at zero displacement) is shown in Figure 3-28b. The moment resisted by the wall above the repair was calculated according to the free-body diagram shown in Figure 3-28b by Equation (3.1):

$$\overrightarrow{M}_{repair} = \overrightarrow{r}_{act} \times \overrightarrow{F}_H + \overrightarrow{r}_{top} \times (\overrightarrow{F}_{v1} + \overrightarrow{F}_{v2}) \quad (4.1)$$

Figure 3-29 shows the calculated base moment resisted by the wall versus the top of the wall’s drift for Repaired Specimen C2. The peak displacements and corresponding base moments for each cycle of the Repaired Specimen C2 test are presented in Table 3-4.

To determine the ductility reached (μ), an effective yield displacement ($\delta_{y,eff}$) was taken as the displacement corresponding to the intersection of a line tangent to the initial slope of the resulting pushover curve and a horizontal line set at the level of the maximum base moment obtained from test, $M_{base,max}$. The

displacement obtained at $0.8M_{base,max}$ after post-peak of the backbone curve of the test setup was taken for the ultimate displacement (δ_u). Then, using Equation 3.2, ductility was calculated as 2.58/-4.22 in the positive and negative directions.

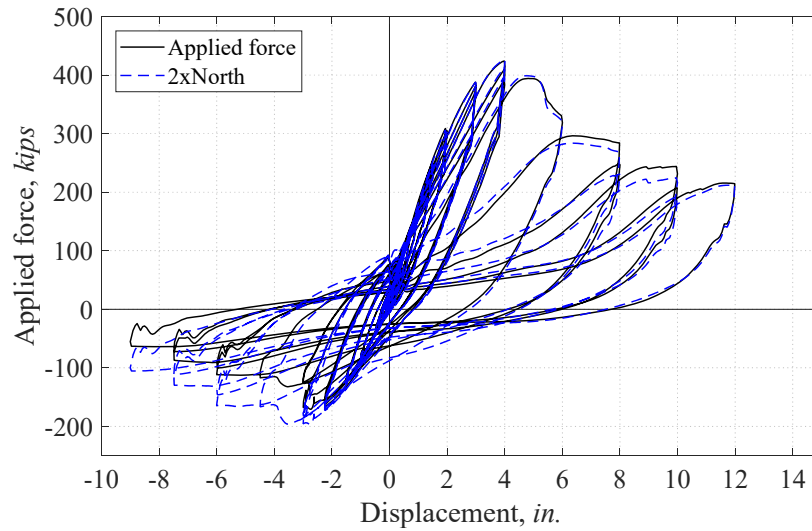


Figure 4-24. Applied lateral force vs. top drift relationship for Repaired Specimen C2

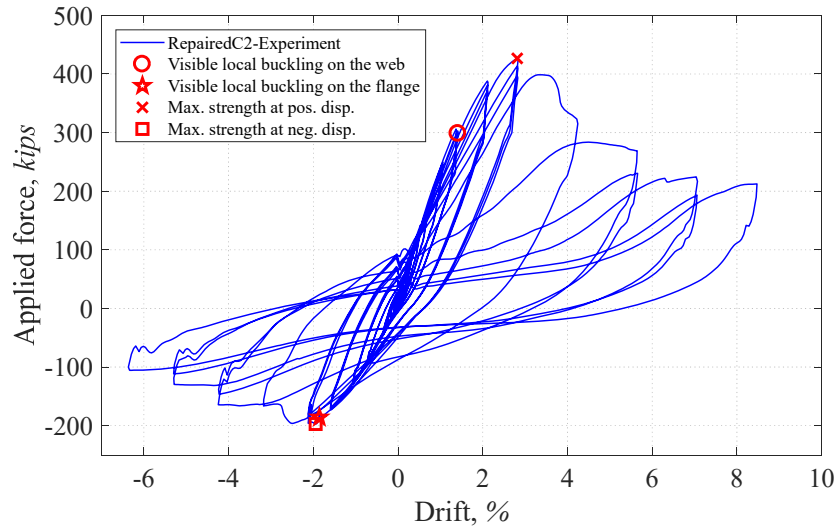


Figure 4-25. Some important points marked in the applied lateral force vs. top drift relationship for Repaired Specimen C2

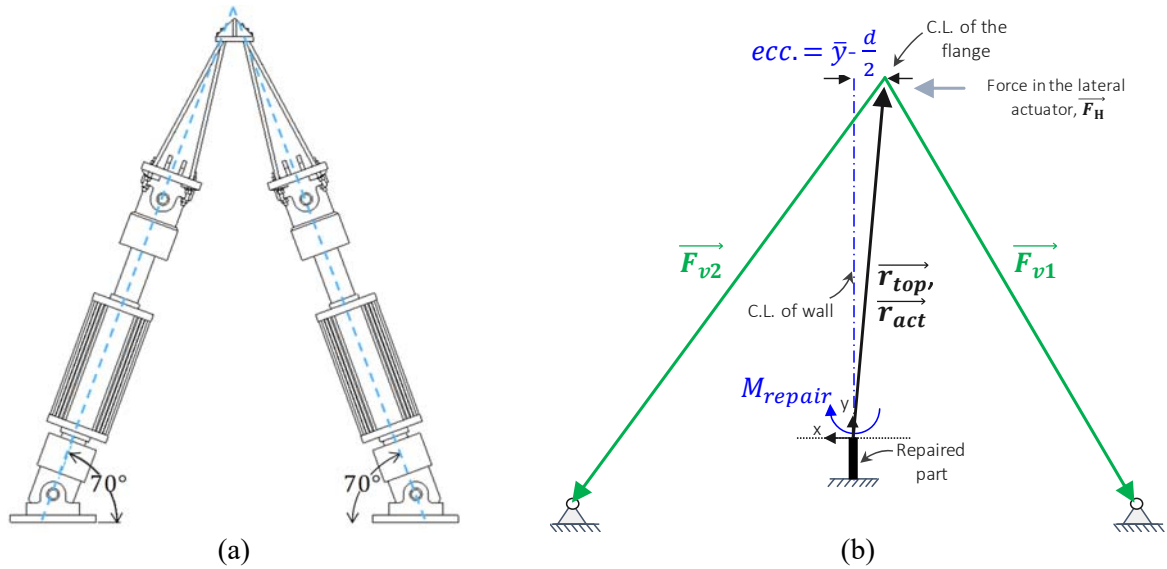


Figure 4-26. (a) Inclination angle of vertical actuators at zero displacement; (b) Free body diagram of the specimen wall at zero displacement

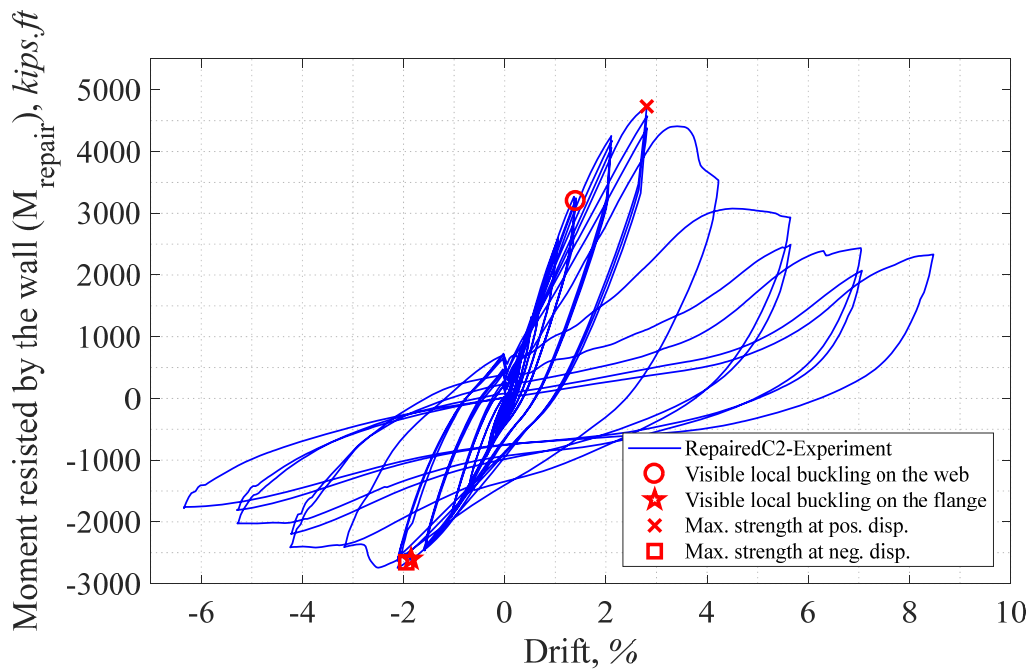


Figure 4-27. Calculated experimental base moment vs. top drift relationship for Repaired Specimen C2

Table 4-2. Peak displacements and corresponding base moments for each cycle of Repaired Specimen C2 test

Cycle	Label	Displacement, <i>in.</i>	Base Moment, <i>kip.ft</i>	Cycle	Label	Displacement, <i>in.</i>	Base Moment, <i>kip.ft</i>
1	C1P	0.24	422	15	C15P	3.0	4176
	C1N	-0.13	-336		C15N	-2.25	-2434
2	C2P	0.25	435	16	C16P	3.0	4062
	C2N	-0.13	-347		C16N	-2.26	-2417
3	C3P	0.50	859	17	C17P	4.0	4732
	C3N	-0.25	-557		C17N	-3.00	-2746
4	C4P	0.50	854	18	C18P	4.0	4571
	C4N	-0.25	-580		C18N	-3.0	-2633
5	C5P	0.75	1323	19	C19P	4.0	4377
	C5N	-0.38	-772		C19N	-3.0	-2588
6	C6P	0.75	1280	20	C20P	6.0	4409
	C6N	-0.38	-770		C20N	-4.5	-2744
7	C7P	1.00	1704	21	C21P	Skipped	NA
	C7N	-0.50	-933		C21N	Skipped	NA
8	C8P	1.00	1660	22	C22P	Skipped	NA
	C8N	-0.50	-919		C22N	Skipped	NA
9	C9P	1.5	2595	23	C23P	8.0	3077
	C9N	-1.00	-1440		C23N	-6.0	-2414
10	C10P	1.5	2555	24	C24P	8.0	2491
	C10N	-1.00	-1431		C24N	-6.0	-2199
11	C11P	1.94	3270	25	C25P	10.0	2432
	C11N	-1.50	-1929		C25N	-7.5	-2024
12	C12P	2.0	3246	26	C26P	10.0	2072
	C12N	-1.50	-1916		C26N	-7.49	-1809
13	C13P	2.0	3205	27	C27P	12.0	2333
	C13N	-1.50	-1911		C27N	-9.0	-1780
14	C14P	3.0	4254	28	C28P	Skipped	NA
	C14N	-2.26	-2465		C28N	Skipped	NA

The strains on the steel plates were recorded by strain gages placed at 5.44, 29.44, and 35.44*in.* from the top of the footing on the webs and flange of the wall. It was observed from the C1 and C2 specimens that the strain profile is symmetric about the mid-length of the Specimen's flange (until local buckling develops, which was not triggered necessarily at the same time on both halves of the specimen). Therefore, only half of the wall was instrumented with strain gauges. In order to check if the repair plate

stayed elastic during the test, strain gauges were mounted 5.44in. from the top of the footing on the surface of the plate. Moreover, in order to track the strains in the plastic hinge region, strain gauges were mounted on the existing steel plate at 29.44in. and 35.44in. from the top of the footing (equal to 4.94in. and 10.94in. from the top of repair plate) between the 1st and 2nd tie bar rows and 2nd and 3rd tie bar rows (more detailed instrumentation plans showing locations of strain gauges and other sensors are included in Appendix E1). The strain profiles recorded at these three heights are shown in Figure 3-30 at the peak displacements of the cycle corresponding to the theoretical first yield points in the positive and negative direction. The vertical axis shows the recorded strain normalized to the yield strain of the steel plate, which was obtained as 0.001951 from the steel coupon tests. At this stage, the strain profiles across the wall cross-section are almost linear. Figures 3-32 and 4-30 respectively show the recorded strains at the peak displacement of the cycle where local buckling was first observed, on the web for positive wall displacements, and on the flange for negative displacements. The strain profiles when maximum resistance was reached are shown in Figure 3-36.

The points of maximum flexural strength experimentally obtained from Repaired Specimen C2 were compared to their corresponding values predicted by theoretical P-M interaction curves. These plots are shown in Figure 3-39 for the Repaired Specimen C2. In calculation of the P-M interaction curves, the actual material properties of the steel plates and concrete infill measured from the tensile coupon and compression cylinder tests were used.

The experimentally obtained moment developing at the cross-section above repair of the walls were also compared to their theoretical resistances calculated using the Plastic Stress Distribution Method (PSDM). The theoretical values were calculated three different way, namely using the actual, nominal, and expected material properties. These comparisons are shown in Figure 3-41 for Repaired Specimen C2. The actual values are those obtained using results from the testing of steel coupons of samples from the wall's web and flanges, and of concrete cylinder cast during construction of the walls and tested on the corresponding specimen test day. The nominal yield value used for the steel plates was equal to 50ksi for

the A572Gr50 steel used in the wall's construction. The nominal value for concrete was taken equal as 6ksi for the specimen, as this was the ordered material (note that cylinder strength on the day of test turned out to be less than this value). The expected values for the steel yield and concrete compressive strengths were calculated by multiplying those values by $R_y=1.1$ and $R_c=1.5 \times 0.85$, respectively. The material property values as well as the calculated theoretical resistances are shown in Table 4-3.

Table 4-3. Actual, nominal, and expected material properties and Calculated flexural resistances for Repaired Specimen C2

Specimen	Material property	Concrete f'_c, ksi	Steel plates F_y, ksi	$M_{PSDM}, kip.ft$		$\frac{M_{PSDM}}{M_{experiment}}$	
				Pos.	Neg.	Pos.	Neg.
Repaired C2	Nominal	6.0	50.0	3567	-2099	0.75	0.76
	Actual	5.1	55.2	3631	-2288	0.77	0.83
	Expected	7.65	55.0	4093	-2322	0.86	0.85

The specimens were inspected after the test. Figure 3-44 shows a schematic of the damage on the steel plates for Repaired Specimen C2. In this figure, the locally buckled areas are marked with dashed line, the fracture lines are shown with solid line, and the tie bar failures are circled. The pictures of the specimen in all directions are also shown in Figure 4-35. Note that these tie bar failures, in all observed cases, were due to weld failure at their connection at only one end of each tie bar. The failed ends of the tie bars are marked in the figure and one example of the weld fracture of tie bar at 3rd row and 1st column from West side of North Web is shown in Figure 4-36.

The rotations of the wall above repair where the plastic hinge was developed was also calculated. This was done using the recorded horizontal movements of the wall from the string pots attached to the wall closest to the foundation, and then dividing its readings by its distance to the top of the repair plate (26in.), which resulted in total rotations at the wall base (i.e., θ_{wt}). Recognizing that this calculated rotation

also included the rotations of the wall-footing connection (i.e., θ_{wf}) and rotation of repair plate (i.e., θ_{wr}), these rotations at the wall-footing connection (θ_{wf}) and at repair plate (i.e., θ_{wr}) were subtracted from the total rotations (θ_{wt}) to obtain the wall rotations at the base (i.e., θ_{wb}). Figure 3-48 shows the composition of the rotations at the base of the wall. Note that there was no slippage between the footing and the strong floor during the test and therefore the lateral displacements of the footing were considered zero in calculation of the rotation.

Note that the rotation at the wall-footing connection (θ_{wf}) could have been calculated at each step of the test using the differences in the recorded displacements from the vertical string pots (i.e., along the axial axis of the wall) that were connected from the wall surface to the foundation's top surface at the east and west elevations of the wall, divided by their distance from each other, but this would have not included rotations introduced locally near the base of the wall due to the flexibility/deformations of the footing itself. Instead, the wall-footing connection rotation was taken into account by substituting the footing and wall-to-footing connection with a linear rotational spring at the base of the wall. The rotational stiffness of this spring was calculated by finding the slope of a line that was fitted to the M_{base} - θ_{wf} relationship curve at the linear cycles (i.e., from the beginning of the test until end of Cycle 7) and then multiplying the rotational stiffness by the base moment (M_{base} , not M_{repair}) at each corresponding step of the test. The rotational spring stiffness was calculated as 1.113×10^6 kip.ft/rad for Repaired Specimen C2. Unfortunately, the accelerometers placed at South web did not run properly for the first four elastic cycles so the calculated rotation spring stiffness of the foundation was only confirmed with the LS-DYNA model of the wall. The rotation of the repair part (i.e., θ_{wr}) was directly obtained from the same method as the calculation of the total rotation of the wall above repair, which was done by using the recorded horizontal top movements of the repair plate from the string pot attached to the wall closest to the foundation, and then dividing its readings by its distance to the top of the footing (23.5in.).

Figure 3-49 shows the calculated moment above repair versus the wall rotations ($M_{repair}-\theta_{wb}$) relationship curve. This curve was compared to the one with total rotations above repair ($M_{repair}-\theta_{wt}$) in Figure 3-50. Note that since the weld connecting the thicker plate to the repair plate had fractured at maximum negative moment, the rotations obtained reached 0.08 rad, which is unrealistic based on the results obtained from C2 Specimen (which had maximum rotation of -0.045 rad). Therefore, the negative rotations after the point of maximum moment should be ignored.

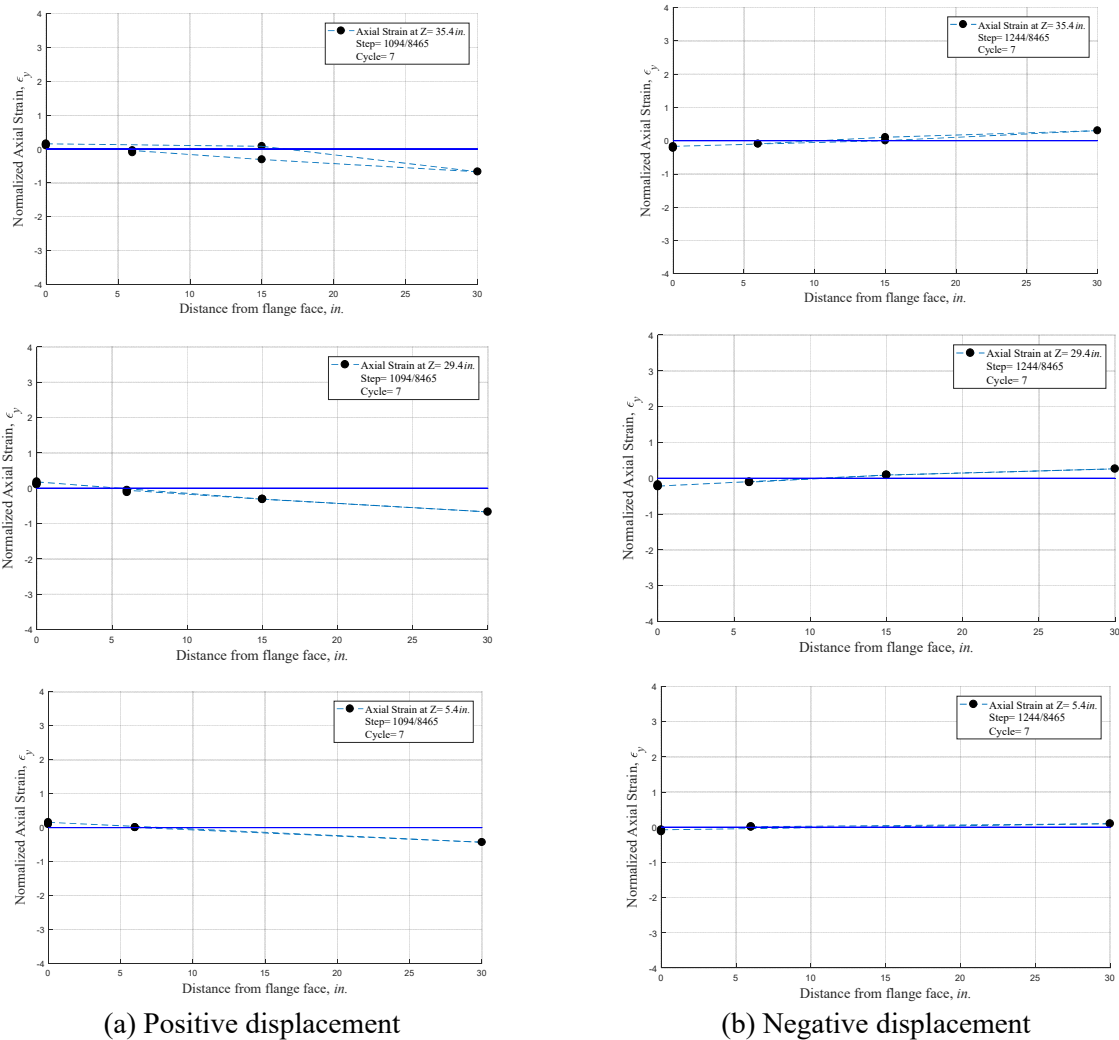
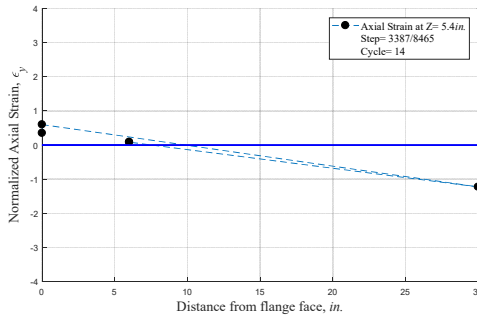
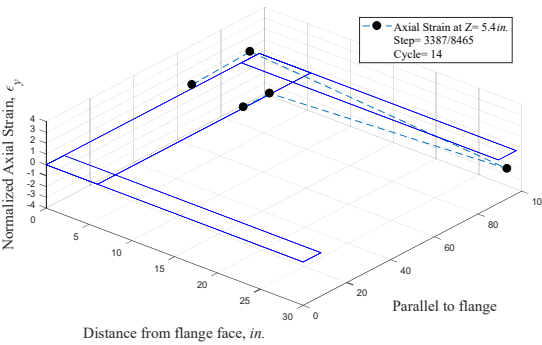
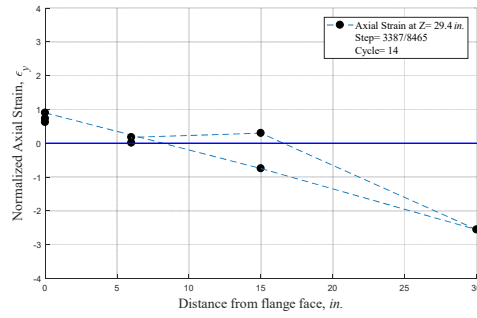
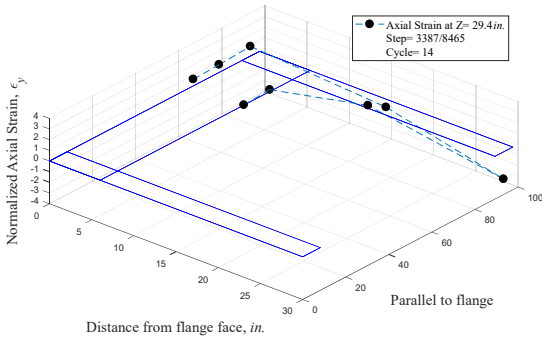
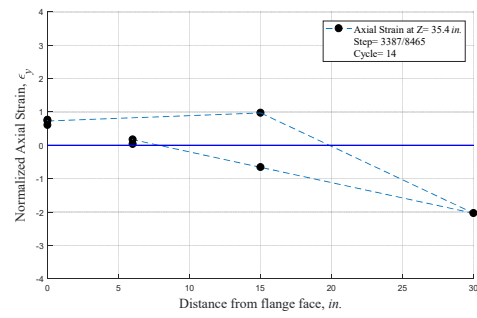
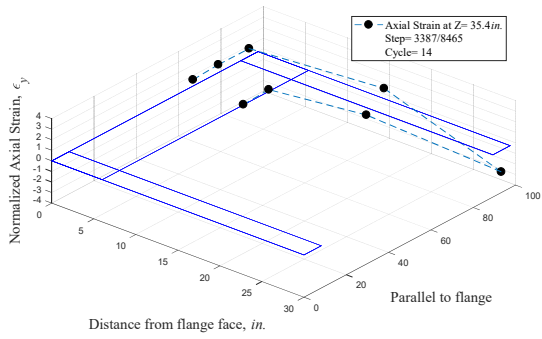


Figure 4-28. Strain profiles at first yield on: (a) positive displacement; (b) negative displacement



3D strain profile

Elevation view of strain profile

Figure 4-29. Strain profiles at the positive peak of Cycle 14 where the local buckling was visually observed on the web

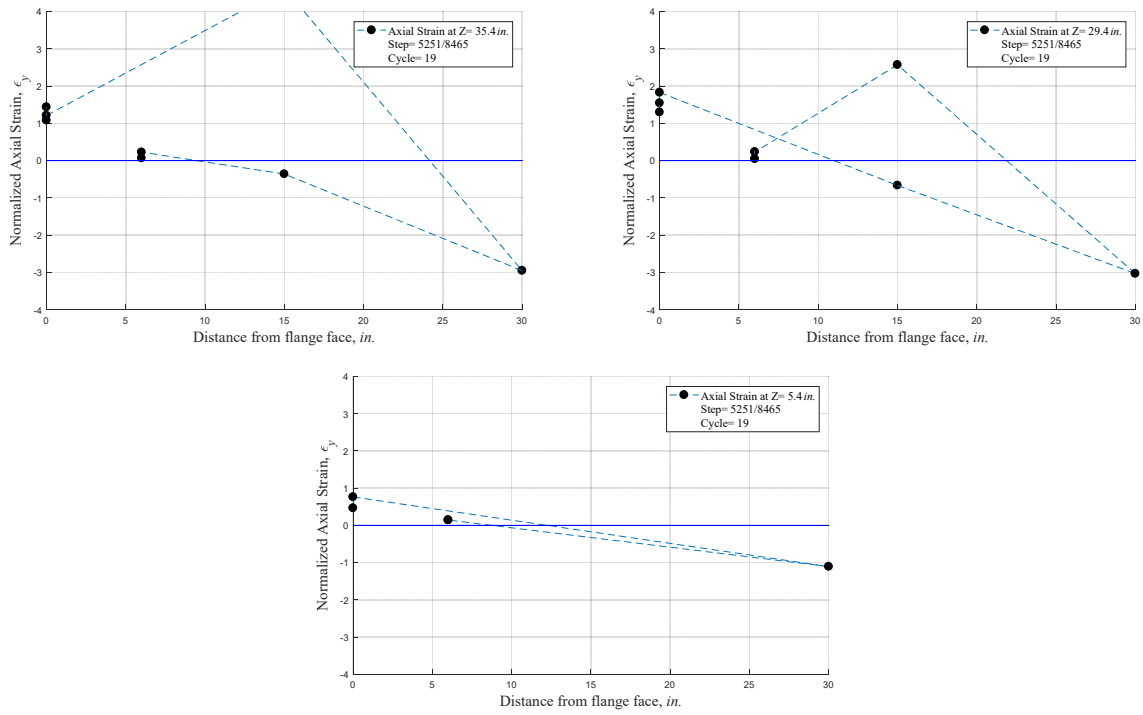
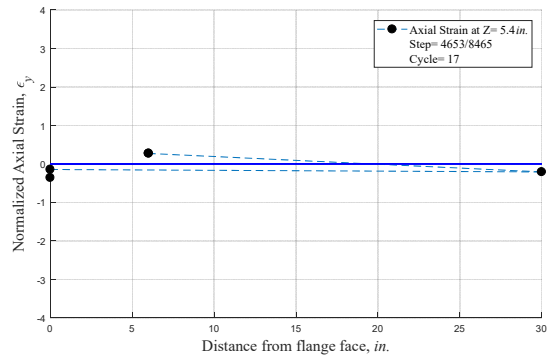
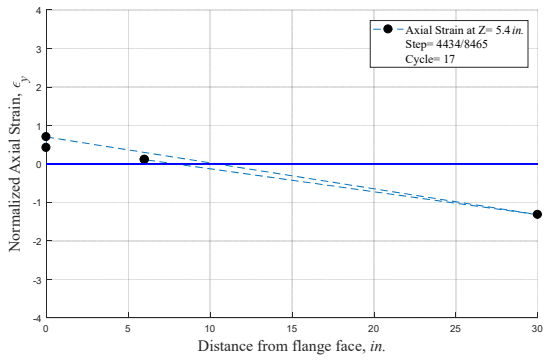
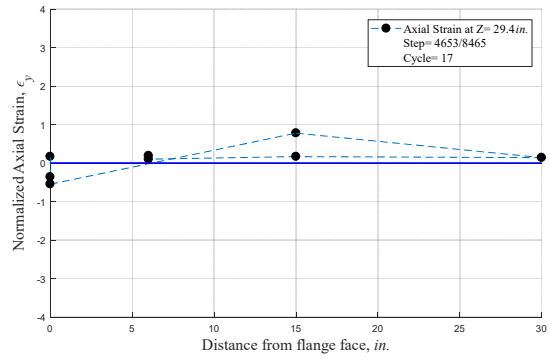
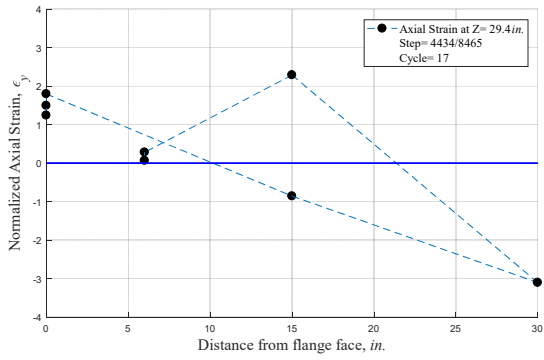
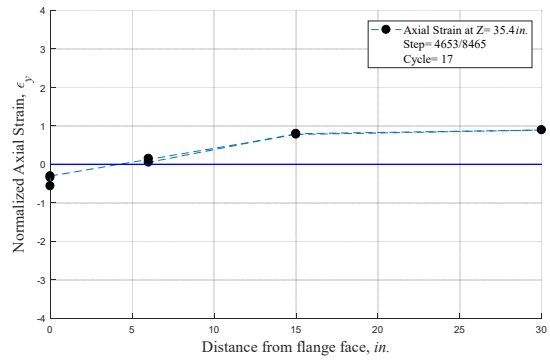
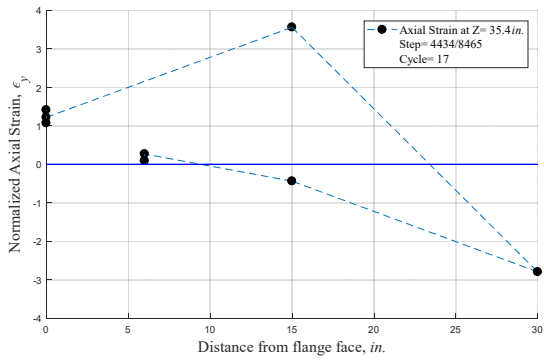


Figure 4-30. Strain profiles at the negative peak of Cycle 19 where the local buckling was visually observed on the flange



(a) Positive maximum strength

(b) Negative maximum strength

Figure 4-31. Strain profiles at: (a) the positive maximum strength point (Cycle 17); (b) the negative maximum strength point (Cycle 17)

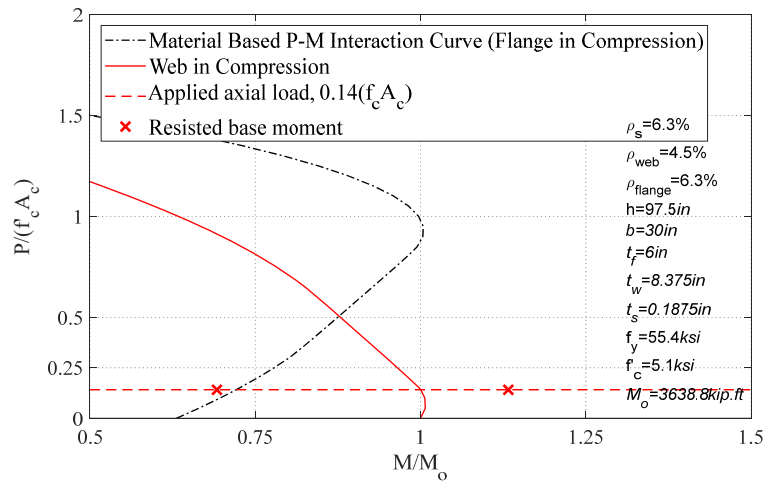


Figure 4-32. Comparison of Repaired Specimen C2 flexural resistances with P-M interaction curve

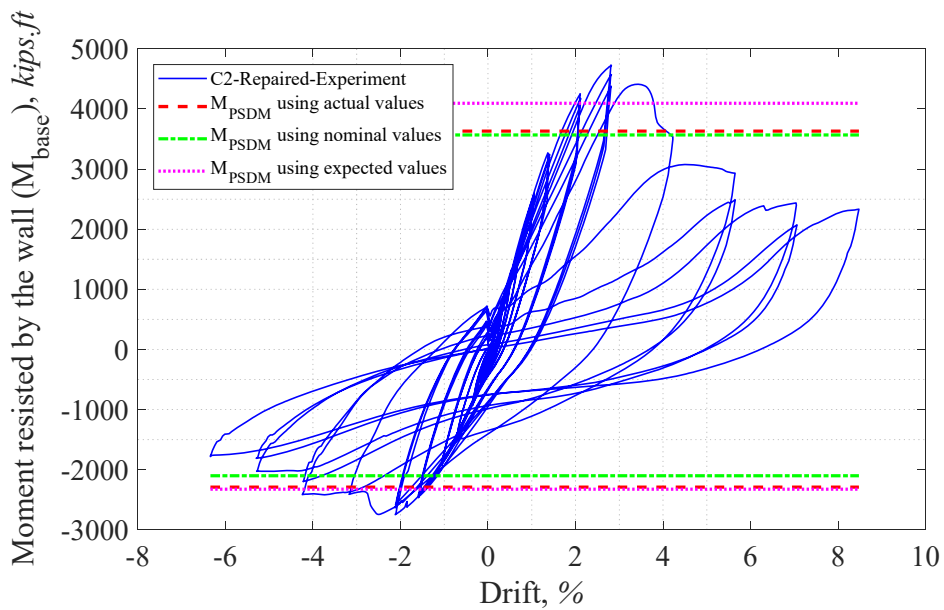


Figure 4-33. Comparison of calculated theoretical resistance moments and the experimental moment at cross-section above repair for Repaired Specimen C2

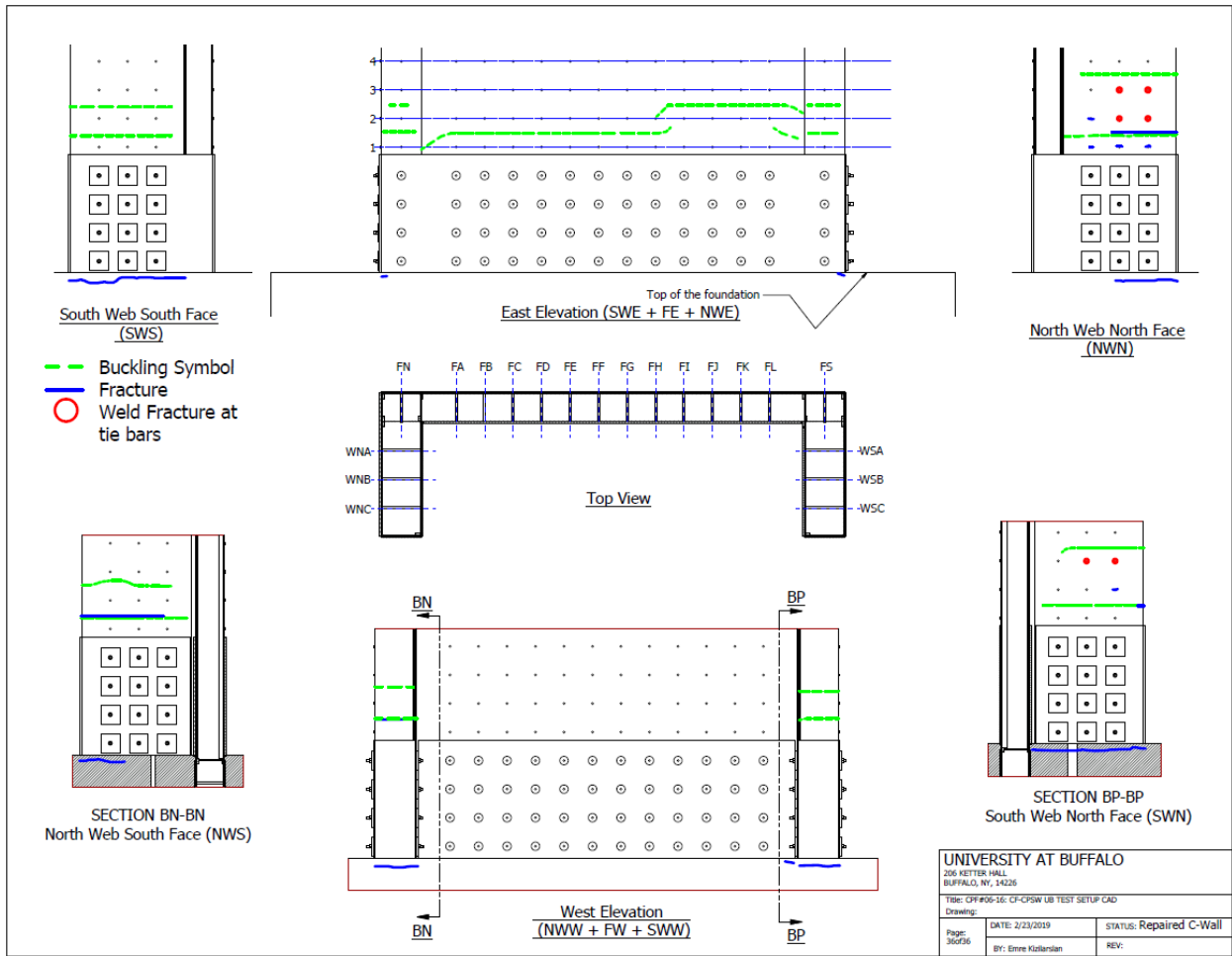


Figure 4-34. Sketch of post-test damage inspection of the wall steel plates for Repaired Specimen C2

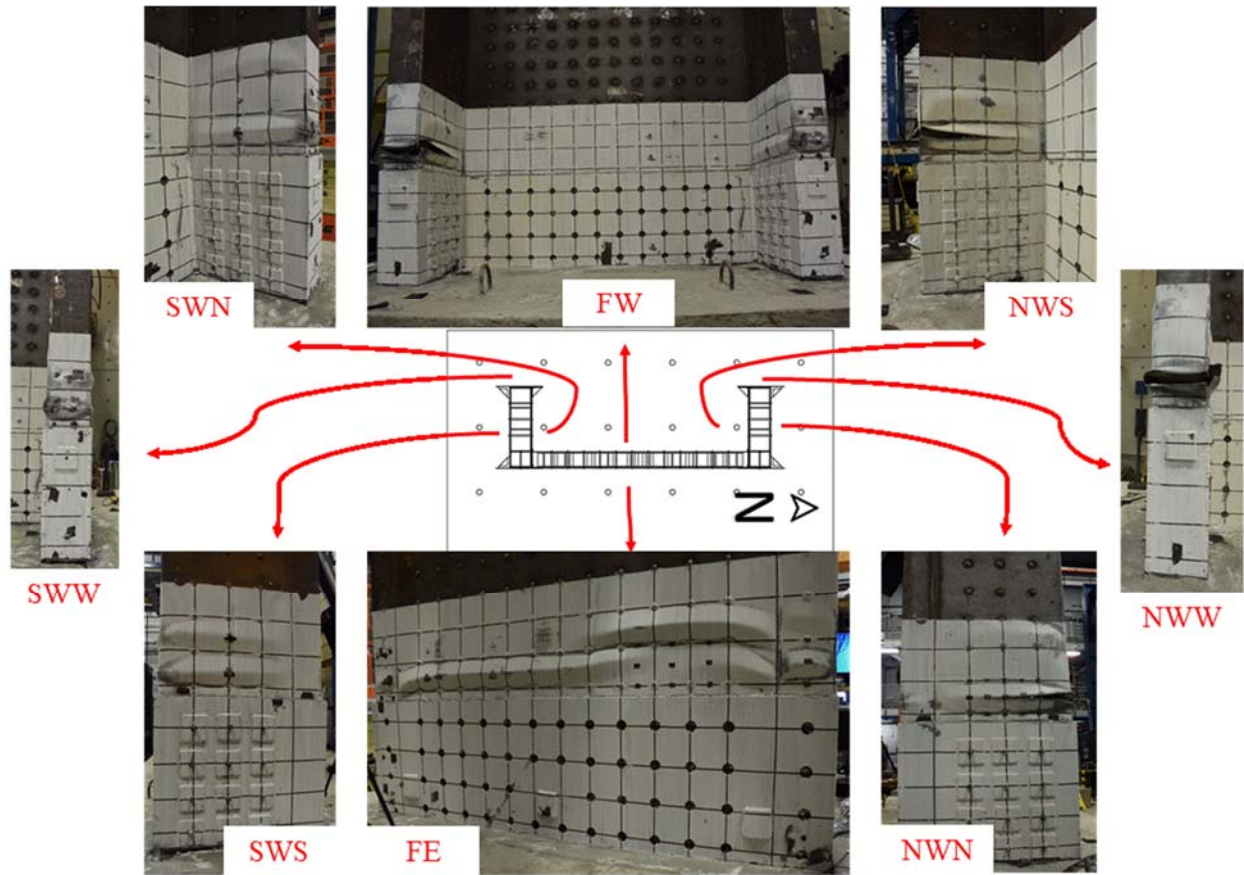


Figure 4-35. Post-test damage inspection of the wall steel plates for Repaired Specimen C2



Figure 4-36. Weld fracture of tie bar at 3rd row and 1st column from West side of North Web.

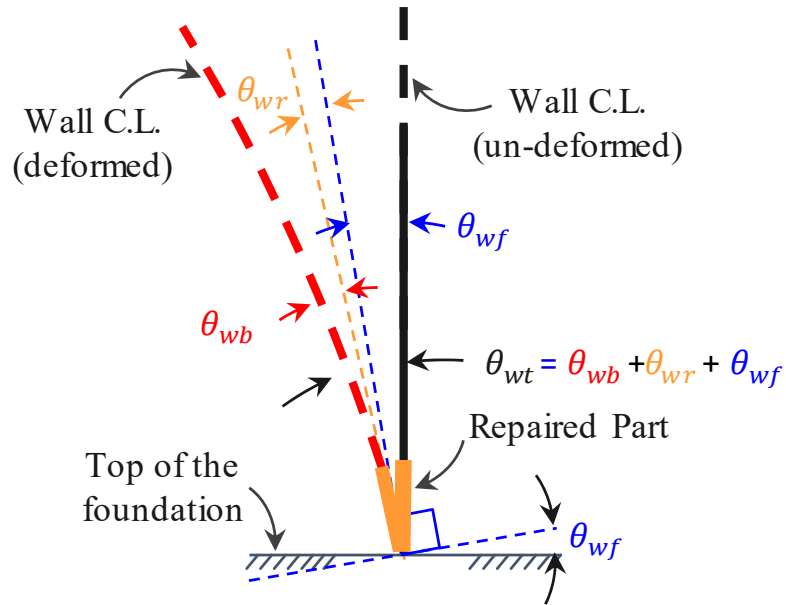


Figure 4-37. Composition of wall rotations above repaired part of the wall

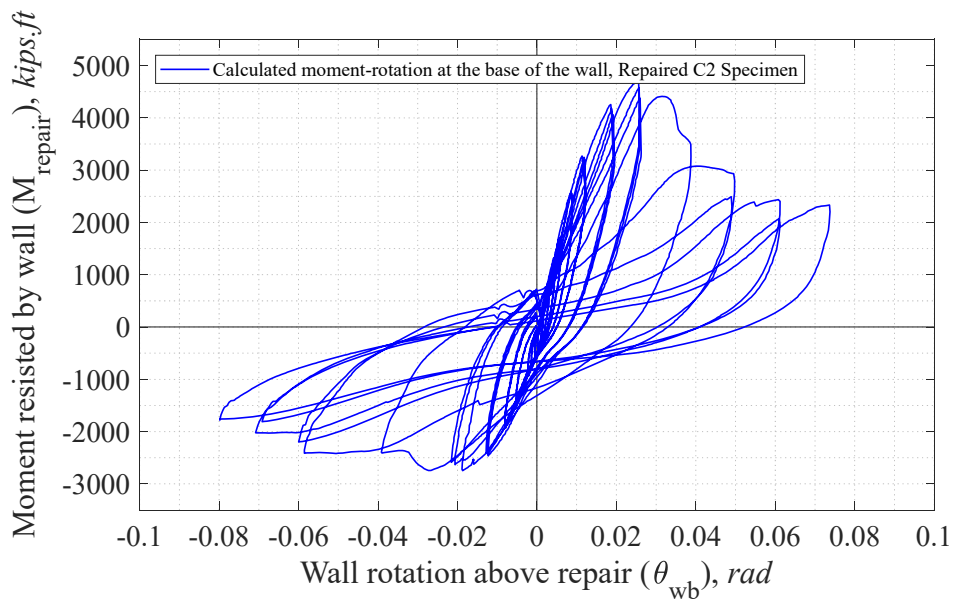


Figure 4-38. Calculated experimental base moment vs. wall rotation above repaired part for Repaired Specimen C2

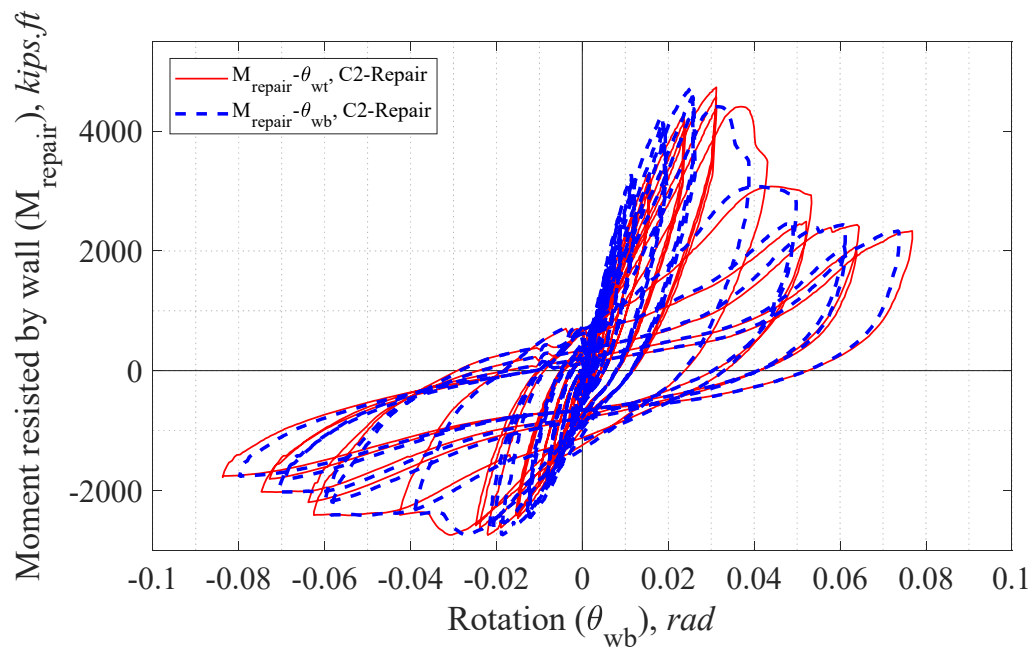


Figure 4-39. Comparison of calculated experimental base moment vs. wall base rotation and vs. total base rotation for Repaired Specimen C2

“This Page Intentionally Left Blank”

SECTION 5

SUMMARY AND CONCLUSIONS

Two large-scale C-shaped Composite Plate Shear Wall/Concrete Filled were subjected to axial and cyclic flexural loading. The walls were subjected to 19% and 15% axial loading before horizontal cyclic loads were applied. Both specimens showed similar buckling and fracture behaviors. Ductility was more than 4 (4.02/-4.3 for positive and negative directions for both specimens) when flexural strength dropped to 80% of the peak value developed, and both specimens reached or exceeded their calculated plastic moment capacities in the positive and negative direction. More specifically:

- Peak strength was reached at drifts of 3.2% in the positive and 2.7% in the negative directions for Specimen C1. On the other hand, the peak strength was observed at 2.1% and 1.8% in the positive and negative directions for Specimen C2.
- Tests showed that even though local buckling started in early cycles after yielding, the capacity of the walls did not drop until fracture of the steel plates.
- The fractures of steel plate were not sudden; it was progressive, meaning that flexural strength degradation was relatively slow.
- A significant portion of web and flange remained unfractured at peak drifts of 6.3/-5.4% when testing was stopped, and a residual flexural strength of 29.7/-31.3% and 32.9/-31.8% of corresponding peak values of Specimens C1 and C2 in the positive and negative directions, respectively, remained after completion of the tests.
- Yielding propagated over roughly 40% of the height of the wall; given that the ratio of Plastic Moment to First Yield Moment was in the range of 1.45 to 1.66 (depending on direction of loading) for the measured material strengths.
- Buckling occurred between multiple layers of tie bars, as a consequence of yielding over a substantial part of the height.

- Even though the main purpose of the tests was to observe the behavior of the walls under different axial loading, the results ended up to be relatively close to each other. However, as it is generally considered essential to achieve replicability of results across multiple specimens, the availability of test results on two specimens that have achieved essentially similar hysteretic behavior is a positive outcome to ensure the reliable seismic performance of the system.

Based on the experimental observations and results obtained, it can be concluded that C-shaped C-PSW/CF can exhibit good cyclic behavior without premature strength degradation, while maintaining their ability to resist large axial load of up to 19% $A_g f'_c$.

Moreover, a large-scale C-shaped Composite Plate Shear Wall/Concrete Filled that had been previously subjected to axial and cyclic flexural loading up to a severe level of damage was repaired and retested, to investigate if this structural system could realistically be returned to a post-earthquake condition having the same capacity and hysteretic behavior. The repaired specimen was subjected to the same loading protocol as the original wall, namely being subjected to 15% of the crushing load of the infill concrete before horizontal cyclic loads were applied.

The repaired specimen exhibited similar yielding, buckling, and fracture behaviors as the originally tested Specimen C2. Ductility reached was 2.58/-4.22 in the positive and negative directions when flexural strength dropped to 80% of the peak value developed, which indicates that the ductility is reduced in the positive direction. This is because the repair weld at the base of one of the webs was not executed as designed and failed prematurely. Nonetheless, the repaired specimen (like the unrepaired one did) reached or exceeded its calculated plastic moment capacities in the positive and negative direction. More specifically, positive peak strength was reached at drifts of 2.1% both Specimen C2 and the Repaired Specimen C2. However, due to fracture at the weld inside footing between the existing steel plate of

Specimen C2 and its repair plate, the data obtained in the negative direction for the Repaired Specimen C2 is not deemed to be representative beyond a drift of 1.8% (Cycle18) and a moment equal to 115% of M_p .

As before, the tests showed that even though local buckling started in early cycles after yielding, the capacity of the walls did not drop until fracture of the steel plates initiated. Likewise, the fractures of steel plate were progressive, flexural strength degradation was relatively slow, and buckling occurred between multiple layers of tie bars, as a consequence of yielding over a substantial part of the height.

Based on the experimental observations and results obtained, it can be concluded that C-shaped C-PSW/CF repaired by the procedure adopted here can exhibit a good cyclic inelastic behavior without premature strength degradation, while maintaining their ability to resist axial load as high as 15% $A_f f'_c$ of the crushing load of the infill concrete.

“This Page Intentionally Left Blank”

SECTION 6

REFERENCES

- ACI "Building code requirements for structural concrete (ACI 318-19) and commentary." American Concrete Institute.
- AISC 341-16 (2016). *Seismic provisions for structural steel buildings*, American Institute of Steel Construction, Chicago, Ill.
- Alzeni, Y., and Bruneau, M. (2014). "Cyclic Inelastic Behavior Of Concrete Filled Sandwich Panel Walls Subjected To In-Plane Flexure." *Technical Rep. MCEER 14-009*, MCEER The State University of New York at Buffalo.
- Bhardwaj, S. R., and Varma, A. H. (2017). *Design of modular steel-plate composite walls for safety-related nuclear facilities*, American Institute of Steel Construction.
- Bowerman, H., and Chapman, J. C. (2002). "Bi-steel steel-concrete-steel sandwich construction." *Composite construction in steel and concrete IV*, 656-667.
- Brown, N., Kowalsky, M., and Nau, J. (2015). "Impact of D/t on seismic behavior of reinforced concrete filled steel tubes." *Journal of constructional steel Research*, 107, 111-123.
- Bruneau, M., and Kizilarslan, E. (2019). "Seismic and Wind Behavior and Design of Coupled CF-CPSW Core Walls for Steel Buildings." *Interim Report No.5 to Charles Pankow Foundation: Grant # 06-15*.
- Cho, S. G., Park, W.-K., So, G.-H., Yi, S.-T., and Kim, D. (2015). "Seismic capacity estimation of Steel Plate Concrete (SC) shear wall specimens by nonlinear static analyses." *KSCE Journal of Civil Engineering*, 19(3), 698-709.

- Denavit, M. D., Hajjar, J. F., and Leon, R. T. (2016). "Cross-Section Strength of Circular Concrete-Filled Steel Tube Beam-Columns." *ENGINEERING JOURNAL-AMERICAN INSTITUTE OF STEEL CONSTRUCTION*, 53(2), 99-105.
- El-Bahey, S., and Bruneau, M. (2011). "Bridge piers with structural fuses and bi-steel columns. I: Experimental testing." *Journal of Bridge Engineering*, 17(1), 25-35.
- Eom, T.-S., Park, H.-G., Lee, C.-H., Kim, J.-H., and Chang, I.-H. (2009). "Behavior of double skin composite wall subjected to in-plane cyclic loading." *Journal of structural engineering*, 135(10), 1239-1249.
- Fujimoto, M., Wada, A., Saeki, E., A., W., and Y., H. (1988). "A study on the unbonded brace encasted in buckling-restrained concrete and steel tube." *Journal of Str. Engineering, AIJ*, 34.
- Hajjar, J. F. (2000). "Concrete - filled steel tube columns under earthquake loads." *Progress in Structural Engineering and Materials*, 2(1), 72-81.
- Iwata, M., Kato, T., and Wada, A. (2000). "Buckling-restrained braces as hysteretic dampers." *Behavior of Steel Structures in Seismic Areas*, 33-38.
- Kenarangi, H., and Bruneau, M. (2019). "Experimental Study on Composite Action in Reinforced Concrete-Filled Steel-Tube Shaft Foundations." *Journal of Bridge Engineering*, 24(7), 04019060.
- Leon, R. T., Kim, D. K., and Hajjar, J. F. (2007). "Limit state response of composite columns and beam-columns part 1: Formulation of design provisions for the 2005 AISC specification." *ENGINEERING JOURNAL-AMERICAN INSTITUTE OF STEEL CONSTRUCTION*, 44(4), 341.
- Mazzoni, S., McKenna, F., Scott, M. H., and Fenves, G. L. (2006). "OpenSees command language manual." *Pacific Earthquake Engineering Research (PEER) Center*.
- MSC (2019). "850-FT-TALL RAINIER SQUARE TOWER TOPS OUT IN ONLY 10 MONTHS." *Modern Steel Construction*, Retrieved from:

<https://www.aisc.org/modernsteel/news/2019/august/rainier-square-tower-tops-out-at-850-ft-in-under-10-months/>.

- Saeki, E., Maeda, Y., Nakamura, H., Midorikawa, M., and Wada, A. (1995). "Experimental study on practical-scale unbonded braces." *Journal of Structural and Constructional Engineering, Architectural Institute of Japan*, 476, 149-158.
- Stephens, M. T., Lehman, D. E., and Roeder, C. W. (2018). "Seismic performance modeling of concrete-filled steel tube bridges: Tools and case study." *Engineering Structures*, 165, 88-105.
- Tsai, K.-C. "Design of steel beam-to-box column connections for seismic load'." *Proc., Proc., First World Conf. Constructional Steel Design, Acapulco, Mexico*, 365-374.
- Usami, T., and Ge, H. (1994). "Ductility of concrete-filled steel box columns under cyclic loading." *Journal of structural engineering*, 120(7), 2021-2040.
- Varma, A. H., Malushte, S. R., Sener, K., and Lai, Z. "Steel-plate composite (SC) walls for safety related nuclear facilities: design for in-plane and out-of-plane demands." *Proc., Proceedings of the 21st IASMiRT Conference (SMiRT 21)*.
- Varma, A. H., Malushte, S. R., Sener, K. C., and Lai, Z. (2014). "Steel-plate composite (SC) walls for safety related nuclear facilities: Design for in-plane forces and out-of-plane moments." *Nuclear Engineering and Design*, 269, 240-249.
- Varma, A. H., Ricles, J. M., Sause, R., and Lu, L.-W. (2002). "Seismic behavior and modeling of high-strength composite concrete-filled steel tube (CFT) beam-columns." *Journal of Constructional Steel Research*, 58(5-8), 725-758.
- Varma, A. H., Ricles, J. M., Sause, R., and Lu, L.-W. (2004). "Seismic behavior and design of high-strength square concrete-filled steel tube beam columns." *Journal of Structural Engineering*, 130(2), 169-179.

Yu, J.-G., Feng, X.-T., Hao, J.-P., and Gao, X. (2019). "Experimental Study of Composite Steel Plate Shear Wall with Flush End-Plate Connection." *International Journal of Steel Structures*, 1-20.

“This Page Intentionally Left Blank”

APPENDIX A

Design details of Initial Specimen (Mathcad sheets)

Mathcad © Enabled Content.

CPF#06-16: C-Shape CF-CPSW Project, Hadi Kenarangi, University at Buffalo, 2017

Calculations for design of C-Shape CF-CPSW test specimens: *Tie bar design*

ⓘ Disclaimer

⌵ User Notices

User Notices

Input variables that need to be defined by the user are highlighted in **YELLOW.**

Key results and design checks are highlighted in **GREEN.**

Intermediate results and checks are highlighted in **BLUE.**

⌴ User Notices

Description

- Lateral Loading System is noted as "**LLS**"
- Axial Loading System is noted as "**ALS**"
- LLS and ALS are designed using Gr. A36 Steel. Other parts are designed using A572 Gr.50 Steel.
- Welds are designed using E70xx electrode

References:

- AISC 360-16 (2016). *Specification for structural steel buildings*, American Institute of Steel Construction, Chicago, Ill.
- AISC 341-16 (2016). *Seismic provisions for structural steel buildings*, American Institute of Steel Construction, Chicago, Ill.

Input

$$t_s := \frac{3}{16} \text{ in}$$

Steel plate thickness

$$F_{yplate} := 50 \text{ ksi}$$

Specified yield strength of steel plate (A572 Grade 50)

$$F_{uplate} := 65 \text{ ksi}$$

Specified ultimate tensile strength of steel plate (A572 Grade 50)

$$E_s := 29000 \text{ ksi}$$

Elastic modulus for steel

$$t_c := 5 \text{ in}$$

Thickness of the concrete core

$$t_w := t_c + 2 \cdot t_s = 5.375 \cdot \text{in}$$

Total thickness of wall

$$w_1 := 8 \text{ in}$$

Vertical spacing of tie bars

$$w_2 := 8 \text{ in}$$

Horizontal spacing of tie bars

$$D_{tie} := \frac{5}{8} \text{ in}$$

Nominal diameter of round tie bars

$$F_{ytie} := 50 \text{ ksi}$$

Specified yield strength of tie bars (A572 Grade 50)

$$F_{utie} := 65 \text{ ksi}$$

Specified ultimate strength of tie bars (A572 Grade 50)

Steel Web Plate of C-PSW/CF with Boundary Elements per AISC341-16 Article: H7.4a.

The maximum spacing of tie bars in vertical and horizontal directions, w_1 , shall be:

$$w_{1\max} := 1.8 \cdot t_s \cdot \sqrt{\frac{E_s}{F_{y\text{plate}}}} = 8.128 \cdot \text{in} \quad \text{AISC341-16 Eq. (H7-1)}$$

$$w_1 := \begin{cases} w_1 & \text{if } w_1 \leq w_{1\max} \\ \text{"Adjust } w_1 \text{ value"} & \text{otherwise} \end{cases}$$

Use tie spacings of: $w_1 = 8 \cdot \text{in}$

Tie Bar Diameter in C-PSW/CF with or without Boundary Elements Tie per AISC341-16 Article: H7.4e.

Tie bars shall be designed to elastically resist the tension force, T_{req} , determined as follows:

$t_s = 0.187 \cdot \text{in}$	Steel plate thickness
$t_c = 5 \cdot \text{in}$	Thickness of the concrete core
$t_w = 5.375 \cdot \text{in}$	Total thickness of wall
$w_2 = 8 \cdot \text{in}$	Horizontal spacing of tie bars
$w_1 = 8 \cdot \text{in}$	Vertical spacing of tie bars
$F_{y\text{plate}} = 50 \cdot \text{ksi}$	Nominal yield strength of steel plate

T_1 is the tension force resulting from the locally buckled web plates developing plastic hinges on horizontal yield lines along the tie bars and at mid-vertical distance between tie-bars, and is determined as follows:

$$T_1 := 2 \cdot \left(\frac{w_2}{w_1} \right) \cdot t_s^2 \cdot F_{y\text{plate}} = 3.516 \cdot \text{kip} \quad \text{AISC341-16 Eq. (H7-5)}$$

T_2 is the tension force that develops to prevent splitting of the concrete element on a plane parallel to the steel plate.

$$T_2 := \left(\frac{t_s \cdot F_{y\text{plate}} \cdot t_w}{4} \right) \cdot \left(\frac{w_2}{w_1} \right) \cdot \left[\frac{6}{18 \cdot \left(\frac{t_w}{\min(w_1, w_2)} \right)^2 + 1} \right] = 8.283 \cdot \text{kip} \quad \text{AISC341-16 Eq. (H7-6)}$$

$$T_{\text{req}} := T_1 + T_2 = 11.799 \cdot \text{kip} \quad \text{AISC341-16 Eq. (H7-4)}$$

$F_{y\text{tie}} = 50 \cdot \text{ksi}$ Nominal yield strength of tie bars

$$A_{\text{req}} := \frac{T_{\text{req}}}{F_{y\text{tie}}} = 0.236 \cdot \text{in}^2 \quad \text{Required tie bar cross-section area}$$

$$D_{\text{req}} := \sqrt{\frac{4 \cdot A_{\text{req}}}{\pi}} = 0.548 \cdot \text{in} \quad \text{Required tie bar diameter}$$

$$D_{\text{tie}} := \begin{cases} D_{\text{tie}} & \text{if } D_{\text{tie}} \geq D_{\text{req}} \\ \text{"Tie diameter is not OK"} & \text{otherwise} \end{cases}$$

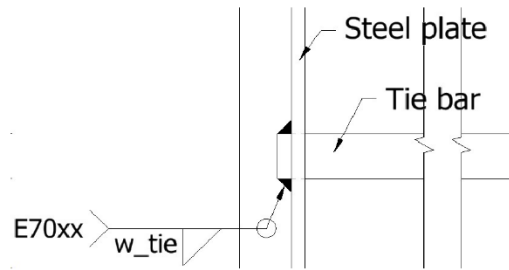
Use $D_{\text{tie}} = 0.625 \cdot \text{in}$ tie bars with yield strength of $F_{y\text{tie}} = 50 \cdot \text{ksi}$

Tie Bar-to-steel plate joint weld design:

$$T_{tie} := \frac{\pi}{4} D_{tie}^2 \cdot F_{ytie} = 15.34 \cdot \text{kip} \quad \text{Tensile strength of tie bars}$$

$$F_{EXX} := 70 \text{ksi} \quad \text{Weld electrode grade}$$

$$w_{tie} := \frac{3}{16} \text{in} \quad \text{Fillet weld size}$$



Weld length considering centerline of the weld:

$$l_w := \pi(D_{tie} + w_{tie}) = 2.553 \cdot \text{in} \quad \text{Weld length}$$

Transverse fillet weld strength:

$$\phi R_{n,weld} := 0.75 \cdot 0.6 \cdot F_{EXX} \cdot \left(1.0 + 0.5 \sin\left(\frac{\pi}{2}\right)^{1.5} \right) \cdot w_{tie} \cdot l_w = 22.614 \cdot \text{kip} \quad \text{AISC 360-10 (J2-5)}$$

$$w_{tie} := \begin{cases} w_{tie} & \text{if } \phi R_{n,weld} \geq T_{tie} \\ \text{"Tie weld size is not OK"} & \text{otherwise} \end{cases}$$

Weld is sufficient to develop the tensile strength of tie bar.

Use $w_{tie} = 0.187 \cdot \text{in}$ fillet weld with $F_{EXX} = 70 \cdot \text{ksi}$

$$\text{Base metal shear yield: } \phi R_{n,bms} := (1.0)(0.6 \cdot F_{yplate}) \cdot t_s \cdot l_w = 14.358 \cdot \text{kip}$$

$$\text{Base metal fracture: } \phi R_{n,bmf} := (0.75)(0.6 \cdot F_{uplate}) \cdot t_s \cdot l_w = 13.999 \cdot \text{kip}$$

Base metal fracture is governing failure mode of the tie-to-steel plate connection

Mathcad © Enabled Content.

CPF#06-16: C-Shape CF-CPSW Project, Hadi Kenarangi, University at Buffalo, 2017

Calculations for design of Axial Loading System: *Top Fixture Design*

Disclaimer

User Notices

User Notices

Input variables that need to be defined by the user are highlighted in **YELLOW**.
Key results and design checks are highlighted in **GREEN**.
Intermediate results and checks are highlighted in **BLUE**.

User Notices

Description

- Lateral Loading System is noted as "**LLS**"
- Axial Loading System is noted as "**ALS**"
- LLS and ALS are designed using Gr. A36 Steel. Other parts are designed using A572 Gr.50 Steel.
- Welds are designed using E70xx electrode

References:

- AISC 360-16 (2016). *Specification for structural steel buildings*, American Institute of Steel Construction, Chicago, Ill.
- AISC 341-16 (2016). *Seismic provisions for structural steel buildings*, American Institute of Steel Construction, Chicago, Ill.

Input

$$d_b := 0.89 \cdot 1.5 \text{ in}$$

Diameter of 1.5 in diameter high impact Threaded Bar (approximation excluding threads)

$$F_{by} := 105 \text{ ksi}$$

Yield strength of the threaded bar

$$A_b := \frac{\pi}{4} \cdot d_b^2 = 1.4 \cdot \text{in}^2$$

Cross-sectional area of the threaded bar

$$I_b := \frac{\pi}{4} \cdot \left(\frac{d_b}{2}\right)^4 = 0.156 \cdot \text{in}^4$$

Area moment of inertia

$$S_{by} := \frac{I_b}{\left(\frac{d_b}{2}\right)} = 0.234 \cdot \text{in}^3$$

Elastic modulus of cross-section

$$M_{by} := F_{by} \cdot S_{by} = 24.526 \cdot \text{kip} \cdot \text{in}$$

Yield moment of the threaded bar

$$P_{by} := F_{by} \cdot A_b = 146.974 \cdot \text{kip}$$

Axial yield load of the threaded bar

$$SF := 1.5$$

Safety factor

$$F_{1v} := P_{by} \cdot SF = 220.462 \cdot \text{kip}$$

Vertical load component of the applied load (Taken equal to yield capacity of threaded bar)

$$F_{2v} := F_{1v}$$

$$t_{wo} := 5 \text{ in} + 2 \cdot 0.19 \text{ in} = 5.38 \cdot \text{in}$$

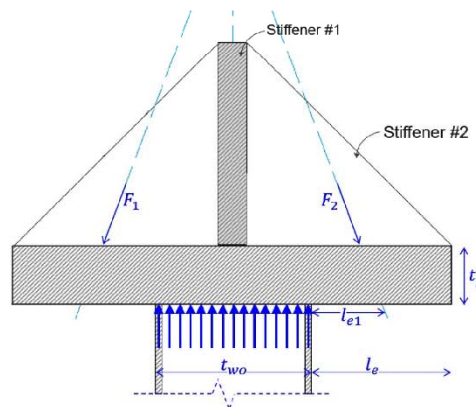
Total thickness of the wall flange

$$l_e := 5 \text{ in}$$

Length of the cantilevering part of the top fixture

$$l_{e1} := \frac{l_e}{2} = 2.5 \cdot \text{in}$$

Distance from center of the threaded bar to the edge of the wall flange



$$M_u := F_{1v} \cdot \left(l_{e1} + \frac{F_{1v}}{F_{1v} + F_{2v}} \cdot \frac{t_{wo}}{2} \right) = 847.675 \cdot \text{kip} \cdot \text{in}$$

Moment demand per threaded bar at one side

$$V_u := \max(F_{1v}, F_{2v}) = 220.462 \cdot \text{kip}$$

Shear demand per threaded bar at one side

$w_p := 67\text{in}$ Cross-length of the top fixture plate (only the length containing the stiffener 1 parts)

$t_p := 2\text{in}$ Thickness of the top plate

$F_{yp} := 36\text{ksi}$ Yield strength of the steel plate (A36 Grade)

$t_{s1} := 1\text{in}$ Thickness of the Stiffener #1

$h_{s1} := 7\text{in}$ Height of the Stiffener #1

$t_{s2} := 1\text{in}$ Thickness of the Stiffener #2

Cross-section properties at a distance x from the edge of the plate:

6 Stiffener #2 was used.

$$h_s(x) := x$$

$$y(x) := \frac{w_p \cdot t_p \cdot \frac{t_p}{2} + 6 \cdot \left[t_{s2} \cdot h_s(x) \cdot \left(t_p + \frac{h_s(x)}{2} \right) \right]}{w_p \cdot t_p + 6 \cdot (t_{s2} \cdot h_s(x))}$$

$$I(x) := \frac{w_p \cdot t_p^3}{12} + w_p \cdot t_p \cdot \left(y(x) - \frac{t_p}{2} \right)^2 + 6 \cdot \left[\frac{t_{s2} \cdot h_s(x)^3}{12} + t_{s2} \cdot h_s(x) \cdot \left[y(x) - \left(\frac{h_s(x)}{2} + t_p \right) \right]^2 \right]$$

$$S(x) := \frac{I(x)}{\max(y(x), t_p + h_s(x) - y(x))}$$

$$M(x) := \begin{cases} 0 & \text{if } 0 \leq x \leq \frac{l_e}{2} \\ 4F_{1v} \cdot \left(x - \frac{l_e}{2} \right) & \text{if } \frac{l_e}{2} \leq x \leq l_e \\ 4F_{1v} \cdot \left(x - \frac{l_e}{2} \right) - \frac{4F_{1v} + 4F_{2v}}{t_{w0}} \cdot \frac{(x - l_e)^2}{2} & \text{if } l_e \leq x \leq l_e + \left(\frac{t_{w0}}{2} - \frac{t_{s1}}{2} \right) \end{cases}$$

Capacity check at the edge of the wall:

$$x_0 := l_e$$

$$S(x_0) = 76.019 \cdot \text{in}^3 \quad M(x_0) = 2.205 \times 10^3 \cdot \text{kip} \cdot \text{in}$$

$$\frac{F_{yp} \cdot S(x_0)}{M(x_0)} = 1.241$$

Capacity check at the edge of the Stiffener #1:

$$x_0 := l_e + \left(\frac{t_{wo}}{2} - \frac{t_{s1}}{2} \right)$$

$$S(x_0) = 130.046 \cdot \text{in}^3 \quad M(x_0) = 3.35 \times 10^3 \cdot \text{kip} \cdot \text{in}$$

$$\frac{F_{yp} \cdot S(x_0)}{M(x_0)} = 1.398$$

Volume of the top plate:

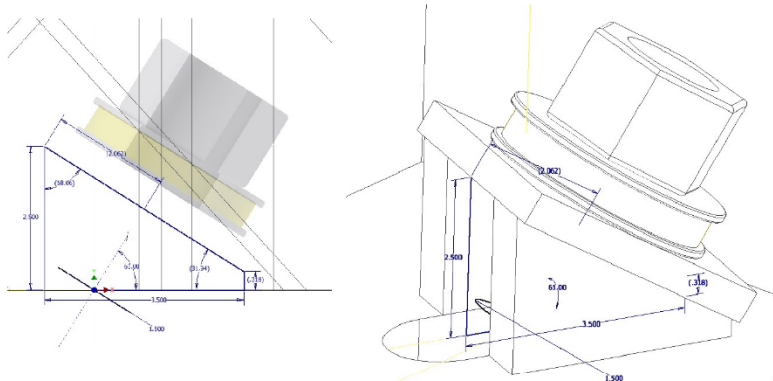
$$w_{\text{total}} := w_p + 4\text{in} + 4\text{in} + 5\text{in} = 80 \cdot \text{in}$$

$$V_{\text{topPlate}} := w_{\text{total}} \cdot (2 \cdot l_e + t_{wo}) t_p + 6 \cdot h_{s1} \cdot \frac{h_{s1}}{2} \cdot t_{s2} + t_{s1} \cdot h_{s1} \cdot w_p = 3.077 \times 10^3 \cdot \text{in}^3$$

$$W_{\text{topPlate}} := 490 \frac{\text{lb}}{\text{ft}^3} \left[w_{\text{total}} \cdot (2 \cdot l_e + t_{wo}) t_p + 6 \cdot h_{s1} \cdot \frac{h_{s1}}{2} \cdot t_{s2} + t_{s1} \cdot h_{s1} \cdot w_p \right] = 872.472 \cdot \text{lb}$$

Required thickness (t_{vs}) for each of the vertical seatings of the side threaded bars:

Note: two vertical seatings are used for each of the side threaded bars



$$\text{SF} := 1.2$$

$$F := P_{by} \cdot \text{SF} = 176.369 \cdot \text{kip}$$

$$t_{vs} := \frac{1}{2} \left[\frac{F \cdot \cos\left(\frac{31}{180} \cdot \pi\right)}{3.5\text{in}} + \frac{F \cdot \cos\left(\frac{59}{180} \cdot \pi\right) \cdot \left(0.318\text{in} + \frac{3.5\text{in}}{2 \cdot \cos\left(\frac{31}{180} \cdot \pi\right)}\right) \cdot \frac{3.5\text{in}}{2}}{\frac{(3.5\text{in})^3}{12}} \right] \cdot \frac{1}{36\text{ksi}} = 2.058 \cdot \text{in}$$

Use 2in. vertical seating plates on each side of the threaded bar.

Mathcad © Enabled Content.

CPF#06-16: C-Shape CF-CPSW Project, Hadi Kenarangi (PhD Candidate), University at Buffalo, 2017

Calculations for design of Axial Loading System: Top Fixture Vertical Anchor Design

Disclaimer

User Notices

User Notices

Input variables that need to be defined by the user are highlighted in **YELLOW**.
Key results and design checks are highlighted in **GREEN**.
Intermediate results and checks are highlighted in **BLUE**.

User Notices

Description

- Lateral Loading System is noted as "**LLS**"
- Axial Loading System is noted as "**ALS**"
- LLS and ALS are designed using Gr. A36 Steel. Other parts are designed using A572 Gr.50 Steel.
- Welds are designed using E70xx electrode

References:

- AISC 360-16 (2016). *Specification for structural steel buildings*, American Institute of Steel Construction, Chicago, Ill.
- AISC 341-16 (2016). *Seismic provisions for structural steel buildings*, American Institute of Steel Construction, Chicago, Ill.

Input

Shear demand on the vertical anchors (results from finite element analysis using LS-Dyna):

$$V := 2 \cdot 150 \text{kip} \cdot \left(\cos\left(\frac{72}{180} \cdot \pi\right) + \cos\left(\frac{56}{180} \cdot \pi\right) \right) - 150 \text{kip} \cdot \left(2 \cdot \cos\left(\frac{83}{180} \cdot \pi\right) + \cos\left(\frac{67}{180} \cdot \pi\right) \right) = 165.292 \cdot \text{kip}$$

Shear strength of one threaded bar:

$F_{y\text{tb}} := 105 \text{ksi}$ Minimum yield stress of threaded bar

$A_{\text{tb}} := 1.4 \text{in}^2$ Nominal area of 1.5in diameter threaded bar

$V_{\text{tb}} := 0.6 \cdot F_{y\text{tb}} \cdot A_{\text{tb}} = 88.2 \cdot \text{kip}$ Shear strength per threaded bar

$N_{\text{tb}} := \text{ceil}\left(\frac{V}{V_{\text{tb}}}\right) = 2$ Required number of threaded bars

$N_{\text{tb_used}} := 3$ Number of used threaded bars

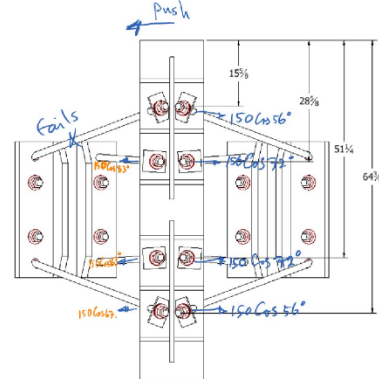


Figure1: Assuming failure of one threaded bar during test.

Required length of embedment:

Assuming a uniform stress distribution along the embedded threaded bar as shown in Figure 2:

$f_c := 4 \text{ksi}$ nominal strength of the concrete

$d_{\text{tb}} := 1.5 \text{in}$ diameter of the threaded bar

$V := \frac{N_{\text{tb}}}{N_{\text{tb_used}}} \cdot V_{\text{tb}} = 58.8 \cdot \text{kip}$ shear force at the top of each threaded bar

$l_{\text{tb}} := 20 \text{in}$ $x_{\text{tb}} := 5 \text{in}$ Trial numbers for below numerical solver

Given

$$V \cdot l_{\text{tb}} + f_c \cdot d_{\text{tb}} \cdot \frac{(l_{\text{tb}} - x_{\text{tb}})^2}{2} - f_c \cdot d_{\text{tb}} \cdot x_{\text{tb}} \cdot \left(l_{\text{tb}} - \frac{x_{\text{tb}}}{2} \right) = 0 \text{kip} \cdot \text{in}$$

$$V + f_c \cdot d_{\text{tb}} \cdot (l_{\text{tb}} - x_{\text{tb}}) - f_c \cdot d_{\text{tb}} \cdot x_{\text{tb}} = 0 \text{kip}$$

Find $(l_{\text{tb}}, x_{\text{tb}}) = \begin{pmatrix} 23.659 \\ 16.73 \end{pmatrix} \cdot \text{in}$

USE 3 1.5in diameter threaded bars with 24in of embedment length.

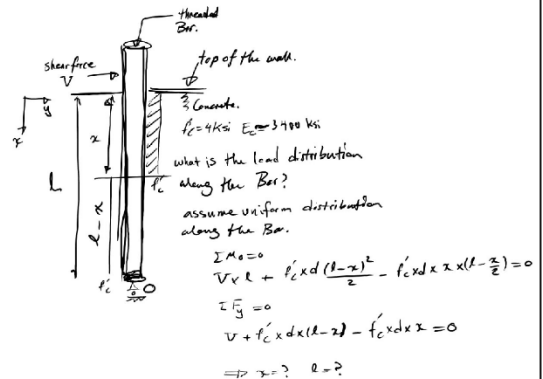


Figure2: Assuming a uniform stress distribution along the embedded bar.

Mathcad © Enabled Content.

CPF#06-16: C-Shape CF-CPSW Project, Hadi Kenarangi (PhD Candidate), University at Buffalo, 2017

Calculations for design of Axial Loading System: Actuator Attachment Plate Design

Disclaimer

User Notices

User Notices

Input variables that need to be defined by the user are highlighted in **YELLOW**.
Key results and design checks are highlighted in **GREEN**.
Intermediate results and checks are highlighted in **BLUE**.

User Notices

Description

- Lateral Loading System is noted as "LLS"
- Axial Loading System is noted as "ALS"
- LLS and ALS are designed using Gr. A36 Steel. Other parts are designed using A572 Gr.50 Steel.
- Welds are designed using E70xx electrode

References:

- AISC 360-16 (2016). *Specification for structural steel buildings*, American Institute of Steel Construction, Chicago, Ill.
- AISC 341-16 (2016). *Seismic provisions for structural steel buildings*, American Institute of Steel Construction, Chicago, Ill.

Input

$d_b := 0.89 \cdot 1.5 \text{ in}$ Diameter of the threaded bar (approximation excluding threads)

$F_{by} := 105 \text{ ksi}$ Yield strength of the threaded bar

$A_b := \frac{\pi}{4} \cdot d_b^2 = 1.4 \cdot \text{in}^2$ Cross-sectional area of the threaded bar

$I_b := \frac{\pi}{4} \cdot \left(\frac{d_b}{2}\right)^4 = 0.156 \cdot \text{in}^4$ Area moment of inertia

$S_{by} := \frac{I_b}{\left(\frac{d_b}{2}\right)} = 0.234 \cdot \text{in}^3$ Elastic modulus of cross-section

$M_{by} := F_{by} \cdot S_{by} = 24.526 \cdot \text{kip} \cdot \text{in}$ Yield moment of the threaded bar

$P_{by} := F_{by} \cdot A_b = 146.974 \cdot \text{kip}$ Axial yield load of the threaded bar

$SF := 1.2$ Safety factor

$F_{1v} := P_{by} \cdot SF = 176.369 \cdot \text{kip}$ Vertical load component of the applied load
(Taken equal to yield capacity of threaded bar)

$l_e := 7.0 \text{ in}$ Hanging length of the baseplate

$b := 2 \cdot 3.5 \text{ in} + 16.5 \text{ in} = 23.5 \cdot \text{in}$ Cross-length of the baseplate.

$F_{yp} := 36 \text{ ksi}$ Yield strength of the baseplate (Grade A36)

$M_u := \frac{2F_{1v} \cdot l_e}{2} + \frac{2F_{1v} \cdot 5 \text{ in}}{2} = 176.369 \cdot \text{kip} \cdot \text{ft}$ Considers two threaded bars acting on the baseplate.

$t_{p_req} := \left[\frac{6 \cdot F_{1v} \cdot (5 \text{ in} + l_e)}{F_{yp} \cdot b} \right]^{0.5} = 3.874 \cdot \text{in}$ Minimum required thickness for the baseplate with no stiffeners

Consider using two vertical stiffeners on the base plate to reduce the base plate thickness. Assume using a 2in. thick plate for the baseplate and:

$b = 23.5 \cdot \text{in}$ Cross-length of the baseplate

$t_p := 3.0 \text{ in}$ Thickness of the baseplate

$t_{s1} := 1.5 \text{ in}$ Thickness of the Stiffener #1

$h_{s1}(x) := 6 \text{ in}$ Height of the Stiffener #1 at distance x from the cross-edge of the base plate

$n_p := 2$ Number of vertical stiffener plates (No. of Stiffener #1)

$$y(x) := \frac{t_p \cdot b \cdot \frac{t_p}{2} + n_p \cdot \left[h_{s1}(x) \cdot t_{s1} \cdot \left(t_p + \frac{h_{s1}(x)}{2} \right) \right]}{t_p \cdot b + n_p \cdot h_{s1}(x) \cdot t_{s1}}$$

$$I(x) := \frac{b \cdot t_p^3}{12} + t_p \cdot b \cdot \left(y(x) - \frac{t_p}{2} \right)^2 + n_p \cdot \left[\frac{t_{s1} \cdot h_{s1}(x)^3}{12} + t_{s1} \cdot h_{s1}(x) \cdot \left(t_p + \frac{h_{s1}(x)}{2} - y(x) \right)^2 \right]$$

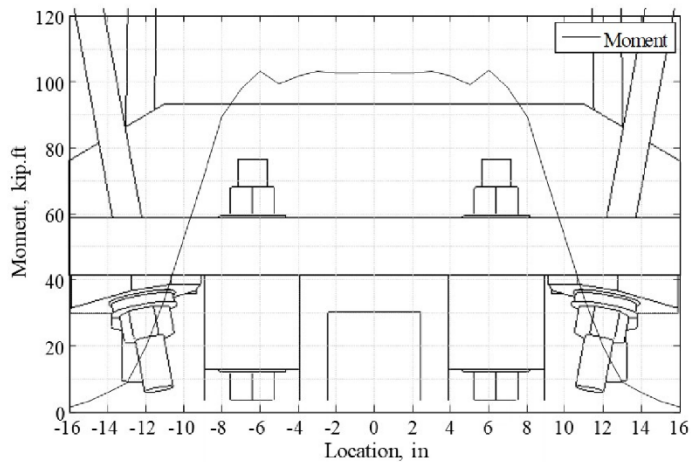
$$S(x) := \frac{I(x)}{\max(y(x), t_p + h_{s1}(x) - y(x))}$$

try $h_{s1}(0) = 6$ in

$$y(0) = 2.415$$
 in

$$S(0) = 60.327$$
 in³

$$M_y := S(0) \cdot F_{yp} = 180.982$$
 kip-ft Moment capacity is OK.




Bending moment along the plate (Analysis results from LS-Dyna)

Mathcad ® Enabled Content.

CPF#06-16: C-Shape CF-CPSW Project, *Hadi Kenarangi (PhD Candidate), University at Buffalo, 2017*

Calculations for design of Lateral Loading System (LLS) set-up

 Disclaimer


 User Notices

User Notices

Input variables that need to be defined by the user are highlighted in **YELLOW.**

Key results and design checks are highlighted in **GREEN.**

Intermediate results and checks are highlighted in **BLUE.**

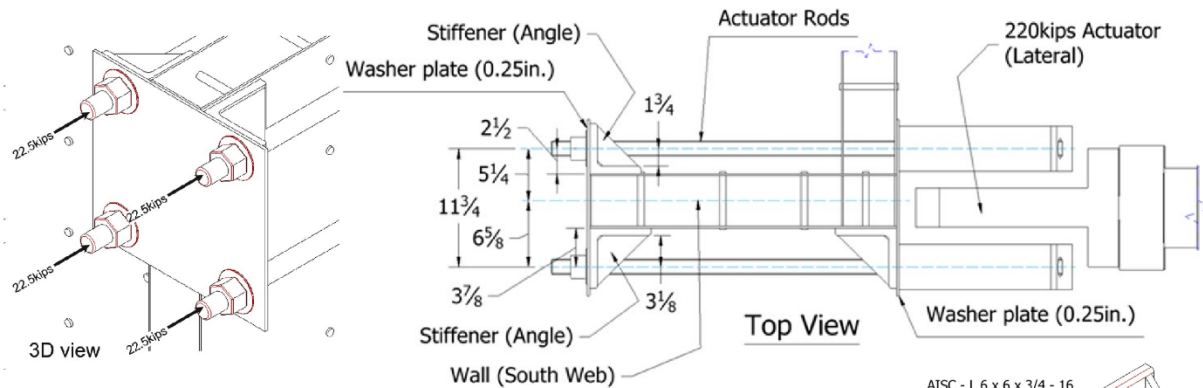
 User Notices

Description

- Lateral Loading System is noted as "**LLS**"
- Axial Loading System is noted as "**ALS**"
- LLS and ALS are designed using Gr. A36 Steel. Other parts are designed using A572 Gr.50 Steel.
- Welds are designed using E70xx electrode

References:

- AISC 360-16 (2016). *Specification for structural steel buildings*, American Institute of Steel Construction, Chicago, Ill.
- AISC 341-16 (2016). *Seismic provisions for structural steel buildings*, American Institute of Steel Construction, Chicago, Ill.

Lateral actuator attachment plate design (check for the critical one):

$$T_{act} := 90\text{kip}$$

Load per actuator

$$T_{rod} := \frac{T_{act}}{4} = 22.5 \cdot \text{kip}$$

Load per threaded rod

$$SF := 2.0$$

Safety factor

$$l := 3.125\text{in}$$

Distance between threaded rod C.L. and critical section

$$M_{req} := SF \cdot 2 \cdot T_{rod} \cdot l = 281.25 \cdot \text{kip} \cdot \text{in} \quad \text{Required flexural strength}$$

$$t_{plate} := 0.25\text{in}$$

Thickness of the washer plate

$$h_{plate} := 16\text{in}$$

Height of the washer plate

$$w_{plate} := 16.75\text{in}$$

Width of the washer plate

$$t_L := 0.75\text{in}$$

Thickness of the angle

$$t_p := t_{plate} + t_L = 1 \cdot \text{in}$$

$$F_{yp} := 36\text{ksi}$$

Yield strength of plate and angle (Gr. A36)

$$F_{up} := 58\text{ksi}$$

Ultimate tensile strength of plate and angle (Gr. A36)

$$t_{s2} := 0.5\text{in}$$

Thickness of the stiffener

$$n := 4$$

Number of the stiffeners

Cross-section properties at critical section from the edge of the plate:

$$h_s := 4.25\text{in} - 1.25\text{in}$$

Height of the stiffeners at the critical section

$$y := \frac{h_{plate} \cdot t_p \cdot \frac{t_p}{2} + n \cdot t_{s2} \cdot h_s \cdot \left(t_p + \frac{h_s}{2} \right)}{h_{plate} \cdot t_p + n \cdot (t_{s2} \cdot h_s)}$$

$$I := \frac{h_{plate} \cdot t_p^3}{12} + h_{plate} \cdot t_p \cdot \left(y - \frac{t_p}{2} \right)^2 + 6 \cdot \left[\frac{t_{s2} \cdot h_s^3}{12} + t_{s2} \cdot h_s \cdot \left[y - \left(\frac{h_s}{2} + t_p \right) \right]^2 \right]$$

AISC - L 6 x 6 x 3/4 - 16

EPP3_S1

AISC - L 5 x 5 x 3/4 - 16

EPN4_S1

$$S := \frac{I}{\max(y, t_p + h_s - y)} = 10.792 \cdot \text{in}^3$$

Capacity check at the critical cross-section:

$$\frac{F_{yp} \cdot S}{M_{req}} = 1.381$$

"OK" if $\frac{F_{yp} \cdot S}{M_{req}} \geq 1.0$ = "OK"
 "NG" otherwise

Lateral actuator attachment plate angle-to-wall web steel faceplate weld design:

$F_{EXX} := 70 \text{ksi}$ Weld electrode grade

$w_{tie} := \frac{3}{16} \text{in}$ Fillet weld size

$l_w := h_{plate} = 16 \cdot \text{in}$ Weld length

Transverse fillet weld strength:

$$\phi R_{n,weld} := 0.75 \cdot 0.6 \cdot F_{EXX} \cdot \left(1.0 + 0.5 \sin \left(\frac{\pi}{2} \right)^{1.5} \right) \cdot w_{tie} \cdot l_w = 141.75 \cdot \text{kip} \quad \text{AISC 360-10 (J2-5)}$$

Base metal shear yield: $\phi R_{n,bms} := (1.0)(0.6 \cdot F_{yp}) \cdot t_L \cdot l_w = 259.2 \cdot \text{kip}$

Base metal fracture: $\phi R_{n,bmf} := (0.75)(0.6 \cdot F_{up}) \cdot t_L \cdot l_w = 313.2 \cdot \text{kip}$

$$\phi R_n := \min(\phi R_{n,weld}, \phi R_{n,bms}, \phi R_{n,bmf}) = 141.75 \cdot \text{kip}$$

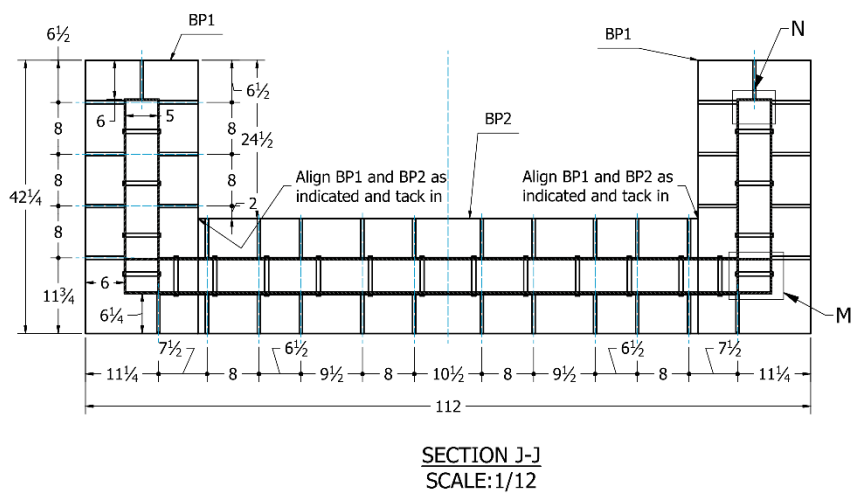
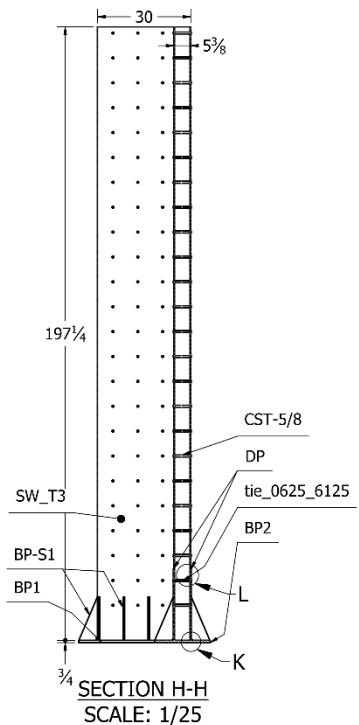
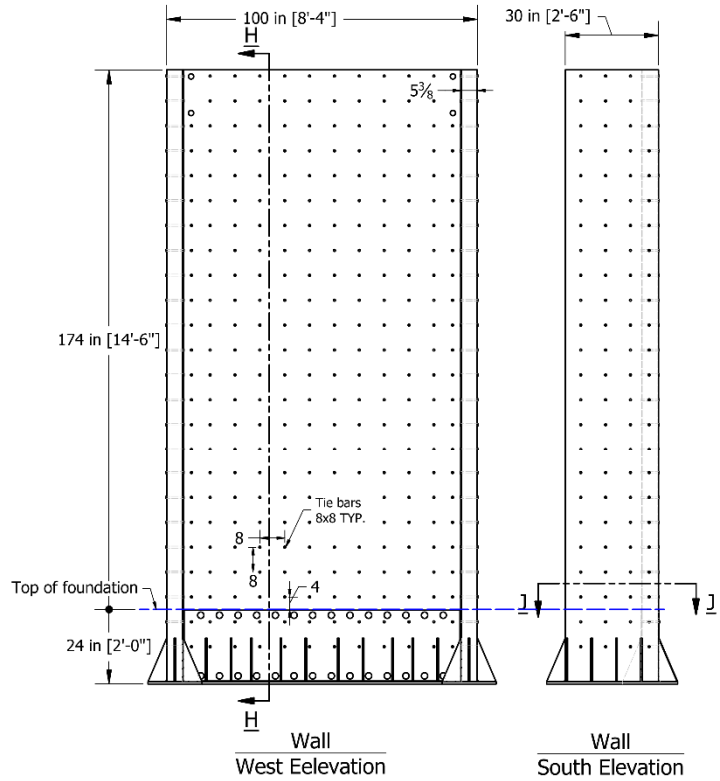
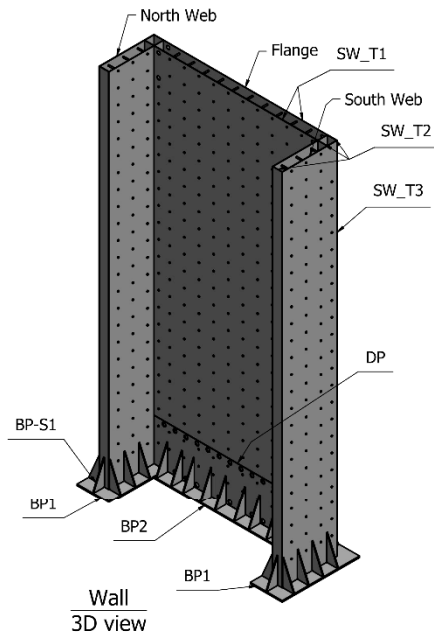
Weld capacity check:

$$\frac{\phi R_n}{SF \cdot 2 \cdot T_{rod}} = 1.575$$

"OK" if $\frac{\phi R_n}{SF \cdot 2 \cdot T_{rod}} \geq 1.0$ = "OK"
 "NG" otherwise

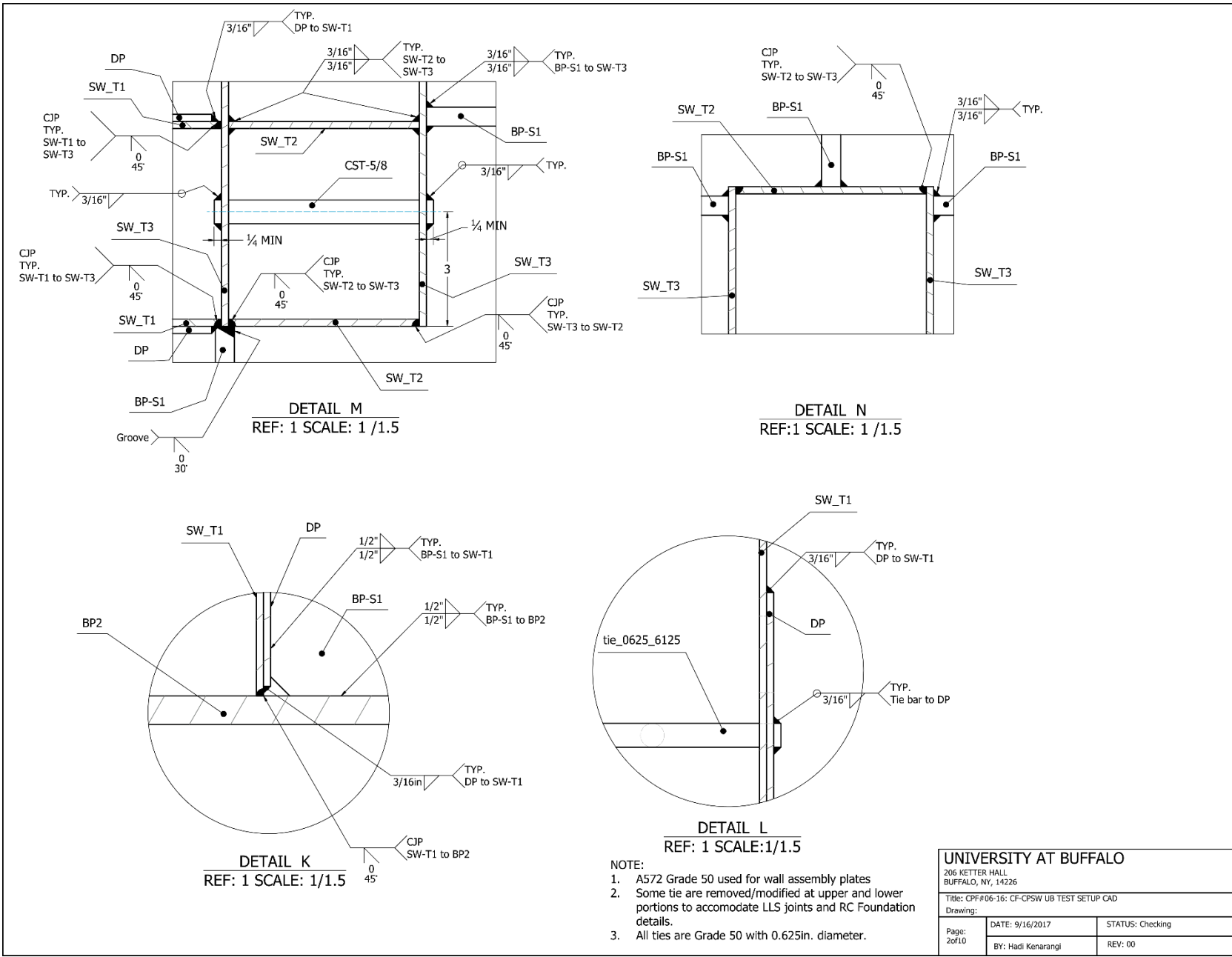
APPENDIX B

Initial Specimen and Initial Test Set-up Details: CAD Drawings



- NOTE:
1. A572 Grade 50 used for wall assembly plates
 2. Some tie are removed/modified at upper and lower portions to accommodate LLS joints and RC Foundation details.
 3. All ties are Grade 50 with 0.625in. diameter.

UNIVERSITY AT BUFFALO		
206 KETTER HALL BUFFALO, NY, 14226		
Title: CPF#06-16: CF-CPSW UB TEST SETUP CAD		
Drawing:		
Page: 1 of 10	DATE: 9/16/2017	STATUS: Checking
	BY: Hadi Kenarangi	REV: 00



DETAIL M
REF: 1 SCALE: 1 / 1.5

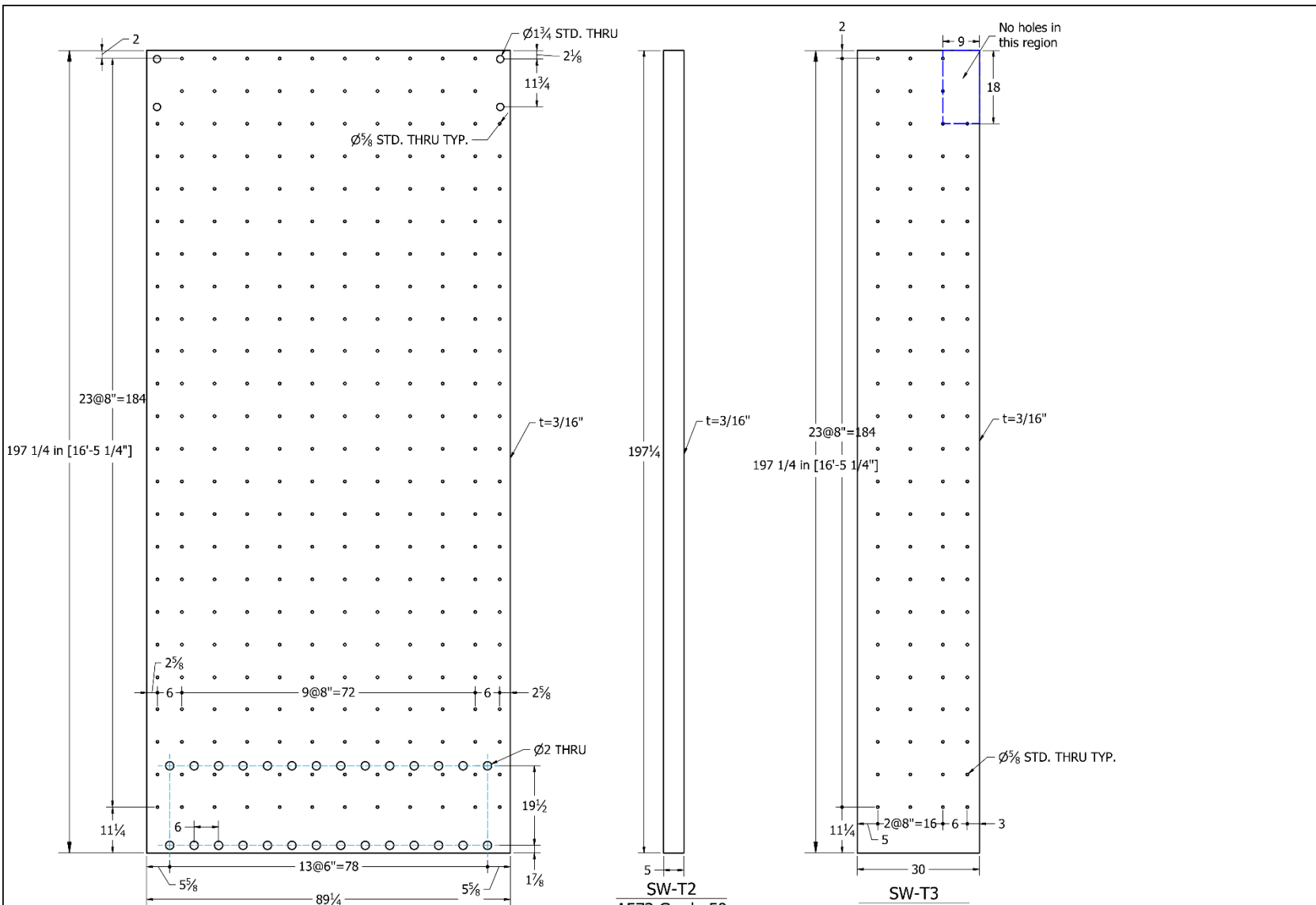
DETAIL N
REF:1 SCALE: 1 / 1.5

DETAIL K
REF: 1 SCALE: 1/1.5

DETAIL L
REF: 1 SCALE: 1/1.5

- NOTE:
1. A572 Grade 50 used for wall assembly plates
 2. Some tie are removed/modified at upper and lower portions to accommodate LLS joints and RC Foundation details.
 3. All ties are Grade 50 with 0.625in. diameter.

UNIVERSITY AT BUFFALO		
206 KETTER HALL BUFFALO, NY, 14226		
Title: CPF#06-16: CF-CPSW UB TEST SETUP CAD		
Drawing:		
Page: 2of10	DATE: 9/16/2017	STATUS: Checking
	BY: Hadi Kenarangi	REV: 00



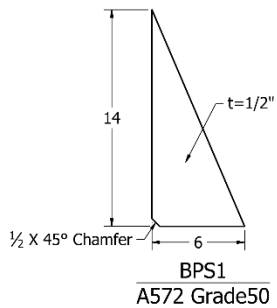
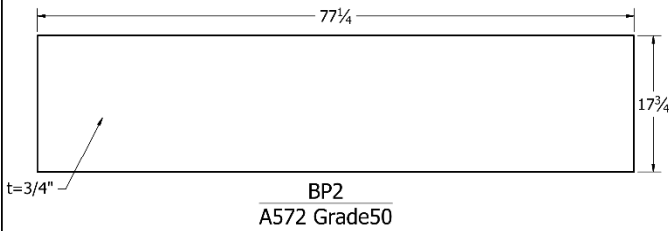
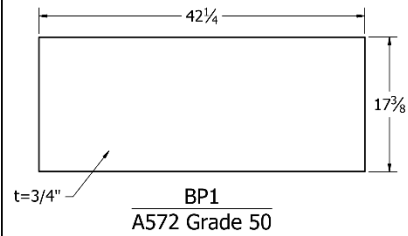
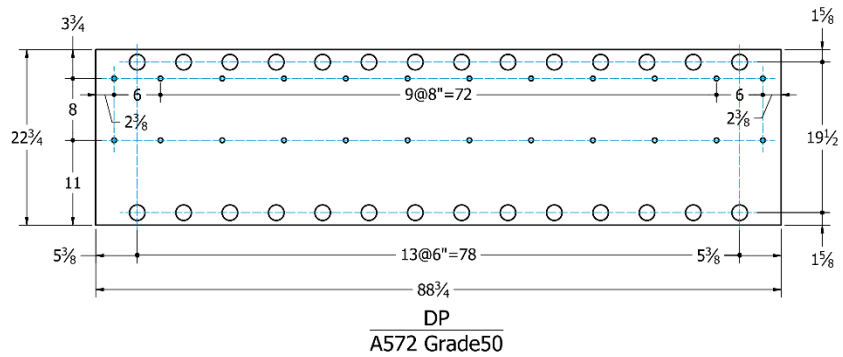
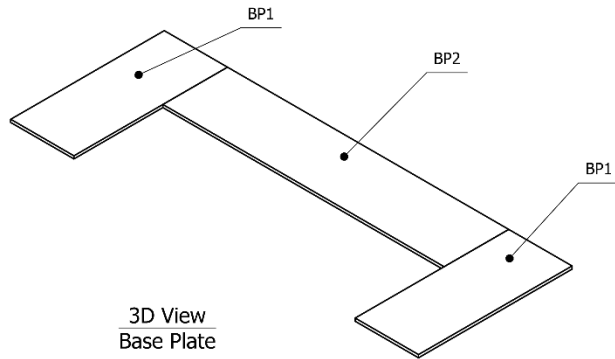
SW-T2
A572 Grade 50

SW-T3
A572 Grade 50

SW-T1
A572 Grade 50

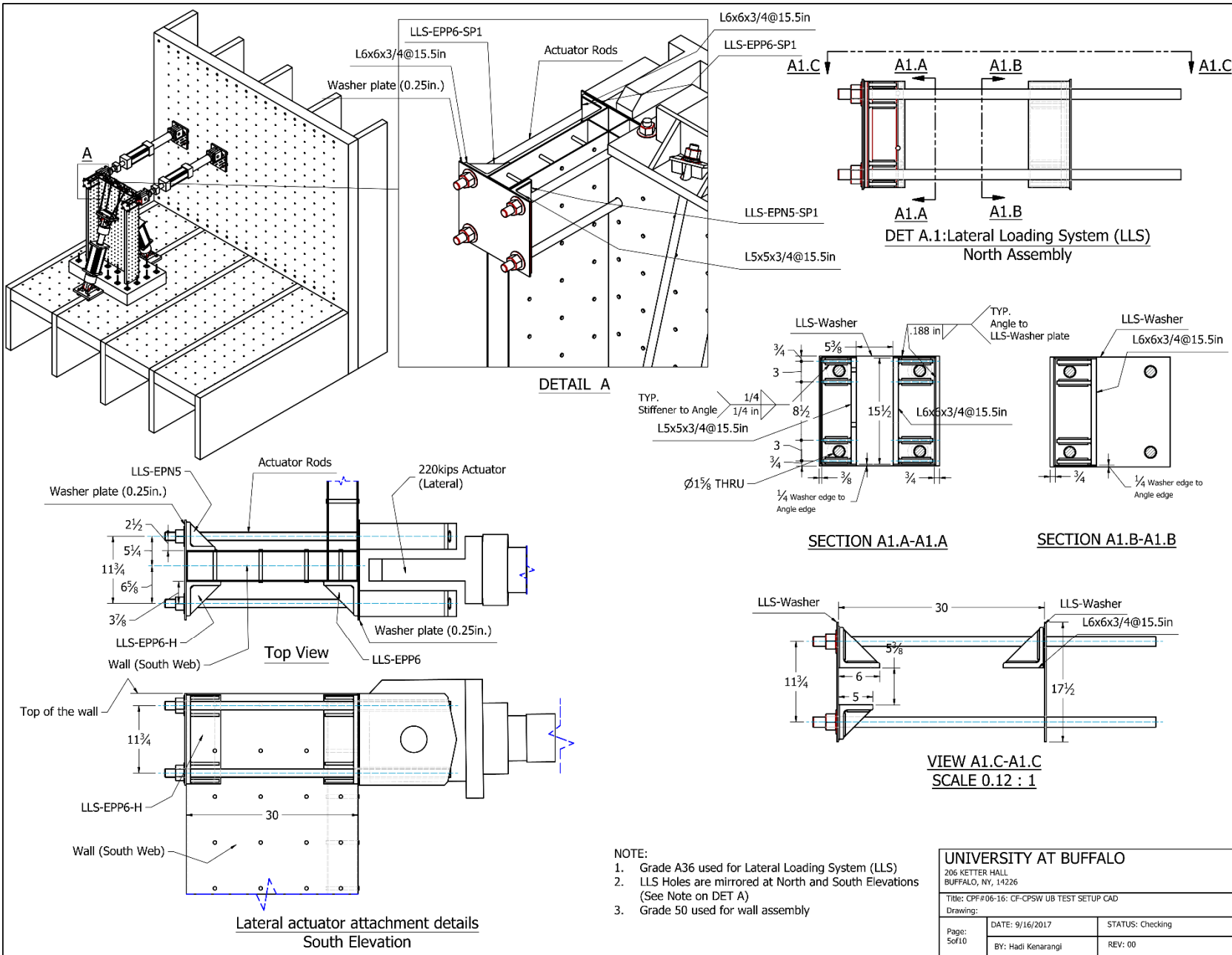
- NOTE:
1. A572 Grade 50 used for wall assembly plates
 2. Some tie are removed/modified at upper and lower portions to accommodate LLS joints and RC Foundation details.
 3. All ties are Grade 50 with 0.625in. diameter.

UNIVERSITY AT BUFFALO		
206 KETTER HALL BUFFALO, NY, 14226		
Title: CPF#06-16: CF-CPSW UB TEST SETUP CAD		
Drawing:		
Page: 3of10	DATE: 9/16/2017	STATUS: Checking
	BY: Hadi Kenarangi	REV: 00

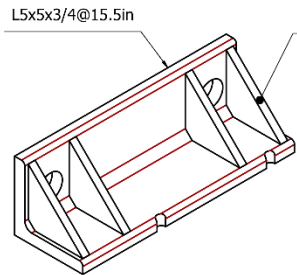


NOTE:
1. A572 Grade 50 used for wall assembly plates

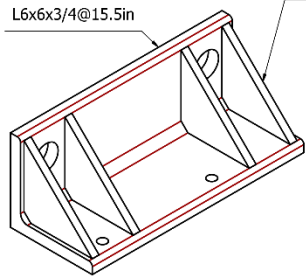
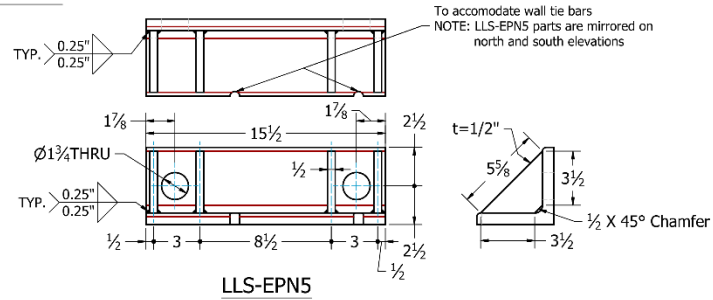
UNIVERSITY AT BUFFALO		
206 KETTER HALL BUFFALO, NY, 14226		
Title: CPF#06-16: CF-CPSW UB TEST SETUP CAD		
Drawing:		
Page: 4 of 10	DATE: 9/16/2017	STATUS: Checking
	BY: Hadi Kenarangi	REV: 00



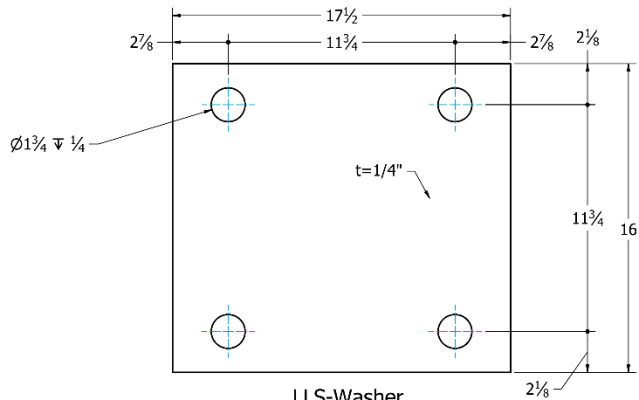
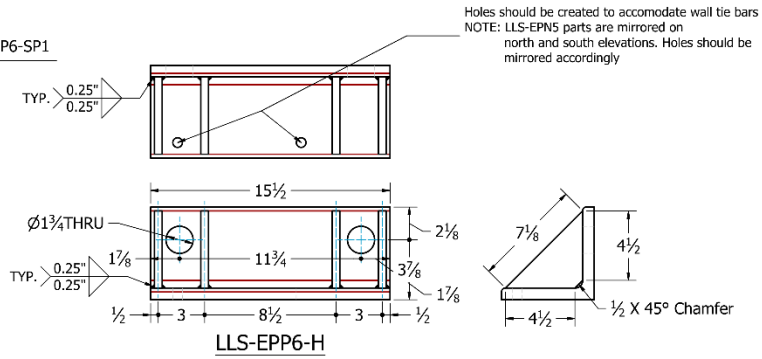
UNIVERSITY AT BUFFALO		
206 KETTER HALL BUFFALO, NY, 14226		
Title: CPF#06-16: CF-CPSW UB TEST SETUP CAD		
Drawing:		
Page: 5 of 10	DATE: 9/16/2017	STATUS: Checking
	BY: Hadi Kenarangi	REV: 00



LLS-EPN5
A36 Grade36

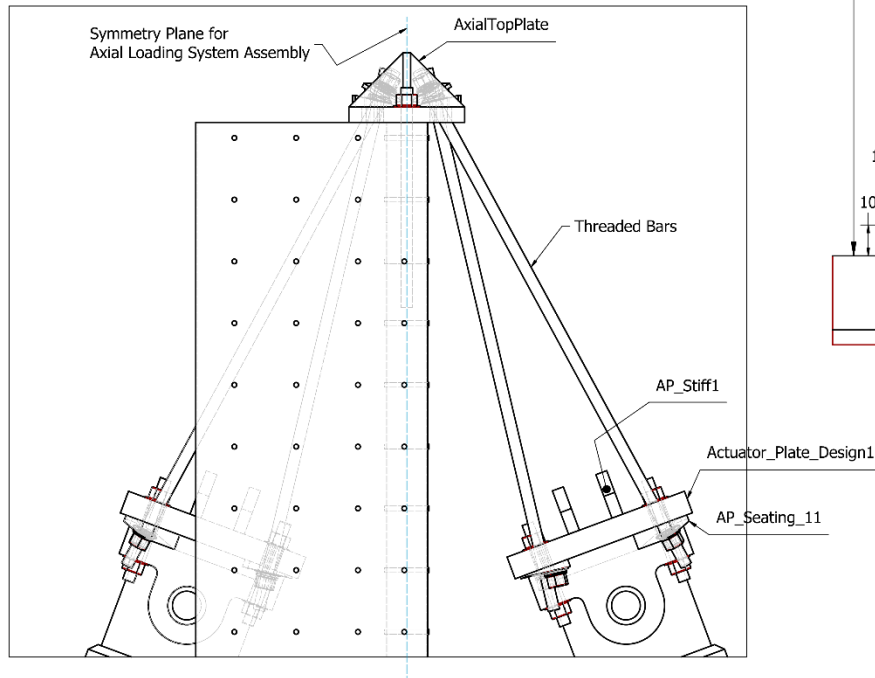
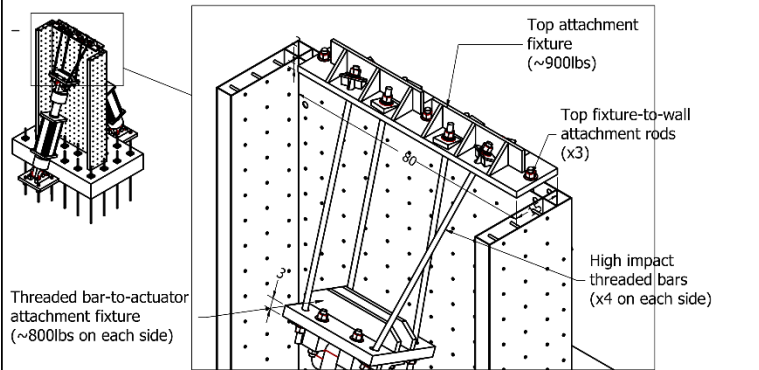


LLS-EPP6-H
A36 Grade36

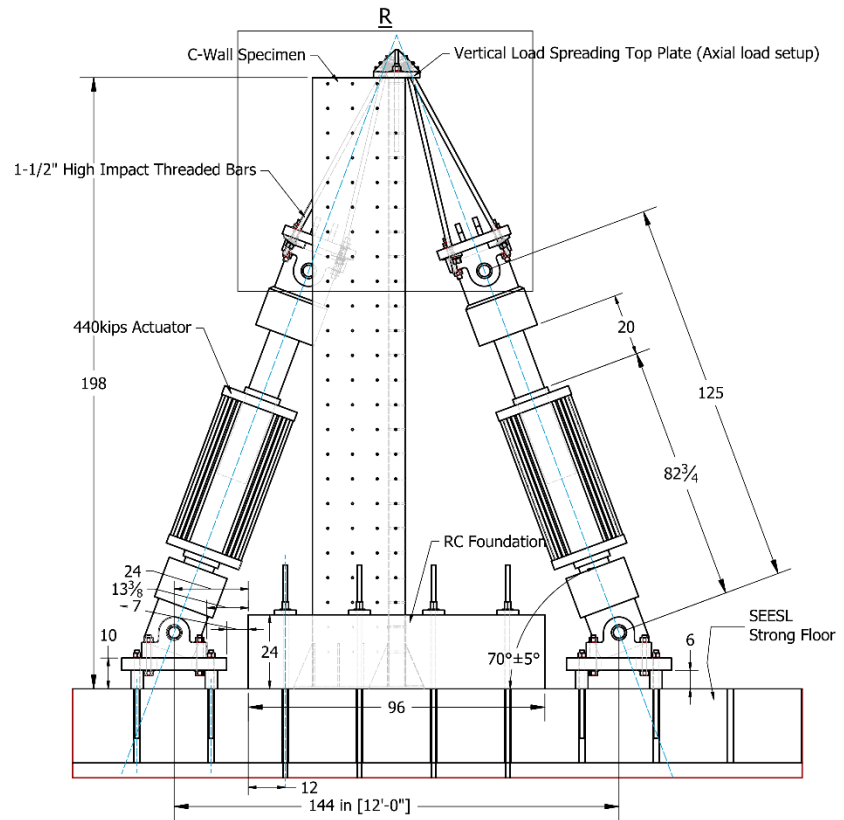


- NOTE:
- Grade A36 used for Lateral Loading System (LLS)
 - LLS Holes are mirrored at North and South Elevations (See Note on DET A)
 - Grade 50 used for wall assembly

UNIVERSITY AT BUFFALO		
206 KETTER HALL BUFFALO, NY, 14226		
Title: CPF#06-16: CF-CPSW UB TEST SETUP CAD		
Drawing:		
Page: 6 of 10	DATE: 9/16/2017	STATUS: Checking
	BY: Hadi Kenarangi	REV: 00



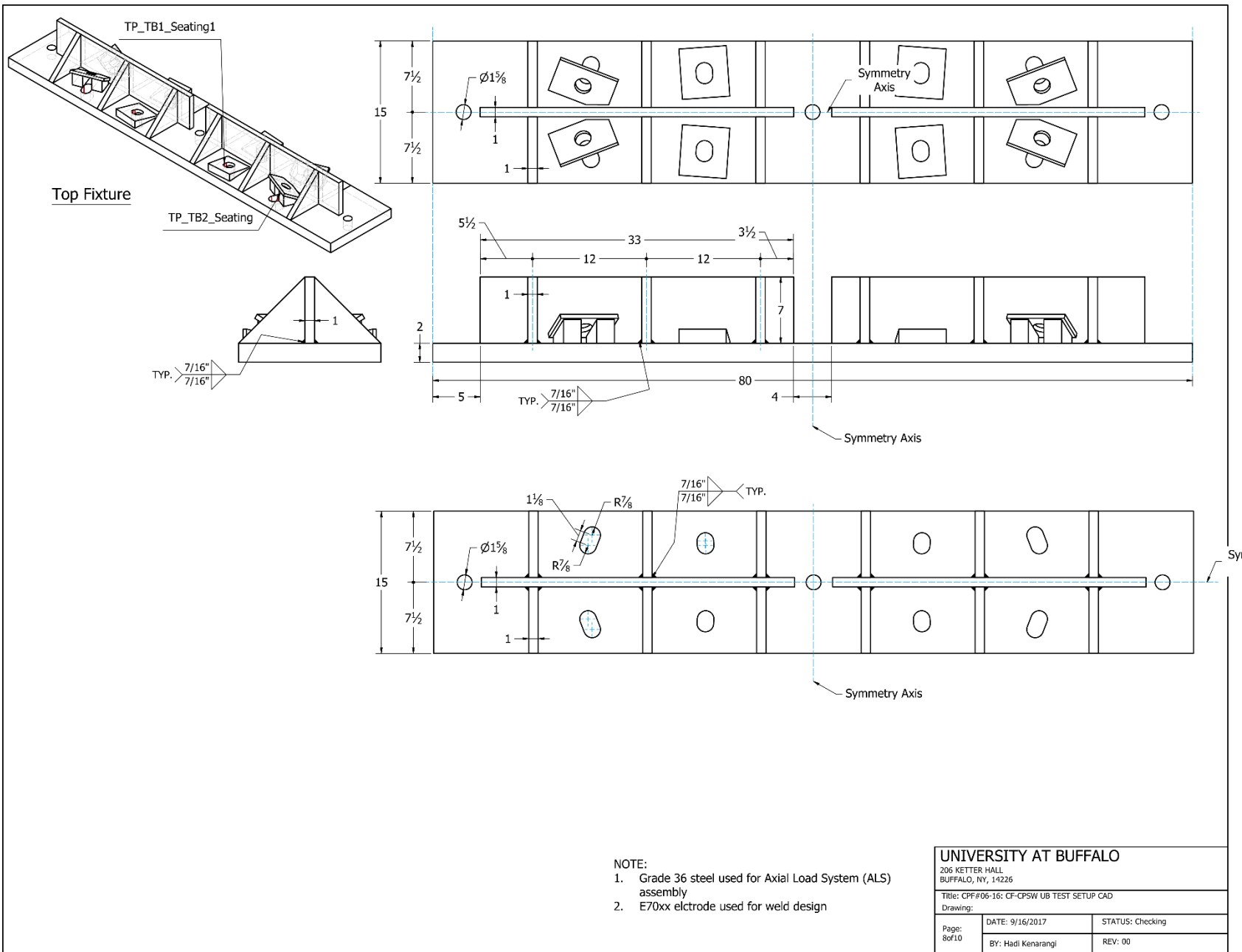
DETAIL R
SCALE: 1 / 10

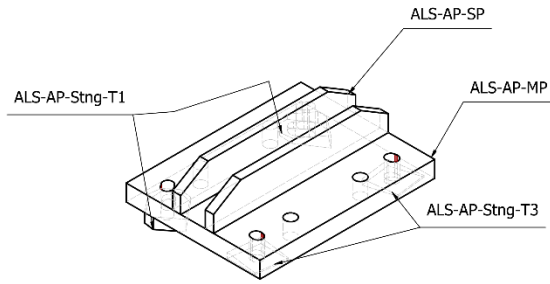


Axial Loading System Assembly
South Elevation

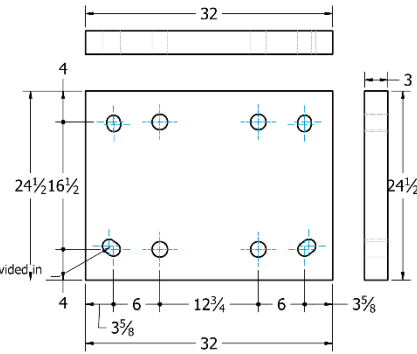
- NOTE:
- Grade 36 steel used for Axial Load System (ALS) assembly
 - E70xx electrode used for weld design

UNIVERSITY AT BUFFALO		
206 KETTER HALL BUFFALO, NY, 14226		
Title: CPF#06-16: CF-CPSW UB TEST SETUP CAD		
Drawing:		
Page: 7 of 10	DATE: 9/16/2017	STATUS: Checking
	BY: Hadi Kenarangi	REV: 00

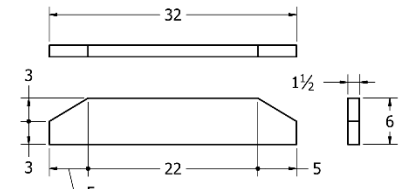




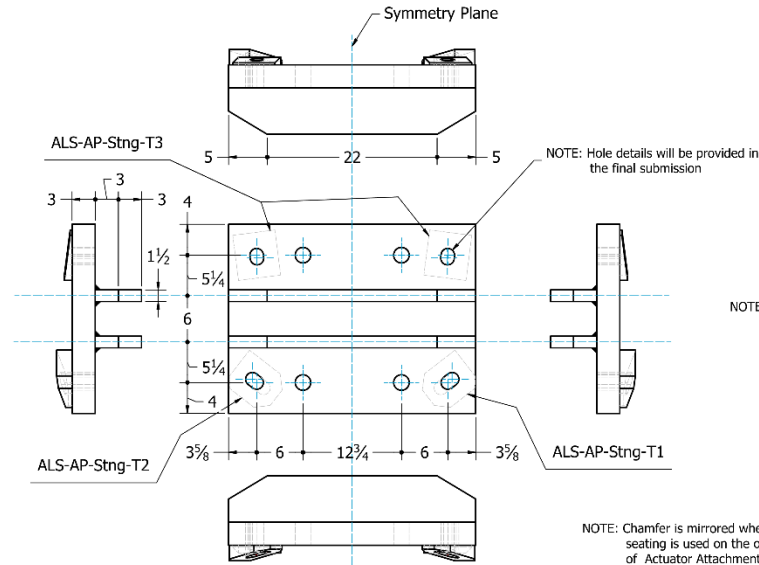
Actuator Attachment Plate



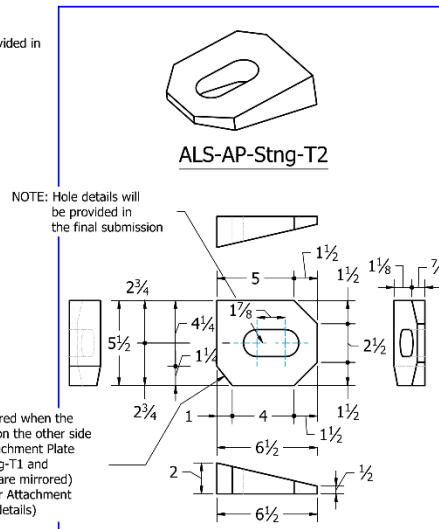
ALS-AP-MP
Grade36ksi



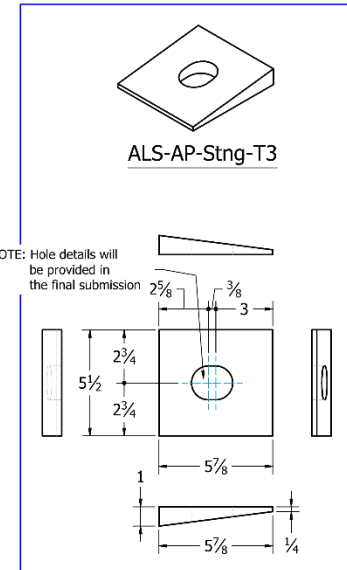
ALS-AP-SP
Grade36ksi



Actuator Attachment Plate Assembly Details
SCALE: 1/10 Grade 36ksi



ALS-AP-Stng-T2



ALS-AP-Stng-T3

- NOTE:
- Grade 36 steel used for Axial Load System (ALS) assembly
 - E70xx electrode used for weld design

UNIVERSITY AT BUFFALO

206 KETTER HALL
BUFFALO, NY, 14226

Title: CPF#06-16: CF-CP5W UB TEST SETUP CAD

Drawing:

Page: 9 of 10	DATE: 9/16/2017	STATUS: Checking
	BY: Hadi Kenarangi	REV: 00

Bill of Material per Specimen						
ITEM	QTY	PART NUMBER	DESCRIPTION	PART WEIGHT, LBS	WEIGHTxQTY, LBS	PART VOLUME, C.IN.
20	2	SW_T1	A572 Gr.50	947.20409	1894.40818	3266.221
43	6	SW_T2	A572 Gr.50	53.62738	321.76428	184.922
37	4	SW_T3	A572 Gr.50	320.19596	1280.78384	1104.124
38	4	Washer plate (0.25in.)	A36	19.60255	78.4102	67.595
23	2	BP1	A572 Gr.50	159.42924	318.85848	549.756
18	1	BP2	A572 Gr.50	298.23339	298.23339	1028.391
56	38	BP-S1	A572 Gr.50	6.07202	230.73676	20.938
59	448	CST-5/8	Circular steel tie bar Gr. 50 #5/8in	0.51156	229.17888	1.764
19	1	ALS top fixture	A36	911.90355	911.90355	3144.495
39	4	ALS-TP-TB1-Stng	A36	5.9566	23.8264	20.54
24	2	ALS-TP-TB2-Stng-T1	A36	8.87603	17.75206	30.607
25	2	ALS-TP-TB2-Stng-T2	A36	8.87603	17.75206	30.607
34	2	ALS-AP-MP	A36	659.46	1318.92	2274
41	4	ALS-AP-SP	A36	76.995	307.98	265.5
35	2	ALS-AP-Stng-T1	A36	48.19307	96.38614	166.183
36	2	ALS-AP-Stng-T2	A36	48.19307	96.38614	166.183
42	4	ALS-AP-Stng-T3	A36	42.19326	168.77304	145.494
61	63.000 in	L6x6x3/4@15.5in	Angle Steel, A36	38.04713	152.18852	131.197
48	16	LLS-EPP6-SP1	A36	1.79452	28.71232	6.188
60	31.500 in	L5x5x3/4@15.5in	Angle Steel, A36	31.30463	125.21852	107.947
46	8	LLS-EPN5-SP1	A36	1.14202	9.13616	3.938
74	2	DP	A572 Gr.50	104.603	209.206	360.7
75	24	tie_0625_6125	Circular steel tie bar Gr. 50 #5/8in	0.54491	13.07784	1.879
T				Total Gr.50	4796.24765	6518.695
T				Total Gr.36	3353.34511	6560.474
T				Total	8149.59276	13079.169

UNIVERSITY AT BUFFALO		
206 KETTER HALL BUFFALO, NY, 14226		
Title: CPF#06-16: CF-CPSW UB TEST SETUP CAD		
Drawing:		
Page: 10of10	DATE: 9/16/2017	STATUS: Checking
	BY: Hadi Kenarangi	REV: 00

APPENDIX C

Final Specimen Design Detail and Drawings

C.1 Tie Bar Design

Mathcad © Enabled Content.

Pankow C-Shape CF-CPSW Project, Hadi Kenarangi, University at Buffalo, 2018

Calculations for design of C-Shape CF-CPSW test specimens

Disclaimer

User Notices

User Notices

Input variables that need to be defined by the user are highlighted in **YELLOW.**
Key results and design checks are highlighted in **GREEN.**
Intermediate results and checks are highlighted in **BLUE.**

User Notices

Description

- Lateral Loading System is noted as "**LLS**"
- Axial Loading System is noted as "**ALS**"
- LLS and ALS are designed using Gr. A36 Steel. Other parts are designed using A572 Gr.50 Steel.
- Welds are designed using E70xx electro.

References:

- AISC 360-16 (2016). *Specification for structural steel buildings*, American Institute of Steel Construction, Chicago, Ill.
- AISC 341-16 (2016). *Seismic provisions for structural steel buildings*, American Institute of Steel Construction, Chicago, Ill.

Input (for post IR1 Specimen)

$$t_s := \frac{3}{16} \text{ in}$$

Steel plate thickness

$$F_{yplate} := 50 \text{ ksi}$$

Specified yield strength of steel plate (A572 Grade 50)

$$F_{uplate} := 65 \text{ ksi}$$

Specified ultimate tensile strength of steel plate (A572 Grade 50)

$$E_s := 29000 \text{ ksi}$$

Elastic modulus for steel

$$t_c := 5.625 \text{ in}$$

Thickness of the concrete infill (for flange part)

$$t_w := t_c + 2 \cdot t_s = 6 \cdot \text{in}$$

Total thickness of wall

$$w_1 := 6 \text{ in}$$

Vertical spacing of tie bars

$$w_2 := 6 \text{ in}$$

Horizontal spacing of tie bars

$$D_{tie} := \frac{7}{16} \text{ in}$$

Nominal diameter of round tie bars

$$F_{ytie} := 55 \text{ ksi}$$

Specified yield strength of tie bars (F1554 Grade 55)

$$F_{utie} := 75 \text{ ksi}$$

Specified ultimate strength of tie bars (F1554 Grade 55)

Steel Web Plate of C-PSW/CF with Boundary Elements per AISC341-16 Article: H7.4a.

The maximum spacing of tie bars in vertical and horizontal directions, w_1 , shall be:

$$w_{1\max} := 1.8 \cdot t_s \sqrt{\frac{E_s}{F_{y\text{plate}}}} = 8.128 \cdot \text{in} \quad \text{AISC341-16 Eq. (H7-1)}$$

$$w_1 := \begin{cases} w_1 & \text{if } w_1 \leq w_{1\max} \\ \text{"Adjust } w_1 \text{ value"} & \text{otherwise} \end{cases}$$

Use tie spacings of: $w_1 = 6 \cdot \text{in}$

Tie Bar Diameter in C-PSW/CF with or without Boundary Elements Tie per AISC341-16 Article: H7.4e.

Tie bars shall be designed to elastically resist the tension force, T_{req} , determined as follows:

$t_s = 0.187 \cdot \text{in}$	Steel plate thickness
$t_c = 5.625 \cdot \text{in}$	Thickness of the concrete core
$t_w = 6 \cdot \text{in}$	Total thickness of wall
$w_2 = 6 \cdot \text{in}$	Horizontal spacing of tie bars
$w_1 = 6 \cdot \text{in}$	Vertical spacing of tie bars
$F_{y\text{plate}} = 50 \cdot \text{ksi}$	Nominal yield strength of steel plate

T_1 is the tension force resulting from the locally buckled web plates developing plastic hinges on horizontal yield lines along the tie bars and at mid-vertical distance between tie-bars, and is determined as follows:

$$T_1 := 2 \cdot \left(\frac{w_2}{w_1} \right) \cdot t_s^2 \cdot F_{y\text{plate}} = 3.516 \cdot \text{kip} \quad \text{AISC341-16 Eq. (H7-5)}$$

T_2 is the tension force that develops to prevent splitting of the concrete element on a plane parallel to the steel plate.

$$T_2 := \left(\frac{t_s \cdot F_{y\text{plate}} \cdot t_w}{4} \right) \cdot \left(\frac{w_2}{w_1} \right) \cdot \left[\frac{6}{18 \cdot \left(\frac{t_w}{\min(w_1, w_2)} \right)^2 + 1} \right] = 4.441 \cdot \text{kip} \quad \text{AISC341-16 Eq. (H7-6)}$$

$$T_{\text{req}} := T_1 + T_2 = 7.956 \cdot \text{kip} \quad \text{AISC341-16 Eq. (H7-4)}$$

$F_{y\text{tie}} = 55 \cdot \text{ksi}$ Nominal yield strength of tie bars

$$A_{\text{req}} := \frac{T_{\text{req}}}{F_{y\text{tie}}} = 0.145 \cdot \text{in}^2 \quad \text{Required tie bar cross-section area}$$

$$D_{\text{req}} := \sqrt{\frac{4 \cdot A_{\text{req}}}{\pi}} = 0.429 \cdot \text{in} \quad \text{Required tie bar diameter}$$

$$D_{\text{tie}} := \begin{cases} D_{\text{tie}} & \text{if } D_{\text{tie}} \geq D_{\text{req}} \\ \text{"Tie diameter is not OK"} & \text{otherwise} \end{cases}$$

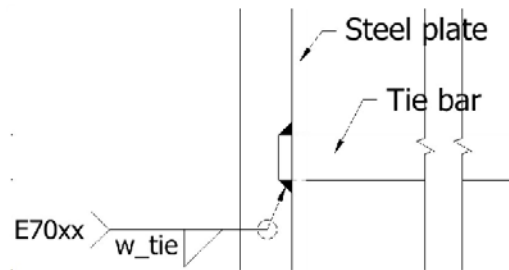
Use $D_{\text{tie}} = 0.438 \cdot \text{in}$ tie bars with yield strength of $F_{y\text{tie}} = 55 \cdot \text{ksi}$

Tie Bar-to-steel plate joint weld design:

$$T_{tie} := \frac{\pi}{4} D_{tie}^2 \cdot F_{ytie} = 8.268 \cdot \text{kip} \quad \text{Tensile strength of tie bars}$$

$$F_{EXX} := 70 \text{ksi} \quad \text{Weld electrode grade}$$

$$w_{tie} := 0.5 \text{in} \quad \text{Fillet weld size}$$



Weld length considering centerline of the weld:

$$l_w := \pi(D_{tie} + w_{tie}) = 2.945 \cdot \text{in} \quad \text{Weld length}$$

Transverse fillet weld strength:

$$\phi R_{n,weld} := 0.75 \cdot 0.6 \cdot F_{EXX} \cdot \left(1.0 + 0.5 \sin\left(\frac{\pi}{2}\right)^{1.5} \right) \cdot w_{tie} \cdot l_w = 69.581 \cdot \text{kip} \quad \text{AISC 360-10 (J2-5)}$$

$$w_{weld} := \begin{cases} w_{tie} & \text{if } \phi R_{n,weld} \geq T_{tie} \\ \text{"Tie weld size is not OK"} & \text{otherwise} \end{cases}$$

Weld is sufficient to develop the tensile strength of tie bar.

Use $w_{tie} = 0.5 \cdot \text{in}$ fillet weld with $F_{EXX} = 70 \cdot \text{ksi}$

$$\text{Base metal shear yield: } \phi R_{n,bms} := (1.0)(0.6 \cdot F_{yplate}) \cdot t_s \cdot l_w = 16.567 \cdot \text{kip}$$

$$\text{Base metal fracture: } \phi R_{n,bmf} := (0.75)(0.6 \cdot F_{uplate}) \cdot t_s \cdot l_w = 16.153 \cdot \text{kip}$$

Base metal fracture is governing failure mode of the tie-to-steel plate connection

C.2 Foundation reinforcing cage details

General Notes:

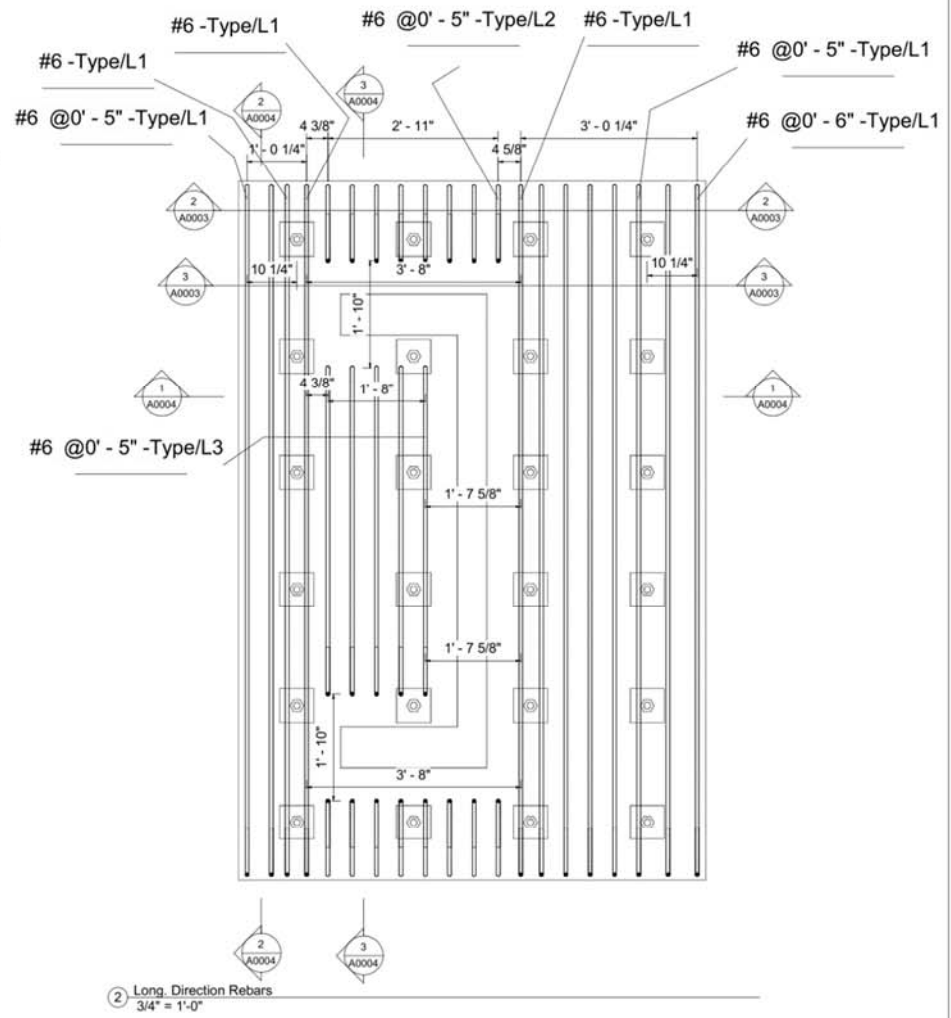
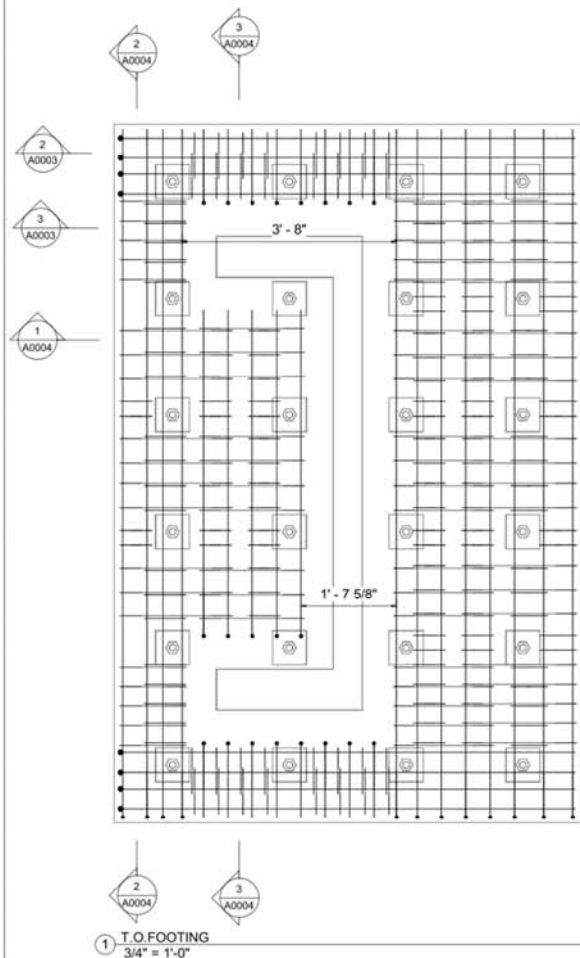
1. All foundation rebars are ASTM A706/A615 Grade 60
2. Specified strength for foundation concrete is 4000psi
3. Rebar bends per ACI 318 unless noted otherwise

UNIVERSITY AT BUFFALO
206 Ketter Hall
Buffalo, NY, 14226

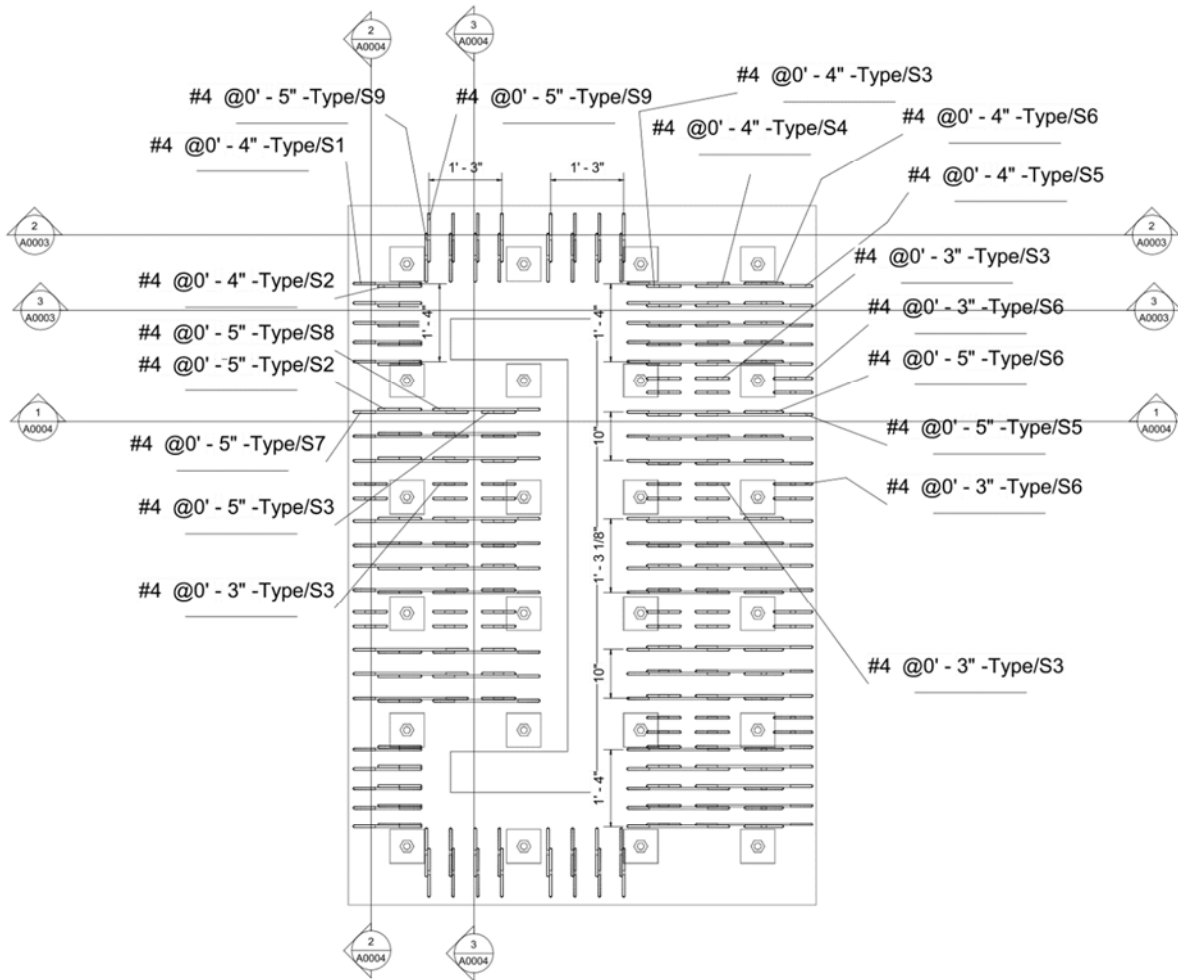
C-Shape Wall Foundation System

General Notes

A0000 Date: 01/01/2017
By: Hadi Kenarangi

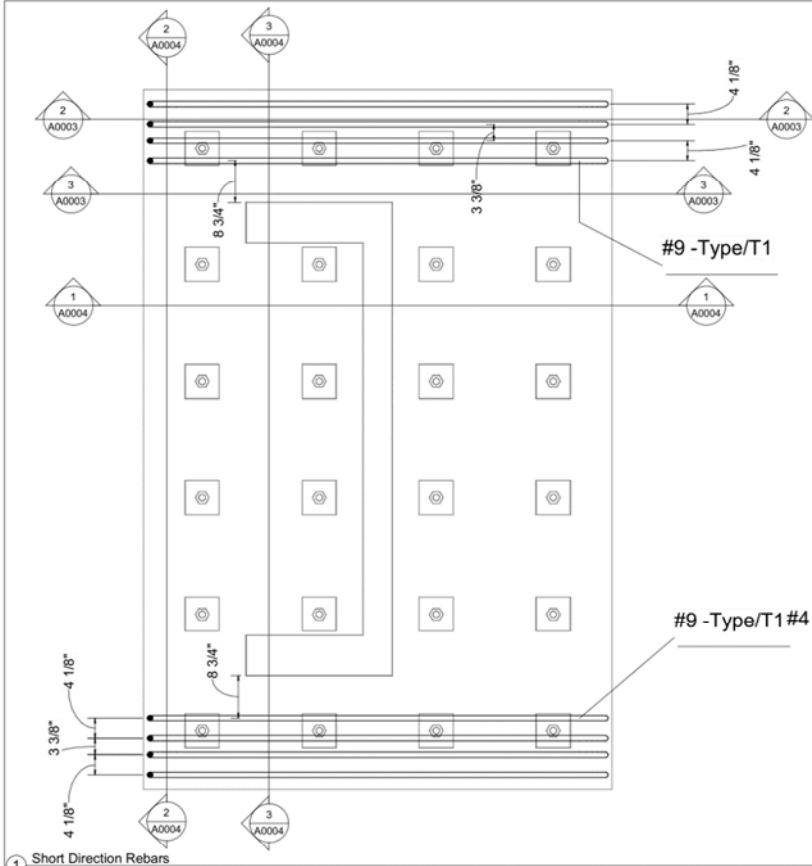


UNIVERSITY AT BUFFALO 206 Ketter Hall Buffalo, NY, 14226	
C-Shape Wall Foundation System	
Rebar Layout 01	
A0001	Date: 01/01/2017
	By: Hadi Kenarangi

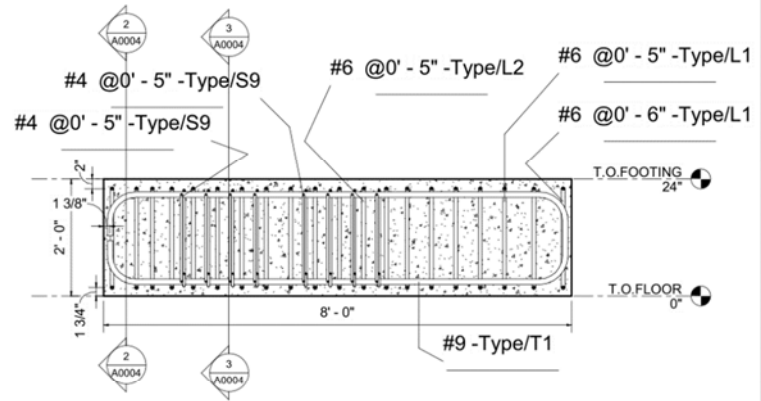


② Shear Rebars
3/4" = 1'-0"

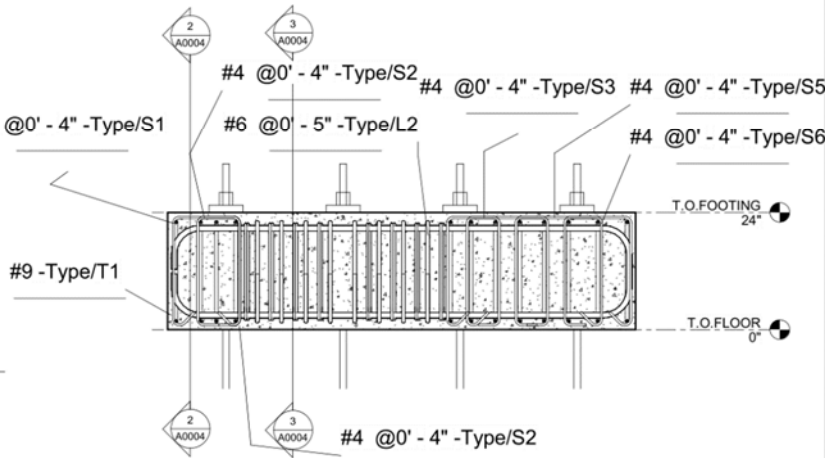
UNIVERSITY AT BUFFALO 206 Ketter Hall Buffalo, NY, 14226	
C-Shape Wall Foundation System	
Rebar Layout 02	
A0002	Date: 01/01/2017
	By: Hadi Kenarangi



① Short Direction Rebars
3/4" = 1'-0"

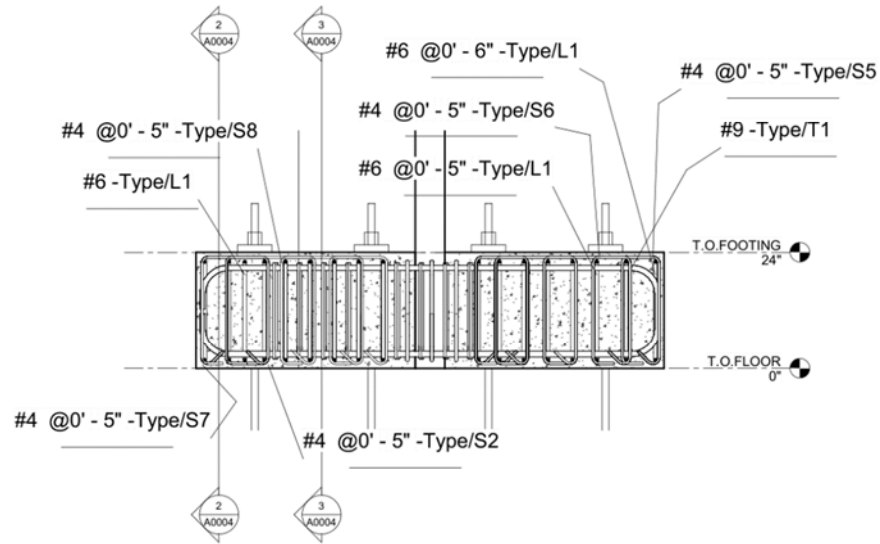


② Section 1
3/4" = 1'-0"

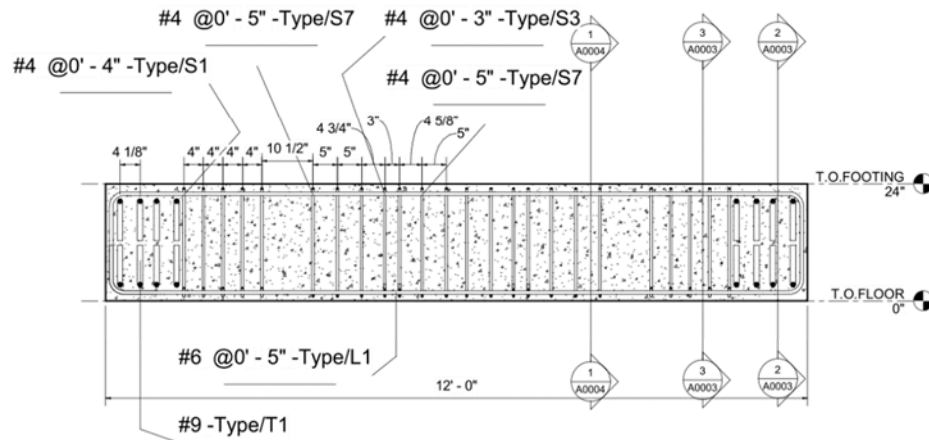


③ Section 2
3/4" = 1'-0"

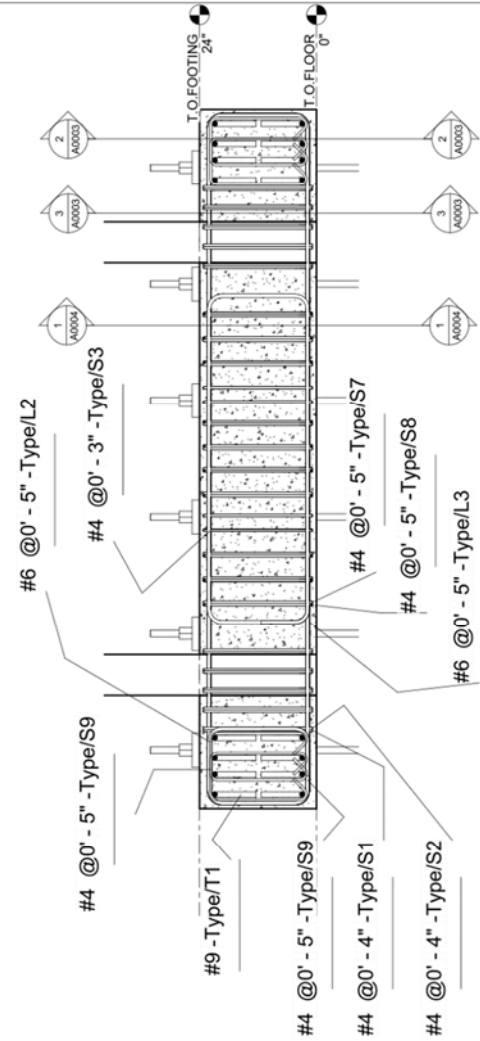
UNIVERSITY AT BUFFALO 206 Ketter Hall Buffalo, NY, 14226	
C-Shape Wall Foundation System	
Rebar Layout 03	
A0003	Date: 01/01/2017
	By: Hadi Kenarangi



① Section 3
3/4" = 1'-0"

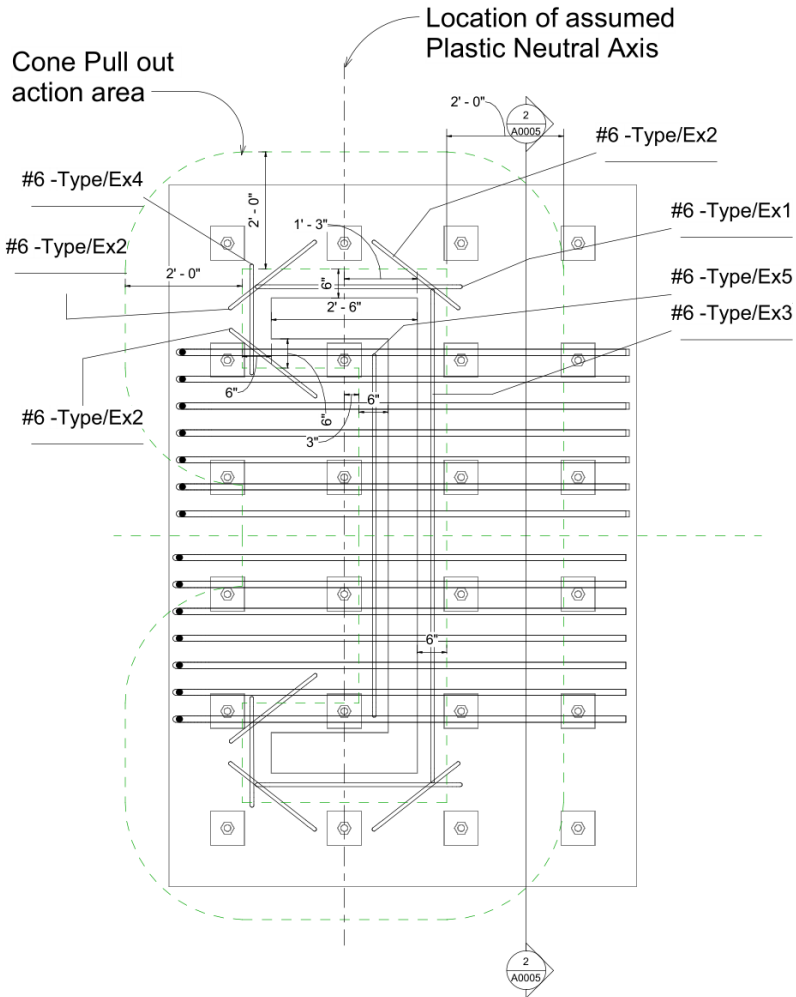


② Section 4
3/4" = 1'-0"



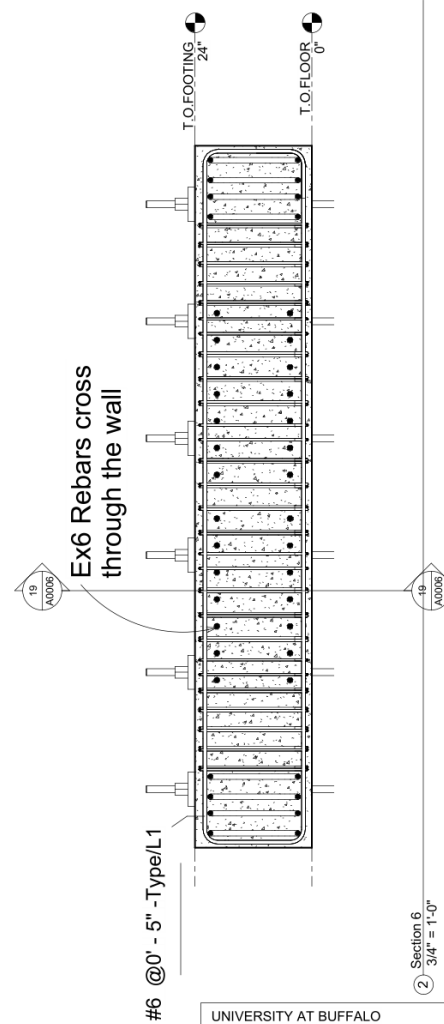
③ Section 5
3/4" = 1'-0"

UNIVERSITY AT BUFFALO 206 Ketter Hall Buffalo, NY, 14226	
C-Shape Wall Foundation System	
Rebar Layout 04	
A0004	Date: 01/01/2017
	By: Hadi Kenarangi



① After Wall Placement Rebars
3/4" = 1'-0"

Elevation 1 - a



Ex6 Rebars cross through the wall

#6 @0' - 5" - Type/L1

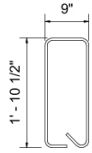
UNIVERSITY AT BUFFALO
206 Ketter Hall
Buffalo, NY, 14226

C-Shape Wall Foundation System

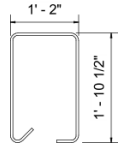
After Wall Placement Reb. Layout 01

A0005

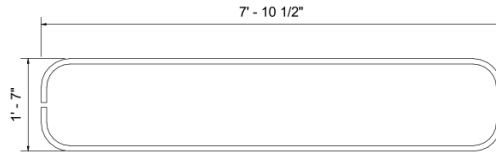
Date: 01/01/2017
By: Hadi Kenarangi



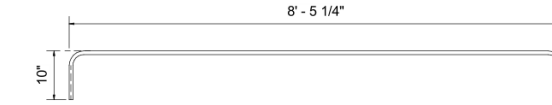
② Type/S2
3/4" = 1'-0"



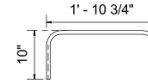
① Type/S1
3/4" = 1'-0"



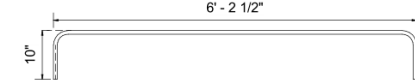
③ Type/T1
3/4" = 1'-0"



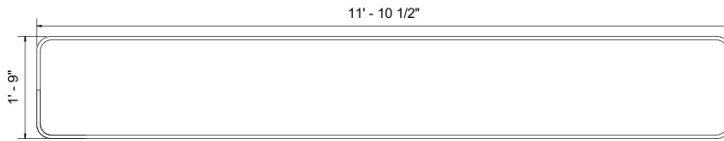
⑯ Type/Ex3
3/4" = 1'-0"



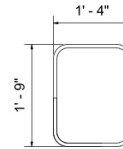
⑰ Type/Ex4
3/4" = 1'-0"



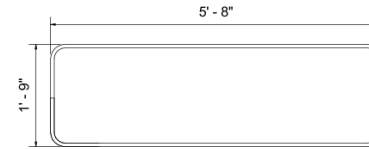
⑱ Type/Ex5
3/4" = 1'-0"



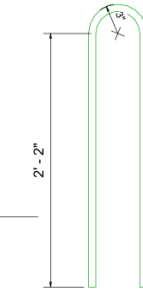
④ Type/L1
3/4" = 1'-0"



⑤ Type/L2
3/4" = 1'-0"



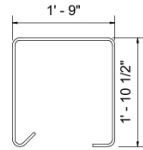
⑥ Type/L3
3/4" = 1'-0"



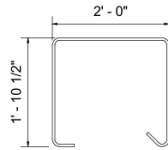
⑳ Lifting Hooks (LH)
1 1/2" = 1'-0"



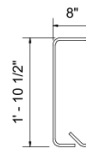
⑦ Type/S3
3/4" = 1'-0"



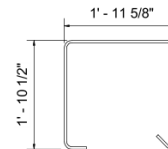
⑧ Type/S4
3/4" = 1'-0"



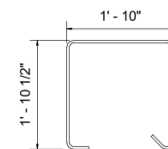
⑨ Type/S5
3/4" = 1'-0"



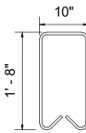
⑩ Type/S6
3/4" = 1'-0"



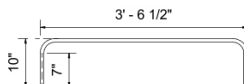
⑪ Type/S7
3/4" = 1'-0"



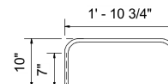
⑫ Type/S8
3/4" = 1'-0"



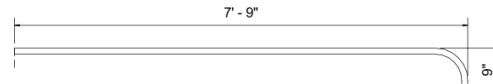
⑬ Type/S9
3/4" = 1'-0"



⑭ Type/Ex1
3/4" = 1'-0"



⑮ Type/Ex2
3/4" = 1'-0"



⑲ Type/Ex6
3/4" = 1'-0"

UNIVERSITY AT BUFFALO
206 Ketter Hall
Buffalo, NY, 14226

C-Shape Wall Foundation System

Rebar Legend

A0006

Date: 01/01/2017

By: Hadi Kenarangi

A	B	C	D	E	F	G	H	Schedule Mark (Type)	Bar Diameter	Bend Type	Quantity By Rebar Set	Bar Length	No.	Vol/bar (in ³)	Vol/bundle (in ³)	Weight/bundle (lbs)
0' - 10"	3' - 6"	0' - 0"	0' - 0"	0' - 0"	0' - 0"	0' - 10"	0' - 0"	Ex1	0.75"	2	2	4' - 11"	#6	26	52	15
0' - 10"	1' - 11"	0' - 0"	0' - 0"	0' - 0"	0' - 0"	0' - 10"	0' - 0"	Ex2	0.75"	2	6	3' - 3"	#6	17	105	29
0' - 10"	8' - 5"	0' - 0"	0' - 0"	0' - 0"	0' - 0"	0' - 10"	0' - 0"	Ex3	0.75"	2	1	9' - 10"	#6	52	52	15
0' - 10"	1' - 11"	0' - 0"	0' - 0"	0' - 0"	0' - 0"	0' - 10"	0' - 0"	Ex4	0.75"	2	2	3' - 3"	#6	17	34	10
0' - 10"	6' - 3"	0' - 0"	0' - 0"	0' - 0"	0' - 0"	0' - 10"	0' - 0"	Ex5	0.75"	2	1	7' - 7"	#6	40	40	11
0' - 0"	7' - 9"	0' - 9"	0' - 0"	0' - 0"	0' - 0"	0' - 0"	0' - 0"	Ex6	1.27"	17A	28	8' - 2"	#10	124	3473	986
0' - 10"	1' - 9"	11' - 11"	1' - 9"	11' - 11"	0' - 0"	0' - 10"	0' - 0"	L1	0.75"	T2	12	28' - 2"	#6	149	1792	509
0' - 10"	1' - 9"	1' - 4"	1' - 9"	1' - 4"	0' - 0"	0' - 10"	0' - 0"	L2	0.75"	T2	16	7' - 1"	#6	38	601	171
0' - 10"	1' - 9"	3' - 8"	1' - 9"	3' - 8"	0' - 0"	0' - 10"	0' - 0"	L3	0.75"	T2	5	15' - 9"	#6	85	417	119
0' - 5"	1' - 11"	1' - 2"	1' - 11"	0' - 0"	0' - 0"	0' - 5"	0' - 3"	S1	0.50"	Rebar Shape 2	10	5' - 5"	#4	15	128	36
0' - 5"	1' - 11"	0' - 9"	1' - 11"	0' - 0"	0' - 0"	0' - 5"	0' - 3"	S2	0.50"	Rebar Shape 2	20	5' - 0"	#4	12	256	67
0' - 5"	1' - 11"	0' - 7"	1' - 11"	0' - 0"	0' - 0"	0' - 5"	0' - 3"	S3	0.50"	Rebar Shape 2	58	4' - 10"	#4	11	661	188
0' - 5"	1' - 11"	1' - 9"	1' - 11"	0' - 0"	0' - 0"	0' - 5"	0' - 3"	S4	0.50"	Rebar Shape 2	20	6' - 0"	#4	14	283	80
0' - 5"	1' - 11"	2' - 0"	1' - 11"	0' - 0"	0' - 0"	0' - 5"	0' - 3"	S5	0.50"	Rebar Shape 2	20	6' - 3"	#4	15	295	84
0' - 5"	1' - 11"	0' - 8"	1' - 11"	0' - 0"	0' - 0"	0' - 5"	0' - 3"	S6	0.50"	Rebar Shape 2	28	4' - 11"	#4	12	324	92
0' - 5"	1' - 11"	2' - 0"	1' - 11"	0' - 0"	0' - 0"	0' - 5"	0' - 3"	S7	0.50"	Rebar Shape 2	10	6' - 2"	#4	15	145	41
0' - 5"	1' - 11"	1' - 10"	1' - 11"	0' - 0"	0' - 0"	0' - 5"	0' - 3"	S8	0.50"	Rebar Shape 2	10	6' - 1"	#4	14	143	41
0' - 5"	1' - 8"	0' - 10"	1' - 8"	0' - 0"	0' - 0"	0' - 5"	0' - 3"	S9	0.50"	S3	32	4' - 9"	#4	11	358	102
0' - 9"	7' - 11"	1' - 7"	7' - 11"	0' - 0"	0' - 0"	0' - 9"	0' - 0"	T1	1.13"	S6	8	17' - 8"	#9	212	1698	482
								LH	0.75"	10	4	4' - 4"	#6	26	104	30
														Grand Total	10940	3107

UNIVERSITY AT BUFFALO
206 Ketter Hall
Buffalo, NY, 14226

C-Shape Wall Foundation System

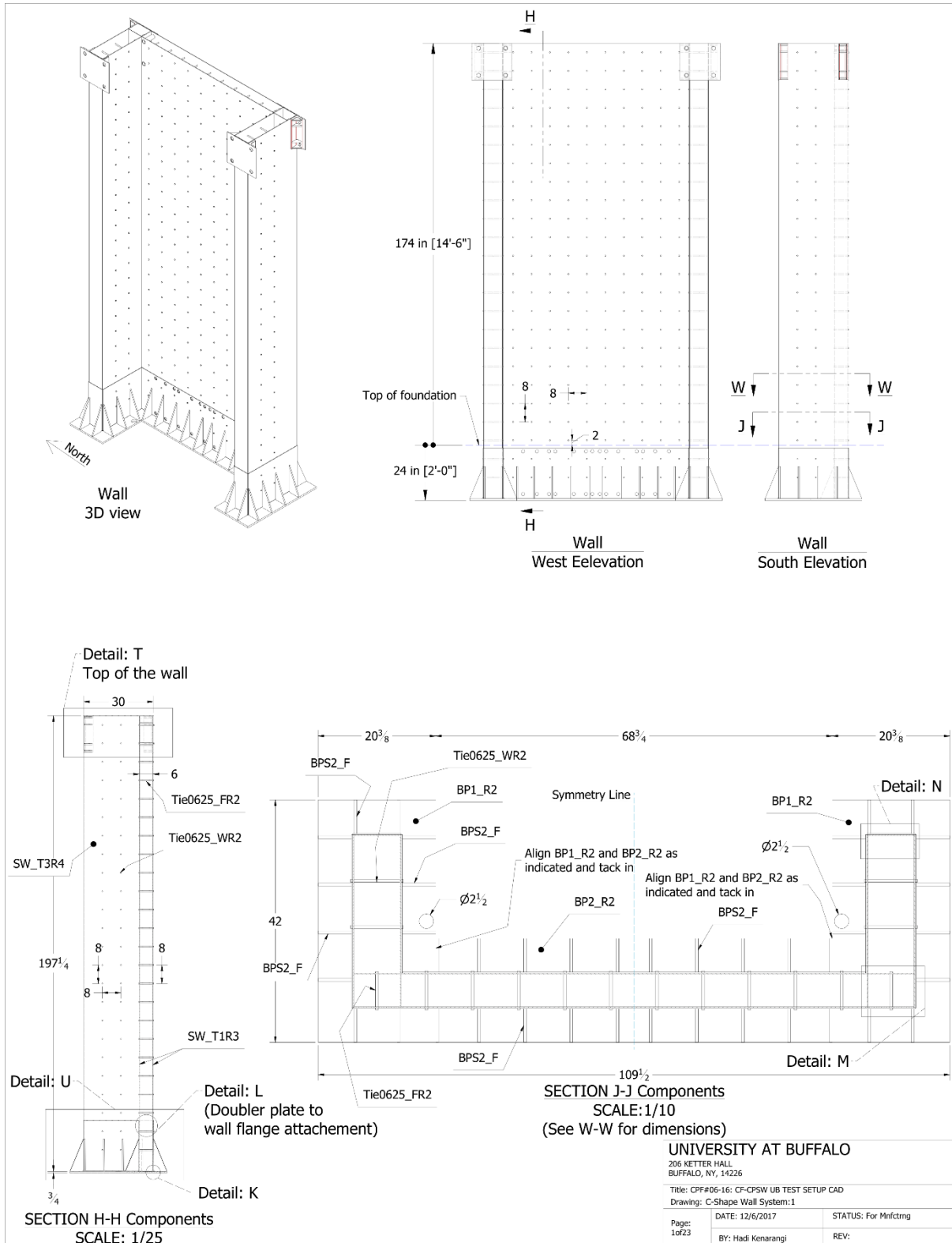
Rebar Schedule

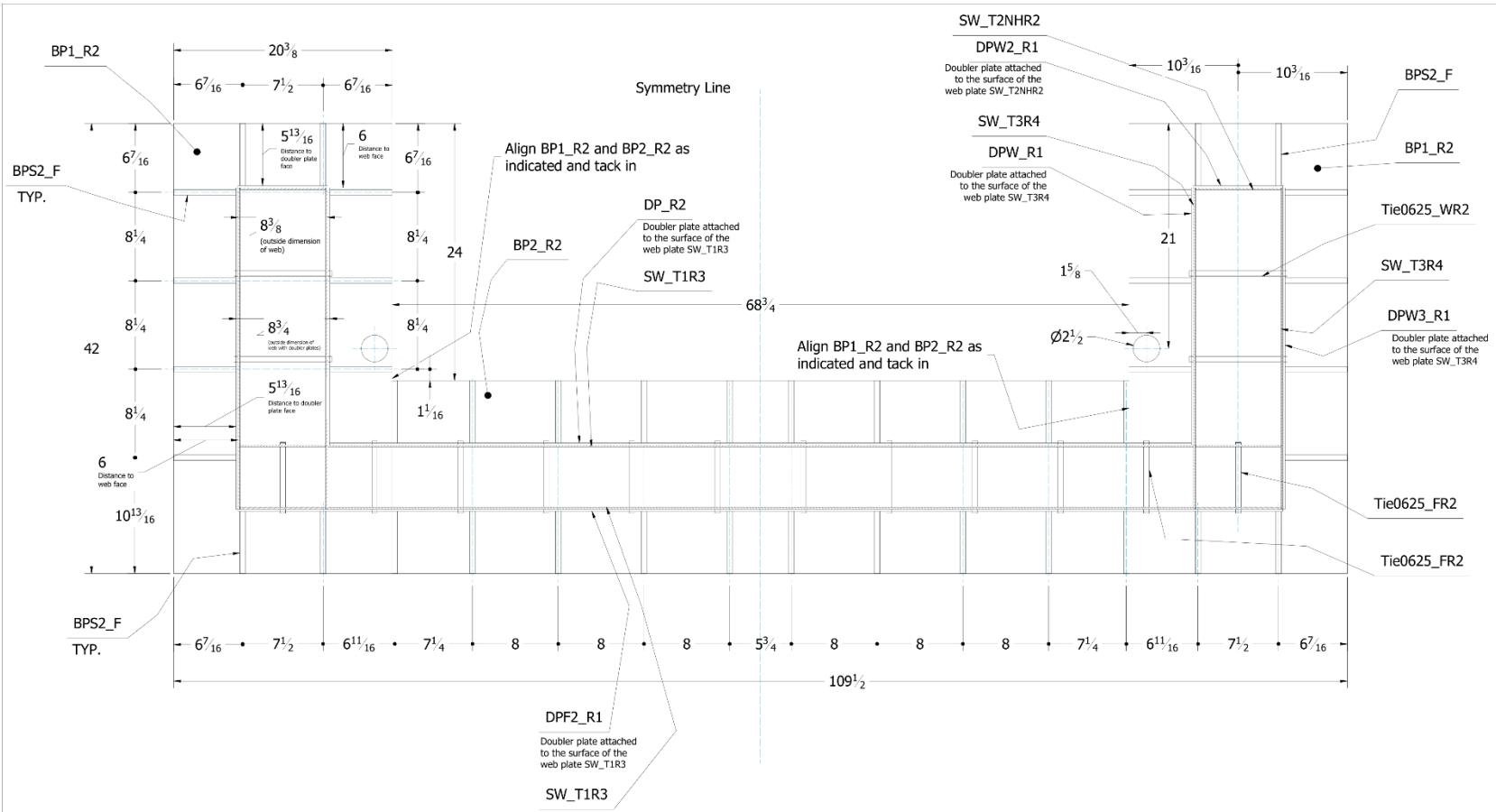
A0007

Date: 01/01/2017

By: Hadi Kenarangi

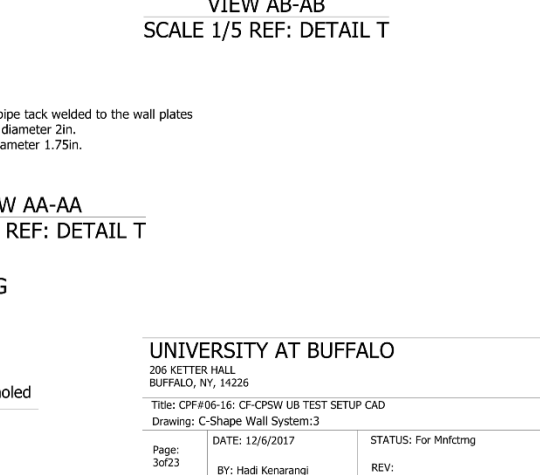
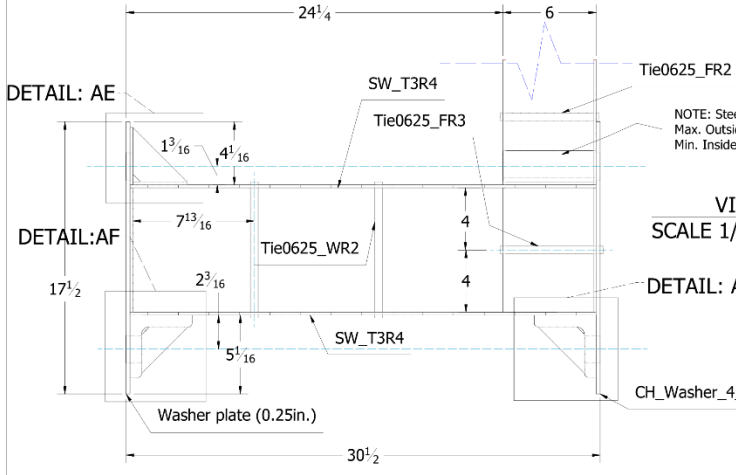
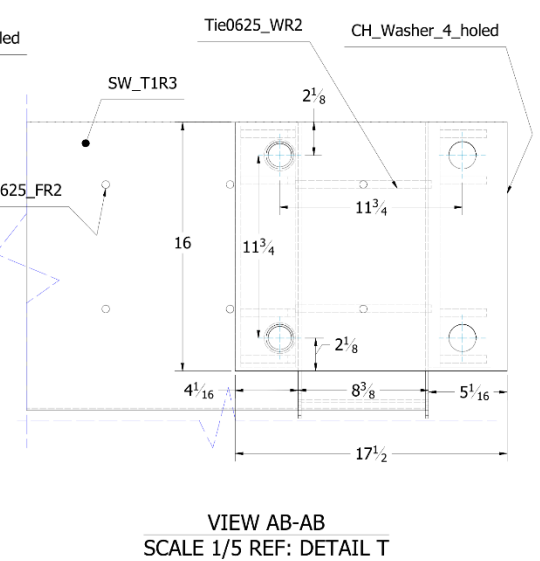
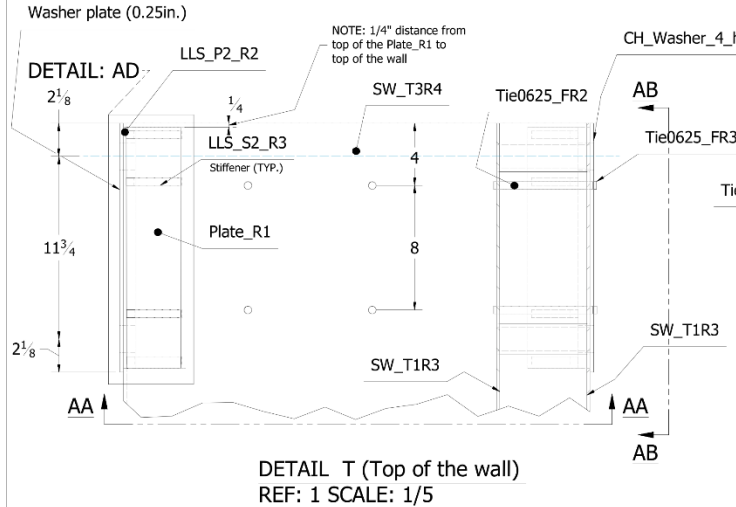
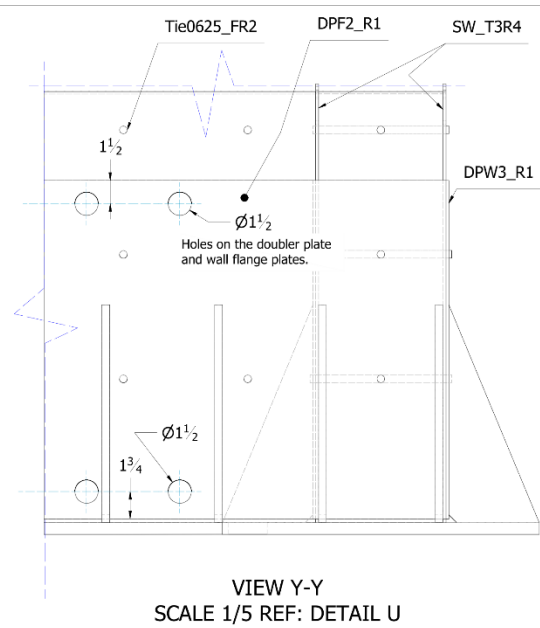
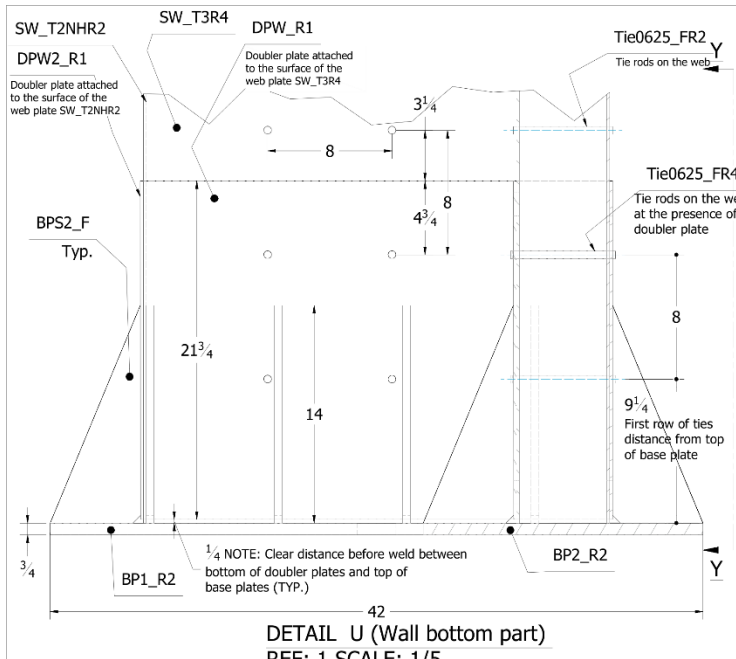
C.3 Test setup and specimens' drawings submitted to fabricator



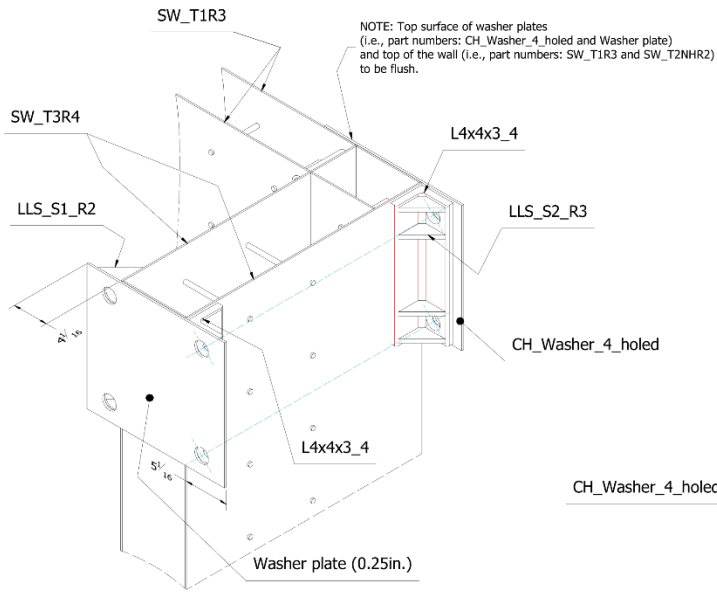


SECTION W-W
 NOTE: arrangements are symmetric
 with respect to shown symmetry line

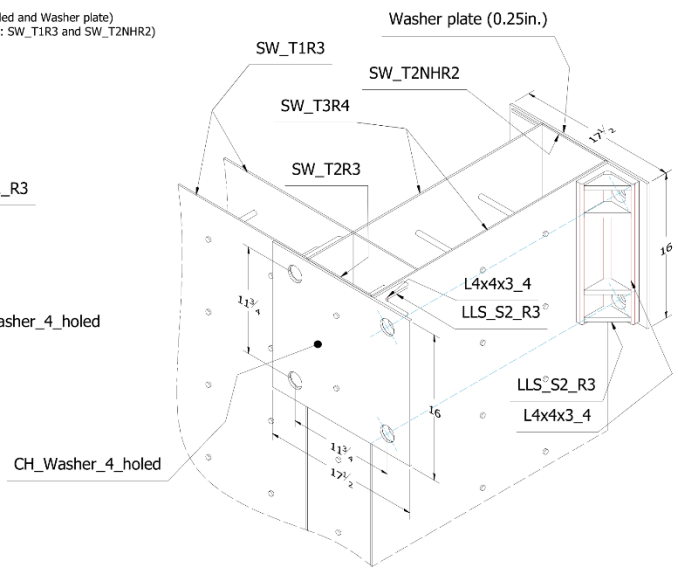
UNIVERSITY AT BUFFALO		
206 KETTER HALL BUFFALO, NY, 14226		
Title: CPF#06-16: CF-CPSW UB TEST SETUP CAD		
Drawing: C-Shape Wall System:2		
Page: 2of23	DATE: 12/6/2017 BY: Hadi Kenarangi	STATUS: For Mnfctmg REV:



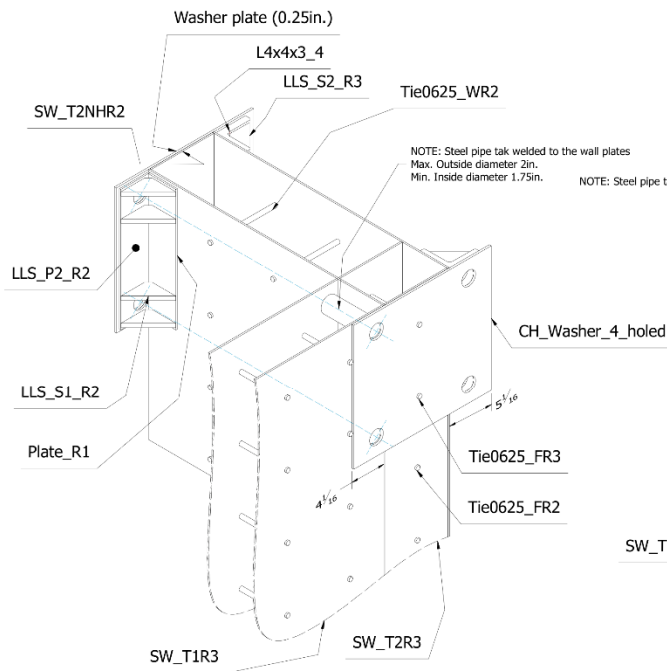
UNIVERSITY AT BUFFALO		
206 KETTER HALL BUFFALO, NY, 14226		
Title: CPF#06-16: CF-CPSW UB TEST SETUP CAD		
Drawing: C-Shape Wall System:3		
Page: 3of23	DATE: 12/6/2017 BY: Hadi Kenarangi	STATUS: For Mnfctrng REV:



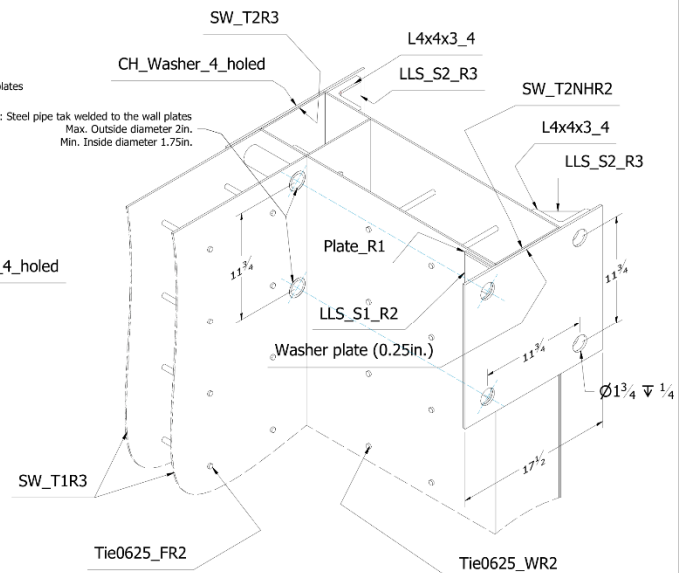
Top of the wall
3D View



Top of the wall
3D View Opposite angle



Top of the wall
3D View



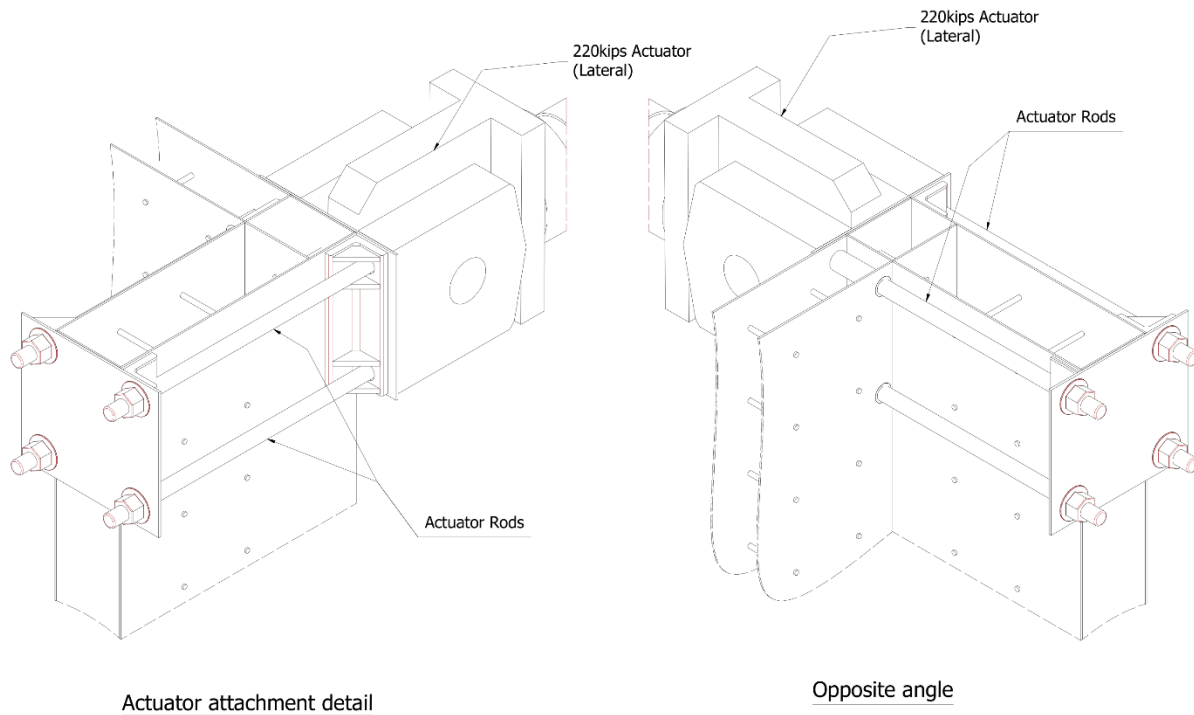
Top of the wall
3D View

UNIVERSITY AT BUFFALO

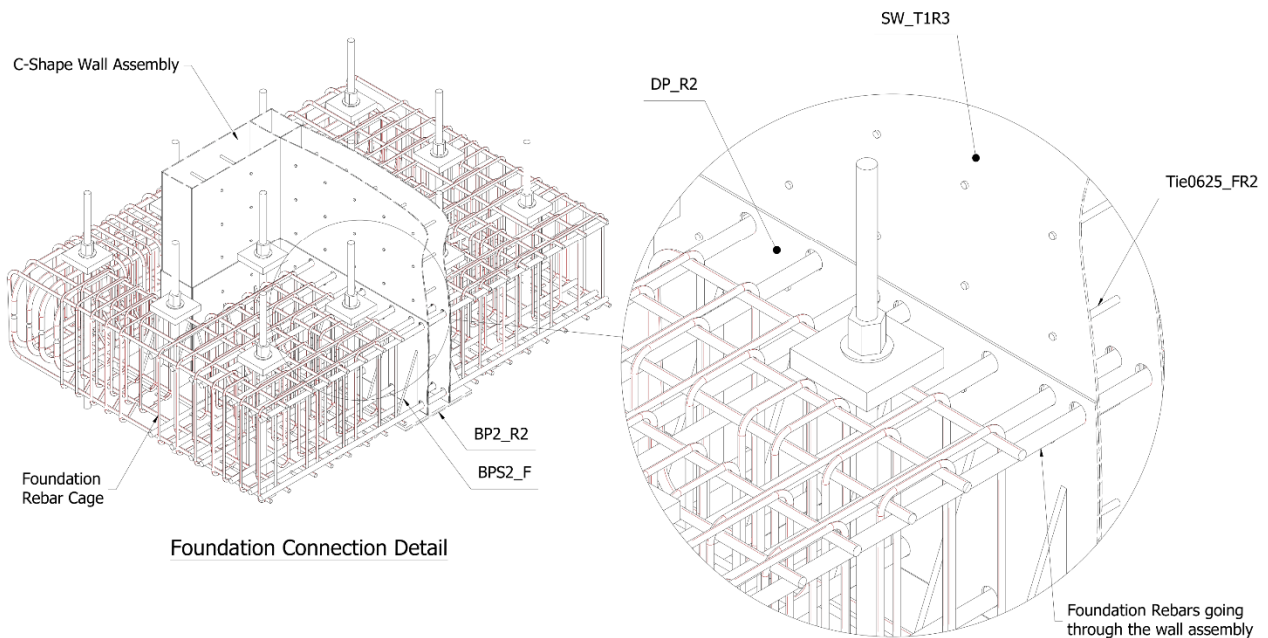
206 KETTER HALL
BUFFALO, NY, 14226

Title: CPF#06-16: CF-CPSW UB TEST SETUP CAD
Drawing: C-Shape Wall System:4

Page: 4of23	DATE: 12/6/2017	STATUS: For Mnfctng
	BY: Hadi Kenarangi	REV:



NOTE: Drawing provided to illustrate the details of the testing actuator attachments at the top of the wall (Holes on the washer plates, stiffeners, and wall flange should be aligned as they will be used with actuator rods as shown)

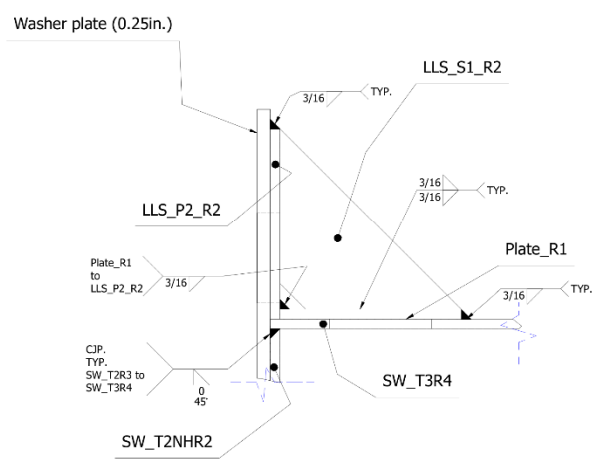
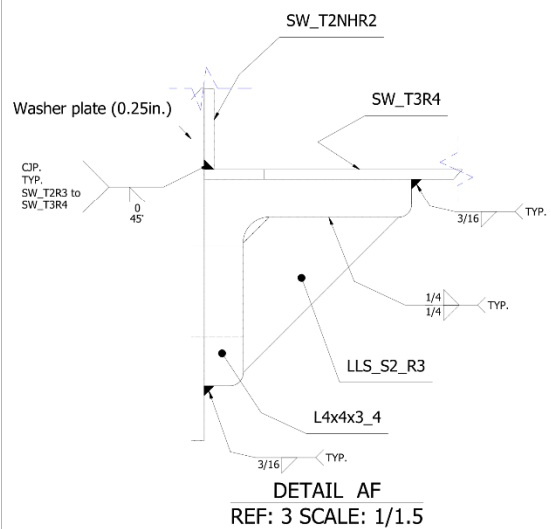
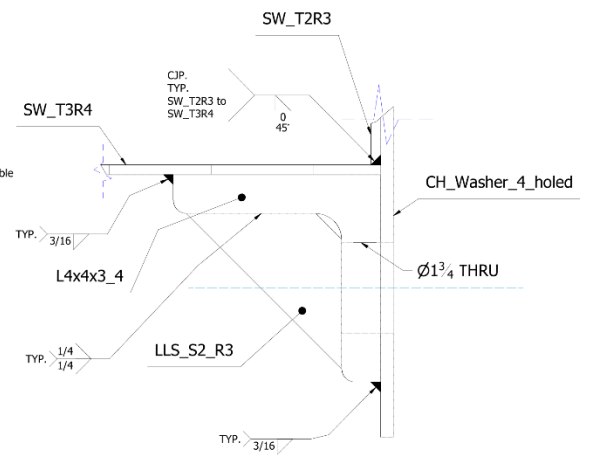
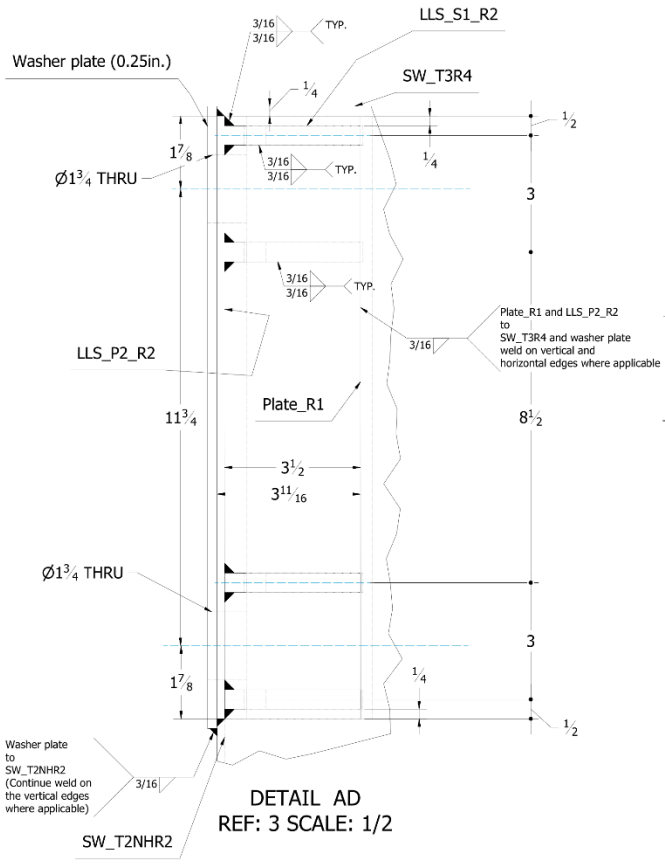


NOTE: Drawing provided to illustrate the details of the Wall assembly-to-RC foundation connection. (Holes on the doubler plates and wall face plates should be aligned to accommodate the shown crossing rebars in the foundation)

UNIVERSITY AT BUFFALO
206 KETTER HALL
BUFFALO, NY, 14226

Title: CPF#06-16: CF-CPSW UB TEST SETUP CAD
Drawing: C-Shape Wall System:5

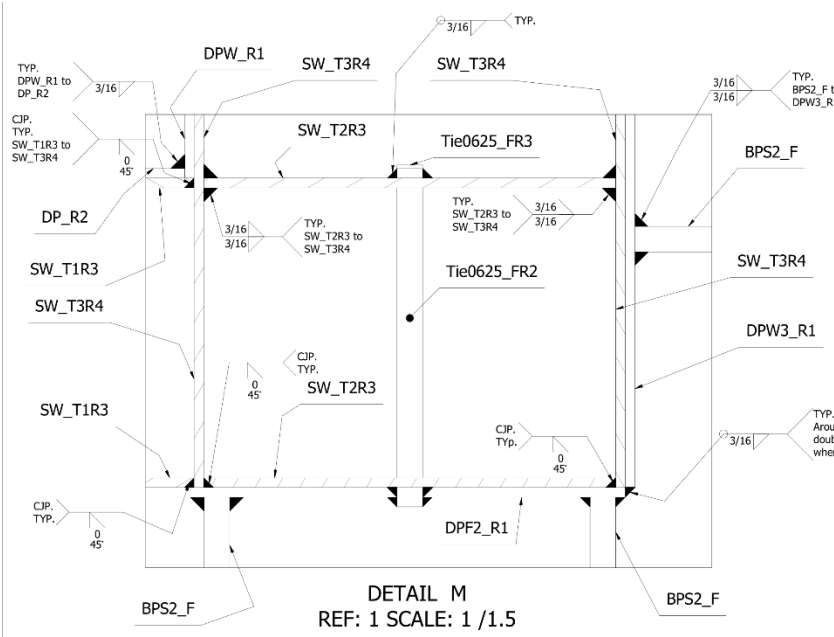
Page: Sof23	DATE: 12/6/2017	STATUS: For Mnfctrng
	BY: Hadi Kenarangi	REV:



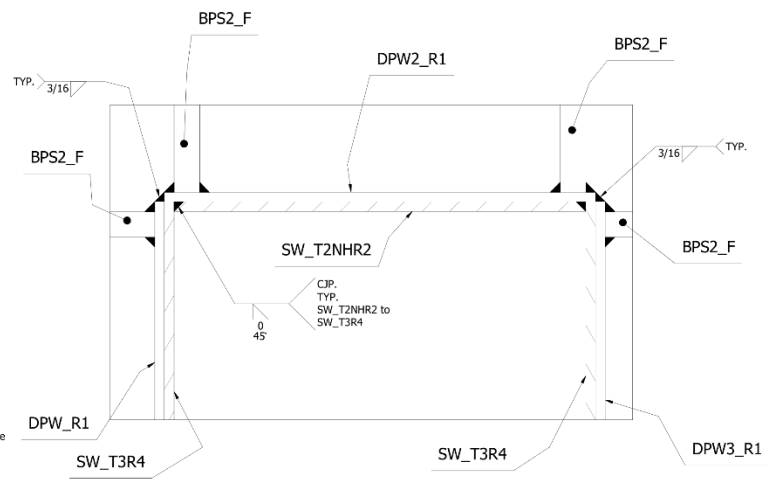
UNIVERSITY AT BUFFALO
206 KETTER HALL
BUFFALO, NY, 14226

Title: CPF#06-16: CF-CPSW UB TEST SETUP CAD
Drawing: C-Shape Wall System_Wediment Details:6

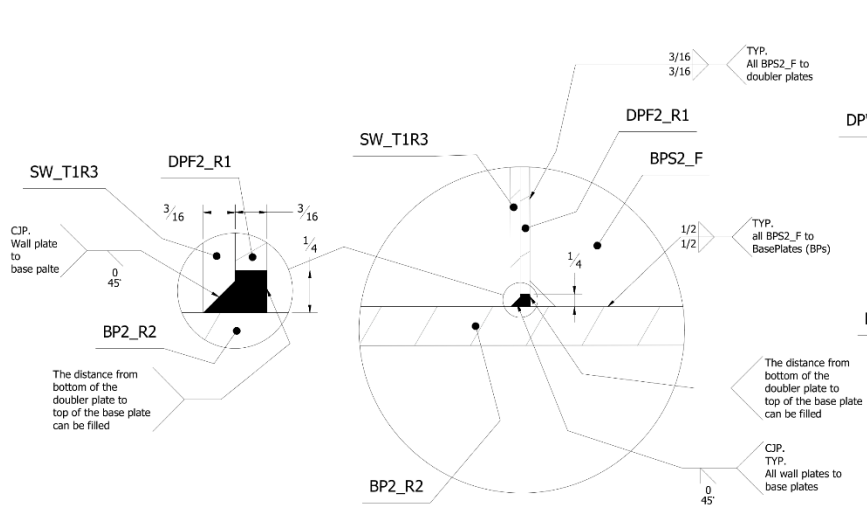
Page: 6of23	DATE: 12/6/2017 BY: Hadi Kenarangi	STATUS: For Mnfctng REV:
----------------	---------------------------------------	-----------------------------



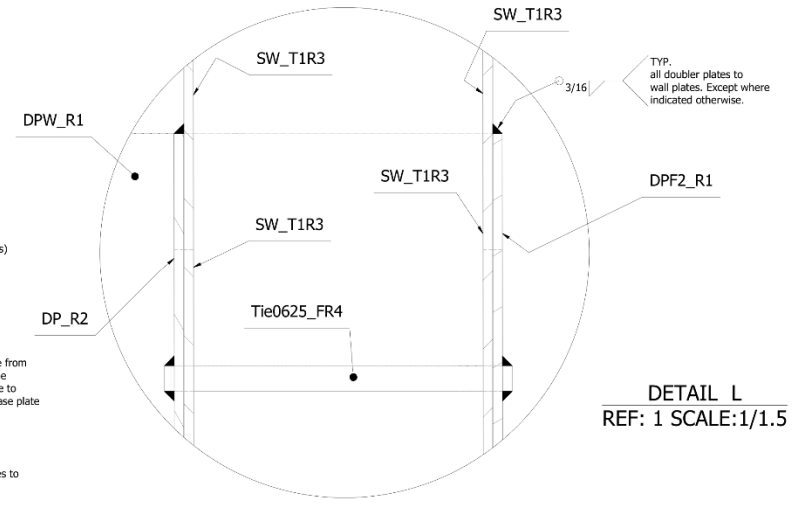
DETAIL M
REF: 1 SCALE: 1 / 1.5



DETAIL N
REF:1 SCALE: 1 / 1.5

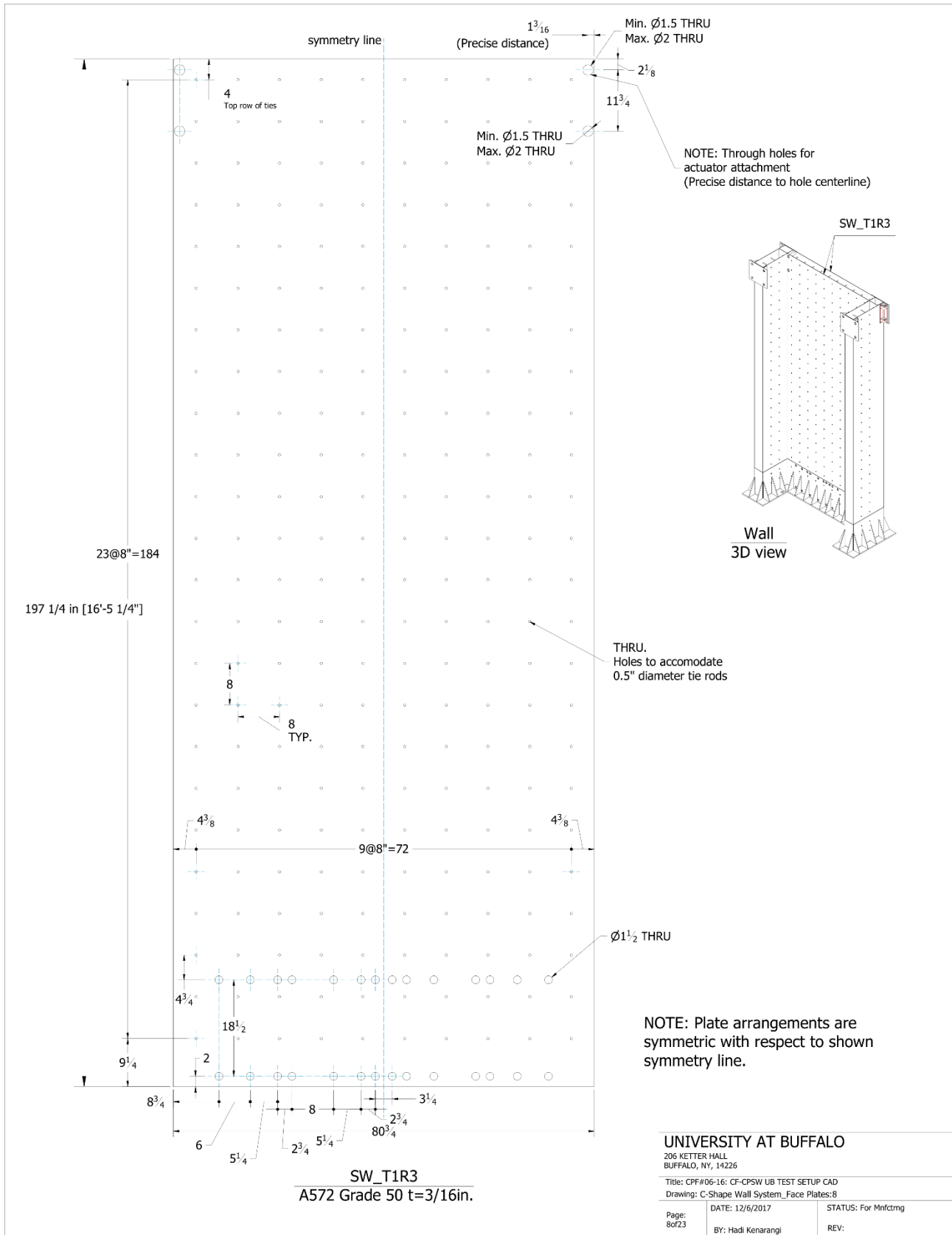


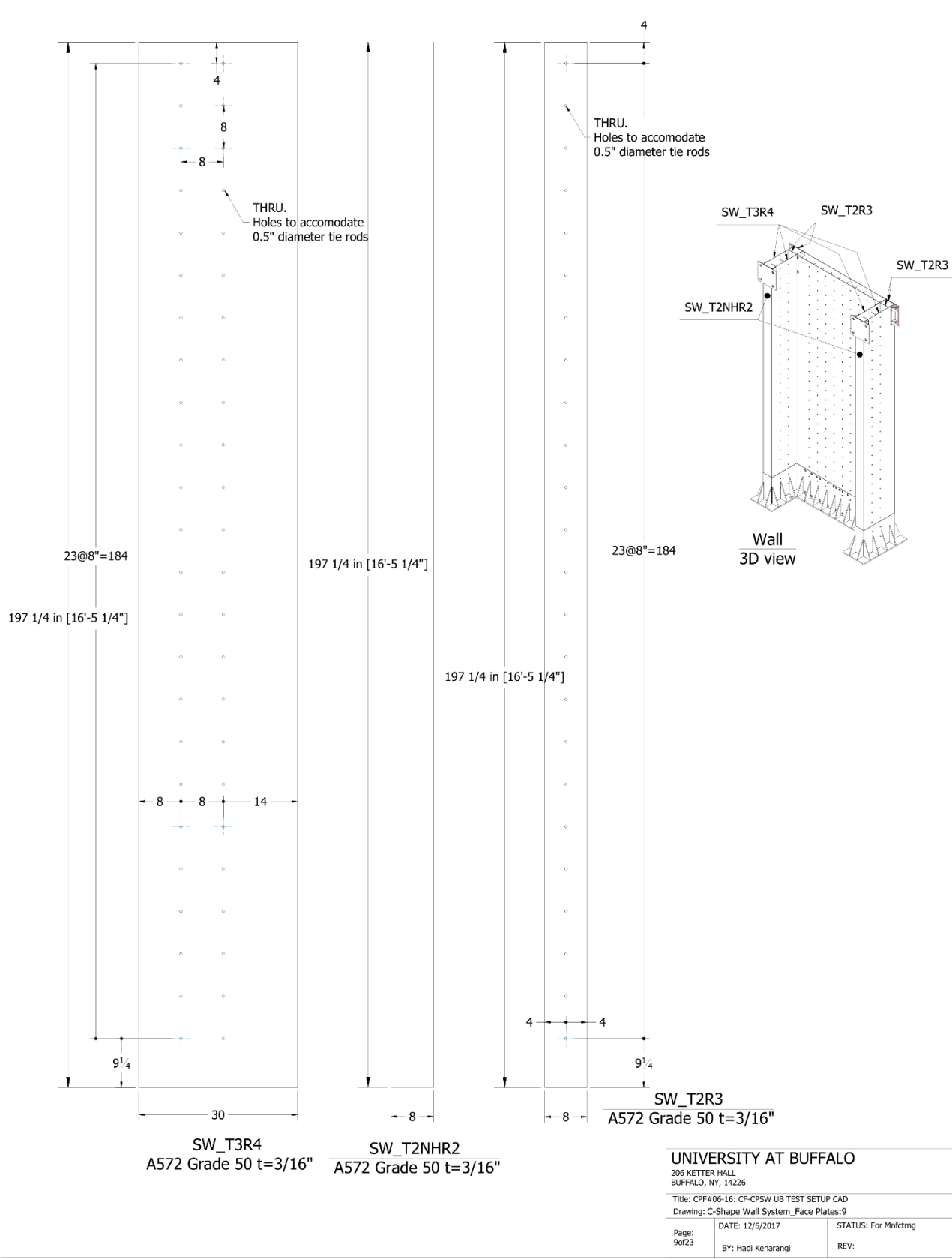
DETAIL K
REF: 1 SCALE: 1/1.5

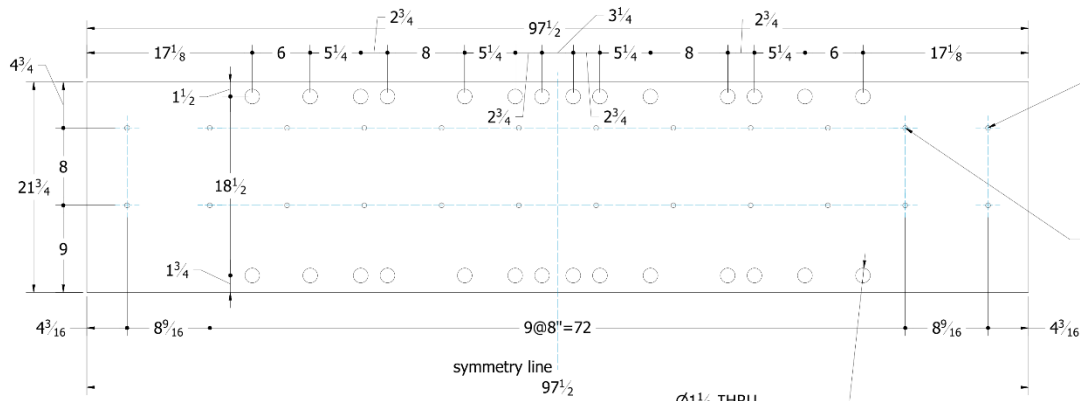


DETAIL L
REF: 1 SCALE: 1/1.5

UNIVERSITY AT BUFFALO		
206 KETTER HALL BUFFALO, NY, 14226		
Title: CPF#06-16: CF-CPSW UB TEST SETUP CAD		
Drawing: C-Shape Wall System_Weldment Details:7		
Page: 7of23	DATE: 12/6/2017	STATUS: For Mnfctng
	BY: Hadi Kenarangi	REV: 00







DPWF2_R1
A572 Grade 50 $t=3/16"$

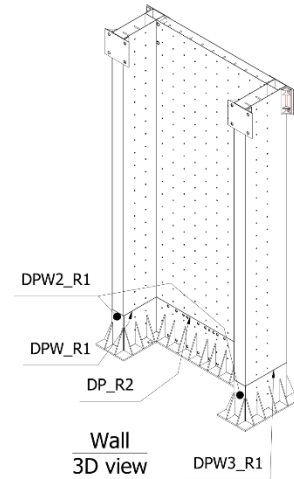
NOTE:

1. Doubler plate DPWF2_R1 to be welded to the flange of the wall.
2. Holes are symmetric with respect to shown symmetry line.
3. Holes on the doubler plate should be aligned with the holes on the wall flange.
4. The hole drilling can be performed before or after welding to the wall flange.

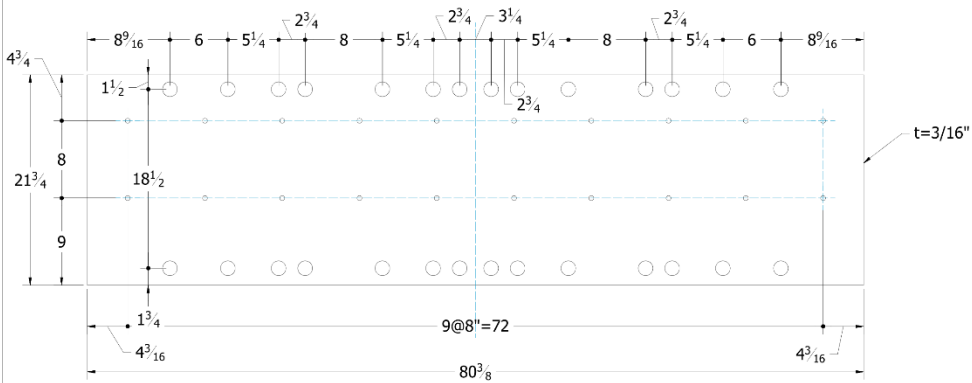
THRU.
Holes to accommodate 0.5" diameter tie rods (NOTE: First and last column Aligned with tie holes on SW_T2R3)

THRU.
Holes to accommodate 0.5" diameter tie rods (NOTE: all holes except first and last columns Aligned with tie holes on SW_T3R4)

$\varnothing 1\frac{1}{2}$ THRU
through doubler plate
and wall flange



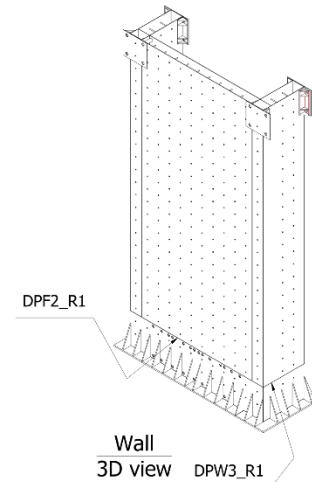
Wall
3D view



DP_R2
A572 Grade 50 $t=3/16"$

NOTE:

1. Doubler plate DP_R2 to be welded to the flange of the wall.
2. Holes are symmetric with respect to shown symmetry line.
3. Holes on the doubler plate should be aligned with the holes on the wall flange.
4. The hole drilling can be performed before or after welding to the wall flange.



Wall
3D view

UNIVERSITY AT BUFFALO

206 KETTER HALL
BUFFALO, NY, 14226

Title: CPF#06-16: CF-CPSW UB TEST SETUP CAD
Drawing: C-Shape Wall System_Doubler Plates:10

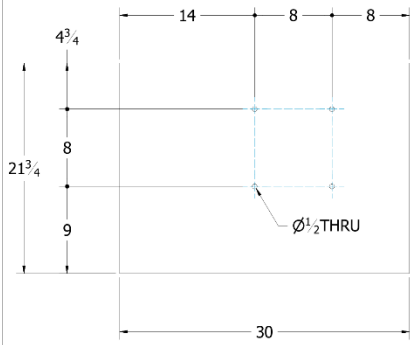
Page:
10of23

DATE: 12/6/2017

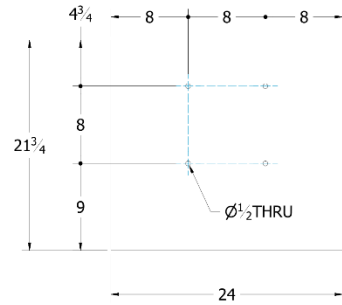
STATUS: For Mfctg

BY: Hadi Kenarangi

REV: 00



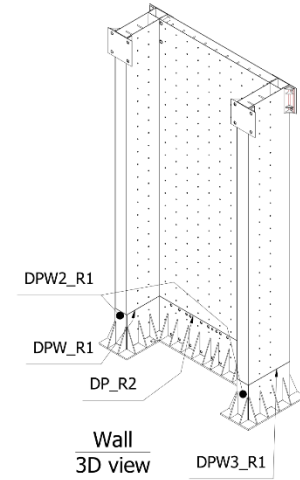
DPW3_R1
A572 Grade 50 t=3/16"



DPW_R1
A572 Grade 50 t=3/16"



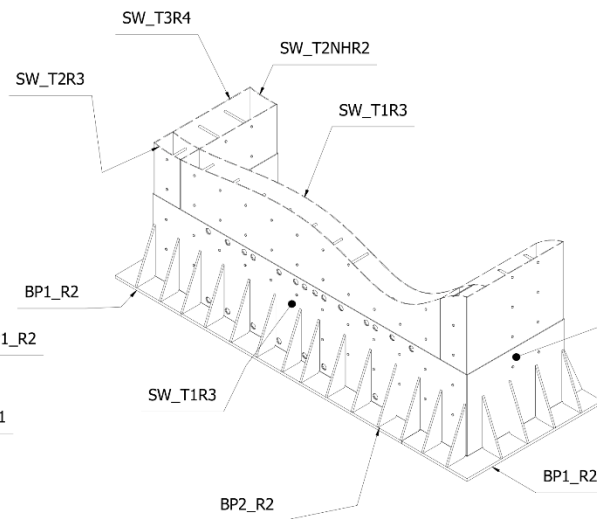
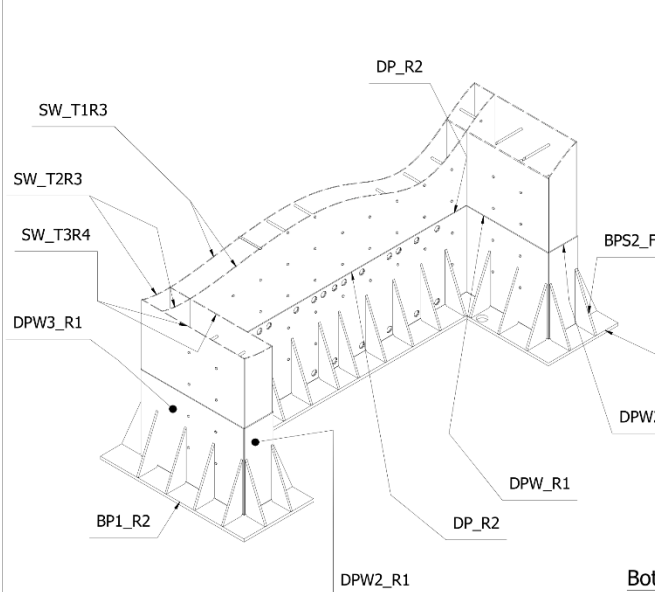
DPW2_R1
A572 Grade 50 t=3/16"



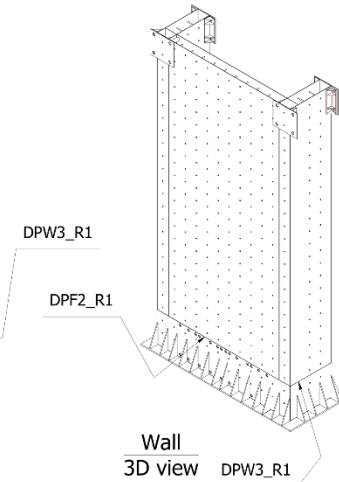
Wall
3D view

NOTE:

1. Doubler plates DPW3_R1 and DPW_R1 to be welded to the web of the wall.
2. Holes on the doubler plate should be aligned with the holes on the wall flange.
3. The hole drilling can be performed before or after welding to the wall flange.



Bottom of the wall
3D view



Wall
3D view

UNIVERSITY AT BUFFALO

206 KETTER HALL
BUFFALO, NY, 14226

Title: CPF#06-16: CF-CPSW UB TEST SETUP CAD
Drawing: C-Shape Wall System_Doubler Plates:11

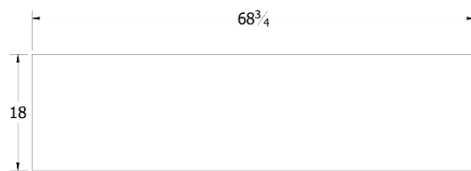
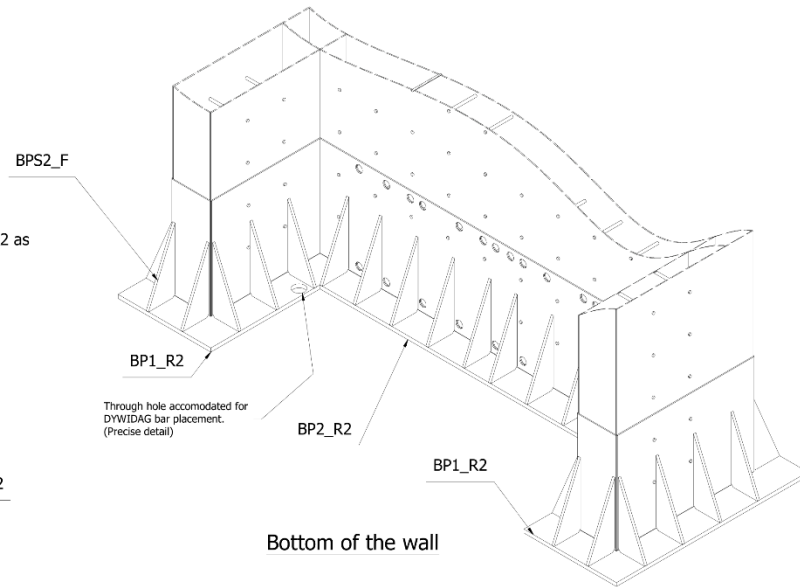
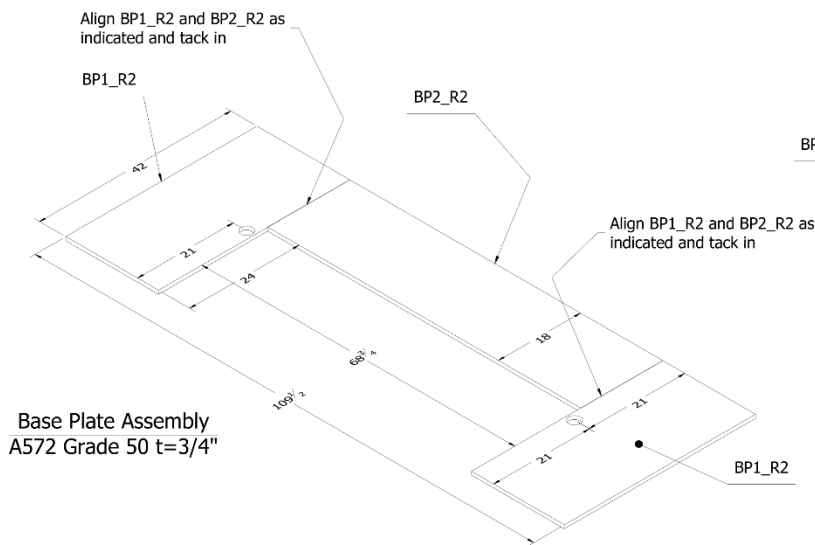
Page:
11of23

DATE: 12/6/2017

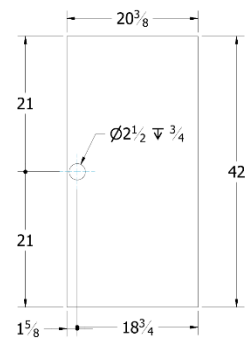
STATUS: For Mnfctng

BY: Hadi Kenarangi

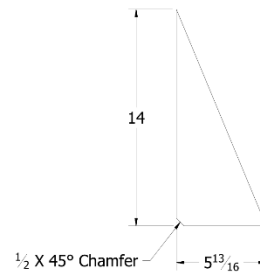
REV:



BP2_R2
A572 Grade 50 t=3/4"

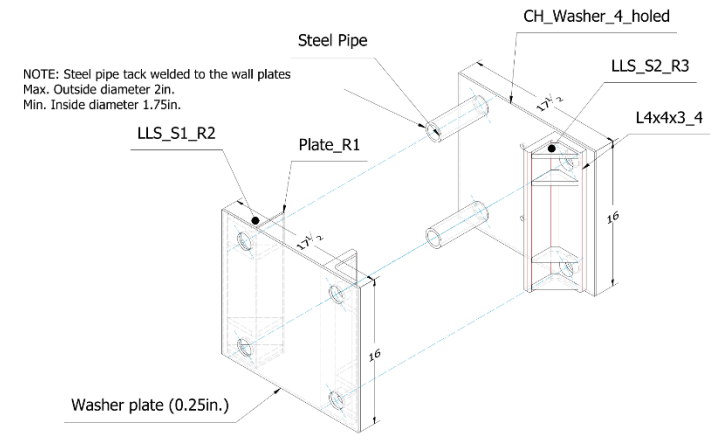
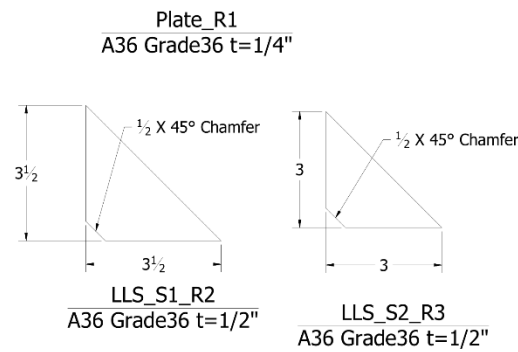
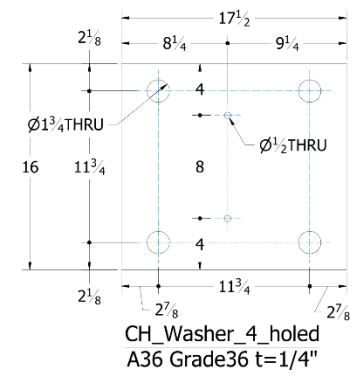
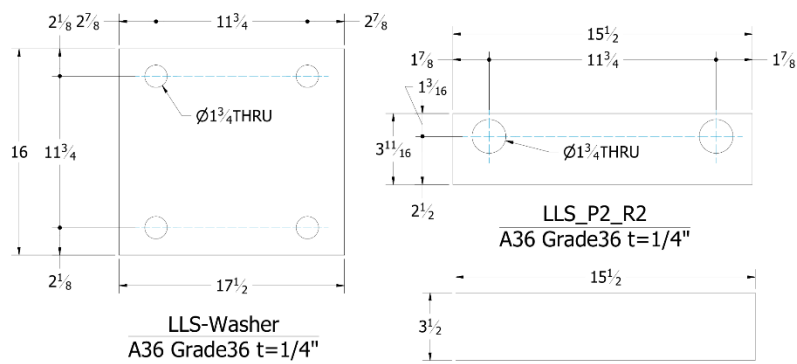


BP1_R2
A572 Grade 50 t=3/4"

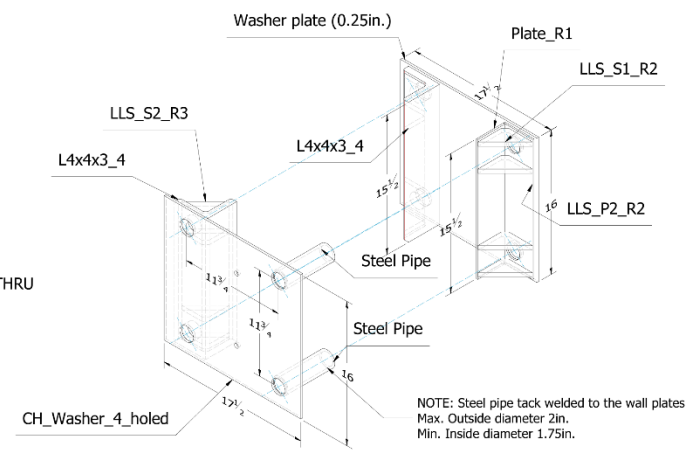
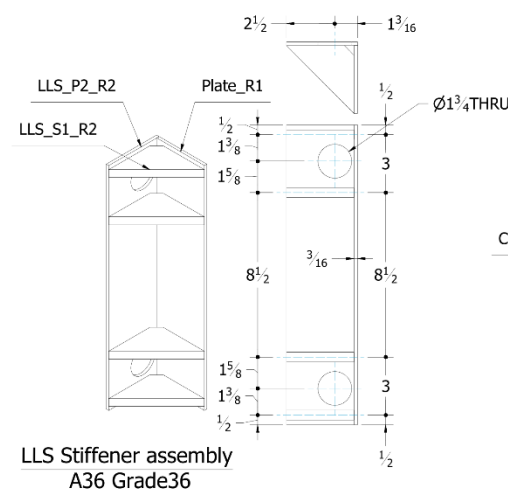
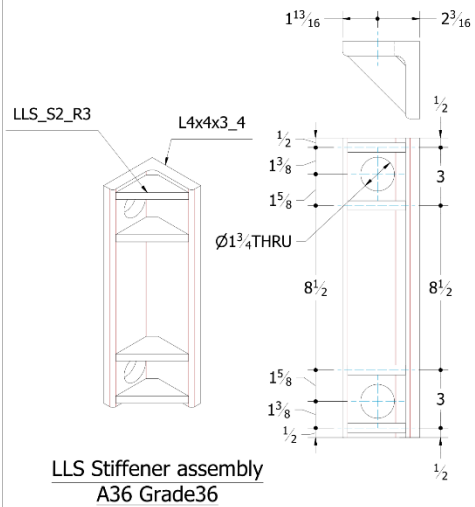


BPS2_F
A572 Grade 50 t=1/2" SCALE:1 / 5

UNIVERSITY AT BUFFALO		
206 KETTER HALL BUFFALO, NY, 14226		
Title: CPF#06-16: CF-CPSW UB TEST SETUP CAD Drawing: C-Shape Wall System_Base Plates:12		
Page: 12of23	DATE: 12/6/2017	STATUS: For Mnfctng
	BY: Hadi Kenarangi	REV:

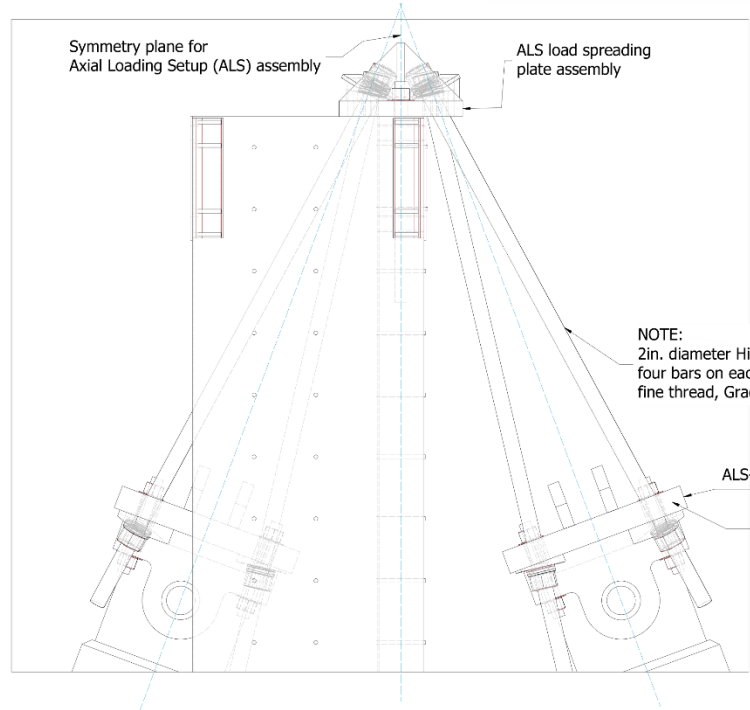
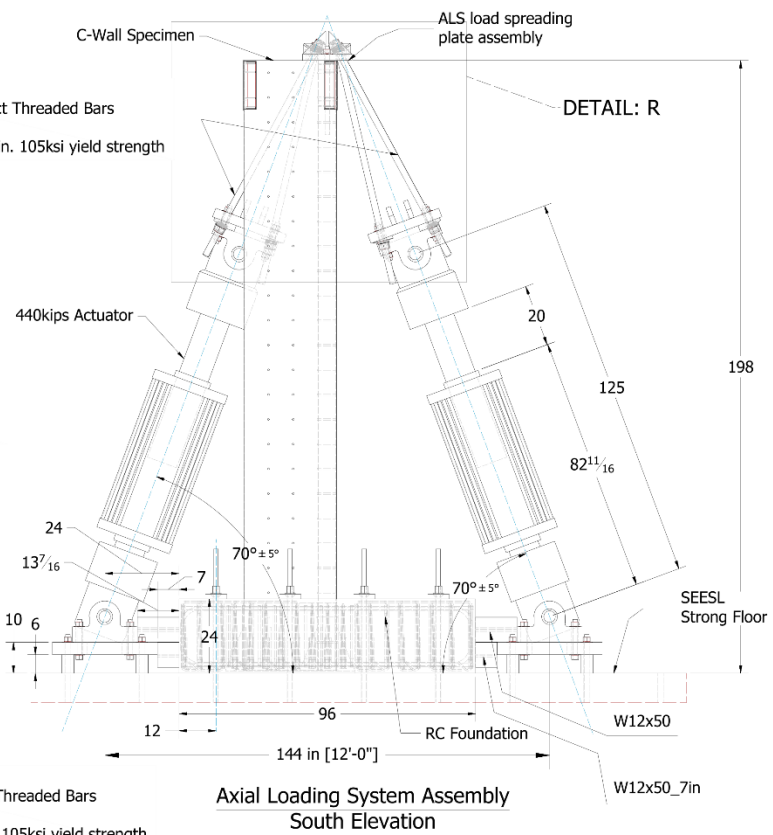
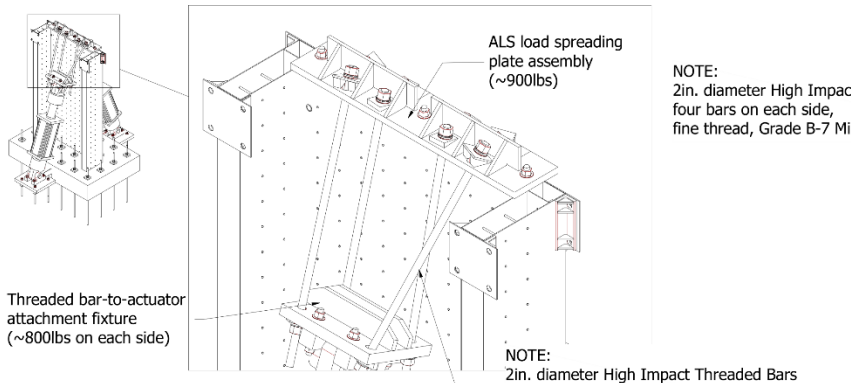


Lateral Loading System (LLS) at top of the wall



Lateral Loading System (LLS) at top of the wall
Opposite angle

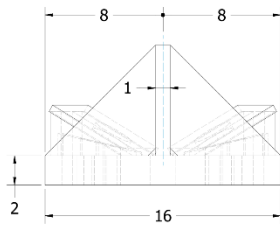
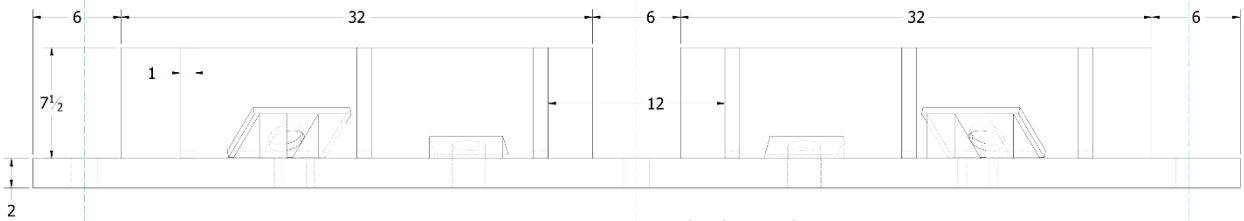
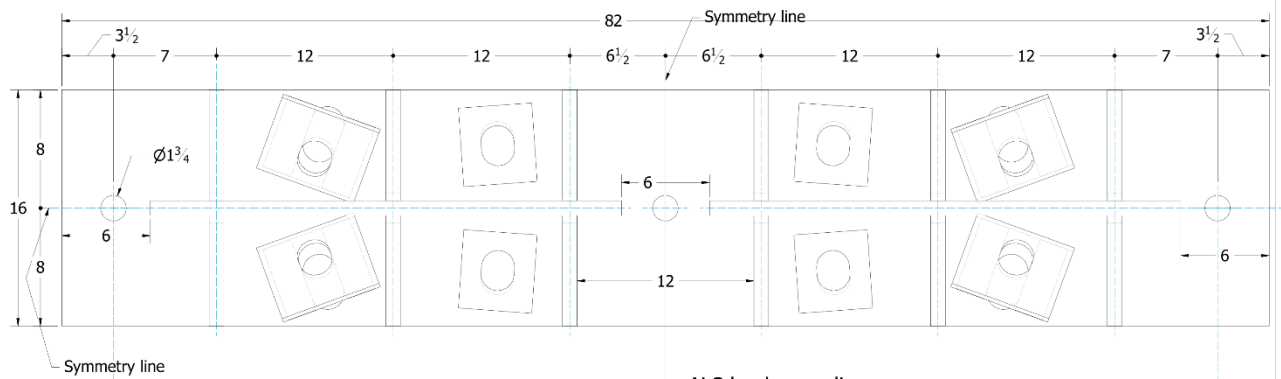
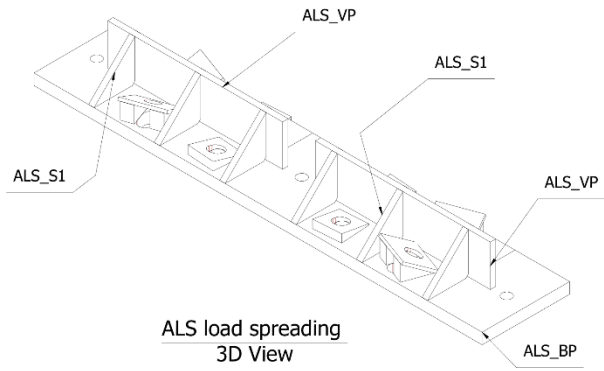
UNIVERSITY AT BUFFALO		
206 KETTER HALL BUFFALO, NY, 14226		
Title: CPF#06-16: CF-CPSW UB TEST SETUP CAD Drawing: C-Shape Wall System_LLS:13		
Page: 13of23	DATE: 12/6/2017	STATUS: For Mnfctrng
	BY: Hadi Kenarangi	REV:



DETAIL R
SCALE: 1 / 10

NOTE: Drawing provided only to illustrate how final parts will be assembled with lab equipment.

UNIVERSITY AT BUFFALO		
206 KETTER HALL BUFFALO, NY, 14226		
Title: CPF#06-16: CF-CPSW UB TEST SETUP CAD		
Drawing:		
Page: 14of23	DATE: 12/6/2017 BY: Hadi Kenarangi	STATUS: For Mnfctng REV: 00



UNIVERSITY AT BUFFALO

206 KETTER HALL
BUFFALO, NY, 14226

Title: CPF#06-16: CF-CPSW UB TEST SETUP CAD

Drawing:

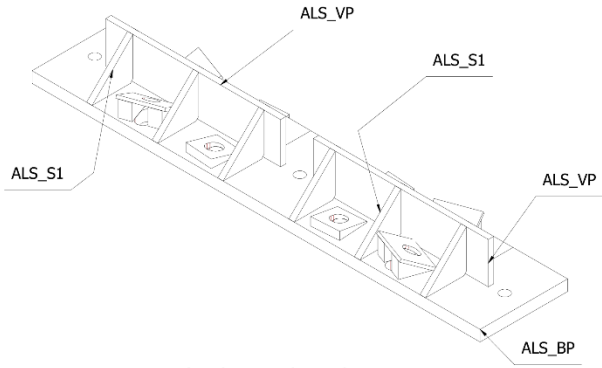
Page:
15of23

DATE: 12/6/2017

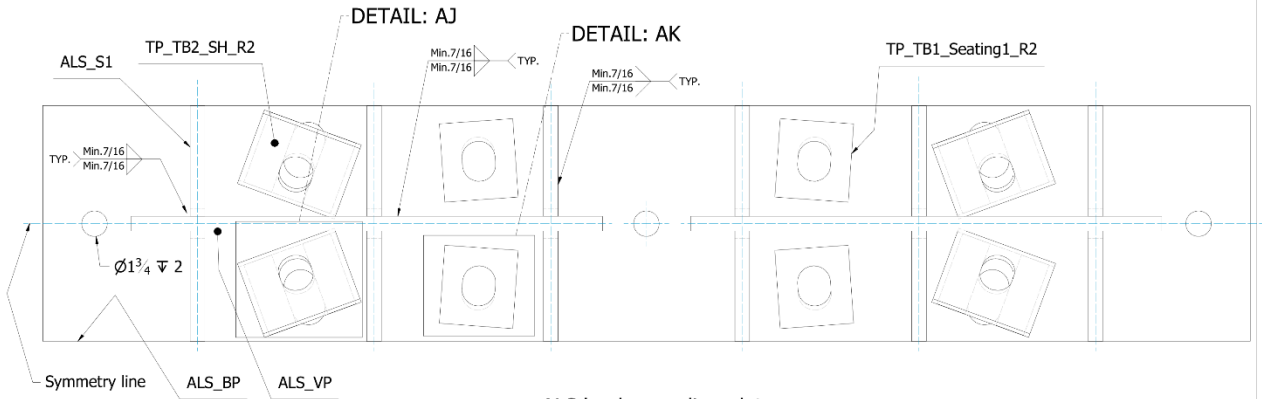
BY: Hadi Kenarangi

STATUS: For Mfrctng

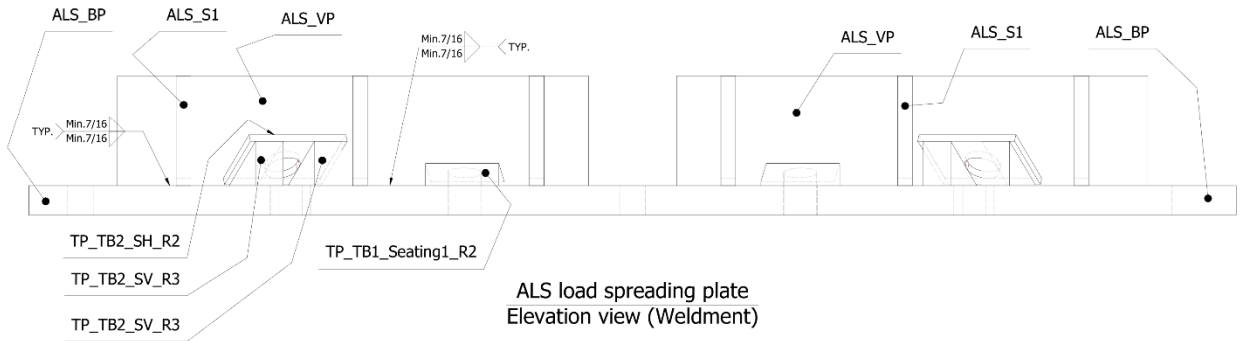
REV:



ALS load spreading plate



ALS load spreading plate
Top view (Weldment)



ALS load spreading plate
Elevation view (Weldment)

UNIVERSITY AT BUFFALO

206 KETTER HALL
BUFFALO, NY, 14226

Title: CPF#06-16: CF-CPSW UB TEST SETUP CAD

Drawing:

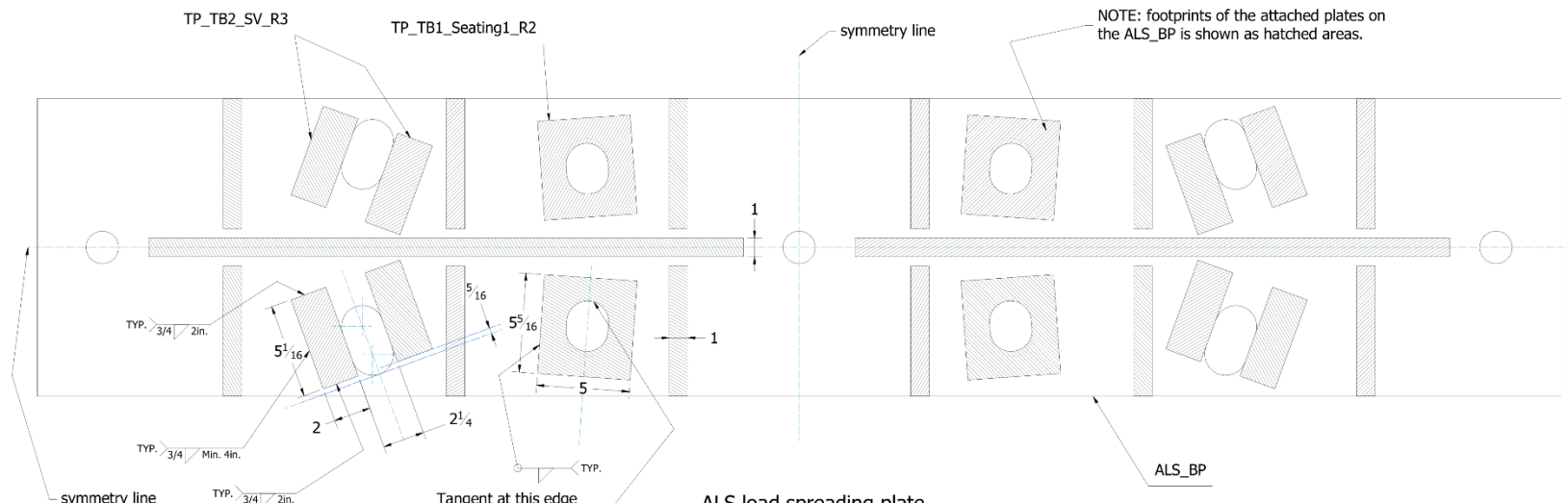
Page:
16of23

DATE: 12/6/2017

BY: Hadi Kenarangi

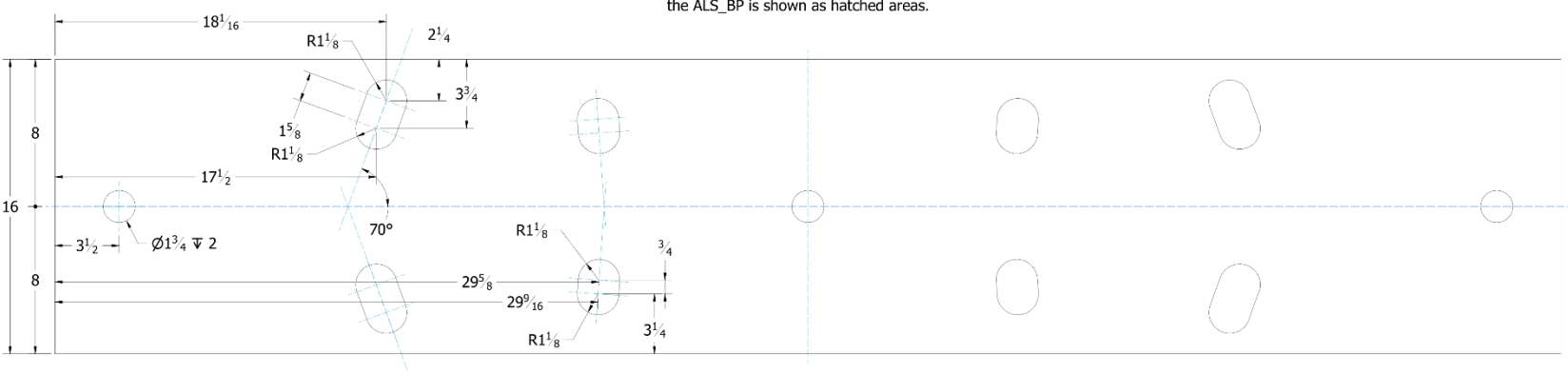
STATUS: For Mnfrctng

REV:



ALS load spreading plate
Top view SCALE: 1/4

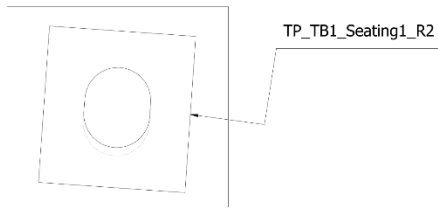
NOTE: footprints of the attached plates on the ALS_BP is shown as hatched areas.



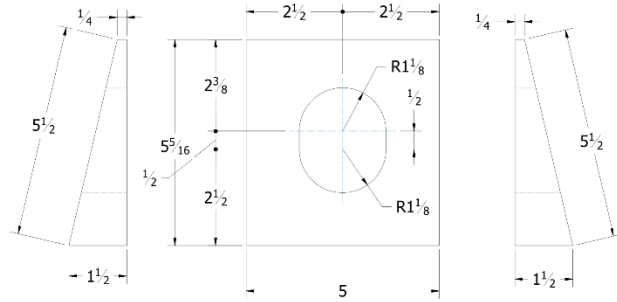
ALS_BP
Top view hole configurations SCALE: 1/4
t=2in. A36 Grade 36

- NOTES:
- Precise detail
 - Hole arrangements are symmetric with respect to shown symmetry lines
 - Allowable tolerance $\pm 1/16$ "

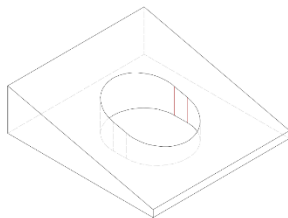
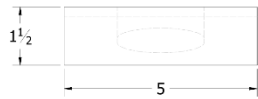
UNIVERSITY AT BUFFALO		
206 KETTER HALL BUFFALO, NY, 14226		
Title: CPF#06-16: CF-CPSW UB TEST SETUP CAD		
Drawing:		
Page: 17of23	DATE: 12/6/2017 BY: Hadi Kenarangi	STATUS: For Mnfctng REV:



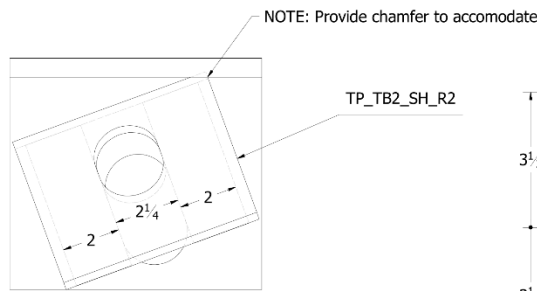
DETAIL AK
REF:16



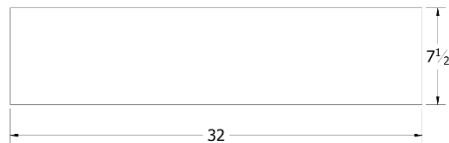
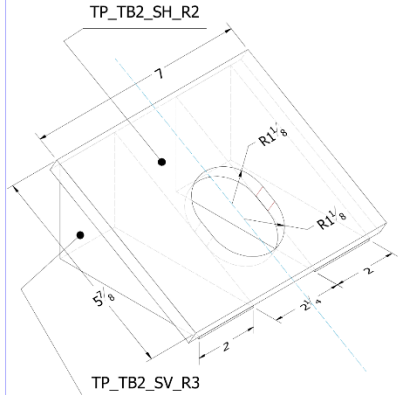
TP_TB1_Seating1_R2



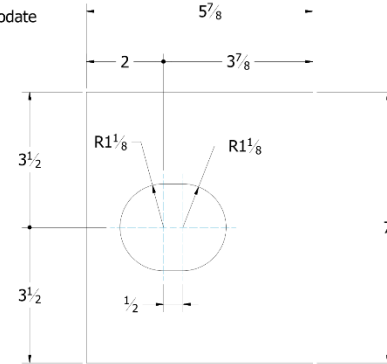
TP_TB1_Seating1_R2
3D view



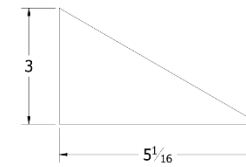
DETAIL AJ
REF: 16



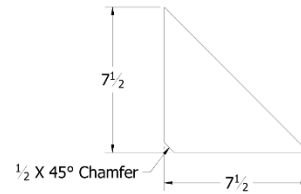
ALS_VP
t=1in., A36 Grade 36ksi



TP_TB2_SH_R2
t=1/2in. Grade A36



TP_TB2_SV_R3
t=2in. Grade A36



ALS_S1
t=1in., A36 Grade 36ksi

UNIVERSITY AT BUFFALO

206 KETTER HALL
BUFFALO, NY, 14226

Title: CPF#06-16: CF-CPSW UB TEST SETUP CAD
Drawing:

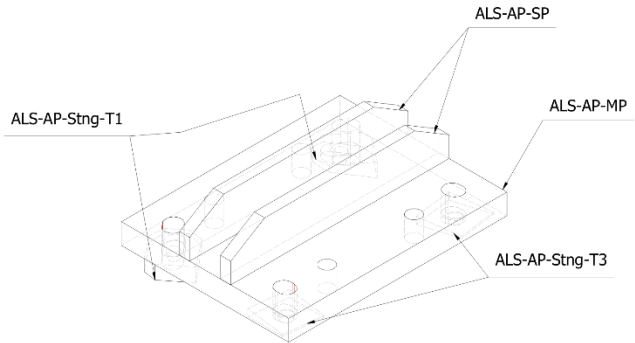
Page:
18of23

DATE: 12/6/2017

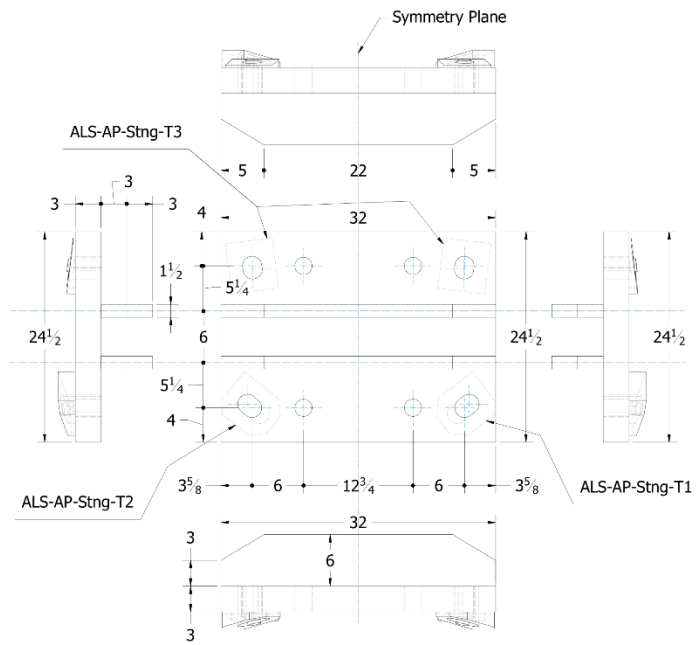
STATUS: For Mnfctng

BY: Hadi Kenarangi

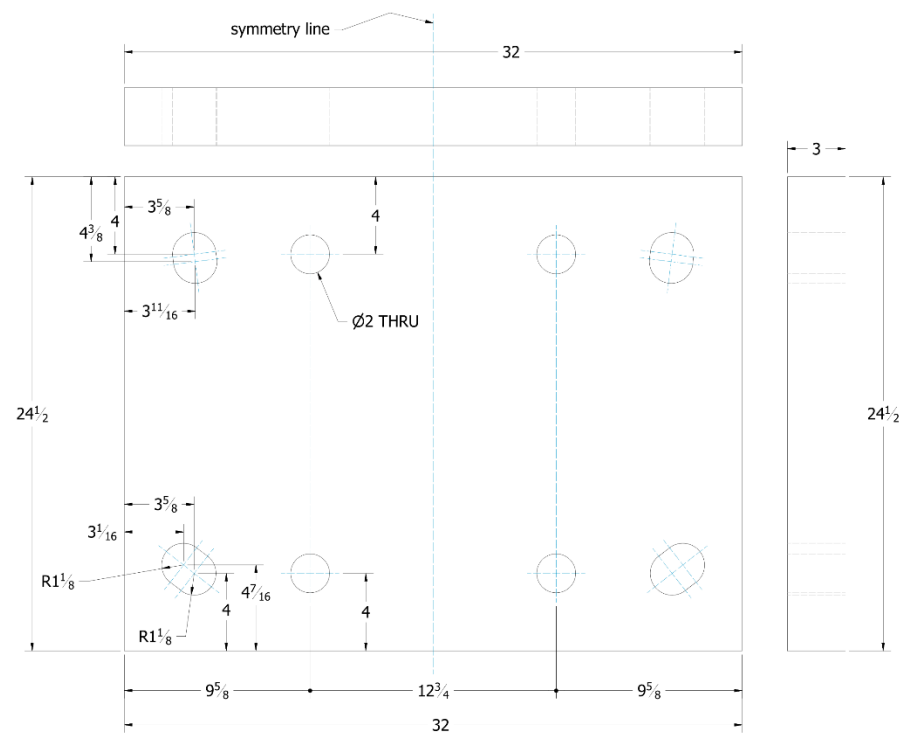
REV:



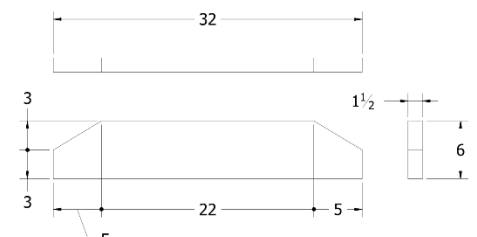
Actuator Attachment Plate



Actuator Attachment Plate Assembly Details
SCALE: 1/9 Grade 36ksi

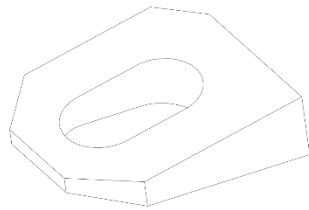


ALS-AP-MP
t=3in. Grade 36ksi SCALE: 1/4

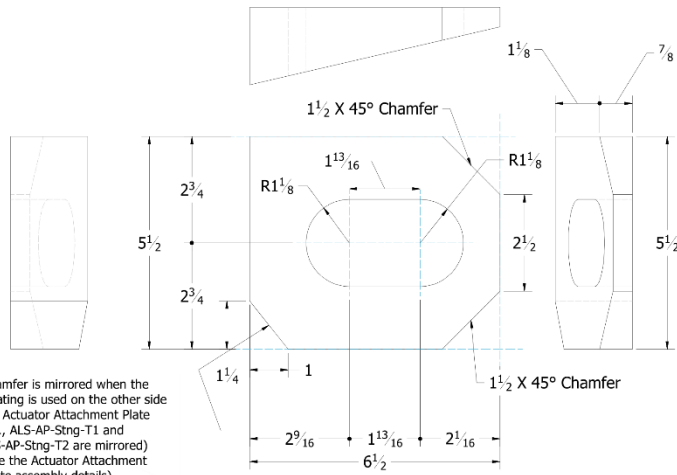


ALS-AP-SP
t=1.5in. Grade 36ksi SCALE: 1/8

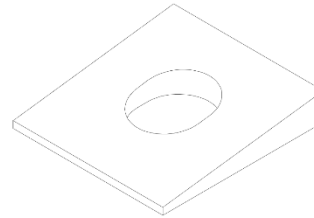
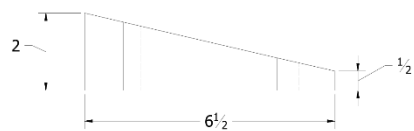
UNIVERSITY AT BUFFALO		
206 KETTER HALL BUFFALO, NY, 14226		
Title: CPF#06-16: CF-CPSW UB TEST SETUP CAD		
Drawing:		
Page: 19of23	DATE: 12/6/2017 BY: Hadi Kenarangi	STATUS: For Mnfctng REV: 00



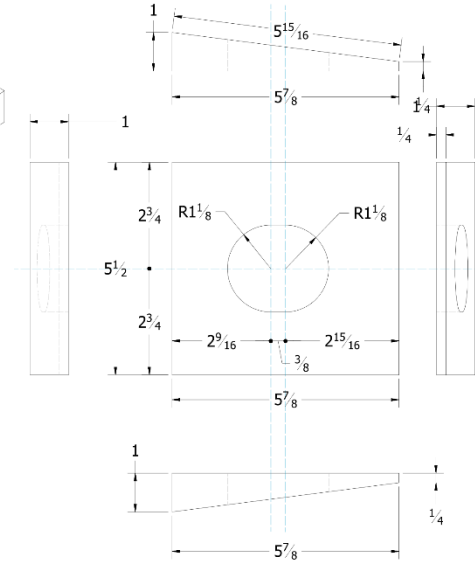
ALS-AP-Stng-T2
and ALS-AP-Stng-T1



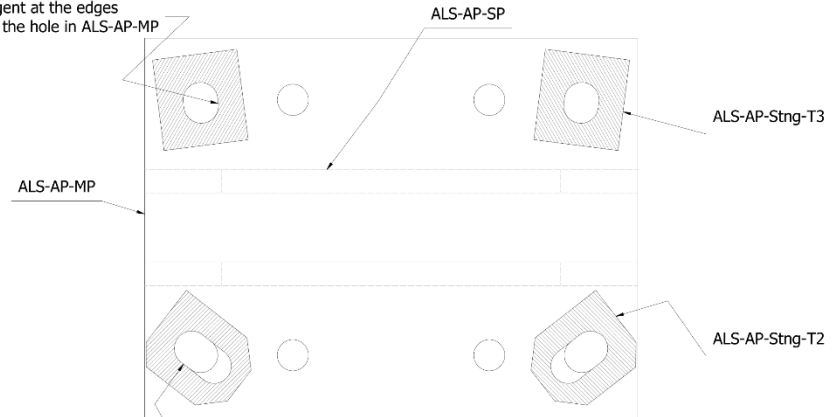
NOTE: Chamfer is mirrored when the seating is used on the other side of Actuator Attachment Plate (i.e., ALS-AP-Stng-T1 and ALS-AP-Stng-T2 are mirrored) (See the Actuator Attachment Plate assembly details)



ALS-AP-Stng-T3



Tangent at the edges
with the hole in ALS-AP-MP



Actuator Attachment Plate Bearing Plates Footprints
SCALE: 1/5 Grade 36ksi

Tangent at the edges
with the hole in ALS-AP-MP

UNIVERSITY AT BUFFALO

206 KETTER HALL
BUFFALO, NY, 14226

Title: CPF#06-16: CF-CPSW UB TEST SETUP CAD

Drawing:

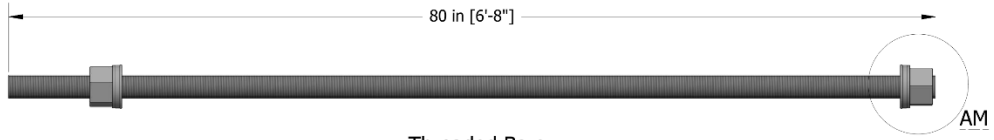
Page:
200fZ3

DATE: 12/6/2017

STATUS: For Mnfctrng

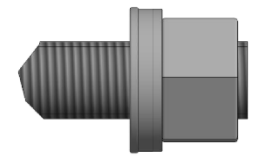
BY: Hadi Kenarangi

REV: 00

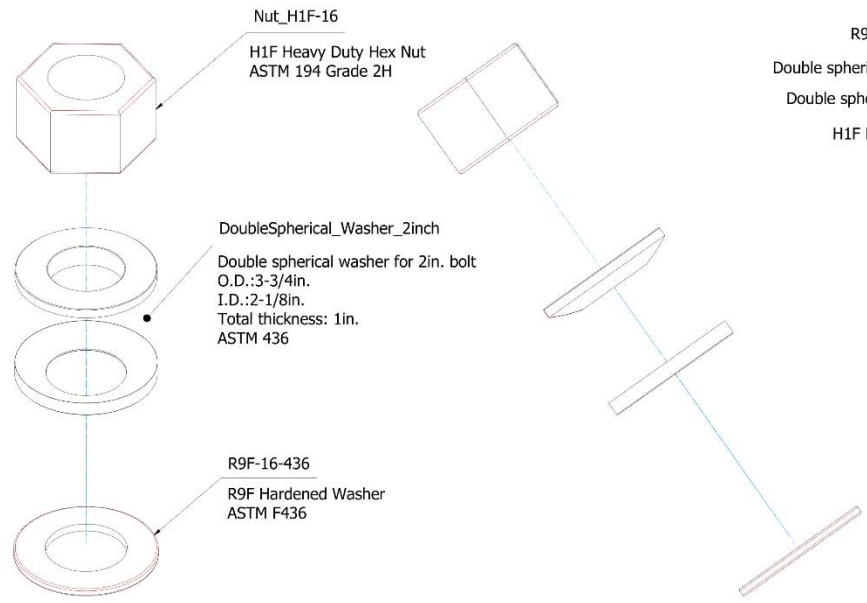
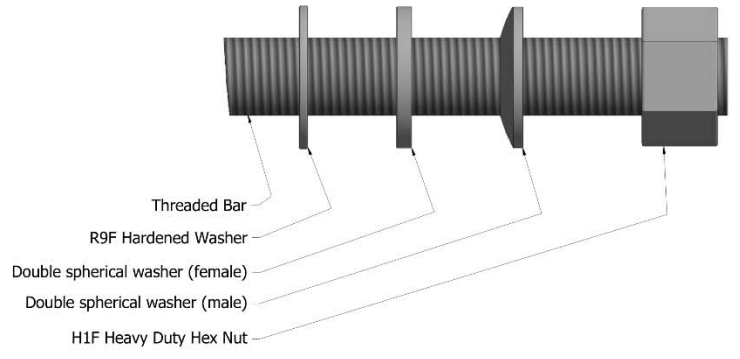


Threaded Bars

- NOTE:
- 2in. diameter high impact threaded bars with fine thread.
 - Material grade: B-7, Min. 105ksi yield strength.
 - Each bar includes two hardened flat washers, two heavy nuts, and two double spherical washers on each side.



DETAIL AM



UNIVERSITY AT BUFFALO		
206 KETTER HALL BUFFALO, NY, 14226		
Title: CPF#06-16: CF-CPSW UB TEST SETUP CAD		
Drawing:		
Page: 21of23	DATE: 12/6/2017 BY: Hadi Kenarangi	STATUS: For Mnfctrng REV:

BOM per C-Shape Wall

Item	Part Number	Unit QTY	QTY	Description	System	REF. Page	Filename	Part Volume, C.in	Part Weight, lbs	WeightsQTY, lbs	Comments
W-1	LLS-Washer	1	2	A36 Gr.36ksi	Wall	13	CH_Washer_4.ipt	67.6	19.2	38.3	
W-2	Plate_R1	1	2	A36 Gr.36ksi	Wall	13	Plate_R1.ipt	10.2	2.9	5.8	
W-3	LLS_S1_R2	1	8	A36 Gr.36ksi	Wall	13	LLS_S1_R2.ipt	3	0.9	6.8	
W-4	LLS_P2_R2	1	2	A36 Gr.36ksi	Wall	13	LLS_P2_R2.ipt	9.8	2.8	5.6	
W-5	CH_Washer_4_holed	1	2	A36 Gr.36ksi	Wall	13	CH_Washer_4_holed.ipt	67.5	19.1	38.3	
W-6	LLS_S2_R3	1	16	A36 Gr.36ksi	Wall	13	LLS_S2_R3.ipt	2.2	0.6	9.9	
W-7	L4x4x3_4	16,000 in	64,000 in	A36 Gr.36ksi, Steel Angle	Wall	13	L4x4x3_4.ipt	84.7	24	96.1	
W-8	DPF2_R1	1	1	A572 Gr. 50ksi. Actual yield strength no more than 60ksi.	Wall	10	DPF2_R1.ipt	387.5	109.9	109.9	
W-9	SW_T3R4	1	4	A572 Gr. 50ksi. Actual yield strength no more than 60ksi.	Wall	9	SW_T3R4.ipt	1107.8	314.2	1256.6	
W-10	SW_T1R3	1	2	A572 Gr. 50ksi. Actual yield strength no more than 60ksi.	Wall	8	SW_T1R3.ipt	2966	841.2	1682.3	
W-11	SW_T2NHR2	1	2	A572 Gr. 50ksi. Actual yield strength no more than 60ksi.	Wall	9	SW_T2NHR2.ipt	295.9	83.9	167.8	
W-12	SW_T2R3	1	4	A572 Gr. 50ksi. Actual yield strength no more than 60ksi.	Wall	9	SW_T2R3.ipt	295	83.7	334.6	
W-13	BP1_R2	1	2	A572 Gr. 50ksi. Actual yield strength no more than 60ksi.	Wall	12	BP1_R2.ipt	638.1	181	361.9	
W-14	BP2_R2	1	1	A572 Gr. 50ksi. Actual yield strength no more than 60ksi.	Wall	12	BP2_R2.ipt	928.1	263.2	263.2	
W-15	BPS2_F	1	42	A572 Gr. 50ksi. Actual yield strength no more than 60ksi.	Wall	12	BPS2_F.ipt	20.3	5.8	241.6	
W-16	DP_R2	1	1	A572 Gr. 50ksi. Actual yield strength no more than 60ksi.	Wall	10	DP_R2.ipt	317.8	90.1	90.1	
W-17	DPW_R1	1	2	A572 Gr. 50ksi. Actual yield strength no more than 60ksi.	Wall	11	DPW_R1.ipt	97.7	27.7	55.4	
W-18	DPW2_R1	1	2	A572 Gr. 50ksi. Actual yield strength no more than 60ksi.	Wall	11	DPW2_R1.ipt	34.2	9.7	19.4	
W-19	DPW3_R1	1	2	A572 Gr. 50ksi. Actual yield strength no more than 60ksi.	Wall	11	DPW3_R1.ipt	122.2	34.7	69.3	
W-20	Steel Pipe	1	4	Any steel grade, steel pipe. See drawings for size limitations.	Wall	13	1.5_PVC_Pipe.ipt	8.2	2.3	9.4	
W-21	Tie0625_FR2	1	260	F1554 Grade 55, 0.5in. diameter tie rods, length:6.375in.	Wall	-	Tie0625_FR2.ipt	1.3	0.4	92.3	
W-22	Tie0625_FR3	1	8	F1554 Grade 55, 0.5in. diameter tie rods, length:6.625in.	Wall	-	Tie0625_FR3.ipt	1.3	0.4	3	
W-23	Tie0625_FR4	1	20	F1554 Grade 55, 0.5in. diameter tie rods, length:6.75in.	Wall	-	Tie0625_FR4.ipt	1.3	0.4	7.5	
W-24	Tie0625_WR2	1	88	F1554 Grade 55, 0.5in. diameter tie rods, length:8.75in.	Wall	-	Tie0625_WR2.ipt	1.7	0.5	42.9	
W-25	Tie0625_WR3	1	8	F1554 Grade 55, 0.5in. diameter tie rods, length:9.125in.	Wall	-	Tie0625_WR3.ipt	1.8	0.5	4.1	
T									Total A36 Gr.36ksi	201	
T									Total A572 Gr. 50ksi	4652	
T									Total F1554 Gr. 55ksi	150	
T									Grand Total	5012	

UNIVERSITY AT BUFFALO
 206 KETTER HALL
 BUFFALO, NY, 14226

Title: CPF#06-16: CF-CPSW UB TEST SETUP CAD
 Drawing:

Page: 22of23	DATE: 12/6/2017	STATUS: For Mnfctrng
	BY: Hadi Kenarangi	REV: 00

BOM for Axial Loading Setup (ALS) System											
Item	Part Number	Unit QTY	QTY	Description	System	REF Page	Filename	Part Volume, C.in	Part Weight, lbs	WeightsQTY, lbs	Comments
A-1	ID2X123X75PR_Female	1	16	ASTM 436 double spherical washer for 2in. diameter rod (female)	ALS	21	ID2X123X75PR_Female.ipt	1.6	0.5	7.2	Part No. ID2X123X75PR from Robt. L. Rowan & Assoc., Inc. or equivalent. www.rlrowan.com
A-2	ID2X123X75PR_Male	1	16	ASTM 436 double spherical washer for 2in. diameter rod (male)	ALS	21	ID2X123X75PR_Male.ipt	3.2	0.9	14.5	Part No. ID2X123X75PR from Robt. L. Rowan & Assoc., Inc. or equivalent. www.rlrowan.com
A-3	ALS_BP	1	1	A36 Gr.36ksi	ALS	17	ALS_BP.ipt	2503.7	710	710	
A-4	ALS_S1	1	12	A36 Gr.36ksi	ALS	18	ALS_S1.ipt	28	7.9	95.3	
A-5	ALS_VP	1	2	A36 Gr.36ksi	ALS	18	ALS_VP.ipt	240	68.1	136.1	
A-6	TP_TB1_Scating1_R2	1	4	A36 Gr.36ksi	ALS	18	TP_TB1_Scating1_R2.ipt	19	5.4	21.5	
A-7	TP_TB2_SH_R2	1	4	A36 Gr.36ksi	ALS	18	TP_TB2_SH_R2.ipt	18	5.1	20.4	
A-8	TP_TB2_SV_R3	1	8	A36 Gr.36ksi	ALS	18	TP_TB2_SV_R3.ipt	15.6	4.4	35.4	
A-9	ALS-AP-MP	1	2	A36 Gr.36ksi	ALS	19	Actuator_Plate_Design1.ipt	2251.9	638.6	1277.3	
A-10	ALS-AP-Stng-T1	1	2	A36 Gr.36ksi	ALS	20	AP_Scating_1.ipt	33.8	9.6	19.2	
A-11	ALS-AP-Stng-T2	1	2	A36 Gr.36ksi	ALS	20	AP_Scating_11.ipt	34.7	9.8	19.7	
A-12	ALS-AP-SP	1	4	A36 Gr.36ksi	ALS	19	AP_Stiff1.ipt	265.5	75.3	301.2	
A-13	ALS-AP-Stng-T3	1	4	A36 Gr.36ksi	ALS	20	AP_Scating_21.ipt	18.4	5.2	20.9	
A-14	B8V-16	1	8	ASTM 193 B8V Grade B7 High Impact Bar, 2in. diameter Fine UNC thread form, Length 80in.	ALS	21	B8V-16.ipt	251.3	71.3	570.2	Part No. B8V-16 from Williams Form Eng. Corp. or equivalent. See: http://www.williamsform.com
A-15	Nut_H1F-16	1	16	ASTM 194 Grade 2H, H1F Heavy Duty Hex Nuts for 2in. bar, Fine thread, Thickness: 1-31/32in.	ALS	21	Nut_H1F-16.ipt	10.4	3	47.4	Part No. H1F-16 from Williams Form Eng. Corp. or equivalent. See: http://www.williamsform.com
A-16	R9F-16-436	1	16	ASTM F436 flat washer for 2in. diameter rod. Thickness: 7/32in.	ALS	21	R9F-16-436.ipt	1.6	0.5	7.4	Part No. RPF-16-436 from Williams Form Eng. Corp. or equivalent. See: http://www.williamsform.com
A-17	W12x50	1	2	W12x50 Grade 50, 13.5in. loose	ALS	-	W12x50.ipt	198	56.2	112.3	Loose part
A-18	W12x50_7in	1	2	W12x50 Grade 50, 7in. loose	ALS	-	W12x50_7in.ipt	102.7	29.1	58.2	Loose part
T									Total A36 Gr.36ksi	2657	
T									Total A572 Gr. 50ksi	170.5	
T									Grand Total	3474	

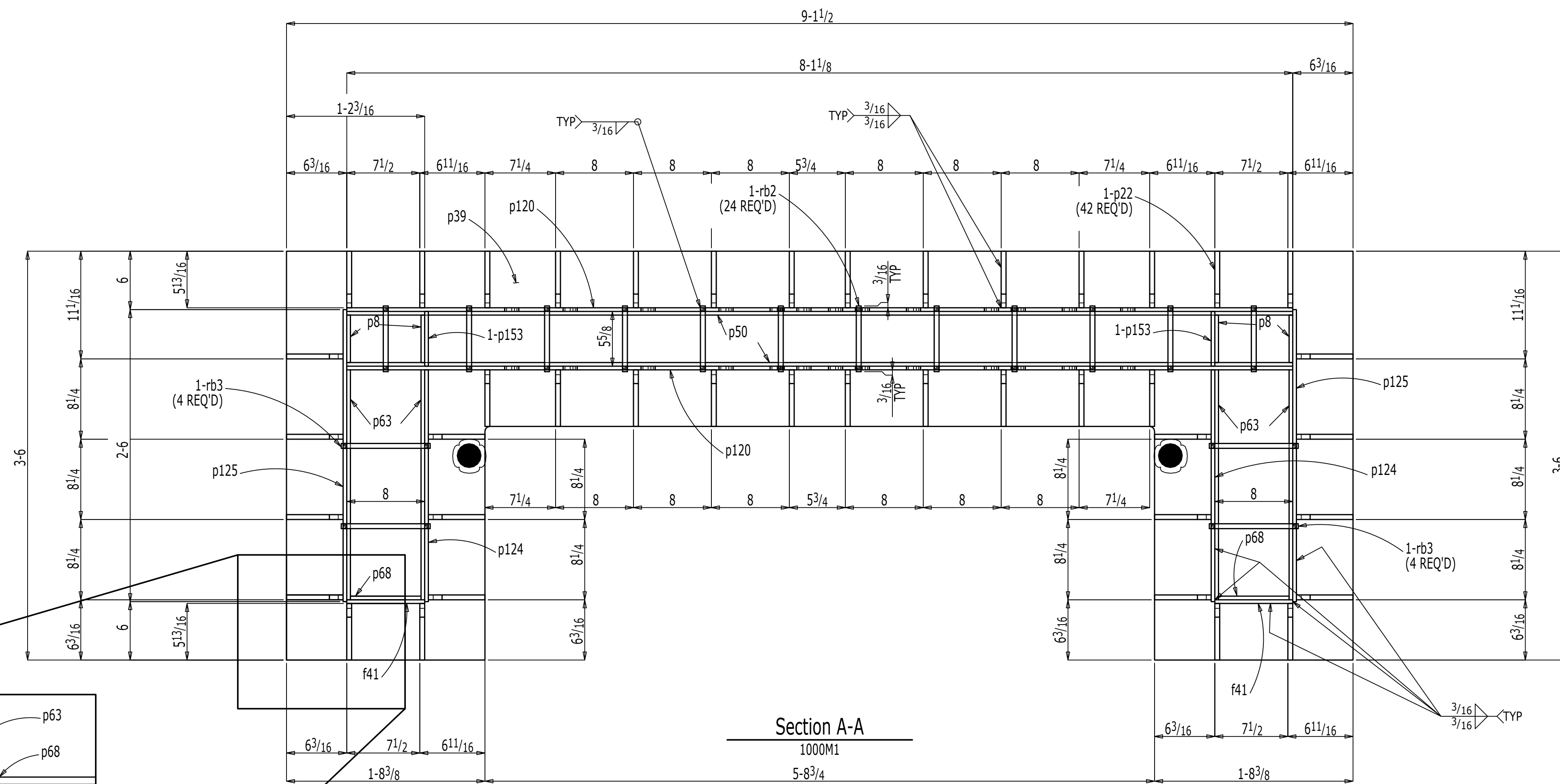
General Notes:

- 2 series of C-shape wall system (See BOM per C-Shape Wall) to be constructed and delivered.
- 1 series of the Axial Loading Setup (ALS) system (See BOM for Axial Loading Setup) to be constructed and delivered.
- E70xx electrode used for all weld designs.
- All tie rods are 0.5in. diameter F1554 Grade 55ksi (Mark AB55 PB).
- For research purposes the actual maximum yield strength of A572 Gr. 50ksi used in wall system should not be more than 60ksi. An actual yield strength closer to 50ksi is desirable.
- For tensile coupon tests in the lab, minimum of two plates of 12x12in. of each A572 Gr. 50ksi steel batch used in the Wall system construction should be included in the product delivery.
- For tensile coupon tests in the lab, minimum of four rods of minimum 12in. long of each F1554 Grade 55ksi used in the construction of wall system should be included in the product delivery.
- For research purposes, Items W-9 to W-12 shown in the BOM per C-Shape Wall (which are the wall steel face plates) must be constructed from one single steel plate batch for both C-Shape wall deliveries.
- For research purposes, Items W-21 to W-25 shown in the BOM per C-Shape Wall (which are the wall tie rods) must be constructed from one single steel batch for both C-Shape wall deliveries.

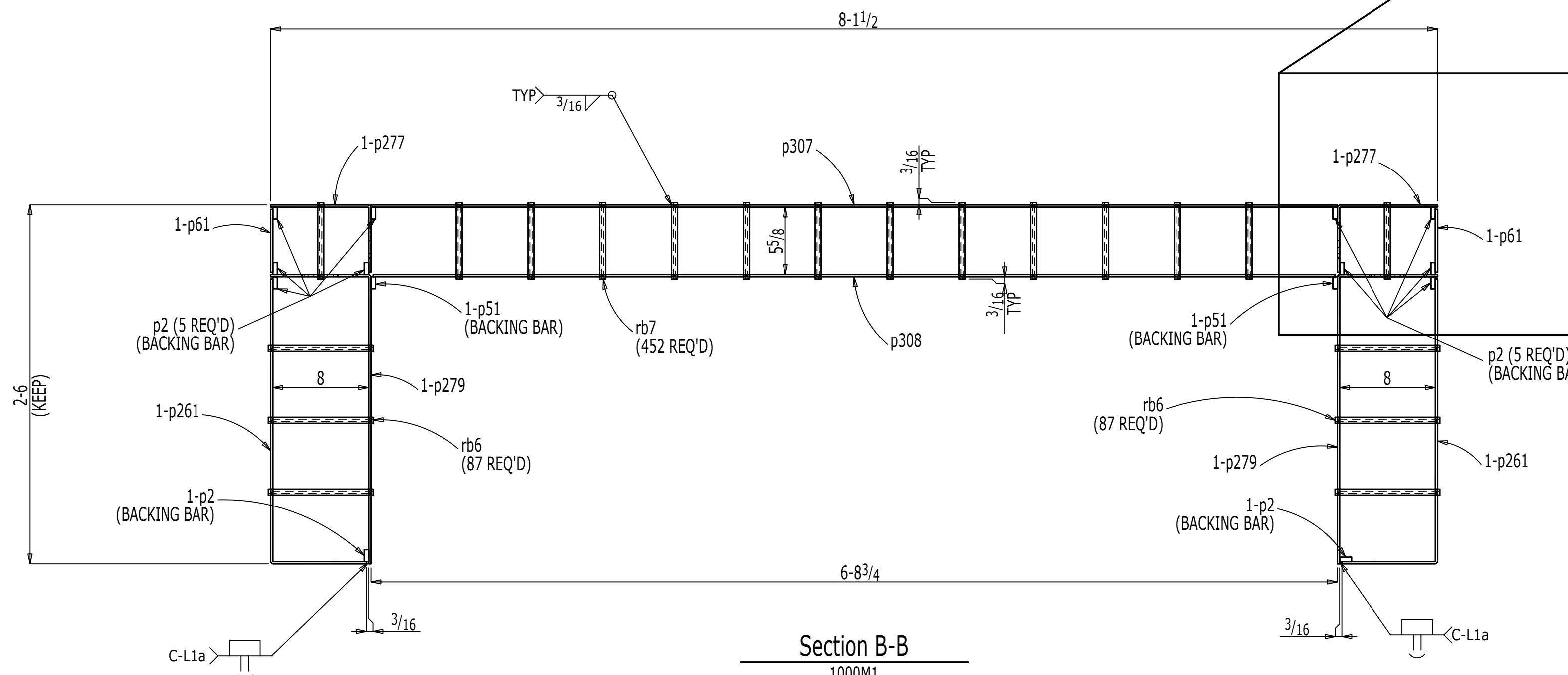
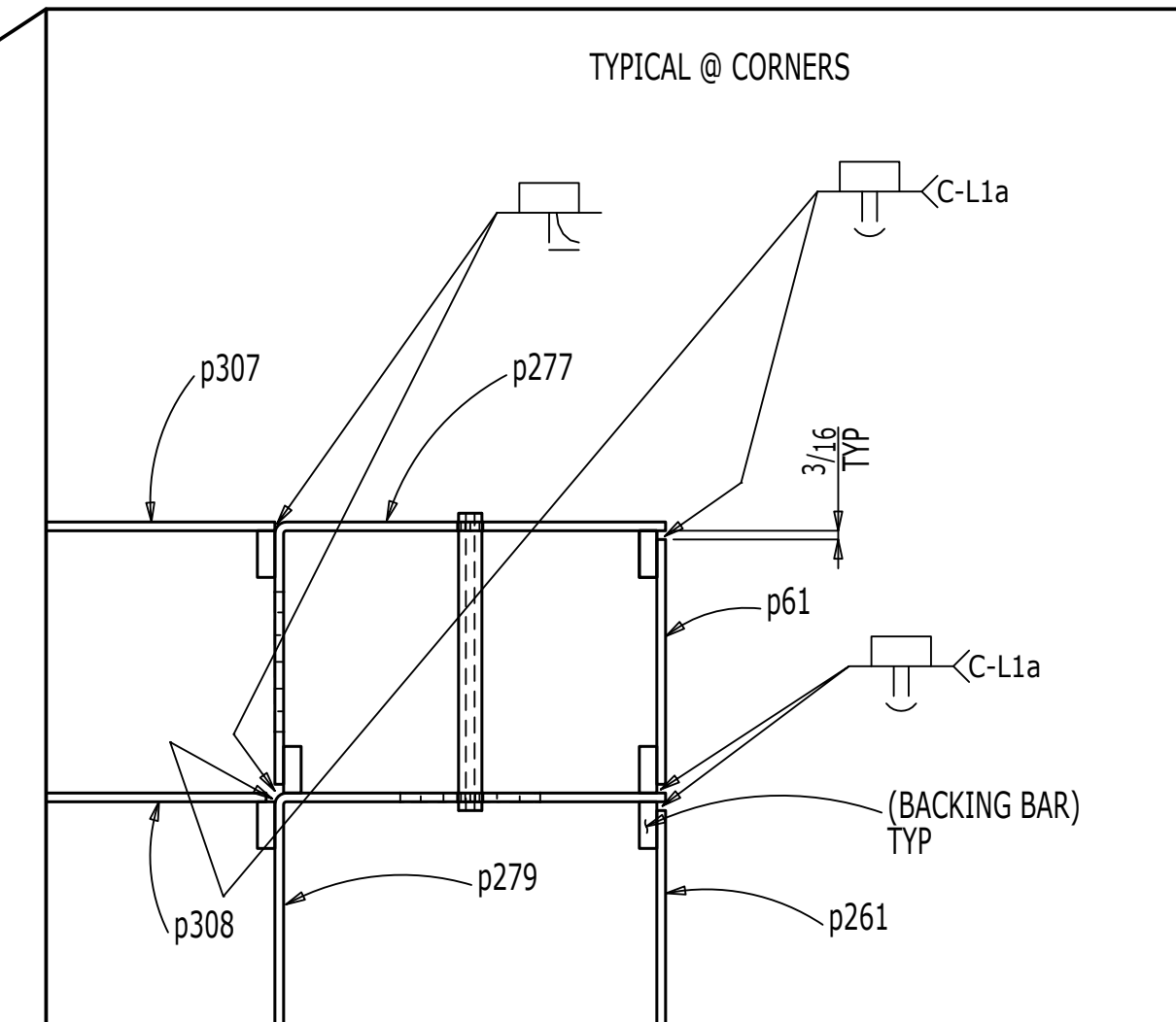
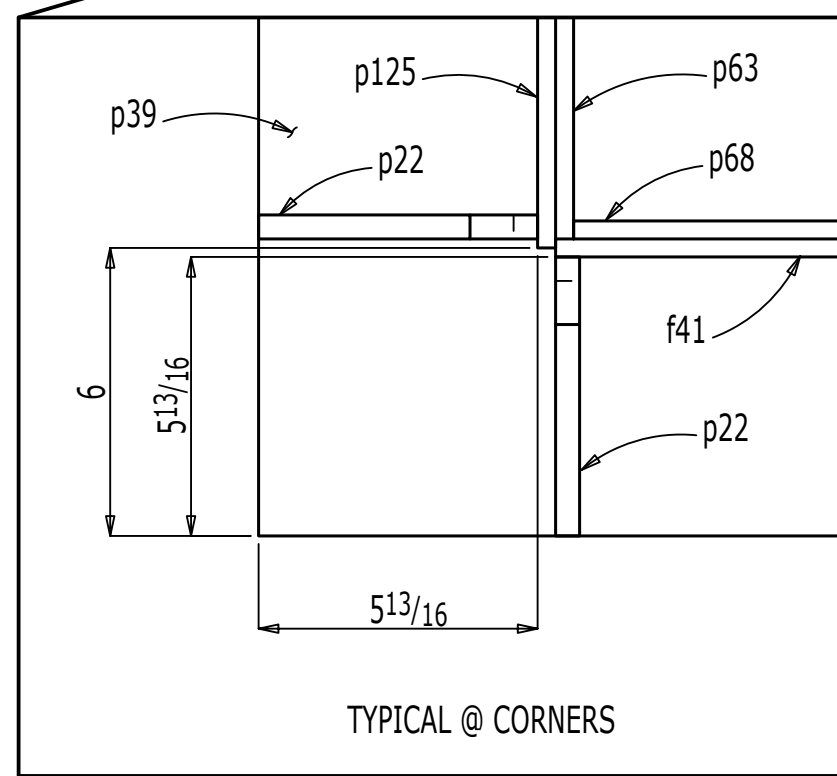
UNIVERSITY AT BUFFALO		
206 KETTER HALL BUFFALO, NY, 14226		
Title: CPF#06-16: CF-CPSW UB TEST SETUP CAD		
Drawing:		
Page: 23of23	DATE: 12/6/2017	STATUS: For Mnfctrng
	BY: Hadi Kenarangi	REV: 00

C.4 Drawings received from fabricator

AB
B
BK
BP
C
CP
F
G
H
LP
M
P
PG
SR
T
TM
V
X
CR
DW
FP
GR
HR
LA
RC
RP
SB
ST
TP



Section A-A
1000M1
5-8 3/4



Section B-B
1000M1
6-8 3/4

ENG. REF. DRG. No. XXXX

REV	REMARKS	DATE	DWN	CHK	APP
A	ISSUED FOR FABRICATION	Mar 14 2018	GS	PR	CLG
0	ORIGINAL ISSUE	Feb 27 2018	GS	PR	CLG

MEMBERS ARE TO BE ERECTED SO THAT MARKED END IS IN SAME LOCATION AS ON ERECTION DRAWING No. XXXX

GENERAL NOTES	
MATERIAL : AS NOTED	ELECTRODES : E70LH
HOLES : 15/16 DIA UNO	BOLTS : 7/80A325N UNO
SURFACE PREPN & PAINT : NO BLAST NO PAINT	
ALL RUNNING DIMENSIONS FROM END OF MAIN MATERIAL. ALL VERTICAL SPACING OF HOLES TO BE 3" UNLESS NOTED. ALL SNIPS TO BE 3/4 x 3/4 UNLESS NOTED. ALL COPIES TO BE RADIUSSED. "S" IN PIECEMARK OF CONNECTION MATERIAL DENOTES SHORT SLOTS. ALL OPEN ENDS TO HAVE TOLERANCE OF (+/- 1/4") UNO. *INDICATES LAYOUT MARK FOR FABRICATION. ALL H.S. SHOP BOLTS TO BE TORQUED UNLESS NOTED.	

DESCRIPTION	DRAWN BY	DATE
DETAILS C-SHAPE <td>GS</td> <td>02-27-18</td>	GS	02-27-18
JOB : UNIVERSITY AT BUFFALO UB SPECIMENS	CHECKED BY	DATE
	PR	02-27-18
	APPROVED BY	DATE
	CLG	02-27-18
CUSTOMER : BOSTON PROPERTIES	JOB NO.	DRG. NO.
	1261	1001
	Fab: Cives 2015.25_Fab Job: UB_Specimens	REV. A

JOB NO.	DRG NO.
1261	1001

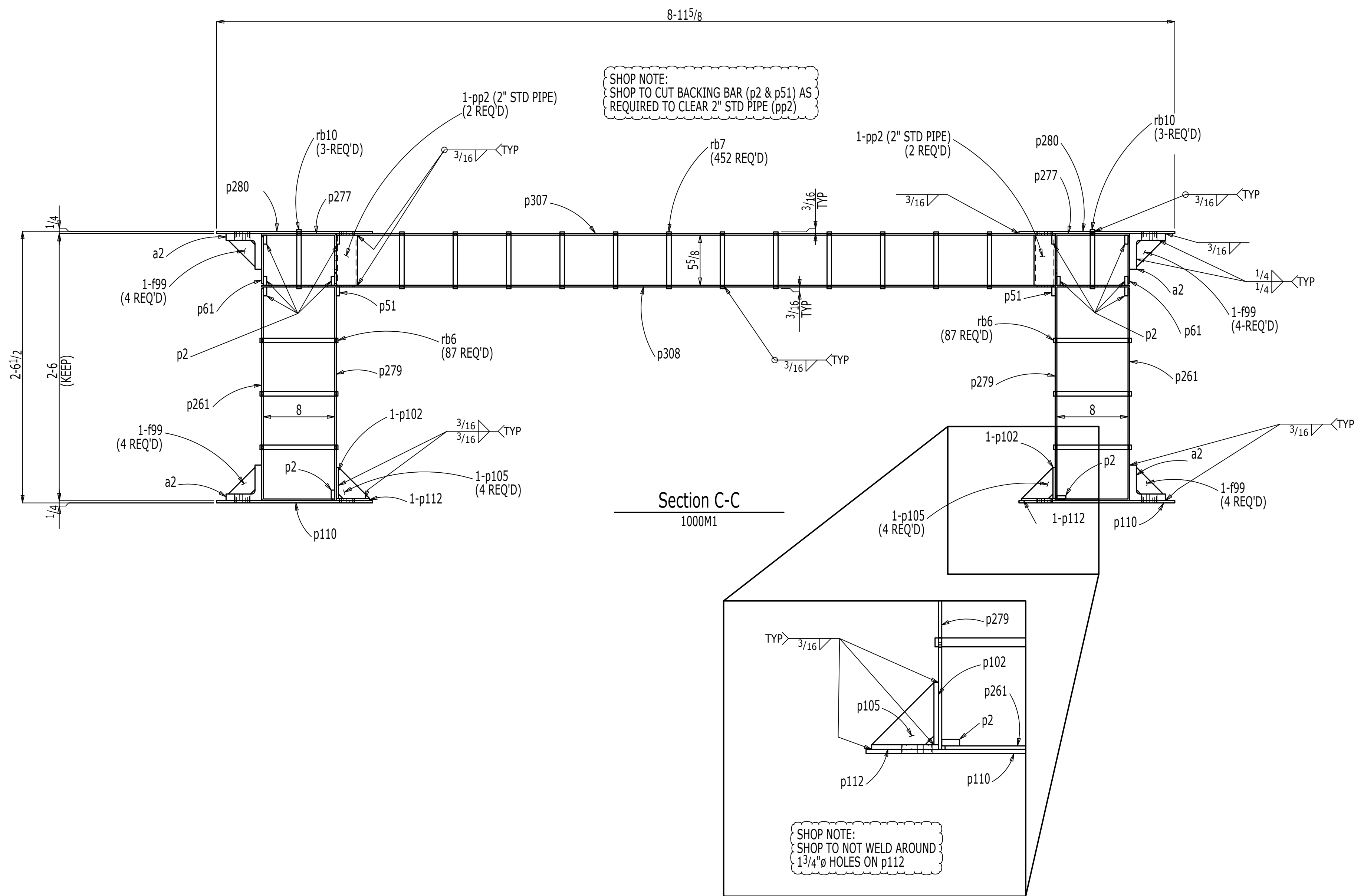
WORK THIS DRAWING WITH DRAWINGS 1000, 1002, 1003 & 1004



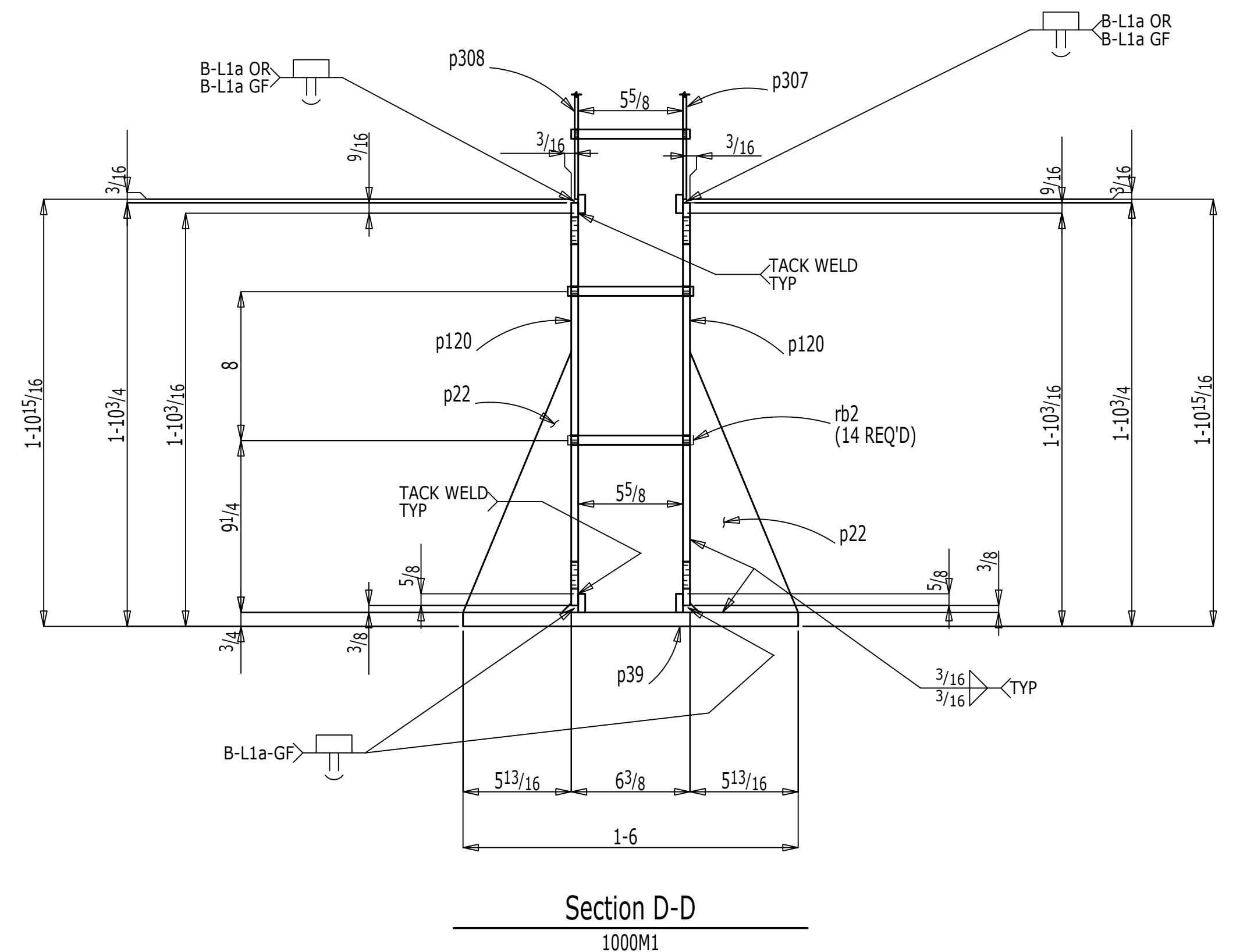
NEW ENGLAND DIVISION



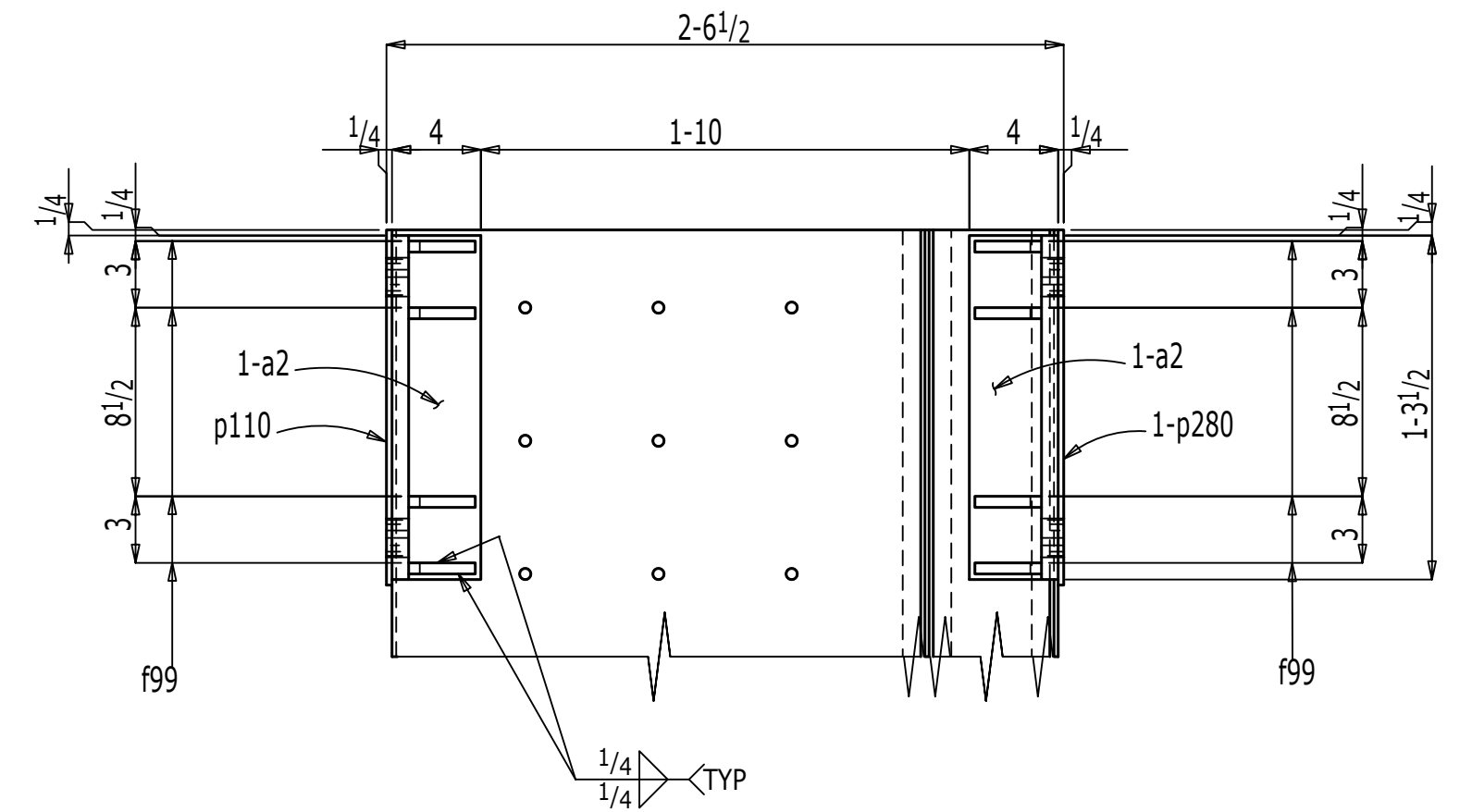
AB
B
BK
BP
C
CP
F
GH
LP
M
P
PG
SR
T
TM
V
X
CR
DW
FP
GR
HR
LA
RC
RP
SB
ST
TP



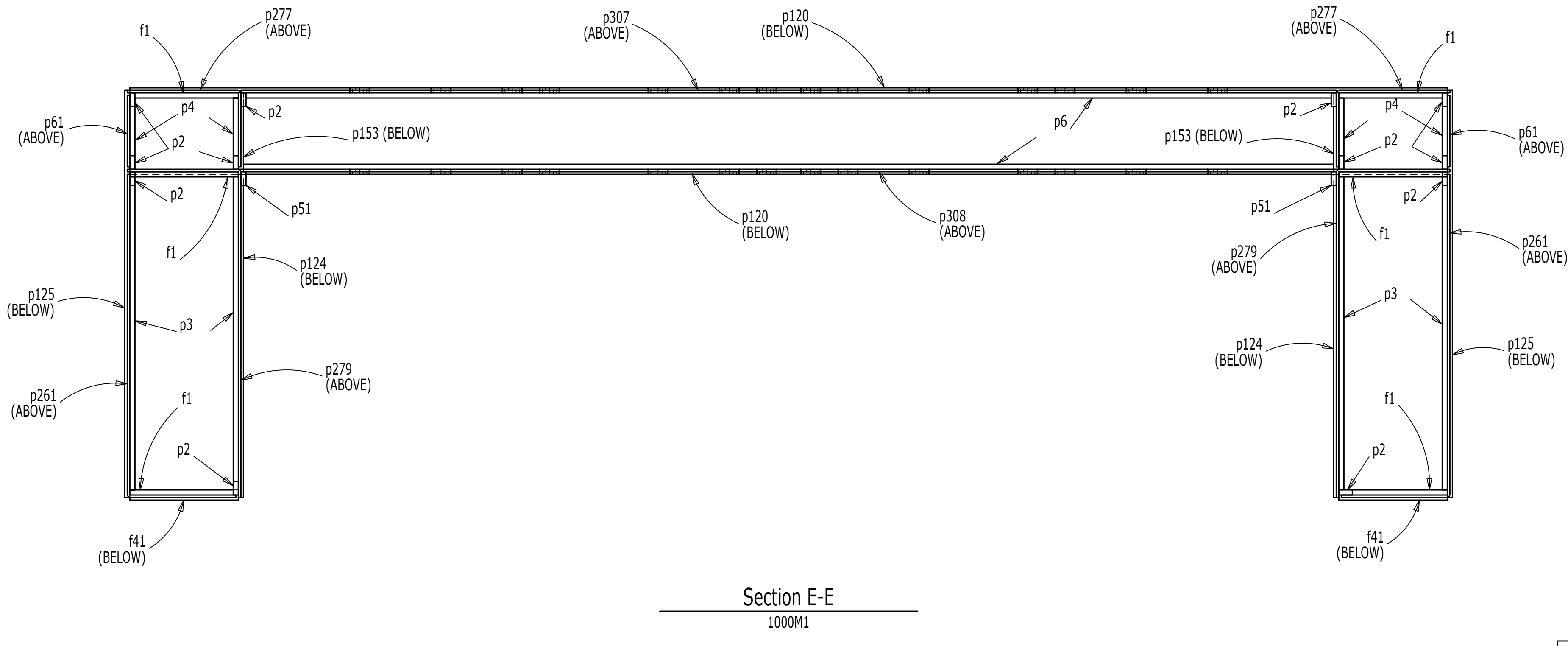
Section C-C
1000M1



Section D-D
1000M1



Section F-F
1000M1



Section E-E
1000M1

ENG. REF. DRG. No. XXXX

A	ISSUED FOR FABRICATION	Mar 14 2018	GS	PR	CLG
0	ORIGINAL ISSUE	Feb 27 2018	GS	PR	CLG
REV	REMARKS	DATE	DWN	CHK	APP

MEMBERS ARE TO BE ERECTED SO THAT MARKED END IS IN SAME LOCATION AS ON ERECTION DRAWING No. XXXX

GENERAL NOTES			
MATERIAL :	AS NOTED	ELECTRODES :	E70LH
HOLES :	15/16 DIA UNO	BOLTS :	7/8A325N UNO
SURFACE PREPN & PAINT :	NO BLAST NO PAINT		
ALL RUNNING DIMENSIONS FROM END OF MAIN MATERIAL. ALL VERTICAL SPACING OF HOLES TO BE 3" UNLESS NOTED. ALL SNIPS TO BE 3/4 x 3/4 UNLESS NOTED. ALL COPIES TO BE RADIUSSED. @ - DENOTES "CONTACT SURFACE" THIS SIDE OF PLATE. "S" IN PIECEMARK OF CONNECTION MATERIAL DENOTES SHORT SLOTS. ALL OPEN ENDS TO HAVE TOLERANCE OF (+/- 1/4") UNO. * INDICATES LAYOUT MARK FOR FABRICATION. ALL H.S. SHOP BOLTS TO BE TORQUED UNLESS NOTED.			

DESCRIPTION :	DETAILS C-SHAPE	DRAWN BY	DATE
JOB :	UNIVERSITY AT BUFFALO UB SPECIMENS	GS	02-27-18
CUSTOMER : BOSTON PROPERTIES		CHECKED BY	DATE
		PR	02-27-18
JOB NO. DRG. NO.		APPROVED BY	DATE
		CLG	02-27-18
JOB NO. DRG. NO.		1261	1002



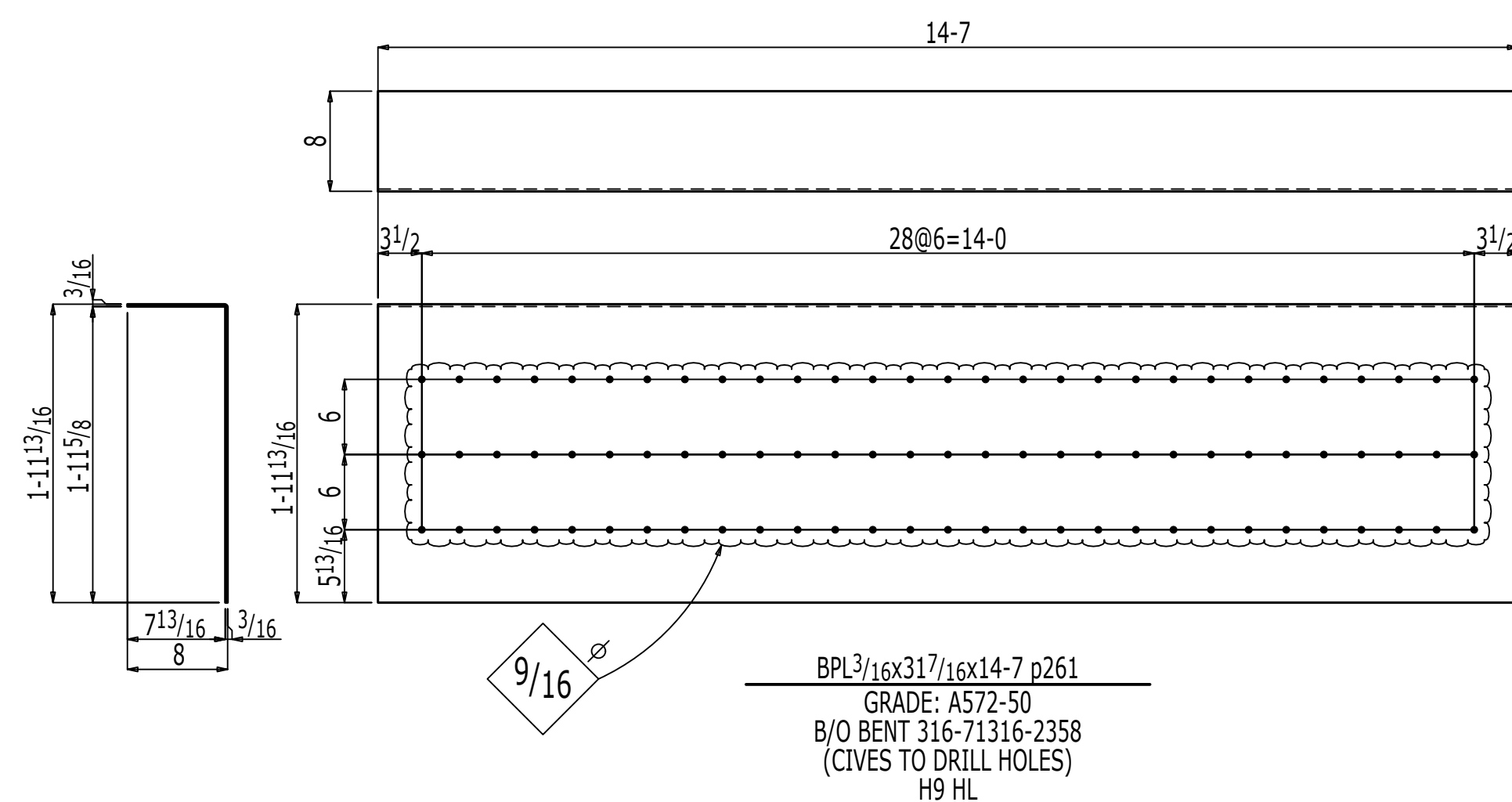
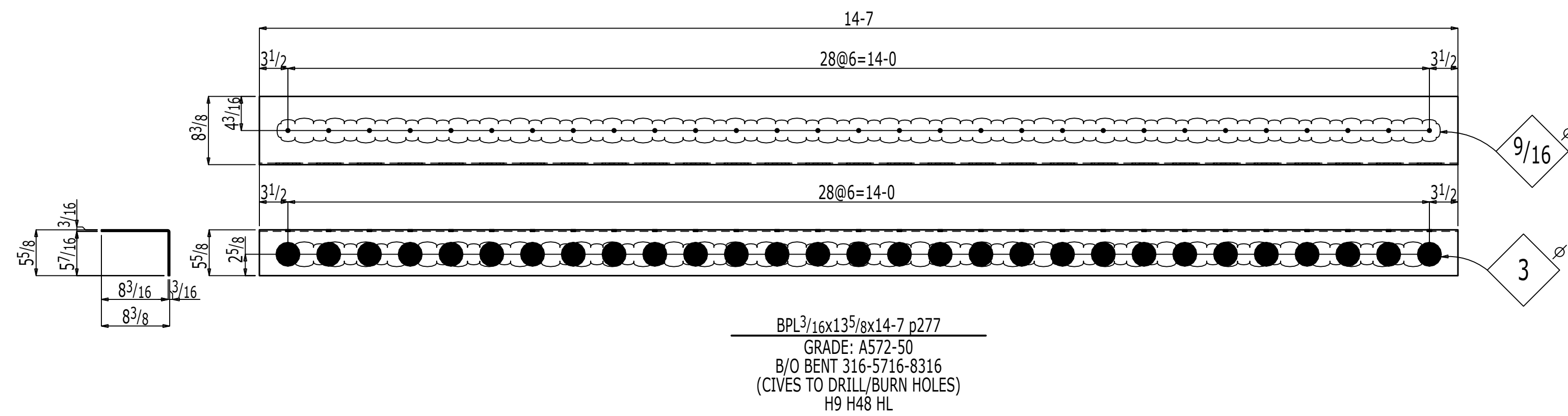
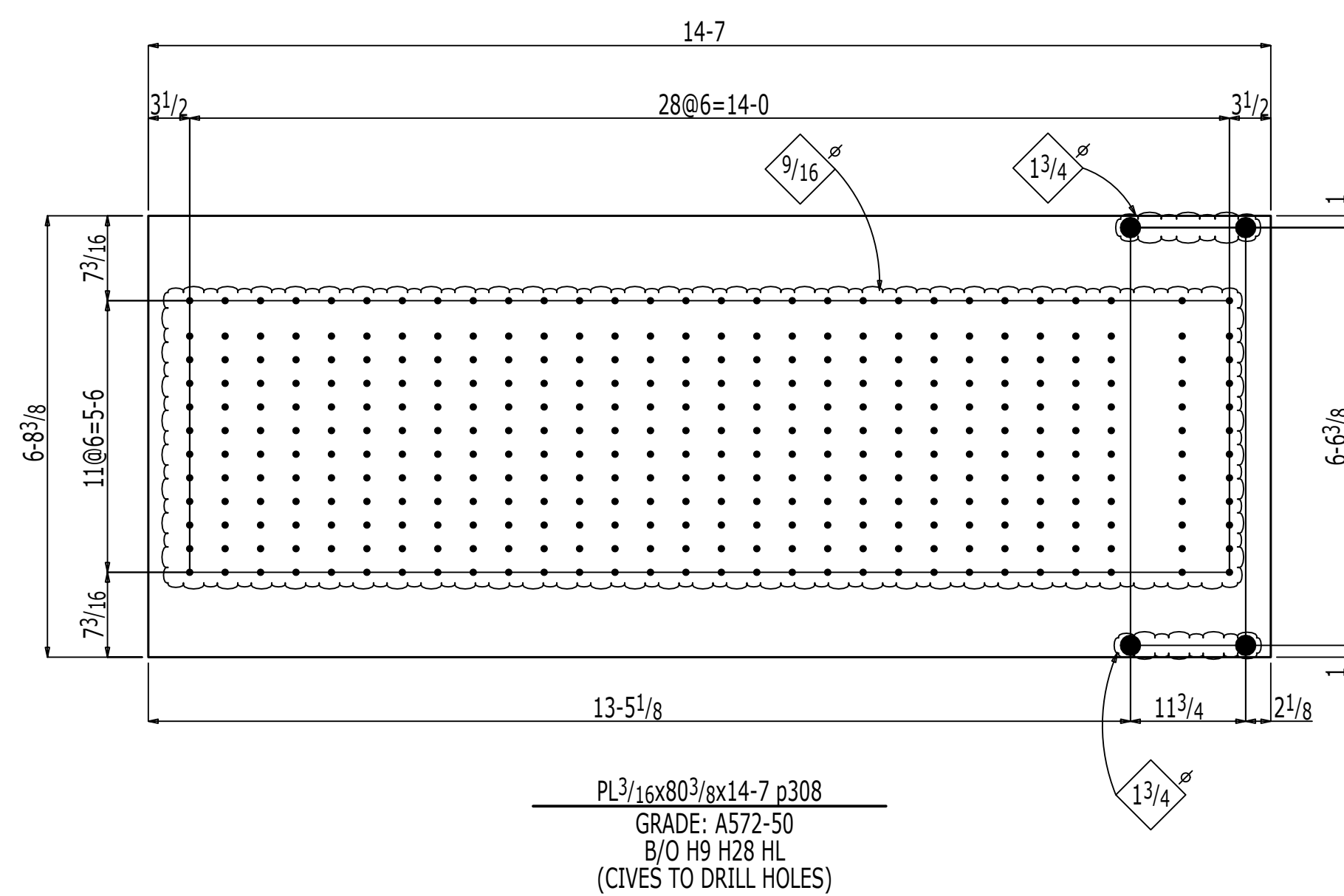
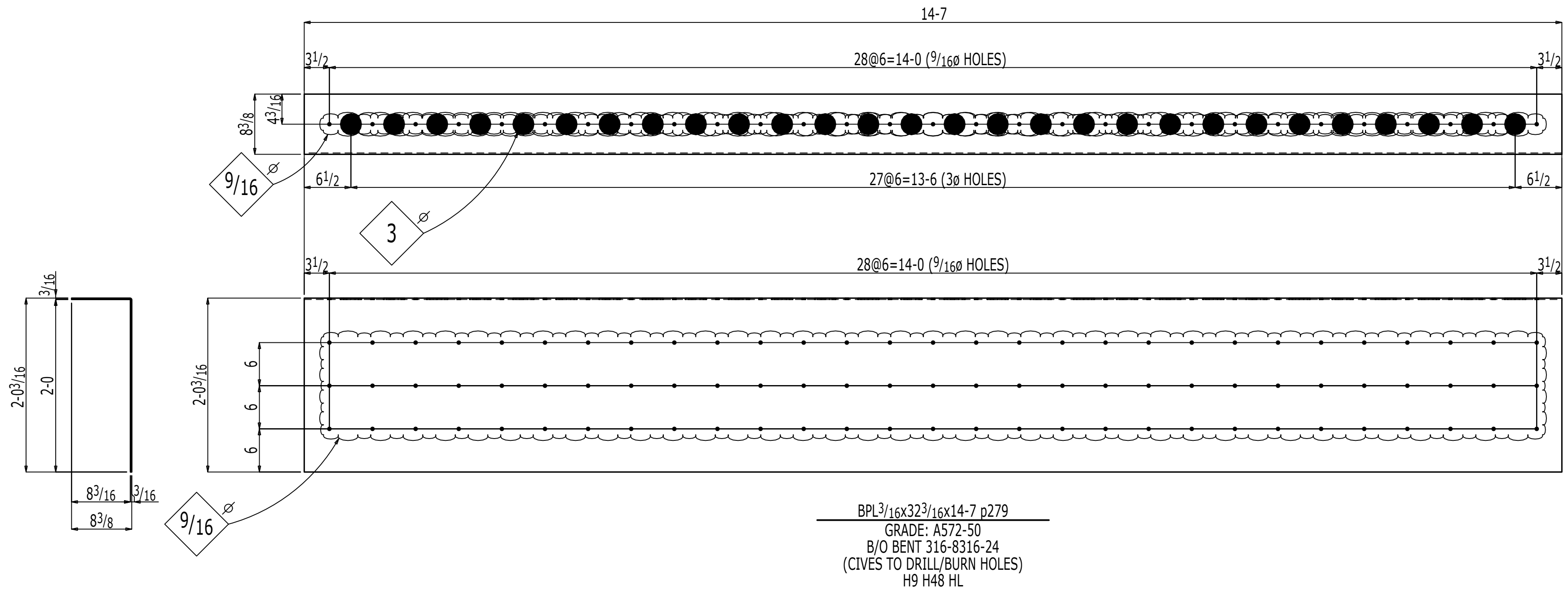
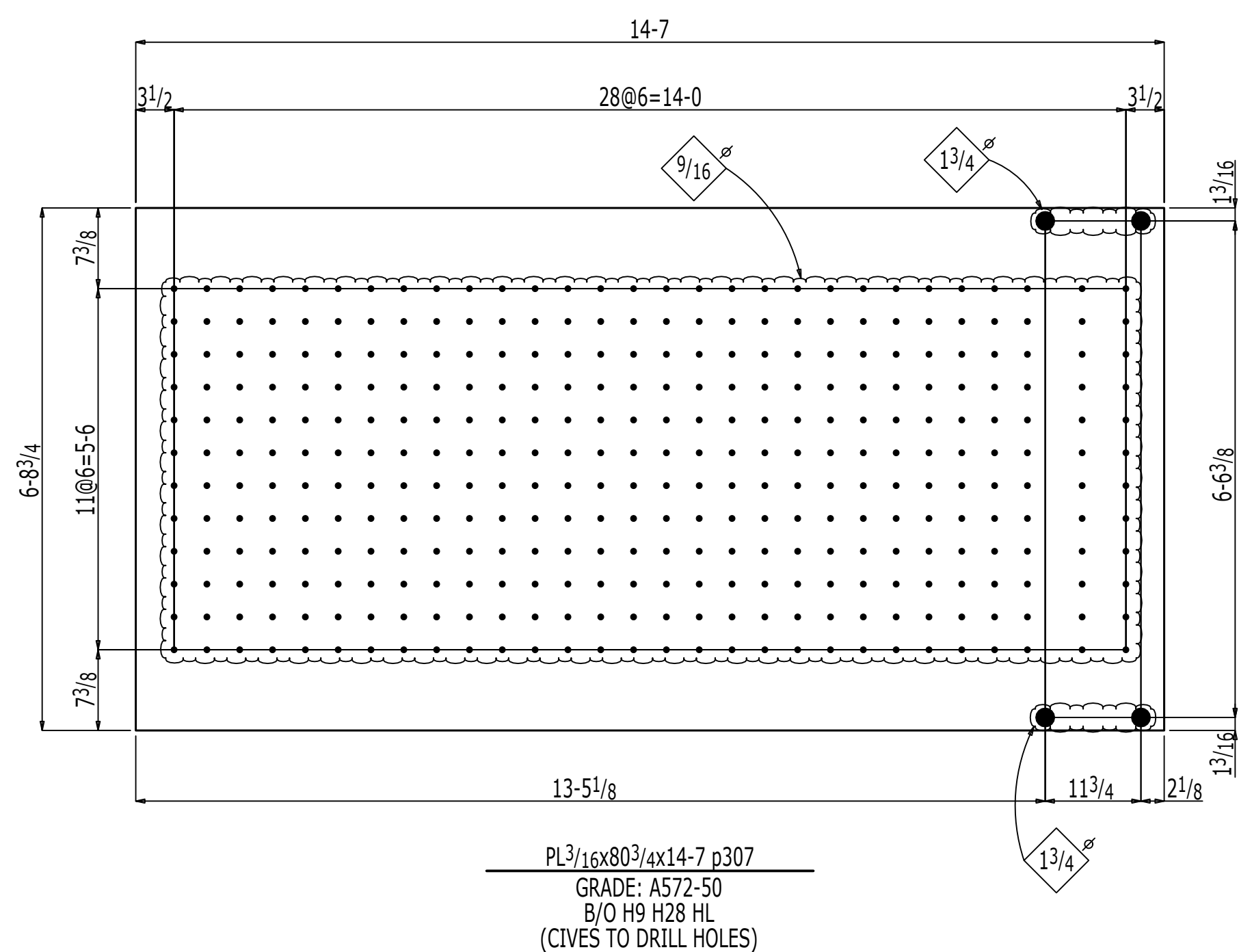
NEW ENGLAND DIVISION

REV. A

WORK THIS DRAWING WITH DRAWINGS 1000, 1001, 1003 & 1004

JOB NO.	DRG. NO.
1261	1002

AB
BK
BP
C
CP
F
GH
LP
M
P
PG
SR
T
TM
V
X
CR
DW
FP
GR
HR
LA
RC
RP
SB
ST
TP



ENG. REF. DRG. No. XXXX

REV	REMARKS	DATE	DWN	CHK	APP
A	ISSUED FOR FABRICATION	Mar 14 2018	GS	PR	CLG
0	ORIGINAL ISSUE	Feb 27 2018	GS	PR	CLG

MEMBERS ARE TO BE ERECTED SO THAT MARKED END IS IN SAME LOCATION AS ON ERECTION DRAWING No. XXXX

GENERAL NOTES

MATERIAL : AS NOTED
ELECTRODES : E70LH
HOLES : 15/16 DIA UNO
BOLTS : 7/8@A325N UNO
SURFACE PREPN & PAINT : **NO BLAST NO PAINT**

ALL RUNNING DIMENSIONS FROM END OF MAIN MATERIAL.
ALL VERTICAL SPACING OF HOLES TO BE 3" UNLESS NOTED.
ALL SNIPS TO BE 3/4 x 3/4 UNLESS NOTED.
ALL COPIES TO BE RADUSED.
⊗ — DENOTES "CONTACT SURFACE" THIS SIDE OF PLATE.
⊗ — IN PIECEMARK OF CONNECTION MATERIAL DENOTES SHORT SLOTS.
ALL OPEN ENDS TO HAVE TOLERANCE OF (+/- 1/4") UNO.
* INDICATES LAYOUT MARK FOR FABRICATION.
ALL H.S. SHOP BOLTS TO BE TORQUED UNLESS NOTED.

DESCRIPTION	DRAWN BY	DATE
DETAILS C-SHAPE	GS	02-27-18
UNIVERSITY AT BUFFALO UB SPECIMENS	PR	02-27-18
BOSTON PROPERTIES	CLG	02-27-18
CUSTOMER : BOSTON PROPERTIES	JOB NO.	DRG. NO.
	1261	1003
	Fab: Cives_2015.25_Fab	REV.
	Job: UB_Specimens	A

WORK THIS DRAWING WITH DRAWINGS 1000, 1001, 1002 & 1004

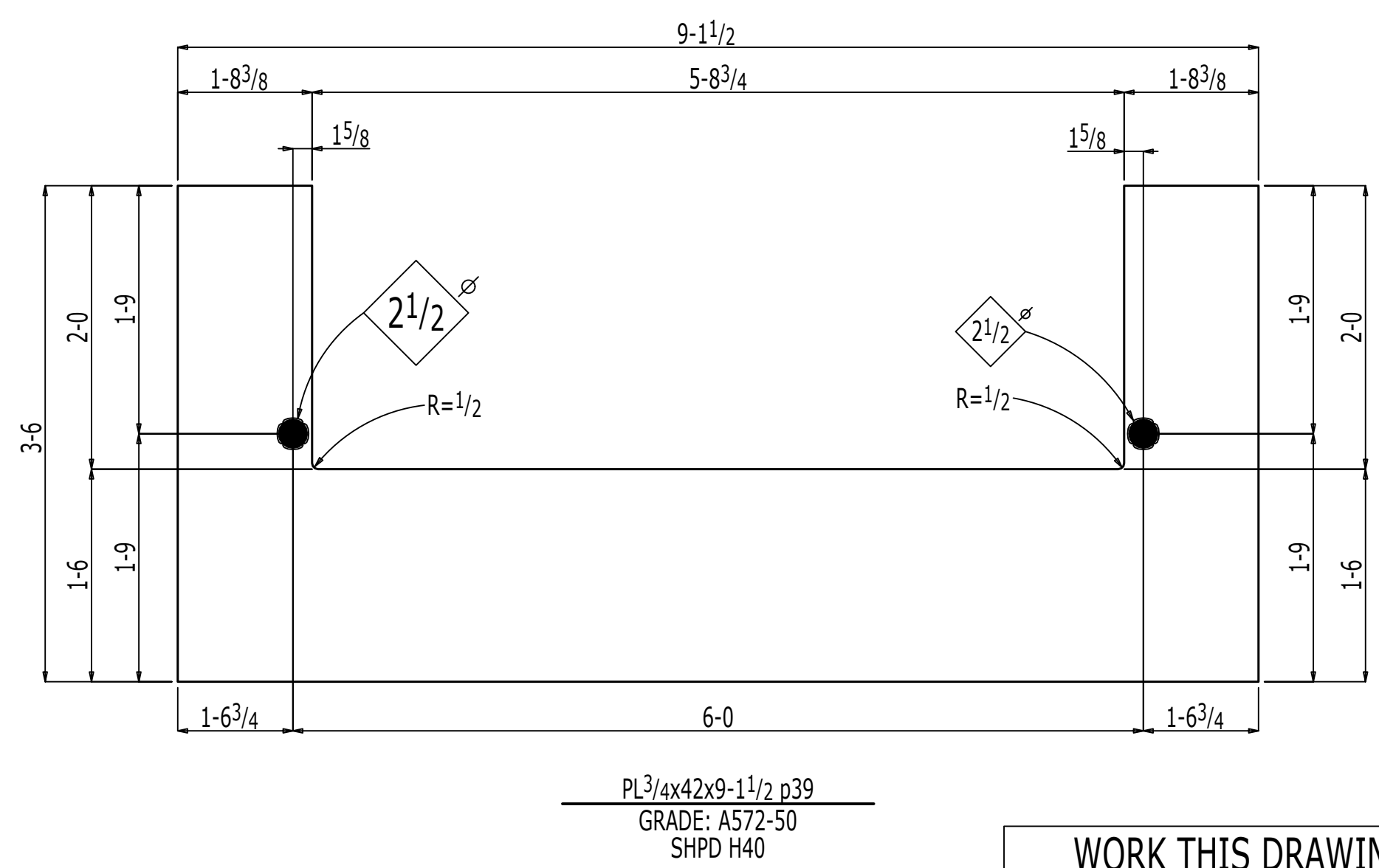
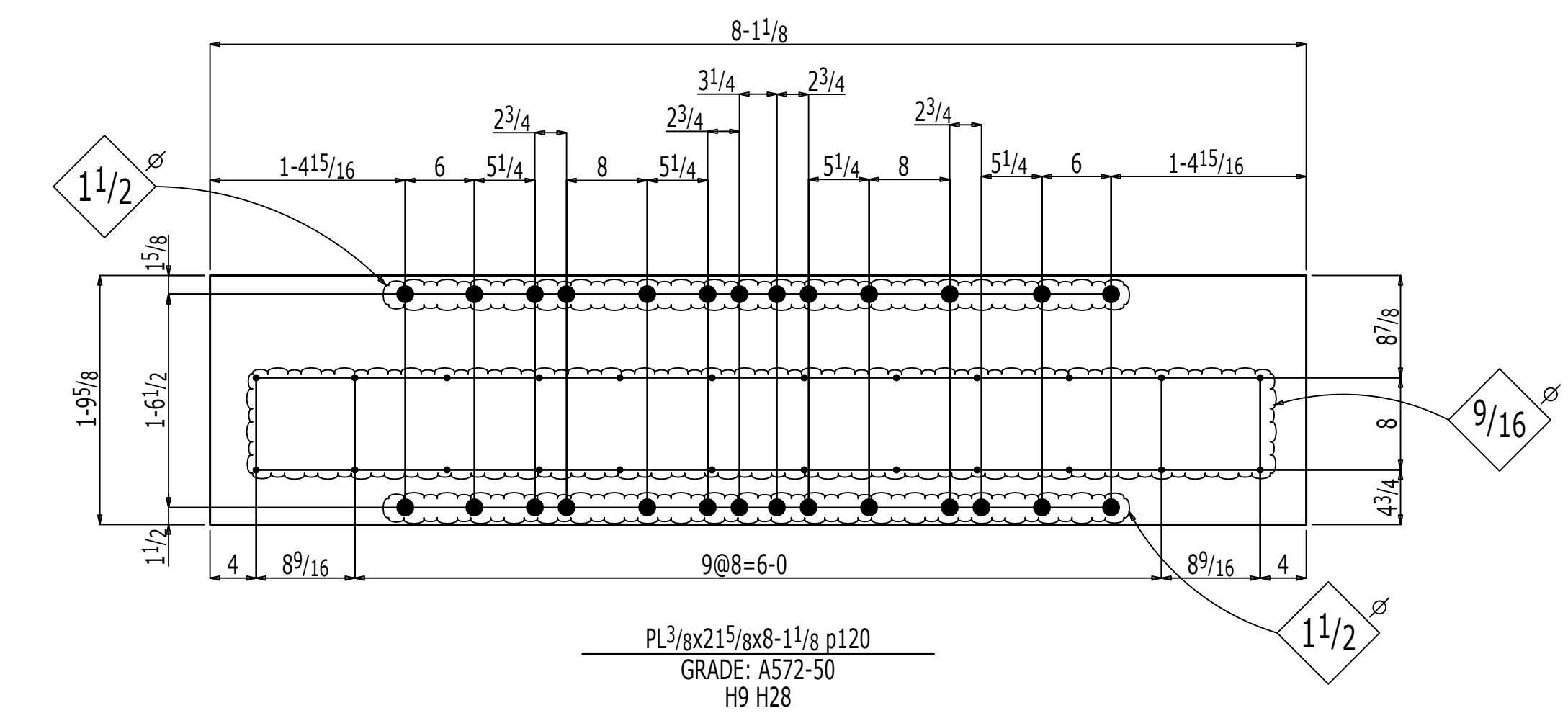
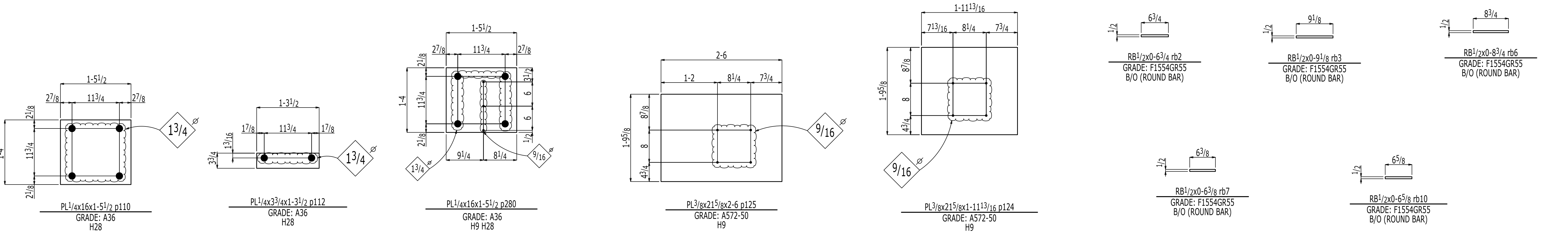
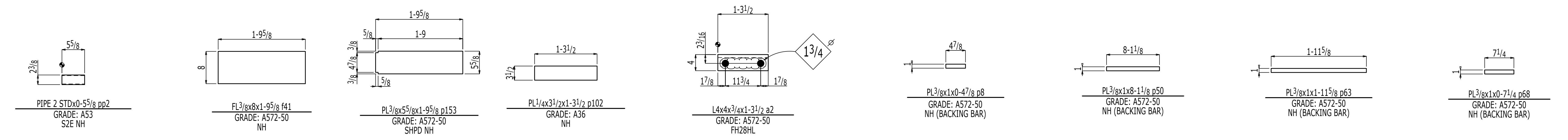
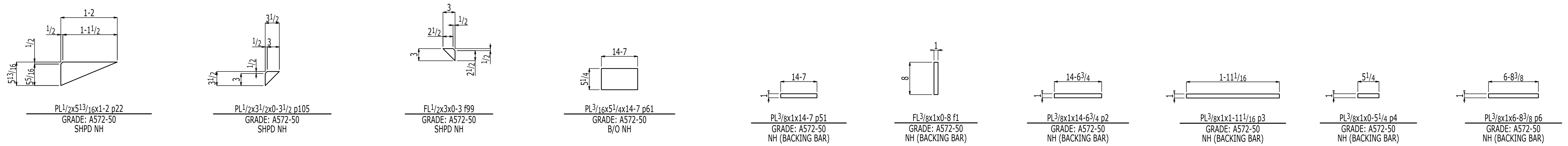


KL

NEW ENGLAND DIVISION

JOB NO.	DRG NO.
1261	1003

AB
BK
BP
C
CP
F
G
H
LP
M
P
PG
SR
T
TM
V
X
CR
DW
FP
GR
HR
LA
RC
RP
SB
ST
TP



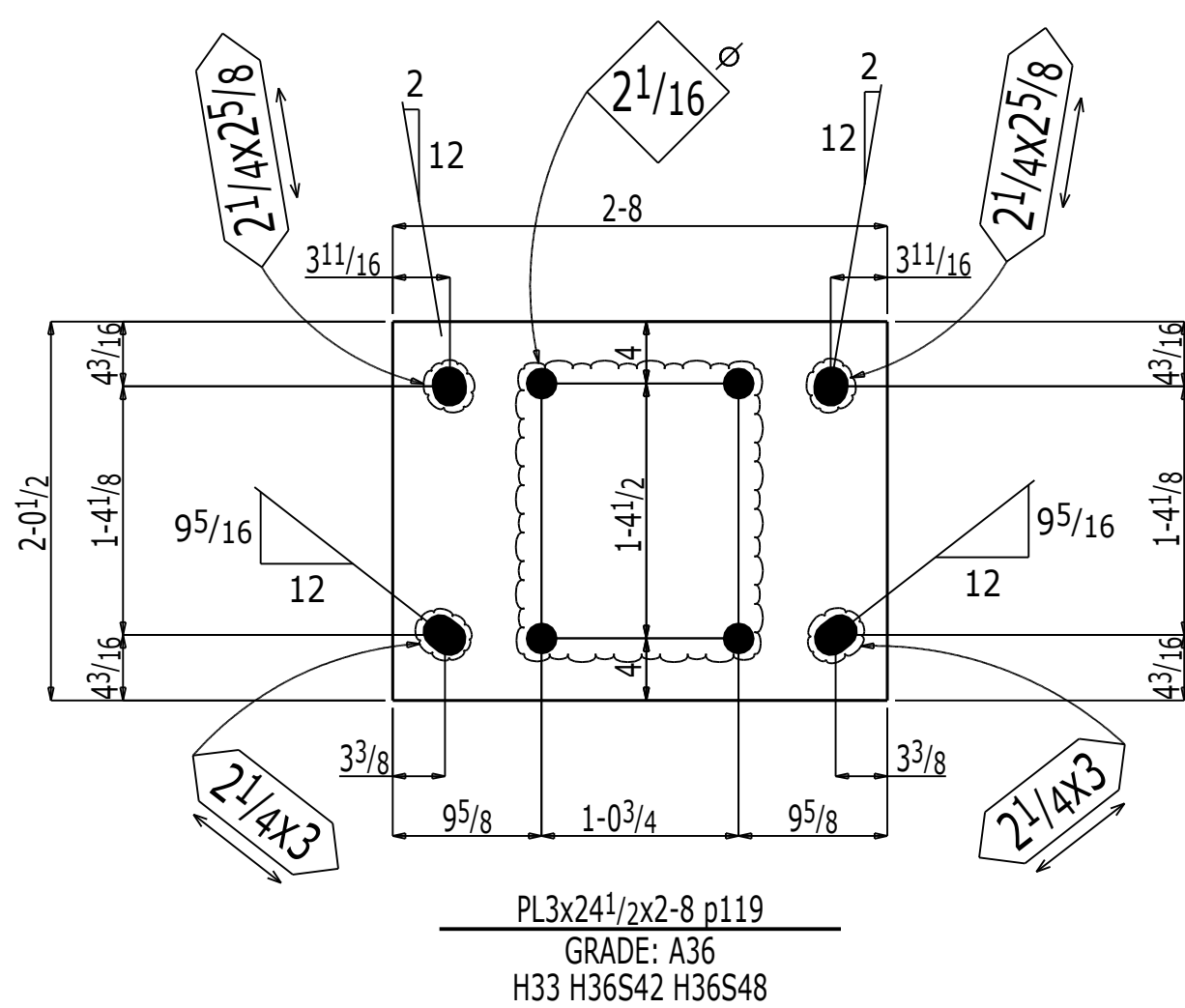
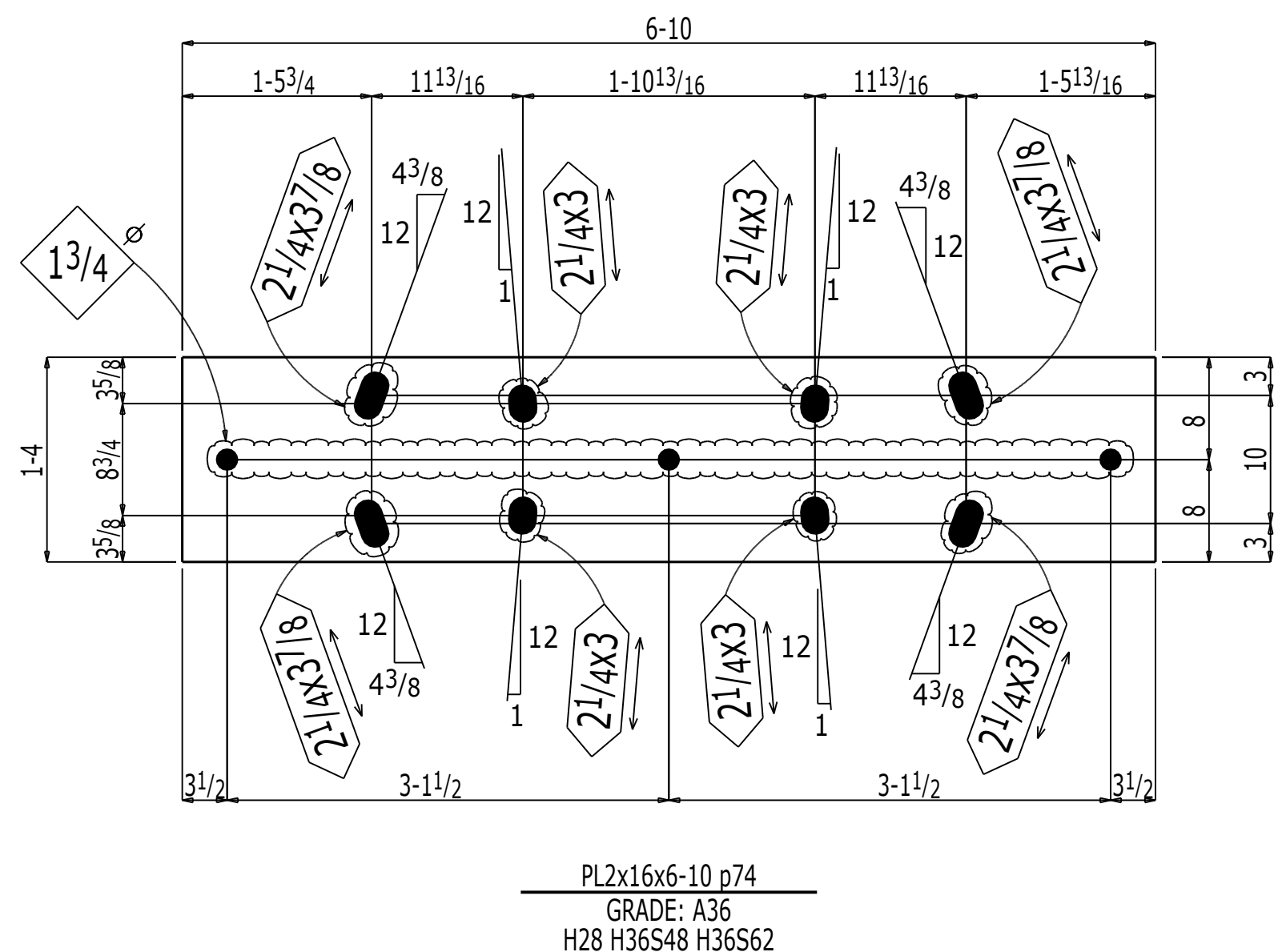
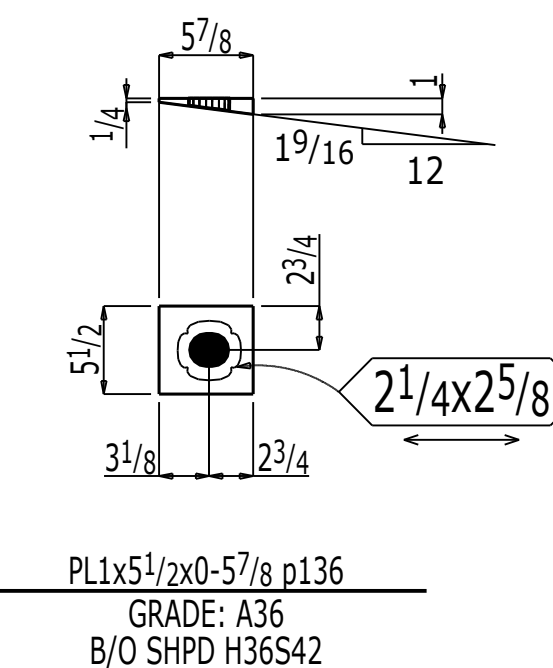
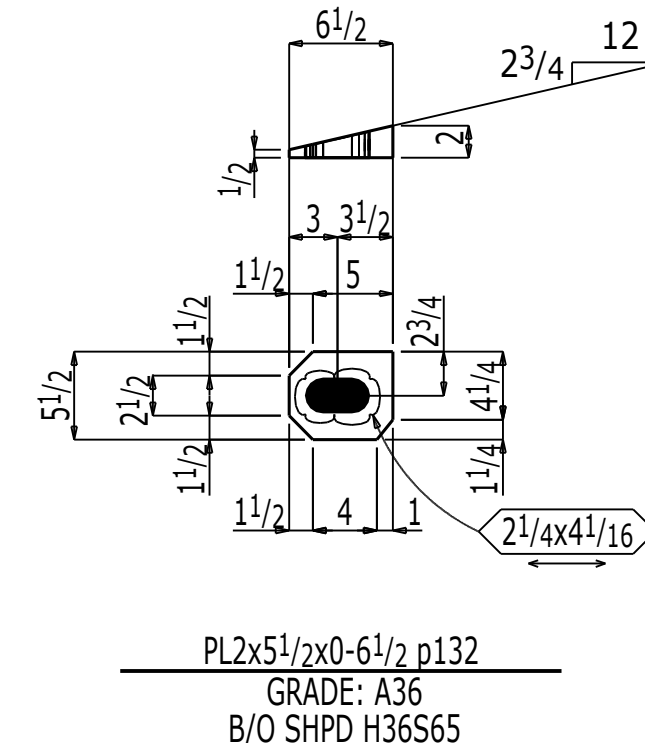
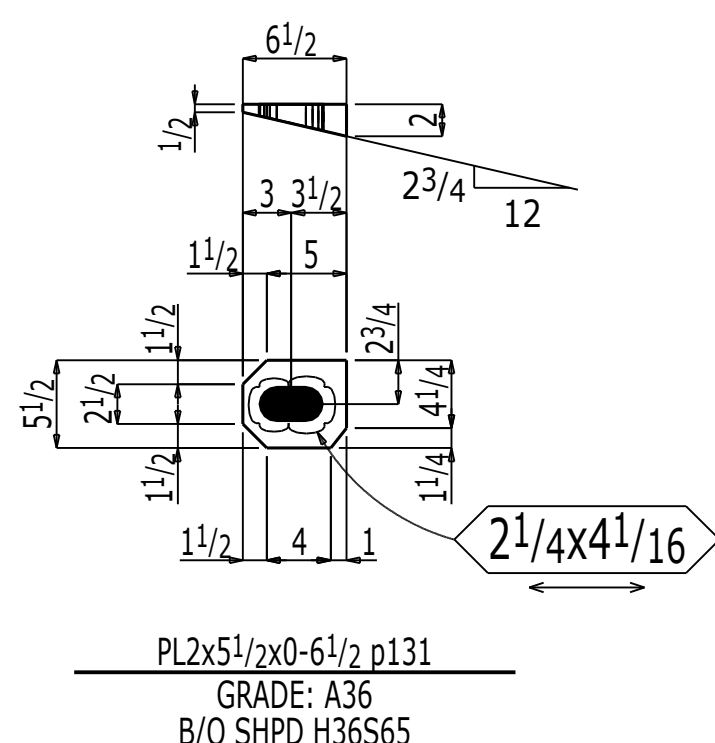
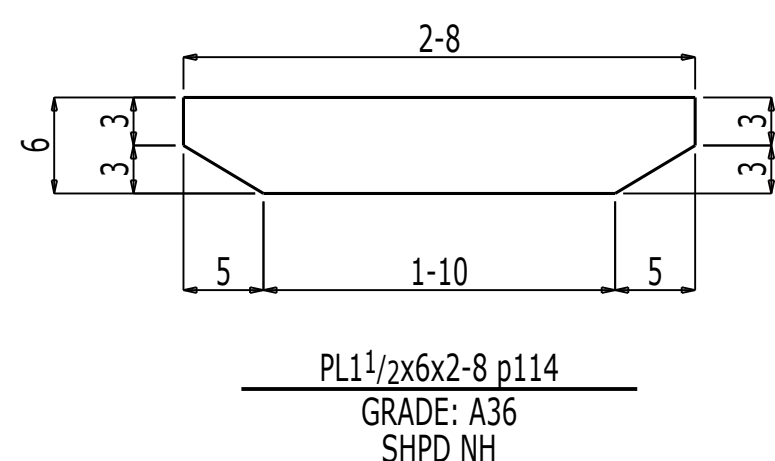
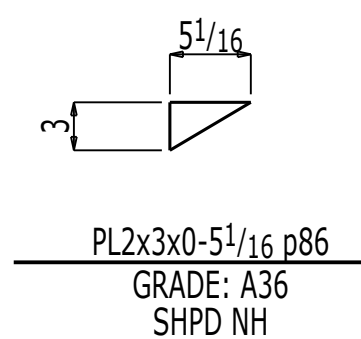
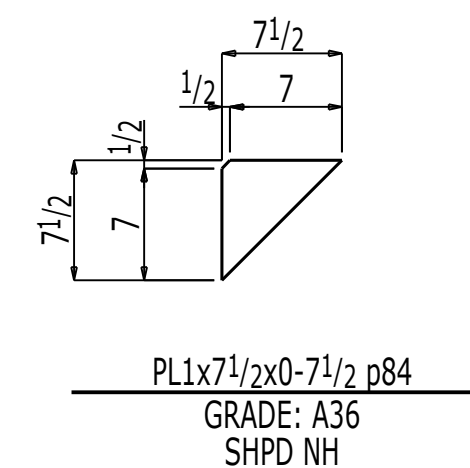
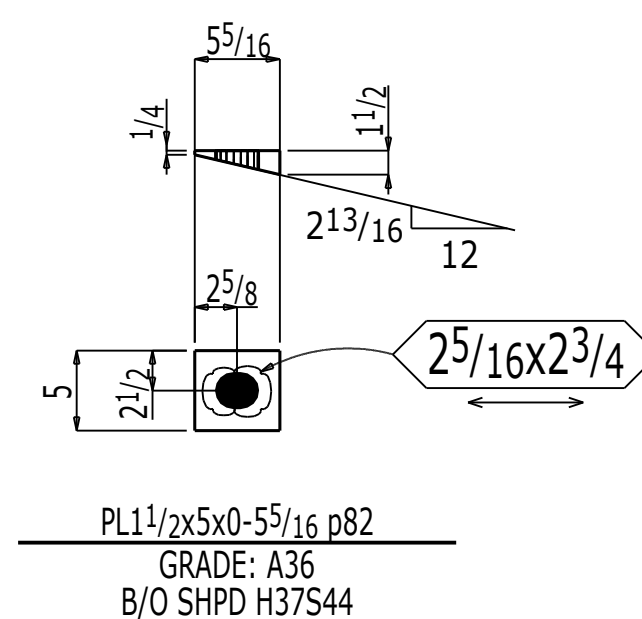
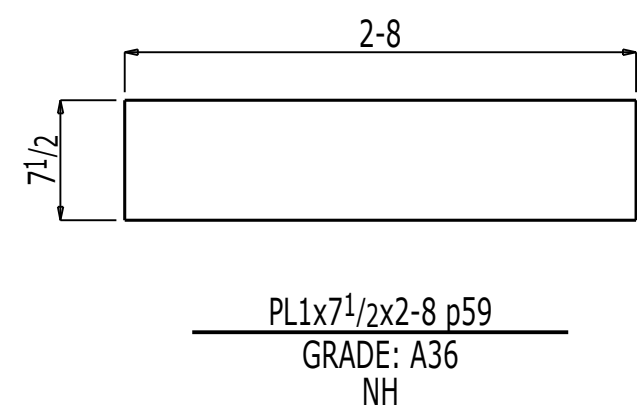
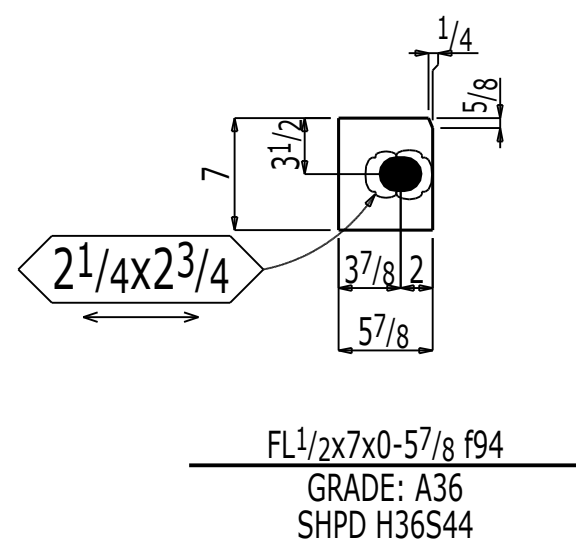
WORK THIS DRAWING WITH
DRAWINGS 1000, 1001, 1002 & 1003

ENG. REF. DRG. No. XXXX

A	ISSUED FOR FABRICATION	Mar 14 2018	GS	PR	CLG	MEMBERS ARE TO BE ERECTED SO THAT MARKED END IS IN SAME LOCATION AS ON ERECTION DRAWING No. XXXX
0	ORIGINAL ISSUE	Feb 27 2018	GS	PR	CLG	
REV	REMARKS	DATE	DWN	CHK	APP	

GENERAL NOTES		DRAWN BY	DATE
MATERIAL :	AS NOTED	GS	02-27-18
ELECTRODES :	E70LH	PR	02-27-18
HOLES :	15/16 DIA UNO	CLG	02-27-18
BOLTS :	7/80A325N UNO	APP	02-27-18
SURFACE PREP & PAINT : NO BLAST NO PAINT		JOB NO.	DRG. NO.
		1261	1004
DESCRIPTION : DETAILS C-SHAPE		Job:	UB Specimens
JOB : UNIVERSITY AT BUFFALO UB SPECIMENS		REV.	A
CUSTOMER : BOSTON PROPERTIES			

JOB NO.	DRG NO.
1261	1004



ENG. REF. DRG. No. XXXX

REV	REMARKS	DATE	SRM	GS	PR	CLG
A	Shop Issue	Mar 23 2018		GS		CLG
0	ORIGINAL ISSUE	Mar 15 2018	GS		PR	CLG

MEMBERS ARE TO BE ERCTED SO THAT MARKED END IS IN SAME LOCATION AS ON ERECTION DRAWING No. XXXX

GENERAL NOTES

MATERIAL : AS NOTED | ELECTRODES : E70LH | ALL RUNNING DIMENSIONS FROM END OF MAIN MATERIAL. ALL VERTICAL SPACING OF HOLES TO BE 3" UNLESS NOTED. ALL SNIPS TO BE 3/4 x 3/4 UNLESS NOTED. ALL COPIES TO BE RADIIUSED.

HOLES : 15/16 DIA UNO | BOLTS : 7/8ØA325N UNO

SURFACE PREP & PAINT : **NO BLAST NO PAINT**

DESCRIPTION : DETAILS C-SHAPE

JOB : UNIVERSITY AT BUFFALO UB SPECIMENS

CUSTOMER : BOSTON PROPERTIES

DRAWN BY : GS | DATE : 03-15-18

CHECKED BY : PR | DATE : 03-15-18

APPROVED BY : CLG | DATE : 03-15-18

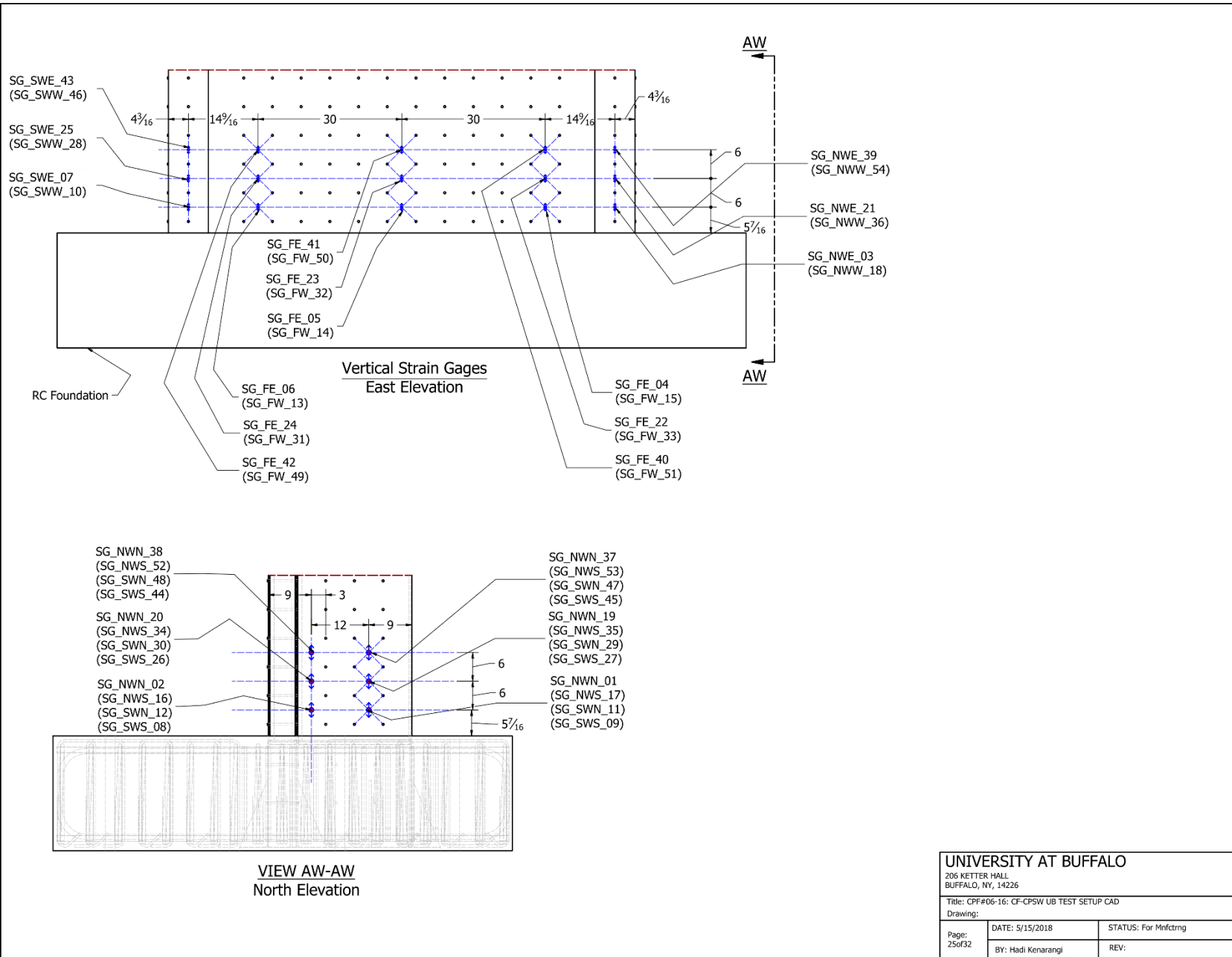
JOB NO. : 1261 | DRG. NO. : 1008

Fab: Cives 2015.25_Fab Job: UB_Specimens REV. : A

WORK THIS DRAWING WITH DRAWING 1007

APPENDIX D

Instrumentation of C-Shaped Walls



UNIVERSITY AT BUFFALO

206 KETTER HALL
BUFFALO, NY, 14226

Title: CPF#06-16: CF-CPSW UB TEST SETUP CAD

Drawing:

Page:
25of32

DATE: 5/15/2018

BY: Hadi Kenarangi

STATUS: For Mnfctng

REV:

Table 1. Strain gauge placement details						Table 1. Strain gauge placement details					
No.	Label	Location, in	Location	Orientation	Elevation	No.	Label	Location, in	Location	Orientation	Elevation
1	SG_NWN_01	5.4375	NWN	Vert.	North	28	SG_SWW_28	11.4375	SWW	Vert.	West
2	SG_NWN_02	5.4375	NWN	Vert.	North	29	SG_SWN_29	11.4375	SWN	Vert.	North
3	SG_NWE_03	1	NEW	Vert.	West	30	SG_SWN_30	11.4375	SWN	Vert.	North
4	SG_FE_04	1	FE	Vert.	East	31	SG_FW_31	11.4375	FW	Vert.	West
5	SG_FE_05	12	FE	Vert.	East	32	SG_FW_32	11.4375	FW	Vert.	West
6	SG_FE_06	12	FE	Vert.	East	33	SG_FW_33	11.4375	FW	Vert.	West
7	SG_SWE_07	12	SWE	Vert.	East	34	SG_NWS_34	11.4375	NWS	Vert.	South
8	SG_SWS_08	12	SWS	Vert.	South	35	SG_NWS_35	11.4375	NWS	Vert.	South
9	SG_SWS_09	24	SWS	Vert.	South	36	SG_NWW_36	11.4375	NWW	Vert.	West
10	SG_SWW_10	24	SWW	Vert.	West	37	SG_NWN_37	17.4375	NWN	Vert.	North
11	SG_SWN_11	5.4375	SWN	Vert.	North	38	SG_NWN_38	17.4375	NWN	Vert.	North
12	SG_SWN_12	5.4375	SWN	Vert.	North	39	SG_NWE_39	17.4375	NEW	Vert.	West
13	SG_FW_13	5.4375	FW	Vert.	West	40	SG_FE_40	17.4375	FE	Vert.	East
14	SG_FW_14	5.4375	FW	Vert.	West	41	SG_FE_41	17.4375	FE	Vert.	East
15	SG_FW_15	5.4375	FW	Vert.	West	42	SG_FE_42	17.4375	FE	Vert.	East
16	SG_NWS_16	5.4375	NWS	Vert.	South	43	SG_SWE_43	17.4375	SWE	Vert.	East
17	SG_NWS_17	5.4375	NWS	Vert.	South	44	SG_SWS_44	17.4375	SWS	Vert.	South
18	SG_NWW_18	5.4375	NWW	Vert.	West	45	SG_SWS_45	17.4375	SWS	Vert.	South
19	SG_NWN_19	11.4375	NWN	Vert.	North	46	SG_SWW_46	17.4375	SWS	Vert.	South
20	SG_NWN_20	11.4375	NWN	Vert.	North	47	SG_SWN_47	17.4375	SWN	Vert.	North
21	SG_NWE_21	11.4375	NEW	Vert.	West	48	SG_SWN_48	17.4375	SWN	Vert.	North
22	SG_FE_22	11.4375	FE	Vert.	East	49	SG_FW_49	17.4375	FW	Vert.	West
23	SG_FE_23	11.4375	FE	Vert.	East	50	SG_FW_50	17.4375	FW	Vert.	West
24	SG_FE_24	11.4375	FE	Vert.	East	51	SG_FW_51	17.4375	FW	Vert.	West
25	SG_SWE_25	11.4375	SWE	Vert.	East	52	SG_NWS_52	17.4375	NWS	Vert.	South
26	SG_SWS_26	11.4375	SWS	Vert.	South	53	SG_NWS_53	17.4375	NWS	Vert.	South
27	SG_SWS_27	11.4375	SWS	Vert.	South	54	SG_NWW_54	17.4375	NWW	Vert.	West

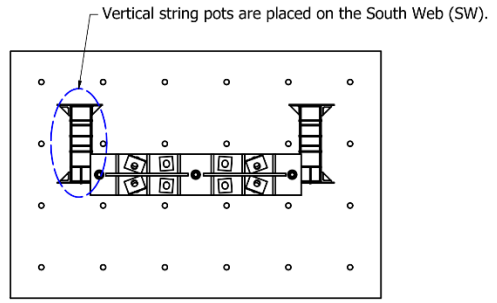
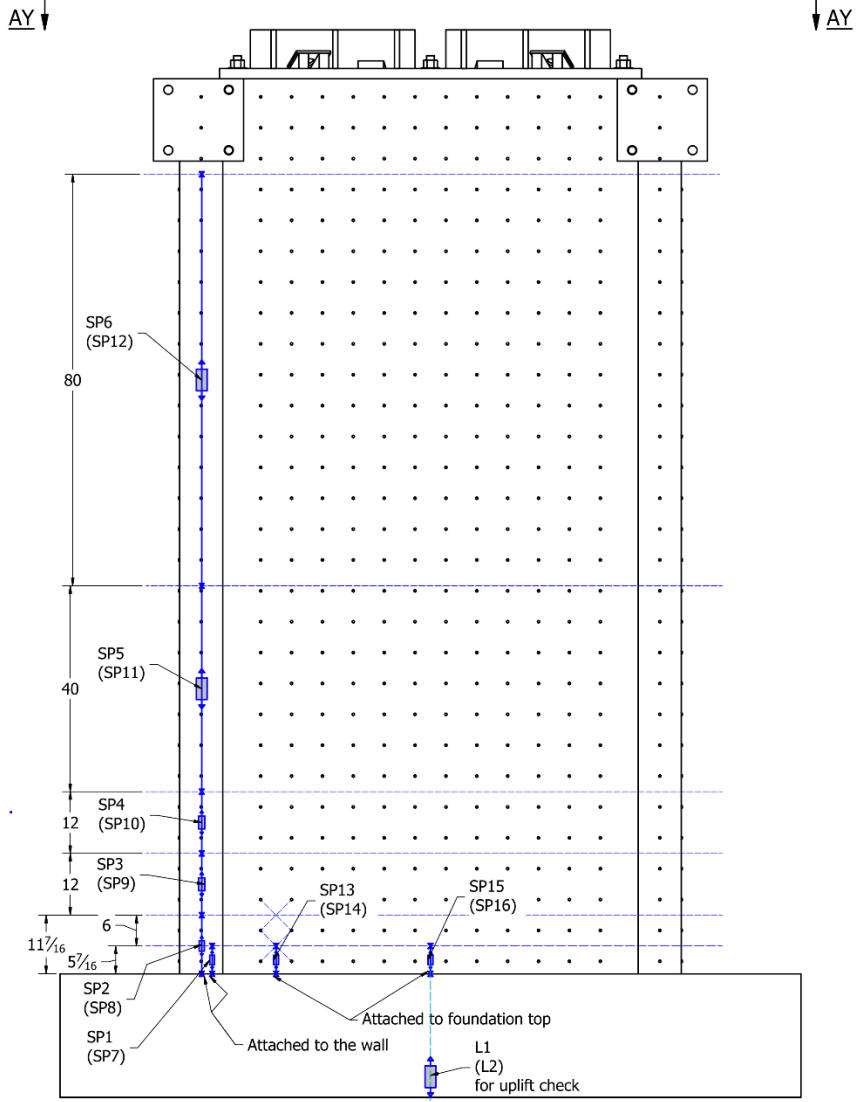
UNIVERSITY AT BUFFALO

206 KETTER HALL
BUFFALO, NY, 14226

Title: CPF#06-16: CF-CPSW UB TEST SETUP CAD

Drawing:

Page: 26of32	DATE: 5/15/2018	STATUS: For Mnfctng
	BY: Hadi Kenarangi	REV:

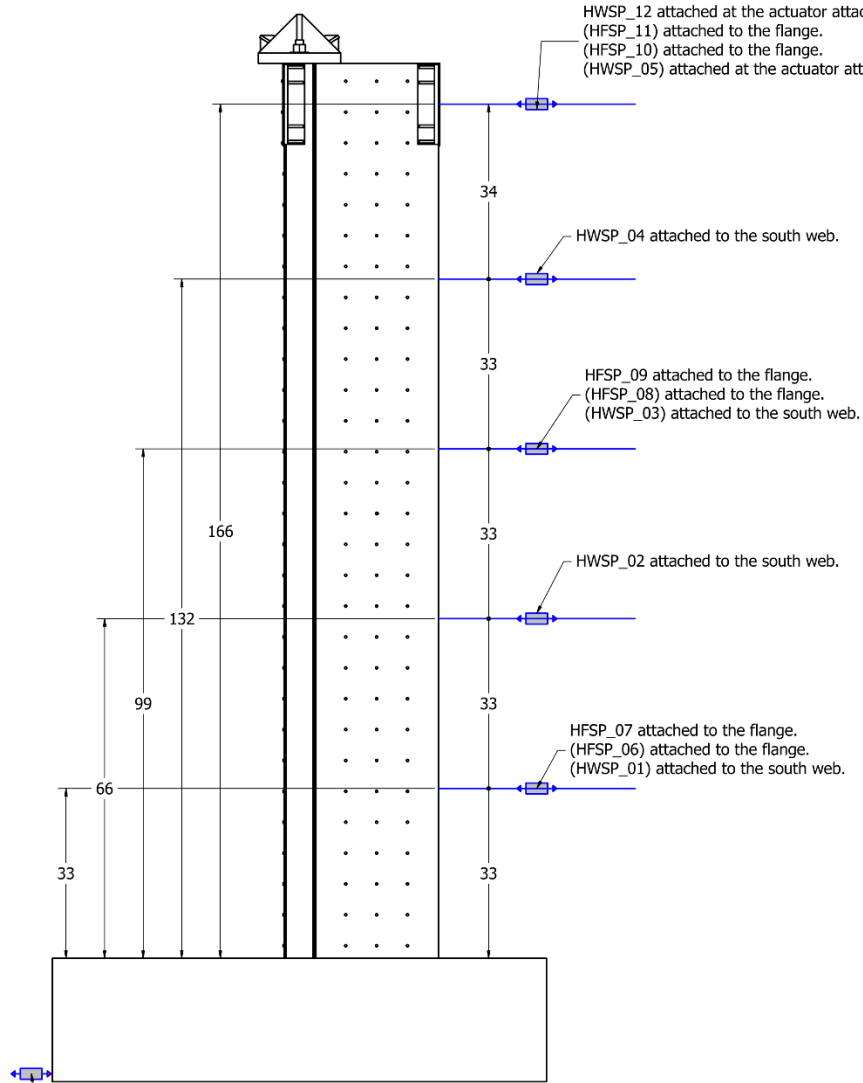


VIEW AY-AY
SCALE 1/30

Vertical String Pots
East Elevation

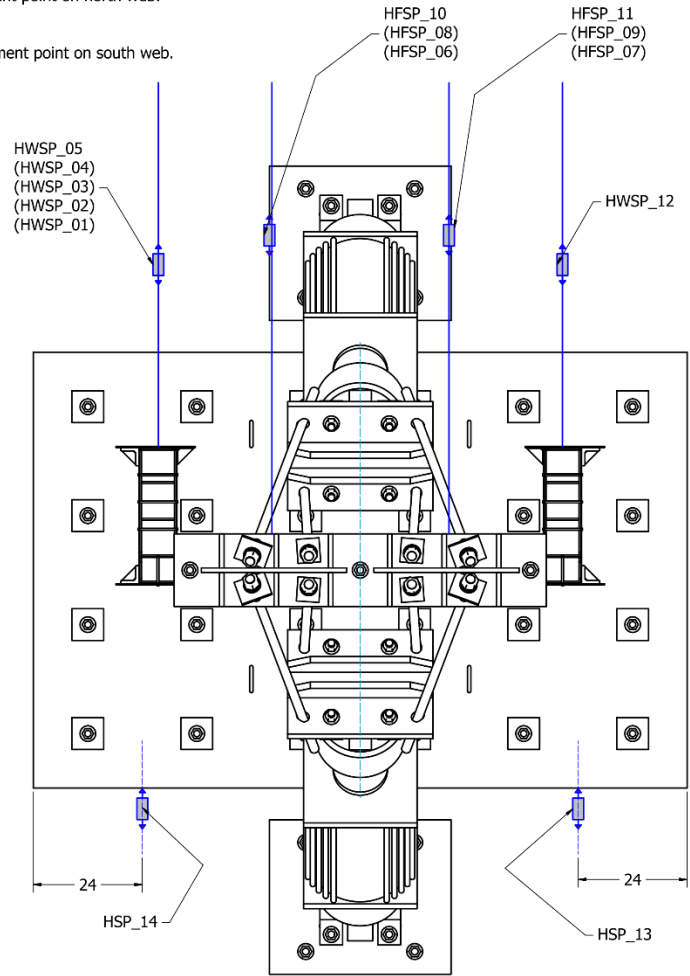
NOTE:
String pots and LVDTs in paranthesis are to be placed on the opposite elevation.

UNIVERSITY AT BUFFALO		
206 KETTER HALL BUFFALO, NY, 14226		
Title: CPF#06-16: CF-CPSW UB TEST SETUP CAD		
Drawing:		
Page: 27 of 32	DATE: 5/15/2018	STATUS: For Mnfctrng
	BY: Hadi Kenarangi	REV:



Horizontal String Pots
 North Elevation

HSP_13 See plan view.
 (HSP_14) See plan view.
 Check for foundation slippage.



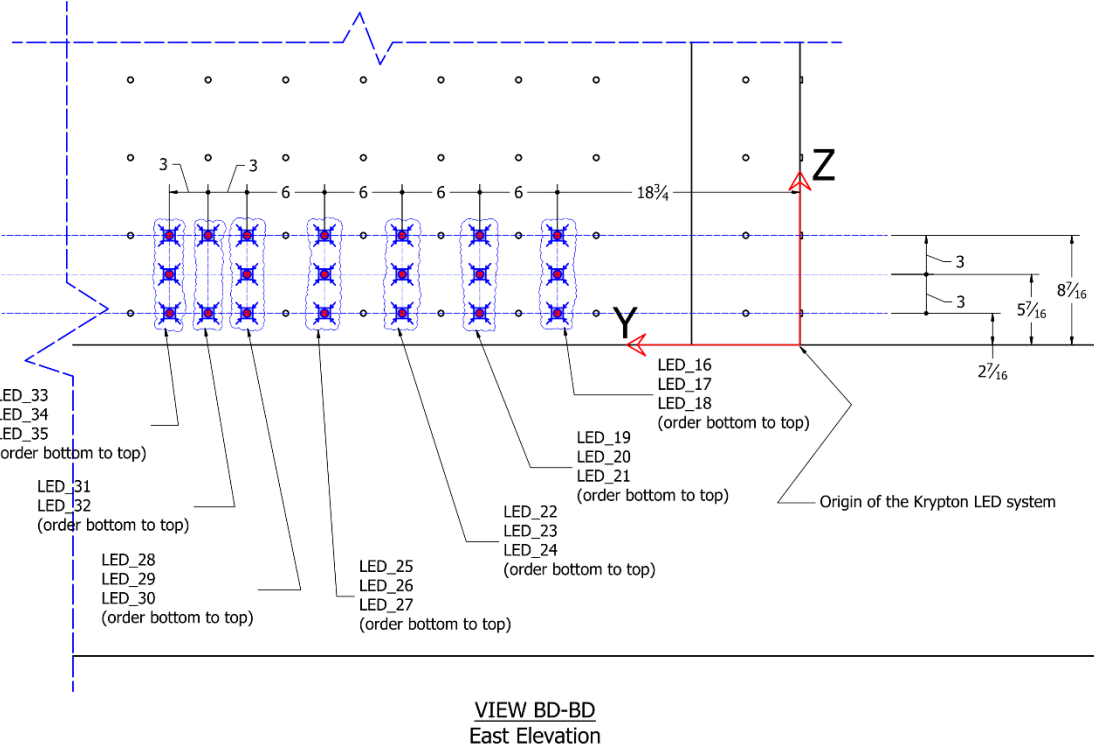
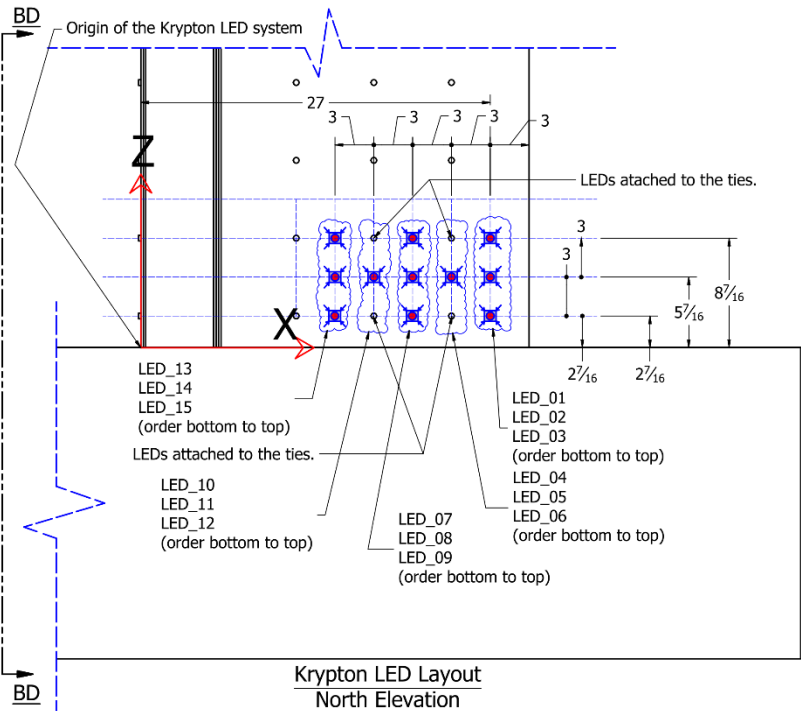
Plan View

UNIVERSITY AT BUFFALO		
206 KETTER HALL BUFFALO, NY, 14226		
Title: CPF#06-16: CF-CPSW UB TEST SETUP CAD		
Drawing:		
Page: 28of32	DATE: 5/15/2018	STATUS: For Mnfctng
	BY: Hadi Kenarangi	REV:

No.	Label	Length, in	Location*, in	Orientation	Elevation
1	L#1	~	SF to F	Vertical uplift	East
2	L#2	~	SF to F	Vertical uplift	East

Table 3. String pot placement details							Table 3. String pot placement details						
No.	Label	Length, in.	Gauge, in.	Location	Orientation	Ele.	No.	Label	Length, in.	Gauge, in.	Location	Orientation	Ele.
1	SP1	5.4375	±1.0	Bottom of the wall to the wall flange	Vertical Def.	E	16	SP16	5.4375	±1.0	Top of the foundation to the wall flange	Vertical Def.	W
2	SP2	11.4375	±1.0	Bottom of the wall to the wall flange	Vertical Def.	E	17	HWSP_01	~	±4.0	South Web, West Elevation	Horizontal Def.	S
3	SP3	12	±1.0	On the wall flange	Vertical Def.	E	18	HWSP_02	~	±8.0	South Web, West Elevation	Horizontal Def.	S
4	SP4	12	±1.0	On the wall flange	Vertical Def.	E	19	HWSP_03	~	±10.0	South Web, West Elevation	Horizontal Def.	S
5	SP5	40	±0.5	On the wall flange	Vertical Def.	E	20	HWSP_04	~	±15.0	South Web, West Elevation	Horizontal Def.	S
6	SP6	80	±0.5	On the wall flange	Vertical Def.	E	21	HWSP_05	~	±15.0	South Web, West Elevation	Horizontal Def.	S
7	SP7	5.4375	±1.0	Bottom of the wall to the wall web	Vertical Def.	W	22	HFSP_06	~	±4.0	Flange, West Elevation	Horizontal Def.	W
8	SP8	11.4375	±1.0	Bottom of the wall to the wall web	Vertical Def.	W	23	HFSP_07	~	±4.0	Flange, West Elevation	Horizontal Def.	W
9	SP9	12	±1.0	On the wall web	Vertical Def.	W	24	HFSP_08	~	±10.0	Flange, West Elevation	Horizontal Def.	W
10	SP10	12	±1.0	On the wall web	Vertical Def.	W	25	HFSP_09	~	±10.0	Flange, West Elevation	Horizontal Def.	W
11	SP11	40	±0.5	On the wall web	Vertical Def.	W	26	HFSP_10	~	±15.0	Flange, West Elevation	Horizontal Def.	W
12	SP12	80	±0.5	On the wall web	Vertical Def.	W	27	HFSP_11	~	±15.0	Flange, West Elevation	Horizontal Def.	W
13	SP13	5.4375	±1.0	Top of the foundation to the wall flange	Vertical Def.	E	28	HWSP_12	~	±15.0	South Web, West Elevation	Horizontal Def.	W
14	SP14	5.4375	±1.0	Top of the foundation to the wall flange	Vertical Def.	W	29	HSP_13	~	±0.5	Strong floor to Found. (slippage check)	Horizontal Slip	E
15	SP15	5.4375	±1.0	Top of the foundation to the wall flange	Vertical Def.	E	30	HSP_14	~	±0.5	Strong floor to Found. (slippage check)	Horizontal Slip	E

UNIVERSITY AT BUFFALO		
206 KETTER HALL BUFFALO, NY, 14226		
Title: CPF#06-16: CF-CPSW UB TEST SETUP CAD		
Drawing:		
Page: 29of32	DATE: 5/15/2018	STATUS: For Mnfctng
	BY: Hadi Kenarangi	REV:



UNIVERSITY AT BUFFALO		
206 KETTER HALL BUFFALO, NY, 14226		
Title: CPF#06-16: CF-CPSW UB TEST SETUP CAD		
Drawing:		
Page: 306/32	DATE: 5/15/2018	STATUS: For Mnfctrng
	BY: Hadi Kenarangi	REV:

Table 4. Krypton LEDs placement details				
No.	Label	Location*, in	Attached to	Elevation
1	LED_01	(27,0,2 7/16)	Web	N
2	LED_02	(27,0,5 7/16)	Web	N
3	LED_03	(27,0,8 7/16)	Web	N
4	LED_04	(24,0,2 7/16)	Web	N
5	LED_05	(24,0,5 7/16)	Web	N
6	LED_06	(24,0,8 7/16)	Web	N
7	LED_07	(21,0,2 7/16)	Web	N
8	LED_08	(21,0,5 7/16)	Web	N
9	LED_09	(21,0,8 7/16)	Web	N
10	LED_10	(18,0,2 7/16)	Web	N
11	LED_11	(18,0,5 7/16)	Web	N
12	LED_12	(18,0,8 7/16)	Web	N
13	LED_13	(15,0,2 7/16)	Web	N
14	LED_14	(15,0,5 7/16)	Web	N
15	LED_15	(15,0,8 7/16)	Web	N
16	LED_16	(0,18 3/4,2 7/16)	Flange	E
17	LED_17	(0,18 3/4,5 7/16)	Flange	E
18	LED_18	(0,18 3/4,8 7/16)	Flange	E
19	LED_19	(0,24 3/4,2 7/16)	Flange	E
20	LED_20	(0,24 3/4,5 7/16)	Flange	E
21	LED_21	(0,24 3/4,8 7/16)	Flange	E
22	LED_22	(0,30 3/4,2 7/16)	Flange	E
23	LED_23	(0,30 3/4,5 7/16)	Flange	E
24	LED_24	(0,30 3/4,8 7/16)	Flange	E
25	LED_25	(0,36 3/4,2 7/16)	Flange	E
26	LED_26	(0,36 3/4,5 7/16)	Flange	E
27	LED_27	(0,36 3/4,8 7/16)	Flange	E
28	LED_28	(0,42 3/4,2 7/16)	Flange	E
29	LED_29	(0,42 3/4,5 7/16)	Flange	E
30	LED_30	(0,42 3/4,8 7/16)	Flange	E
31	LED_31	(0,45 3/4,2 7/16)	Flange	E
32	LED_32	(0,45 3/4,8 7/16)	Flange	E
33	LED_33	(0,48 3/4,2 7/16)	Flange	E
34	LED_34	(0,48 3/4,5 7/16)	Flange	E
35	LED_35	(0,48 3/4,8 7/16)	Flange	E

* From the defined origin on the foundation (X,Y,Z).

UNIVERSITY AT BUFFALO		
205 KETTER HALL BUFFALO, NY, 14226		
Title: CFF#06-16: CF-CPSW UB TEST SETUP CAD		
Drawing:		
Page: 31 of 32	DATE: 5/15/2018	STATUS: For Mofcmrg
	BY: Hadi Kinarangi	REV:

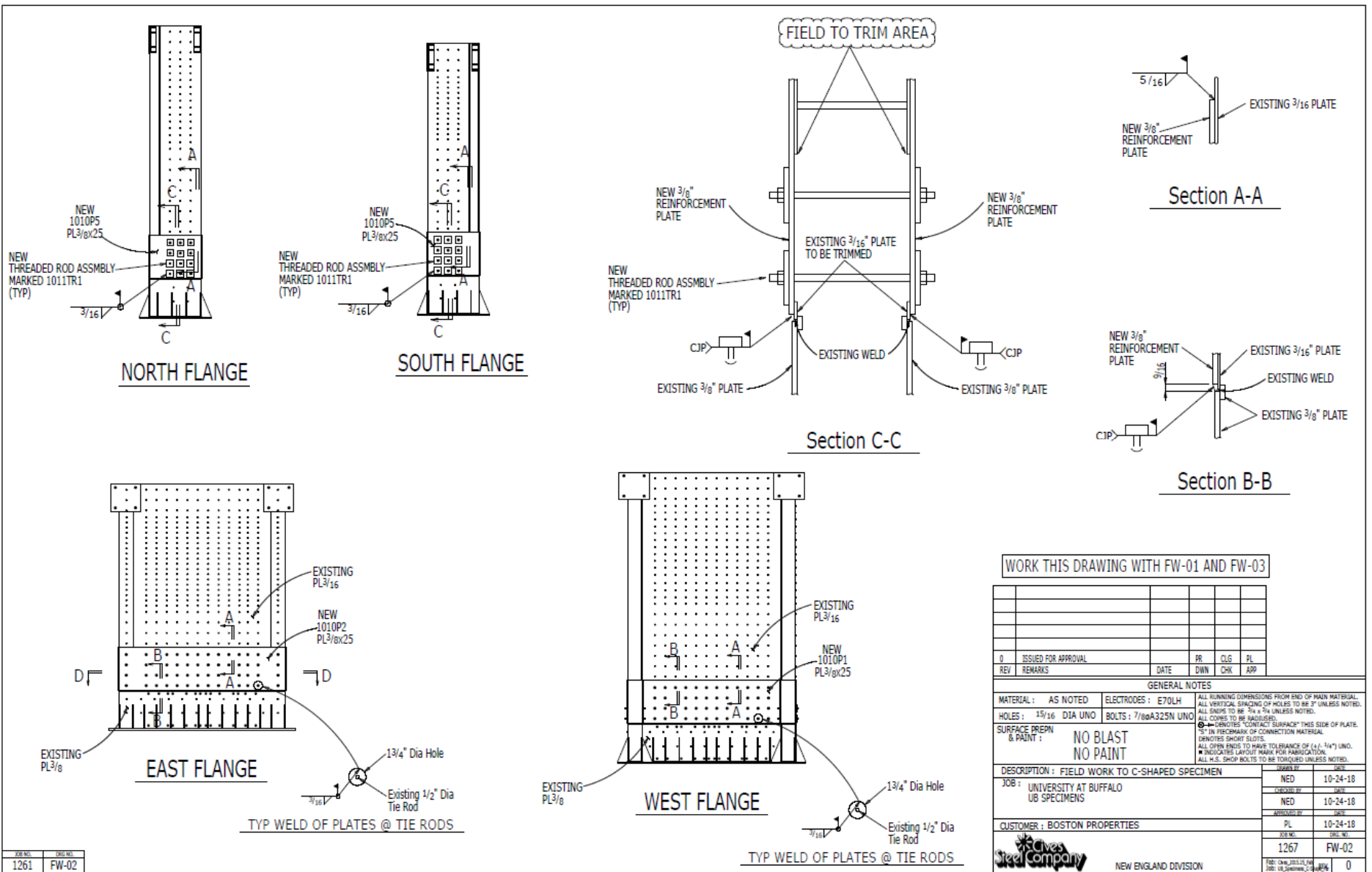
APPENDIX E

Drawings of Repaired C-Shaped Wall

This Appendix includes drawings of the repaired wall specimen and the dimensions of the splice (repair) steel plates. These drawings were produced by Cives Steel Company, but have been modified by the authors as indicated below to reflect the final as-built repair implementation:

- Missing additional square washers and threaded bars in the 3rd and 4th rows of the webs were added to the original drawing.
- The fillet weld size at the top of the splice plate was changed to $5/16in.$ instead of $3/16in.$
- The number of tie bars were changed to 24 instead of 12.

Furthermore, even though it is not shown in the drawings, the bottom of the splice plates were beveled to facilitate their welding to the thicker wall plate in the footing.



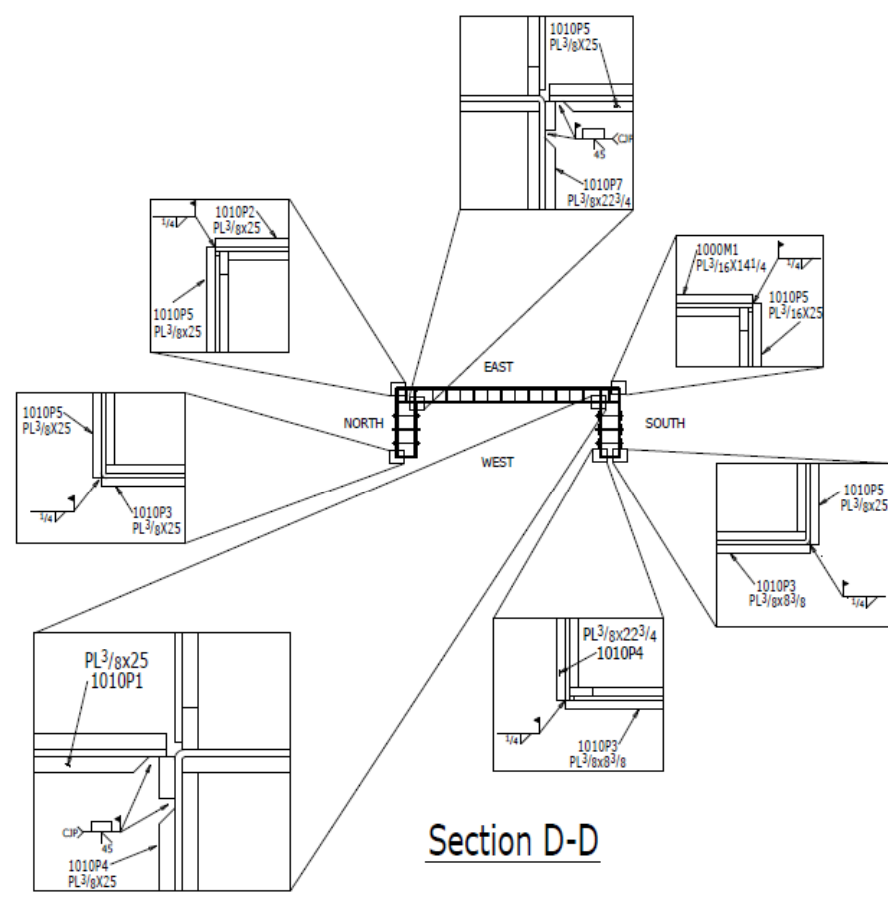
WORK THIS DRAWING WITH FW-01 AND FW-03

REV	ISSUED FOR APPROVAL	DATE	PR	CLG	PL
0	ISSUED FOR APPROVAL				
1	REVISION				

GENERAL NOTES	
MATERIAL: AS NOTED	ELECTRODES: E70LH
HOLES: 15/16 DIA UNO	BOLTS: 7/8x3/25N UNO
SURFACE PREP & PAINT: NO BLAST NO PAINT	
<small> ALL RUNNING DIMENSIONS FROM END OF MAIN MATERIAL. ALL VERTICAL SPACING OF HOLES TO BE 2" UNLESS NOTED. ALL SHIMS TO BE 3/4" x 3/4" UNLESS NOTED. ALL CORNERS TO BE RADIUS. (C) INDICATES CONTACT SURFACE THIS SIDE OF PLATE. * IN PISCENARK OF CONNECTION MATERIAL. DIMENSIONS SHORT SLITS. ALL OPEN ENDS TO HAVE TOLERANCE OF (1/4" - 1/4") UNO. * INDICATES LAYOUT MARK FOR FABRICATION. ALL U.S. SHOP BOLTS TO BE TORQUED UNLESS NOTED. </small>	
DESCRIPTION: FIELD WORK TO C-SHAPED SPECIMEN	ISSUED BY: NED DATE: 10-24-18
JOB: UNIVERSITY AT BUFFALO UB SPECIMENS	DESIGNED BY: NED DATE: 10-24-18
CUSTOMER: BOSTON PROPERTIES	APPROVED BY: PL DATE: 10-24-18
	DATE: 1267 DATE: FW-02
	FOR: CHS, LLC, 11/14/18 JOB: UB, SPECIMEN, C-1, 11/14/18 0

DWG NO.	REV NO.
1261	FW-02

A B C D E F G H I J K L M N P Q R S T U V W X Y Z AA AB AC AD AE AF AG AH AI AJ AK AL AM AN AO AP



Section D-D

ISSUED FOR APPROVAL	04/23/2018	NE	CL	PL
REV	REVISIONS	DATE	BY	APP

GENERAL NOTES	
MATERIAL : AS NOTED	ELECTRODES : E70LH
HOLES : 15/16" DIA UNO	BOLTS : 7/8x3/25M UNO
SURFACE PREP & PAINT :	NO BLAST NO PAINT

DESCRIPTION : DETAILS	DATE	
	BY	DATE
JOB : UNIVERSITY AT BUFFALO UB SPECIMENS	NE	10-24-18
CUSTOMER : BOSTON PROPERTIES	PL	10-24-18

1267	FW-03	0
------	-------	---

1267	FW-03
------	-------

WORK THIS DRAWING WITH FW-01 AND FW-02



NEW ENGLAND DIVISION

E.1 Repaired C-Shaped Specimen: Instrumentation Plan

Instrumentation Plan of Repaired C-Shaped Wall This Appendix B includes the instrumentation plans for the strain gauges, and string and linear potentiometers for the repaired wall specimen.

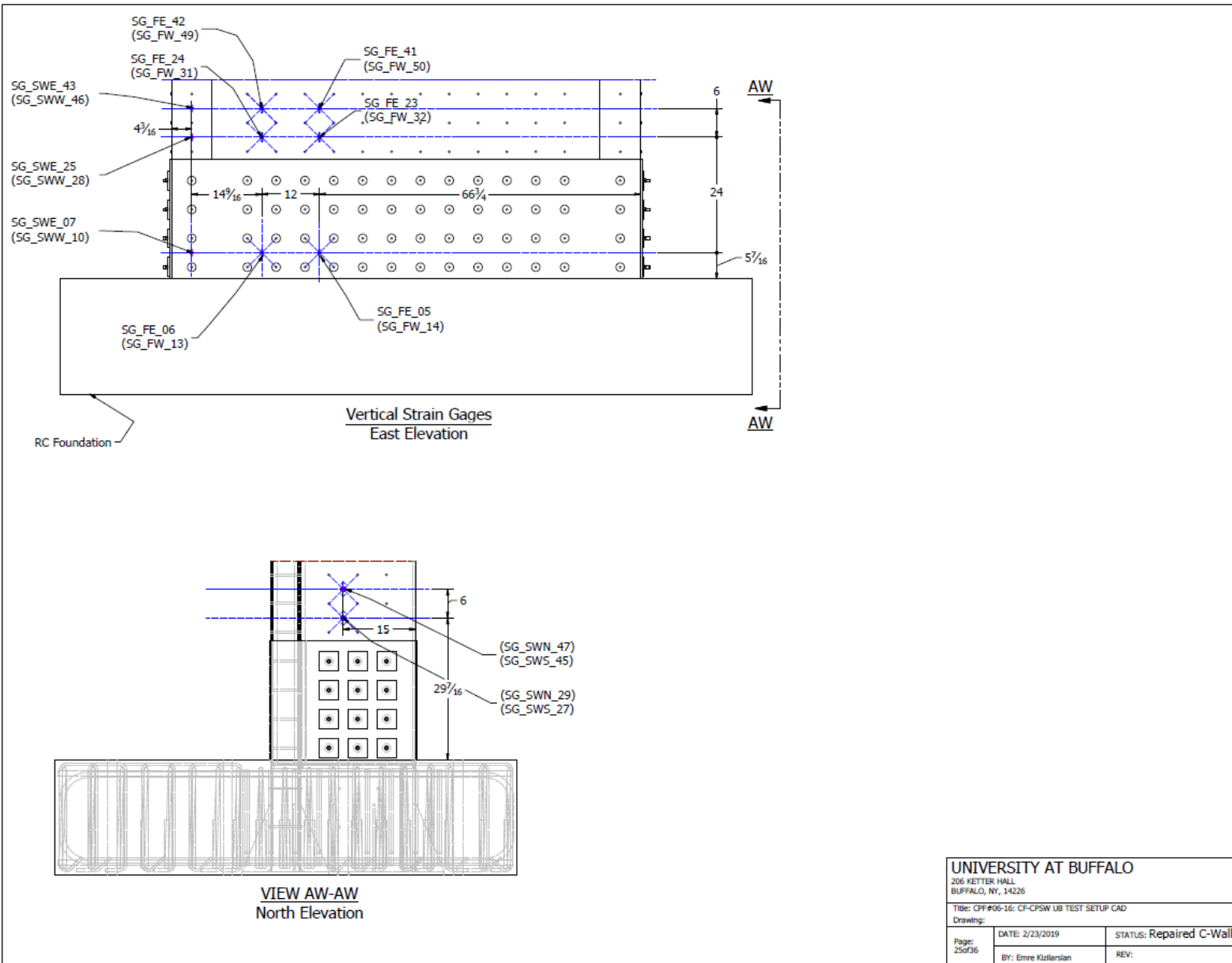
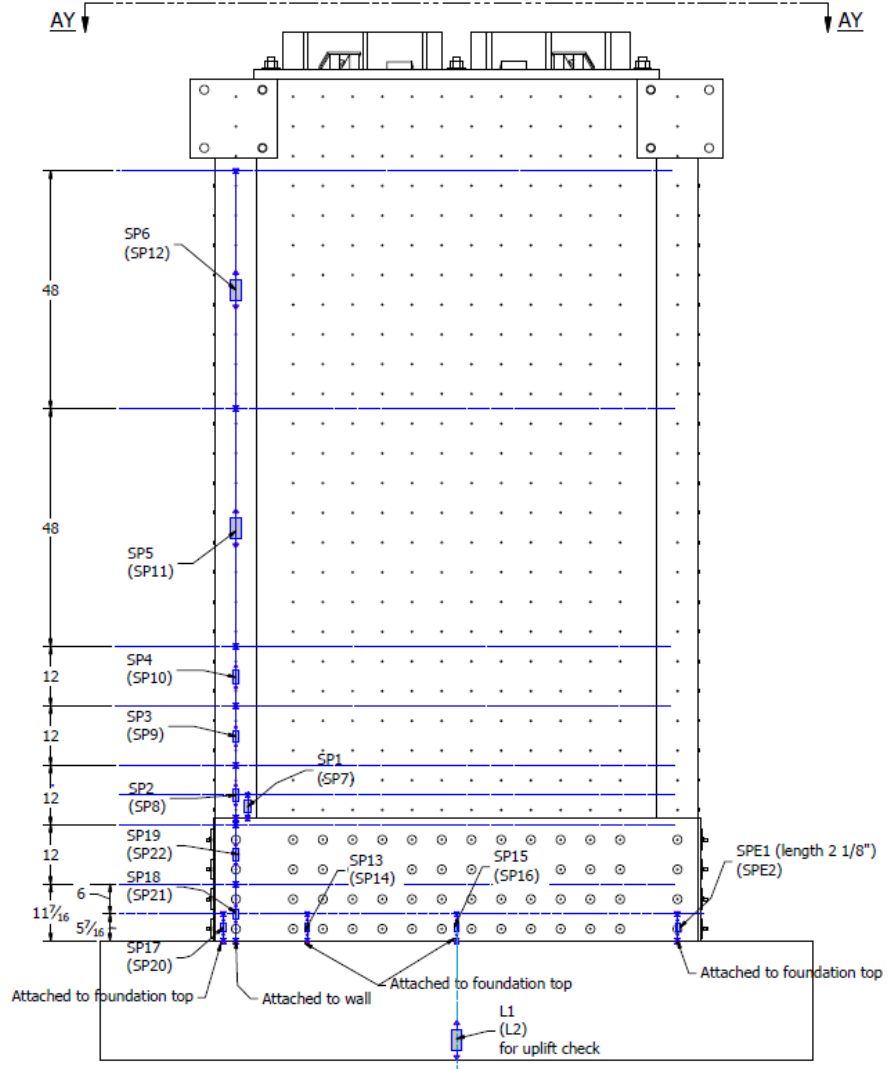
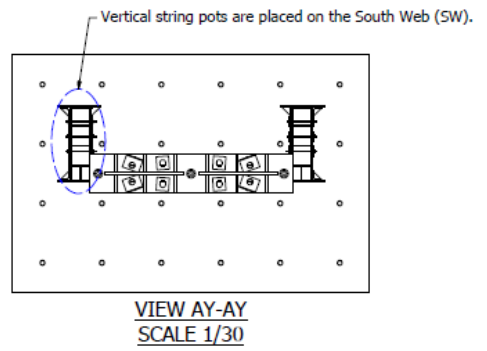


Table 1. Strain Gauge List					
No.	Label	Location	Orientation	Elevation	Distance, in
1	SG_FE_06	FE	Vert.	East	5.4375
2	SG_FW_13	FW	Vert.	West	5.4375
3	SG_SWE_07	SWE	Vert.	East	5.4375
4	SG_SWW_10	SWW	Vert.	West	5.4375
5	SG_FE_05	FE	Vert.	East	5.4375
6	SG_FW_14	FW	Vert.	West	5.4375
7	SG_SWE_25	SWE	Vert.	East	29.4375
8	SG_SWW_28	SWW	Vert.	West	29.4375
9	SG_FE_24	FE	Vert.	East	29.4375
10	SG_FW_31	FW	Vert.	West	29.4375
11	SG_FE_23	FE	Vert.	East	29.4375
12	SG_FW_32	FW	Vert.	West	29.4375
13	SG_SWN_29	SWN	Vert.	North	29.4375
14	SG_SWS_27	SWS	Vert.	South	29.4375
15	SG_SWE_43	SWE	Vert.	East	35.4375
16	SG_SWW_46	SWW	Vert.	West	35.4375
17	SG_FE_42	FE	Vert.	East	35.4375
18	SG_FW_49	FW	Vert.	West	35.4375
19	SG_FE_41	FE	Vert.	East	35.4375
20	SG_FW_50	FW	Vert.	West	35.4375
21	SG_SWN_47	SWN	Vert.	North	35.4375
22	SG_SWS_45	SWS	Vert.	South	35.4375

UNIVERSITY AT BUFFALO		
206 KETTER HALL BUFFALO, NY, 14226		
Title: CFF#06-16: CF-CPSW UB TEST SETUP CAD		
Drawing:		
Page: 26of36	DATE: 2/23/2019	STATUS: Repaired C-Wall
	BY: Emre Kizilaslan	REV:

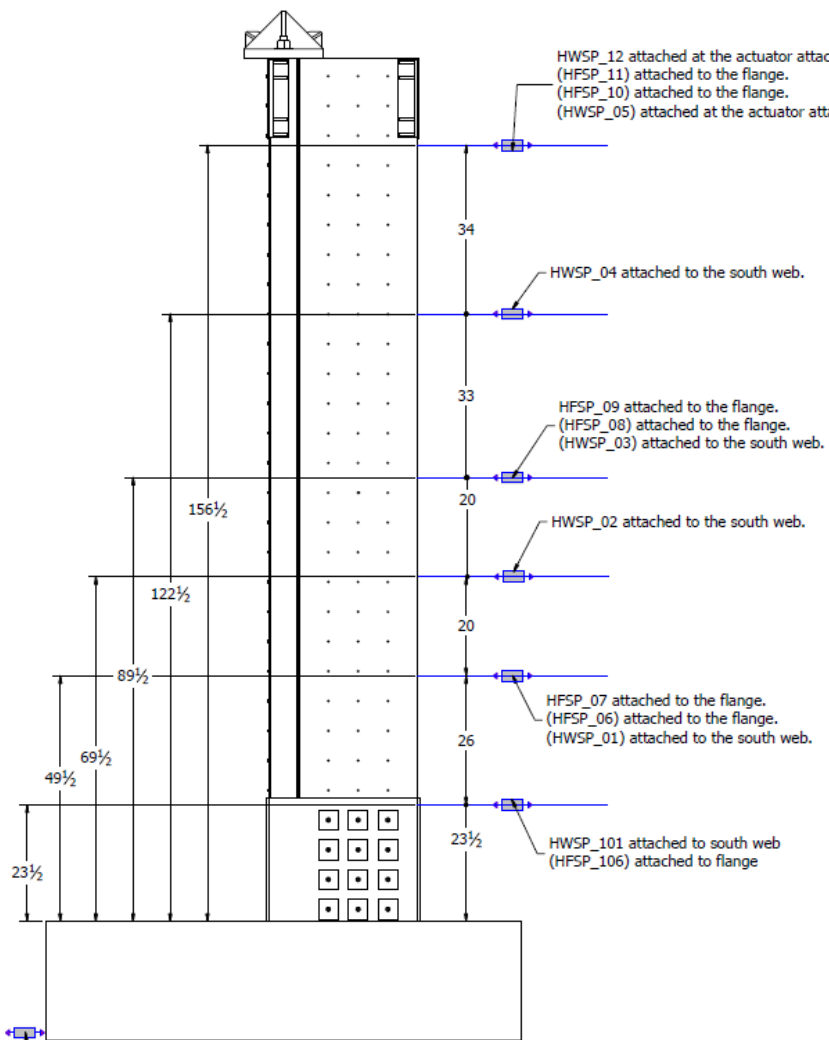


Vertical String Pots
East Elevation



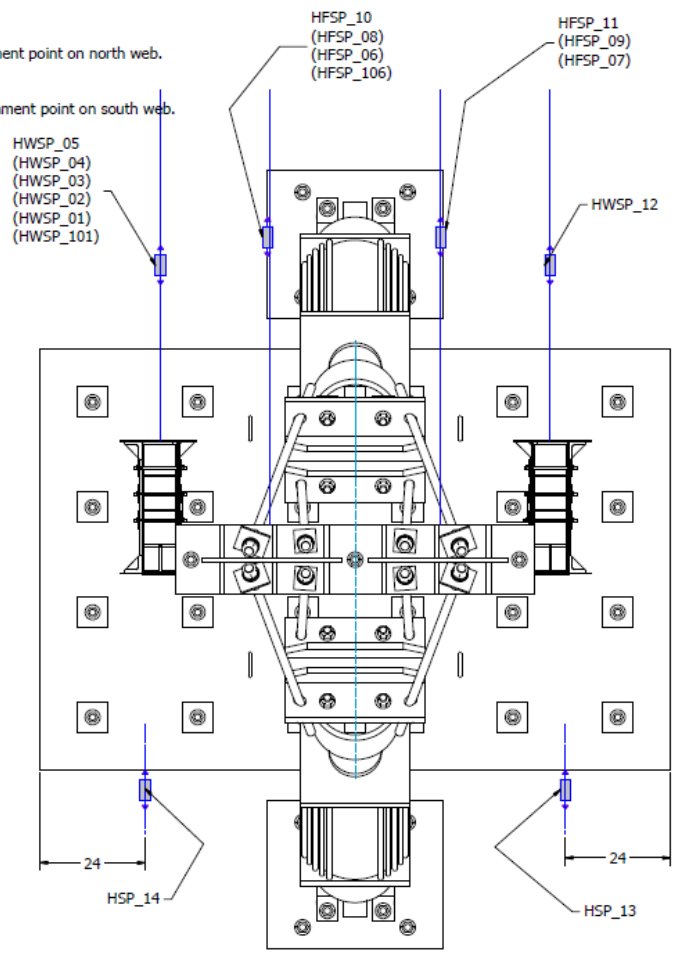
NOTE:
String pots and LVDTs in paranthesis are to be placed on the opposite elevation.

UNIVERSITY AT BUFFALO		
206 KETTER HALL BUFFALO, NY, 14226		
Title: CFF#06-16: CF-CPSW UB TEST SETUP CAD		
Drawing:		
Page: 27of36	DATE: 2/23/2019	STATUS: Repaired C-Wall
	BY: Emre Kizilarslan	REV:



Horizontal String Pots
North Elevation

HSP_13 See plan view.
(HSP_14) See plan view.
Check for foundation slippage.



Plan View

UNIVERSITY AT BUFFALO		
206 KETTER HALL BUFFALO, NY, 14226		
Title: CFF#06-16: CF-CPSW UB TEST SETUP CAD		
Drawing:		
Page: 28of36	DATE: 2/23/2019	STATUS: Repaired C-Wall
BY: Emre Kizilarslan		REV:

No.	Label	Location	Orientation	Elevation	Length, in
1	L1	Attached to the footing	Vertical Def.	East	2 ± 1
2	L2	Attached to the footing	Vertical Def.	West	2 ± 1
3	SPE1	Attached to the North web	Vertical Def.	East	2 ± 1
4	SPE2	Attached to the North web	Vertical Def.	West	2 ± 1

No.	Label	Location	Orientation	Elevation	Length, in
1	SP1	On existing steel plate above repaired part	Vertical Def.	East	4.6875
2	SP2	On existing steel plate above repaired part	Vertical Def.	East	9.6875
3	SP3	On existing steel plate above repaired part	Vertical Def.	East	12
4	SP4	On existing steel plate above repaired part	Vertical Def.	East	12
5	SP5	On existing steel plate above repaired part	Vertical Def.	East	48
6	SP6	On existing steel plate above repaired part	Vertical Def.	East	48
7	SP7	On existing steel plate above repaired part	Vertical Def.	West	4.6875
8	SP8	On existing steel plate above repaired part	Vertical Def.	West	9.6875
9	SP9	On existing steel plate above repaired part	Vertical Def.	West	12
10	SP10	On existing steel plate above repaired part	Vertical Def.	West	12
11	SP11	On existing steel plate above repaired part	Vertical Def.	West	48
12	SP12	On existing steel plate above repaired part	Vertical Def.	West	48
13	SP13	On repaired steel plate	Vertical Def.	East	5.4375
14	SP14	On repaired steel plate	Vertical Def.	West	5.4375
15	SP15	On repaired steel plate	Vertical Def.	East	5.4375
16	SP16	On repaired steel plate	Vertical Def.	West	5.4375
17	SP17	On repaired steel plate	Vertical Def.	East	5.4375
18	SP18	On repaired steel plate	Vertical Def.	East	11.4375
19	SP19	On repaired steel plate	Vertical Def.	East	12
20	SP20	On repaired steel plate	Vertical Def.	West	5.4375
21	SP21	On repaired steel plate	Vertical Def.	West	11.4375
22	SP22	On repaired steel plate	Vertical Def.	West	12

No.	Label	Location	Orientation	Elevation	Length, in	Distance from top of footing, in
1	HWSP_101	Attached to the South web	Horizontal Def.	West	20 ± 1	23.5
2	HWSP_01	Attached to the South web	Horizontal Def.	West	20 ± 1	49.5
3	HWSP_02	Attached to the South web	Horizontal Def.	West	20 ± 1	69.5
4	HWSP_03	Attached to the South web	Horizontal Def.	West	20 ± 1	89.5
5	HWSP_04	Attached to the South web	Horizontal Def.	West	20 ± 1	122.5
6	HWSP_05	Attached to the South web	Horizontal Def.	West	20 ± 1	156.5
7	HFSP_106	Attached to the West Flange	Horizontal Def.	West	20 ± 1	23.5
8	HFSP_06	Attached to the West Flange	Horizontal Def.	West	20 ± 1	49.5
9	HFSP_07	Attached to the West Flange	Horizontal Def.	West	20 ± 1	49.5
10	HFSP_08	Attached to the West Flange	Horizontal Def.	West	20 ± 1	89.5
11	HFSP_09	Attached to the West Flange	Horizontal Def.	West	20 ± 1	89.5
12	HFSP_10	Attached to the West Flange	Horizontal Def.	West	20 ± 1	156.5
13	HFSP_11	Attached to the West Flange	Horizontal Def.	West	20 ± 1	156.5
14	HWSP_12	Attached to the North Web	Horizontal Def.	West	20 ± 1	156.5
13	HSP_13	Attached to the footing	Horizontal Def.	East	20 ± 1	3 (from strong floor)
14	HSP_14	Attached to the footing	Horizontal Def.	East	20 ± 1	3 (from strong floor)

UNIVERSITY AT BUFFALO		
206 KETTER HALL BUFFALO, NY, 14226		
Title: OPF #06-16: CF-CPSW UB TEST SETUP CAD		
Drawing:		
Page: 29of36	DATE: 2/23/2019	STATUS: Repaired C-Wall
	BY: Emre Kizilarslan	REV: